

Marc J. M. Abadie · Mariana Pinteala ·
Alexandru Rotaru *Editors*

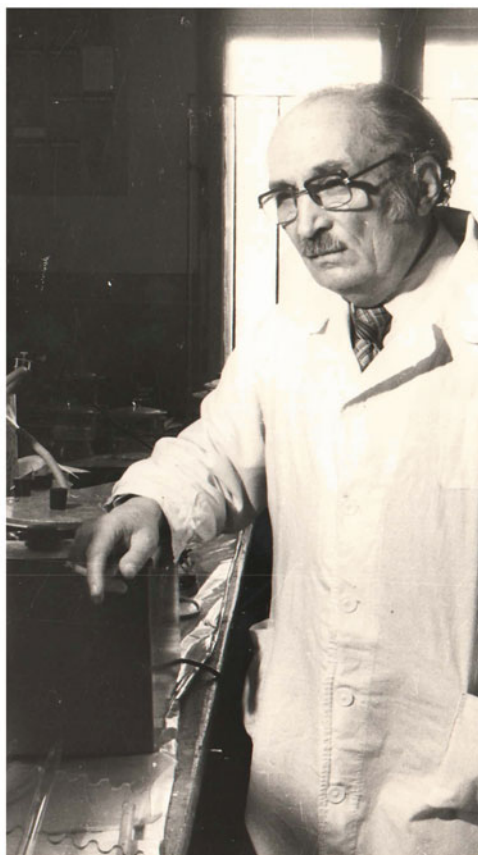
New Trends in Macromolecular and Supramolecular Chemistry for Biological Applications

 Springer

New Trends in Macromolecular and Supramolecular Chemistry for Biological Applications



"Petru Poni"
Institute of Macromolecular Chemistry



*The book is dedicated to the memory of Acad. Prof. Dr. Eng. Cristofor I. Simionescu (1920–2020)
and to the commemorative celebration of the century of his birth.*

A Man Ahead his Time, A Great Spirit & Visionary

Marc J. M. Abadie · Mariana Pinteala ·
Alexandru Rotaru
Editors

New Trends in Macromolecular and Supramolecular Chemistry for Biological Applications





This Book is part of a project that has received funding
from the **European Union's Horizon 2020 research
and innovation programme** under grant agreement
N°667387

 Springer

Editors

Marc J. M. Abadie
SupraChem Lab
“Petru Poni” Institute of Macromolecular
Chemistry
Iasi, Romania

Mariana Pinteala 
SupraChem Lab
“Petru Poni” Institute of Macromolecular
Chemistry
Iasi, Romania

Alexandru Rotaru 
SupraChem Lab
“Petru Poni” Institute of Macromolecular
Chemistry
Iasi, Romania

ISBN 978-3-030-57455-0 ISBN 978-3-030-57456-7 (eBook)
<https://doi.org/10.1007/978-3-030-57456-7>

© The Editor(s) (if applicable) and The Author(s), under exclusive license
to Springer Nature Switzerland AG 2021

This work is subject to copyright. All rights are solely and exclusively licensed by the Publisher, whether the whole or part of the material is concerned, specifically the rights of translation, reprinting, reuse of illustrations, recitation, broadcasting, reproduction on microfilms or in any other physical way, and transmission or information storage and retrieval, electronic adaptation, computer software, or by similar or dissimilar methodology now known or hereafter developed.

The use of general descriptive names, registered names, trademarks, service marks, etc. in this publication does not imply, even in the absence of a specific statement, that such names are exempt from the relevant protective laws and regulations and therefore free for general use.

The publisher, the authors and the editors are safe to assume that the advice and information in this book are believed to be true and accurate at the date of publication. Neither the publisher nor the authors or the editors give a warranty, expressed or implied, with respect to the material contained herein or for any errors or omissions that may have been made. The publisher remains neutral with regard to jurisdictional claims in published maps and institutional affiliations.

This Springer imprint is published by the registered company Springer Nature Switzerland AG
The registered company address is: Gewerbestrasse 11, 6330 Cham, Switzerland

Preface

“Supramolecular” chemistry is the study of weakly interacting assemblies of molecules. It has many potential applications in medicine as well as in materials science and catalysis. Supramolecular chemistry was very quickly used to simulate cohesion and transport mechanisms in the human body for biomedical and therapeutic purposes. This modern chemistry has the ability to mimic the complex mechanisms at work within the organism in order to better study and understand them and to provide the appropriate treatments for better regeneration of the sick living cell.

We present a series of papers on various subjects concerning medical applications that should have been the subject of an international symposium “New Trends in Macromolecular and Supramolecular Chemistry for Biomedical Applications” to be held in Iasi, Romania, on June 7–8, 2020, and which was postponed to 2022, due to the COVID-19 pandemic.

Moreover, this book is the result of the research undertaken at the SupraChem Lab, *Laboratory of Supramolecular Chemistry for Adaptive Delivery Systems*, led by **Dr. Mariana Pinteala** and managed by **Dr. Teodora Rusu** in ICM “Petru Poni,” Iasi (RO). SupraChem Lab project has benefited for the financial support from the H2020 WIDESPREAD 2-2014: ERA Chairs Project no 667387: SupraChem Lab Laboratory of Supramolecular Chemistry for Adaptive Delivery Systems ERA Chair initiative.

This 5-year programme (2015-2020) has enabled some thirty researchers to address the design, synthesis, and characterization of supramolecular entities for biomedical applications such as gene therapy, mechanisms of transport through tissues, supramolecular non-viral vector, DNA transfection, hydrogels for drug delivery, tissue engineering, stimuli-responsive polymers, antimicrobial agents, and markers for diagnostics.

We have brought in scientific personalities who have been willing to contribute their experience and expertise but also to help our young, dynamic, and competent team. Some of these extraordinary personalities are: Prof. Nadine Millot (ICB, University of Bourgogne, Dijon–France), Prof. Luisa De Cola (ISIS Institut des

Sciences et d'Ingenierie Supramoleculaires, University Louis Pasteur, Strasbourg—France), Dr. Sylvia Wagner (Fraunhofer-Institut für Biomedizinische Technik IBMT, Sulzbach—Germany), Prof. Claudiu T. Supuran (University of Florence—Italy), Prof. Aatto Laaksonen (Institutionen för Material, University of Stockholm—Sweden), Prof. Ulrich Scherf (Bergische Universität Wuppertal, Wuppertal—Germany), Dr. Marc Baaden (Laboratoire de Biochimie Théorique, UPR 9080 CNRS, Institut de Biologie Physico-Chimique, Paris—France), Prof. Christoph Janiak (Heinrich-Heine-Universität Düsseldorf HHU, Düsseldorf—Germany), Prof. Simon Webb (University of Manchester, Manchester—UK), Prof. Sinda Lepetre-Mouelhi (Galien Institute, Paris-Sud U., Paris 11, Orsay—France), Prof. Kurt V. Gothelf (University of Aarhus, Aarhus—Denmark), Prof. Stephane Vincent (University of Namur, Namur—Belgium), and Prof. Ulrich S. Schubert (University of Jena, Jena—Germany).

We would like to thank all the contributors who made this book a reality.

June 2020

Marc J. M. Abadie
ERA Chair



SupraChem Lab—Laboratory of Supramolecular Chemistry for Adaptive Delivery Systems—ERA Chair initiative

2020 marks the end of the implementation period of the Horizon 2020 SupraChem Lab ERA Chair initiative. In just five years, the project has reached its main objective—the creation of a group of young researchers in the field of supramolecular chemistry with applications in nanomedicine in the Macromolecular Chemistry Institute Petru Poni, Iasi, Romania. Financed by the European Union under the ERA Chair Initiative Horizon 2020 H2020-WIDESPREAD-2014-2 CONTRACT NO 667387, the project has been a tremendous success under the attentive guidance of **Prof. Emeritus Dr. Marc JM Abadie University of Montpellier.**

This initiative had benefited from the top infrastructure of the newly built IntelCentre (Centre of Advanced Research in Bionanoconjugates and Biopolymers) —a 5 M Euro Structural Funds investment. The **Project Coordinator, Dr. Mariana Pinteala, together with the Project Manager, Dr. Teodora Rusu,** managed to provide the newly created team with all the necessary conditions to conduct high-level research.

During this fantastic period, 28 young researchers had been given the opportunity to receive a head start in applying the insights of supramolecular chemistry to biomedical applications such as gene therapy, mechanisms of transport through tissues, supramolecular non-viral vector, DNA transfection, hydrogels for drug delivery, tissue engineering, stimuli responsive polymers, anti-microbial agents and markers for diagnostics.

So, let us put SupraChem Lab under a microscope and see what it has accomplished throughout these wonderful five years:



73 articles published in scientific peer review journals
3 book chapters



28 young researchers
4 training & team building sessions
18 trainings organized within ICMP
12 participations in trainings organized by partner institutions
21 internships abroad
8 round table events and **5 events**



145 Participations - national and international **conferences**
19 regional networking events
21 international meetings participation
9 Meetings organised with the support of SupraChem Lab project
11 Meetings (non-scientific) organised within the SupraChem Lab project
52 Participation in meeting (non-scientific) organised by other institutions



10 PHD thesis (6 completed and defended)

Looking forward to the future

SupraChem Lab has made a solid start in its five years of existence, managing to find ways to self-sustain and grow; therefore, we are looking with great confidence forward. Several prestigious names from both scientific and policy-making sectors have been linked to SupraChem Lab. We can mention here Prof. Jean-Marie Lehn, Nobel prize laureate 1987 in Chemistry, and Signe Ratso, Deputy Director-General of the Directorate-General “Research and Innovation” (RTD).

Thus, the networking and connections developed during the project has helped in the creation of scientific ties that in turn lead to winning important research projects (ex. mimicking living matter mechanisms by five-dimensional chemistry, acronym 5D-nanoP project, coordinated by Prof. Aatto Laaksonen, Stockholm University, Sweden, or a PD project: metal-organic frameworks based on fluorinated terphenylic ligands for gas storage and separation, acronym: FluoroMOF, having Prof. Christoph Janiak as a mentor, Düsseldorf University, Germany, etc.), projects that will ensure the sustainability of SupraChem Lab in the future.

There had been a few bumps along the road, the biggest one being the fact that *the Final Conference on “New trends in Macromolecular and Supramolecular Chemistry for Biomedical Applications” had to be postponed to June 2022*, due to the current COVID-19 pandemic. As a response to this situation, the book at hand will provide an overview of the investigations conducted within the SupraChem Lab together with notable research in the field developed by its collaborators outside the project, paving the way towards a fruitful conference in the following year.

Overall, the exploitation of results from this project can lead to the creation of spin-off/start-up, new product, patent, PhD thesis/post, standard, service, societal activity, open/copyleft licenses, further research, policy change, etc. In the long term, our research will help in gene therapy, drug delivery, tissue engineering, antimicrobial agents, and markers for diagnostics.

Olaru Natalia Loana

Contents

Approaches Towards Synthetic Signal Transduction in Phospholipid Bilayers	1
Flavio della Sala, David P. Tilly, and Simon J. Webb	
Measuring Ionic Transport Through Lipid Bilayers	25
Radu Zonda, Sorin-Alexandru Ibanescu, Mihaela Silion, Adina Coroaba, Dragos-Lucian Isac, Marc J. M. Abadie, and Mariana Pinteala	
Stability and Structure of Adaptive Self-organized Supramolecular Artificial Water Channels in Lipid Bilayers	51
A. Hardiagon, S. Murail, L. Huang, M. Barboiu, F. Sterpone, and M. Baaden	
Functional Microporous Polymer Networks: Synthesis and Applications	65
Alex Palma-Cando and Ullrich Scherf	
Mixed-Matrix Membranes	87
Alexander Nuhnen and Christoph Janiak	
A Story on Carbon Dioxide and Its Hydration	115
Claudiu T. Supuran	
Polymeric Carriers for Transporting Nucleic Acids—Contributions to the Field	133
Lilia Clima, Andrei Ioan Dascalu, Bogdan Florin Craciun, and Mariana Pinteala	
Development of Novel Versatile Theranostic Platforms Based on Titanate Nanotubes: Towards Safe Nanocarriers for Biomedical Applications	151
Julien Boudon, Fadoua Sallem, Alexis Loiseau, Lionel Maurizi, Anne-Laure Papa, and Nadine Millot	

A Microbiological Epilogue—Nosocomial Infections	179
Irina Rosca, Elena-Laura Ursu, and Adrian Fifere	
New Enkephalin Nanomedicines for Pain Alleviation, Overcoming the Side Effects of Morphine	191
Sinda Lepetre-Mouelhi, Jiao Feng, and Patrick Couvreur	
Inverse Problems and Hierarchical Multiscale Modelling of Biological Matter	213
Alexander Lyubartsev and Aatto Laaksonen	
Non-viral Vectors and Drug Delivery: In Vitro Assessment	239
Dragos Peptanariu, Marc J. M. Abadie, and Mariana Pinteala	
Biodegradable Nanoparticles for Specific Drug Transport	255
Karin Danz, Hagen von Briesen, and Sylvia Wagner	
Smart Polymeric Materials for Drug Delivery	275
Gheorghe Fundueanu, Sanda Bucatariu, and Marieta Constantin	
Inorganic Nanoparticles as Free Radical Scavengers	295
Adrian Fifere, Ioana-Andreea Turin Moleavin, Ana-Lacramioara Lungoci, Narcisa Laura Marangoci, and Mariana Pinteala	
Supramolecular Guanosine-Quadruplex Hydrogels and Hydrogel Composites for Cell Growth Applications	331
Elena Laura Ursu and Alexandru Rotaru	
Hydrogelation of Chitosan with Monoaldehydes Towards Biomaterials with Tuned Properties	345
Luminita Marin, Daniela Ailincăi, Manuela Maria Iftime, Anda-Mihaela Craciun, Andrei Bejan, Mariana Pinteala, and Marc Jean M. Abadie	
Molecular Dynamics Simulations and <i>in silico</i> Analysis of Supramolecular Self-assembled Structures	357
Corneliu Cojocaru, Andrei Neamtu, Tudor Vasiliu, Dragos Lucian Isac, and Mariana Pinteala	

Approaches Towards Synthetic Signal Transduction in Phospholipid Bilayers



Flavio della Sala, David P. Tilly, and Simon J. Webb

Abstract Synthetic signal transduction is an exciting new research field that applies supramolecular chemistry in a membrane environment to provide insight into the physical processes involved in natural signal transduction and to open new opportunities in synthetic biology, for example the integration of artificial signaling pathways into cells. Although it is still a developing field, we discuss a selection of recent stimuli-responsive supramolecular constructs that, when embedded in the phospholipid bilayer, can mimic aspects of the behavior of different natural signaling proteins, including ligand-gated ion channels, G-protein coupled receptors and receptor tyrosine kinases. The lipid bilayer plays a key part in these biomimetic systems, as this complex anisotropic environment provides challenges both when designing supramolecular systems that function in the bilayer and when analyzing the data they provide. Nonetheless these recent studies have provided key insights into how the bilayer affects binding to, the conformation of, and catalysis by membrane-embedded supramolecular constructs. If successful, these model systems promise to be key components for bottom-up synthetic biology, the creation of artificial cells and devices starting from molecular components.

Keywords Phospholipid bilayers · Vesicles · Supramolecular chemistry · Biomimetic chemistry · Signal transduction

Abbreviations

Aib	α -amino- <i>iso</i> -butyric acid
ATP	adenosine triphosphate
CFTR	cystic fibrosis transmembrane conductance regulator

F. della Sala · D. P. Tilly · S. J. Webb (✉)
School of Chemistry, University of Manchester, Oxford Road, Manchester M13 9PL, UK
e-mail: S.Webb@manchester.ac.uk

Manchester Institute of Biotechnology, University of Manchester,
131 Princess Street, Manchester M1 7DN, UK

DET	diethylenetriamine
DMPC	1,2-dimyristoyl- <i>sn</i> -glycero-3-phosphocholine
DNA	deoxyribonucleic acid
DOPC	1,2-dioleoyl- <i>sn</i> -glycero-3-phosphocholine
DOPE	1,2-dioleoyl- <i>sn</i> -glycero-3-phosphoethanolamine
PPC	1,2-dipalmitoyl- <i>sn</i> -glycero-3-phosphocholine
<i>E/M</i>	excimer/monomer
EDTA	ethylenediaminetetraacetic acid
EGFR	epidermal growth factor receptor
FRET	Förster resonance energy transfer
GABA	γ -aminobutyric acid
GDP	guanosine diphosphate
GPCR	G-protein coupled receptor
GTP	guanosine triphosphate
<i>h.e.</i>	helical excess
HPTS	8-hydroxypyrene-1,3,6-trisulfonic acid
HRE	hormone responsive element
IR	insulin receptor
nAChR	nicotinic acetylcholine receptor
NMR	nuclear magnetic resonance
PA	2-phenethylamine
PBC	planar bilayer conductance
pLGIC	pentameric ligand-gated ion channel
RTK	receptor tyrosine kinase
SHR	steroid hormone receptor
ss-NMR	solid state nuclear magnetic resonance

1 Introduction

The cell membrane is a semipermeable physical barrier that defines the cell, giving it a compartmentalized network of chemical reactions that do not freely interact with constituents of the extracellular environment. The major component of the cell membrane is a phospholipid bilayer, a noncovalent fluid assembly that is typically 3 to 4 nm thick and largely impermeable to hydrophilic molecules and small inorganic ions. This impermeability to ions gives the membrane a key role in energy storage, through the maintenance of transmembrane concentration gradients. The membrane is also home to a large number of biomolecules including proteins, carbohydrates and steroids, which have specific functions such as regulating interactions with the extracellular environment, biocatalysis and using concentration gradients to drive biosynthesis (Luckey 2008).

This barrier has to have controllable permeability, however, to allow specific molecules to enter and exit the cell according to the demands of cellular metabolism.

Some of the molecules that translocate through the bilayer act as messengers, and the communication of information across the cell membrane is essential to coordinate biological events with other cells and adapt to changes in the external environment. Nature has developed many sophisticated mechanisms to sense, transduce and process external signals, before converting them into complex intracellular responses. The translocation of messenger molecules across the membrane can occur by diffusion through the hydrophobic core of the bilayer (alone or when complexed to carrier proteins) or by passage through a hydrophilic channel within a transmembrane protein (either passive or active transport). Alternatively, the messenger molecules may regulate the opening/closing (“gating”) of a channel protein to allow the transit of other molecules.

Instead of physical mass transfer, the binding of messenger molecules to receptors at the outer surface of the cells can initiate the transfer of information via transmembrane domains. Binding to a primary messenger can alter the conformation, orientation or position of the transmembrane domains, and these global changes are necessarily transmitted to the far side of the bilayer. This mechanism also allows for signal amplification, as binding to the primary messenger molecule outside the cell can initiate the catalytic production of a large number of secondary messengers inside the cell. Despite being some of the most intensely studied protein families in the proteome, the complexity of signal transduction processes involving large proteins within a self-assembled lipid matrix makes the unambiguous interpretation of biophysical data challenging.

Self-assembled artificial vesicles doped with synthetic molecules are widely used to construct simplified systems that mimic aspects of the behavior of cell membranes. Phospholipid vesicles reproduce some basic features of the cell membrane, an internal aqueous compartment surrounded by a semipermeable barrier, yet are less complex and simple to fabricate. Despite their apparent simplicity, the physical properties of these self-assembled soft materials, such as anisotropy, chirality, low fluidity, low permeability and variable thickness, make bilayers more complex environments than isotropic solvent. Several of these properties depend on bilayer composition and temperature, and can determine the behavior of any synthetic molecules within the bilayers (Pintre and Webb 2013). Nonetheless since the receipt and relay of messages is fundamental to the function of living organisms, a detailed understanding of the physical processes that produce these features is a key objective in biomimetic chemistry.

In this review we discuss a selection of recently published supramolecular approaches to mimicking signal transduction processes, with a focus on systems that are controlled by external stimuli, such as messenger molecules or light. There are other recent reviews both in this area (Bekus and Schrader 2020; Vanuytsel et al. 2019) and in other related contexts, such as synthetic ion channels (Zheng et al. 2021) and supramolecular chemistry in biomembranes (Webb 2013; Barba-Bon et al. 2020), which can provide useful alternative narratives. These recent reviews reflect rapidly growing interest in this area, an area that is inspired by the complexity and elegance of biological signaling processes.

2 Natural Transmembrane Signaling Mechanisms

2.1 Protein Ion Channels

Natural ion channels regulate many key functions, such as the transmission of electric signals across the membranes of neurons and other excitable cells (Unwin 1989). Other important examples include the cystic fibrosis transmembrane conductance regulator (CFTR), which controls secretion and absorption in different types of epithelial tissue (Saint-Criq and Gray 2017). It is not surprising that unregulated function of ion channels gives rise to a series of diseases collectively known as channelopathies (e.g. epilepsy, myotonia, ataxia cardiac, arrhythmia and cystic fibrosis) (Ptáček 1997; Gadsby et al. 2006). Many protein ion channels have a relatively similar structure, with homologous domains within the membrane that delineate a central pore for the channel. Passage through these protein ion channels is usually “gated”, *i.e.* the channels are opened and closed by specific stimuli. Depending on the gating mechanism, natural ion channels can be classified as being voltage-gated, ligand-gated, light-gated or mechano-sensitive. Such gating is usually mediated by a conformational change rather than a change in the extent of self-association of multisubunit channels (Fig. 1a).

Voltage-gated ion channels form a large family whose gating activity depends on changes in the potential difference across the membrane, and regulate the flux of Na^+ , Ca^{2+} and K^+ across the cellular membrane. The structure of voltage-gated K^+ ion channels has been elucidated in recent years, (Gulbis et al. 1999; Sands et al. 2005) and a proposed mode of action described. The canonical model describes voltage-gated K^+ channels as transmembrane pores composed of four identical subunits around a central ion conduction pathway. Each subunit consists of six α -helices (S1–S6), with helices S5–S6 in the pore domain and transmembrane helices S1–S4 forming the voltage-sensing domain. The arginine-rich S4 helices are sensitive to membrane (de)polarization, and are proposed to slide or screw in the direction of the extracellular surface with subsequent relocation of the arginine residues to externally

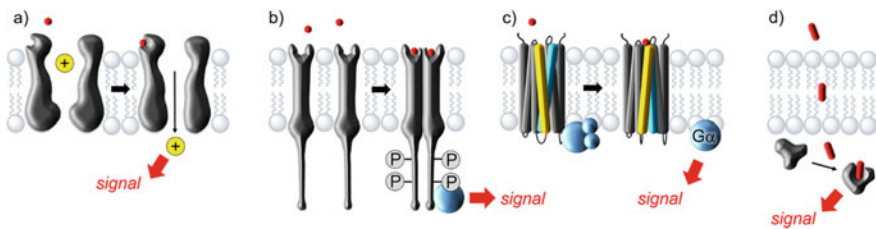


Fig. 1 Schematic representations of **a** Ligand binding to an ion channel to allow passage of cations. **b** Ligand induced dimerization of receptor tyrosine kinases (RTKs). P = phosphate. **c** Ligand induced change in the conformational states of a G-protein coupled receptor (GPCR). **d** Ligand (steroid) translocation through a membrane and binding to a steroid hormone receptor (SHR)

facing pockets. This overall conformational change results in channel opening and the diffusion of K^+ ions down a concentration gradient.

Ligand-gated ion channels include cystic fibrosis transmembrane conductance regulator (CFTR, ATP-gated) and nicotinic acetylcholine receptors (nAChRs, acetylcholine-gated). The latter belongs to the pentameric ligand-gated ion channel (pLGICs) class, which are involved in processes where a neurotransmitter released by synapses induces the transmission of action potential between neurons or between a neuron and a muscle (Herrington and Arey 2014). Channels binding γ -aminobutyric acid (GABA), serotonin, glycine and glutamate also belong to this class of gated ion channels. The general structure comprises five subunits that form a pentameric channel. Each subunit contains a large extracellular domain with a characteristic disulfide bridge formed by a pair of cysteine residues. The structure of glutamate receptors is slightly different, with a large extracellular domain, an extracellular ligand binding domain and a characteristic transmembrane domain formed by two helical subunits that open/close the channels in a 'clamshell' fashion (Zhu et al. 2016).

Light-gated ion channels are extremely rare in nature, with channelrhodopsin the only example currently known (Nagel et al. 2002). Structurally similar to rhodopsin (see below), channelrhodopsin contains all-*trans*-retinal as the isomerizable chromophore. The chromophore domain is covalently linked to a seven-segment transmembrane domain, and upon absorption of blue light a configurational change from all-*trans* to 13-*cis*-retinal induces conformational change of the transmembrane domain with consequent opening of the pore.

Mechano-sensitive channels are a class of membrane-embedded proteins whose gating mechanism is dependent on external mechanical stimuli (Haswell et al. 2011). Senses of touch, hearing and balance involve the presence of mechano-sensitive channels, as well as the regulation of the cardiovascular system and osmotic homeostasis. Several models are proposed for the functioning of mechano-sensitive channels. One relies on the change of membrane tension caused by application of mechanical stress, which induces channel opening as a result of the transmitted force producing a conformational change in the membrane-embedded domains. Alternatively, the transmembrane channel can have an extracellular gating system connected to an extramembrane structural component (*e.g.* cytoskeleton or peptidoglycan). In this case movement of the extracellular component transfers mechanical force to the extracellular gating system, resulting in the regulation of the channel activity.

2.2 Receptor Tyrosine Kinases (RTKs)

Receptor Tyrosine Kinases (RTKs) are a large family containing important receptors such as the epidermal growth factor receptor (EGFR) and the insulin receptor (IR).

RTKs play a crucial role in several cellular activities from cell growth to differentiation, migration and metabolism (Schlessinger 2000). RTKs are strongly associated with tyrosine kinases, enzymes which catalyze phosphoryl transfer to tyrosine residues from ATP.

The general structure of RTKs comprises an extracellular binding domain connected to a cytoplasmic domain by a single transmembrane helix (Fig. 1b). The activation mechanism relies on the binding of a ligand to the RTK extracellular binding domain. For instance, EGF binding induces dimerization of the RTK monomers, as a result of lateral movement of the transmembrane helices. Alternatively, the ligand can induce conformational change of a pre-formed inactive dimer, as in the case of insulin (Hubbard 2004). The active dimer induces the switch-on of the catalytic activity of tyrosine kinases and, hence, the activation of domains towards cytoplasmic enzymes that migrate to the membrane. The result is the onset of multiple signal cascades from a single extracellular binding event, providing the characteristic signal amplification properties showed by RTKs.

2.3 *G-Protein Coupled Receptors (GPCRs)*

G-Protein Coupled Receptors (GPCRs) are a family of seven-transmembrane domain receptors that associate with heterotrimeric proteins able to bind guanosine triphosphate (GTP), known as G-proteins. GPCRs are evolutionary conserved in many species and are important for the senses of light, smell and taste (Fig. 1c) (Tompa 2016). GPCRs respond to a large variety of external primary messengers, which activate multiple signal cascades. The binding of an agonist to an extracellular domain induces a subsequent conformational change in the transmembrane domains, producing a net change in the relative positions of some transmembrane domains. Thus, the binding event is transmitted from the cell exterior, through the membrane to activate a specific intracellular response. In the basal state, three subunits are associated ($G\alpha\beta\gamma$). Upon binding of the incoming ligand, $G\alpha$ undergoes a conformational change, exchanges its bound GDP for GTP and dissociates from the $\beta\gamma$ heterodimer. In this activated state, both $G\alpha$ and $G\beta\gamma$ subunits can independently interact with effector proteins. For instance, transmembrane adenylyl cyclase binds the $G\alpha$ subunit by means of its cytoplasmic catalytic domain (Tesmer et al. 1997). The domain undergoes a conformational change to activate the production of cyclic adenosine monophosphate (cAMP), which is involved in muscle relaxation. On the other hand, the $G\beta\gamma$ subunit has been found associated to voltage-dependent Ca^{2+} channels for the controlled release of neurotransmitters at synapses (De Waard et al. 1997).

Rhodopsin, which is involved in the sensing of light, is probably the most studied GPCR (Manglik and Kobilka 2014; Palczewski et al. 2000). Rhodopsin is bound to 11-*cis*-retinal, which upon illumination by light isomerizes to all-*trans*-retinal and induces a conformational change in the neighboring rhodopsin domain. The net change in rhodopsin shape allows binding and activation of the G-protein transducin.

In this light-activated mode, it has been established that a single rhodopsin can activate hundreds of transducin proteins resulting in highly efficient amplification of the signal.

2.4 Steroid Hormone Receptors (SHRs)

The activation of signal proteins as a result of translocation of a messenger molecule is an alternative mechanism of signal transduction. This behavior is clearly elucidated by steroid hormone receptors (SHRs) (Klinge 2018; Griekspoor et al. 2007). SHRs are a large family of nuclear receptors that play a key role in physiological functions such as organ development and metabolite homeostasis. Alterations in these functions are involved several diseases, for instance breast cancer.

The general structure of SHRs comprises many independent functional domains. The DNA-binding domain is the most conserved among all SHRs with characteristic zinc-finger motifs. The ligand-binding domain is usually formed by twelve α -helices.

All SHRs share a similar mechanism of activation (Fig. 1d). Upon translocation to the cytoplasm by passive diffusion, the hormone binds the ligand-binding domain followed by a rapid relocation of the SHR to the nucleus. Here, SHRs undergo homologous dimerization form active species that are able to bind specific DNA regions, called Hormone Responsive Elements (HREs), through the zinc-finger motifs. This binding event induces recruitment of other co-factors which regulate gene transcription. Location to the nucleus is ligand- and concentration-dependent. Gene transcription can be modulated by receptor antagonists, proteasomes, and other signaling pathways.

3 Artificial Signal Transduction

3.1 Reversible Control over Synthetic Ion Channels

Much like the natural examples, the activity of artificial voltage-gated ion channels is regulated by the transmembrane potential. An early example was reported by Kobuke and co-workers (Kobuke et al. 1995). The system comprises ion pairs of tetra(butylene-1,4-glycol) monobutyl ether phosphate monoesters and di(octadecyl)dimethylammonium cations. Planar bilayer conductance (PBC) studies of these ion pairs revealed a positive voltage dependence of the opening and closing times, with the ion channels in an open state at higher voltages. It was suggested that the amphiphilic molecules self-assemble with a tail-to-tail orientation to form half-channels in each membrane leaflet. Upon application of a voltage, the half-channels move laterally to form supramolecular constructs with an uneven charge density at the two sides of the bilayer, resulting in a net dipole moment. The mechanism was

further clarified by inserting asymmetric derivatives in a planar bilayer (Goto et al. 2001). These species bear a combination of carboxylate and phosphate groups whose different extent of deprotonation at slightly basic pH allowed voltage-gated ion channels with rectifying properties to form. The concept of asymmetry was further investigated by Fyles and co-workers, who reported voltage-gated ion channels formed by bis-macrocyclic bolaamphiphiles (Fyles et al. 1998). PBC studies showed a current-voltage response similar to that shown by the archetypical peptaibol alamethicin, which has well-studied ion channel activity (Woolley and Wallace 1992). Matile and co-workers proposed an alternative design based on rigid rod-like *p*-octiphenyl scaffolds able to completely span the bilayer (Sakai et al. 2001, 2003). A series of pendant azacrown moieties provided a unimolecular ion-conductive pathway. PBC and fluorescence-based studies, performed using both planar bilayers and synthetic vesicles, confirmed that the voltage-gated ion channel activity is closely related to the alignment of the axial rods upon application of a transmembrane potential. The ion channel activity was similar to that shown by α -helical natural antibiotics (Kobayashi et al. 2000). Hou and co-workers proposed an alternative strategy, using voltage to reversibly control the insertion of channel molecules within lipid bilayers (Fig. 2a) (Si et al. 2014). Inspired by the arginine-rich S4 domain of natural voltage-gated K^+ channel (see above), Hou designed a series of arginine-rich pillar[5]arene transmembrane species (**1a–1d**). Similarly to its natural counterpart, these pillar[5]arene species can be reversibly inserted/removed from the bilayer by applying voltages of, respectively, -100 and $+100$ mV. Recently, Roh, Kim and co-workers showed that shape-resistant organic cages can give weakly voltage-gated channels (Benke et al. 2017). These cages, based on porphyrin units, are assembled by dynamic covalent chemistry and showed selectivity for anions. Successfully incorporated into cellular membranes, these porphyrin cages mediated iodide flux across the cell membrane.

The ligand-mediated formation of artificial ion channels has been very popular in the last two decades and many examples are now available (Talukdar et al. 2005). Nonetheless, achieving reversible ion channel activity by addition/removal of these ligands has proved to be more challenging. Futaki and co-workers designed an artificial channel peptide with an alamethicin segment connected through a flexible tetraglycine to a leucine zipper portion derived from the cFos protein (Fig. 2b) (Kiwada et al. 2006). The alamethicin portion inserts within the membrane. The extramembrane leucine zipper bears a pair of lysine side-chains functionalized with iminodiacetic acid (**Ida**), which are able to complex Fe(III) ions. In the absence of Fe(III) ions, the extramembrane leucine zipper adopts a helical conformation that promotes self-association. This conformation is destabilized upon complexation to Fe(III) ions, which allows a channel to open and is revealed by PBC studies as an increase in the channel current level. The ion channel opening was reversed upon the addition of excess EDTA, which complexes the Fe(III) ions and regenerates the helical conformation of the extramembrane segment; an elegant example of changes in conformation producing switching of channel activity. An assembly/disassembly approach to cation-mediated artificial ion channel formation was developed by Webb and co-workers, who created pyridyl-cholate conjugates able to be dimerized within the membrane by Pd(II) ions (Wilson and Webb 2008; Wilson et al. 2011). The

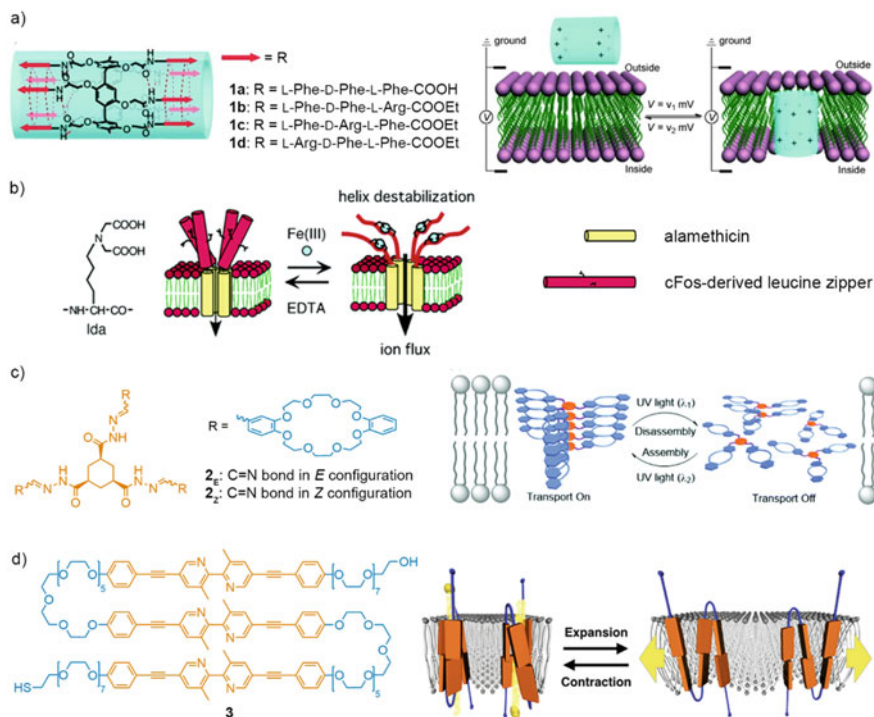


Fig. 2 Artificial ion channels with reversible control. **a** Voltage-gated ion channels. Adapted with permission from reference (Si et al. 2014). Copyright 2014 John Wiley and Sons. **b** Ligand-gated ion channels. Adapted with permission from reference (Kiwada et al. 2006). Copyright 2006 American Chemical Society. **c** Light-gated ion channels. Adapted with permission from reference (Zhou et al. 2017). Copyright 2017 Royal Society of Chemistry. **d** Mechano-sensitive ion channel. Adapted with permission from reference (Muraoka et al. 2017). Copyright 2017 American Chemical Society

activity of these self-assembled multimeric ion channels could be reversed by addition of hexathia-18-crown-6, which as strong chelator for Pd(II) ions dissociated the membrane-spanning complexes. More recently, Peters et al. showed that metal ion-gated artificial ion channels could also have antibiotic activity. They demonstrated the switch-on of ion channel activity by Cu(II) complexation to chelating octameric α -aminoisobutyric (Aib) foldamers (Peters et al. 2020). PBC and vesicle studies showed that complexation increased ionophoric activity, with X-ray crystallographic analysis supporting the formation of multimeric channels by the Cu(II) complexes as well as a direct interaction between anions and the foldamer backbone. Activity in vesicles could be reversed upon EDTA addition, and the increased activity of the Cu(II) complexes in vesicles corresponded with increased antibiotic activity.

Ion channel activity can be controlled by organic ligands instead of metal ions. Recently, Kinbara and co-workers illustrated this principle using synthetic chiral receptors able to bind 2-phenethylamine (PA) (Muraoka et al. 2014). The channel

monomer is an amphiphile that adopts a bent conformation when embedded in artificial vesicles due to stacking of its diphenylacetylene units. Conductance studies of the vesicle-embedded systems in the presence of PA showed ion channel activity, which could be reversed after addition of β -cyclodextrin, a good host for PA (Rekharsky et al. 1995). Alternatively, organic ligands can be used in a blocking/unblocking approach to switching activity. An elegant example of an organic ligand-gated artificial ion channel has been recently reported by Nitschke and co-workers (Haynes et al. 2017). The channel is formed through the self-assembly of pyridyl ligands (L) around Zn(II). X-ray crystallography showed $Zn_{10}L_{15}$ pentagonal prisms with bromide accommodated in the channel-like cavity. PBC measurements of $Zn_{10}L_{15}$ showed channel behavior, while HPTS assays revealed selective transport of halide anions ($Cl^- < Br^- < I^-$) over larger anions. Crucially, channel activity could be switched off by the addition of dodecyl sulfate, which was proposed to block the entrances and exits of the membrane-embedded channels. Calixarenes can also give efficient artificial ion channels, as reported by Li, Chen and co-workers (Hu et al. 2019). In this case, ion channel activity could be switched off by addition of methylene blue, a common cavity binder for calixarenes.

Unlike in the natural world, several examples of synthetic light-switchable ion channels are known. Schreiber and co-workers reported an example of a light-gated artificial ion channel in 1991 (Stankovic et al. 1991). They functionalized gramicidin monomers with the linker 3,3'-azobis(benzeneacetic acid) to give photoactive dimers. Photoisomerization and conductance studies of the azo-linked dimer in artificial vesicles in the dark demonstrated that unimolecular ion channels did not form as the molecules are in the inactive *trans* configuration. Photoactivation to the *cis* form produces a relative change of position of the gramicidin subunits, inducing alignment of their interior pores and ion channel activity. The *cis/trans* isomerization of azobenzene moieties is a versatile switch, and has also been exploited in channels reported by Woolley, (Lien et al. 1996) Kobuke, (Kobuke and Ohgoshi 2000) and Gin (Jog and Gin 2008). Alternatively, Hou, Liu and co-workers exploited the light-induced *E/Z* isomerization of the C=N bonds of acylhydrazone units to realize light-gated reversible ion channels (Fig. 2c) (Zhou et al. 2017). Acylhydrazone substituted crown ether triads stack on top of each other (2_E) to give a self-assembled supramolecular transmembrane channel with selectivity for NH_4^+ and K^+ ions. However, this ion transport could be switched off by irradiation with 320 nm UV light (to give 2_z), then switched back on by 365 nm UV light.

Studies on mechano-sensitive artificial channels are rare, but an example has been reported by Kinbara and co-workers (Fig. 2d) (Muraoka et al. 2017). These artificial channels, formed by oligomers composed of alternating oligo(ethylene glycol) chains and 3,3'-dimethyl-5,5'-bis(phenylethynyl)-2,2'-bipyridine units (**3**) in membranes, mimic the domain structure of multipass transmembrane proteins. When embedded in synthetic bilayers, changes in membrane tension cause these amphiphiles to change the extent of stacking interactions between "domains", which modulates ion transportation.

3.2 *Mimics of TKRs*

Instead of ligand-induced changes in conformation allowing a chemical message to pass through the bilayer, TKRs use ligand-induced changes in position in the membrane to relay a message. The formation of a termolecular (or higher order) active complex involving two or more membrane-embedded components makes this a mechanistically distinct process. The membrane phase state or extent of phase separation in the membrane should play a key role in these intermembrane aggregation processes. Furthermore, unlike ion channels, TKR-mediated signal transduction occurs without physical transport of molecules or ions across the membrane.

Hunter, Williams and co-workers were the first to explore these issues, by creating a simple mimic of TKR-mediated signal transduction (Fig. 3a) (Barton et al. 2002). In the place of the membrane-spanning domains of TKRs, a transmembrane section was formed by linking two molecules of cholenic acid through a tail-to-tail dialkyne bridge. The two termini were decorated with cysteine residues to give **6** and provide access to thiol-disulfide exchange chemistry, with the termini of one portion of dimer **6** transformed into a chromogenic disulfide (*i.e.* **6** to **4**). Both **6** and **4** were embedded in artificial vesicles, then the system activated by tri(3-sulfonatophenyl)phosphane under slightly acidic conditions, a charged reducing agent that does not cross the lipid membrane. This phosphane reduces any external disulfides to the corresponding thiols (*i.e.* **4** to **5**) but leaves the internal disulfides intact. Now 'activated', the external thiols are oxidized to disulfides, such as **5•6** by the addition of potassium ferricyanide (*i.e.* the external messenger, step [O] in Fig. 3a). This oxidative sensing event induces dimerization of the membrane-spanning bis(steroids). The external dimerization pulls the reactive groups at the interior of the membrane into close proximity, accelerating the release of the secondary messenger (the chromophore pyridine-2-thiol, **7**) as this thiol/disulfide displacement becomes a fast intramolecular reaction.

In a following study, the membrane-spanning bis(steroid) unit was re-designed to demonstrate that this dimerization process shows cooperativity (Fig. 3b) (Dijkstra et al. 2007). The bis(steroid) core was labelled at the termini with fluorescent dansyl groups, with copper(II) ions acting as messengers that quench the fluorescence upon binding with the dansyl group. Due the formation of higher stoichiometry complexes, (Doyle et al. 2003) binding to Cu(II) induces aggregation of the membrane-spanning bis(steroid) molecules (Fig. 3b, *left*). Comparison with a control monomer that does not span the membrane revealed that affinity for Cu(II) was higher for the membrane-spanning dimers, as shown by stronger fluorescence quenching. This increase in affinity (*i.e.* high K^{int} , Fig. 3b, *left*) was attributed to transmembrane cooperativity producing tighter binding to Cu(II) in the vesicle lumen. Unlike the thiol/disulfide system developed previously, this artificial signal event involves species at equilibrium; a messenger on one side of the membrane leads to cooperative binding on the opposite side of the membrane.

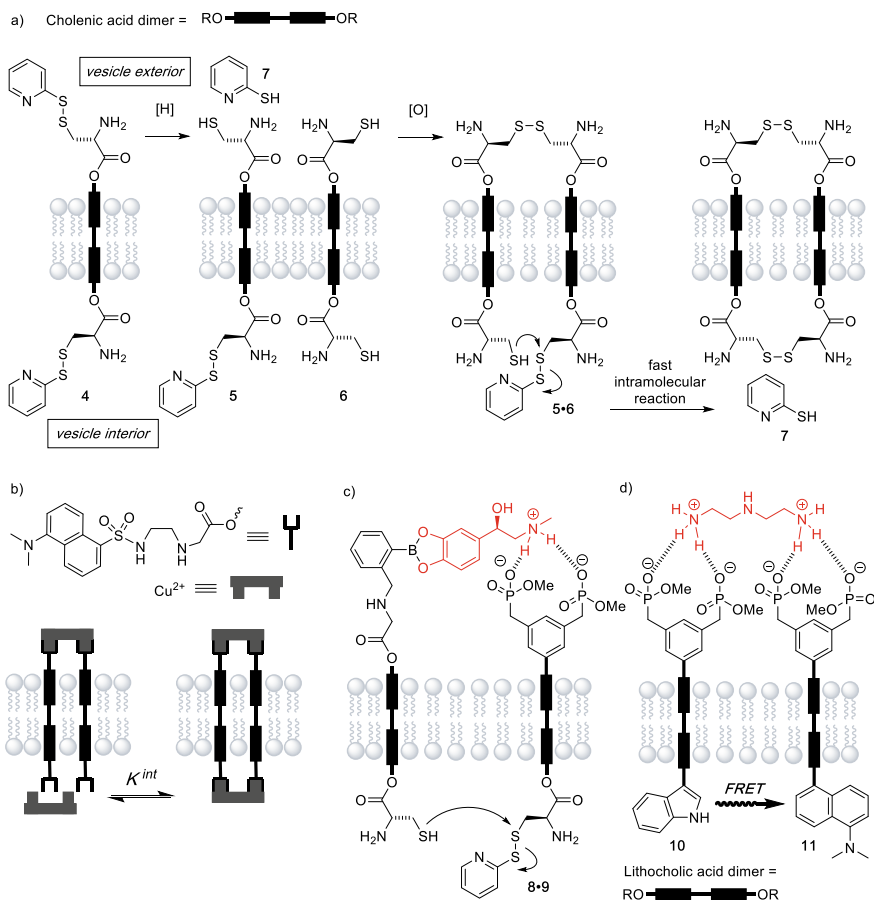


Fig. 3 Schematic representations of bio-inspired signal transduction based on dimerization of membrane-spanning systems within artificial bilayers. **a** Release of a secondary messenger as result of membrane-spanning dimerization (Barton et al. 2002). **b** Cooperativity of transmembrane spanning receptors (Dijkstra et al. 2007). **c** Complexation of adrenaline (red) inducing release of a secondary messenger (Schrader et al. 2006). **d** FRET induced by formation of ternary complex with DET (red) (Bernitzki and Schrader 2009)

In the quest to develop systems able to recognize natural primary messengers, Schrader and co-workers modified bis(lithocholate) membrane-spanning molecules to introduce an alternative non-covalent approach for signal transduction (Schrader et al. 2006). They decorated the terminus facing the exterior of the bilayer with *m*-xylylene bisphosphonate dianion and aminomethylphenylboronic acid moieties (Fig. 3c); these two fragments were designed to form a ternary complex with adrenaline. In this way, an excess of adrenaline (the primary messenger) facilitated the dimerization of vesicle-embedded bis(steroid) lipids by forming a supramolecular complex (8•9). This external dimerization induced intermolecular

cyclization at the vesicle interior as described above, with release of pyridine-2-thiol **7** as secondary messenger. However, the release of the secondary messenger could not be unambiguously proven because the detection system was not sufficiently specific and sensitive. This issue led to a re-design of the membrane-spanning systems to demonstrate that their non-covalent approach was indeed capable of signal transduction (Bernitzki and Schrader 2009). They developed two different unsymmetrical transmembrane units (**10** and **11**, Fig. 3d) in order to have the recognition system for the primary messenger at the vesicle exterior and a FRET couple at the interior. In this way, the formation of the ternary complex of the primary messenger facilitated the dimerization of the membrane-spanning systems, bringing the fluorescence dyes into sufficient proximity to observe FRET. Further studies demonstrated that the binding of the primary messenger, the resulting signal transmission, and subsequent release of the secondary messenger are strictly unidirectional. Importantly the effect of membrane fluidity on this intramembrane reaction was explored, with fluid DMPC bilayers providing a background reaction that is too high but gel-phase DPPC bilayers slowing the signaling reaction too much; a 3:1 mixture of the two was the optimized mixture (Bernitzki et al. 2012).

3.3 *Mimics of GPCRs*

Unlike mimics of RTKs, where bringing two transmembrane units together may be very sensitive to membrane fluidity and phase separation, mimics of GPCRs should combine binding of an external ligand with conformational change in a single embedded transmembrane molecule. To this end, Clayden, Webb and co-workers have explored an artificial transmembrane signaling strategy that employs dynamic foldamers with two interconverting conformations (Le Bailly and Clayden 2016). These synthetic receptors are 3_{10} helical α -aminoisobutyric acid (Aib) oligopeptides able to alter their screw sense distribution in response to specific chemical or physical stimuli. The stereochemical information inherent in 3_{10} helix handedness is transduced over distances commensurate with the foldamer length (rise per residue 0.194 nm), where it can be translated into specific outputs. These hydrophobic foldamers are soluble in several organic solvents and the Aib oligopeptide also acts as a hydrophobic anchor that promotes receptor insertion into the phospholipid bilayer; indeed natural Aib-rich peptaibols work as membrane-disrupting fungal antibiotics (Toniolo and Benedetti 1991). Aib oligopeptides of ≥ 4 residues adopt stable hydrogen-bonded 3_{10} helical conformations with no inherent screw sense preference. The two helix conformations (*M* and *P* enantiomers) have a low energy barrier of inversion ($\Delta G^\ddagger = 46 \text{ kJ mol}^{-1}$ at $-8 \text{ }^\circ\text{C}$) (Solà et al. 2011) and interconvert on a timescale of submilliseconds at ambient temperature. Aib is achiral, so both *P* and *M* helices are present in equal proportion. However, a chiral amino acid at a terminus (typically the N-terminus) induces a preference for either the left- or the right-handed screw sense (Pengo et al. 1998).

To this Aib foldamer core, C-terminal spectroscopic probes can be added to report on changes in the relative populations of *M* and *P* helices. ^1H , ^{13}C and ^{19}F NMR spectroscopic probes have been extensively used to quantify this helical excess (*h.e.*, the fractional excess of *P* or *M* helices), including probes that are inherently achiral (*e.g.* the methylene protons of glycine) or chiral (*e.g.* Aib enantioselectively ^{13}C labeled at a methyl group); the latter can identify which helical conformation predominates (Solà et al. 2011; Clayden et al. 2009; Solà et al. 2010; Pike et al. 2013). More recently, fluorescent probes have been developed, which can be employed in complex environments and can provide additional information, *e.g.* allowing visualization in bilayers by fluorescence microscopy. However, unlike NMR probes, a fluorescent probe needs to be chiral to allow changes in the *P* to *M* helical ratio to be detected using standard fluorescence spectroscopy. One example of this is a conformationally sensitive bis(pyrene) probe (Fig. 4b, blue) that exploited the high sensitivity of excimer emission to interpyrene distance. A series of Aib foldamers were attached at their C-terminus to the acetamide of (*S,S*)-1,2-bis(pyren-1'-yl)ethylenediamine. X-ray crystal structures indicated that one helix screw sense gave widely separated pyrene groups while the other had these groups close in space. Fluorescence emission mirrored these observations, with an increase in excimer/monomer (*E/M*) fluorescence emission ratio correlating with an increase in the proportion of *P* helix. Transfer of these receptors to a bilayer environment showed that this correlation of *E/M* with *h.e.* was maintained, although the spectroscopic changes were weaker and an *M* helix gave the higher *E/M* ratio. The latter effect was the reverse of that observed

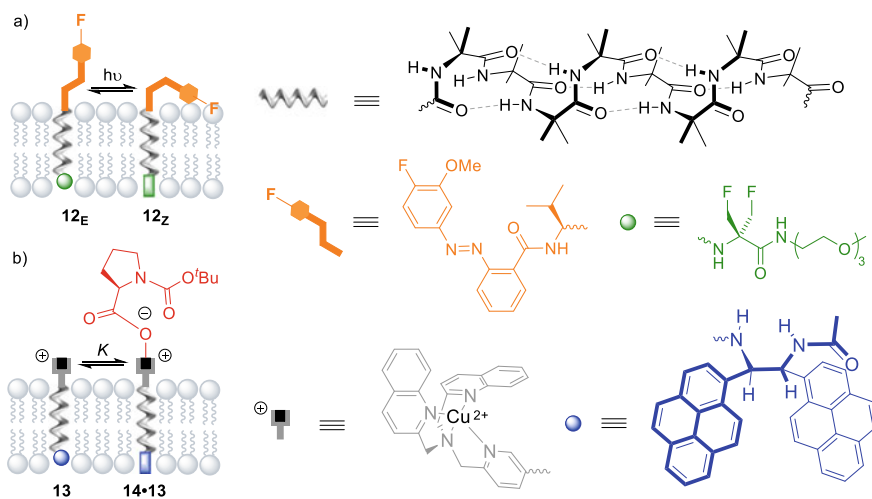


Fig. 4 Schematic representations of approaches to bio-inspired signal transduction based on conformational change of membrane-spanning systems. **a** Light induces a conformational change in an azo-benzene (orange) substituted Aib foldamer **12** that bears a ^{19}F ss-NMR reporter (green) (De Poli et al. 2016). **b** Binding to chiral carboxylate **14** (red) induces conformational change in a Aib foldamer **13** that bears a metal complex (grey) and a bis(pyrene) fluorescence reporter (blue) (Lister et al. 2017)

in organic solvent and was ascribed to changes in the reporter conformation (Lister et al. 2018). It was also found that phospholipid chirality had an influence on global conformation, although it is unclear how strong this influence is.

Several types of stimuli for responsive Aib foldamers were investigated in solution prior to membrane studies (Le Bailly and Clayden 2016). An important example had a boron-containing N-terminus that bound chiral diols. Competitive reversible binding to diols was demonstrated in methanol, including of adenosine, which is a natural signaling molecule for purinergic receptors. Successive displacement of diols with low association constants by more strongly coordinating diols of opposite configuration allowing switching of the helix between left- and right-handedness (Brown et al. 2013). Despite these promising observations, the diol/boronic acid interaction was found to be much weaker at a bilayer interface, which prevented development of these receptors into mimics of ligand-activated GPCRs.

Not all GPCRs are ligand activated, however; rhodopsin undergoes a conformational change in response to light-induced photoisomerization (Manglik and Kobilka 2014; Palczewski et al. 2000). This was the inspiration for photo-responsive GPCR mimic **12** (Fig. 4a) consisting of an Aib foldamer core, with an azobenzene-2-carboxamide capped L-valine residue at its N-terminus and a ^{19}F NMR probe at the C-terminus (De Poli et al. 2016). Validation studies in methanol showed that *E/Z* photo-isomerization of the azobenzene altered the global conformation of the helix: azobenzene in its *Z* configuration gave no measurable preference for a *P* or an *M* helix, while the *E* configuration induced a preference for a left-handed helix. For membrane studies, a 2,2'-difluoroAib probe was used as lipid signals obscure most ^1H and ^{13}C NMR probe signals and the membrane environment broadens ^1H NMR signals. The receptors were embedded in the membranes of multilamellar vesicles prepared from 1,2-dioleoyl-*sn*-glycero-3-phosphocholine (DOPC, hydrophobic region ca. 2.88 nm thick). DOPC was hoped to provide a very fluid matrix, which would permit fast conformational interchange on the NMR timescale. The NMR experiments confirmed that the foldamers localized in the bilayer and the chirality of the DOPC had no significant influence on the screw sense of these helical compounds. Furthermore, linear dichroism showed that an Aib₈ core favors a perpendicular orientation relative to the bilayer surface (Lizio et al. 2021). The change in population distribution between *M* and *P* helices upon light irradiation was monitored by solid-state magic angle spinning ^{19}F NMR spectroscopy (^{19}F ss-NMR). Using foldamers made of four Aib units, they showed azobenzene photo-isomerization (illumination at 365 nm for 5 min) in the membrane altered the helical conformation, going from 65% *M* population for the *E* isomer to an almost equal population of *P* and *M* helices for the *Z* isomer. Illumination at 455 nm switched the azobenzene back to an *E* configuration and restored the initial screw sense preference; multiple photo-switching cycles could be carried out. A longer foldamer made of eight Aib units (three helical turns, with a length commensurate with the hydrophobic region thickness) showed similar behavior in membranes, switching from a screw-sense preference to no preference and back. Thus, the system communicates conformational information along its several nanometer length within a membrane environment, although there was clearly weaker conformational induction. Solid-state NMR was

shown to be an important analytical tool in the field, but also to have a number of practical disadvantages: it requires high concentrations of vesicles, conditions that can perturb the vesicle structure (spinning rate of 10 kHz) and long acquisition times that prevent real-time dynamic detection of conformational change.

The (*S,S*-BisPyrEt)NHAc reporter (Fig. 4b, blue) can overcome many of these signal reporting issues. An Aib₈ oligopeptide with this fluorescent reporter at its C-terminus was equipped at its N-terminus with a water compatible, Cu(II)-containing binding pocket (Lister et al. 2017). This metallofoldamer was studied first in acetonitrile and then in the membranes of large unilamellar DOPC vesicles. In organic solvent, the addition of chiral carboxylate (either Boc-L-Pro or Boc-D-Pro **14**) to the metallofoldamer induced circular dichroism signals of opposite sign at 239 nm, as binding to the messengers led to opposite propeller conformations around the binding pocket. Crucially, non-covalent binding of these messengers also led to a change in *E/M* emission ratio from the distant C-terminal reporter. These studies in organic solvent confirmed that local conformational preferences are relayed to the remote fluorescent probe through a global change in helical handedness. Furthermore, analysis of the binding data obtained showed that this reversible non-covalent binding was tight in acetonitrile, with estimated affinities of 10⁶ M⁻¹; much stronger than the diol/boronate interaction studied previously.

The artificial receptors were added to a suspension of DOPC vesicles and the migration into the phospholipid bilayers was monitored by fluorescence microscopy. Analysis of the spectral emission suggested that the C-terminal pyrenes were in a polar environment, perhaps close to the interface with water at the inner side of the membrane. The receptor-embedded vesicles were titrated with L-Pro or D-Pro carboxylates, and circular dichroism showed that the propeller induction at the binding site occurred with the same sense as in solution. Binding to the messenger molecules also induced a relay of conformational change along the receptor deep into the bilayer, transducing the stereochemical information in the messengers to the pyrene fluorophores positioned ~2.6 nm away. As found for the covalently controlled analogues (Lister et al. 2018), the effect of the ligands on the reporter emission spectra was opposite to that observed in acetonitrile, with D-Pro now increasing the excimer emission. Competitive binding between an ‘agonist’ and an ‘antagonist’ was also demonstrated: the addition of the messenger molecule Leu-enkephalin (a natural agonist for the μ - and δ -opioid receptors) resulted in an increase in *E/M* ratio, which could be inverted by competitive binding of L-BocPro. The work shows both the binding and conformation relay of GPCRs can be mimicked with synthetic molecules (albeit with weaker ligand affinities and a weaker relay), although further essential functions need to be added, such as signal amplification.

4 Translocation Approaches

Hunter, Williams and co-workers created a new type of transmembrane signal transduction, with transmission of information across vesicle bilayers without transfer of

physical matter into the aqueous lumen, which although related to steroid translocation is largely orthogonal to known biological signaling processes. Importantly, this system is able to catalytically generate secondary messengers, a signal cascade that has analogy with biological transduction mechanisms. This work also illustrates how a purely synthetic approach can give access to signal transduction pathways beyond those found in biology.

Their strategy features the controlled translocation across a membrane of a synthetic transducer that is embedded within a bilayer but too short to span it (Fig. 5a) (Langton et al. 2017a). The transducer is equipped with two different functional groups. One is a sensor head that reads extracellular signals, and the second functional group is a pro-catalyst, either in its inactive form when buried within the bilayer or in its active form when protruding at the inner surface of the vesicle bilayer into

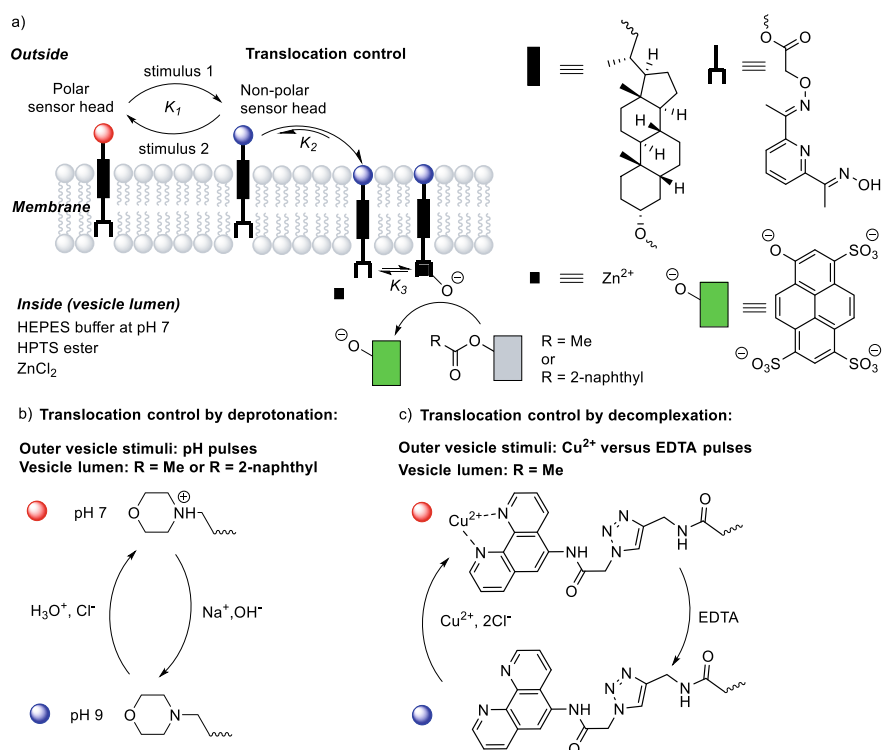


Fig. 5 Schematic representations of approaches to bio-inspired signal transduction based on translocation of a catalytically active steroid. **a** A stimulus outside the vesicle controls the translocation of the steroid into the lumen, where it complexes to Zn(II) (black square) to make a catalytically active oximate that hydrolyses an internal ester (grey). R = Me for the generation of the HPTS fluorescent probe (green) only or R = 2-naphthyl for the co-generation of a surfactant that permeabilizes the bilayer (Langton et al. 2017a, b). **b** Translocation control exerted by protonation/deprotonation (Langton et al. 2017a). **c** Translocation control exerted by Cu(II) complexation/decomplexation (Langton et al. 2017c)

the vesicle lumen. The motion of the transducer between the outer and the inner surface of the lipid bilayer is driven by extravesicular signals.

The transducer core is made of lithocholic acid; its planar structure is thought to favor a perpendicular orientation in the bilayer. The rigidity and length of the steroid core should allow only one of the functionalized termini to stick out into aqueous solution at any time. Vesicles were prepared from mixtures of the transducer with DOPC and 1,2-dioleoyl-*sn*-glycero-3-phosphoethanolamine (DOPE) and encapsulated a pH 7 buffered aqueous solution containing zinc cations and a reactant. The choice of lipid is crucial, as this mixture should be fluid yet also maintain a transmembrane pH gradient. Although a statistical distribution of orientations within the lipid bilayer is obtained, only the transducers with sensor heads pointing outwards can respond to exterior chemical signals. The polarity of the sensor head switches by interacting with chemical signals from outside of the vesicle (Fig. 5b,c); the other end bears the non-polar pro-catalyst that becomes polar upon coordination to Zn(II) inside the vesicle. Control over molecular motion across the lipid bilayer exploits the preference of polar groups to sit in an aqueous phase and non-polar groups to be embedded in the bilayer core.

Initially *N*-alkylmorpholine (pK_a 7.4) was chosen as a sensor head as changing the pH (between 7 and 9) outside the vesicles switched the polarity of the head group by protonation/deprotonation (Fig. 5b). For example, receipt of an external pH 9 signal decreases the polarity of the sensor heads through deprotonation; this switching from polar to non-polar gives transducers with two non-polar termini, which are free to diffuse across the bilayer. Now the pro-catalyst group (an oxime) can be activated by complexation to the zinc(II) cofactor in the aqueous lumen, to give a polar catalyst head that locates the transducer at the inner surface of the vesicle bilayer. This Zn(II) oximate in turn catalyzes the hydrolysis of a non-fluorescent ester inside the vesicle aqueous lumen to produce a fluorescent second messenger. Both the reactant and the hydrolysis product were chosen to be highly charged so they could not leak out of the vesicles, and the reaction inside the vesicles could be monitored by fluorescence microscopy. The position of the transducer is under equilibrium control, so loss of the chemical signal outside the vesicle reverses translocation of the transducer. A lower external pH switches off catalysis due to the affinity of the sensor head (amine) for the extra-vesicular signal (H^+) being higher than that of the pro-catalyst for Zn(II). Multiple cycles of pH variation outside of the vesicles led to reversible switching of the hydrolysis reaction inside the vesicles, indicating that the controlled reversible translocation of molecular shuttles across a lipid bilayer is an effective signal transduction mechanism. The catalyzed hydrolysis inside the vesicles produced a large number of secondary messengers; such amplified output signal is reminiscent of amplification processes commonly exploited by biological signal transduction pathways, with binding of a single molecule generating a large number of output molecules. The system also cleverly exploits the high effective molarity of membrane-embedded reactive groups relative to the small volume of the vesicle lumen.

Subsequent studies used a different ester substrate, which was converted into a surfactant (2-naphthoic acid) upon hydrolysis (Langton et al. 2017b). A pH increase

outside of the vesicle triggered the catalytic production of 2-naphthoic acid inside the vesicle by the Zn(II) oximate. The 2-naphthoic acid produced then permeabilized the vesicles without disrupting the membranes, which enabled the efflux of encapsulated calcein from vesicles and a fluorescence signal due to the relief of self-quenching. This cooperative chemical system demonstrated controlled release of cargo molecules as a response to a chemical signal.

The sensor head can also be varied, as exemplified by phenanthroline bearing transducers (Fig. 5c) (Langton et al. 2017c). For transducers of the correct orientation, the phenanthroline group coordinated to external Cu(II) ions to form a charged polar head at the vesicle outer surface. This Cu(II) messenger could be sequestered using EDTA, producing a polarity switch that released the transducer from the vesicle outer surface. The active catalyst then formed at the inner surface of the vesicle and once again catalyzed the hydrolysis of a non-fluorescent ester to form a fluorescent product. As in the previous example, transducers of the wrong orientation were inactive. The system also relies on the high affinity of phenanthroline for Cu(II) ions to prevent poisoning of the catalytic terminus by complexation to Cu(II) in the place of Zn(II). The intra-vesicular catalysis was repeatedly turned ON by addition of EDTA and OFF by addition of CuCl₂ to the external solution.

Beyond switching the polarity of sensor heads to control transducer translocation, Williams and Hunter further advanced their dynamic signal transduction system by introducing biological molecular recognition (Ding et al. 2019). In one population of vesicles, transducers with desthiobiotin as the sensor head were embedded in the membrane, with complexation to external NeutrAvidin fixing transducers with the right orientation to the vesicle outer surface. The addition of a second population of vesicles that presented high affinity biotin signals at their surface led to NeutrAvidin sequestration, releasing the transducers from the outer surface of the first set of vesicles and activating intra-vesicular catalytic signaling. This ingenious inter-vesicle signaling system is reminiscent of some biological cell-to-cell signaling processes.

5 Future Perspectives

The development of supramolecular systems able to mimic aspects of biological signal transduction is still in an early stage, but several important design principles are becoming apparent. Although studies in isotropic organic solvent are a useful guide, the complex anisotropic environment of the bilayer necessitates additional important considerations when designing membrane-active systems and interpreting the data they provide. Bilayer fluidity is lower than many organic solvents and can vary by three orders of magnitude between bilayer types, (Pintre and Webb 2013) altering the rates of conformational change, lateral (across membrane) diffusion and transverse (through membrane) diffusion. The preferred orientation and location of any synthetic components added to the bilayer should be determined, for example by covalent labeling (Lin and London 2014) although linear dichroism looks to be a useful spectroscopic alternative (Lizio et al. 2021). A specific consideration

for ligand-gated systems is the effect of the bilayer on any binding interactions between aqueous components (the ligand) and components that are embedded in the membrane (the synthetic receptor). The membrane can provide a significant steric barrier as well as much lower polarity compared to bulk aqueous solution, but on the other hand intramembrane interactions can benefit from the high effective molarities of membrane-bound components (Doyle et al. 2003). An often overlooked factor when using bilayers composed of natural phospholipids is the chirality of these molecules (*sn* phospholipids have an (*R*) configuration), and this can influence the conformation of membrane-bound components.

Several parts of the field stand out as needing further development, including increasing the number of systems able to catalytically generate second messengers on the far side of the membrane and the introduction of information-processing molecular machines into the bilayer; the molecular shuttle of Chen et al. indicates a pathway towards the latter (Chen et al. 2018). Finally, a link between a transmembrane information relay and out-of-equilibrium chemical networks in the vesicle membrane (Scheming et al. 1995) or lumen would be an exciting step towards mimicking the behavior of biochemical networks in cells.

Should these hurdles be overcome, the rewards will be significant. Artificial signal transduction would facilitate communication between compartments in artificial tissues (Villar et al. 2013; Booth et al. 2017) or even allow orthogonal signaling pathways to be introduced into cells, “short-circuiting” their signaling networks. For this ambitious goal to be realized, very robust signaling systems will have to be developed that can operate in the very complex and crowded milieu of the cell membrane. Synthetic signal transduction will be a key component needed for bottom-up synthetic biology, the creation of artificial cells and devices starting from molecular components. For example, artificial vesicles capable of maintaining (or even generating) transmembrane concentration gradients, controlling molecular ingress/egress and exchanging information across the bilayer could give stimuli-responsive dynamic cell-like systems with emergent features.

Acknowledgements FDS, DPT and SJW thank the EPSRC (grant EP/P027067/1) for financial support.

References

- Barba-Bon A, Nilam M, Hennig A (2020) Supramolecular chemistry in the biomembrane. *ChemBioChem* 21:886–910. <https://doi.org/10.1002/cbic.201900646>
- Barton P, Hunter CA, Potter TJ, Webb SJ, Williams NH (2002) Transmembrane signalling. *Angew Chem Int Ed* 41:3878–3881. [https://doi.org/10.1002/1521-3773\(20021018\)41:20<3878::AID-ANIE3878>3.0.CO;2-F](https://doi.org/10.1002/1521-3773(20021018)41:20<3878::AID-ANIE3878>3.0.CO;2-F)
- Bekus R, Schrader T (2020) Artificial signal transduction. *ChemistryOpen* 9:667–682. <https://doi.org/10.1002/open.201900367>

- Benke BP, Aich P, Kim Y, Kim KL, Rohman R, Hong S, Hwang I-C, Lee EH, Roh JH, Kim K (2017) Iodide-selective synthetic ion channels based on shape-persistent organic cages. *J Am Chem Soc* 139:7432–7435. <https://doi.org/10.1021/jacs.7b02708>
- Bernitzki K, Schrader T (2009) Entirely artificial signal transduction with a primary messenger. *Angew Chem Int Ed* 48:8001–8005. <https://doi.org/10.1002/anie.200902973>
- Bernitzki K, Maue M, Schrader T (2012) Artificial signal transduction with primary and secondary messengers. *Chem Eur J* 18:13412–13417. <https://doi.org/10.1002/chem.201200623>
- Booth MJ, Restrepo Schild V, Box SJ, Bayley H (2017) Light-patterning of synthetic tissues with single droplet resolution. *Sci Rep* 7:9315. <https://doi.org/10.1038/s41598-017-09394-9>
- Brown RA, Diemer V, Webb SJ, Clayden J (2013) End-to-end conformational communication through a synthetic purinergic receptor by ligand-induced helicity switching. *Nat Chem* 5:853–860. <https://doi.org/10.1038/nchem.1747>
- Chen S, Wang Y, Nie T, Bao C, Wang C, Xu T, Lin Q, Qu D-H, Gong X, Yang Y, Zhu L, Tian H (2018) An artificial molecular shuttle operates in lipid bilayers for ion transport. *J Am Chem Soc* 140:17992–17998. <https://doi.org/10.1021/jacs.8b09580>
- Clayden J, Castellanos A, Solà J, Morris GA (2009) Quantifying end-to-end conformational communication of chirality through an achiral peptide chain. *Angew Chem Int Ed* 48:5962–5965. <https://doi.org/10.1002/anie.200901892>
- De Poli M, Zawodny W, Quinonero O, Lorch M, Webb SJ, Clayden J (2016) Conformational photoswitching of a synthetic peptide foldamer bound within a phospholipid bilayer. *Science* 352:575–580. <https://doi.org/10.1126/science.aad8352>
- De Waard M, Liu H, Walker D, Scott VES, Gurnett CA, Campbell KP (1997) Direct binding of G-protein $\beta\gamma$ complex to voltage-dependent calcium channel. *Nature* 385:446–450. <https://doi.org/10.1038/385446a0>
- Dijkstra HP, Hutchinson JJ, Hunter CA, Qin H, Tomas S, Webb SJ, Williams NH (2007) Transmission of binding information across lipid bilayers. *Chem Eur J* 13:7215–7222. <https://doi.org/10.1002/chem.200601723>
- Ding Y, Williams NH, Hunter CA (2019) A synthetic vesicle-to-vesicle communication system. *J Am Chem Soc* 141:17847–17853. <https://doi.org/10.1021/jacs.9b09102>
- Doyle EL, Hunter CA, Phillips HC, Webb SJ, Williams NH (2003) Cooperative binding at lipid bilayer membrane surfaces. *J Am Chem Soc* 125:4593–4599. <https://doi.org/10.1021/ja021048a>
- Fyles TM, Loock D, Zhou X (1998) A voltage-gated ion channel based on a bis-macrocyclic bolaamphiphile. *J Am Chem Soc* 120:2997–3003. <https://doi.org/10.1021/ja972648q>
- Gadsby DC, Vergani P, Csanády L (2006) The ABC protein turned chloride channel whose failure causes cystic fibrosis. *Nature* 440:477–483. <https://doi.org/10.1038/nature04712>
- Goto C, Yamamura M, Satake A, Kobuke Y (2001) Artificial ion channels showing rectified current behavior. *J Am Chem Soc* 123:12152–12159. <https://doi.org/10.1021/ja010761h>
- Griekspoor A, Zwart W, Neeffjes J, Michalides R (2007) Visualizing the action of steroid hormone receptors in living cells. *Nucl Recept Signal* 5: <https://doi.org/10.1621/nrs.05003>
- Gulbis JM, Mann S, Mackinnon R (1999) Voltage-dependent K^+ channel β subunit. *Cell* 97:943–952. [https://doi.org/10.1016/S0092-8674\(00\)80805-3](https://doi.org/10.1016/S0092-8674(00)80805-3)
- Haswell ES, Phillips R, Rees DC (2011) Mechanosensitive channels: what can they do and how do they do it? *Structure* 19:1356–1369. <https://doi.org/10.1016/j.str.2011.09.005>
- Haynes CJE, Zhu J, Chimere C, Hernández-Ainsa S, Riddell IA, Ronson TK, Keyser UF, Nitschke JR (2017) Blockable $Zn_{10}L_{15}$ ion channels through subcomponent self-assembly. *Angew Chem Int Ed* 56:15388–15392. <https://doi.org/10.1002/anie.201709544>
- Herrington J, Arey BJ (2014) Conformational mechanisms of signaling bias of ion channels. In: Arey B (ed) *Biased signaling in physiology, pharmacology and therapeutics*. Elsevier, pp 173–207. <https://doi.org/10.1016/B978-0-12-411460-9.00006-9>
- Hu X, Liu N, Yang H, Wu F, Chen X, Li C, Chen X (2019) A reversible ion transportation switch of ON-OFF-ON type by a ligand-gated calix[6]arene channel. *Chem Commun* 55:3008–3011. <https://doi.org/10.1039/c9cc00732f>

- Hubbard SR (2004) Juxtamembrane autoinhibition in receptor tyrosine kinases. *Nat Rev Mol Cell Biol* 5:464–470. <https://doi.org/10.1038/nrm1399>
- Jog PV, Gin MS (2008) A light-gated synthetic ion channel. *Org Lett* 10:3693–3696. <https://doi.org/10.1021/ol8013045>
- Kiwada T, Sonomura K, Sugiura Y, Asami K, Futaki S (2006) Transmission of extramembrane conformational change into current: construction of metal-gated ion channel. *J Am Chem Soc* 128:6010–6011. <https://doi.org/10.1021/ja060515b>
- Klinge CM (2018) Steroid hormone receptors and signal transduction processes. In: Belfiore A, LeRoith D. (eds) *Principles of endocrinology and hormone action*. Endocrinology. Springer, pp 187–232. https://doi.org/10.1007/978-3-319-44675-2_9
- Kobayashi S, Takeshima K, Bae Park C, Chang Kim S, Matsuzaki K (2000) Interactions of the novel antimicrobial peptide Buforin 2 with lipid bilayers: proline as a translocation promoting factor. *Biochemistry* 39:8648–8654. <https://doi.org/10.1021/bi0004549>
- Kobuke Y, Ohgoshi A (2000) Supramolecular ion channel containing trans-azobenzene for photo-control of ionic fluxes. *Colloids Surf A Physicochem Eng Asp* 169:187–197. [https://doi.org/10.1016/S0927-7757\(00\)00435-0](https://doi.org/10.1016/S0927-7757(00)00435-0)
- Kobuke Y, Ueda K, Sokabe M (1995) Totally synthetic voltage dependent ion channel. *Chem Lett* 24:435–436. <https://doi.org/10.1246/cl.1995.435>
- Langton MJ, Keymeulen F, Ciaccia M, Williams NH, Hunter CA (2017a) Controlled membrane translocation provides a mechanism for signal transduction and amplification. *Nat Chem* 9:426–430. <https://doi.org/10.1038/nchem.2678>
- Langton MJ, Scriven LM, Williams NH, Hunter CA (2017b) Triggered release from lipid bilayer vesicles by an artificial transmembrane signal transduction system. *J Am Chem Soc* 139:15768–15773. <https://doi.org/10.1021/jacs.7b07747>
- Langton MJ, Williams NH, Hunter CA (2017c) Recognition-controlled membrane translocation for signal transduction across lipid bilayers. *J Am Chem Soc* 139:6461–6466. <https://doi.org/10.1021/jacs.7b02345>
- Le Bailly BAF, Clayden J (2016) Dynamic foldamer chemistry. *Chem Commun* 52:4852–4863. <https://doi.org/10.1039/C6CC00788K>
- Lien L, Jaikaran DCJ, Zhang Z, Woolley GA (1996) Photomodulated blocking of gramicidin ion channels. *J Am Chem Soc* 118:12222–12223. <https://doi.org/10.1021/ja962217s>
- Lin Q, London E (2014) preparation of artificial plasma membrane mimicking vesicles with lipid asymmetry. *PLoS ONE* 9: <https://doi.org/10.1371/journal.pone.0087903>
- Lister FGA, Le Bailly BAF, Webb SJ, Clayden J (2017) Ligand-modulated conformational switching in a fully synthetic membrane-bound receptor. *Nat Chem* 9:420–425. <https://doi.org/10.1038/nchem.2736>
- Lister FGA, Eccles N, Pike SJ, Brown RA, Whitehead GFS, Raftery J, Webb SJ, Clayden J (2018) Bis-pyrene probes of foldamer conformation in solution and in phospholipid bilayers. *Chem Sci* 9:6860–6870. <https://doi.org/10.1039/C8SC02532K>
- Lizio MG, Campana M, De Poli M, Jefferies DF, Cullen W, Andrushchenko V, Chmel NP, Bouř P, Khalid S, Clayden J, Blanch E, Rodger A, Webb SJ (2021, in press) Insight into mechanism of action and peptide-membrane interactions of Aib-rich peptides: multi-technique experimental and theoretical analysis. <https://doi.org/10.1002/cbic.202000834>
- Luckey M (2008) *Membrane structural biology with biochemical and biophysical foundations*. Cambridge University Press, New York
- Manglik A, Kobilka B (2014) The role of protein dynamics in GPCR function: insights from the β_2 AR and rhodopsin. *Curr Opin Cell Biol* 27:136–143. <https://doi.org/10.1016/J.CEB.2014.01.008>
- Muraoka T, Endo T, Tabata KV, Noji H, Nagatoishi S, Tsumoto K, Li R, Kinbara K (2014) Reversible ion transportation switch by a ligand-gated synthetic supramolecular ion channel. *J Am Chem Soc* 136:15584–15595. <https://doi.org/10.1021/ja5070312>

- Muraoka T, Umetsu K, Tabata KV, Hamada T, Noji H, Yamashita T, Kinbara K (2017) Mechano-sensitive synthetic ion channels. *J Am Chem Soc* 139:18016–18023. <https://doi.org/10.1021/jacs.7b09515>
- Nagel G, Ollig D, Fuhrmann M, Kateriya S, Musti AM, Bamberg E, Hegemann P (2002) Channelrhodopsin-1: a light-gated proton channel in green algae. *Science* 296:2395–2398. <https://doi.org/10.1126/science.1072068>
- Palczewski K, Kumasaka T, Hori T, Behnke CA, Motoshima H, Fox BA, Le Trong I, Teller DC, Okada T, Stenkamp RE, Yamamoto M, Miyano M (2000) Crystal structure of rhodopsin: a G protein-coupled receptor. *Science* 289:739–745. <https://doi.org/10.1126/science.289.5480.739>
- Pengo B, Formaggio F, Crisma M, Toniolo C, Bonora GM, Broxterman QB, Kamphius J, Saviano M, Iacovino R, Rossi F, Benedetti E (1998) Linear oligopeptides. Part 406.1 helical screw sense of peptide molecules: the pentapeptide system (Aib)₄/L-Val[L-(α Me)Val] in solution. *J Chem Soc, Perkin Trans 2*:1651–1658. <https://doi.org/10.1039/A800653I>
- Peters AD, Borsley S, della Sala F, Cairns-Gibson DF, Leonidou M, Clayden J, Whitehead GFS, Vitórica-Yrezábal IJ, Takano E, Burtham J, Cockcroft SL, Webb SJ (2020) Switchable foldamer ion channels with antibacterial activity. *Chem Sci* 11:7023–7030. <https://doi.org/10.1039/D0SC02393K>
- Pike SJ, De Poli M, Zawodny W, Raftery J, Webb SJ, Clayden J (2013) Diastereotopic fluorine substituents as ¹⁹F NMR probes of screw-sense preference in helical foldamers. *Org Biomol Chem* 11:3168–3176. <https://doi.org/10.1039/c3ob40463c>
- Pintre IC, Webb SJ (2013) Binding and reactivity at bilayer membranes. *Adv Phys Org Chem* 47:129–183. <https://doi.org/10.1016/B978-0-12-407754-6.00003-X>
- Pláček LJ (1997) Channelopathies: ion channel disorders of muscle as a paradigm for paroxysmal disorders of the nervous system. *Neuromuscul Disord* 7:250–255. [https://doi.org/10.1016/S0960-8966\(97\)00046-1](https://doi.org/10.1016/S0960-8966(97)00046-1)
- Rekharsky MV, Goldberg RN, Schwarz FP, Tewari YB, Ross PD, Yamashoji Y, Inoue Y (1995) Thermodynamic and nuclear magnetic resonance study of the interactions of α - and β -cyclodextrin with model substances: phenethylamine, ephedrine, and related substances. *J Am Chem Soc* 117:8830–8840. <https://doi.org/10.1021/ja00139a017>
- Saint-Criq V, Gray MA (2017) Role of CFTR in epithelial physiology. *Cell Mol Life Sci* 74:93–115. <https://doi.org/10.1007/s00018-016-2391-y>
- Sakai N, Gerard D, Matile S (2001) Electrostatics of cell membrane recognition: structure and activity of neutral and cationic rigid push-pull rods in isoelectric, anionic, and polarized lipid bilayer membranes. *J Am Chem Soc* 123:2517–2524. <https://doi.org/10.1021/ja003141>
- Sakai N, Houdebert D, Matile S (2003) Voltage-dependent formation of anion channels by synthetic rigid-rod push-pull β -barrels. *Chem Eur J* 9:223–232. <https://doi.org/10.1002/chem.200390016>
- Sands Z, Grottesi A, Sansom MSP (2005) Voltage-gated ion channels. *Curr Biol* 15:R44–R47. <https://doi.org/10.1016/j.cub.2004.12.050>
- Scheming APHJ, Lutje Spelberg JH, Driessen MCPF, Hauser MJB, Feiters MC, Nolte RJM (1995) Enzyme mimic displaying oscillatory behavior. oscillating reduction of Manganese(III) Porphyrin in a membrane-bound Cytochrome P-450 model system. *J Am Chem Soc* 117:12655–12656. <https://doi.org/10.1021/ja00155a600>
- Schlessinger J (2000) Cell signaling by receptor tyrosine kinases. *Cell* 103:211–225. <https://doi.org/10.1016/j.cell.2010.06.011>
- Schrader T, Maue M, Ellermann M (2006) Entirely artificial signal transduction with adrenaline. *J Recept Signal Transduct* 26:473–485. <https://doi.org/10.1080/10799890600950545>
- Si W, Li ZT, Hou JL (2014) Voltage-driven reversible insertion into and leaving from a lipid bilayer: tuning transmembrane transport of artificial channels. *Angew Chem Int Ed* 53:4578–4581. <https://doi.org/10.1002/anie.201311249>
- Solà J, Fletcher SP, Castellanos A, Clayden J (2010) Nanometer-range communication of stereochemical information by reversible switching of molecular helicity. *Angew Chem Int Ed* 49:6836–6839. <https://doi.org/10.1002/anie.201001130>

- Solà J, Morris GA, Clayden J (2011) Measuring screw-sense preference in a helical oligomer by comparison of ^{13}C NMR signal separation at slow and fast exchange. *J Am Chem Soc* 133:3712–3715. <https://doi.org/10.1021/ja1097034>
- Stankovic CJ, Heinemann SH, Schreiber SL (1991) Photo-modulated ion channels based on covalently linked gramicidins. *Biochim Biophys Acta* 1061:163–170. [https://doi.org/10.1016/0005-2736\(91\)90281-C](https://doi.org/10.1016/0005-2736(91)90281-C)
- Talukdar P, Bollot G, Mareda J, Sakai N, Matile S (2005) Ligand-gated synthetic ion channels. *Chem Eur J* 11:6525–6532. <https://doi.org/10.1002/chem.200500516>
- Tesmer JGG, Sunahara RK, Gilman AG, Sprang SR (1997) Crystal structure of the catalytic domains of adenylyl cyclase in a complex with $\text{G}_{\text{S}\alpha}$ -GTP γ S. *Science* 278:1907–1916. <https://doi.org/10.1126/science.278.5345.1907>
- Tompa P (2016) The principle of conformational signaling. *Chem Soc Rev* 45:4252–4284. <https://doi.org/10.1039/C6CS00011H>
- Toniolo C, Benedetti E (1991) The polypeptide 3_{10} -helix. *Trends Biochem Sci* 16:350–353. [https://doi.org/10.1016/0968-0004\(91\)90142-I](https://doi.org/10.1016/0968-0004(91)90142-I)
- Unwin N (1989) The structure of ion channels in membranes of excitable cells. *Neuron* 3:665–676. [https://doi.org/10.1016/0896-6273\(89\)90235-3](https://doi.org/10.1016/0896-6273(89)90235-3)
- Vanuytsel S, Carniello J, Wallace MI (2019) Artificial signal transduction across membranes. *ChemBioChem* 20:2569–2580. <https://doi.org/10.1002/cbic.201900254>
- Villar G, Graham AD, Bayley H (2013) A tissue-like printed material. *Science* 340:48–52. <https://doi.org/10.1126/science.1229495>
- Webb SJ (2013) Supramolecular approaches to combining membrane transport with adhesion. *Acc Chem Res* 46:2878–2887. <https://doi.org/10.1021/ar400032c>
- Wilson CP, Webb SJ (2008) Palladium(II)-gated ion channels. *Chem Commun* 34:4007–4009. <https://doi.org/10.1039/b809087d>
- Wilson CP, Boglio C, Ma L, Cockroft SL, Webb SJ (2011) Palladium(II)-mediated assembly of biotinylated ion channels. *Chem Eur J* 17:3465–3473. <https://doi.org/10.1002/chem.201002031>
- Woolley GA, Wallace BA (1992) Membrane biology topical review model ion channels: Gramicidin and Alamethicin. *J Membr Biol* 129:109–136. <https://doi.org/10.1007/BF00219508>
- Zheng S-P, Huang L-B, Sun Z, Barboiu M (2021) Self-assembled artificial ion-channels toward natural selection of functions. *Angew Chem Int Ed* 60:566–597. <https://doi.org/10.1002/anie.201915287>
- Zhou Y, Chen Y, Zhu P-P, Si W, Hou J-L, Liu Y (2017) Reversible photo-gated transmembrane channel assembled from an acylhydrazone-containing crown ether triad. *Chem Commun* 53:3681–3684. <https://doi.org/10.1039/c7cc01123g>
- Zhu S, Stein RA, Yoshioka C, Lee C-H, Goehring A, Mchaourab HS, Gouaux E (2016) Mechanism of NMDA receptor inhibition and activation. *Cell* 165:704–714. <https://doi.org/10.1016/j.cell.2016.03.028>

Measuring Ionic Transport Through Lipid Bilayers



Radu Zonda, Sorin-Alexandru Ibanescu, Mihaela Silion, Adina Coroaba, Dragos-Lucian Isac, Marc J. M. Abadie, and Mariana Pinteala

Abstract Natural ion channels are of outstanding importance in all living cells. Based on them more and more artificial ion channels are prepared for many biomedical and bioengineering applications, separation devices, environmental monitoring, food safety and so on. Moreover, the comprehensive study of their mechanism of action can lead to deep understanding of life at the cellular level. Unfortunately, ion transport across lipid bilayer membranes is an elusive phenomena difficult to evidence. This review focuses on the main techniques suitable to evidence it starting from liposomes as biomimetic model for the cellular membrane and going to the use of fluorescence spectroscopy to study membrane active molecules.

Keywords Ion transport · Lipid bilayers · Liposomes · Fluorescence spectroscopy

Abbreviations

AFM	Atomic force microscopy
ATP	Adenosine triphosphate
BLM	Black lipid membrane
CD	Circular dichroism
CL	Cardiolipin
CH	Cholesterol
DAG	Diacylglycerol
DLPC	1,2-Dilauroyl-sn-glycero-3-phosphocholine
DPPC	Dipalmitoylphosphatidylcholine
DLS	Dynamic Light Scattering
EC ₅₀	Effective concentration
GUV	Giant unilamellar vesicles

R. Zonda · S.-A. Ibanescu · M. Silion · A. Coroaba (✉) · D.-L. Isac · M. J. M. Abadie · M. Pinteala

Centre of Advanced Research in Bionanoconjugates and Biopolymers, “Petru Poni” Institute of Macromolecular Chemistry, 700487 Iasi, Romania

e-mail: adina.coroaba@icmpp.ro

HPTS	8-Hydroxypyrene-1,3,6-trisulfonic acid
QCM-D	Quartz crystal microbalance with dissipation
LUV	Large unilamellar vesicles
PBS	Phosphate-buffered saline
PC	Phosphatidylcholine
PE	Phosphatidylethanolamine
PS	Phosphatidylserine
PI	Phosphatidylinositol
PG	Phosphatidylglycerol
PBC	Planar bilayer conductance
SAXS	Small-angle X-ray scattering
SEC	Size exclusion chromatography
SEM	Scanning electron microscopy
SLM	Supported lipid membranes
SUV	Small unilamellar vesicles
TEM	Transmission electron microscopy

1 Introduction

For living beings in nature, ion transport plays an essential role, ensuring the electrolyte balance of cells. The ion channel that is a molecule or a system of molecules crossing the cell membrane able to selectively transport ion species from one side of the cell membrane to another represents the driving force for ion transport. The comprehensive study of ion channels allowed deep understanding of life at the cellular level. Researchers such as Kenneth Cole (Cole 1939), Alan Hodgkin and Andrew Huxley (Hodgkin and Huxley 1952) or Erwin Neher and Bert Sakmann, who also won the Nobel Prize in 1991 or Masaharu Noda (Noda et al. 1983a,1984), Irwin Levitan (Levitan 1985) or Declan Doyle (Doyle et al. 1998) continued their pioneering work in the discovery and investigation of ion channels.

Natural ion channels, taken out of the context of purely biological function, can be adapted to the requirements of the laboratory or of the industrial, pharmaceutical, etc. environment, by functionalization or various other modifications. Isolation of natural ion channels can be a difficult process, hence necessitating laboratory restoration (Biron et al. 2004). The difference between artificial and natural channels is thus distorted; it cannot be clearly decided the degree of proteins modification necessary to make them artificial. Supramolecular chemistry offers the opportunity to build artificial ion channels from simpler, cheaper and easier to integrate molecules into self-assembling systems (Lu et al. 2020; Sun and Barboiu 2019; Fang et al. 2019).

Selective ion transport lies beneath many systems for different applications, from detection or separation devices (Dyer et al. 2000; Strathmann 2005) of different chemical species (Kim et al. 2018; Calvo and Otero 2008; Steller et al. 2012), to the study of biological phenomena involving ion migrations (Williamson et al. 2003; Gonen and Walz 2006; Bezaniilla 2008).

Taking all this into account this chapter aims to present several principles and molecules used for ion transport across lipid bilayers, with focus on the main techniques suitable to evidence their ion transport properties. Starting from the function of the natural cellular membranes this work reviews several strategies to prepare artificial lipid bilayers and characterize them. The last part presents the most used analytical techniques available to estimate the ion transport across lipid bilayers explaining the most important parameters that can be obtained from them.

1.1 Channel Types

In nature there is a multitude of molecular constructions which fulfill the role of ion channels in the cell membrane. Natural ion channels are regulated through complex mechanisms by the biological system in which they are contained, and their isolation for the purpose of individual study or application in an artificial setting might alter their functionality. Thus, their structure needs to be modified to a greater or lesser (Renart et al. 2020) extent in order to adjust to the conditions of the new system. In this way the difference between the artificial and the natural channels is diminished, making it difficult to establish at which extent of modification certain compounds can be called artificial. Of course, entirely artificial ion channels do exist, and they are obtained by new molecules, which reproduce the functions of natural ion channels (Zheng et al. 2020; Muraoka et al. 2020).

Depending on their morphology, ion channels can be divided into unimolecular channels and ion channels formed by self-assembly of several molecules.

Even though they are composed of only one molecule, unimolecular ion channels have the ability of intramolecular self-assembly to form a stable structure which can cross the membrane and is capable of selective ion transport. Crown ethers (Fyles 2007) and *pillar-arene* (Hu et al. 2012) based compounds are examples for this type of channels (Fig. 1).

Whether formed of a single or more molecules, the composing units tend to associate in supramolecular structures to form channels of different types. Depending on the association of different component units, the following forms of channels can be distinguished (Fig. 2a): compact, barrel-stave, barrel-hoop, barrel-rozette and micellar (Schalley 2012; Malla et al. 2020a). An example of *barrel stave* self-assembly is presented in Fig. 2b.

These structures are based on non-covalent intermolecular interactions, that are most often in a dynamic monomer/supramolecular structure equilibrium influenced by environmental conditions. Many structures have been developed to have selective ion transport through lipid bilayers. Table 1 presents several examples of molecules used to form ion channels and method used to study their activity.

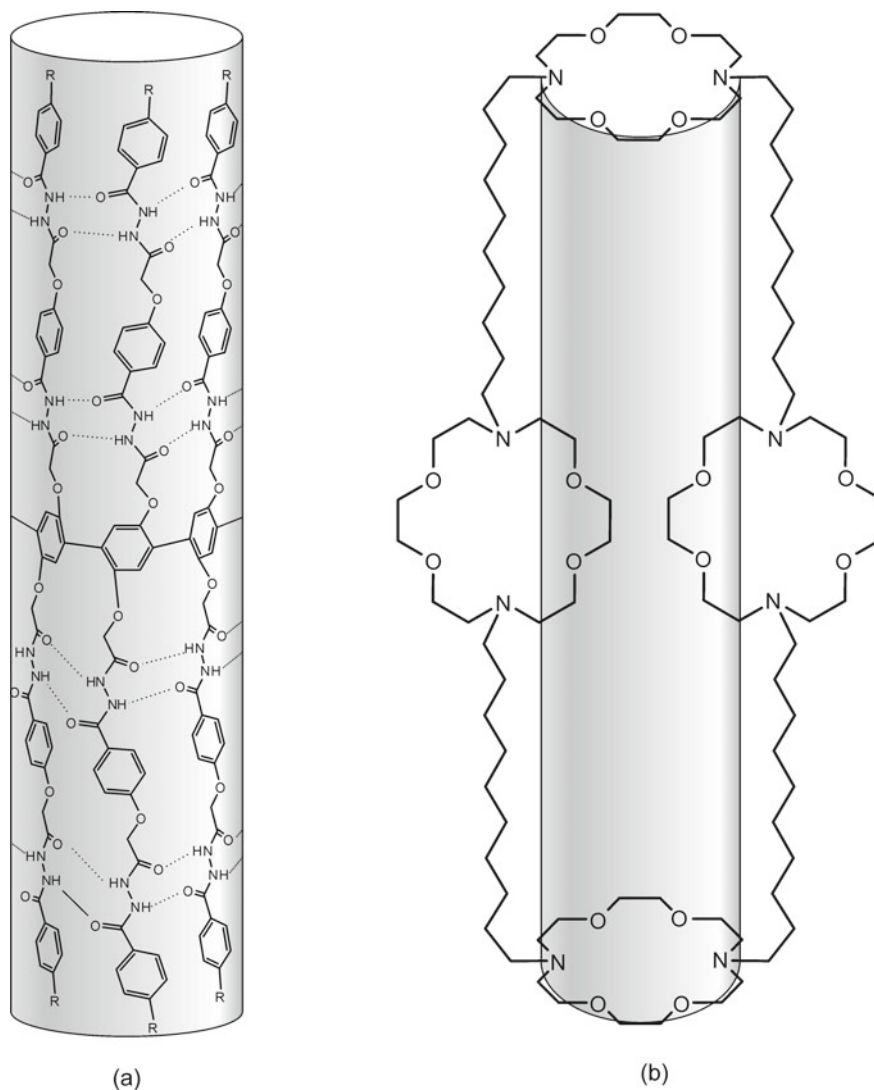
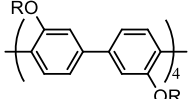


Fig. 1 Unimolecular channels based on *pillar-arenes* (a) and *crown ethers* (b)

1.2 Assessment of Water and Ion Transport Through Double Layer Lipid Membranes

In artificial solid membranes transport mechanisms depend only on the membrane's porosity or, in the case of compact membranes, the transport is accomplished by dialysis. However, in double layer lipid membranes, simple diffusion across the membrane is not a definitive phenomenon for the transport of chemical species, and

Table 1 Structure of natural and artificial ion channels and methods used to test their activity

Ion channel	Ion transport method of investigation	Reference
Natural ion channels		
Gramicidin	Planar Bilayer Conductance (PBC) assay	Ashrafuzzaman et al. (2008); Hladky and Haydon (1972)
	HPTS assay	Shen et al. (2020)
KcsA (Potassium channel of streptomyces A)	PBC assay	Thompson et al. (2008)
Fluc family channels	PBC assay Light Scattering Assay of F – Efflux	Last et al. (2017); Stockbridge et al. (2012)
Artificial ion channels		
Alkyl-benzoureido-crown-ethers	HPTS assay	Gilles and Barboiu (2016); Zonda et al. (2018)
Columnar self-assemblies of triarylamin derivatives	HPTS assay, PBC assay	Schneider et al. (2017)
Peptaibol-mimetic Aib foldamers	HPTS assay PBC assay	Adam et al. (2018)
3 ₁₀ -Helical α -Aminoisobutyric Acid Foldamers	HPTS assay PBC assay	Jones et al. (2016)
Hydrazide-appended pillar[5]arene derivatives (Fig. 1a)	HPTS assay	Hu et al. (2012)
2-hydroxy-N1, N3-diarylisophthalamide-based compounds	HPTS assay PBC assay	Malla et al. (2020b)
Polyhydrazide-Based Organic Nanotubes	HPTS assay PBC assay	Roy et al. (2020)
Narrow Diameter Carbon Nanotube Porins	Stopped flow assay	Li et al. (2020)
Potassium-templated self-assembly of 50 -guanosine monophosphate	Pore activity by circular dichroism	Hennig and Matile (2008)
Dendritic Folate Rosettes	HPTS assay PBC assay	Sakai et al. (2006)
Rigid-Rod Molecules based arenes backbone  R = peptide, crown ether	HPTS assay PBC assay	Sakai and Matile (2002); Sakai et al. (2001)

the pores are not a constitutive part of the membrane, but mostly mediators that promote transport. These mediators are involved in two types of transport – active and passive.

1. In *passive transport*, the mediators form channels or pores in the lipid membrane and specifically allow the transported species to cross spontaneously the membrane, in order to compensate the entropy gradient between the two sides. The transport may occur directly through the structure/mass of the membrane, or it can be mediated by various molecules, through pores, water or ion channels or a carrier mechanism.
2. *Active transport* relies on a complex mechanism by which a certain chemical species is shifted from one side of the membrane to the other with energy consumption from the mediator molecule. Usually active transport occurs against the concentration gradient. In nature there are two variations – primary active transport, promoted by ATP (adenosine triphosphate) and secondary active transport, which relies on the existence of an electrochemical gradient.

2 Lipid Bilayers

2.1 Natural Lipid Bilayers - Cell Membrane

The cell membrane plays a key role in the existence and functioning of the cell, ensuring its integrity and at the same time allowing selective exchange between the interior and exterior of the cell. The cellular wall has a complex structure, but at its base lies the double layer lipid membrane. The cellular membrane is a complex structure made of phospholipids - compounds formed by a glycerin unit which usually binds two chains of fatty acids (diacylglycerol - DAG) and a phosphate group with a polar group like choline attached to it (Fig. 3a). The two aliphatic chains form a hydrophobic tail, and with the phosphoric end representing the hydrophilic part, the molecule has an amphipathic behavior. Amphipathic molecules tend to self-organize in an aqueous environment in micelles or vesicles. Micelles are globular formations consisting of molecules oriented with their hydrophilic side towards the outer aqueous environment, and the hydrophobic end inwards. The vesicles have a double layer membrane, with the phospholipids oriented with their hydrophobic tail towards the interior, and the hydrophilic side towards the exterior to the aqueous environment (Fig. 3b). The aqueous medium of the vesicle may differ by the outer aqueous environment.

The cellular membrane contains several phospholipid species, which differ by both the length of the fatty acid chain and the nature of the polar group. Thus, the aliphatic chains that form the hydrophobic tail regularly contain 14 to 24 carbon atoms and can be either saturated or unsaturated. The presence of the unsaturated bonds may generate cis-trans isomers. Both the cis-trans isomerism and the length of the chain can influence the properties of the membrane (Meer et al. 2008; Harayama and

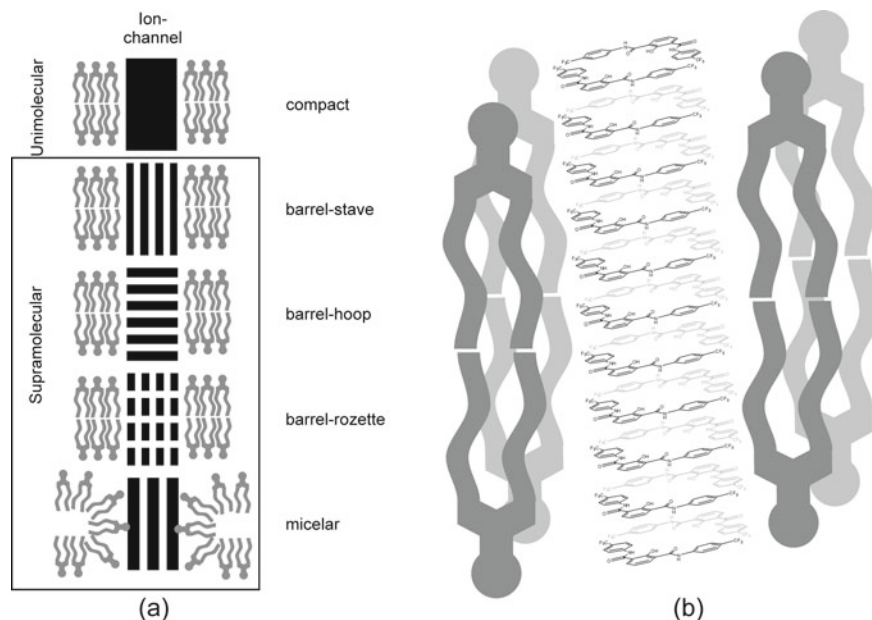


Fig. 2 (a) Pore structure depending on the supramolecular association of composing units; (b) Example of self-assembling barrel-rozette synthetic pore from 2-hydroxy-N1,N3-bis[4-(trifluoromethyl)phenyl]benzene-1,3-dicarboxamide monomer

Riezman 2018). The phospholipid composition of the cell membrane significantly differs from one cell type to another. Thus, most eukaryotic cellular membranes generally contain phosphatidylcholine (PC), phosphatidylethanolamine (PE), phosphatidylserine (PS) and phosphatidylinositol (PI). In some cell types the membrane is asymmetric, the two lipid layers having different compositions. This feature has been studied mainly in erythrocyte (Kahlenberg et al. 1974). Besides phospholipids, the cellular membrane contains other chemical species such as cholesterol (CH), sugars, proteins (Fig. 4) (Cooper and Hausman 2007).

Diversity in the structure of the cellular membrane is also seen in prokaryotes. Thus, the Gram-positive bacteria wall is mainly made of anionic lipids like phosphatidylglycerol (PG) and cardiolipin (CL) and only a small amount of zwitterionic lipids like PE. In the case of Gram-negative bacteria the proportion is reversed, zwitterionic lipids being dominant (Table 2) (Gabriel et al. 2007).

Table 2 Distribution of the lipids in the membrane of different type of cells

Cell type	PC (%)	PE (%)	PG (%)	PS (%)	CL (%)	CH (%)
<i>E. coli</i> (Gram-negative)	–	80	20	–	5	–
<i>S. aureus</i> (Gram-positive)	–	–	57	–	43	–
Erythrocytes (exterior layer)	33	9	–	–	–	25
Erythrocytes (interior layer)	10	25	–	10	–	–

2.2 Artificial Lipid Bilayers

2.2.1 Spherical – Liposomes

Liposomes are the most used systems in the study of lipid bilayer membranes. They are defined as spherical vesicles with a diameter ranging from 30 nm to several microns (Akbarzadeh et al. 2013). Liposomes are formed by one or more bilayer lipid membranes usually dispersed in aqueous environment. Their organization is biomimetic similar to that of the cellular membrane. This makes them ideal for the simulation of membrane biologic processes but they can also be used as carrier for active compounds, due to their high biocompatibility, or even as sensors for the detection of certain chemical species. One advantage of using liposomes is avoiding the biological risks involved in using bacterial cells, for example in the study of antimicrobial peptides (Gabriel et al. 2007; Pinheiro et al. 2019). Other advantages come for their high reproducibility and ease of manipulation.

Regarding their structure, liposomes can be unilamellar, with a single bilayer lipid membrane (Fig. 5a), multilamellar with concentric lipid membranes distribution, alternating the lipid layer with aqueous medium (Fig. 5b) or multivesicular when they are composed from vesicles including other vesicles (Fig. 5c) (Akbarzadeh et al. 2013).

Their size is a key parameter for practical applications, generally being divided into (Stein et al. 2017):

- *Giant Unilamellar Vesicles* (GUV) with a diameter over 1 μm ;
- *Large Unilamellar Vesicles* (LUV) with diameter between 100 and 1000 nm;
- *Small Unilamellar Vesicles* (SUV) with a diameter less than 100 nm.

Depending on their structure, application and desired size there are different methods of liposome preparation, generally involving four main steps: drying the lipids, their dispersion in water, purification and characterization.

Drying Down Lipids from Organic Solvent

Commercially available lipids usually come as methanol or chloroform solutions and are dried generally using a rotary evaporator system to form a lipid film. Several common lipids used in the preparation of membranes are: phospholipids, glycolipids, fatty acids, glycerophospholipid, sphingolipid and sterols (Li et al. 2015). The most

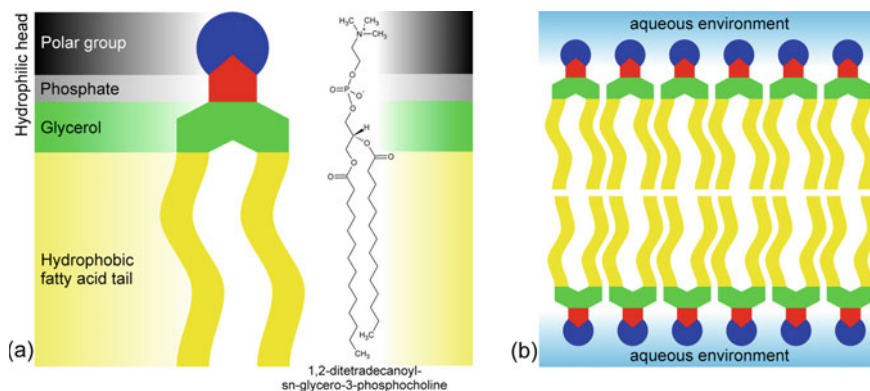


Fig. 3 (a) The structure of a phospholipid molecule together with an example (1,2-ditetradecanoyl-sn-glycero-3-phosphocholine); (b) Arrangement of the phospholipids within the double layer lipid membrane

used are phospholipids especially phosphatidylcholine, phosphatidylethanolamine, phosphatidylinositol and phosphatidylserine.

Dispersing the Lipid in Aqueous Media

This stage is the most important one determining the type of final liposome. Several methods can be used to achieve this goal, generally divided into mechanical methods such as sonication, extrusion through French pressure cell extrusion or freeze-thaw cycles, and solvent assisted methods such as injection from ether or ethanol and reverse phase evaporation (Akbarzadeh et al. 2013). Liposomes are prepared by using one or combinations of more of the above mentioned methods.

When *sonication* is involved this operation can be performed either by using a bath sonicator or a probe sonicator. The liposomes obtained by this method are usually small (SUV). This method, although easy to use, has several disadvantages such as low yield for the vesicles due to the high probability for membrane degradation, hazard of contamination with metals from the sonication probe as well as a high number of multilamellar vesicles remaining in the vesicle suspension (Akbarzadeh et al. 2013). Also, when it is desired to incorporate molecules such as proteins in the lipid bilayer there is a risk of denaturation through energy transfer (Mayer et al. 1986). Obtaining liposomes by *extrusion* involves passing the redispersed lipid solution through a polycarbonate membrane with a known porosity (Riaz 1996) generally leading to LUVs (Anwekar et al. 2011). When proteins are involved, this method avoids the risk of their denaturation. The *freeze thaw cycles* of vesicles is recommended to obtain LUVs by SUVs fusion. This method has limitation in regard to the phospholipid concentration and ionic strength of the environment (Pick 1981).

The *solvent assisted method* involves the rapid injection of lipid solution in an organic solvent to the aqueous media followed by the removal of the organic solvent and the formation of the liposomes. Usual solvents are diethyl ether, diethyl ether/methanol mixture, ethanol, isopropyl ether or isopropyl ether/chloroform

mixture. Generally, the ether route supposes slow injection of the organic phase with fast solvent removal, at 55 °C to 65 °C, leading to a heterogenous liposomal population between 70 to 200 nm (Deamer and Bangham 1976; Schieren et al. 1978). The ethanol route supposes the fast addition of the lipid solution, at a very low ratio, to the aqueous media. This produces a very dilute solution of smaller liposomes, between 30 to 110 nm. The fact that ethanol and water form an azeotrope creates the risk of contamination of the final liposome with ethanol (Batzri and Korn 1973). The reverse phase evaporation route uses a high excess of organic phase to the aqueous media, leading in a first step to the formation of inversed micelles. The slow evaporation of the solvent determines the formation of a gel and when even more solvent is removed the gel collapses and the excess lipids completes the bilayer. This method represented a big advancement in solvent assisted techniques, making achievable highly concentrated liposome suspensions (Anwekar et al. 2011).

Liposome Purification

Separation of liposomes from the medium in which they were constructed, which contains the same elements both inside and outside of the liposomes, is essential in order to obtain a high quality liposomes suspension. The most commonly used methods for purification of liposomes suspensions are centrifugation, ultrafiltration, dialysis and size exclusion chromatography (SEC).

Centrifugation is the easiest and readily available method for separation of liposomes. It is based on the density difference between the liposome and outer medium. The solution containing the liposomes is centrifuged at high speed (approximately 10,000 g) for 30 s to a few minutes, until the liposomes drop to the bottom of the recipient, then the supernatant is removed. The liposomes are resuspended in an isotonic solution free of stain or other elements contained in them. This technique has the advantage of being fast, but it also has some disadvantages. The density difference between the liposome and the exterior environment, usually aqueous, is not significant (density of phosphatidylcholine is 1.08 mmol/L (Schmitz et al. 1983)), hence the difficulty of narrowing the density gradient of the liposomes, yielding a low separation efficiency. Another problem is represented by destructureation of liposomes caused by the high centrifuge force. This method is used mainly for purification of liposomes derived from red blood cells or other natural cell types (Schwoch and Passow 1973; Hu et al. 2011).

Ultrafiltration of the liposomes containing suspension is performed by centrifugation using special column membranes. Due to the centrifuge force, the liquid surrounding the liposomes is pushed through the membrane and the liposomes remain inside the column, and are subsequently recovered and resuspended in a fresh solution. Comparing with centrifugation, this technique has the advantage of a superior separation, but all the other disadvantages mentioned above remain.

Dialysis is a method of purification that uses the osmotic pressure difference existing between two liquid media separated by a specific membrane. It is less commonly used due to the prolonged necessary time, which causes structural modifications of the liposomal membrane or loss of content from the liposome inner

medium. It is usually used for purification of liposomes conceived for controlled release, because these are designed to be more resistant over time.

Separation by SEC is the most frequently used purification method especially for fluorescent marked liposomes. It has the advantage of being fast, selective and minimally invasive to the liposomes. It is based on the difference in size of the particles (including fluorophores) contained in the solution of liposomes, passed through a column with controlled porosity (with pores smaller in diameter than the liposomes). The smaller particles will enter deep into the pores and will flow more slowly, meanwhile the larger components, like the liposomes, will flow more rapidly through the column, as they do not penetrate the pores. Thus, the separation is accomplished due to the difference of the speed at which the solution components pass through the chromatography column. The most frequently used columns are those with Sephadex (Gilles and Barboiu 2016) or dextran (Zonda et al. 2018).

Analyzing the Final Product

The last step in liposome preparation is to verify the quality of the final product. There are few analytical techniques suited for achieving this purpose. Dynamic Light Scattering (DLS) can be used to study the size and dimensional polydispersity of the liposomes and several imaging methods can give local information about morphology and topography of the obtained membranes (Bibi et al. 2011).

DSL analysis is generally recommended in the study of monodisperse particles because in highly polydisperse systems smaller particles can go undetected (Goreham et al. 2019). This makes DLS suited for the measurement of liposomes size and stability in time but not for detecting released particles (Saha et al. 2018).

Figure 6 offers a suggestive overview on the scale of detection ability offered by different microscopical methods. *Classical optical microscopy* uses only visible light to generate magnified images. In this way information about the shape and homogeneity of liposome suspensions can be obtained. Unfortunately the scale does not allow observation of changes in the structure of the lipid membrane but images of multilamellar liposomes were obtained (Nallamotheu et al. 2006). *Polarized light microscopy* takes advantage of the special interaction between polarized light and polarizable bonds in ordered molecules (Murphy and Davidson 2012). Liposomes are very well suited for this type of analysis since the polarized light perpendicularly crossing the lamellar wall interferes with each different layer creating the so called “Maltese cross” as result of lipid birefringence (Placzek and Kosela 2016). *Fluorescence microscopy* is widely used in the study of liposomes offering information about the structure and dynamic of the membranes (Bouvrais et al. 2010) but it requires the use of fluorescent markers (Bibi et al. 2011; Murphy and Davidson 2012; Bouvrais et al. 2010). The *time lapse* technique, developed in the late '90s, allows monitoring of enzymatic processes inside vesicles in real time (Wick et al. 1996). *Confocal microscopy* can build tridimensional images from scanning multiple in depth layers, making possible vesicle visualization from all angles. Using this method it was possible to observe two distinct coexisting phases in liposomes made from 1,2-dilauroyl-sn-glycero-3-phosphocholine (DLPC), Dipalmitoylphosphatidylcholine (DPPC) and cholesterol (Korlach et al. 1999).

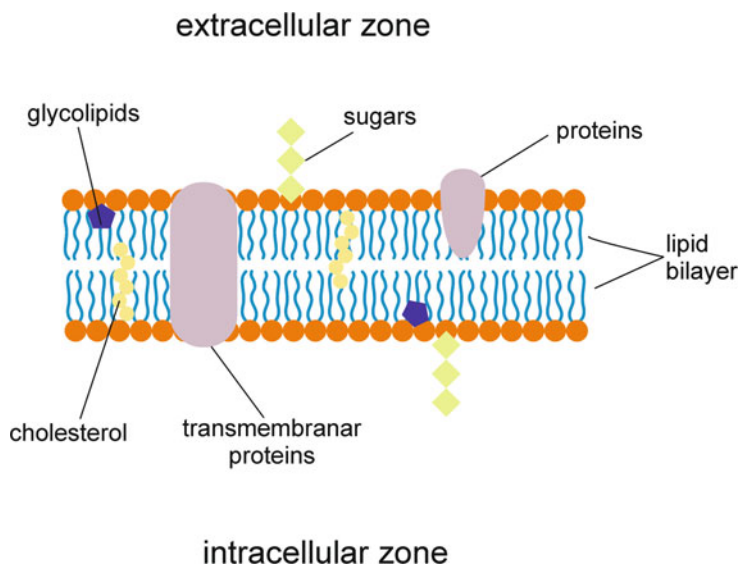


Fig. 4 Generic structure of the cellular membrane

The high vacuum used in *electron microscopy* techniques makes them difficult to use on liposomal systems. Even so there are few special approaches to visualize vesicles by using these methods, Fig. 7 showing some examples (Bibi et al. 2011). In *Transmission Electron Microscopy (TEM)* the use of contrast markers for the medium allowed visualization of vesicles (Bibi et al. 2011; Placzek and Kosela 2016). Also sample manipulation or deposition such as *CryoTEM* or *Cryofracture* made it possible to obtain clear images of liposomes. Advances in *Scanning Electron Microscopy (SEM)* such as *Environmental SEM* made it possible to record images in aqueous environment circumventing some of the limitation in the liposome visualization of the classical technique (Ruozi et al. 2011; Dragnevski and Donald 2008). In *Atomic Force Microscopy (AFM)* tridimensional images with good topographic contrast can be obtained without major environmental limitations and sample preparation. This could represent a good alternative to electron microscopy methods but there is the risk of liposome deformation caused by the interaction between the cantilever and the vesicle (Ruozi et al. 2011).

2.2.2 Planar Membranes

In the study of lipid membranes bilayers processes an alternative to liposomes are planar membranes (Steller et al. 2012). They allow the use of other analysis techniques, not applicable for suspensions, such as conductivity measurements in the *patch clamp* method for the evaluation of ion transport (described in Sect. 3.4) or Quartz Crystal Microbalance with Dissipation (QCM-D) for the study of membrane

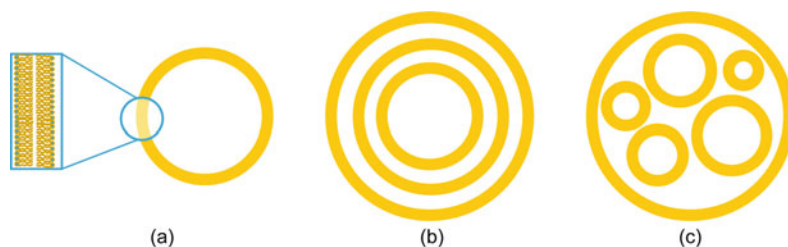


Fig. 5 Schematic representation of liposomes: (a) unilamellar (zoom the the organization of the lipid bilayer); (b) multilamellar; (c) multivesicular

active molecules (McCubbin et al. 2011). Another advantage of planar membranes over liposomes is the ability to better control their properties such as size and lamellarity (Suzuki and Takeuchi 2008). On the other hand, they lack the possibility to entrap molecules as they don't present a tridimensional model and the molecules to be tested may be directly exposed to the environment (Bally et al. 2010). There are several ways to prepare planar lipid bilayers with the most common ones being black lipid membrane (BLM) whose name comes from its opaque appearance. They were first discovered by Mueller and Rudin (Mueller and Rudin 1963; Mueller et al. 1962) and they are usually formed by brushing a solution of lipids (in pentane, decane, hexadecane or mixture of ethanol, methanol with chloroform, pentane, decane, hexadecane) over the gap separating two chambers to be later filled with the aqueous phase. Measuring a change of property for one of the chambers to the other gives information about the membrane. The disadvantage of these type of membranes is their poor stability, corrected by supported lipid membranes (SLM). These are usually formed by bursting GUV from aqueous solution on top of a surface such as microporous polymer films if the transport through the membrane is of interest (Touaj et al. 2009), or glass if the change in the membrane is of interest. Also lipids can be transferred to the surface from the air-water interface by the Langmuir–Blodgett technique (Florin and Gaub 1993; Plant et al. 1994). SLM can be analyzed by AFM or QCM-D. It is also possible to form tethered bilayer lipid membranes (t-BLM) by using lipids modified at the hydrophilic end with a reactive group such as thiols or disulfide. These can react with gold surfaces to create the hydrophobic environment necessary to form the lipid bilayer (Baumgart et al. 2003; Schiller et al. 2003).

3 Assessment of Ion Transport

Depending on the properties of the transported species or the nature of the transport phenomenon, there are several ways to assess transport through lipid membranes.

3.1 Assessment of Ion Transport by Fluorescence Spectroscopy

This method implies using LUV vesicles which contain a fluorophore sensitive to specific environmental factors (pH, concentration, redox etc.) and it is generally employed for the study of ion channels. Its basic principle is represented by detection of variation in a parameter like pH within the vesicle when ion transport occurs. The most used fluorophores are 8-hydroxy-1,3,6-piren trisulfonate (HTPS), 8 aminonaphthalene-1,3,6-trisulfonat (ANTS), 5(6)-carboxyfluorescein (CF) or Safranin O.

This assay relies on the equilibrium between the protonate and the deprotonate form of the fluorophore and its capacity to change its fluorescence properties by shifting from one form to the other. Therefore, the method requires a fluorimeter capable to measure the intensities of light emitted by the two species, depending on the different wave length of the corresponding exciting beam, with a high enough frequency to allow the approximation of the two measurements as being concomitant (Fig. 8). The intensity of the emitted beam corresponding to the two forms of the fluorophore (I_1 - protonated and I_2 - deprotonated) is measured and the ratio (I_1/I_2) is calculated, followed by the calculation of the pH of the environment containing the fluorophore.

The gold standard fluorophore for analysis of ionic transport by detection of pH shifting within the liposomes is HPTS, due to its excellent water solubility and value

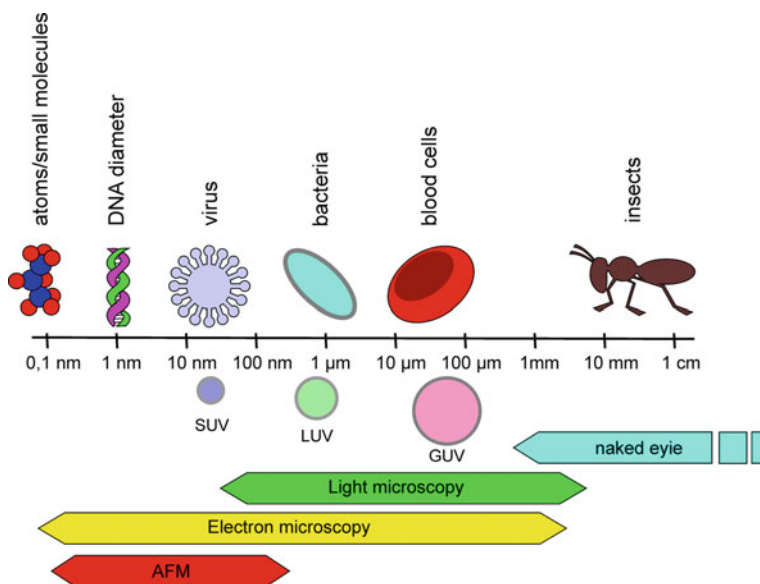


Fig. 6 Correlation between magnification scale of different microscopic methods and the dimension of some biological entities and liposomes

of acid-base dissociation constant (pKa) of approximately 7.3, which permits its inclusion in biomimetic systems.

Assessment of ion transport by HPTS consists of several experimental steps (Fig. 9) (Zonda et al. 2018). The evolution of the I_1/I_2 ratio is monitored through the entire assay. First (t_0), the liposomes suspension is homogenized and stabilized by gentle agitation. After homogenization, at t_1 , the compound evaluated as mediator for ion transport is added to the liposomes suspension. At this time, a change in the I_1/I_2 ratio can be observed as a result of a spontaneous transport. Until the system is stabilized, a step of a few dozen seconds for homogenization should be introduced. At t_2 an aqueous solution containing a strong base or acid is added, with a concentration and volume calculated in order to modify the pH of the liposomes outer environment by one unit. The pH difference causes migration of ions through the liposome membrane in the direction of pH gradient compensation. As a result of this transport, the inner pH of the liposomes changes, and this is reflected in the modification of the I_1/I_2 ratio. At t_3 , empirically determined, a detergent, usually Triton $\times 100$, is added to induce lysis of the liposomes and to determine the I_1/I_2 ratio at the final pH of the outer solution, to be used as reference of the maximum/minimum pH level of the system. After a waiting period of a few dozen seconds for system stabilization, the experiment is ended, at t_4 . The experiment is repeated for different concentrations of the transport mediator in the liposomes suspension.

The outer pH is considered not to be influenced by the ion exchange. The pH within the vesicle is calculated from the time versus I_1/I_2 plot. The formula is obtained after calibrating the intensity of the HPTS emission corresponding to the protonated (I_1) and deprotonated form (I_2) respectively.

$$pH = 1.1684 \times \log(I_1/I_2) + 6.9807$$

The formula is based on the Henderson-Hasselbalch (Paxton et al. 2013) relation and represents the result of the I_1/I_2 calibration in PBS for different pH values, as shown in Fig. 10.

Several important parameters can be extracted from these measurements:

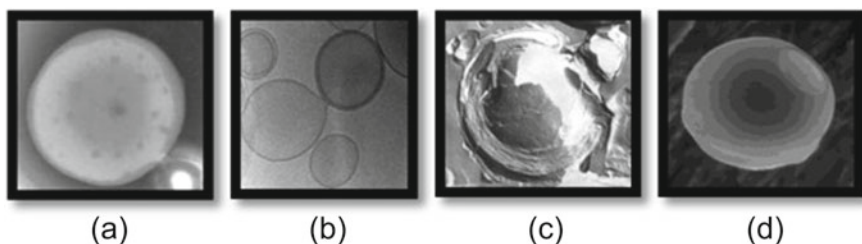


Fig. 7 Vesical images acquired by different electron microscopy techniques (a) TEM (b) Cryo-TEM (c) Cryofracture (d) ESEM. Reproduced from International Journal of Pharmaceutics; Bibi, S. et al., Microscopy imaging of liposomes: From coverslips to environmental SEM, 417, 138–150. Copyright 2011, with permission from Elsevier (Bibi et al. 2011)

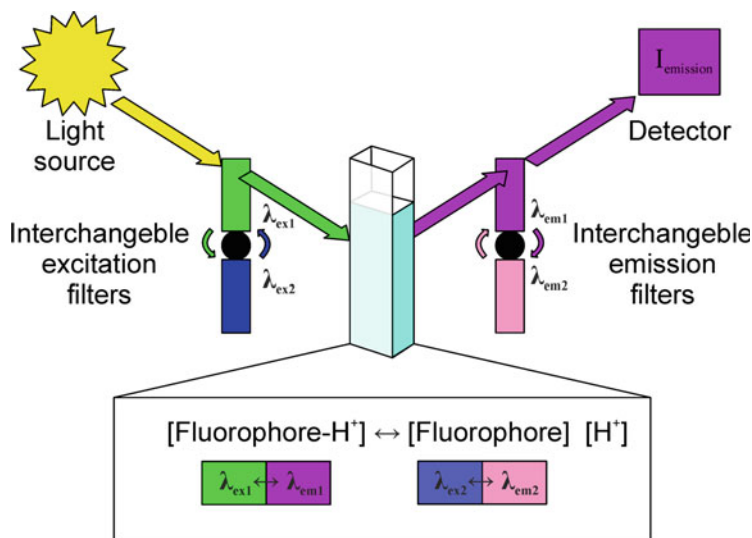


Fig. 8 Schematic representation of the principle used in the pH evaluation by fluorimetric method

The pseudo-first-order rate constant (k) provides information about the kinetics of ion transport through the lipid membrane. Taking into account that the ion transport speed can be determined only indirectly, by monitoring the pH value within the vesicle, the kinetics of the process is expressed as a function of H^+ concentration, suggesting a pseudo-first-order kinetics. Thus, k is calculated from the section immediately following the application of the pH gradient, taking into consideration only the linear area of pH increase. A high value of k reflects a more rapid transport of ions through the lipid membrane.

Fractional activity (Y) is used to compare the ion transport activity based on concentration. It is calculated by the normalization of the fluorescence intensity before the lysis of the liposomes, depending on the concentration of the compound used, considering 0 for blank intensity and 1 for the value corresponding to the highest mediator concentrations that have already reached a maximum constant value. The fractional activity can be expressed under the form of a Hill equation, by plotting $\lg(Y)$ as a function of the concentration. Thus, it is possible to calculate the effective concentration (EC_{50}) as being the intercept between the line and the concentration axis and the Hill coefficient (n) as the slope.

Effective concentration (EC_{50}) represents the concentration required to achieve 50% of the transport activity (Schalley 2012; Gilles and Barboiu 2016; Zonda et al. 2018). EC_{50} assesses the efficiency of the transport process. It is preferable that a smaller concentration of compound to accomplish a high transport. The smaller the EC_{50} value, the more efficient is the transport.

Hill coefficient (n) provides information on the efficiency of cooperation between different part of the transport mechanism. The response of the ion channel to different

chemical stimuli such as variation of the pH is usually in gating/blockage the ion transport. Hill coefficient describes the number of molecules necessary for transport. Ion channels have a discontinuous dynamic action, determined by several factors, like the quantity of mediator integrated in the membrane, supramolecular association of the mediator for ion channels formation, thermodynamic activation of the ion channels or mediator-transported ion interaction. The Hill coefficient connects all these phenomena, generating an overview of the entire transport mechanism.

3.2 Leakage Test

Leakage-test is a fluorimetric method that detects massive leakage of the vesicles content. For this purpose, a self-inhibiting fluorophore like carboxyfluorescein or calcein is introduced into the vesicles. In the vesicles, the fluorophore reaches concentrations high enough for self-inhibition to occur. Loss of vesicle content in the outer environment leads to the release of the fluorophore from the liposome and its consecutive dilution, resulting in the disappearance of self-inhibition. Detection of fluorescence signals the occurrence of non-selective pores or vesicles lysis (Fig. 11).

Leakage test is necessary for the verification of existence of false-positive signals in ion channels transport testing experiments. This is a complementary and also a necessary test for checking unexpected massive leakages through the lipidic membrane, independent from the ion channel transport. This test is also used for other experiments, such as integrity tests of the liposomal membrane.

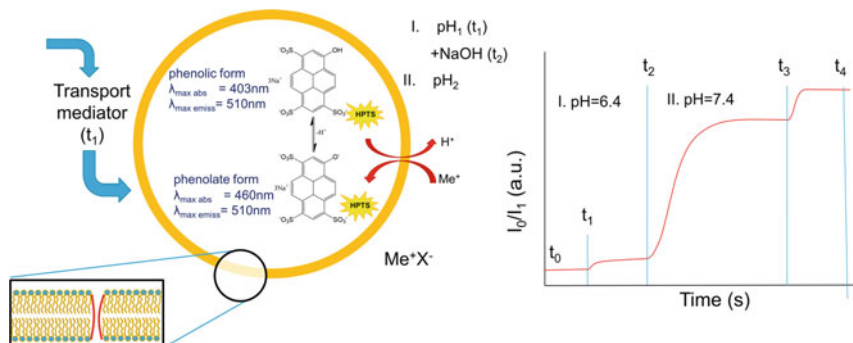


Fig. 9 Principle of the cationic transport assay by HTPS

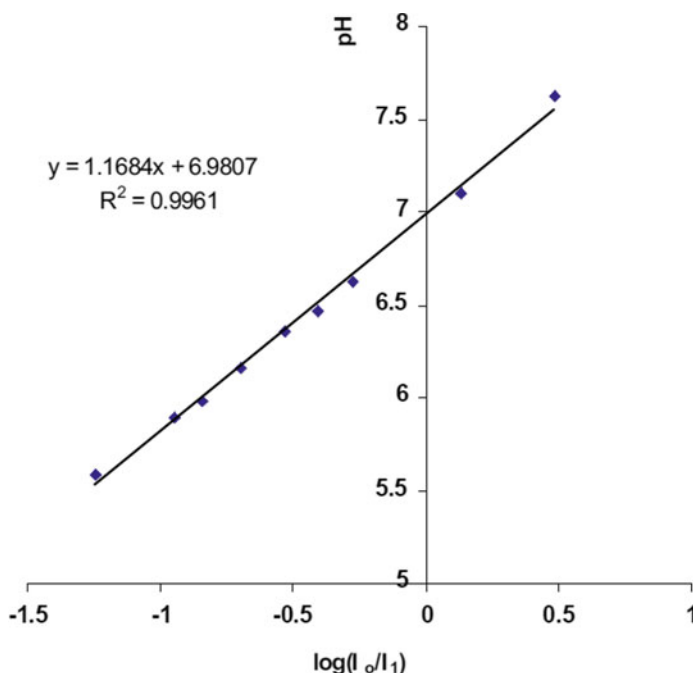


Fig. 10 HPTS calibration curve based on emission intensity ratio for different pH values. Adapted with permission from Chloride transport across lipid bilayers and transmembrane potential induction by an oligophenoxyacetamide; (Sidorov et al. 2003) Copyright 2003 American Chemical Society (Sidorov et al. 2003)

3.3 Analysis of Lipid Membrane Permeability by Stopped-Flow Method

This technique is based on the rapid mixing of the vesicles solution with another solution that abruptly modifies a parameter from outside the vesicle (concentration, osmotic pressure etc.), which would determine the migration of a species through the lipid membrane to compensate the difference between the interior and exterior. Depending on the type of the detector, there are several analysis techniques:

- Light diffusion and circular dichroism (CD) (Licsandru et al. 2016)
- Fluorescence spectroscopy (Posson et al. 2018)
- Small-angle X-ray scattering (SAXS) (West et al. 2008)

This is the most common method in testing the water transport through liposomal membrane (Licsandru et al. 2016). In this case, an abruptly difference of osmotic pressure is applied from outside to inside of liposome, that determine a migration of the water molecules through membrane to the interior of the vesicles, where the osmotic pressure is bigger, in order to compensate the difference. Thus, an increase

of the size of the liposome is detected by light diffusion device and makes possible to calculate the permeability by the follow relation:

$$P_f = \frac{k}{\frac{S}{V_0} * V_w * \Delta_{osm}}$$

where P_f = membrane permeability.

k = exponential coefficient of the change in the light scattering.

S = vesicle surface.

V_0 = initial volume of the vesicle.

V_w = water molar volume.

Δ_{osm} = difference of the induced osmolarity.

Imidazole derivatives are good candidates for mediating water transport through lipid membranes (Licsandru et al. 2016; Leduc et al. 2011). Licsandru et al. compared self-assembled water channels formed by optical active derivative of imidazole and non-chiral alkyl imidazoles using stopped flow assay. They observed in this way a better transport rate of optical active compounds due to the steric advantage in forming ion channels (Licsandru et al. 2016).

3.4 Planar Bilayer Conductance (PBC) Assay. Patch-Clamp Technique

PBC or patch-clamp technique is a good approach in studying planar membranes. This method involves two chambers, *cis* and *trans*, filled with buffered solutions, separated by a planar double-layered lipidic membrane formed in a small hole in the wall between chambers Schalley 2012), as it described in the Fig. 13.

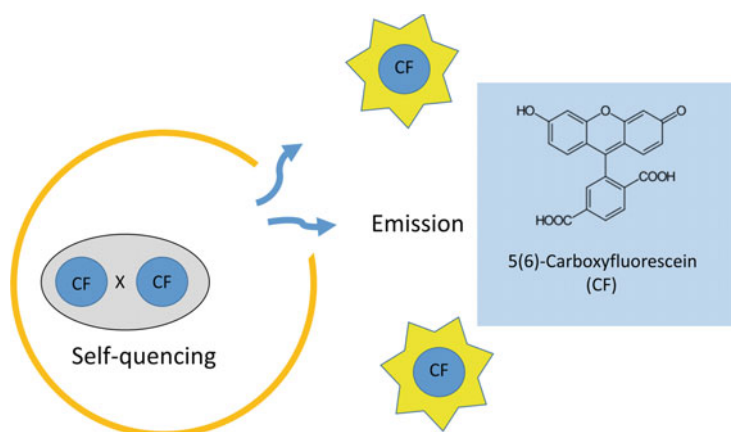


Fig. 11 Principle of the *leakage-test*

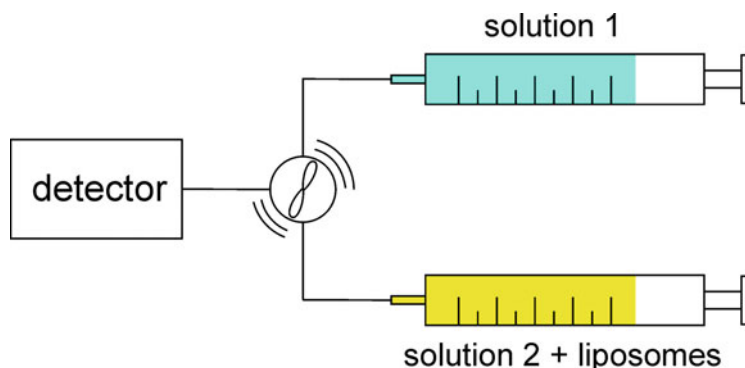


Fig. 12 Schematic representation of water transport through liposome membrane by using the stopped flow method

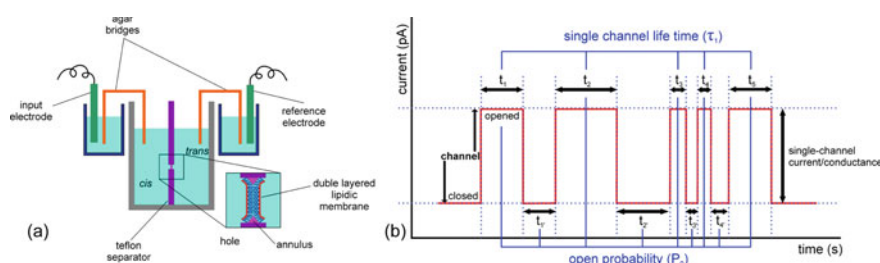


Fig. 13 Schematic representation of Planar Bilayer Conductance assay principle (a) and ideal representation of results obtained (b)

A system formed by a pair of electrodes is set in the two chambers in order to measure the electric conductance of the membrane. Lipid membrane is a medium with a high resistance to electric current flow. Ion transport across the membrane involves the transfer of electric charge between the two sides, resulting in a modification of membrane conductance. This can be used for the detection of ion channel formation, by measuring the conductivity between the cis-trans chambers separated by the lipid membrane. The occurrence of transfer through ion channels can be detected by measuring the pico-/nano amperes order increase of the intensity of the electric current crossing the membrane (Fig. 13 b). Ion channels behave differently depending of their nature. Some are permanently open, others are activated only under certain thermodynamic, steric or chemical conditions. *Patch-clamp* technique is well suited for the study of the ion channels activation mechanism, as it is highly sensitive and detects small variations of current in a very short period of time. Thus, an abrupt rise in conductance from *closed* ($t_1', t_2', t_3',$ etc.) to *open* ($t_1, t_2, t_3,$ etc.) can be observed. The mentioned times represent the life span of an individual ion channel and have very small values (the current leap varies within 10–500 ms interval). Because of this, in order to provide a global picture of the ion transfer, a statistical analysis

of the signals measured by conductance is necessary (channel opening probability calculus, P_0) (Fyles 2007).

This method allows monitoring of ion transport through individual channel but also offers a larger view over the whole process through statistical analysis. Unfortunately, no instruments are commercial available and BLM deposition is highly dependent on the skill and experience of the operator.

4 Conclusions

Ion transport across lipid bilayers is an extremely important process with applications in many fields ranging from sensors to novel drugs preparation and delivery. There are different types of molecules able to selectively transport ions through lipid membranes. Unfortunately, ion transport is an elusive phenomena difficult to evidence. Several indirect techniques were presented that allow observation of these and calculation of some important kinetic parameters involved in ion transport. All available techniques use a simplified, biomimetic model for the cellular membrane, with the most used being liposomes. Due to their biocompatibility many applications make use of liposomes so this chapter tried to present their preparation, purification and characterization before moving on to their use in the study of ion transport. Loading liposomes with pH sensitive fluorescent dyes allowed fluorescent spectroscopy to become a valuable tool in detecting ion transport across lipid bilayer next to the already established patch clamp technique. As more and more teams prepare membrane active molecules, able to selectively transport ions across lipid bilayers, we hope this chapter will facilitate the testing of such molecules and will lead to a standardization.

Acknowledgements The project leading to this application has received funding from the H2020 ERA Chairs Project no 667387: SupraChem Lab Laboratory of Supramolecular Chemistry for Adaptive Delivery Systems ERA Chair initiative. This work was also supported by a grant within the frame of the Complex Projects Partnership Program - PCCDI, under authority of Romanian National Authority for Scientific Research - UEFISCDI, project code PN-III-P1-1.2-PCCDI-2017-0083 (37PCCDI/2018).

References

- Adam C, Peters AD, Lizio MG, Whitehead GFS, Diemer V, Cooper JA, Cockroft SL, Clayden J, Webb SJ (2018) The role of terminal functionality in the membrane and antibacterial activity of peptaibol-mimetic aib foldamers. *Chem Eur J* 24:2249–2256. <https://doi.org/10.1002/chem.201705299>
- Akbarzadeh A, Rezaei-Sadabady R, Davaran S, Joo SW, Zarghami N, Hanifehpour Y, Samiei M, Kouhi M, Nejati-Koshki K (2013) Liposome: classification, preparation, and applications. *Nanoscale Res Lett* 8:102. <https://doi.org/10.1186/1556-276X-8-102>
- Anwekar H, Patel S, Singhai AK (2011) Liposome-as drug carriers. *Int J Pharm Life Sci* 2:945–951

- Ashrafuzzaman M, Andersen OS, McElhaney RN (2008) The antimicrobial peptide gramicidin S permeabilizes phospholipid bilayer membranes without forming discrete ion channels. *Biochim Biophys Acta - Biomembr* 1778:2814–2822. <https://doi.org/10.1016/j.bbamem.2008.08.017>
- Bally M, Bailey K, Sugihara K, Grieshaber D, Vörös J, Stäler B (2010) Liposome and lipid bilayer arrays towards biosensing applications. *Small* 6:2481–2497. <https://doi.org/10.1002/sml.201000644>
- Batzri S, Korn ED (1973) Single bilayer liposomes prepared without sonication. *BBA Biomembr* 298:1015–1019. [https://doi.org/10.1016/0005-2736\(73\)90408-2](https://doi.org/10.1016/0005-2736(73)90408-2)
- Baumgart T, Kreiter M, Lauer H, Naumann R, Jung G, Jonczyk A, Offenhäusser A, Knoll W (2003) Fusion of small unilamellar vesicles onto laterally mixed self-assembled monolayers of thiolopeptides. *J Colloid Interface Sci* 258:298–309. [https://doi.org/10.1016/S0021-9797\(02\)00098-X](https://doi.org/10.1016/S0021-9797(02)00098-X)
- Bezanilla F (2008) How membrane proteins sense voltage. *Nat Rev Mol Cell Biol* 9:323–332. <https://doi.org/10.1038/nrm2376>
- Bibi S, Kaur R, Henriksen-Lacey M, McNeil SE, Wilkhu J, Lattmann E, Christensen D, Mohammed AR, Perrie Y (2011) Microscopy imaging of liposomes: from coverslips to environmental SEM. *Int J Pharm* 417:138–150. <https://doi.org/10.1016/j.ijpharm.2010.12.021>
- Biron E, Otis F, Meillon JC, Robitaille M, Lamothe J, Van Hove P, Cormier ME, Voyer N (2004) Design, synthesis, and characterization of peptide nanostructures having ion channel activity. *Bioorganic Med Chem* 12:1279–1290. <https://doi.org/10.1016/j.bmc.2003.08.037>
- Bouvrans H, Pott T, Bagatolli LA, Ipsen JH, Méléard P (2010) Impact of membrane-anchored fluorescent probes on the mechanical properties of lipid bilayers. *Biochim Biophys Acta Biomembr* 1798:1333–1337. <https://doi.org/10.1016/j.bbamem.2010.03.026>
- Calvo EJ, Otero M (2008) Chemical sensors. In: *Piezoelectric transducers and applications*. https://doi.org/10.1007/978-3-540-77508-9_9
- Cole KS (1939) Electric impedance of the squid giant axon during activity. *J Gen Physiol* 22:649–670. <https://doi.org/10.1085/jgp.22.5.649>
- Cooper GM, Hausman RE (2007) *The cell: a molecular approach* 2nd edn. Sinauer Assoc
- Deamer D, Bangham AD (1976) Large volume liposomes by an ether vaporization method. *BBA Biomembr* 443:629–634. [https://doi.org/10.1016/0005-2736\(76\)90483-1](https://doi.org/10.1016/0005-2736(76)90483-1)
- Doyle DA, Cabral JM, Pfuetzner RA, Kuo A, Gulbis JM, Cohen SL, Chait BT, MacKinnon R (1998) The structure of the potassium channel: Molecular basis of K⁺ conduction and selectivity. *Science* (80-)280:69–77. <https://doi.org/10.1126/science.280.5360.69>
- Dragnevski KI, Donald AM (2008) Applications of environmental scanning electron microscopy (ESEM) in the study of novel drying latex films. *J Phys Conf Ser* 126:012077. <https://doi.org/10.1088/1742-6596/126/1/012077>
- Dyer PN, Richards RE, Russek SL, Taylor DM (2000) Ion transport membrane technology for oxygen separation and syngas production. *Solid State Ionics* 134:21–33. [https://doi.org/10.1016/S0167-2738\(00\)00710-4](https://doi.org/10.1016/S0167-2738(00)00710-4)
- Fang A, Kroenlein K, Riccardi D, Smolyanitsky A (2019) Highly mechanosensitive ion channels from graphene-embedded crown ethers. *Nat Mater* 18:76–81. <https://doi.org/10.1038/s41563-018-0220-4>
- Florin EL, Gaub HE (1993) Painted supported lipid membranes. *Biophys J* 64:375–383. [https://doi.org/10.1016/S0006-3495\(93\)81378-X](https://doi.org/10.1016/S0006-3495(93)81378-X)
- Fyles TM (2007) Synthetic ion channels in bilayer membranes. *Chem Soc Rev* 36:335–347. <https://doi.org/10.1039/b603256g>
- Gabriel GJ, Som A, Madkour AE, Eren T, Tew GN (2007) Infectious disease: Connecting innate immunity to biocidal polymers. *Mater Sci Eng R Reports* 57:28–64. <https://doi.org/10.1016/j.mser.2007.03.002>
- Gilles A, Barboiu M (2016) Highly selective artificial K⁺ channels: an example of selectivity-induced transmembrane potential. *J Am Chem Soc* 138:426–432. <https://doi.org/10.1021/jacs.5b11743>

- Gonen T, Walz T (2006) The structure of aquaporins. *Q Rev Biophys* 39:361. <https://doi.org/10.1017/S0033583506004458>
- Goreham RV, Ayed Z, Ayupova D, Dobhal G (2019) Extracellular vesicles: nature's own nanoparticles. *Compr Nanosci Nanotechnol* 3:27–48. <https://doi.org/10.1016/B978-0-12-803581-8.10412-6>
- Harayama T, Riezman H (2018) Understanding the diversity of membrane lipid composition. *Nat Rev Mol Cell Biol* 19:281–296. <https://doi.org/10.1038/nrm.2017.138>
- Hennig A, Matile S (2008) Detection of the activity of ion channels and pores by circular dichroism spectroscopy: G-quartets as functional CD probes within chirogenic vesicles. *Chirality* 20:932–937. <https://doi.org/10.1002/chir.20526>
- Hladky SB, Haydon DA (1972) Ion transfer across lipid membranes in the presence of gramicidin A. I. Studies of the unit conductance channel. *BBA Biomembr* 274:294–312. [https://doi.org/10.1016/0005-2736\(72\)90178-2](https://doi.org/10.1016/0005-2736(72)90178-2)
- Hodgkin AL, Huxley AF (1952) Currents carried by sodium and potassium ions through the membrane of the giant axon of Loligo. *J Physiol* 116:449–472. <https://doi.org/10.1113/jphysiol.1952.sp004717>
- Hu CMJ, Zhang L, Aryal S, Cheung C, Fang RH, Zhang L (2011) Erythrocyte membrane-camouflaged polymeric nanoparticles as a biomimetic delivery platform. *Proc Natl Acad Sci U S A* 108:10980–10985. <https://doi.org/10.1073/pnas.1106634108>
- Hu X, Chen Z, Tang G, Hou J-L, Li Z (2012) Single-molecular artificial transmembrane water channels. *J Am Chem Soc* 1:10–13. <https://doi.org/10.1021/ja302292c>
- Jones JE, Diemer V, Adam C, Raftery J, Ruscoe RE, Sengel JT, Wallace MI, Bader A, Cockroft SL, Clayden J, Webb SJ (2016) Length-dependent formation of transmembrane pores by 310-helical α -aminoisobutyric acid foldamers. *J Am Chem Soc* 138:688–695. <https://doi.org/10.1021/jacs.5b12057>
- Kahlenberg A, Walker C, Rohrlack R (1974) Evidence for an asymmetric distribution of phospholipids in the human erythrocyte membrane. *Can J Biochem* 52:803–806. <https://doi.org/10.1139/o74-114>
- Kim JS, Chun KY, Han CS (2018) Ion channel-based flexible temperature sensor with humidity insensitivity. *Sens Actuators Phys* 271:139–145. <https://doi.org/10.1016/j.sna.2018.01.025>
- Korlach J, Schwille P, Webb WW, Feigenson GW (1999) Characterization of lipid bilayer phases by confocal microscopy and fluorescence correlation spectroscopy. *Proc Natl Acad Sci U S A* 96:8461–8466. <https://doi.org/10.1073/pnas.96.15.8461>
- Last NB, Sun S, Pham MC, Miller C (2017) Molecular determinants of permeation in a fluoride-specific ion channel. *Elife* 6. <https://doi.org/10.7554/eLife.31259>
- Leduc Y, Michau M, Gilles A, Gence V, Legrand YM, Vanderlee A, Tingry S, Barboiu M (2011) Imidazole-quartet water and proton dipolar channels. *Angew Chemie Int Ed* 50:11366–11372. <https://doi.org/10.1002/anie.201103312>
- Levitan IB (1985) Phosphorylation of ion channels. *J Membr Biol* 87:177–190. <https://doi.org/10.1007/BF01871217>
- Li J, Wang X, Zhang T, Wang C, Huang Z, Luo X, Deng Y (2015) A review on phospholipids and their main applications in drug delivery systems. *Asian J Pharm Sci* 10:81–98. <https://doi.org/10.1016/j.ajps.2014.09.004>
- Li Z, Li Y, Yao YC, Aydin F, Zhan C, Chen Y, Elimelech M, Pham TA, Noy A (2020) Strong differential monovalent anion selectivity in narrow diameter carbon nanotube porins. *ACS Nano* 14:6269–6275. <https://doi.org/10.1021/acs.nano.0c02423>
- Licsandru E, Kocsis I, Shen YX, Murail S, Legrand YM, Van Der Lee A, Tsai D, Baaden M, Kumar M, Barboiu M (2016) Salt-excluding artificial water channels exhibiting enhanced dipolar water and proton translocation. *J Am Chem Soc* 138:5403–5409. <https://doi.org/10.1021/jacs.6b01811>
- Lu J, Zhang H, Hou J, Li X, Hu X, Hu Y, Easton CD, Li Q, Sun C, Thornton AW, Hill MR, Zhang X, Jiang G, Liu JZ, Hill AJ, Freeman BD, Jiang L, Wang H (2020) Efficient metal ion sieving in rectifying subnanochannels enabled by metal–organic frameworks. *Nat Mater* 19:767–774. <https://doi.org/10.1038/s41563-020-0634-7>

- Malla JA, Umesh RM, Vijay A, Mukherjee A, Lahiri M, Talukdar P (2020a) Apoptosis-inducing activity of a fluorescent barrel-roseette M⁺/Cl⁻ channel. *Chem Sci*. <https://doi.org/10.1039/c9sc06520b>
- Malla JA, Umesh RM, Vijay A, Mukherjee A, Lahiri M, Talukdar P (2020b) Apoptosis-inducing activity of a fluorescent barrel-roseette M⁺/Cl⁻ channel. *Chem Sci* 11:2420–2428. <https://doi.org/10.1039/c9sc06520b>
- Mayer LD, Bally MB, Hope MJ, Cullis PR (1986) Techniques for encapsulating bioactive agents into liposomes. *Chem Phys Lipids* 40:333–345. [https://doi.org/10.1016/0009-3084\(86\)90077-0](https://doi.org/10.1016/0009-3084(86)90077-0)
- McCubbin GA, Praporski S, Piantavigna S, Knappe D, Hoffmann R, Bowie JH, Separovic F, Martin LL (2011) QCM-D fingerprinting of membrane-active peptides. *Eur Biophys J* 40:437–446. <https://doi.org/10.1007/s00249-010-0652-5>
- Mueller P, Rudin DO (1963) Induced excitability in reconstituted cell membrane structure. *J Theor Biol* 4:268–280. [https://doi.org/10.1016/0022-5193\(63\)90006-7](https://doi.org/10.1016/0022-5193(63)90006-7)
- Mueller P, Rudin DO, Ti Tien H, Wescott WC (1962) Reconstitution of cell membrane structure in vitro and its transformation into an excitable system. *Nature* 194:979–980. <https://doi.org/10.1038/194979a0>
- Muraoka T, Noguchi D, Kasai RS, Sato K, Sasaki R, Tabata KV, Ekimoto T, Ikeguchi M, Kamagata K, Hoshino N, Noji H, Akutagawa T, Ichimura K, Kinbara K (2020) A synthetic ion channel with anisotropic ligand response. *Nat Commun* 11:2924. <https://doi.org/10.1038/s41467-020-16770-z>
- Murphy DB, Davidson MW (2012) Fundamentals of light microscopy and electronic imaging, 2nd edn. <https://doi.org/10.1002/9781118382905>
- Nallamothu R, Wood GC, Pattillo CB, Scott RC, Kiani MF, Moore BM, Thoma LA (2006) A tumor vasculature targeted liposome delivery system for combretastatin A4: design, characterization, and in vitro evaluation. *AAPS PharmSciTech* 7:E7–E16. <https://doi.org/10.1208/pt070232>
- Noda M, Takahashi H, Tanabe T, Toyosato M, Kikuyotani S, Hirose T, Asai M, Takashima H, Inayama S, Miyata T, Numa S (1983a) Primary structures of β - And δ -subunit precursors of Torpedo californica acetylcholine receptor deduced from cDNA sequences. *Nature* 301:251–255. <https://doi.org/10.1038/301251a0>
- Noda M, Takahashi H, Tanabe T, Toyosato M, Kikuyotani S, Furutani Y, Hirose T, Takashima H, Inayama S, Miyata T, Numa S (1983b) Structural homology of Torpedo californica acetylcholine receptor subunits. *Nature* 302:528–532. <https://doi.org/10.1038/302528a0>
- Noda M, Shimizu S, Tanabe T, Takai T, Kayano T, Ikeda T, Takahashi H, Nakayama H, Kanaoka Y, Minamino N, Kangawa K, Matsuo H, Raftery MA, Hirose T, Inayama S, Hayashida H, Miyata T, Numa S (1984) Primary structure of Electrophorus electricus sodium channel deduced from cDNA sequence. *Nature* 312:121–127. <https://doi.org/10.1038/312121a0>
- Paxton WF, Price D, Richardson NJ (2013) Hydroxide ion flux and pH-gradient driven ester hydrolysis in polymer vesicle reactors. *Soft Matter* 9:11295. <https://doi.org/10.1039/c3sm51575c>
- Pick U (1981) Liposomes with a large trapping capacity prepared by freezing and thawing of sonicated phospholipid mixtures. *Arch Biochem Biophys* 212:186–194. [https://doi.org/10.1016/0003-9861\(81\)90358-1](https://doi.org/10.1016/0003-9861(81)90358-1)
- Pinheiro M, Magalhães J, Reis S (2019) Antibiotic interactions using liposomes as model lipid membranes. *Chem Phys Lipids* 222:36–46. <https://doi.org/10.1016/j.chemphyslip.2019.05.002>
- Placzek M, Kosela M (2016) Microscopic methods in analysis of submicron phospholipid dispersions. *Acta Pharm* 66:1–22. <https://doi.org/10.1515/acph-2016-0003>
- Plant AL, Gueguetchkeri M, Yap W (1994) Supported phospholipid/alkanethiol biomimetic membranes: insulating properties. *Biophys J* 67:1126–1133. [https://doi.org/10.1016/S0006-3495\(94\)80579-X](https://doi.org/10.1016/S0006-3495(94)80579-X)

- Posson DJ, Rusinova R, Andersen OS, Nimigean CM (2018) Stopped-flow fluorometric ion flux assay for ligand-gated ion channel studies. In: Shyng S-L, Valiyaveetil FI, Whorton M (eds) Potassium channels: methods and protocols. Springer, New York, pp 223. https://doi.org/10.1007/978-1-4939-7362-0_17
- Renart ML, Giudici AM, Díaz-García C, Molina ML, Morales A, González-Ros JM, Poveda JA (2020) Modulation of function, structure and clustering of K⁺ channels by lipids: Lessons learnt from KcsA. *Int J Mol Sci* 21:2554. <https://doi.org/10.3390/ijms21072554>
- Riaz M (1996) Liposome preparation methods. *Pak J Pharm Sci* 9:65–77. <https://doi.org/10.1021/la901789h>
- Roy A, Joshi H, Ye R, Shen J, Chen F, Aksimentiev A, Zeng H (2020) Polyhydrazide-based organic nanotubes as efficient and selective artificial iodide channels. *Angew Chemie Int Ed* 59:4806–4813. <https://doi.org/10.1002/anie.201916287>
- Ruozzi B, Belletti D, Tombesi A, Tosi G, Bondioli L, Forni F, Vandelli MA (2011) AFM, ESEM, TEM, and CLSM in liposomal characterization: a comparative study. *Int J Nanomed* 6:557–563. <https://doi.org/10.2147/IJN.S14615>
- Saha A, Panda S, Pradhan N, Kalita K, Trivedi V, Manna D (2018) Azidophosphonate chemistry as a route for a novel class of vesicle-forming phosphonolipids. *Chem Eur J* 24:1121–1127. <https://doi.org/10.1002/chem.201704000>
- Sakai N, Matile S (2002) Recognition of polarized lipid bilayers by p-oligophenyl ion channels: from push-pull rods to push-pull barrels. *J Am Chem Soc* 124:1184–51185. <https://doi.org/10.1021/ja017497c>
- Sakai N, Gerard D, Matile S (2001) Electrostatics of cell membrane recognition: structure and activity of neutral and cationic rigid push-pull rods in isoelectric, anionic, and polarized lipid bilayer membranes. *J Am Chem Soc* 123:2517–2524. <https://doi.org/10.1021/ja003141+>
- Sakai N, Kamikawa Y, Nishii M, Matsuoka T, Kato T, Matile S (2006) Dendritic folate rosettes as ion channels in lipid bilayers. *J Am Chem Soc* 128:2218–2219. <https://doi.org/10.1021/ja058157k>
- Schalley C (2012) Analytical methods in supramolecular chemistry, 2nd. Compl Ed. <https://doi.org/10.1002/9783527644131>
- Schieren H, Rudolph S, Finkelstein M, Coleman P, Weissmann G (1978) Comparison of large unilamellar vesicles prepared by a petroleum ether vaporization method with multilamellar vesicles. ESR, diffusion and entrapment analyses. *BBA Gen Subj* 542:137–153. [https://doi.org/10.1016/0304-4165\(78\)90240-4](https://doi.org/10.1016/0304-4165(78)90240-4)
- Schiller SM, Naumann R, Lovejoy K, Kunz H, Knoll W (2003) Archaea analogue thiolipids for tethered bilayer lipid membranes on ultrasmooth gold surfaces. *Angew Chemie Int Ed* 13:208–211. <https://doi.org/10.1002/anie.200390080>
- Schmitz G, Jabs HU, Assmann G (1983) Densitometry of phosphatidylcholine and sphingomyelin in high-density lipoproteins. *Clin Chem* 29:1435–1437
- Schneider S, Licsandru ED, Kocsis I, Gilles A, Dumitru F, Moulin E, Tan J, Lehn JM, Giuseppone N, Barboiu M (2017) Columnar self-assemblies of triarylaminines as scaffolds for artificial biomimetic channels for ion and for water transport. *J Am Chem Soc* 139:3721–3727. <https://doi.org/10.1021/jacs.6b12094>
- Schwoch G, Passow H (1973) Preparation and properties of human erythrocyte ghosts. *Mol Cell Biochem* 2:197–218. <https://doi.org/10.1007/BF01795474>
- Shen Y, Zhong Y, Fei F, Sun J, Czajkowsky DM, Gong B, Shao Z (2020) Ultrasensitive liposome-based assay for the quantification of fundamental ion channel properties. *Anal Chim Acta* 1112:8–15. <https://doi.org/10.1016/j.aca.2020.03.044>
- Sidorov V, Kotch FW, Kuebler JL, Lam YF, Davis JT (2003) Chloride transport across lipid bilayers and transmembrane potential induction by an oligophenoxacetamide. *J Am Chem Soc* 125:2840–2841. <https://doi.org/10.1021/ja029372t>
- Stein H, Spindler S, Bonakdar N, Wang C, Sandoghdar V (2017) Production of isolated giant unilamellar vesicles under high salt concentrations. *Front Physiol* 8:1–16. <https://doi.org/10.3389/fphys.2017.00063>

- Steller L, Kreir M, Salzer R (2012) Natural and artificial ion channels for biosensing platforms. *Anal Bioanal Chem* 402:209–230. <https://doi.org/10.1007/s00216-011-5517-y>
- Stockbridge RB, Lim HH, Otten R, Williams C, Shane T, Weinberg Z, Miller C (2012) Fluoride resistance and transport by riboswitch-controlled CLC antiporters. *Proc Natl Acad Sci U S A* 109:15289–15294. <https://doi.org/10.1073/pnas.1210896109>
- Strathmann H (2005) Membranes and membrane separation processes. In: Ullmann's encyclopedia of industrial chemistry. https://doi.org/10.1002/14356007.a16_187.pub2
- Sun Z, Barboiu M (2019) Artificial Gramicidins. *Front Chem* 4:611. <https://doi.org/10.3389/fchem.2019.00611>
- Suzuki H, Takeuchi S (2008) Microtechnologies for membrane protein studies. *Anal Bioanal Chem* 391:2695–2702. <https://doi.org/10.1007/s00216-008-1916-0>
- Thompson AN, Posson DJ, Parsa PV, Nimigean CM (2008) Molecular mechanism of pH sensing in KcsA potassium channels. *Proc Natl Acad Sci U S A* 105:6900–6905. <https://doi.org/10.1073/pnas.0800873105>
- Touaj K, Tbeur N, Hor M, Verchère JF, Hlaïbi M (2009) A supported liquid membrane (SLM) with resorcinarene for facilitated transport of methyl glycopyranosides: Parameters and mechanism relating to the transport. *J Memb Sci* 337:28–38. <https://doi.org/10.1016/j.memsci.2009.03.014>
- van Meer G, Voelker DR, Feigenson GW (2008) Membrane lipids: where they are and how they behave. *Nat Rev Mol Cell Biol* 9:112–124. <https://doi.org/10.1038/nrm2330>
- West JM, Xia J, Tsuruta H, Guo W, O'Day EM, Kantrowitz ER (2008) Time evolution of the quaternary structure of *Escherichia coli* aspartate transcarbamoylase upon reaction with the natural substrates and a slow, tight-binding inhibitor. *J Mol Biol* 384:206–218. <https://doi.org/10.1016/j.jmb.2008.09.022>
- Wick R, Angelova MI, Walde P, Luisi PL (1996) Microinjection into giant vesicles and light microscopy investigation of enzyme-mediated vesicle transformations. *Chem Biol* 3:105–110. [https://doi.org/10.1016/S1074-5521\(96\)90286-0](https://doi.org/10.1016/S1074-5521(96)90286-0)
- Williamson IM, Alvis SJ, East JM, Lee AG (2003) The potassium channel KcsA and its interaction with the lipid bilayer. *Cell Mol Life Sci* 60:1581–1590. <https://doi.org/10.1007/s00018-003-3172-y>
- Zheng S-P, Huang L-B, Sun Z, Barboiu M (2020) Self-assembled artificial ion-channels toward natural selection of functions. *Angew Chemie Int Ed*. <https://doi.org/10.1002/anie.201915287>
- Zonda R, Coroaba A, Ibanescu S, Vasiliu T, Neamtu A, Silion M, Rusu T, Pinteala M (2018) Cation transport activity of the alkyl-ureido-benzo-15-crown-5-ethers through double layer lipid membranes. *Rev Roum Chim* 63:665–672

Stability and Structure of Adaptive Self-organized Supramolecular Artificial Water Channels in Lipid Bilayers



A. Hardiagon, S. Murail, L. Huang, M. Barboiu, F. Sterpone, and M. Baaden

Abstract Nanopores that efficiently and selectively transport water have been intensively studied at the nanoscale level. A key challenge relates to linking the nanoscale to the compound's macroscopic properties, which are hardly accessible at the smaller scale. Here we numerically investigate the influence of varying the dimensions of a self-assembled Imidazole I-quartet (I_4) aggregate in lipid bilayers on the water permeation properties of these highly packed water channels. Quantitative transport studies reveal that water pathways in I_4 crystal-like packing are not affected by small scaling factors, despite non-uniform contributions between central channels shielded from the bilayer and lateral, exposed channels. The permeation rate computed in simulations overestimates the experimental value by an order of magnitude, yet these *in silico* properties are very dependent on the force field parameters. The diversity of observed water pathways in such a small-scale *in silico* experiment yields some insights into modifying the current molecular designs in order to considerably improve water transport in scalable membranes.

Keywords Artificial water channels · Self-assembly · Molecular dynamics simulations

A. Hardiagon · F. Sterpone (✉) · M. Baaden (✉)
CNRS, Université de Paris, UPR 9080, Laboratoire de Biochimie Théorique,
13 rue Pierre et Marie Curie, 75005 Paris, France
e-mail: baaden@smpliuix.de; marc.baaden@ibpc.fr

Institut de Biologie Physico-Chimique-Fondation Edmond de Rotschild, PSL Research University, Paris, France

S. Murail
Université de Paris, CNRS, INSERM, Biologie Fonctionnelle Et Adaptative, UMR 8251,
Computational Modeling of Protein Ligand Interactions U1133, 75205 Paris, France

L. Huang · M. Barboiu
Institut Européen Des Membranes, Adaptive Supramolecular Nanosystems Group, Université de Montpellier, ENSCM, CNRS, Place Eugene Bataillon CC047, 34095 Montpellier, France

1 Introduction

The quality and purity of available water resources is one of the biggest challenges of our current societies. The increasing water demand has stimulated the development of new technologies such as ultra-purification of water for medical usage or water desalination reverse osmosis. Inspired by recent work on biological systems, new expectations in terms of feasibility and functionality brought researchers towards artificial waterchannel (AWC) systems. Indeed AWCs have the advantage to present a diversity of properties due to their chemical synthesis and they are easily encapsulated in lipids and polymer membranes (Tan et al. 2018). Following suggestions about size scaling effects in carbon nanotubes (Garate et al. 2009; Köfingner et al. 2008) and recent studies on monomeric superstructures of AWCs (Noy and Wanunu 2020), we propose to study the dimensional scalability and the robustness of empirical models using an artificial multimeric channel aggregate. Imidazole I₄-quartets (I₄) form a class of artificial waterchannels that experimentally show high selectivity and water conductance (Licsandru et al. 2016). Previous studies have simulated the nanoscopic water transport and the packing of water in similar systems (Licsandru et al. 2016; Kocsis et al. 2018). We have previously shown that, depending on the morphology of the synthesized compound (Murail et al. 2018; Sun et al. 2018), self-assembled structures in crystalline and amorphous phases account for single water-wire and associated water transport properties.

Experimental evidence mainly comes from stopped-flow experiments in which compounds are assembled in lipid mixtures into monodisperse liposomes of ~100 nm diameter. This technique employs the use of osmotic gradients to shrink or inflate liposomes. The permeability of the channels embedded in lipids are extracted from the inflation rate probed by light-scattering analysis.

In order to bridge the gap between experimental measurements occurring at the macroscopic scale and the atomistic description, we propose to study the eventual finite-size effects generated by the boundary conditions chosen for molecular dynamics (MD) simulations of these objects, a method of choice to investigate nanoscale membrane aggregates. We have submitted the selected systems to a series of tests by varying force field parameters to determine their relevance.

We show that growing structures up to 10 nm long does not lead to pronounced variability in terms of permeation per channel, despite the increase in surface-to-volume ratio. Accordingly, we observe that simulations of larger systems enable us to explore rare permeation events occurring in regions shielded from lipid interactions thanks to an increase in sampling statistics. Furthermore such an approach paves the way to further investigate spatial correlations between adjacent channels in these highly packed structures.

The influence of a range of parameters in the model, such as water molecule representation and force fields for the I₄ compounds demonstrate the sensitivity of these models and the complex diversity of water transport mechanisms that arise at such a small spatial scale.

2 Materials and Methods

All molecular dynamics simulations were performed under periodic boundary conditions with constant pressure. The CHARMM-36 force field (Klauda et al. 2010) was used for lipid molecules and the TIP3P and SPC/E models were chosen (Jorgensen et al. 1983) for water. To represent S-HC8 molecules and generate their topologies, we used the CHARMM General Force Field (Vanommeslaeghe and MacKerell 2012) together with the ParamChem web service (Vanommeslaeghe et al. 2012). The GROMACS 2018.7 and 2019.2 softwares were used to run the simulations with all atoms, with an integration time step of 2 fs. All bonds were constrained using the LINear Constraint Solver algorithm. Particle mesh Ewald electrostatics was used with a 12 Å cutoff with the Verlet buffer scheme for nonbonded interactions; the neighbor list was updated every 20 steps. Three baths (imidazoles, lipids, and water and ions) were coupled to a temperature of 310 K using the Nosé-Hoover thermostat with a time constant $t = 1$ ps and a chain length of 4. Pressure in the x/y dimensions was scaled isotropically with Parrinello-Rahman barostat at 1 bar, and the z dimension was coupled independently to a reference pressure of 1 bar, $t = 5.0$ ps, and compressibility of $4.5 \cdot 10^{-5} \text{ bar}^{-1}$. All systems were minimized for 5000 steps with a steepest descent algorithm and equilibrated for 2 ns, using decreasing position restraints of 1000, 400, 200, 100, 40 $\text{kJ mol}^{-1} \text{ nm}^{-2}$ on heavy atoms, with the crystal structure as a reference. Production runs were finally computed for 1000 to 2000 ns without any position restraints.

The previous results we compared to were obtained using initial I-quartet channel patches of 3 nm width inserted (Murail et al. 2018). The packing of the initial patch was based on X-ray structures and the composition of lipids follows the one used experimentally. This composition of the lipid mixture is the same as before with a respective molar ratio 5:4:1 for Chl:PC:PS. The molar ratio between compounds and lipids was previously based on an estimation of the insertion efficiency and initial concentrations inserted (Licsandru et al. 2016). In this new series of simulations, we varied the size of the patch along the two directions of the crystal parallel to the bilayer membrane. The size effect was only investigated in the case of the S-HC8 compound since this structure was the most stable structure of the crystal form observed in previous results. The molar ratio of lipid:compound was multiplied by a factor 2 in simulation sim5, with the same initial patch of circa 3 nm width. The height of the crystal patch was kept constant and is assumed to be close to the thickness of the lipid bilayer.

All systems have been hydrated with a constant molar ratio of lipid:water equal to 28. We checked in additional simulations that no other long-range effects on the z axis and through periodic boundary conditions occur, by changing this latter molar ratio to 54. Na^+ and Cl^- ions have been inserted using a Monte-Carlo scheme to neutralize the system and to obtain a concentration of solute equal to 0.15 M.

All setups were assembled using the CHARMM-GUI web interface (Jo et al. 2008) and format files were adapted to the Gromacs software using the online tool services (Lee et al. 2016).

The molecular dynamics trajectories were visually inspected and analyzed using the VMD software (Humphrey et al. 1996). Analysis of the trajectories for RMSD and permeation calculations were performed using custom scripts for the MDAnalysis library (Gowers et al. 2016; Michaud-Agrawal et al. 2011). The accuracy of the analysis was first tested by varying the sampling time. Fast computation and accuracy were accessed both using 0.1 ns as a sampling time for the analysis of water permeations. The analysis of pore radius was performed using the HOLE software (Smart et al. 1996). Due to large fluctuations of channel components on the lateral sides of the patch, mean pore radius values were relevant only for central channels.

3 Water Conductance and Dimensional Scaling

To evaluate the transport activity of the membrane in simulation, we computed the average number of permeation events in one direction or water conductance q_0 (see Table 1). This number is related to the diffusional permeability p_d which quantifies the number of water molecules that exited a channel on one side of the membrane once they entered through the opposite side of the membrane (Zhu et al. 2004). We will further discuss the implications of this specific choice of permeation measurement.

We observed that all systems are stable in the bilayer during 1000 ns simulation, based on their low root mean square deviation from the starting point. There is no major rearrangement of compounds in the membrane, except for very few compounds that move freely within the membrane. A crystal structure arrangement is dominant; we observed very similar water pathways as in previous studies of similar patch configurations (sim1) (Murail et al. 2018). In Fig. 2 we reported the evolution of water permeation events during the time of each simulation (from 1000 to 2000 ns). We observed that an equilibrium regime is reached on a range of time between 500 and 1000 ns depending on the simulation.

All simulations were performed under equilibrium conditions, therefore we expect that the net flow through the channels is null on average after a certain time. Indeed, we observed that the net flow cancellation coincides with the convergence of permeation rates to a constant value. Regarding these observations, we extracted water conduction using water molecule trajectories taken above a time offset considered as equilibration period. We combine linear regression and a bootstrap method to compute estimates of water conductance and their confidence intervals (Haslwanter 2016). We computed conductance values reported in Table 1 using the following relation:

$$q_0 = \frac{N_{perm}}{2N_c}$$

where N_{perm} relates to the number of permeation events per second (in both directions), N_c relates to the effective number of channels. We consider a ‘‘permeation event’’ as a complete transport of a water molecule through the channel delimited

Table 1 Water conductance values reported for the whole set of simulations. Some results from previous studies and from previous experimental measurements are mentioned for comparison. Water conductance values are computed using number of permeation events in a time window normalized by the number of effective channels in the pre-formed crystal patch. The last two columns account for the distribution of events between lateral and central channel as defined in the article text

Simulation acronym	System description	Force Field	Water Model	Permeation regime	Conductance			
					$\times 10^6$ H2O/s/channel		lateral	central
					q0	std		
	AQP1	–	–	–	$\sim 10^3$	–	–	–
	S-HC8 – Exp (7)	–	–	osmotic	1,4	0,1	–	–
sim1	S-HC8 – 6 channels - no defects	CgenFF	TIP3P	diffusive	19.5	0.2	99%	1%
sim2	S-HC8 – 6 channels - with defects	CgenFF	TIP3P	diffusive	22.2	0.2	99%	1%
sim3	S-HC8 – 2 \times 6 channels	CgenFF	TIP3P	diffusive	22.5	0.1	82%	18%
sim4	SHC8 – 12 channels	CgenFF	TIP3P	diffusive	20.8	0.1	72%	28%
sim5	S-HC8 – 6 channels - large membrane	CgenFF	TIP3P	diffusive	20.5	0.1	98%	2%
sim6	S-HC8 – 6 channels	CgenFF	SPC/E	diffusive	10.1	0.1	76%	14%
sim7	S-HC8 – 6 channels	GAFF	TIP3P	diffusive	65.0	0.3	78%	28%

by the mean position of phosphorus atoms in the lipid bilayer in both leaflets. The number of effective channels in our simulations was estimated by visual examination. Thereby we defined an effective channel as an I4- (or lipid-)bounded area within which water wires are located; the “effective” attribute characterizing channels delimited by both compound molecules and hydrophobic tails of lipid molecules that allow water to cross the membrane. Despite basing the structure of the central channel on X-ray data, the behavior of the channels exposed to lipids was first unclear to us. As most of the permeation events occur in these regions, we tested two different setups: one patch with the lateral, exposed channels defined by exactly four imidazole molecules and one patch with exposed lateral channels defined by three imidazole molecules, see Fig. 1 a) b), the latter setup was already used in previous studies (Murail et al. 2018). Both configurations remain stable during 1000 ns and we notice higher thermal fluctuations for the imidazole column in the first setup, resulting in

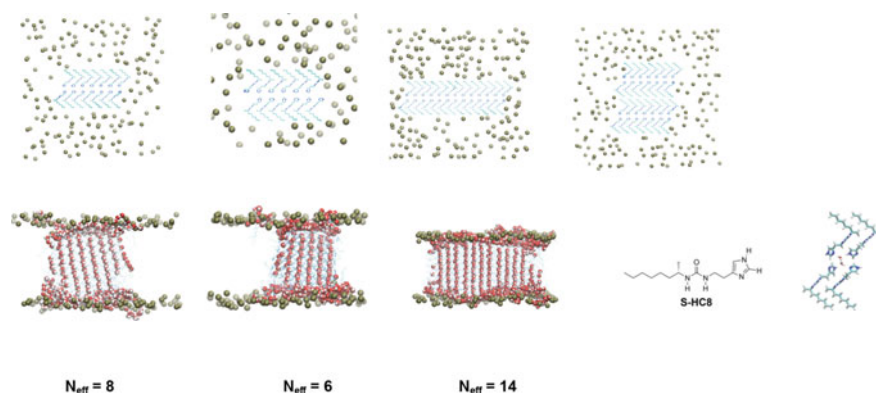


Fig. 1 Initial aggregation setups of the S-HC8 compound (see panels h and i) used for molecular dynamics simulations. Top view (a) sim1 (b) sim2 (c) sim3 (d) sim4. Lateral view (e) sim1 (f) sim2 (g) sim3. Only molecules of the I4 compounds and the phosphorus atoms of the lipids are represented in the upper panels; water molecules close to polar heads of the imidazole compound are added in the bottom panels. All other molecules are omitted in the pictures for clarity. Below each bottom panel, the estimated number of effective water channels is shown

only one lateral-exposed channel and a reduced number of effective channels, see Fig. 1.

Interestingly, in the second regime we observed that the normalized number of permeation events grows with a similar rate independently of the size of either the membrane or the patch. In the next section, we further discuss different considerations about the water pathways in order to better understand these results.

In previous results, simulations were performed using a larger lateral pressure in x/y directions (10 atm) compared to normal pressure (1 atm). Our motivation for this choice was to compensate for the relatively small size of the aggregates. Indeed, it has been shown that small compounds tend to remain in crystal form under higher lateral pressure. In the present simulations, we did not need to increase lateral pressure since the crystal form was already stable at 1 atm. Some preliminary simulations have been performed at higher lateral pressure (10 atm) but no significant changes

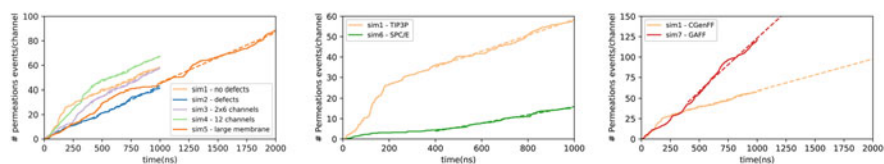


Fig. 2 Time series of number of permeation events normalized over the total number of pre-formed imidazole I4 channels in the membrane. The permeation rates are grouped together with respect to several varying factors: size of the patch and lipid/compound ratio (a), water model (b) and force field parameters (c). Achieving a constant permeation rate after an initial time offset provides a simple measure that the system reaches a converged transport state. Water conductance values associated to each simulation are reported in Table 1

in both stability and permeations were observed. One of the simulation outcomes (sim5) with a larger lipid membrane indicates that the number of lipids does not play a role in the overall stability since permeation pathways are very similar to observations in sim1. We believe that the coupling between chiral crystal and induced chiral water single-wire is enforcing the stability of this chiral structure (Kocsis et al. 2018), resulting in the observed robustness of the permeation mechanism. At this stage, we plan to perform a more detailed analysis of the contribution of each Van der Waals and Coulomb interaction between compound/compound, compound/lipid and compound/water pairs. This breakdown will allow us to understand the key mechanism for stability and permeation in these structures.

4 Permeation Pathways: Lateral Versus Central

In all simulations we observed a much larger number of permeations in lateral channels compared to central channels. Due to the multimeric nature of the patch, channels were identified based on geometrical aspects given the position of each water molecule permeating in the half-time of its course through the membrane. Considering the array-like alignment of channels in one direction in the membrane plane, we considered as “lateral channel” either an exposed channel with walls sharing lipid atoms and compound atoms, or the first channel with walls made by compound molecules. This choice was motivated by observations of water molecules jumping laterally from one channel to another in this region. Note that the average duration of permeation events, despite a broad range of deviations is always bigger in central channels (10–500 ns) than in lateral channels (1–50 ns). These values are reported qualitatively here, despite the lack of statistics on these timescales to distinguish water permeation mechanisms between central and lateral channels.

Following the last two columns of Table 1, we noticed that systems with bigger size patches display more central permeation events. Interestingly, the permeation in central channels is not equally distributed among the central channels and only a few of them are activated (see Fig. 3). An analysis of the pore radius was performed on a trajectory obtained from sim4 and was correlated with the permeation events. Over 10 central channels, only two pairs of adjacent channels remain active in the second part of the simulation (channels 3,4 and 7,8); the activity being related to the water permeability. For these channels, the mean pore radius is $1.36 \pm 0.1 \text{ \AA}$ and for inactive channels the mean pore radius is $1.31 \pm 0.1 \text{ \AA}$ (see Fig. 3). Thus, central permeation events are correlated to fluctuations of the pore size.

In several simulations not reported here, we observed an increase of central channel radius up to 1.5 \AA which is accompanied by a much faster transport of water with a change of conformation of the water packing inside a channel. These results suggest that the patch could undergo some structural transitions at room temperature. However, we want to warn the reader that further investigation of these dynamical processes is still to be investigated. Indeed the statistics of central permeation events

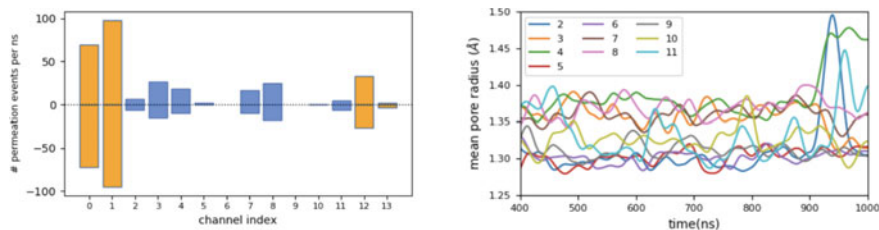


Fig. 3 (a) water conductance per channel (12 aligned channels) during the time window 400–1000 ns. Channel indices follow the spatial order, the channels 0 and 13 are effective channels delimited by both lipids and S-HC8 molecules. Lateral channels are colored in orange and central channels are colored in blue. Positive values account for water molecules entering the lower leaflet and exiting the channel on the upper leaflet, and negative values are defined accordingly. (b) Time series of mean pore radius for each labeled central channel. Lateral mean pore radius for lateral channels was not represented, indeed higher fluctuations of channel walls reduces considerably the accuracy of this measure. Only the time window corresponding to a constant water flow is considered. For convenience, data is averaged on a time window of 50 ns.

at these timescales remain too low to ensure the system to be in a stationary state, and therefore compute a stationary permeation rate.

In order to characterize the permeation pathways, we also computed the unidirectional flow for both directions along the z axis on the time window where the absolute flow is constant. We observed the water flow to be almost symmetric for all lateral channels. Moreover we noticed that central channels in large systems could maintain a positive net flow in the active channel during more than 400 ns (see Fig. 3). Still, there is no evidence that water flow in one direction could be energetically favored in this equilibrium-MD simulation. To confirm this hypothesis, it could be interesting to extend the simulations considering its limitations due to the small amount of statistics for central channels in the current study.

5 Discussion on the Model

We showed that for the scales investigated the overall water conductance scales linearly with the size of the patch. At first sight, if we suppose that all channels of the patch contribute independently to the overall water flow, these results seem natural. However a detailed analysis of individual channel permeation has revealed that lateral channels contribute significantly contribute for more permeation events than central channels. If we consider simulation sim4 (see Fig. 1), the setup has the same number of lateral channels as in sim1, but with almost the double number of central channels. First, we were expecting that the water conductance will scale with the number of lateral channels, but simulations show that it scales with the total number of channels. One hypothesis to understand these results is to suggest that permeation in these crystal-like structures is a collective phenomenon between adjacent channels. This vision is supported by the comparison between simulations

Table 2 Self-diffusion of water in the bulk calculated for two water models and experimental reference value (Mahoney and Jorgensen 2000)

Water Model	Self-diffusion (10^{-5} cm ² /s)
experimental	2.30
TIP3P	5.19
SPC/E	2.49

sim1 and sim2 where the local change of the lateral channel conformation does not seem to disturb overall water conductance. So, in order to understand the mechanism of water flow at larger scales, one has to consider the spatial correlations of such crystal-like molecular assemblies.

As shown in Fig. 1, the choice of the water model has a significant impact on the permeation rate. Water conduction is twice stronger using the TIP3P water model compared to the SPC/E model given all other setup features being equal. It is well-known that water transport in confined geometries is strongly dependent on hydrogen bonds that water molecules form within their close environment (Horner et al. 2015; Alexiadis and Kassinos 2008). Yet the number of hydrogen-bonds in S-HC8 channels is very close to the number of hydrogen bonds in the bulk. Hence we expect that the diffusion in the channels at equilibrium will be affected correspondingly to the bulk diffusion. Indeed, as shown in Table 2, the ratio between self-diffusion coefficients between TIP3P and SPC/E model is 2.1 which is consistent with our results. Moreover, as the SPC/E water model is more faithful to real data concerning transport properties, we keep in mind that almost all simulations performed here with the TIP3P model would overestimate transport properties.

In order to test the sensitivity of the model coefficients, we compared the water conductance in two similar setups varying force field parameters for the imidazole compounds using either CGenFF (Caleman et al. 2012) or GAFF (Wang et al. 2004). Results in Fig. 1 show that permeability is more than three times larger when using the GAFF force field. Using GAFF parameters, we noticed the crystal patch to be less flexible under thermal fluctuations; almost no imidazole molecules are moving freely in the lipid bilayer. We expect that GAFF parameters reinforce long-range electrostatics interactions resulting in even more stable crystal-like patches embedded in the lipid bilayer. This freezing effect of the surrounding architecture could contribute to increase water conductance both in lateral and central channels. However, further considerations about energetics and experimental data is under investigation to validate and study the influence of both LJ coefficients and partial charges of these two models.

Furthermore, experimental data is required to assess the validity of the modeled aggregates. Despite the estimation from experimental results of the molar ratio between lipids and compound molecules, the average size of these membrane-embedded objects actually remains unknown. Two scenarios arise at this stage, one assuming the existence of small patches with large surface-to-volume-ratio effect and therefore a particular role of the interaction between lipids and the compound patch on permeation rate, the other scenario assuming the presence of large crystal patches where surface-to-volume-ratio effects are negligible. In order to validate the second scenario, we would need above-mentioned experimental data. Furthermore

a coarse-grain approach could be adopted to simulate larger systems, however the forcefield issue then becomes even more stringent as all relevant physico-chemical properties of the imidazole compounds will have to be captured in the simplified representation. Somehow we would have to find a compromise between the loss of atomistic description for water dynamics and the gain in the amount of statistics.

Although the size of the embedded system does not seem to play a significant role in the permeation rate in our simulations, we keep in mind that it essentially concerns the hypothesis based on crystal configuration at small timescale. The major difficulty in reproducing the experimental conditions relates to the unknown average size and distribution of compound assemblies embedded in the liposomes, the radius of which is distributed around 100 nm. In our simulations, the patch size does not exceed 10 nm and timescales accessible to all-atoms descriptions are bounded to a few microseconds. Given the small values of the scaling factor we used in this study, we do not exclude some important surface-to-volume effects when we scale the system up to experimental ones. For the time being, we cannot resolve the question of long-term events such as the rearrangement of the structure inside the membrane without validating a proper force field. We already know from previous results related to other compounds (Murail et al. 2018) that disordered aggregates may also display high water conductance and ion selectivity but these structures have shown limited robustness under application of the current force field. This observation emphasizes the difficulty to validate the force field choice at these small timescales.

Regarding the test series we performed on the S-HC8 compound, we can minimize the actual mismatch between experimental results in stopped-flow experiments and our simulations where we found a water conductance of one to two orders of magnitude larger than the experimental value. Indeed, the choice of the model needs to be understood in order to correctly reproduce tendencies of the experiments. Moreover, the current studies were only tackling the stability and permeation mechanisms at equilibrium. Yet structural changes of such systems composed by a large number of interacting molecules has to be challenged under non-equilibrium conditions such as osmotic gradients or hydrostatic pressure (Kalra et al. 2003; Yoshida et al. 2017). Such considerations as a comparison between diffusional and osmotic single-channel permeabilities need to be clarified on these systems, in order to enlighten experimental observations in real systems. Although these dynamical aspects have been intensively studied in carbon nanotubes and biological channels (Horner et al. 2015), a long road to understand stability and water permeation mechanisms in molecular self-assemblies remains.

6 Conclusion and Perspectives

By varying the size of the patch of crystal-like assemblies of I_4 channels using MD simulations, we found that permeation rate scales with the total of number of channels. Large surface-to-volume-ratio in these *in silico* model systems could induce an overestimation of the permeation rate in contrast to experiments on liposome

substrates. Surprisingly, finite-size effects do not seem to be ruled out by the particular morphology of the more active channels. These findings suggest that collective effects that imply long-range interactions between compounds and lipid/compound interfacial energies have to be carefully investigated. Indeed, the scaling of these seed structures to a larger scale remains a challenge given the number of uncertainties related to the phase state of large self-assemblies in lipid bilayers. Although X-ray data provide a crystalline structure that displays permeation properties, we showed that the force field parameters that describe interactions between I_4 compounds is determinant to allow stability within the lipid bilayer and therefore control the permeation rate. Flexibility and mutual effects between hydrophobic and hydrophilic regions in these packed channels have shown to be a major asset to increase single-channel permeability. Simulations will play an important role in elaborating future designs of self-assembled compounds with improved properties. Previous and present studies rely on a static approach, therefore out-of-equilibrium simulations will confirm and complete the current scenario. Furthermore, Van der Waals interactions and electrostatic interactions will be investigated to calibrate the force field with respect to experimental data. At last, larger scales will be assessed by coarse-grained approaches (Chan and Král 2018; Brandner et al. 2019) in order to study the feasibility of scalable membrane constructs linking to the macro-scale (Kumar et al. 2012; Shen et al. 2018).

Acknowledgements This work was conducted within the ANR-15-CE29-0009 DYNAFUN (Mihail Barboiu) and ANR-18-CE06-0004 WATERCHANNELS (Fabio Sterpone) projects. The study was further supported by the “Initiative d’Excellence” program from the French State (Grant “DYNAMO”, ANR-11-LABX-0011 and grant “CACISICE”, ANR-11-EQPX-0008). A.H. and M.B. thank Sesame Ile-de-France for co-funding the display wall used for data analysis. Computational work was performed using HPC resources from GENCI-CINES (grant number A0070701714) to Marc Baaden. This publication received support from the H2020 ERA Chairs Project no 667387: SupraChem Lab Laboratory of Supramolecular Chemistry for Adaptive Delivery Systems ERA Chair initiative.

References

- Tan Z, Chen S, Peng X et al (2018) Polyamide membranes with nanoscale Turing structures for water purification. *Science* 360:518–521. <https://doi.org/10.1126/science.aar6308>
- Garate J-A, English NJ, MacElroy JMD (2009) Static and alternating electric field and distance-dependent effects on carbon nanotube-assisted water self-diffusion across lipid membranes. *J Chem Phys* 131:114508. <https://doi.org/10.1063/1.3227042>
- Köfinger J, Hummer G, Dellago C (2008) Macroscopically ordered water in nanopores. *Proc Natl Acad Sci* 105:13218–13222. <https://doi.org/10.1073/pnas.0801448105>
- Noy A, Wanunu M (2020) A new type of artificial water channels. *Nat Nanotechnol* 15:9–10. <https://doi.org/10.1038/s41565-019-0617-5>
- Licsandru E, Kocsis I, Shen Y et al (2016) Salt-excluding artificial water channels exhibiting enhanced dipolar water and proton translocation. *J Am Chem Soc* 138:5403–5409. <https://doi.org/10.1021/jacs.6b01811>

- Kocsis I, Sorci M, Vanselow H, et al (2018) Oriented chiral water wires in artificial transmembrane channels. *Sci Adv* 4:eao5603. <https://doi.org/10.1126/sciadv.aao5603>
- Murail S, Vasiliu T, Neamtu A et al (2018) Water permeation across artificial I-quartet membrane channels: from structure to disorder. *Faraday Discuss* 209:125–148. <https://doi.org/10.1039/C8FD00046H>
- Sun Z, Kocsis I, Li Y et al (2018) Imidazole derivatives as artificial water channel building-blocks: structural design influence on water permeability. *Faraday Discuss* 209:113–124. <https://doi.org/10.1039/C8FD00024G>
- Klauda JB, Venable RM, Freites JA et al (2010) Update of the CHARMM all-atom additive force field for lipids: validation on six lipid types. *J Phys Chem B* 114:7830–7843. <https://doi.org/10.1021/jp101759q>
- Jorgensen WL, Chandrasekhar J, Madura JD et al (1983) Comparison of simple potential functions for simulating liquid water. *J Chem Phys* 79:926–935. <https://doi.org/10.1063/1.445869>
- Vanommeslaeghe K, MacKerell AD (2012) Automation of the CHARMM General Force Field (CGenFF) I: bond perception and atom typing. *J Chem Inf Model* 52:3144–3154. <https://doi.org/10.1021/ci300363c>
- Vanommeslaeghe K, Raman EP, MacKerell AD (2012) Automation of the CHARMM General Force Field (CGenFF) II: assignment of bonded parameters and partial atomic charges. *J Chem Inf Model* 52:3155–3168. <https://doi.org/10.1021/ci3003649>
- Jo S, Kim T, Iyer VG, Im W (2008) CHARMM-GUI: a web-based graphical user interface for CHARMM. *J Comput Chem* 29:1859–1865. <https://doi.org/10.1002/jcc.20945>
- Lee J, Cheng X, Swails JM et al (2016) CHARMM-GUI input generator for NAMD, GROMACS, AMBER, OpenMM, and CHARMM/OpenMM simulations using the CHARMM36 additive force field. *J Chem Theory Comput* 12:405–413. <https://doi.org/10.1021/acs.jctc.5b00935>
- Humphrey W, Dalke A, Schulten K (1996) VMD: visual molecular dynamics. *J Mol Graph* 14:33–38. [https://doi.org/10.1016/0263-7855\(96\)00018-5](https://doi.org/10.1016/0263-7855(96)00018-5)
- Gowers RJ, Linke M, Barnoud J, et al (2016) MDAnalysis: a Python package for the rapid analysis of molecular dynamics simulations. In: *Proceedings of the 15th Python Science Conference*, pp 98–105. <https://doi.org/10.25080/Majors-629e541a-00e>
- Michaud-Agrawal N, Denning EJ, Woolf TB, Beckstein O (2011) MDAnalysis: a toolkit for the analysis of molecular dynamics simulations. *J Comput Chem* 32:2319–2327. <https://doi.org/10.1002/jcc.21787>
- Smart OS, Neduvelil JG, Wang X et al (1996) HOLE: a program for the analysis of the pore dimensions of ion channel structural models. *J Mol Graph* 14:354–360. [https://doi.org/10.1016/S0263-7855\(97\)00009-X](https://doi.org/10.1016/S0263-7855(97)00009-X)
- Zhu F, Tajkhorshid E, Schulten K (2004) Theory and simulation of water permeation in aquaporin-1. *Biophys J* 86:50–57. [https://doi.org/10.1016/S0006-3495\(04\)74082-5](https://doi.org/10.1016/S0006-3495(04)74082-5)
- Haslwanter T (2016) Linear regression models. In: Haslwanter T (ed) *An introduction to statistics with Python: with applications in the life sciences*. Springer International Publishing, Cham, pp 183–220
- Horner A, Zocher F, Preiner J et al (2015) The mobility of single-file water molecules is governed by the number of H-bonds they may form with channel-lining residues. *Sci Adv* 1:e1400083. <https://doi.org/10.1126/sciadv.1400083>
- Alexiadis A, Kassinos S (2008) Self-diffusivity, hydrogen bonding and density of different water models in carbon nanotubes. *Mol Simul* 34:671–678. <https://doi.org/10.1080/08927020802073057>
- Caleman C, van Maaren PJ, Hong M et al (2012) Force field benchmark of organic liquids: density, enthalpy of vaporization, heat capacities, surface tension, isothermal compressibility, volumetric expansion coefficient, and dielectric constant. *J Chem Theory Comput* 8:61–74. <https://doi.org/10.1021/ct200731v>
- Wang J, Wolf RM, Caldwell JW et al (2004) Development and testing of a general amber force field. *J Comput Chem* 25:1157–1174. <https://doi.org/10.1002/jcc.20035>

- Kalra A, Garde S, Hummer G (2003) Osmotic water transport through carbon nanotube membranes. *Proc Natl Acad Sci U S A* 100:10175–10180. <https://doi.org/10.1073/pnas.1633354100>
- Yoshida H, Marbach S, Bocquet L (2017) Osmotic and diffusio-osmotic flow generation at high solute concentration. II. Molecular dynamics simulations. *J Chem Phys* 146:194702. <https://doi.org/10.1063/1.4981794>
- Chan H, Král P (2018) Nanoparticles self-assembly within lipid bilayers. *ACS Omega* 3:10631–10637. <https://doi.org/10.1021/acsomega.8b01445>
- Brandner AF, Timr A, Melchionna S, et al (2019) Modelling lipid systems in fluid with Lattice Boltzmann Molecular Dynamics simulations and hydrodynamics. *Sci Rep* 9:16450. <https://doi.org/10.1038/s41598-019-52760-y>
- Kumar M, Habel JEO, Shen Y et al (2012) High-density reconstitution of functional water channels into vesicular and planar block copolymer membranes. *J Am Chem Soc* 134:18631–18637. <https://doi.org/10.1021/ja304721r>
- Shen Y, Song W, Barden DR et al (2018) Achieving high permeability and enhanced selectivity for Angstrom-scale separations using artificial water channel membranes. *Nat Commun* 9:1–11. <https://doi.org/10.1038/s41467-018-04604-y>
- Mahoney MW, Jorgensen WL (2000) Diffusion constant of the TIP5P model of liquid water. *J Chem Phys* 114:363–366. <https://doi.org/10.1063/1.1329346>

Functional Microporous Polymer Networks: Synthesis and Applications



Alex Palma-Cando and Ullrich Scherf

Abstract Microporous polymer networks (MPNs) possess a high potential for such applications where high specific surface areas and extended π -conjugation (causing semiconductive properties) are a must. Some relevant experimental results for chemical and electrochemical generation of functional microporous polymer networks gathered during the last decade in our groups are here presented. Smart design of rigid 3D building blocks (tectons) allows to produce microporous polymers with specific surface areas up to $2200 \text{ m}^2 \text{ g}^{-1}$. Microporous monoliths have been e.g. used for oil trapping from aqueous mixtures while thin MPN films showed a high potential in the optical and electrochemical detection of nitroaromatic explosives up to low ppb concentrations.

Keywords Microporous Polymer Networks (MPNs) · Electrodeposition · Electrochemical sensing · Optical sensing · Nitroaromatic analytes · Thin film sensors · Polymer monoliths

Abbreviations

AFM	Atomic force microscopy
AIE	Aggregation-induced emission
BFEE	Boron trifluoride ethyl etherate
CMP	Conjugated microporous polymer
CPMAS	Cross-polarization magic-angle spinning
DCM	Dichloromethane

A. Palma-Cando
School of Chemical Sciences and Engineering, Materials and Processes Applied Research Group (GIAMP), Yachay Tech University, Hda. San José s/n y Proyecto Yachay, 100119 Urcuquí, Ecuador

U. Scherf (✉)
Macromolecular Chemistry Group and Wuppertal Institute for Smart Materials and Systems, Bergische Universität Wuppertal, Gaußstraße 20, 42119 Wuppertal, Germany
e-mail: scherf@uni-wuppertal.de

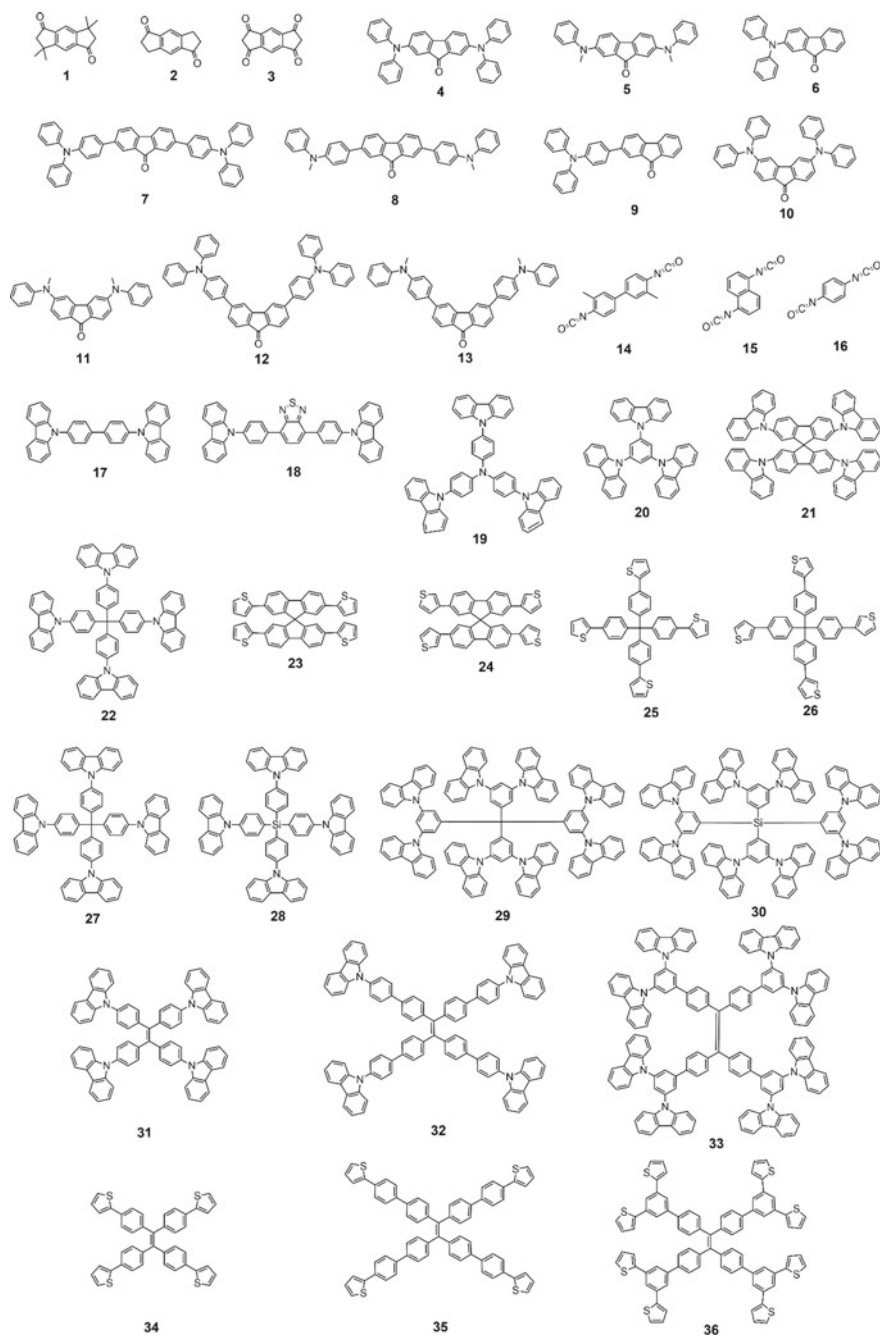
DMI	1,3-Dimethyl-2-imidazolidinone
DNB	1,3-Dinitrobenzene
DNT	2,4-Dinitrotoluene
EQCM	Electrochemical quartz-crystal microbalance
GC	Glassy Carbon
HCP	Hypercrosslinked polymers
ITO	Indium tin oxide
LSV	Linear sweep voltammetry
MPN	Microporous polymer network
NB	Nitrobenzene
ODB	1,2-Dichlorobenzene
PAF	Porous aromatic framework
PL	Photoluminescence
<i>p</i> -TolSO ₂ Na	Sodium <i>p</i> -toluenesulfinate
Rq	Root-mean-square roughness
S _{BET}	Brunauer–Emmett–Teller specific surface areas
TBABF ₄	Tetrabutylammonium tetrafluoroborate
TBAF	Tetrabutylammonium fluoride
TBAP	Tetrabutylammonium perchlorate
TDAE	Tetrakis(dimethylamino)ethylene
THF	Tetrahydrofuran
TNB	1,3,5-Trinitrobenzene
TNP	2,4,6-Trinitrophenol
TNT	2,4,6-Trinitrotoluene
TPE	Tetraphenylethylene
WE	Working electrode

1 Introduction

Polymerization of bifunctional monomers usually leads to the formation of 1D-linear or branched, non-porous polymers. By chemical modification of a precursor polymer, hypercrosslinked polymers (HCPs) have been produced using different cross-linkers (Tan and Tan 2017). These HCPs showed *high Brunauer–Emmett–Teller* (BET)-derived surface areas (S_{BET}) up to 3000 m² g⁻¹ (Wang et al. 2017). A different approach for synthesizing porous polymer structures is based on the polymerization of rigid, multifunctional 3D monomers. The resulting, mostly amorphous materials are covalently bond and highly crosslinked organic structures that present inherent microporosity (porous diameter < 2 nm) (Sing et al. 1984) and high surface areas (Preis et al. 2015a). Conjugated microporous polymers (CMPs) (Lee and Cooper 2020) and porous aromatic frameworks (PAFs) (Yuan and Zhu 2019) are common names used to described these type of polymer networks. Only difference between CMPs and PAFs is the occurrence/non-occurrence of extended π -conjugation thus

causing problems in the classification of (micro)porous polymers (Jiang et al. 2007). To avoid misunderstandings, we have opted for a different terminology, Microporous Polymer Networks (MPNs), which includes both CMPs and PAFs. MPNs have shown application potential in gas storage and separation (Lu et al. 2010), adsorption and encapsulation of chemicals (Wang et al. 2013), heterogeneous catalysis (Xie et al. 2013), photoredox catalysis (Zhang et al. 2013), light emittance (Bonillo et al. 2016), chemo- and biosensing (Geng et al. 2016), energy storage (Zhang et al. 2018), and in biological applications (Bhunia et al. 2018). Synthesis chemical routes for the production of MPNs are mainly dealing with C-C coupling or C-N coupling reactions such as Sonogashira-Hagihara coupling (Trunk et al. 2016), Suzuki-Miyaura coupling (Chen et al. 2010), Yamamoto coupling (Schmidt et al. 2009), Heck coupling (Sun et al. 2013), cyclotrimerizations (Buyukcakir et al. 2019), phenazine ring fusion (Marco et al. 2017), Schiff-base condensations (Xu and Hedin 2013), heterocycle linkages (Biswal et al. 2018), alkyne metathesis (Lu et al. 2015), Buchwald-Hartwig amination (Liao et al. 2018), direct arylation (Liu et al. 2013), polyolefinations (Preis et al. 2015a), and oxidative couplings (Qiao et al. 2014). MPNs produced by these chemical routes are usually insoluble and practically intractable powders or monoliths that cannot be processed into thin films for applications in the field of organic electronics. Electrochemical, oxidative generation of MPNs has proved to be an promising technique for the preparation of high quality thin MPN films (Suresh and Scherf 2018). The electropolymerization method allows for simultaneous MPN formation and deposition under mild and catalyst-free conditions, and in short times. Anodic electropolymerization is accomplished by oxidation of multifunctional monomers at the electrode followed by cascades of radical ion-radical ion coupling reactions which leads to dimers, trimers, tetramers, oligomers up to polymer networks (Ibanez et al. 2018). A controlled deposition of the growing thin MPN films on the electrode surface is driven by a progressively reduced solubility of the coupling products (Heinze et al. 2010). Thiophenes and carbazoles are the most used electroactive motifs with low oxidation potential, that are applied in combination with suitable linkers in the electrogeneration of MPN films (Palma-Cando et al. 2019a; Zhang et al. 2015).

Hereinafter, we discuss some of our efforts and contributions in the synthesis, characterization and application of microporous polymer networks during the past decade. A library of diverse monomers utilized for the generation of MPNs is presented in Scheme 1. In the first part, we review some examples of chemically synthesized MPNs based on cyclotrimerizations and Friedel-Craft-type polycondensations. Then, we will focus on the electrochemical generation of thin MPN films based on multifunctional carbazole- and thiophene-based rigid monomers and their application as luminescent or electrochemical sensors for nitroaromatic analytes. Both oxidative chemical or electrochemical polymerizations have been comparatively studied, e.g. concerning the inherent porosity of bulk powders and thin MPN films, respectively.



Scheme 1 Chemical structures of chemically or electrochemically polymerized monomers for generation of microporous polymer networks (MPNs)

2 Chemically Synthesized Microporous Polymer Networks

A first selected approach in the synthesis of microporous polymer networks is based on a well-known synthesis of truxene derivatives by cyclotrimerization, here by using bifunctional *s*-indacene monomers (Sprick et al. 2010). Truxene itself is obtained in the cyclotrimerization of indan-1-one with protic (Dehmlow and Kelle 1997) or Lewis acids (Ansems et al. 2000), while truxenone can be synthesized in the condensation of indan-1,3-dione with protic acids (Sanguinet et al. 2006). Figure 1 shows the chemical structures of our bifunctional monomers **1–3**. Polycondensation of monomer **1** was tested under different acidic conditions resulting in a MPN yield of ca. 85% by using titanium tetrachloride as Lewis acidic catalyst in 1,2-dichlorobenzene (180 °C, 72 h). Monomers **2** and **3** were polymerized under similar conditions using titanium tetrachloride (for 72 h) or methanensulfonic acid (for 3 h), respectively, with a quantitative polymer yield. Idealized structures of the resulting ladder-type MPNs are shown in Fig. 1. These network polymers showed excellent thermal stability in air up to 330 °C. Solid state $^{13}\text{C}\{^1\text{H}\}$ cross-polarization magic-angle spinning (CPMAS) NMR spectroscopy confirmed the formation of the idealized structural motifs including low-intensity carbonyl-related end group signals. Surface area (S_{BET}) values of the bulk polymers were obtained by applying the Brunauer–Emmett–Teller equation to the corresponding nitrogen adsorption isotherms. **P1** showed a S_{BET} value of 395 m^2g^{-1} which was much lower than the S_{BET} values of 1165 m^2g^{-1} for **P2** possibly related to the presence of bulkier methyl substituents that support pore formation. **P3** showed the highest S_{BET} value of 1650 m^2g^{-1} for a MPN powder obtained in a metal-free, acid catalyzed cyclotrimerization.

As second example of our selection, acid-catalysed Friedel–Craft-type polycondensations were applied to a series of 10 multifunctional arylamino-substituted fluorenone monomers (see monomers **4–13** in Scheme 1) and binary mixtures of them

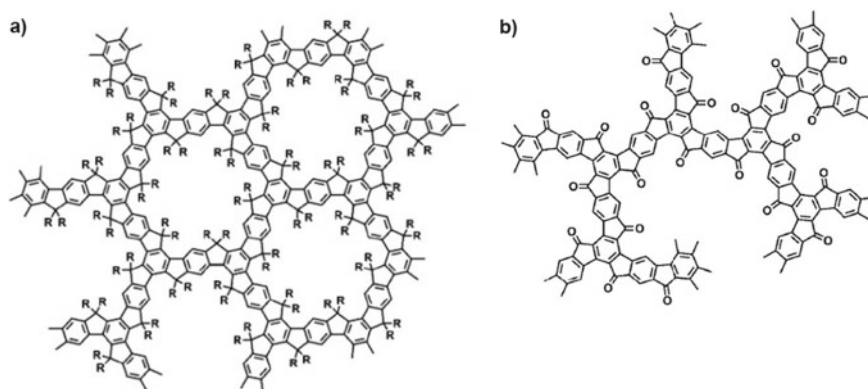


Fig. 1 Idealized chemical structures of MPNs **a** P1 and P2 (P1: R = CH₃, P2: R = H), and **b** P3. (Sprick et al. 2010). Reproduced with permission of The Royal Society of Chemistry

(Preis et al. 2011). $A_2 + B_2$ and AB_2 polycondensations under Friedel-Craft reaction conditions between aromatic ketones and bifunctional aromatic moieties lead to the formation of linear, high molecular weight polymers (Zolotukhin et al. 2004) and hyperbranched polymers, (Smet et al. 2002) respectively. We used the similar synthetic principles for the generation of MPNs (for **P4–P6** see Fig. 2) starting from A_4B_2 and A_2B_2 monomers, carried out with methane sulfonic acid as catalyst in 1,2-dichlorobenzene (at 140 °C). Formation of rigid, three-dimensional (3D) structures was obtained in a single reaction step under formation of 9,9-diphenylfluorene knot motifs in nearly quantitative yields. Thermogravimetric analysis showed good stability of the MPNs up to 250 °C. Solid-state $^{13}\text{C}\{^1\text{H}\}$ CPMAS NMR spectra for **P4** showed a broad signal with three maxima at 129 ppm, 138 ppm and 148 ppm for the aromatic carbons and a weak signal at 63 ppm assigned to the aliphatic tetragonal carbon that is formed during condensation. The resulting MPN (**P4**) showed maximum S_{BET} values of $1420 \text{ m}^2 \text{ g}^{-1}$ for homopolymers due to the rigidity and high cross-linking density of the MPNs. Copolymerization of two different monomers followed by supercritical CO_2 treatment (sc CO_2 washing) led to optimized S_{BET} values up to $1775 \text{ m}^2 \text{ g}^{-1}$ for a copolymer from monomers **1/3** (1:1 w/w). For comparison, the same, non-sc CO_2 -washed copolymer showed a reduced S_{BET} of $718 \text{ m}^2 \text{ g}^{-1}$. Therefore, exchange of leftover organic solvents by sc CO_2 distinctly increases the accessible S_{BET} surface area of the MPNs. This effect was more noticeable for MPNs of lower less cross-linking density in comparison to highly cross-linked MPNs. Optimized homopolymerization of monomer **4** (Scheme 1) with trifluoromethane sulfonic acid as catalyst in 1,2-dichlorobenzene at 140 °C led to MPNs showing high S_{BET} values of up to $2250 \text{ m}^2 \text{ g}^{-1}$ (Preis et al. 2013). Maximum pore volume and hydrogen storage capacity determined for this MPN (**P4**) are $2.16 \text{ cm}^3 \text{ g}^{-1}$ and 1.68%, respectively.

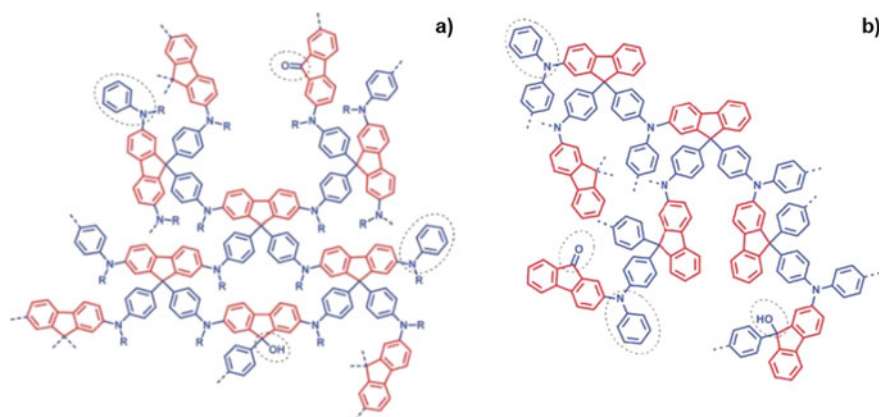


Fig. 2 Idealized chemical structures of MPNs **a** P4 and P5 (P4: R = phenyl and P5: R = methyl), and **b** P6. Unreacted aromatic, keto units and 9-monosubstituted fluorene cores that form end groups cores are encircled. Modified with permission (Preis et al. 2011). Reproduced with permission of The Royal Society of Chemistry

As third example of MPN generation, the metal-free cyclotrimerization of three different aromatic diisocyanate monomers (see monomers **14–16** in Scheme 1) allows for the generation of monolithic MPNs (Preis et al. 2015b). These commercial low-priced monomers undergo cyclotrimerization under triarylcyanurate formation (see Fig. 3a), by using three different catalyst systems: sodium p-toluenesulfinate (p-TolSO₂Na), (Moritsugu et al. 2011) tetrabutylammonium fluoride (TBAF) (Nambu and Endo 1993), or tetrakis(dimethylamino)ethylene (TDAE) (Giuglio-Tonolo et al. 2014). A 3 × 7 experimental matrix was set up under variation of monomers, catalysts, solvents, and reaction temperature. Five of the monolithic MPNs obtained from monomer **14** showed a combination of high yield and high S_{BET} surface areas; **P14-1** (92% yield and S_{BET} 783 m² g⁻¹: with 10% TBAF in DMI at 150 °C), **P14-2** (92%; 971 m² g⁻¹: with 10% TBAF in ODB at 150 °C), **P14-3** (98%; 216 m² g⁻¹: with 10% TBAF in THF at 150 °C), **P14-4** (100%; 115 m² g⁻¹: with 10% p-TolSO₂Na in DMI at 150 °C), and **P14-5** (86%; 711 m² g⁻¹: with 10% TDAE in DMI at room temperature). A second 3 × 15 experimental matrix was applied to optimize the catalyst concentrations (10%, 5% and 1%) for the five promising polymerization conditions. Herein, **P14-6** was obtained under similar condition as **P14-4** with a 1% TBAF resulting in a monolithic MPN with quantitative yield and a S_{BET} value of 1320 m² g⁻¹ thus demonstrating the influence of the catalyst/monomer ratio on the cross-linking density of the resulting polymer networks (more than one order of magnitude of improvement in S_{BET}). This easily produced MPN **P14-6** shows reasonably high gas uptakes of 1.3 wt%, 1.1 wt%, and 14.4 wt% for hydrogen (at 77 K), methane (at 273 K), and carbon dioxide (at 273 K), respectively. Moreover, up-scaling the production of **P14-6** was demonstrated by using a 100 g monomer batch resulting in compact, monolithic MPN chunks with a slightly increased S_{BET} of 1510 m² g⁻¹. These results suggested potential applications of such MPN monoliths for the capture and storage of gases. It was found that increasing the monomer concentration over a certain threshold leads to the formation of MPNs of higher surface area. This behavior is probably related to an increased cross-linking density.

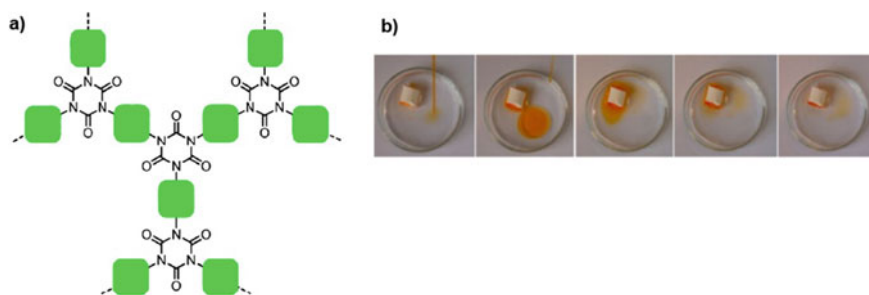


Fig. 3 **a** Idealized chemical structure of the MPNs P14-P16 made from rigid, aromatic diisocyanates (green rectangle represents the aromatic cores: (in P14) 2,2'-dimethyl-biphenyl-1,1'-diyl, (in P15) 1,5-naphthylene and (in P16) 1,4-phenylene, and **b** photographs showing dodecane (dyed with Sudan I) sorption into a microporous, monolithic P14 chunk from aqueous mixture (Preis et al. 2015b). Reproduced with permission of the American Chemical Society

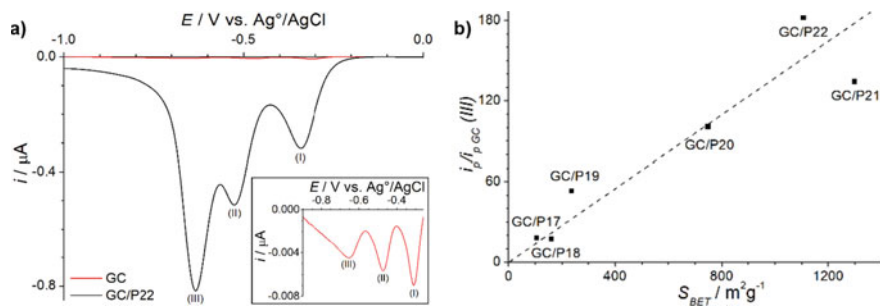


Fig. 4 **a** Linear scan voltammograms (after background correction) for reduction of 0.5 μM aqueous TNB solution at P22-modified and bare (at scan rate of 0.01 V s^{-1}) and **b** current ratio of the third reduction peak of TNB at MPN-modified and bare glassy carbon electrodes versus S_{BET} of the MPN films (Palma-Cando and Scherf 2015). Adapted with permission of the American Chemical Society

Removal of oily contaminants from aqueous mixtures was investigated for such **P14** monoliths. Figure 3b shows photographs for the dodecane (as model for an oily contamination, dyed with Sudan I) sorption from an aqueous mixture using microporous **P14** chunks. Hereby, the low-density MPN material (0.18 g cm^{-3}) is floating on the water surface and is completely trapping the oily pollutant (within short times of less than one minute, under up to fourfold mass increase).

3 Electrochemically Synthesized Microporous Polymer Networks

Electrochemical oxidative polymerization of multifunctional monomers with low oxidation potential leads directly to the formation of thin MPN films, while the wet-chemistry based oxidative coupling produces MPN powders (or, in some cases, monoliths) (Palma-Cando and Scherf 2016). Hereby, non-aqueous monomer solutions are usually applied at low concentrations (μM) with supporting organic electrolytes based on tetrabutylammonium salts (Palma-Cando et al. 2014). MPN films can favorably be generated in a three-electrode cell connected to a potentiostat/galvanostat which controls potential and current applied to the system. Microporous polymer films are deposited on the working electrode (WE) by oxidative polymerization. Electronic conductors used as inert WE are usually made of gold, platinum, glassy carbon or ITO (Gurunathan et al. 1999). Our first approach into the generation of MPN films dealt with the electrochemical polymerization of multifunctional carbazole monomers (for the six investigated monomers see **17–22** in Scheme 1) containing two, three and four carbazole units (Palma-Cando and Scherf 2015). Ambrose and Nelson described the mechanism for the electrochemical oxidative coupling of carbazoles under formation of cation radicals that experience

radicalion-radicalion couplings into 3,3'-bicarbazole dimers (Ambrose and Nelson 1968). Dimers can undergo further reactions such as 6,6'-couplings, into extended oligomers and polymers. In the polymerization of monomers **17–22** we first studied the influence of the number of carbazoles attached to the core of the tectons on the resulting surface area of the deposited microporous polymers. Nitrogen and krypton adsorption isotherms were recorded for the six different MPNs made both by bulk chemical polymerization with FeCl_3 (for comparison) and potentiostatic electrochemical polymerization, respectively. Electrogenerated MPN films were synthesized from diluted monomer solutions in acetonitrile/dichloromethane mixtures. Adsorption isotherms of films and powders showed similar trends with a fast N_2 or Kr uptake at low relative pressure (<0.1) which is characteristic for the occurrence of permanent microporosity (Sing et al. 2008). Table 1 lists the S_{BET} values for bulk microporous polymer powders and the respective MPN films. Similar surface area values for bulk polymers and thin films were obtained for the tetrasubstituted MPNs (**P21** and **P22**). On the other hand, decreased S_{BET} values were determined for films generated from bi- and trisubstituted monomers if compared to the corresponding MPN powders (**P17–P20**). Reduced cross-linking density for the electrogenerated films is most probably caused by an exclusive formation of carbazole dimers while FeCl_3 bulk polymerization also yields 3,5-disubstituted carbazoles (Chen et al. 2012). Moreover, a direct relationship between the number of carbazole groups in the monomers and the S_{BET} values of the resulting MPN films was observed based on increased cross-linking density and rigidity of the MPNs when increasing the functionality of the monomers. Tetrafunctionalized monomers provide an optimum amount of possible cross-linking sites (Zhang et al. 2014).

Electrogenerated polymer films are very promising materials for the fabrication of electrochemical sensors and biosensors (Terán-Alcocer et al. 2021) for various analytes such as neurotransmitters (Moon et al. 2018), pharmaceuticals (Eslami and Alizadeh 2016), glucose (Naveen et al. 2017), hydrogen peroxide (Park et al. 2016), nitrites (Ge et al. 2020), or nitroaromatic compounds (Guo et al. 2015). We used thin, carbazole-based MPN films for the electrochemical detection of 1,3,5-trinitrobenzene (TNB) as prototypical nitroaromatic compound in aqueous solution, based on its cathodic reduction. An increased current response of up to 182 times was observed for **P22** films on glassy carbon (GC) electrodes when contacted with aqueous TNB solutions, if compared to the current response of bare GC electrodes (see Fig. 4a). An interesting correlation was found between the current response increase (bare GC vs. MPN coated GC electrodes) and the S_{BET} of the MPN films (see Fig. 4b). Hereby, the formation of charge-transfer complexes between the electron-poor nitroaromatic analytes and the electron-rich MPN films is boosted by the much higher electroactive surface area at the MPN-modified electrodes where the analyte reduction takes place (Evans et al. 2002; Zhang et al. 2006; Shamsipur et al. 2015).

Regarding civil and environmental security, the detection of explosives in the gas-phase is highly desirable (Sun et al. 2015). Here, fluorescent polymers networks have shown high application potential as luminescent sensor for explosive traces (Liu et al. 2012). We used spirobifluorene-cored MPN films (**P21**) for the gas-phase detection of nitroaromatic explosives due to their intense inherent fluorescence and high S_{BET}

Table 1 Calculated specific BET surface areas S_{BET} of chemically synthesized bulk polymer powders as well as of electrogenerated MPN films using N_2 or Kr gas sorption, respectively

Polymer	Number of electroactive units	S_{BET} powder ($m^2 g^{-1}$)	S_{BET} film ($m^2 g^{-1}$)	Polymer	Number of electroactive units	S_{BET} powder ($m^2 g^{-1}$)	S_{BET} film ($m^2 g^{-1}$)
P17	2	225	104	P27	4	1322	1106
P18	2	324	159	P28	4	574	492
P19	3	1065	236	P29	8	1331	1027
P20	3	1647	748	P30	8	1194	872
P21	4	1249	1297	P31	4	1097	979
P22	4	1322	1106	P32	4	1039	874
P23	4	1153	815 ^a 1240 ^b	P33	8	2203	2170
P24	4	1102	1099 ^a 1576 ^b	P34	4	1085	433
P25	4	2020	1258 ^a 2135 ^b	P35	4	956	–
P26	4	1390	927 ^a 1114 ^b	P36	8	1767	1634

^aSolvent: dichloromethane; ^bSolvent: DCM/BFEE

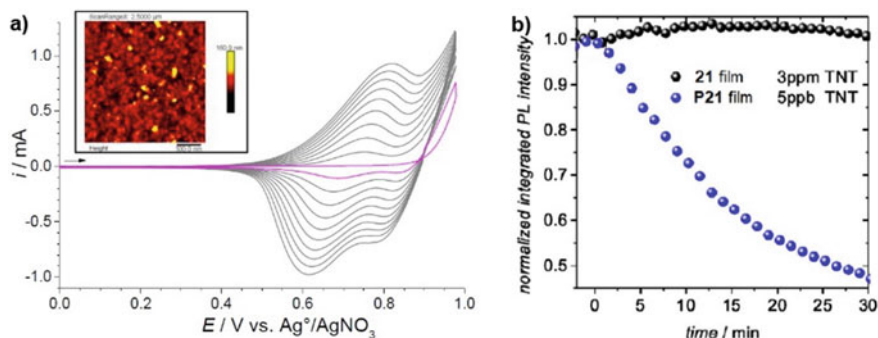


Fig. 5 **a** Ten successive cyclic voltammograms at an ITO electrode for 0.5 mM solution of monomer **21** in acetonitrile/dichloromethane (1:4) and 0.1 M TBAP as supporting electrolyte, potential range: 0–0.98 V, scan rate: 0.10 Vs^{-1} . The inset shows a tapping mode AFM image of the resulting MPN film. **b** Integrated PL response to different TNT vapor concentrations (455–480 nm) for a vapor-deposited non-porous film of monomer **21** (black dots) and a microporous P21-film (blue dots) (Räupke et al. 2016). Reproduced with permission

surface area ($1297 \text{ m}^2 \text{ g}^{-1}$) (Räupke et al. 2016). Figure 5a shows 10 successive voltammetric cycles for the electrochemical polymerization of a 0.5 mM solution of monomer **21** in acetonitrile/dichloromethane (1:4) on ITO electrodes. **P21** thin films with thickness of ca. 50 nm are formed by cycling in a potential range of 0 V–0.98 V with a scan rate of 0.10 Vs^{-1} . A so-called nucleation loop with a crossing effect between the first anodic scan and the reverse sweep is observed during the first cycle. This phenomenon might be related to an autocatalytic reaction between oligomeric intermediates and monomers (Heinze et al. 2007). Tapping mode AFM image shows a rather smooth morphology with a mean roughness R_q of ~ 14 nm (see inset Fig. 5a). For the sensing experiment, analytes were placed in a closed chamber (analyte chamber) that is connected via a needle valve to a second chamber containing the **P21** films on ITO (sample chamber). Each chamber can be separately heated. Photoluminescence (PL) spectra of a **P21** film upon excitation at 355 nm show a PL peak centered at 472 nm. The so-called quenching efficiency of the **P21** PL upon exposure to different analytes (e.g. acetone, ethanol, toluene, benzene, nitrobenzene—NB, and 2,4-dinitrotoluene—DNT) were found to be >1 for electron-poor nitroaromatic analytes (NB and DNT), while for the other analytes only a slight effect on the PL was observed. A possible mechanism of PL quenching is an energy transfer between the excited, electron-rich host and the electron-poor nitroaromatic quencher (Toal and Trogler 2006). The higher quenching efficiency (DNT *vs.* NB) for the energy transfer from the LUMO level of **P21** (-2.58 eV) to the LUMO level of DNT (-3.22 eV) might be ascribed to a deeper lying LUMO level of DNT if compared to the LUMO level position of NB (-2.91 eV). Finally, gas-phase detection of 2,4,6-trinitrotoluene (TNT) at low concentrations down to 5 ppb (room temperature vapor pressure) was investigated. Our **P21** films showed a maximum quenching of ca. 50% after 30 min by contact with TNT vapors (see Fig. 5b). Already after 2–3 min

a significant PL quenching response was recorded. For comparison, PL quenching was not detectable for non-porous films, vapor-deposited films of monomer **21** at even much higher TNT concentration of 3 ppm (3 orders of magnitude increased concentration). These results clearly demonstrate the crucial role of microporosity and high surface area of the films by facilitating the interaction between the MPN surface and the quencher molecules.

In a second attempt, we studied the electrochemical, oxidative polymerization of tetrathienyl-substituted spirobifluorene- and tetraphenylmethane-cored monomers (see monomers **23–26** in Scheme 1) both in pure dichloromethane and dichloromethane/boron trifluoride ethyl etherate (DCM/BFFE) mixtures (Palma-Cando et al. 2015). The coupling mechanism for electron-rich heteroaromatics such as thiophenes is described in a similar way as done for carbazole-based monomers (Diaz et al. 1981). The potential required for the oxidation of the monomer is always higher than potential needed for oxidation of the oligomeric species that are formed in a cascade of condensation reactions toward formation of polymeric chains. It has been demonstrated that the addition of boron trifluoride decreases the needed potential for monomer coupling by reducing the aromaticity of the system through BF_3 interaction with the lone electron pair at the thiophene sulfur (Shi et al. 1995, 1999). The resulting surface areas extracted from nitrogen or krypton sorption measurements of thin, electrogenerated MPN films and, for comparison, of bulk MPN powders obtained by wet-chemical coupling with FeCl_3 , respectively, are listed in Table 1. The highest S_{BET} surface areas for thin MPN films were achieved for deposition from DCM/BFFE mixtures with S_{BET} values like that of the corresponding bulk polymer powders. This finding indicates the importance of reducing the potential for the monomer oxidation. The connectivity of the networks made from the 3-thienylbased monomers (**24** and **26**) was significantly affected by the presence of boron trifluoride. The formation of hyperbranched oligothiophene structures containing 2,3,5-trisubstituted thiophene units was obtained in electrochemical polymerization in DCM (see Fig. 6a). However, MPN deposition from **24** and **26** in DCM/BFEE mixtures preferably led to the formation of 2,2'-bithiophene links similar to that what is generally observed for the corresponding 2-thienyl-substituted monomers **23** and **25** (see Fig. 6b and c). Moreover, electrochemical reduction of TNB at **P25**-modified GC electrodes showed a linear relationship between current response and thickness of the microporous deposits. These results confirm the role of the donor–acceptor interaction between electron-poor nitroaromatic and electron-rich moieties after modifying GC electrodes with **P25**-films.

In a further study we utilized tetra- and octacarbazole-functionalized monomers with three dimensional, rigid tetraphenylmethane and tetraphenylsilane cores for electrochemical (and wet-chemical) MPN generation (see monomers **27–30** in Scheme 1) (Palma-Cando et al. 2016). Bulk polymer powders were isolated in high yields for the oxidative coupling of these multifunctional monomers with FeCl_3 . MPN powders showed good thermal stability and intense photoluminescence (PL) with maxima at 444 nm (**P27**), 473 nm (**P28**), 482 nm (**P29**), and 471 nm (**P30**). In addition, a reasonable CO_2 trapping capacity was shown for **P29** with a storage

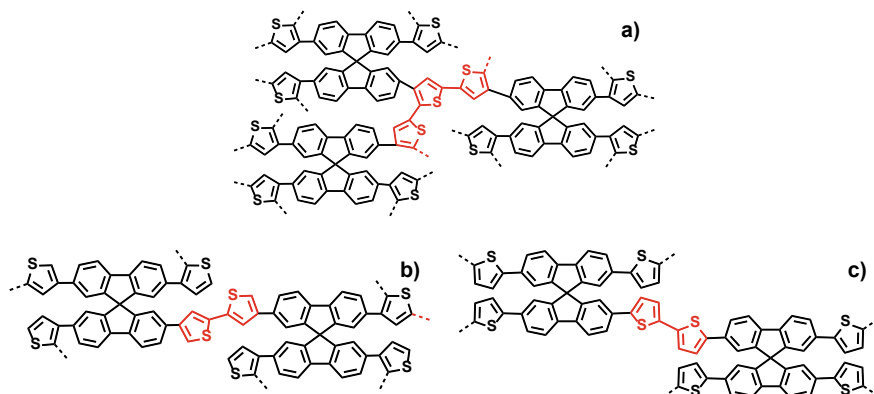


Fig. 6 Idealized chemical structure of the thienyl-thienyl links in microporous films **a** electrochemically prepared P24 in DCM, **b** electrochemically prepared P24 in DCM/BFEE mixture, and **c** wet-chemically prepared P23 (Palma-Cando et al. 2015). Adapted with permission of The American Chemical Society

capacity of up to ca. 9 wt%. Quartz-crystal microbalance measurements simultaneously coupled to the electrochemical film deposition (EQCM) was used for gaining more insight into the growth of the MPN films during the electropolymerization of our multifunctional monomers. The anodic scan in the first cyclic voltammogram for polymerization of monomer **27** showed a decrease in the EQCM frequency starting at the peak potential onset at ca. 0.9 V vs. Ag/AgNO₃ (see Fig. 7a). This frequency dropping is related to a mass increase that can be estimated by the Sauerbrey equation (Sauerbrey 1959) thus documenting oxidative coupling of carbazole units and subsequent irreversible deposition of a **P27** layer on the Pt/quartz electrode. A continuously increasing mass was observed indicating a homogeneous film growth overlaid by a reversible uptake and release of perchlorate counteranions due to doping/dedoping events in the as-grown **P27** layer. Nitrogen or krypton adsorption isotherms at 77 K for wet-chemically made bulk polymer powders or electrodeposited MPN films are depicted in Fig. 7b and c, respectively. Main gas capture at low relative pressure of <0.1 verifies the microporous nature of the materials. Slightly reduced specific surface areas were found for the electrodeposited MPN films if compared to the bulk polymer powders (see Table 1). **P29** made from octacarbazoly-substituted tetraphenylmethane tectons showed the highest S_{BET} of 1331 m² g⁻¹. Both silicon-cored MPNs displayed increased S_{BET} value in relation to the respective silicon-cored MPNs. This result can be related to electronic $\sigma - \pi$ -interactions of aromatic substituents through the silicon centers thus decreasing the reactivity of the carbazoly groups and leading to a lower cross-linking density (Traylor et al. 1970). Electrochemical sensing experiments for various nitroaromatic analytes were carried out on glassy carbon electrodes modified with microporous **P29** films. Figure 8b depicts linear scan voltammograms for the electrochemical reduction of 0.1 μM solutions

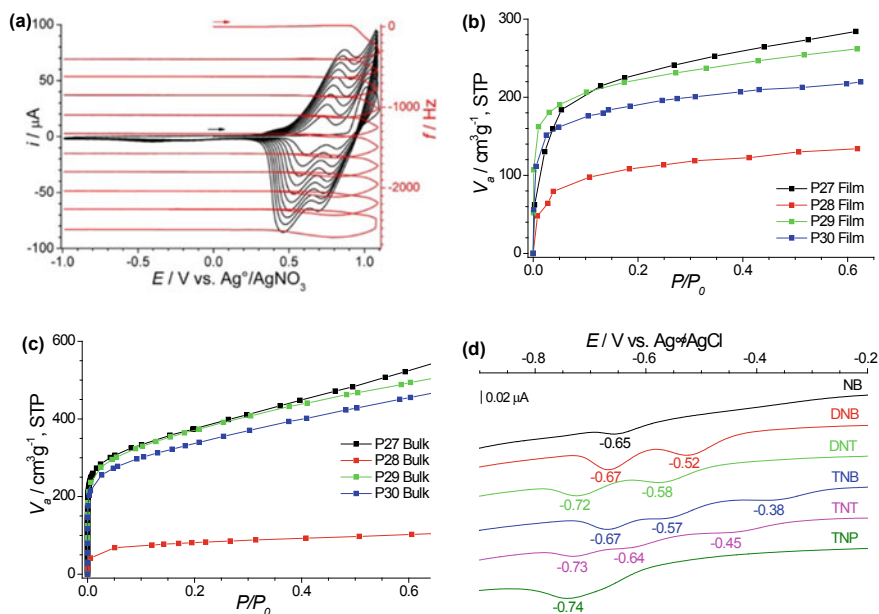


Fig. 7 a Ten cyclic voltammograms (black lines) and EQCM frequency changes (red lines), that reflect the mass accumulation in the electrochemical polymerization of 0.1 mM solutions of 27. Adsorption isotherms of **b** electropolymerized MPN films (Kr sorption) and **c** corresponding bulk polymer powders synthesized by oxidative coupling with $FeCl_3$ (N_2 sorption). **d** Linear scan voltammograms for the reduction of 0.1 μM solutions of various nitroaromatic analytes at P29-modified GC electrodes in buffered aqueous solution (pH 7.4). LSVs were obtained with a scan rate of 0.01 $V s^{-1}$ (Palma-Cando et al. 2016). Adapted with permission of the American Chemical Society

of nitrobenzene (NB), 1,3-dinitrobenzene (DNB), 2,4-dinitrotoluene (DNT), 1,3,5-trinitrobenzene (TNB), 2,4,6-trinitrophenol (TNP), and 2,4,6-trinitrotoluene (TNT) at P29-modified GC electrodes in an aqueous environment. A series of reduction peaks corresponding to the number of nitro functions in the analyte was observed for sub- μM concentrations of the analytes. Hereby, the position of the first reduction peak potential drops by increasing the number of nitro substituents in the analyte molecules, that means, less energy is required for the initial, interfacial charge transfer between the microporous polymer containing electron-rich bicarbazole-units and the electron-poor nitroaromatic compounds (Shamsipur et al. 2015). Similar results were reported by us for polymer networks deposited from multifunctional monomers with three or six carbazole units (Palma-Cando et al. 2019b).

In a follow-on study, we converted wet-chemically as well as electrochemically a series of six tetra- or octa-substituted carbazole- or thiophene-based, tetraphenylethylene (TPE)-cored monomers (see monomers 31–36 in Scheme 1) into microporous polymer materials (Palma-Cando et al. 2017). TPE is a prominent propeller-shaped structural motif that shows the so-called aggregation-induced emission (AIE)

phenomenon in the solid state. Main reason for occurrence of AIE effects is the restriction of intramolecular rotations and vibrations (Mei et al. 2014). Since early reports of the AIE effect, (Luo et al. 2001; Sharafy and Muszkat 1971) AIE phenomena received enormous attention from the scientific community due to potential applications in different fields (Jimenez and Rodríguez 2020). In our study, luminescent MPN powders based on TPE-cored tectons were obtained by wet-chemical oxidative coupling of monomers **31–36** with FeCl_3 , resulting in materials that are thermally stable up to 300 °C. Electrochemical, oxidative polymerization of the carbazole-based monomers **31–33** were carried out in dichloromethane solutions containing tetrabutylammonium tetrafluoroborate (TBABF_4) as electrolyte, while the thiophene-based monomers **34–36** required the addition of 20% (V/V) BFEE to the solution for effective film formation. Nitrogen or krypton gas adsorption data at 77 K within the relative pressure window of 0–0.6 were determined for bulk polymer powders and MPN films, respectively. A fast gas uptake at low relative pressures documents the microporous nature of the materials. Slightly reduced S_{BET} values were observed for the electrogenerated MPN films if compared to the corresponding bulk powders (see Table 1), probably indicating a reduced cross-linking density. The bulk polymer powders **P31** and **P34** showed quite similar S_{BET} values of ca. $1100 \text{ m}^2 \text{ g}^{-1}$, both containing tectons that are fourfold carbazolyl- or thienyl-substituted with the substituents directly attached to the TPE core. **P32** and **P35** polymers both containing 1,4-phenylene spacers between the electroactive units and the TPE core showed slightly reduced surface areas of $1039 \text{ m}^2 \text{ g}^{-1}$ and $956 \text{ m}^2 \text{ g}^{-1}$, respectively, for the bulk materials/powders. Electrochemically generated **P34** films, as an example for electrodeposited MPN films, display a clearly lowered surface area of only $433 \text{ m}^2 \text{ g}^{-1}$ possibly related to overoxidation effects due to the high monomer oxidation potential of 1.4 V needed for generation of the thin MPN films and/or to a reduced cross-linking density. By doubling the number of electroactive carbazolyl or thienyl substituents in one monomer, remarkably high S_{BET} values were obtained for **P33** ($2203 \text{ m}^2 \text{ g}^{-1}$) and **P36** polymer powders of ($1767 \text{ m}^2 \text{ g}^{-1}$) indicating high cross-linking density and high rigidity. The presence of the 1,3,5-trisubstituted aromatic spacer units between core fragment and electroactive, peripheral substituents plays, probably, a crucial role concerning the resulting specific surface area: by decreasing the probability for chain intercalation. Within this series, the electrogenerated, carbazole-based MPN films show an intense photoluminescence. The combination of high permanent microporosity and intense PL seems promising for PL sensing applications. Thin MPN films emit green to yellow PL with maxima centered at 527 nm for **P31**, 542 nm for **P32**, and 529 nm for **P33**. Electrogenerated **P33** films were tested as chemical sensors for TNT detection in solution, please note the importance to public health and security (Fei et al. 2014). Figure 8a shows the continuously dropped PL intensity for ppm concentrations of the TNT analyte with a clearly detectable quenching already for a concentration of ~1 ppm TNT. The sensing mechanism can be related to excited state energy transfer between the electron-rich bicarbazole units of the MPN films and the electron-poor

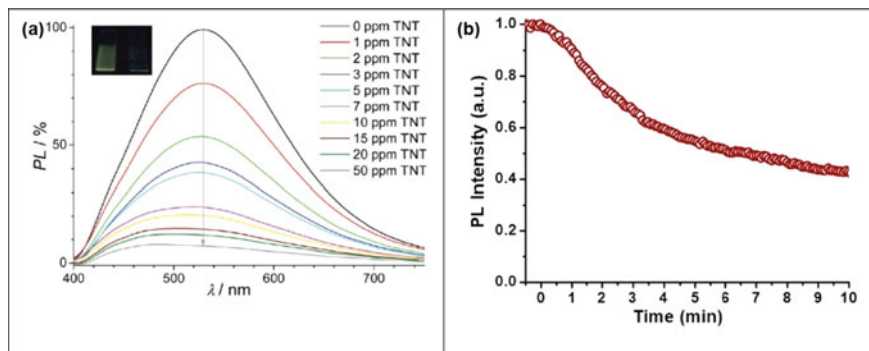


Fig. 8 **a** PL spectra (upon excitation at 340 nm) of P33 films after immersing the films into TNB solutions of different concentrations. The inset shows photographic photoluminescence images of P33 films, in the pristine state and after exposure to 50 ppm TNT solutions. Reproduced with permission (Palma-Cando et al. 2017) Reproduced by permission of The Royal Society of Chemistry. **b** Time trace of the fluorescence quenching of a P31 film in the presence of TNT vapors at a concentration of 10 ppb (Mothika et al. 2018). Reproduced with permission of the American Chemical Society

quencher (TNT). Optimized gas-phase detection conditions for TNT in electrogenerated **P31** films allowed us to detect this harmful analyte up to the 10 ppb level, in a few seconds (see Fig. 8b) (Mothika et al. 2018).

4 Conclusions and Perspectives

During the last decade, our research groups have tested a broad library of new monomers for oxidative generation of microporous polymer networks (MPNs) in wet-chemical and electrochemical strategies. Microporous materials both showing high specific surface areas of up to $2200 \text{ m}^2 \text{ g}^{-1}$ and intense photoluminescence are accessible by a smart design of the tectons that form the MPN framework (in the case of **P33**, for example, by combining a tetraphenylethylene (TPE) core, phenylene spacers and eight electroactive carbazole units in the periphery). Potential applications in the field of optical or electrochemical sensors for detection of nitroaromatic compounds (including explosives) have been systematically explored, finally allowing for a vapor detection with sensitivities down to a few ppb (e.g. for TNT gas-phase detection). We still see big opportunities in the exploration of related MPNs nanocomposites in fields such as electrochemical sensors, supercapacitors, or heterogeneous catalysis, based e.g. on inherent microporosity, efficient photoluminescence and semiconducting nature of the films. The electrosynthesis of thin MPN films, is, hereby, an elegant and straightforward method to combine MPN synthesis directly with thin film formation.

Acknowledgements A. P.-C. thanks University Yachay Tech for the internal grant No. Chem19-08 and Chem19-17.

References

- Ambrose JF, Nelson RF (1968) Anodic oxidation pathways of carbazoles: I. carbazole and N-substituted derivatives. *J Electrochem Soc* 115:1159–1164. <https://jes.ecsdl.org/content/115/11/1159.abstractN2>. Electrochemical and spectroscopic techniques have been employed in elucidating the anodic oxidation pathways of carbazole and several N-substituted derivatives. For carbazole and the N-alkyl or N-aryl
- Ansems RBM, Scott LT (2000) Circumtrindene: a geodesic dome of molecular dimensions. Rational synthesis of 60 of C₆₀ I, *J Am Chem Soc* 122:2719–2724. <https://doi.org/10.1021/ja993028n>
- Bhunia S, Dey N, Pradhan A, Bhattacharya S (2018) A conjugated microporous polymer based visual sensing platform for aminoglycoside antibiotics in water. *Chem Commun* 54:7495–7498. <https://doi.org/10.1039/C8CC02865F>
- Biswal BP, Becker D, Chandrasekhar N, Seenath JS, Paasch S, Machill S, Hennersdorf F, Brunner E, Weigand JJ, Berger R, Feng X (2018) Exploration of thiazolo[5,4-d]thiazole linkages in conjugated porous organic polymers for chemoselective molecular sieving. *Chem A Eur J* 24:10868–10875. <https://doi.org/10.1002/chem.201802631>
- Bonillo B, Sprick RS, Cooper AI (2016) Tuning photophysical properties in conjugated microporous polymers by comonomer doping strategies. *Chem Mater* 28:3469–3480. <https://doi.org/10.1021/acs.chemmater.6b01195>
- Buyukcakir O, Yuksel R, Jiang Y, Lee SH, Seong WK, Chen X, Ruoff RS (2019) Synthesis of porous covalent quinazoline networks (CQNs) and their gas sorption properties. *Angew Chemie Int Ed* 58:872–876. <https://doi.org/10.1002/anie.201813075>
- Chen L, Honsho Y, Seki S, Jiang D (2010) Light-harvesting conjugated microporous polymers: rapid and highly efficient flow of light energy with a porous polyphenylene framework as antenna. *J Am Chem Soc* 132:6742–6748. <https://doi.org/10.1021/ja100327h>
- Chen Q, Luo M, Hammershøj P, Zhou D, Han Y, Laursen BW, Yan C-G, Han B-H (2012) Microporous polycarbazole with high specific surface area for gas storage and separation. *J Am Chem Soc* 134:6084–6087. <https://doi.org/10.1021/ja300438w>
- Dehmloew EV, Kelle T (1997) Synthesis of new truxene derivatives: possible precursors of fullerene partial structures? *Synth Commun* 27:2021–2031. <https://doi.org/10.1080/00397919708006804>
- Diaz AF, Castillo JI, Logan JA, Lee W-Y (1981) Electrochemistry of conducting polypyrrole films. *J Electroanal Chem Interfacial Electrochem* 129:115–132. [https://dx.doi.org/10.1016/S0022-0728\(81\)80008-3](https://dx.doi.org/10.1016/S0022-0728(81)80008-3)
- Eslami MR, Alizadeh N (2016) Nanostructured conducting molecularly imprinted polypyrrole based quartz crystal microbalance sensor for naproxen determination and its electrochemical impedance study. *RSC Adv* 6:9387–9395. <https://doi.org/10.1039/c5ra21489k>
- Evans SAG, Elliott JM, Andrews LM, Bartlett PN, Doyle PJ, Denuault G (2002) Detection of hydrogen peroxide at mesoporous platinum microelectrodes. *Anal Chem* 74:1322–1326. <https://doi.org/10.1021/ac011052p>
- Fei T, Jiang K, Zhang T (2014) Highly sensitive TNT photoluminescent sensing by a phosphorescent complex. *Sens. Actuators B Chem* 199:148–153. <https://dx.doi.org/10.1016/j.snb.2014.03.088>
- Ge Y, Jamal R, Zhang R, Zhang W, Yu Z, Yan Y, Liu Y, Abdiryim T (2020) Electrochemical synthesis of multilayered PEDOT/PEDOT-SH/Au nanocomposites for electrochemical sensing of nitrite. *Microchim Acta* 187:248. <https://doi.org/10.1007/s00604-020-4211-1>
- Geng T-M, Zhu H, Song W, Zhu F, Wang Y (2016) Conjugated microporous polymer-based carbazole derivatives as fluorescence chemosensors for picronic acid. *J Mater Sci* 51:4104–4114. <https://doi.org/10.1007/s10853-016-9732-y>

- Giuglio-Tonolo AG, Spitz C, Terme T, Vanelle P (2014) An expeditious method for the selective cyclotrimerization of isocyanates initiated by TDAE. *Tetrahedron Lett* 55:2700–2702. <https://doi.org/10.1016/j.tetlet.2014.03.045>
- Guo Z, Florea A, Cristea C, Bessueille F, Vocanson F, Goutaland F, Zhang A, Săndulescu R, Lagarde F, Jaffrezic-Renault N (2015) 1,3,5-Trinitrotoluene detection by a molecularly imprinted polymer sensor based on electropolymerization of a microporous-metal-organic framework. *Sens Actuators B Chem* 207:960–966. <https://doi.org/10.1016/j.snb.2014.06.137>
- Gurunathan K, Murugan AV, Marimuthu R, Mulik UP, Amalnerkar DP (1999) Electrochemically synthesised conducting polymeric materials for applications towards technology in electronics, optoelectronics and energy storage devices. *Mater Chem Phys* 61:173–191. [https://dx.doi.org/10.1016/S0254-0584\(99\)00081-4](https://dx.doi.org/10.1016/S0254-0584(99)00081-4)
- Heinze J, Rasche A, Pagels M, Geschke B (2007) On the origin of the so-called nucleation loop during electropolymerization of conducting polymers. *J Phys Chem B* 111:989–997. <https://doi.org/10.1021/jp066413p>
- Heinze J, Frontana-Urbe BA, Ludwigs S (2010) Electrochemistry of conducting polymers-persistent models and new concepts. *Chem Rev* 110:4724–4771. <https://doi.org/10.1021/cr900226k>
- Ibanez JG, Rincón ME, Gutierrez-Granados S, Chahma M, Jaramillo-Quintero OA, Frontana-Urbe BA (2018) Conducting polymers in the fields of energy, environmental remediation, and chemical-chiral sensors. *Chem Rev* 118:4731–4816. <https://doi.org/10.1021/acs.chemrev.7b00482>
- Jiang J-X, Su F, Trewin A, Wood CD, Campbell NL, Niu H, Dickinson C, Ganin AY, Rosseinsky MJ, Khimyak YZ, Cooper AI (2007) Conjugated microporous poly(aryleneethynylene) networks. *Angew Chemie* 119:8728–8732. <https://doi.org/10.1002/ange.200701595>
- Jimenez ER, Rodríguez H (2020) Aggregation-induced emission: a review of promising cyano-functionalized AIEgens. *J Mater Sci* 55:1366–1387. <https://doi.org/10.1007/s10853-019-04157-5>
- Lee J-SM, Cooper AI (2020) Advances in conjugated microporous polymers. *Chem Rev* 120:2171–2214. <https://doi.org/10.1021/acs.chemrev.9b00399>
- Liao Y, Wang H, Zhu M, Thomas A (2018) Efficient supercapacitor energy storage using conjugated microporous polymer networks synthesized from Buchwald-Hartwig coupling. *Adv Mater* 30:1705710. <https://doi.org/10.1002/adma.201705710>
- Liu X, Xu Y, Jiang D (2012) Conjugated microporous polymers as molecular sensing devices: microporous architecture enables rapid response and enhances sensitivity in fluorescence-on and fluorescence-off sensing. *J Am Chem Soc* 134:8738–8741. <https://doi.org/10.1021/ja303448r>
- Liu D-P, Chen Q, Zhao Y-C, Zhang L-M, Qi A-D, Han B-H (2013) Fluorinated porous organic polymers via direct C-H arylation polycondensation. *ACS Macro Lett* 2:522–526. <https://doi.org/10.1021/mz4001699>
- Lu W, Yuan D, Zhao D, Schilling CI, Plietzsch O, Muller T, Bräse S, Guenther J, Blümel J, Krishna R, Li Z, Zhou H-C (2010) Porous polymer networks: synthesis, porosity, and applications in gas storage/separation. *Chem Mater* 22:5964–5972. <https://doi.org/10.1021/cm1021068>
- Lu G, Yang H, Zhu Y, Huggins T, Ren ZJ, Liu Z, Zhang W (2015) Synthesis of a conjugated porous Co(II) porphyrinylene-ethynylene framework through alkyne metathesis and its catalytic activity study. *J Mater Chem A* 3:4954–4959. <https://doi.org/10.1039/C4TA06231K>
- Luo J, Xie Z, Lam JW, Cheng L, Chen H, Qiu C, Kwok HS, Zhan X, Liu Y, Zhu D, Tang BZ (2001) Aggregation-induced emission of 1-methyl-1,2,3,4,5-pentaphenylsilole. *Chem Commun* 1740–1741. <https://doi.org/10.1039/B105159H>
- Marco AB, Cortizo-Lacalle D, Perez-Miqueo I, Valenti G, Boni A, Plas J, Strutyński K, De Feyter S, Paolucci F, Montes M, Khlobystov AN, Melle-Franco M, Mateo-Alonso A (2017) Twisted aromatic frameworks: readily exfoliable and solution-processable two-dimensional conjugated microporous polymers. *Angew Chemie* 129:7050–7055. <https://doi.org/10.1002/ange.201700271>
- Mei J, Hong Y, Lam JWY, Qin A, Tang Y, Tang BZ (2014) Aggregation-induced emission: the whole is more brilliant than the parts. *Adv Mater* 26:5429–5479. <https://doi.org/10.1002/adma.201401356>

- Moon J-M, Thapliyal N, Hussain KK, Goyal RN, Shim Y-B (2018) Conducting polymer-based electrochemical biosensors for neurotransmitters: a review. *Biosens Bioelectron* 102:540–552. <https://doi.org/10.1016/j.bios.2017.11.069>
- Moritsugu M, Sudo A, Endo T (2011) Development of high-performance networked polymers consisting of isocyanurate structures based on selective cyclotrimerization of isocyanates. *J Polym Sci Part A Polym Chem* 49:5186–5191. <https://doi.org/10.1002/pola.24987>
- Mothika VS, Raupke A, Brinkmann KO, Riedl T, Brunklaus G, Scherf U (2018) Nanometer-thick conjugated microporous polymer films for selective and sensitive vapor-phase TNT detection. *ACS Appl Nano Mater* 1:6483–6492. <https://doi.org/10.1021/acsanm.8b01779>
- Nambu Y, Endo T (1993) Synthesis of novel aromatic isocyanurates by the fluoride-catalyzed selective trimerization of isocyanates. *J Org Chem* 58:1932–1934. <https://doi.org/10.1021/jo00059a055>
- Naveen MH, Gurudatt NG, Shim Y-B (2017) Applications of conducting polymer composites to electrochemical sensors: a review. *Appl Mater Today* 9:419–433. <https://doi.org/10.1016/j.apmt.2017.09.001>
- Palma-Cando A, Scherf U (2015) Electrogenerated Thin Films of Microporous Polymer Networks with Remarkably Increased Electrochemical Response to Nitroaromatic Analytes. *ACS Appl. Mater. Interfaces*. 7:11127–11133. <https://doi.org/10.1021/acsnami.5b02233>
- Palma-Cando A, Scherf U (2016) Electrochemically generated thin films of microporous polymer networks: synthesis, properties, and applications. *Macromol Chem Phys* 217:827–841. <https://doi.org/10.1002/macp.201500484>
- Palma-Cando AU, Frontana-Uribe BA, Maldonado JL, Hernandez MR (2014) Control of thickness of PEDOT electrodeposits on glass/ITO electrodes from organic solutions and its use as anode in organic solar cells. *Procedia Chem* 12:92–99. <https://doi.org/10.1016/j.proche.2014.12.046>
- Palma-Cando A, Brunklaus G, Scherf U (2015) Thiophene-based microporous polymer networks via chemical or electrochemical oxidative coupling. *Macromolecules*. 48. <https://doi.org/10.1021/acs.macromol.5b01821>
- Palma-Cando A, Preis E, Scherf U (2016), Silicon- or carbon-cored multifunctional carbazolyli monomers for the electrochemical generation of microporous polymer films. *Macromolecules*. 49. <https://doi.org/10.1021/acs.macromol.6b02025>
- Palma-Cando A, Woitassek D, Brunklaus G, Scherf U (2017) Luminescent tetraphenylethene-cored, carbazole- and thiophene-based microporous polymer films for the chemosensing of nitroaromatic analytes. *Mater Chem Front* 1:1118–1124. <https://doi.org/10.1039/C6QM00281A>
- Palma-Cando A, Rendon-Enriquez I, Tausch M, Scherf U (2019b) Thin functional polymer films by electropolymerization. *Nanomaterials* 9:1125. <https://doi.org/10.3390/nano9081125>
- Palma-Cando A, Frontana-Uribe BA, Varela-Guerrero V (2019) Relationship between charge transfer diffusion coefficients and doping level for electrogenerated thin PEDOT films on ITO. *Bionatura* 2. <https://doi.org/10.21931/RB/CS/2019.02.01.8>
- Park CS, Lee C, Kwon OS (2016) Conducting polymer based nanobiosensors, *Polymers (Basel)* 8. <https://doi.org/10.3390/polym8070249>
- Preis E, Widling C, Scherf U, Patil S, Brunklaus G, Schmidt J, Thomas A (2011) Aromatic, microporous polymer networks with high surface area generated in Friedel–Crafts-type Polycondensations. *Polym Chem* 2:2186–2189. <https://doi.org/10.1039/C1PY00251A>
- Preis E, Widling C, Brunklaus G, Schmidt J, Thomas A, Scherf U (2013) Microporous polymer networks (MPNs) made in metal-free regimes: systematic optimization of a synthetic protocol toward N-arylcarbazole-based MPNs. *ACS Macro Lett* 2:380–383. <https://doi.org/10.1021/mz400126f>
- Preis E, Dong W, Brunklaus G, Scherf U (2015a) Microporous, tetraarylethylene-based polymer networks generated in a reductive polyolefination process. *J Mater Chem C* 3:1582–1587. <https://doi.org/10.1039/C4TC02664K>
- Preis E, Schindler N, Adrian S, Scherf U (2015b) Microporous polymer networks made by cyclotrimerization of commercial, aromatic diisocyanates. *ACS Macro Lett* 4:1268–1272. <https://doi.org/10.1021/acsmacrolett.5b00726>

- Qiao S, Du Z, Yang R (2014) Design and synthesis of novel carbazole-spacer-carbazole type conjugated microporous networks for gas storage and separation. *J Mater Chem A* 2:1877–1885. <https://doi.org/10.1039/C3TA14017B>
- Räupke A, Palma-Cando A, Shkura E, Teckhausen P, Polywka A, Görrn P, Scherf U, Riedl T (2016) Highly sensitive gas-phase explosive detection by luminescent microporous polymer networks. *Sci Rep* 6:29118. <https://doi.org/10.1038/srep29118>
- Sanguinet L, Williams JC, Yang Z, Twieg RJ, Mao G, Singer KD, Wiggers G, Petschek RG (2006) Synthesis and characterization of new truxenones for nonlinear optical applications. *Chem Mater* 18:4259–4269. <https://doi.org/10.1021/cm0601887>
- Sauerbrey G (1959) Use of quartz vibration for weighing thin films on a microbalance. *Zeitschrift Für Phys* 155:206–212
- Schmidt J, Werner M, Thomas A (2009) Conjugated microporous polymer networks via yamamoto polymerization. *Macromolecules* 42:4426–4429. <https://doi.org/10.1021/ma9005473>
- Shamsipur M, Tabrizi MA, Mahkam M, Aboudi J (2015) A high sensitive TNT sensor based on electrochemically reduced graphene oxide-poly(amidoamine) modified electrode. *Electroanalysis* 27:1466–1472. <https://doi.org/10.1002/elan.201400634>
- Sharafy S, Muszkat KA (1971) Viscosity dependence of fluorescence quantum yields. *J Am Chem Soc* 93:4119–4125. <https://doi.org/10.1021/ja00746a004>
- Shi G, Jin S, Xue G, Li C (1995) A conducting polymer film stronger than aluminium. *Science* (80-.) 267:994–996. <https://doi.org/10.1126/science.267.5200.994>
- Shi G, Li C, Liang Y (1999) High-strength conducting polymers prepared by electrochemical polymerization in boron trifluoride diethyl etherate solution. *Adv Mater* 11:1145–1146. [https://doi.org/10.1002/\(SICI\)1521-4095\(199909\)11:13%3c1145::AID-ADMA1145%3e3.0.CO;2-T](https://doi.org/10.1002/(SICI)1521-4095(199909)11:13%3c1145::AID-ADMA1145%3e3.0.CO;2-T)
- Sing KSW (1985) Reporting physisorption data for gas/solid systems with special reference to the determination of surface area and porosity (recommendations 1984). *Pure Appl Chem* 57:603–619. <https://doi.org/10.1351/pac198254112201>
- K.S.W. Sing, D.H. Everett, R.A.W. Haul, L. Moscou, R.A. Pierotti, J. Rouquerol, T. Siemieniewska, Reporting Physisorption Data for Gas/Solid Systems, in: *Handb. Heterog. Catal.*, Wiley-VCH Verlag GmbH & Co. KGaA, Weinheim, 2008. <https://doi.org/https://doi.org/10.1002/9783527610044.hetcat0065>.
- Smet M, Schacht E, Dehaen W (2002) Synthesis, characterization, and modification of hyperbranched poly(arylene oxindoles) with a degree of branching of 100%. *Angew Chemie Int Ed* 41:4547–4550. [https://doi.org/10.1002/1521-3773\(20021202\)41:23%3e4547::AID-ANI E4547%3e3.0.CO;2-A](https://doi.org/10.1002/1521-3773(20021202)41:23%3e4547::AID-ANI E4547%3e3.0.CO;2-A)
- Sprick RS, Thomas A, Scherf U (2010) Acid catalyzed synthesis of carbonyl-functionalized microporous ladder polymers with high surface area. *Polym Chem* 1:283–285. <https://doi.org/10.1039/B9PY00375D>
- Sun L, Liang Z, Yu J, Xu R (2013) Luminescent microporous organic polymers containing the 1,3,5-tri(4-ethenylphenyl)benzene unit constructed by Heck coupling reaction. *Polym Chem* 4:1932. <https://doi.org/10.1039/c2py21034g>
- Sun X, Wang Y, Lei Y (2015) Fluorescence based explosive detection: from mechanisms to sensory materials. *Chem Soc Rev* 44:8019–8061. <https://doi.org/10.1039/C5CS00496A>
- Suresh VM, Scherf U (2018) Electrochemically generated conjugated microporous polymer network thin films for chemical sensor applications. *Macromol Chem Phys* 219. <https://doi.org/10.1002/macp.201800207>
- Tan L, Tan B (2017) Hypercrosslinked porous polymer materials: design, synthesis, and applications. *Chem Soc Rev* 46:3322–3356. <https://doi.org/10.1039/C6CS00851H>
- Terán-Alcocer A, Bravo-Plascencia F, Cevallos-Morillo C, Palma-Cando A (2021) Electrochemical sensors based on conducting polymers for the aqueous detection of biologically relevant molecules. *Nanomaterials* 11:252. <https://doi.org/10.3390/NANO11010252>
- Toal SJ, Trogler WC (2006) Polymer sensors for nitroaromatic explosives detection. *J Mater Chem* 16:2871–2883. <https://doi.org/10.1039/B517953J>

- Traylor TG, Hanstein WG, Berwin HJ (1970) σ - π conjugation of carbon-metal bonds. Stereo-electronic and inductive effects. *J Am Chem Soc* **92**:7476–7477. <https://doi.org/10.1021/ja00728a044>
- Trunk M, Herrmann A, Bildirir H, Yassin A, Schmidt J, Thomas A (2016) Copper-free sonogashira coupling for high-surface-area conjugated microporous poly(aryleneethynylene) networks. *Chem A Eur J* **22**:7179–7183. <https://doi.org/10.1002/chem.201600783>
- Wang X-S, Liu J, Bonenfant JM, Yuan D-Q, Thallapally PK, Ma S (2013) A porous covalent porphyrin framework with exceptional uptake capacity of saturated hydrocarbons for oil spill cleanup. *Chem Commun* **49**:1533. <https://doi.org/10.1039/c2cc38067f>
- Wang S, Zhang C, Shu Y, Jiang S, Xia Q, Chen L, Jin S, Hussain I, Cooper AI, Tan B (2017) Layered microporous polymers by solvent knitting method. *Sci Adv* **3**:e1602610. <https://doi.org/10.1126/sciadv.1602610>
- Xie Y, Wang T-T, Liu X-H, Zou K, Deng W-Q (2013) Capture and conversion of CO₂ at ambient conditions by a conjugated microporous polymer. *Nat Commun* **4**:1960. <https://doi.org/10.1038/ncomms2960>
- Xu C, Hedin N (2013) Synthesis of microporous organic polymers with high CO₂-over-N₂ selectivity and CO₂ adsorption. *J Mater Chem A* **1**:3406. <https://doi.org/10.1039/c3ta01160g>
- Yuan Y, Zhu G (2019) Porous aromatic frameworks as a platform for multifunctional applications. *ACS Cent Sci* **5**:409–418. <https://doi.org/10.1021/acscentsci.9b00047>
- Zhang H-X, Cao A-M, Hu J-S, Wan L-J, Lee S-T (2006) Electrochemical sensor for detecting ultratrace nitroaromatic compounds using mesoporous SiO₂-modified electrode. *Anal Chem* **78**:1967–1971. <https://doi.org/10.1021/ac051826s>
- Zhang K, Kopetzki D, Seeberger PH, Antonietti M, Vilela F (2013) Surface area control and photocatalytic activity of conjugated microporous poly(benzothiadiazole) networks. *Angew Chemie Int Ed* **52**:1432–1436. <https://doi.org/10.1002/anie.201207163>
- Zhang X, Lu J, Zhang J (2014) Porosity enhancement of carbazolic porous organic frameworks using dendritic building blocks for gas storage and separation. *Chem Mater* **26**:4023–4029. <https://doi.org/10.1021/cm501717c>
- Zhang H, Zhang Y, Gu C, Ma Y (2015) Electropolymerized conjugated microporous poly(zinc-porphyrin) films as potential electrode materials in supercapacitors. *Adv Energy Mater* **5**:1402175–1402180. <https://doi.org/10.1002/aenm.201402175>
- Zhang C, He Y, Mu P, Wang X, He Q, Chen Y, Zeng J, Wang F, Xu Y, Jiang J-X (2018) Toward high performance thiophene-containing conjugated microporous polymer anodes for lithium-ion batteries through structure design. *Adv Funct Mater* **28**:1705432. <https://doi.org/10.1002/adfm.201705432>
- Zolotukhin MG, Fomina L, Salcedo R, Sansores LE, Colquhoun HM, Khalilov LM (2004) Super-electrophiles in polymer chemistry a novel, one-pot synthesis of high-T-g, high-temperature polymers. *Macromolecules* **37**:5140–5141. <https://doi.org/10.1021/ma0495902>

Mixed-Matrix Membranes



Alexander Nuhnen and Christoph Janiak

Abstract Molecular separations are of significant industrial importance and membrane processes offer great potential for such energy-saving separations but pure polymer membranes are limited by their compromise between gas permeability and selectivity, and the aging processes that some high performing materials undergo. Mixed-matrix membranes (MMMs) combine a continuous organic polymer phase with a dispersed porous additive, i.e. filler, and synergistically the easy processability of polymers and the superior gas separation performance of various porous filler materials. MMMs may provide separation properties which can surpass the selectivity/permeability trade-off which is empirically observed for pure polymer membranes. This chapter briefly introduces membrane separation and mixed-matrix membranes. Then, metal-organic frameworks (MOFs) as novel additives with high porosity and tunable pore size for MMMs are described which are supposed to outperform other porous fillers. In particular, the fraction of these MOF-polymer MMM studies for CO₂/CH₄ and CO₂/N₂ separation is reported where both improved permeability and selectivity have been observed. A thorough investigation on a MOF-Matrimid MMM is highlighted where the same Al-fumarate MOF in a porous state and in a non-porous (because solvent-filled) state was used to quantify the contribution of MOF porosity relative to polymer porosity for the permeability in the MMM and which also showed that the interface volume (the so-called void volume) contributes roughly only 10% to the available free volume in the MMM.

Keywords Mixed-matrix membranes · Separation · Permeation · Permeability · Selectivity · Porosity · Metal-organic frameworks · MOFs · Polymer · Carbon dioxide · CO₂ separation · Interface · Fractional volume · Void volume

A. Nuhnen · C. Janiak (✉)

Institut für Anorganische Chemie und Strukturchemie, Heinrich-Heine-Universität Düsseldorf,
40204 Düsseldorf, Germany

e-mail: janiak@uni-duesseldorf.de

1 Introduction

Industrial separation processes are commonly carried out with methods, such as, distillation, drying, evaporation, crystallization or absorption, which are energy intensive. Chemical separations are, for example, responsible for about half of the industrial energy which is used in the USA and 10–15% of the total energy consumption in the USA. Alternative separation methods that require less thermal energy could make the majority of these separations much more energy efficient (Sholl and Lively 2016). The need for greater energy efficiency and limited resources has focused attention on improved separation technologies. Membranes can provide enhanced separation performance and can lead to more energy-efficient, sustainable, and cost-effective commercial applications.

Membranes are thin layers which provide a resistance to the passage of different substances. All membrane separation processes are based on controlling the permeation rate of chemical species through the membrane. With the development of an ultra-thin, defect-free, high-flow membrane for osmosis, Loeb and Sourirajan helped membrane technology achieve the industrial breakthrough in the 1960s (Loeb and Sourirajan 1963). The high flow rate with sufficient selectivity was achieved by a thin surface film stabilized by a microporous carrier. Building on the work of Loeb and Sourirajan, gas separation using membranes also became economically interesting, so that in 1980 the first membrane for the separation of hydrogen, H_2 and nitrogen, N_2 was used by Monsanto under the name Prism®. Shortly thereafter, Dow developed processes for gas separation of N_2 from air and Cyanara successfully separated CO_2 from natural gas (mainly methane, CH_4) using membranes (Bernardo et al. 2009).

Artificial membranes are now frequently used in chemical industrial processes. The use of membrane separation processes is advantageous for many applications. Particularly the lower costs, the lower energy consumption and simpler process conditions make membrane separation processes a preferred technology for the purification of mixtures (Koros and Mahajan 2000). Membrane separation processes can achieve energy savings of up to 50% of the production cost over other separation technologies (Buonomenna 2013). The superiority of membrane separation processes over conventional processes is mainly explained by the avoidance of energy-intensive phase conversions.

Some of the most important examples of membrane applications are gas purification, the production of drinking water from seawater (water desalination), the purification of sewage or the recovery of fuel vapors (Abetz et al. 2006). Membrane processes, which are already in place in industry, include the removal of CO_2 from natural gas (before the natural gas can be passed to the pipeline), the isolation and recovery of hydrogen (for example in cracking processes), and oxygen/nitrogen separation from air (for enriched oxygen in medical devices and enriched nitrogen used for oxygen sensitive materials) (Koros and Mahajan 2000; He and Hägg 2012). Membrane processes for vapor (Ohlrogge and Stürken 2001) or monomer recovery, e.g. ethylene/ N_2 or propylene/ N_2 separation (Baker 2002; BORSIG Membrane Technology GmbH 2020) or for water desalination are increasingly applied.

Organic polymers are typically used for commercial membranes as they are inexpensive and easy to manufacture. Research into the development of new membrane materials mostly focuses on the development of dense polymer membranes. Current challenges for membrane technologies lie primarily in the degrading performance over longer periods of time. The loss of performance results either from impurities and partial degradation of the membranes by corrosive, sulphurous gases such as H_2S and SO_2 or from the accumulation of slowly permeating species in the membrane, resulting in lower transport rates for all gases (Bernardo et al. 2009).

2 Separation by Membranes

Mass transfer through membranes depends fundamentally on the type of membrane used. A distinction is made between porous and non-porous (dense) membranes. The porous membranes are then divided into further subclasses according to their transport mechanism. Figure 1 shows the most relevant diffusion mechanisms in porous membranes (Kluiters 2004).

The transport mechanism for dense, non-porous membranes is generally described in the literature as a solution-diffusion process (Javid 2005). Mass transfer through the membrane takes place in three steps (Fig. 2).

First, the gas molecules are adsorbed on the membrane surface on the high-pressure side (upstream, *feed*). Then the gas molecules diffuse through the polymer matrix before desorbing on the low-pressure side (downstream, *permeate*) of the membrane in the last step. The driving force for the described process is a gradient in pressure, temperature or concentration. In accordance with the solution-diffusion

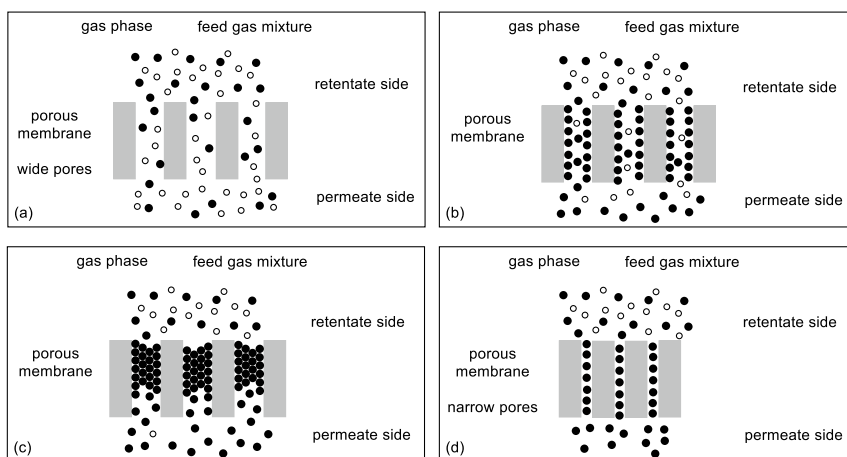


Fig. 1 Schematic representation of the transport mechanism in porous membranes. **a** Knudsen diffusion, **b** surface diffusion, **c** capillary condensation, **d** molecular sieve

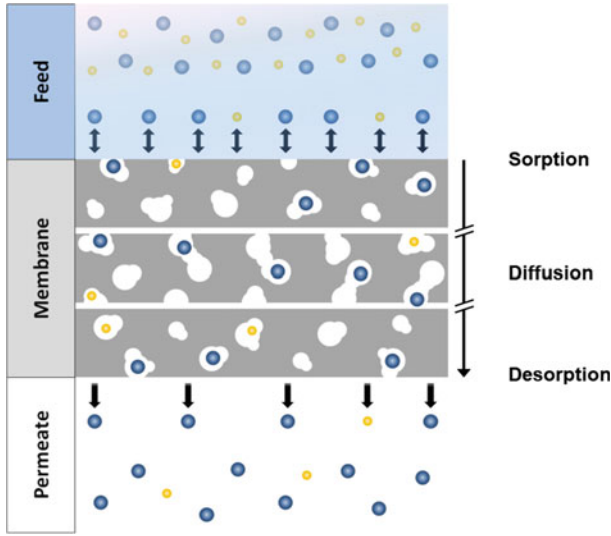


Fig. 2 Schematic representation of the transport mechanism by means of solution-diffusion through dense membranes. Based on the representation from Ref. (Sieffert 2013). The blue and yellow spheres represent different chemical species. The white space in the ‘dense’ membrane, which hosts the blue and yellow spheres, depicts the free volume space inside the polymer.

model, the permeability P of a gas i depends on two factors, the diffusion coefficient D and the solubility coefficient S (Eq. 1):

$$P_i = D_i \times S_i \tag{1}$$

The diffusion of the gas molecules, more specifically the thermally induced movement of the polymer chains through the gas molecules, is usually the rate determining step in the permeation through a dense membrane. As indicated by the white areas around the gas molecules in Fig. 2, the free volume in the polymer matrix is shifted along the gradient by the gas molecules. Accordingly, a molecule permeating through a membrane is located in the free volume space, i.e., micro voids of the polymer. These voids are a result of suboptimal chain stacking and their sum is also referred to as the free volume of the polymer. Due to the thermally induced statistical movement of chain segments micro canals are formed between micro voids. This allows a molecule to move across the membrane from one void to another corresponding to the applied driving force. To visualize this model the membrane in Fig. 2 shows micro voids as white areas. In the middle of the membrane the passage of a molecule (blue sphere) is illustrated from the upper micro void to the lower one by formation of micro canals in between.

The permeability P of a component i can also be formulated as flux normalized to the thickness of the membrane l and the applied pressure difference Δp between feed and permeate, as shown in Eq. 2:

$$P_i = \frac{(\text{flux}_i \times l)}{(\Delta p_i)} \quad (2)$$

The ratio of the permeability P of two gases i, j indicates the ideal permselectivity or selectivity α of the membrane (Eq. 3):

$$\alpha_{i/j} = \frac{P_i}{P_j} \quad (3)$$

Dense membranes often show a low permeability (slow diffusion) but a high selectivity compared to porous membranes. Because of this and in contrast to the microporous membrane, it is also possible to separate molecules of almost the same size and molecular weight, if their solubility in the membrane material differs significantly. In other words, it is mainly the solubility of the gases that determines the possible separation performance of the membrane in terms of selectivity. The thickness of the membrane in turn determines the permeability or effective flow. For this reason, asymmetric membranes are particularly advantageous and widely used in industry. Asymmetric membranes combine high flow rates with good mechanical stability. Structurally, they are composed of a dense, selective layer (0.1–1 μm , in thickness) supported by a porous substrate (50–200 μm). In the selective part of the membrane the permeation is based on the solution-diffusion model and in the porous section on the Knudsen diffusion model. The preferred form of such membranes is the hollow fiber to allow even higher flow rates.

Besides the structure, chemical and physical properties of the membrane play an important role for the separation properties. Membranes should be defect-free, selective, highly permeable, and exhibit high thermal, mechanical and chemical stability. If membranes are classified according to their material type, a distinction is typically made between polymer membranes and inorganic membranes. Inorganic materials include metal oxides, silicates and zeolites, which exhibit high thermal and chemical stability combined with high permselectivity (Li et al. 2005; Carreon et al. 2012). However, amorphous inorganic membranes in particular have low mechanical stability and are often too brittle for common shaping processes (McLeary et al. 2006). Nevertheless, microporous inorganic membranes with pore diameters <1 nm show a high potential for gas separation applications due to their molecular sieving effect combined with high flow rates. Their mechanical strength can be significantly increased by porous support materials.

3 Organic Polymer Membranes

Organic polymer-based membranes are the most commonly used membrane types for gas separation in industry today (Nunes and Peinemann 2006). Figure 3 shows examples of chemical structures of polymer materials for the production of membranes for gas separation.

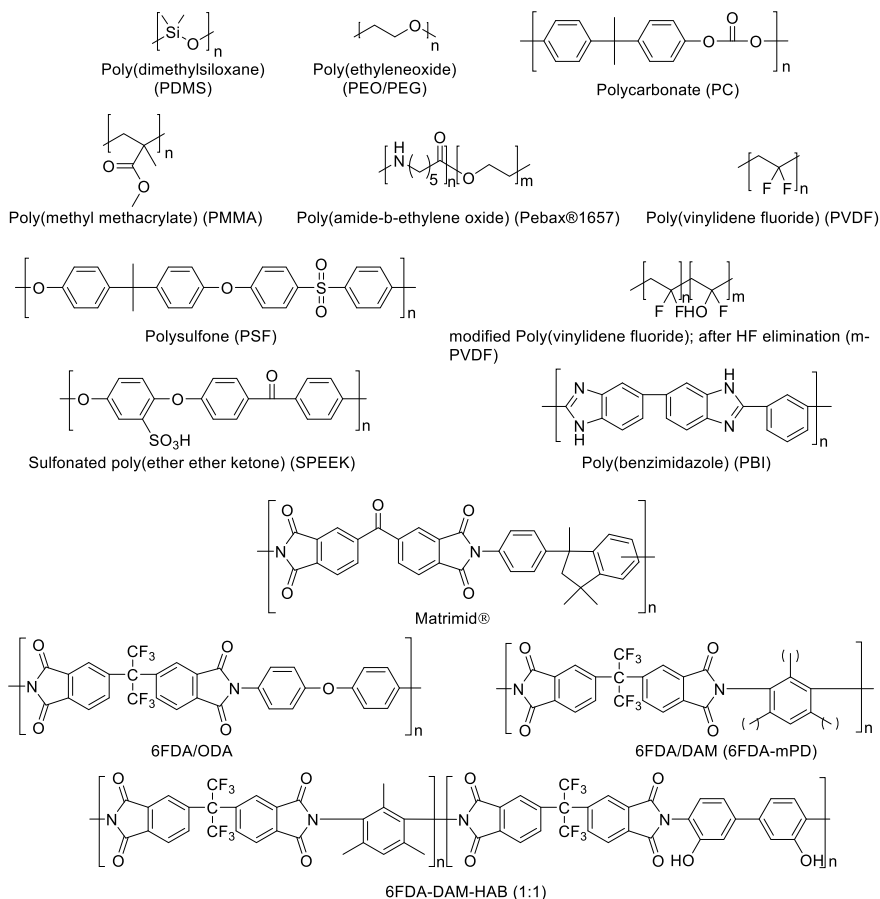


Fig. 3 Chemical structures of frequently used polymers for membrane production for gas separation, also for MOF-polymer MMMs (Dechnik et al. 2017). Abbreviations: 6FDA = 2,2'-bis(3,4-carboxyphenyl)hexafluoropropane dianhydride, ODA = 4,4'-oxydianiline, DAM = diaminomesitylene, mPD = m-phenylenediamine, HAB = 3,3'-dihydroxy-4,4'-diamino-biphenyl

An important constraint in the development of membrane applications is the inverse correlation between permeability and selectivity. Organic polymer membranes are particularly susceptible to this inverse gas permeability and selectivity relationship, such that membranes with high permeability have a low selectivity and vice versa. The compromise between permeability and selectivity for polymer-based membranes in gas separation was graphically worked out by Robeson in 1991 and again in 2008 (Robeson 1991, 2008). Robeson plotted the selectivity of a gas pair logarithmically against the permeability of the faster permeating gas, which makes the trade-off between permeability and selectivity for polymer membranes apparent (Fig. 4). The well-known Robeson upper-bound plots (Robeson 1991, 2008) for gas pairs summarize the permeability and selectivity of reported dense pure polymer

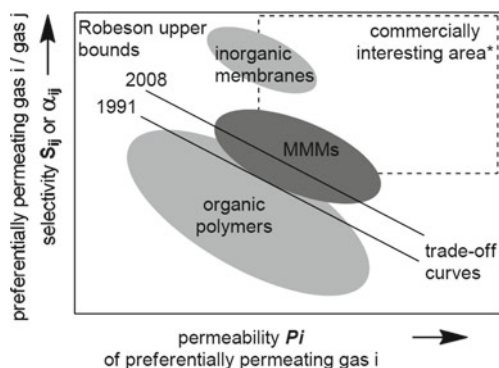


Fig. 4 Schematic representation of the Robeson upper bounds (trade-off curves) of 1991 and 2008 (Robeson 1991, 2008). (*Distance or position of a specific membrane relative to the upper bound can vary depending on the separation problem.) Reprinted from Ref. (Dechnik et al. 2017a) with permission. Copyright 2017 John Wiley and Sons

membranes and thereby illustrate that as permeability increases the selectivity of the membrane decreases, giving an ‘upper bound’ of membrane performance (Fig. 4). These upper bounds of performance for organic polymer membranes increase gradually over the years with further development but still do not approach the performances observed by other materials, for example inorganic membranes (Dechnik et al. 2017b).

Commercially, higher permeability allows the membrane surface area to be reduced for a given gas flow, thus reducing investment costs in the membrane unit. Increased selectivity in turn results in higher purity of the desired product. Depending on the separation problem, a suitable compromise between permeability and selectivity must be found for polymer membranes. The commercially interesting area for gas separation, shown in Fig. 4, is already reached by inorganic materials such as zeolites (Li et al. 2005; McLeary et al. 2006). However, inorganic (ceramic) materials are often brittle and have poor shaping properties.

4 Mixed-Matrix Membranes

Efforts to overcome the ‘Robeson upper bound’ and enter the commercially interesting area (Fig. 4) led to the preparation of composite membranes, which consist of (porous) inorganic fillers embedded in a polymer matrix, the so-called mixed-matrix membranes (MMMs). The organic polymer matrix is also called the continuous phase, and the (porous) inorganic or organic/inorganic hybrid materials, as fillers form the dispersed or discrete phase of the membrane. The schematic structure of MMMs is shown in Fig. 5.

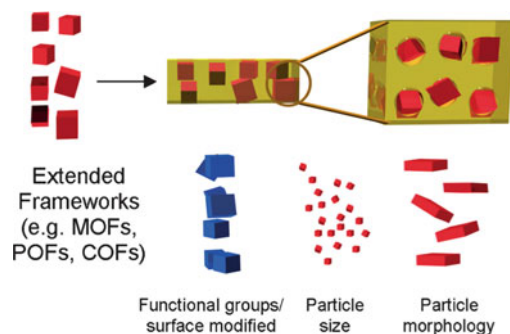


Fig. 5 Schematic structure of mixed-matrix membranes (MMMs) with relevant filler properties, such as type (MOF = metal-organic framework, POF = porous organic framework, COF = covalent organic framework), functional (surface) groups, particle size and morphology). Reprinted from Ref. (Dechnik et al. 2017a) with permission. Copyright 2017 John Wiley and Sons

In the field of gas separation, the concept of MMMs serves to combine the positive properties of the inorganic (filler) and organic polymer (continuous) material types and to overcome both the compromise between permeability and selectivity for organic polymer membranes and the limited formability of the inorganic membranes. The first research on such composite membranes was carried out in the 1970s by Paul and Kemp (1973). They discovered that the time lag, that is, the time it originally takes for a gas to permeate through the membrane, was significantly increased for four different gases by incorporating inorganic zeolite 5A in the polydimethylsiloxane (PDMS) polymer. The increased diffusion time can be explained by adsorption of the gases in the activated pores of the filler. No influence on the gas permeation in the steady state was found. The first work with indications of improved permeation properties of MMMs goes back to studies by Kulprathipanja et al. in the 1980s (Kulprathipanja et al. 1988). They could increase the selectivity of pure cellulose acetate membranes for O_2/N_2 gas separation from 3.0 to 4.3 by intercalation of silicate particles.

The incorporation of fillers in a polymer matrix can have different effects on the permeability of gases, depending on the filler properties. In general, a distinction can be made between porous and non-porous fillers. Porous fillers, with pore sizes close to the kinetic diameter of the gas molecules, can act as molecular sieves and thus promote selection by size exclusion (Vu et al. 2003). Embedding such fillers is therefore particularly advantageous for the separation of the smaller components. Furthermore, porous fillers can promote the selective transport of more easily condensable molecules. This is achieved by a higher affinity of the fillers to the more easily condensable component, which favors their solubility and/or transport through the filler. Especially for the separation of easily polarizable molecules, such as CO_2 with its quadrupole moment, from poorly polarizable gases (N_2 , CH_4), the affinity to polarizable gases can be increased by incorporating functional groups into fillers (Torrissi et al. 2010; Banerjee et al. 2009). If there is no particular interaction between

filler and gas molecules, the incorporation of porous fillers only increases the free volume in the MMM, which gradually increases the permeability as the volume of the discrete phase increases. In this case, however, the selectivity remains at the level of the pure polymer membrane. Non-porous particles show two opposite properties, depending on the nature of the polymer. On the one hand, they can disrupt the polymer chains, especially of semi-crystalline, glassy polymers, thus increasing the permeability of MMM compared to the pure polymer (Merkel et al. 2002; Ahn et al. 2008). On the other hand, they can act as a barrier for the gas molecules, preventing them from permeating through the membrane and thereby reducing the permeability (Sadeghi et al. 2011).

A mathematical description and prediction of the effective permeability P_{eff} for low filler loadings in MMMs with a spherical filler can be performed using the Maxwell model based on Eq. 4:

$$P_{eff} = P_c \times \frac{P_d + 2P_c - 2\phi_d \times (P_c - P_d)}{P_d + 2P_c + \phi_d \times (P_c - P_d)} \quad (4)$$

Here P_c stands for the permeability of the continuous, pure polymer phase, P_d for the permeability of the dispersed (filler) phase and ϕ_d for the volume fraction of the dispersed phase. The volume fraction ϕ_d of the filler can be calculated as follows using the density ρ_d and ρ_c , and the mass percent w_d and w_c of the filler and the polymer, respectively (Eq. 5):

$$\phi_d = \frac{w_d / \rho_d}{\frac{w_c}{\rho_c} + \frac{w_d}{\rho_d}} \quad (5)$$

For porous and non-porous fillers one can define limiting cases within the Maxwell model. With Eq. 6, the relative permeability of the MMM (P_{eff}/P_c) can be approximated for porous fillers whose permeability is significantly higher than that of the pure polymer ($P_d \gg P_c$).

$$P_d \gg P_c : \frac{P_{eff}}{P_c} = \frac{1 + 2\phi_d}{1 - \phi_d} \quad (6)$$

For non-porous fillers with the property $P_d \ll P_c$, that is, a significantly lower permeability of the filler compared to the polymer, the permeability of the composite membrane is calculated according to Eq. 7.

$$P_d \ll P_c : \frac{P_{eff}}{P_c} = \frac{2 - 2\phi_d}{2 + \phi_d} \quad (7)$$

The Maxwell model does not consider interactions between the individual filler particles and is therefore only suitable for low filler loadings. Instead, it is based on the assumption that the particles are isolated from each other. At higher filler loadings, however, strands or clusters of interconnected particles can form, which

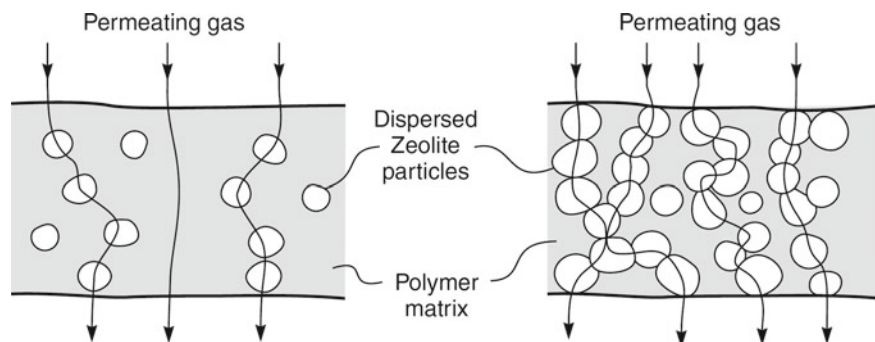


Fig. 6 Gas permeation through mixed-matrix membranes with different loads of porous (zeolite) particles. Left: Isolated dispersed particles with a solution-diffusion mechanism (in the polymer) combined with a partial gas transport according to a porous membrane type (the filler). Right: interconnected particles leading to transport mechanisms as in microporous membranes (cf. Fig. 1). Reprinted with permission from Ref. (Baker 2004). 2004 Copyright John Wiley and Sons

eventually grow into continuous channels and thus trigger an alternative mechanism of gas transport, akin to microporous membranes (Fig. 6, cf. Fig. 1).

The interconnection threshold is different for each composite material, but is often in the range of 30 vol.% of the filler. For predicting the permeability of MMMs with higher loads, other models such as the Bruggeman model can be used, as they also consider interactions between the filler particles (Bánhegyi 1986; Shen and Lua 2013).

An essential factor in the successful production of MMMs is the appropriate combination of polymer and filler, taking into account the physical properties of the inorganic filler and the interface between polymer and filler particle. Gas molecules naturally always choose the route with the least resistance when permeating through a membrane. Consequently, in a MMM made of a combination of the highly permeable but only moderately selective polydimethylsiloxane (PDMS, silicone) rubber and a zeolite with high selectivity and average permeability, gas molecules will prefer diffusion through the polymer matrix. This prevents a possible positive effect of the filler. Duval et al. were able to show that this theoretical consideration can actually be observed in practice by means of the incorporation of zeolite 5A in PDMS (Duval et al. 1993).

PDMS/5A-MMMs showed almost no improvement of the separation properties due to the extremely fast permeation through the polymer. On the other hand, the separation properties for various gas components of the glassy, moderately permeable polymer membrane made of polyethersulfone (PES) could be significantly improved by adding zeolite 5A as filler (Li et al. 2005). Therefore components should be selected careful to ensure a similarly high permeability for the faster permeating gas.

Concerning the interface between polymer and filler particle four different case scenarios can be envisioned which are schematically depicted in Fig. 7 (Chung et al. 2007).

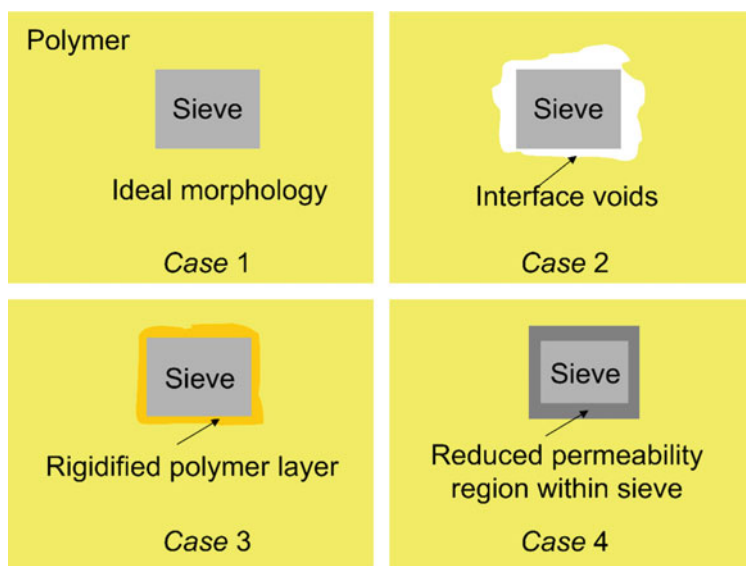


Fig. 7 Schematic representation of different case scenarios of the interface between polymer and filler in an MMM. Reprinted with permission of Ref. (Chung et al. 2007). 2007 Copyright Elsevier

In case 1, the filler is perfectly embedded into the polymer matrix. With such an ideal interface, the permeation properties, at low volume fractions of the filler, should follow the Maxwell model and should depend only on the properties of the respective components. In case 2, there are voids present between the two phases. This effect can be caused in particular by repulsive interactions between filler and polymer, as Barrer and James have shown for the mixture of polymer and zeolite powders by means of electrostatic resistance measurements (Barrer and James 1960). The poor adhesion between the two phases thus leads to free volume around the particles, which results in increased permeability with simultaneous loss of selectivity. For glass-like polymers this case occurs particularly frequently, compared to the elastic rubber-like polymers. It is therefore assumed that in glassy, rigid polymers, when particles are embedded during crystallization, cavities are formed in the vicinity of the particles due to the lack of flexibility of the polymer chains (Vankelecom et al. 1995). Experimental proof of the formation of cavities, apart from the loss of selectivity, is difficult. A possible approach correlates the increase in free volume with a decrease in density in the composite membrane. Thus Paul et al. and Ahn et al. tried to quantify the voids by determining the ratio of the ideal density to the measured density of MMMs (Ahn et al. 2008; Takahashi and Paul 2006).

Case 3 and 4 require a certain affinity between polymer and filler, since attractive interactions between continuous polymer and dispersed filler phase either trigger rigidification of the polymer chains or partial pore blockage of the filler by polymer chains. If, as shown in case 3, the mobility of the polymer chain is reduced by adsorption on the surface of the filler, this leads to an increased selectivity of the

composite membranes, as shown in the work of Koros et al. and Kulprathipanja et al. (Li et al. 2005; Moaddeb and Koros 1997). The rigidified polymer chains show reduced diffusion, especially for the less diffusive component, which leads to an overall decrease in permeability. Rigidification of the polymer chains can be experimentally demonstrated by determining the glass transition temperature T_g . For example, an increased T_g of the MMM compared to the pure polymer indicates a poorer mobility of the polymer chains and thus a rigidification of the polymer chains (Li et al. 2005). The use of porous fillers for the production of MMMs can, depending on the pore size of the particles, lead to a partial or complete blocking of the pores by polymer strands. A complete blockage of the pores leads accordingly to a decrease in permeability, since the formerly porous filler now behaves like a non-porous filler. For example, the incorporation of the porous zeolite NaX, with pore sizes between 7 and 13 Å, into a PDMS matrix led to a considerable loss of permeability with increasing volume fraction of NaX, while maintaining the same selectivity (Clarizia et al. 2004). A partial blocking of the pore structures of fillers with pore diameters close to the kinetic diameter of the gas molecules to be separated is definitely advantageous. As a result, fillers with pores that were originally too large can now act as molecular sieves, resulting in increased selectivity of the composite membrane (Chung et al. 2007). The main goal of the production of MMMs is to improve the separation properties compared to polymer membranes by the influence of porous filler particles. Therefore, the interface morphology of an ideal MMM should promote transport through the porous dispersed phase.

5 Metal-Organic Frameworks as Filler in MMMs

Metal-organic frameworks (MOFs) (Schoedel and Rajeh 2020; Evans et al. 2019; Zhou and Kitagawa 2014; Long and Yaghi 2009) with a high internal surface area and a large pore volume, originally developed for gas storage and separation, (Getman et al. 2012; Adil et al. 2017) catalysis, (Rogge et al. 2017) drug delivery etc., (Janiak 2003; Janiak and Vieth 2010) opened up new perspectives for fillers in MMMs (Tanh Jeazet et al. 2012; Hunger et al. 2012). MOFs are potentially porous coordination networks composed of metal nodes and organic linkers that self-assemble into an extended (crystalline) two- or three-dimensional network (Fig. 8) (Batten et al. 2013). Their precisely adjustable three-dimensional structure and tunable inner and outer microenvironment make MOFs perfectly suitable as a filler in polymer based MMMs (Tanh Jeazet and Janiak 2014a, b).

Given the chemical and structural mutability and notable porosity, MOFs have been identified as promising filler components for high-performance mixed-matrix membranes (MMM). MOFs in MMMs are added as porous fillers which possess molecular sieving properties and are combined with polymers to achieve enhanced separation performance of the obtained hybrid membrane (Fig. 4) (Dechnik et al. 2017a, b). This field of MOF-MMM research has produced a large number of different membranes and many MOF/polymer combinations have been tested and are

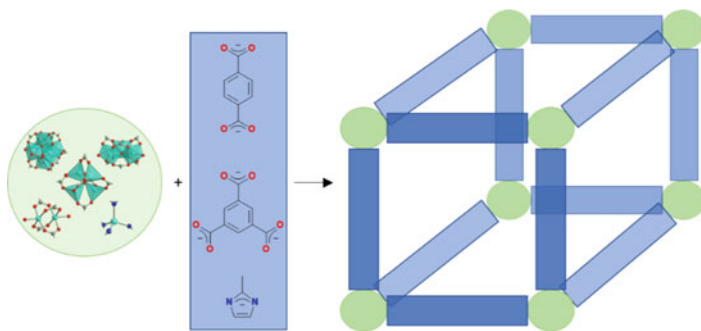


Fig. 8 Construction principle of MOFs from metal clusters or metal atoms and organic ligands (linkers) into a three-dimensional porous framework

reported towards potential application for relevant gas separations. Such membrane polymers prominently include polyimides, for example Matrimid®, 6FDA/ODA or 6FDA/DAM (cf. Fig. 3) (Dechnik et al. 2017b).

MOFs are additives which are expected to be superior to other porous fillers because MOFs feature higher porosity and tunable pore size. Still, only a few MOF-MMM papers report both an increased permeability and selectivity. The separation performance of the MOF filler and the compatibility between the organic polymer and the inorganic-organic hybrid MOF still leave room for optimization. Research in MMMs has focused on enhancing the chemical compatibility between the MOF and polymer phase by judiciously functionalizing the organic linkers of the MOF, modifying the MOF surface chemistry and, more recently, exploring how particle size, morphology and distribution enhance separation performance. An increased compatibility could be achieved in polyimides, in particular, by hydrogen-bonding interactions between the polymer backbone and bringing appropriate surface-functional groups onto the MOF filler particles.

Adjustment of the outer MOF surface was, for example, done by synthesizing the MOF in the presence of modulators, such as monodentate carboxylate ligands, monoatomic anions or surfactants. The modulators influence the MOF crystallite nucleation and growth as they also bind to the metal atoms and compete with the actual linkers for coordination. Thereby, modulators can control the particle size, lead to defects in MOFs and cover the outside surface of MOF particles (Schaate et al. 2011).

In the synthesis of UiO-66(Zr) (Valenzano et al. 2011) and NH₂-UiO-66(Zr) (Schaate et al. 2011) the modulators benzoic acid (BA) and 4-aminobenzoic acid (ABA) were added in a high (50:1) molar ratio relative to the linker. The modulator ABA gave rise to accessible amino groups on the outer MOF surface. The ABA-modified UiO-66(Zr)-ABA and NH₂-UiO-66(Zr)-ABA MOFs could then react with Matrimid under formation of amide groups as was seen in the IR spectra of Matrimid

MMMs with these MOFs at high filler loading. The membrane of $\text{NH}_2\text{-UiO-66(Zr)}$ -ABA/Matrimid was over 50% more selective and 540% more permeable in mixed- CO_2/CH_4 gas separations than the neat Matrimid membrane. This membrane was also 30% more selective and 140% more permeable than the non-modulated and non-functionalized UiO-66(Zr) /Matrimid membrane (Fig. 9) (Anjum et al. 2015).

$\text{NH}_2\text{-UiO-66(Zr)}$ was post-synthetically reacted with formation of amide bonds with polar succinic acid ($\text{HO}_2\text{C}-(\text{CHOH})_2\text{-CO}_2\text{H}$), non-polar decanoyl chloride ($n\text{-C}_9\text{H}_{17}\text{COCl}$) or aromatic phenyl acetyl chloride (PhCH_2COCl). The larger molecules PhCH_2COCl and $n\text{-C}_9\text{H}_{17}\text{COCl}$ could not diffuse into the MOF and reacted only with the amine groups on the outer surface of the particles. Only the smaller succinic acid reacted also with the internal amino groups. The post-synthetic modification should improve the compatibility with the polymer in an MMM. The such modified $\text{NH}_2\text{-UiO-66(Zr)}$ was then combined with Matrimid into a composite membrane for CO_2/N_2 single gas permeation studies (Venna et al. 2015). The imide groups in the Matrimid polymer should be able to form hydrogen bonds with the NH_2 groups or post-synthetically introduced-amide groups. The aromatic rings in Matrimid and the aromatic rings from PhCH_2CO -could interact through π -stacking (Fig. 10, left). Unfortunately, these anticipated and aimed-for MOF-polymer interactions could not be spectroscopically authenticated. Yet, Matrimid and post-synthetically modified $\text{NH}_2\text{-UiO-66(Zr)}$ yielded defect-free membrane films. No interfacial space, i.e. void volume was seen around the particles by scanning electron microscopy (SEM).

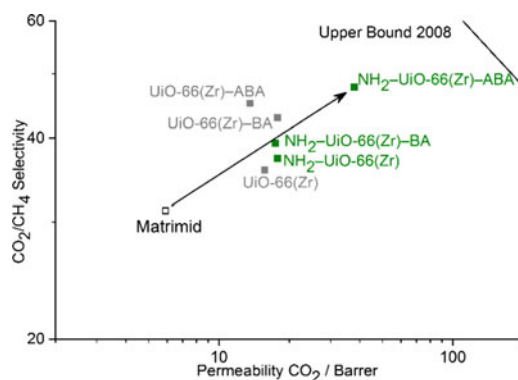


Fig. 9 Comparative CO_2/CH_4 selectivity and permeability for UiO/Matrimid MMMs with 30 wt% standard UiO-66(Zr) (grey) and amino-functionalized $\text{NH}_2\text{-UiO-66(Zr)}$ (green) which were further synthesized also with benzoic acid (BA) or aminobenzoic acid (ABA) as modulator (Anjum et al. 2015). The Robeson Upper bound from 2008 is included for comparison. Figure adapted from Ref. (Dechnik et al. 2017b), <https://pubs.acs.org/doi/10.1021/acs.cgd.7b00595>, further permissions related to the material excerpted should be directed to the ACS, copyright American Chemical Society, 2017

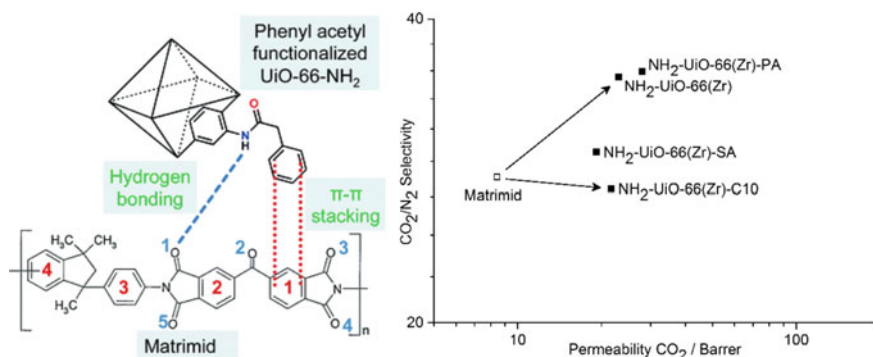


Fig. 10 Left: Possible interactions between Matrimid and phenyl acetyl (PA) functionalized NH₂-UiO-66(Zr). Left figure part reproduced from ref. (Venna et al. 2015), copyright Royal Society of Chemistry, 2015. Right: Comparative CO₂/N₂ selectivity and permeability for Matrimid MMMs with NH₂-UiO-66(Zr) which was post-synthetically reacted with succinic acid (SA, HO₂C-(CHOH)₂-CO₂H), decanoyl chloride (C10, n-C₉H₁₇COCl) or phenyl acetyl chloride (PA, PhCH₂COCl) (Venna et al. 2015). Right figure part taken from ref. (Dechnik et al. 2017b), <https://pubs.acs.org/doi/10.1021/acs.cgd.7b00595>, further permissions related to the material excerpted should be directed to the ACS, copyright American Chemical Society, 2017

MMMs with the aromatic phenyl acetyl (PA) functionalized, PhCH₂CO-NH-UiO-66(Zr) (= NH₂-UiO-66(Zr)-PA in Fig. 10, right) showed an improved CO₂ permeability and CO₂/N₂ selectivity over NH₂-UiO-66(Zr). On the other hand, the pore-filling succinic acid (SA) but also the larger, albeit non-polar decanoyl chloride (C10) modified MOFs NH₂-UiO-66(Zr)-SA and NH₂-UiO-66(Zr)-C10 gave a decrease in selectivity (Fig. 10, right).

In a complementary approach, common polymer structures can be modified by grafting of functional groups onto the polymer chain or by replacement with a copolymer containing functional monomer units to enhance the filler-polymer compatibility. The effect of different diamine monomers in polyimide copolymers with 6FDA was studied in MMMs with NH₂-MIL-53 (Tien-Binh et al. 2015). The CO₂ permeability of 6FDA-ODA (6FDA = 4,4'-hexafluoroisopropylidene diphthalic anhydride, ODA = 4,4'-oxydianiline, cf. Fig. 3) as MMMs was very low with 15 Barrer (Fig. 11). At the same time the MOF particles had agglomerated due to weak polymer-MOF interaction (Chen et al. 2012). Similarly, in the NH₂-MIL-53/6FDA-DAM membrane (DAM = 2,4-diaminomesitylene) the MOF particles formed clusters and did not adhere to the polymer (Tien-Binh et al. 2015). On the other hand, the copolyimide 6FDA-DAM-HAB (1:1) (HAB = 3,3'-dihydroxy-4,4'-diamino-biphenyl, cf. Fig. 3) with NH₂-MIL-53 in a 10 wt% composite membrane came close to the 2008 Robeson's upper bound (Fig. 11). The better polymer-MOF interaction was traced to the hydroxyl groups in the HAB part. No interfacial voids were seen in the NH₂-MIL-53/6FDA-DAM-HAB membrane due to a good particle dispersion (Tien-Binh et al. 2015).

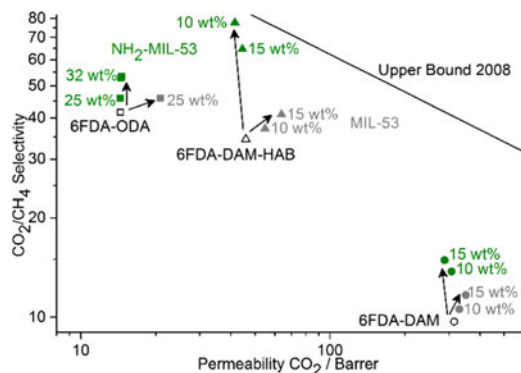


Fig. 11 CO_2/CH_4 permeability and selectivity for MMMs with 6-FDA based co-polyimides with the diamine co-monomers ODA (squares), DAM (circles) and DAM/HAB (triangles) and MIL-53 (grey) and NH_2 -MIL-53 (green) with different MOF/MMM mass fractions (Tien-Binh et al. 2015). Figure taken from ref. (Dechnik et al. 2017b), <https://pubs.acs.org/doi/10.1021/acs.cgd.7b00595>, further permissions related to the material excerpted should be directed to the ACS, copyright American Chemical Society, 2017

When gases adsorb at high pressure in a polymer the motion of the polymer chain segments can be increased, leading in turn to an increase in permeability and to a decrease in selectivity. This effect is called plasticization. Also the thermal annealing of membranes changes the plasticization, the mechanical polymer stability and its permeability and selectivity. High annealing temperatures also crosslink the polyimide chains in Matrimid. During the heat treatment adjacent polymer chains become mobile and the aromatic imide and phenylene groups from neighboring chains can enter in π - π -interaction. Thereby, annealing increases the packing density of the polymer chains and decreases the free volume resulting in an increased size selectivity for the different gas molecules (Zhou and Koros 2006; Bos et al. 1998). The MOF filler has an additional influence on the annealing process in Matrimid-based MMMs (Mahdi and Tan 2016). Both the addition of ZIF-8 nanoparticles and annealing improve the gas selectivity. An annealed 10 wt% ZIF-8/Matrimid MMM gave the best results, including tolerance to damage and mechanical robustness, similar to annealed neat Matrimid. For higher wt% of filler loading, the fracture energy and strength decreased considerably (Fig. 12).

For the preparation of ZIF-8/Matrimid MMMs, first a Matrimid polymer was grafted with 1-(3-aminopropyl)-imidazole which was intended to act as terminal linker and anchor group towards Zn in ZIF-8 (Fig. 13). The ZIF-8 nanoparticles were then grown around the polymer particles. Subsequently, the ZIF-8/Matrimid particle composite was fused and annealed to a dense MMM in a DMF-vapor environment. Thereby, higher filler loadings and an improved membrane morphology were tried to achieve for an enhanced CO_2/CH_4 separation performance (Shahid et al. 2015).

Indeed, the imidazole-grafted Matrimid allowed for in situ formed ZIF-8 loadings up to 30 wt% without any loss in selectivity. In the separation of CO_2/CH_4 mixtures the CO_2 permeability for these 30 wt% ZIF-8/Matrimid MMMs had increased up

Fig. 12 Comparison of gas selectivity data of annealed ZIF-8/Matrimid membranes with annealed neat Matrimid (0 wt%) and the mechanical fracture energy and strengths of the membranes. Figure taken from ref. (Mahdi and Tan 2016), copyright Elsevier 2016

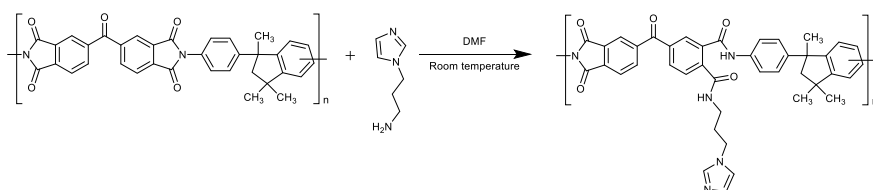
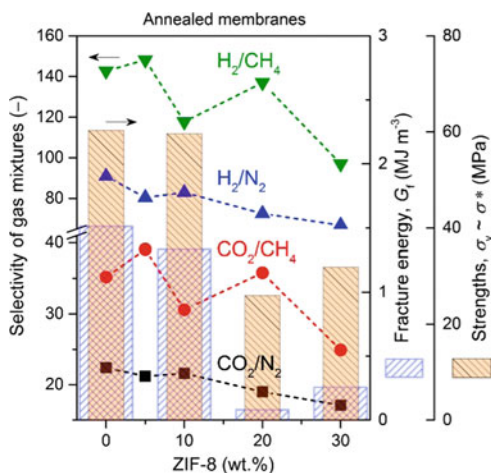


Fig. 13 Grafting of 1-(3-aminopropyl)-imidazole on Matrimid

to 200% and the CO_2/CH_4 selectivity 65%, compared to a neat polymer Matrimid membrane. The MMM from grafted Matrimid with in situ grown ZIF-8 had also a higher permeability and selectivity than membranes prepared conventionally from ZIF-8 and Matrimid albeit with an already optimized protocol concerning dispersion and slow evaporation of the solvent (Fig. 14) (Shahid and Nijmeijer 2014). Thus, higher performing MMMs can be achieved with nearly the same MOF and polymer through enhanced dispersion and higher filler loading by using novel membrane fabrication techniques which avoid interfacial defects.

The MOF $[\text{Co}_4(\mu_4\text{-O})(\text{Me}_2\text{pzba})_3]$ is more air/moisture stable than its MOF-5 analog, which made the Co-MOF suitable for embedding in a Matrimid mixed-matrix membrane. The compound $[\text{Co}_4(\mu_4\text{-O})(\text{Me}_2\text{pzba})_3]$ could be manipulated without working under inert conditions. The small Co-MOF particles could be well dispersed in the polymer because of the good compatibility between MOF and polymer. No aggregation was seen by SEM-EDX (Fig. 15, left). The $[\text{Co}_4(\mu_4\text{-O})(\text{Me}_2\text{pzba})_3]/\text{Matrimid}$ membranes exhibited a better CO_2/CH_4 permeability and selectivity compared to a neat Matrimid membrane (Fig. 15, right). At a pressure difference of 3 bar over the membrane the mixed-gas selectivity (S) was increased from 41 for Matrimid to 60 for the 24 wt % MMM. This selectivity for the Co-MOF/Matrimid MMM is also higher than the selectivities which were reported for

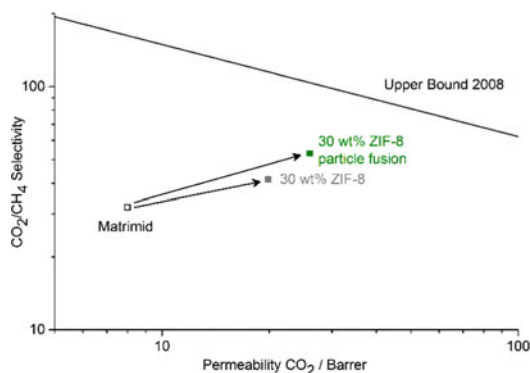


Fig. 14 Permeability and selectivity of a 30 wt% Matrimid/ZIF-8 MMM (Shahid and Nijmeijer 2014) prepared by conventional filler dispersion and solvent evaporation (grey) and prepared by in-situ ZIF-8 growth around grafted Matrimid followed by particle fusion and MMM formation in DMF vapor (green) (Shahid et al. 2015). Figure taken from ref. (Dechnik et al. 2017b), <https://pubs.acs.org/doi/10.1021/acs.cgd.7b00595>, further permissions related to the material excerpted should be directed to the ACS, copyright American Chemical Society, 2017

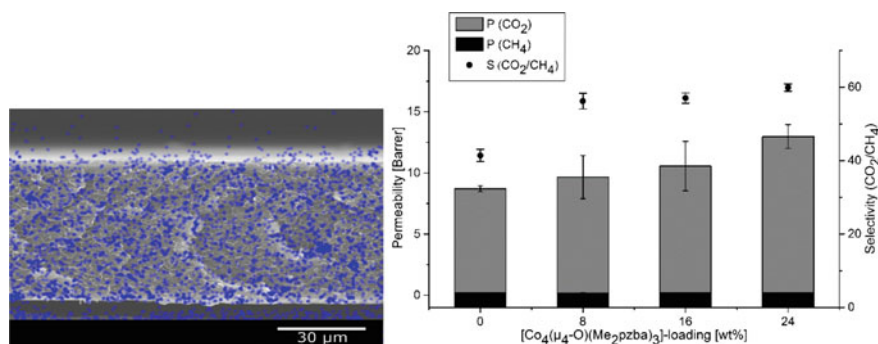


Fig. 15 Left: energy-dispersive X-ray spectrometric (SEM-EDX)-mapping of cobalt (blue) in MMM cross sections with 8 wt% $[\text{Co}_4(\mu_4\text{-O})(\text{Me}_2\text{pzba})_3]$. The Co which is detected below and above the membrane cross section is an artefact and stems from reflection of the electron beam on the sample holder. The top of the cross-section is also the top of the membrane when casted. Right: CO_2/CH_4 permeability (P, left ordinate) and selectivity (S, right ordinate) for neat Matrimid (0 wt%) and $[\text{Co}_4(\mu_4\text{-O})(\text{Me}_2\text{pzba})_3]/\text{Matrimid}$ MMMs with 8, 16 and 24 wt% $[\text{Co}_4(\mu_4\text{-O})(\text{Me}_2\text{pzba})_3]$ loading. The separation of CO_2 was measured from a 50:50 v:v CO_2/CH_4 mixed gas, temperature 25 °C, transmembrane pressure 3 bar. The standard deviations are given as error bars. Figure from Ref. (Dechnik et al. 2017c), copyright American Chemical Society, 2017

MOF-5/Matrimid membranes (maximum $S = 45$), where the MOF-5 degrades with moisture (Dechnik et al. 2017c).

The influence of the free volume within the polymer (cf. Fig. 2) on the gas separation properties is controversial and was, so far, not clearly proven. The free volume within a polymer is used synonymously with the fractional free volume (FFV) v_f , which is dimensionless ($\text{cm}^3 \text{cm}^{-3}$) and can be calculated as follows (Eq. 8):

$$v_f = \frac{v - 1.3 \cdot v_0}{v} \quad (8)$$

where v is the specific volume of the polymer (in $\text{cm}^3 \text{g}^{-1}$), i.e. the reciprocal density, and v_0 represents the occupied volume of the molecules of the polymer (in $\text{cm}^3 \text{g}^{-1}$). The occupied volume of the molecules can be obtained from the van-der-Waals radii calculated by Bondi and van Krevelen for certain chemical groups divided by the molar mass of the same. The volume thus calculated is higher by a factor of 1.3 than the van-der-Waals volumes of the chemical groups, since even at 0 K there is free volume between the polymer molecules.

A further still not fully settled question is the influence of porous and non-porous fillers in MMMs with respect to the possible role of the polymer-filler interface, that is, the void volume. Recently, we compared the same MOF filler in a porous and non-porous state, so as to rule out artefacts from a different polymer-filler interface. MMMs were prepared based on the polymer Matrimid and with the porous MOF aluminum fumarate (Al-fum) as filler or with a non-porous because dimethylsulfoxide solvent-filled aluminum fumarate (Al-fum(DMSO)). In both cases the filler contents ranged from 4 to 24 wt%. The CO_2/CH_4 separation characteristics of both MMMs were measured using a binary gas mixture. The mixed-gas permeation in both the porous and non-porous filler membranes followed the theoretical prediction by the Maxwell model. MMMs with the porous Al-fum dispersed phase displayed an increased CO_2 and CH_4 permeability and a moderate rise in selectivity with increasing filler fraction (Fig. 16).

Conversely, the MMMs with the non-porous dispersed phase Al-fum(DMSO) exhibited a reduction in permeability but had the same selectivity as the pure polymer membrane (Fig. 17).

The Maxwell model can be applied to composite membranes to predict its permeability (see above). Previous work often gave only poor or qualitative trend agreements for porous and non-porous fillers compared to the predicted values of the Maxwell model (Shen and Lua 2013; Rafiq et al. 2015; Sadeghi et al. 2016; Tanh

Fig. 16 CO_2/CH_4 separation performance of porous Al-fum/Matrimid MMMs with different loadings of Al-fum. To verify the reproducibility and significance of the selectivity drop for the 24 wt% membrane, this membrane was prepared and measured four times

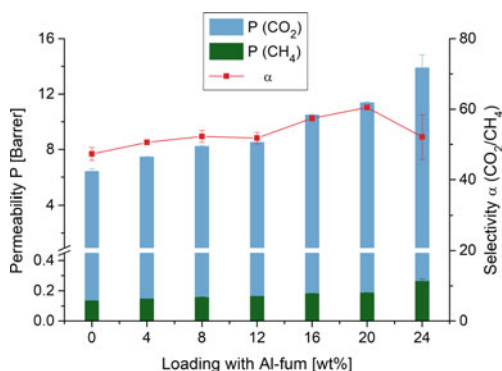
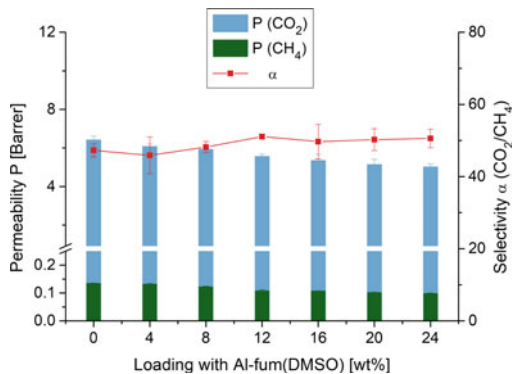


Fig. 17 CO₂/CH₄ separation performance of non-porous Al-fum(DMSO)/Matrimid MMMs as a function of Al-fum(DMSO) loadings



Jeazet et al. 2013). The observed permeability values could often not be quantitatively reproduced with the model. This discrepancy between model and experiment can be due to deviations from the assumptions underlying the Maxwell model. The Maxwell model assumes, for example, a spherical particle geometry, an ideal dispersion and a maximum filler loading corresponding to a volume fraction ϕ_d of 0.2. Also, unaccounted microdefects, that is, void volume due to poor interaction between filler and polymer invalidates the Maxwell model. Figure 18 depicts the comparison between the Maxwell model predicted and the experimental relative CO₂ permeabilities for the mixed-matrix membranes with porous Al-fum and non-porous Al-fum(DMSO) fillers. The measured relative CO₂ permeabilities for porous Al-fum/Matrimid composite membranes match the calculated values from the Maxwell

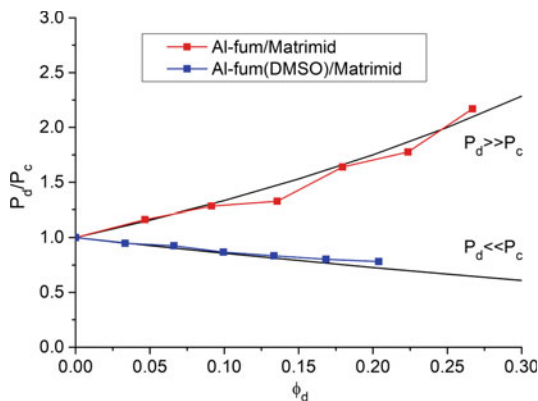


Fig. 18 Relative experimental CO₂ permeabilities P_d/P_c versus filler volume fraction ϕ_d for porous Al-fum/Matrimid (red) and non-porous Al-fum(DMSO)/Matrimid MMMs (blue). The black lines represent the prediction by the Maxwell model for the relative CO₂ permeabilities for porous filler ($P_d \gg P_c$) and non-porous fillers ($P_d \ll P_c$). The higher density of the non-porous Al-fum(DMSO) over the porous Al-fum filler leads to a lower filler volume fraction of the former for the same MOF weight percent

model for porous fillers which are much more permeable than the polymer, that is $P_d \gg P_c$ (cf. Eq. 6). Accordingly, the non-porous Al-fum(DMSO)/Matrimid membranes follow the Maxwell model for non-porous fillers where the filler is non-permeable or $P_d \ll P_c$ (cf. Eq. 7). The decrease of the relative experimental CO_2 permeability P_d/P_c for the non-porous Al-fum(DMSO)/Matrimid MMMs is also a good indicator for the homogeneously distributed filler particles with good MOF-polymer interactions (case 1 in Fig. 7). Non-selective voids (case 2 in Fig. 7) would have resulted in increased permeabilities and reduced selectivity. Rigidification of the polymer chains (case 3 in Fig. 7) would have led to reduced permeability and increased selectivity which was also not observed (cf. Fig. 17).

On the other hand, if the logarithm of the permeability, $\lg P$ has a linear relation with the reciprocal specific free fractional volume ($1/s\text{FFV}$) (Fig. 19), then there is no significant contribution from a (non-selective) void volume (case 1 in Fig. 7). The $s\text{FFV}$ consists of the free volume of the polymer and the MOF; it does not include the polymer-filler interface volume which is also termed void volume. For a 24 wt% porous Al-fum/Matrimid membrane the $s\text{FFV}$ was calculated as $0.23 \text{ cm}^3 \text{ g}^{-1}$ and for a 24 wt% non-porous Al-fum(DMSO)/Matrimid membrane as $0.12 \text{ cm}^3 \text{ g}^{-1}$. Further, a good agreement between the theoretical and experimental density of the Al-fum and Al-fum(DMSO) composite membranes supports the presence of

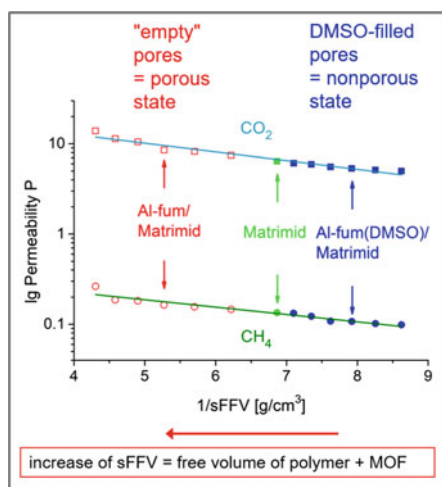


Fig. 19 Linear correlation of $\lg \text{Permeability}$ for CO_2 (upper line) and CH_4 (lower line) to the reciprocal specific free fractional volume ($s\text{FFV}$)—both for the porous Al-fum (left, red data points) and non-porous Al-fum (DMSO) MOF (right blue data points)—each up to 24 wt% MOF content in the MMM. The $s\text{FFV}$ contains the specific polymer and MOF porosity. This linear dependence of $\log P$ versus $1/s\text{FFV}$ excludes a significant contribution from a void volume, that is, the polymer-filler interface volume. For pure Matrimid $1/s\text{FFV} = 6.9$, for 24 wt% Al-fum MMM $1/s\text{FFV} = 4.3$, for 24 wt% Al-fum (DMSO) MMM $1/s\text{FFV} = 8.6$. Points in-between are for the 4, 8, 12, 16 and 20 wt% MMMs. Figure taken from Ref. (Nuhnen et al. 2018), copyright American Chemical Society, 2018

only small interface/void volume. The MMMs of both filler types exhibited specific interface/void volumes below $0.02 \text{ cm}^3 \text{ g}^{-1}$ and often even below $0.01 \text{ cm}^3 \text{ g}^{-1}$ (Nuhnen et al. 2018).

6 Summary

Combining MOFs and polymers to mixed-matrix membranes (MMMs) can help to overcome the trade-off between permeability and selectivity for pure organic polymers and to obtain materials with separation properties exceeding the Robeson upper bound. Most work on such MOF-polymer MMMs deals with the separation of CO_2/CH_4 for natural gas sweetening or CO_2/N_2 separation for the purification of flue gases. Even if MOF-polymer MMMs exhibit enhanced separation performance it should be emphasized that testing gas permeation under industrially relevant conditions should be developed. Also, mixed gas permeation and the influence of contaminants on the separation performance should be evaluated.

The permeability of an MMM can be approximated by the Maxwell model which predicts an increase in gas permeability for porous fillers and a decrease for non-porous fillers, respectively. The increase and decrease in gas permeability is in general due to the difference in free fractional volume (FFV). The FFV combines the free volume of the polymer and filler. In contrast, the interfacial/void volume between filler and polymer contributes only about 10% to the available free volume in a well-prepared MMM.

A challenge with MOF-polymer MMMs is still the increase in selectivity. In cases, where a selectivity increase has been seen with MOF-polymer composite membranes, the following reasons were given for the increase in selectivity: (Nuhnen et al. 2020) (i) Polymer chain rigidification could have been induced by the filler. This results in a higher glass temperature T_g and in general a high T_g goes together with low permeability and high selectivity and vice versa (Li et al. 2005). (ii) Polymer chains can block the MOF channels to some degree and make them size discriminating. Thus, the MOF assumes molecular sieving properties. The smaller gas molecules are transported better relative to the larger ones (Feijani et al. 2015). (iii) An adsorption affinity of the MOF filler for one gas over the other increases the transport of the former over the latter through the membrane (Jacques et al. 2018; Abedini et al. 2018).

Acknowledgements C.J. thanks the German Research Foundation, DFG for support through grant Ja466/29-1 and the Anton-Betz Foundation.

Conflict of interest The authors declare no conflict of interest.

Ethical approval The authors declare that this article does not contain any studies with human participants or animals.

References

- Abedini R, Mosayebi A, Mokhtari M (2018) Improved CO₂ separation of azide cross-linked PMP mixed matrix membrane embedded by nano-CuBTC metal organic framework. *Process Safety Environ Protect* 114:229–239. <https://doi.org/10.1016/j.psep.2017.12.025>
- Abetz V, Brinkmann T, Dijkstra M, Ebert K, Fritsch D, Ohlrogge K, Paul D, Peinemann KV, Pereira-Nunes S, Scharnagl N, Schossig M (2006) Developments in membrane research: from material via process design to industrial application. *Adv Eng Mater* 8:328–358. <https://doi.org/10.1002/adem.200600032>
- Adil K, Belmabkhout Y, Pillai RS, Cadiau A, Bhatt PM, Assen AH, Maurin G, Eddaoudi M (2017) Gas/vapour separation using ultra-microporous metal-organic frameworks: insights into the structure/separation relationship. *Chem Soc Rev* 46:3402–3430. <https://doi.org/10.1039/c7cs00153c>
- Ahn J, Chung WJ, Pinnau I, Guiver MD (2008) Polysulfone/silica nanoparticle mixed-matrix membranes for gas separation. *J Membr Sci* 314:123–133. <https://doi.org/10.1016/j.memsci.2008.01.031>
- Anjum MW, Vermoortele F, Khan AL, Bueken B, De Vos DE, Vankelecom IFJ (2015) Modulated UiO-66-based mixed-matrix membranes for CO₂ separation. *ACS Appl Mater Interfaces* 7:25193–25201. <https://doi.org/10.1021/acsami.5b08964>
- Baker RW (2002) Future directions of membrane gas separation technology. *Ind Eng Chem Res* 41:1393–1411. <https://doi.org/10.1021/ie0108088>
- Baker RW (2004) *Membrane technology and application*, 2nd ed. Wiley-VCH, Chichester. <https://www.wiley.com/en-us/Membrane+Technology+and+Applications%2C+2nd+Edition-p-9780470020388>
- Banerjee R, Furukawa H, Britt D, Knobler C, O’Keeffe M, Yaghi OM (2009) Control of pore size and functionality in isoreticular zeolitic imidazolate frameworks and their carbon dioxide selective capture properties. *J Am Chem Soc* 131:3875–3877. <https://doi.org/10.1021/ja809459e>
- Bánhegyi G (1986) Comparison of electrical mixture rules for composites. *Colloid Polym Sci* 264:1030–1050. <https://doi.org/10.1007/BF01410321>
- Barrer RM, James SD (1960) Electrochemistry of crystal-polymer membranes. Part I. Resistance measurements. *J Phys Chem* 64:417–421. <https://pubs.acs.org/doi/pdf/10.1021/j100833a010>
- Batten SR, Champness NR, Chen XM, Garcia-Martinez J, Kitagawa S, Öhrström L, O’Keeffe M, Paik Suh M, Reedijk J (2013) Terminology of metal-organic frameworks and coordination polymers (IUPAC Recommendations 2013). *Pure Appl Chem* 85:1715–1724. <https://doi.org/10.1351/PAC-REC-12-11-20>
- Bernardo P, Drioli E, Golemme G (2009) Membrane gas separation: a review/state of the art. *Ind Eng Chem Res* 48:4638–4663. <https://doi.org/10.1021/ie8019032>
- BORSIG Membrane Technology GmbH. <https://www.borsig.de/en/borsig-membrane-technology-gmbh/#productrecovery>. Accessed Aug 2020
- Bos A, Pünt IGM, Wessling M, Strathmann H (1998) Plasticization-resistant glassy polyimide membranes for CO₂/CO₄ separations. *Sep Purif Technol* 14:27–39. [https://doi.org/10.1016/S1383-5866\(98\)00057-4](https://doi.org/10.1016/S1383-5866(98)00057-4)
- Buonomenna MG (2013) Membrane processes for a sustainable industrial growth. *RSC Adv* 3:5694–5740. <https://doi.org/10.1039/C2RA22580H>
- Carreon ML, Li S, Carreon MA (2012) AIPO-18 membranes for CO₂/CH₄ separation. *Chem Commun* 48:2310–2312. <https://doi.org/10.1039/C2CC17249F>
- Chen XY, Vinh-Thang H, Rodrigue D, Kaliaguine S (2012) Amine-functionalized MIL-53 metal-organic framework in polyimide mixed matrix membranes for CO₂/CH₄ separation. *Ind Eng Chem Res* 51:6895–6906. <https://doi.org/10.1021/ie3004336>
- Chung TS, Jiang LY, Li Y, Kulprathipanja S (2007) Mixed matrix membranes (MMMs) comprising organic polymers with dispersed inorganic fillers for gas separation. *Prog Polym Sci* 32:483–507. <https://doi.org/10.1016/j.progpolymsci.2007.01.008>

- Clarizia G, Algieri C, Drioli E (2004) Filler-polymer combination: a route to modify gas transport properties of a polymeric membrane. *Polymer* 45:5671–5681. <https://doi.org/10.1016/j.polymer.2004.06.001>
- Dechnik J, Gascon J, Doonan CJ, Janiak C, Sumby CJ (2017a) Mixed-matrix membranes. *Angew Chem Int Ed* 56:9292–9310. <https://doi.org/10.1002/anie.201701109>
- Dechnik J, Sumby CJ, Janiak C (2017b) enhancing mixed-matrix membrane performance with metal-organic framework additives. *Cryst Growth Des* 17:4467–4488. <https://doi.org/10.1021/acs.cgd.7b00595>
- Dechnik J, Nuhnen A, Janiak C (2017) Mixed-matrix membranes of the air-stable MOF-5 analog [Co₄(μ₄-O)(Me₂pzba)₃] with mixed-functional pyrazolate-carboxylate linker for CO₂/CH₄ separation. *Cryst Growth Des* 17:4090–4099. <https://doi.org/10.1021/acs.cgd.7b00202>
- Duval JM, Folkers B, Mulder MHV, Desgrandchamps G, Smolders CA (1993) Adsorbent filled membranes for gas separation. Part 1. Improvement of the gas separation properties of polymeric membranes by incorporation of microporous adsorbents. *J Membr Sci* 80:189–198. [https://doi.org/10.1016/0376-7388\(93\)85143-K](https://doi.org/10.1016/0376-7388(93)85143-K)
- Evans JD, Garai B, Reinsch H, Li W, Dissegna S, Bon V, Senkovska I, Fischer RA, Kaskel S, Janiak C, Stock N, Volkmer D (2019) Metal-organic frameworks in Germany: from synthesis to function. *Coord Chem Rev* 380:378–418. <https://doi.org/10.1016/j.ccr.2018.10.002>
- Feijani EA, Mahdavi H, Tavasoli A (2015) Poly(vinylidene fluoride) based mixed matrix membranes comprising metal organic frameworks for gas separation applications. *Chem Eng Res Des* 96:87–102. <https://doi.org/10.1016/j.cherd.2015.02.009>
- Getman RB, Bae YS, Wilmer CE, Snurr RQ (2012) Review and analysis of molecular simulations of methane, hydrogen, and acetylene storage in metal-organic frameworks. *Chem Rev* 112:703–723. <https://doi.org/10.1021/cr200217c>
- He X, Hägg MB (2012) Membranes for environmentally friendly energy processes. *Membranes* 2:706–726. <https://doi.org/10.3390/membranes2040706>
- Hunger K, Schmeling N, Tanh Jeazet HB, Janiak C, Staudt C, Kleinermanns K (2012) Investigation of cross-linked and additive containing polymer materials for membranes with improved performance in pervaporation and gas separation. *Membranes* 2:727–763. <https://doi.org/10.3390/membranes2040727>
- Jacques NM, Rought PRE, Fritsch D, Savage M, Godfrey HGW, Li L, Mitra T, Frogley MD, Clinque G, Yang S, Schröder M (2018) Locating the binding domains in a highly selective mixed matrix membrane via synchrotron IR microspectroscopy. *Chem Commun* 54:2866–2869. <https://doi.org/10.1039/C7CC08932E>
- Janiak C (2003) Engineering coordination polymers towards applications. *Dalton Trans* 14:2781–2804. <https://doi.org/10.1039/b305705b>
- Janiak C, Vieth JK (2010) MOFs, MILs and more: concepts, properties and applications for porous coordination networks (PCNs). *New J Chem* 34:2366–2388. <https://doi.org/10.1039/C0NJ00275E>
- Javid A (2005) Membranes for solubility-based gas separation applications. *Chem Eng J* 112:219–226. <https://doi.org/10.1016/j.cej.2005.07.010>
- Kluiters SCA (2004) Status review on membrane systems for hydrogen separation. Intermediate report EU project MIGREYD NNE5-2001-670, ECN-C-04-102. <http://www.ecn.nl/publications>
- Koros WJ, Mahajan R (2000) Pushing the limits on possibilities for large scale gas separation: which strategies? *J Membr Sci* 175:181–196. [https://doi.org/10.1016/S0376-7388\(00\)00418-X](https://doi.org/10.1016/S0376-7388(00)00418-X)
- Kulprathipanja S, Neuzil RW, Li NN (1988) Separation of fluids by means of mixed matrix membranes. US patent 4740219A. <https://patents.google.com/patent/US4740219A/en>. Accessed Aug 2020
- Li S, Martinek JG, Falconer JL, Noble RD, Gardner TQ (2005a) Modeling permeation of CO₂/CH₄, CO₂/N₂, and N₂/CH₄ mixtures across SAPO-34 membrane with the Maxwell-Stefan equations. *Ind Eng Chem Res* 44:3220–3228. <https://doi.org/10.1021/ie0610703>

- Li Y, Chung TS, Cao C, Kulprathipanja S (2005b) The effects of polymer chain rigidification, zeolite pore size and pore blockage on polyethersulfone (PES)-zeolite a mixed matrix membranes. *J Membr Sci* 260:45–55. <https://doi.org/10.1016/j.memsci.2005.03.019>
- Loeb S, Sourirajan S (1963) Sea water demineralization by means of an osmotic membrane. *Adv Chem* 28:117–132. <https://doi.org/10.1021/ba-1963-0038.ch009>
- Long JR, Yaghi OM (2009) The pervasive chemistry of metal–organic frameworks (Editorial). *Chem Soc Rev* 38:1213–1214. <https://doi.org/10.1039/B903811F>
- Mahdi EM, Tan JC (2016) Mixed-matrix membranes of zeolitic imidazolate framework (ZIF-8)/Matrimid nanocomposite: thermo-mechanical stability and viscoelasticity underpinning membrane separation performance. *J Membr Sci* 498:276–290. <https://doi.org/10.1016/j.memsci.2015.09.066>
- McLeary EE, Jansen JC, Kapteijn F (2006) Zeolite based films, membranes and membrane reactors: Progress and prospects. *Microporous Mesoporous Mater* 90:198–220. <https://doi.org/10.1016/j.micromeso.2005.10.050>
- Merkel TC, Freeman BD, Spontak RJ, He Z, Pinnau I, Meakin P, Hill AJ (2002) Ultrapermeable, reverse-selective nanocomposite membranes. *Science* 296:519–522. <https://doi.org/10.1126/science.1069580>
- Moaddeb M, Koros WJ (1997) Gas transport properties of thin polymeric membranes in the presence of silicon dioxide particles. *J Membr Sci* 125:143–163. [https://doi.org/10.1016/S0376-7388\(96\)00251-7](https://doi.org/10.1016/S0376-7388(96)00251-7)
- Nuhnen A, Dietrich D, Millan S, Janiak C (2018) Role of filler porosity and filler/polymer interface volume in metal-organic framework/polymer mixed-matrix membranes for gas separation. *ACS Appl Mater Interfaces* 10:33589–33600. <https://doi.org/10.1021/acsami.8b12938>
- Nuhnen A, Klopotowski M, Tanh Jeazet HB, Sorribas S, Zornoza B, Téllez C, Coronas J, Janiak C (2020) High performance MIL-101(Cr)@6FDA-mPD and MOF-199@6FDA-mPD mixed-matrix membranes for CO₂/CH₄ separation. *Dalton Trans* 49:1822–1829. <https://doi.org/10.1039/C9DT03222C>
- Nunes SP, Peinemann KV (eds) (2006) *Membrane technology in the Chemical Industry*, 2nd ed. Wiley-VCH, Weinheim. <https://www.wiley.com/en-us/Membrane+Technology%3A+in+the+Chemical+Industry%2C+2nd%2C+Revised+and+Enlarged+Edition-p-9783527313167>
- Ohlrogge K, Stürken K (2001) The separation of organic vapors from gas streams by means of membranes. In: Nunes SP, Peinemann KV (eds) *Membrane Technology*. Wiley-VCH Verlag GmbH, Weinheim, pp 69–94
- Paul DR, Kemp DR (1973) The diffusion time lag in polymer membranes containing adsorptive fillers. *J Polym Sci Polym Phys* 41:79–93. <https://doi.org/10.1002/polc.5070410109>
- Rafiq S, Maulud A, Man Z, Mutalib MIA, Ahmad F, Khan AU, Khan AL, Ghauri M, Muhammad N (2015) Modelling in mixed matrix membranes for gas separation. *Can J Chem Eng* 93:88–95. <https://doi.org/10.1002/cjce.22111>
- Robeson LM (1991) Correlation of separation factor versus permeability for polymeric membranes. *J Membr Sci* 62:165–185. [https://doi.org/10.1016/0376-7388\(91\)80060-J](https://doi.org/10.1016/0376-7388(91)80060-J)
- Robeson LM (2008) The upper bound revisited. *J Membr Sci* 320:390–400. <https://doi.org/10.1016/j.memsci.2008.04.030>
- Rogge SMJ, Bavykina A, Hajek J, Garcia H, Olivos-Suarez AI, Sepúlveda-Escribano A, Vimont A, Clet G, Bazin P, Kapteijn F, Daturi M, Ramos-Fernandez EV, Llabrés i Xamena FX, Van Speybroeck V, Gascon J (2017) Metal-organic and covalent organic frameworks as single-site catalysts. *Chem Soc Rev* 46:3134–3184. <https://doi.org/10.1039/c7cs00033b>
- Sadeghi M, Semsarzadeh MA, Barikani M, Chenar MP (2011) Gas separation properties of polyether-based polyurethane–silica nanocomposite membranes. *J Membr Sci* 376:188–195. <https://doi.org/10.1016/j.memsci.2011.04.021>
- Sadeghi Z, Omidkhan M, Masoumi ME, Abedini R (2016) Modification of existing permeation models of mixed matrix membranes filled with porous particles for gas separation. *Can J Chem Eng* 94:547–555. <https://doi.org/10.1002/cjce.22414>

- Schaate A, Roy P, Godt A, Lippke J, Waltz F, Wiebcke M, Behrens P (2011) Modulated synthesis of Zr-based metal-organic frameworks: from nano to single crystals. *Chem Eur J* 17:6643–6651. <https://doi.org/10.1002/chem.201003211>
- Schoedel A, Rajeh S (2020) Why design matters: from decorated metal oxide clusters to functional metal-organic frameworks. *Top Curr Chem* 378:19. <https://doi.org/10.1007/s41061-020-0281-0>
- Shahid S, Nijmeijer K (2014) Performance and plasticization behavior of polymer-MOF membranes for gas separation at elevated pressures. *J Membr Sci* 470:166–177. <https://doi.org/10.1016/j.memsci.2014.07.034>
- Shahid S, Nijmeijer K, Nehache S, Vankelecom I, Deratani A, Quemener D (2015) MOF-mixed matrix membranes: precise dispersion of MOF particles with better compatibility via a particle fusion approach for enhanced gas separation properties. *J Membr Sci* 492:21–31. <https://doi.org/10.1016/j.memsci.2015.05.015>
- Shen Y, Lua AC (2013) Theoretical and experimental studies on the gas transport properties of mixed matrix membranes based on polyvinylidene fluoride. *AIChE J* 59:4715–4726. <https://doi.org/10.1002/aic.14186>
- Sholl DS, Lively RP (2016) Seven chemical separations to change the world. *Nature* 532:435–437. <https://doi.org/10.1038/532435a>
- Sieffert D (2013) Nanocomposite materials for membrane separation processes. Dissertation, Heinrich-Heine-Universität Düsseldorf, Düsseldorf, Germany. <https://docserv.uni-duesseldorf.de/servlets/DocumentServlet?id=26268>
- Takahashi S, Paul DR (2006) Gas permeation in poly(ether imide) nanocomposite membranes based on surface-treated silica. Part 2: with chemical coupling to matrix. *Polymer* 47:7519–7535. <https://doi.org/10.1016/j.polymer.2006.08.036>
- Tanh Jeazet HB, Janiak C (2014a) Metal-organic frameworks in mixed-matrix membranes. In: Metal organic framework materials MacGillivray LR, Lukehart C (eds) Wiley, Chichester, pp 403–418. <https://www.wiley.com/en-us/Metal+Organic+Framework+Materials-p-9781119952893>. ISBN 978-1-119-95289-3
- Tanh Jeazet HB, Janiak C (2014b) Metal-organic frameworks: frameworks in mixed-matrix membranes. In: MacGillivray LR, Lukehart CM (eds) Encyclopedia of inorganic and bioinorganic chemistry. Wiley, Chichester. <http://dx.doi.org/10.1002/9781119951438.eibc2219>
- Tanh Jeazet HB, Staudt C, Janiak C (2012) Metal-organic frameworks in mixed-matrix membranes for gas separation. *Dalton Trans* 41:14003–14027. <https://doi.org/10.1039/C2DT31550E>
- Tanh Jeazet HB, Koschine T, Staudt C, Raetzke K, Janiak C (2013) Correlation of gas permeability in a metal-organic framework MIL-101(Cr)-Polysulfone mixed-matrix membrane with free volume measurements by positron annihilation lifetime spectroscopy (PALS). *Membranes (Basel)* 3:331–353. <https://doi.org/10.3390/membranes3040331>
- Tien-Binh N, Vinh-Thang H, Chen XY, Rodrigue D, Kaliaguine S (2015) Polymer functionalization to enhance interface quality of mixed matrix membranes for high CO₂/CH₄ gas separation. *J Mater Chem A* 3:15202–15213. <https://doi.org/10.1039/C5TA01597A>
- Torrìsì A, Mellot-Draznieks C, Bell RG (2010) Impact of ligands on CO₂ adsorption in metal-organic frameworks: first principles study of the interaction of CO₂ with functionalized benzenes. II. Effect of polar and acidic substituents. *J Chem Phys* 132:044705. <https://doi.org/10.1063/1.3276105>
- Valenzano L, Civalleri B, Chavan S, Bordiga S, Nilsen MH, Jakobsen S, Lillerud KP, Lamberti C (2011) Disclosing the complex structure of UiO-66 metal organic framework: a synergic combination of experiment and theory. *Chem Mater* 23:1700–1718. <https://doi.org/10.1021/cm1022882>
- Vankelecom IFJ, Merckx E, Luts M, Uytterhoeven JB (1995) Incorporation of zeolites in polyimide membranes. *J Phys Chem* 99:13187–13192. <https://doi.org/10.1021/j100035a023>
- Venna SR, Lartey M, Li T, Spore A, Kumar S, Nulwala HB, Luebke DR, Rosi NL, Albenze E (2015) Fabrication of MMMs with improved gas separation properties using externally-functionalized MOF particles. *J Mater Chem A* 3:5014–5022. <https://doi.org/10.1039/C4TA05225K>

- Vu DQ, Koros WJ, Miller SJ (2003) Mixed matrix membranes using carbon molecular sieves: I. Preparation and experimental results. *J Membr Sci* 211:311–334. [https://doi.org/10.1016/S0376-7388\(02\)00429-5](https://doi.org/10.1016/S0376-7388(02)00429-5)
- Zhou HC, Kitagawa S (2014) Metal-organic frameworks (MOFs) (Editorial). *Chem Soc Rev* 43:5415–5418. <https://doi.org/10.1039/C4CS90059F>
- Zhou F, Koros WJ (2006) Study of thermal annealing on Matrimid® fiber performance in pervaporation of acetic acid and water mixtures. *Polymer* 47:280–288. <https://doi.org/10.1016/j.polymer.2005.11.017>

A Story on Carbon Dioxide and Its Hydration



Claudiu T. Supuran

Abstract CO₂ is one of the fundamental molecules on earth, being a widespread and highly stable form of carbon. It is hydrated slowly to bicarbonate and protons, which is not enough for most life forms in which this simple molecules plays relevant functions. Thus, the enzymes carbonic anhydrases (CAs) evolved, and they efficiently catalyze the hydration of CO₂. CAs are involved in many physiological and pathological events in organisms all over the phylogenetic tree. Over the last three decades I was involved in unravelling the biochemical basic phenomena connected to these enzymes and in drug design of modulators of their activity (inhibitors and activators). The various approaches I developed were applied to many types of such enzymes and allowed the discovery of many classes of highly isoform-selective inhibitors. This afforded new applications of the inhibitors for the management of hypoxic tumors, neuropathic pain, cerebral ischemia, arthritis, degenerative disorders apart the classical ones connected with these drugs (diuretics, anti-glaucoma, anti-epileptic and anti-obesity action). The study of CA activators showed that these enzymes may represent a crucial family of new targets for improving cognition as well as in therapeutic areas, such as generalized anxiety, post-traumatic stress, obsessive-compulsive disorder or phobias for which few efficient therapies are available.

Keywords Carbonic anhydrase · Inhibition · Inhibitor · Activation · Anticancer drug · Neuropathic pain · Neurodegeneration · Memory therapy · SLC-0111

1 Introduction

I started to work on the metalloenzyme carbonic anhydrase (CAs, EC 4.2.1.1) in 1987 and in the first 15 years of my research the constant leitmotiv was “when will you stop working on such a simple and well-known enzyme”? Such queries came from friends, collaborators and sometimes professors with a much more important experience in chemical/biomedical research than myself. In fact, CAs are present

C. T. Supuran (✉)

Department of NEUROFARBA, Section of Pharmaceutical and Nutraceutical Sciences,
University of Florence, via Ugo Schiff 6, 50019 Sesto Fiorentino, Florence, Italy
e-mail: claudiu.supuran@unifi.it

© The Author(s), under exclusive license to Springer Nature Switzerland AG 2021
M. J. M. Abadie et al. (eds.), *New Trends in Macromolecular and Supramolecular Chemistry for Biological Applications*, https://doi.org/10.1007/978-3-030-57456-7_6

115

in all living organism, acting as catalysts for the reversible hydration of CO₂ to bicarbonate and protons, an exquisitely simple chemical transformation (Supuran 2017, 2020a, 2016a, 2008; Neri and Supuran 2011). CA was discovered in 1930s, its most relevant inhibitors (the primary sulfonamides) were known since the '40s and the first clinically used agents based on CA inhibitors (CAIs) were launched in the 50s (Supuran 2017, 2020a, 2016a, 2008; Neri and Supuran 2011; Alterio et al. 2012). Thus, the expressed doubts were in fact quite reasonable, but fortunately did not stop me for continuing my trip in exploring CAs, their inhibitors, activators and their pharmacological/ biotechnological applications (Supuran 2016b, 2018a; Nocentini and Supuran 2019; Berrino and Supuran 2019). Why are CAs relevant may be understood from the fact that these enzymes act on carbon dioxide and water, two neutral molecules, which are very efficiently converted to bicarbonate and H⁺ ions, generating a weak base and a very strong acid (Neri and Supuran 2011; Alterio et al. 2012; Supuran 2016b, 2018a; Nocentini and Supuran 2019; Berrino and Supuran 2019). As a consequence, and due to the high availability of CO₂ from metabolic processes, this reaction constitutes the basis of pH regulation in all living organism (Supuran 2017, 2020a, 2016a, 2008). Furthermore, CAs are metabolic enzymes (Berrino and Supuran 2019), being involved in many other processes apart pH regulation, as I proposed and demonstrated recently, mainly but not exclusively in the tumor metabolism (Supuran 2017, 2020a, 2016a).

Today, there are 8 (α -, β -, γ -, δ -, ζ -, η , θ , and ι -CA) different CA genetic families reported in various organisms (De Simone et al. 2015; Kikutani et al. 2016; Jensen et al. 2019; De Prete et al. 2016, 2019; Aspatwar et al. 2018; Capasso and Supuran 2015). The distribution of these enzymes is rather variegated in most investigated organisms, and except animals, most of them possess multiple representatives of two or more genetic families (Supuran 2017, 2020a, 2016a, 2008, 2016b, 2018a; Neri and Supuran 2011; Alterio et al. 2012; Nocentini and Supuran 2019; Berrino and Supuran 2019; De Simone et al. 2015). For example, in some diatoms 5 different CA classes with multiple isoforms were described (Kikutani et al. 2016; Jensen et al. 2019).

CAs, or at least the human isoforms, are drug targets for more than 70 years by now, as all clinically used diuretics were developed from acetazolamide **1**, the first sulfonamide CAI to be used clinically (Supuran 2017, 2020a, 2016a, 2008; Neri and Supuran 2011; Alterio et al. 2012). Presently, many types of CAIs are employed in various clinical settings, as diuretics (Supuran 2018b, 2018c), anti-glaucoma agents (Carta et al. 2012a; Supuran et al. 2019; Supuran 2019), anti-epileptic drugs (Aggarwal et al. 2013), and anti-obesity agents (Scozzafava et al. 2013; Costa et al. 2019), and for the management of hypoxic, metastatic tumors (Supuran et al. 2018; Supuran 2018d; Nocentini and Supuran 2018; Ruzzolini et al. 2020). Recently, classical chemotypes but also some new classes of CAIs were shown to be useful for the management of neuropathic pain (Carta et al. 2015; Supuran 2016c), cerebral ischemia (Di Cesare Mannelli et al. 2016), and some forms of arthritis (Margheri et al. 2016; Akgul et al. 2018; Bua et al. 2017; De Simone and Supuran 2012). These developments were only possible due to the fact that several

new CA inhibition mechanism have been discovered (Supuran 2017, 2020a, 2016a, 2008; Neri and Supuran 2011; Alterio et al. 2012).

2 CA Inhibition/Activation Mechanisms

In Fig. 1 the 4 CA inhibition mechanisms and the CA activation mechanism are presented schematically, based on kinetic and crystallographic data obtained over the last 25 years (Supuran 2017, 2020a, 2016a, 2008; Neri and Supuran 2011; Alterio et al. 2012).

2.1 Zinc Binders

Sulfonamides and their isosteres (sulfamiedes, sulfamates, substituted sulfamides), inorganic complexing anions (halides, pseudohalides but also many complex, heavy metal containing anions, etc. (Simone and Supuran 2012; Winum and Supuran 2015; Supuran 2018e); various sulfur-based, carbon-based (Supuran 2018e), phosphorus-based (Nocentini et al. 2019) and boron-based (Alterio et al. 2016; Nocentini et al. 2018a) ZBGs, of the N-hydroxy-sulfonamide, sulfonyl-hydrazide (Supuran 2018e), benzenephosponamidate (Nocentini et al. 2019), mono- and dithiocarbamate (Carta et al. 2012b; Vullo et al. 2016), xanthate (Carta et al. 2013), benzoxaborole (Alterio et al. 2016; Nocentini et al. 2018a), thiol, selenol (Angeli et al. 2019a; Tanini et al. 2020), carboxylate (Langella et al. 2016; Sechi et al. 2012; Cadoni et al. 2017), ninhydrin (Bouzina et al. 2021), hydroxamate (Fiore et al. 2012) and carbamate (De Simone et al. 2018) belong to this group of CAIs. As shown in Fig. 1A, they coordinate the metal ion from the enzyme active site in a monodentate fashion, substituting the water molecule or hydroxide ion involved in the catalytic cycle, i.e., CO₂ hydration (Supuran 2017, 2020a, 2016a, 2008; Neri and Supuran 2011; Alterio et al. 2012). For the α -CAs, as shown in the figure, two amino acid residues, Thr199-Asp106, are also involved in the binding of inhibitors, with which they engage in a hydrogen bond network which stabilized the enzyme-inhibitor adduct. The sulfonamides are by far the most clinically relevant inhibitors, with many such drugs being used for the treatment of conditions mentioned above (Supuran 2018b, 2018c, 2019, 2018d; Carta et al. 2012a; Supuran et al. 2019, 2018; Aggarwal et al. 2013; Scozzafava et al. 2013; Costa et al. 2019; Nocentini and Supuran 2018; Ruzzolini et al. 2020).

2.2 CAIs Which Anchor to the Zinc-Bound Water Molecule

As shown in Fig. 1B, these CAIs are anchored by means of hydrogen bonds to the water molecule or hydroxide anion coordinated to the zinc, by using the AG

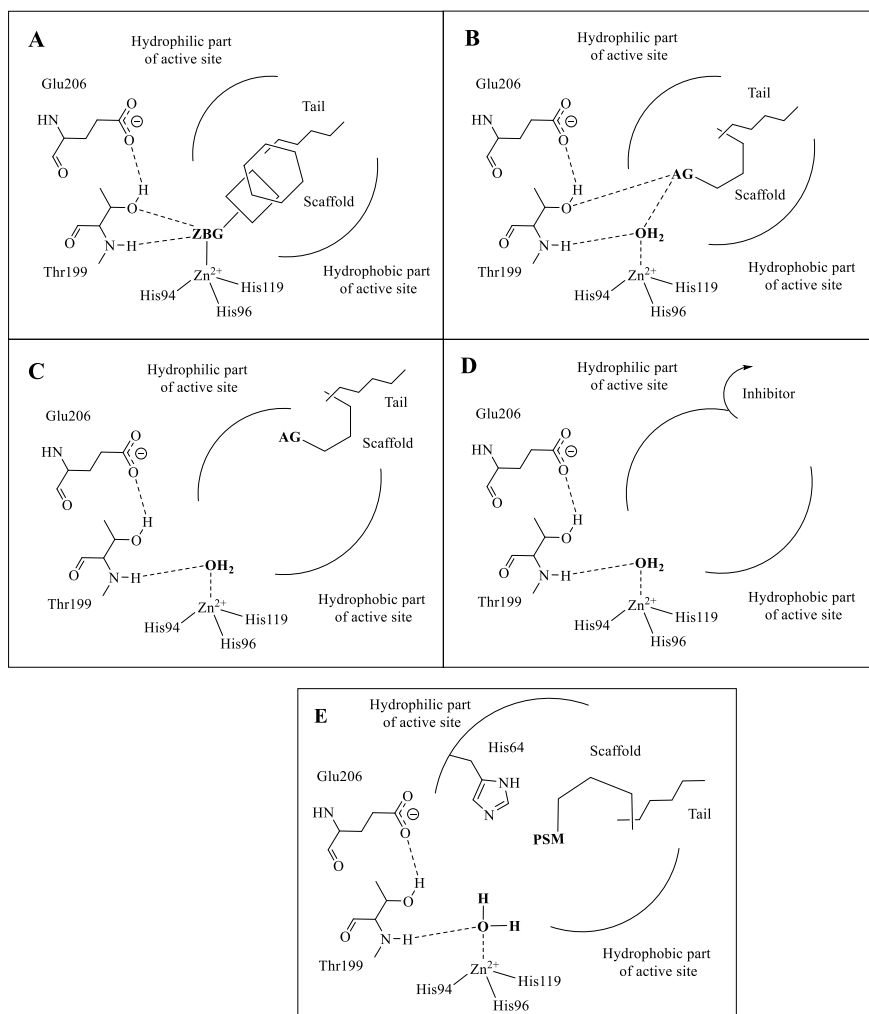


Fig. 1 The main CA inhibition (A–D) and the CA activation mechanism (E) known to date. **A** zinc binders, which incorporate a zinc-binding group (ZBG); **B** compounds which anchor to the zinc-bound water, and possess an anchoring group (AG); **C** inhibitors which occlude the entrance to active site (contain an AG moiety); **D** inhibitors binding outside the active site; **E** CA activators (CAAs) incorporate proton shuttle moieties (PSMs) and bind as inhibitors of type (C)

moiety present in their scaffold. To this class of CAIs belong the phenols (Nair et al. 1994; Innocenti et al. 2008a, b; Bayram et al. 2008; Nocentini et al. 2018b; Karioti et al. 2016), polyamines of the spermine/spermidine type (Carta et al. 2010), the sulfocoumarins which are hydrolyzed to sulfonates acting this as prodrug inhibitors (Tars et al. 2013), but also some thioxocoumarins (Ferraroni et al. 2016; Nocentini et al. 2018c) and several carboxylic acid derivatives (Langella et al. 2016).

2.3 CAIs Which Occlude the Entrance to the Active Site Cavity

As shown in Fig. 1C, these compounds bind far away from the metal ion and its coordinated water molecule, at the entrance of the CA active site cavity, a region which is also quite variable between the various α -CA isoforms. Coumarins and some of their derivatives were discovered to possess this peculiar inhibition mechanism (Maresca et al. 2009, 2010a, 2010b; Temperini et al. 2010; Touisni et al. 2011; Bonneau et al. 2013; Sharma et al. 2014; Maresca and Supuran 2010; Fois et al. 2020; Carta et al. 2012c; Isik et al. 2015; Davis et al. 2013). The coumarin is in fact hydrolyzed by the esterase CA activity, with formation of *cis/trans*-2-hydroxycinnamic acid derivatives (Maresca et al. 2009; Isik et al. 2015; Davis et al. 2013; Nocentini et al. 2015; Küçükbay et al. 2016; Angeli et al. 2018a; D'Ambrosio et al. 2015; Supuran 2018f; Briganti et al. 1997; Temperini et al. 2006b), which thereafter binds at the entrance of the cavity. Many coumarins act as isoform-selective CAIs for the different human isoforms, due to the fact that they bind in this variable region of the active site, interacting thus with diverse amino acid residues of the various isoforms (Supuran 2017, 2016b; Alterio et al. 2012; Nocentini and Supuran 2019; Maresca et al. 2009, 2010a, 2010b; Temperini et al. 2010; Touisni et al. 2011; Bonneau et al. 2013; Sharma et al. 2014; Maresca and Supuran 2010; Fois et al. 2020). Other compounds possessing a similar CA inhibition mechanism are the 5- and 6-ring lactones/thiolactones (Carta et al. 2012c), 3,4-dihydro-1H-quinoline-2-ones (Isik et al. 2015), some heterocoumarins incorporating selenium, tellurium (Davis et al. 2013; Nocentini et al. 2015; Küçükbay et al. 2016), and the substituted quinoline-2(1H)-ones (Angeli et al. 2018a).

2.4 Out of the Active Site Binding CAIs

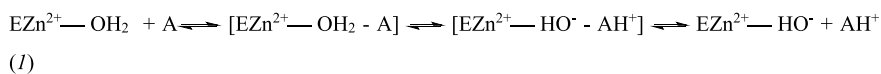
Few derivatives were observed so far to bind out of the active site (Fig. 1D), in a hydrophobic pocket adjacent to the main CA active site entrance. 2-(Benzylsulfinyl)benzoic acid was co-crystallized bound to CA II in this way (D'Ambrosio et al. 2015), with its COOH moiety hydrogen-bonding the imidazole of His64, an important residue for the CA catalytic mechanism (see next paragraph). In this way the proton shuttling is blocked and the catalytic cycle collapses, effectively inhibiting then enzyme catalytic activity (D'Ambrosio et al. 2015).

2.5 CA Activation

The CA activation process is shown schematically in Fig. 1E. The activator binding site coincides with that of inhibitors occluding the active site entrance (Maresca et al.

2009; Supuran 2018f). Most biogenic primary amines (catecholamines, serotonin histamine, etc.), natural and non-natural amino acids, some oligopeptides, or small proteins represent the main classes of CA activator (CAAs) (Supuran 2018f; Briganti et al. 1997).

Equation 1 shows the rationale behind the CA activation phenomenon (Supuran 2018f; Briganti et al. 1997).



enzyme - activator complexes

(1)

The CAA binds to the enzyme, forming enzyme – activator complexes. The activator incorporates a proton shuttling moiety, PSM (Fig. 1E) which participates to the rate-determining step of the catalytic cycle. This is the proton shuttling from the zinc-coordinated water to the reaction medium (Supuran 2018f; Briganti et al. 1997). His64 plays the role of natural proton shuttle, being situated in the middle of the active site cavity and having a flexible side chain of the imidazole type, which is able to participate in proton transfer processes (Supuran 2017, 2020a, 2016a, 2018f; Briganti et al. 1997). In the enzyme-activator complexes this process which is assisted by the activator is an intramolecular, and not intermolecular reaction, which may explain the kinetic activating effect (Temperini et al. 2006a, b, 2008; Vistoli et al. 2020). X-ray crystal structures of CAs with activators bound, of the amine and amino acid type are known to date, such as those with histamine, L- and D-His, L- and D-Phe, L-adrenaline, D-Trp, etc. (Supuran 2018f; Briganti et al. 1997; Temperini et al. 2006a, b, 2008; Vistoli et al. 2020). All catalytically active mammalian CAs, were shown to be activatable by natural amino acids and amines (Briganti et al. 1997; Temperini et al. 2006a, b, 2008; Vistoli et al. 2020). CAAs (such as D-Phe) may have applications in pharmacology for the management of various diseases (Canto de Souza et al. 2017). In fact, the activators were shown to induce an increased ERK phosphorylation which is involved in memory consolidation, opening the possibility of using CAA-based therapies for obsessive–compulsive disorder, post-traumatic stress disorders, phobias, generalized anxiety, etc. (Canto de Souza et al. 2017).

3 Clinically Used CAIs

The primary sulfonamides/sulfamates/sulfamides in clinical use for decades or in clinical development as novel agents, are shown in Fig. 2.

They include: acetazolamide **1**, methazolamide **2**, ethoxzolamide **3**, sulthiame **4**, dichlorophenamide **5**, dorzolamide **6** and brinzolamide **7**) (Supuran 2017, 2020a, 2016a, 2008, 2016b; Neri and Supuran 2011; Alterio et al. 2012; Nocentini and Supuran 2019), sulpiride **8** (Abbate et al. 2004), the antiepileptics with CA inhibitory

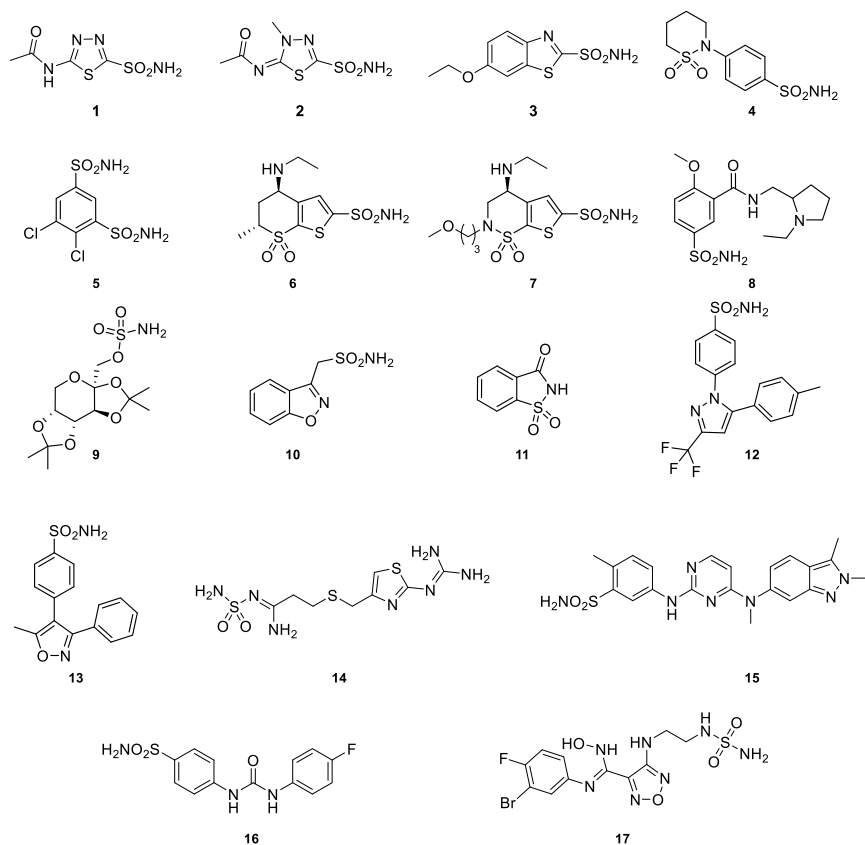


Fig. 2 CAIs 1–15 used clinically, or in clinical development, SLC-0111 **16** and epacadostat **17**

action such as topiramate **9** (Casini et al. 2003) and zonisamide **10** (De Simone et al. 2005), sweeteners such as saccharine **11** (Köhler et al. 2007), CA/COX-2 selective inhibitors, such as celecoxib **12** (Weber et al. 2004) and valdecoxib **13** (De Fiore et al. 2006), histamine H₂-receptor antagonists with CA inhibitory action, such as famotidine **14** (Angeli et al. 2018b), tyrosine kinase/CA pan-inhibitors, such as pazopanib **15** (Winum et al. 2012), SLC-0111 (**16**), in Phase Ib/II clinical trials as an antitumor/antimetastatic agent (Pacchiano et al. 2011, 2010; Lou et al. 2011; McDonald et al. 2020), as well as the CA/indoleamine-2,3-dioxygenase inhibitor epacadostat **17**, in Phase III clinical trials as an antitumor agent (Angeli et al. 2019b; Scozzafava et al. 1999a, b; Supuran et al. 1999; Menabuoni et al. 1999; Abbate et al. 2003; Güzel et al. 2008; Avvaru et al. 2010; Carta et al. 2011; Menchise et al. 2005; Alterio et al. 2006; Tanpure et al. 2015; Wilkinson et al. 2006; Eldehna et al. 2019).

4 Novel Applications of the Isoform-Selective CAIs Targeting Human Enzymes

4.1 *Cancer and Metastasis*

The transmembrane isoforms CA IX and XII were demonstrated to be involved in tumorigenesis as they regulate the tumor pH, both within the cell and in the extracellular space (Supuran 2008, 2018a; Svastová et al. 2004; Ditte et al. 2011; Cianchi et al. 2010). They also participate in the tumor metabolism, which is different of the normal one due to the low levels of O₂ (hypoxia) (Berrino and Supuran 2019; Angeli et al. 2020). Both these enzymes are overexpressed in tumors due to hypoxia, as their gene expression is regulated by the transcription factor HIF-1 α (hypoxia inducible factor-1 α) (Supuran 2017, 2020a, 2016a, 2008; Svastová et al. 2004). CA IX/XII inhibition leads to an inhibition of the growth of primary tumors and metastases (Pacchiano et al. 2011; Lou et al. 2011), which favored the development of new inhibitors, among which SLC-0111 is nowadays in Phase Ib/II clinical trials for the management of metastatic advanced solid tumors (McDonald et al. 2020). This compound is effective mainly in combination with other antitumor agents and may lead to a revolutionary new approach in the management of hypoxic tumors, which poorly respond to classical chemo- and radiotherapy (McDonald et al. 2020; Angeli et al. 2020; Supuran 2020b).

4.2 *Cerebral Ischemia*

In cerebral ischemia there is also an impaired/insufficient blood and O₂ supply to the brain, which leads to overexpression of HIF-1 α targets mentioned above, CA IX and XII (Di Cesare Mannelli et al. 2016). It has been shown that sulfonamide or coumarin inhibitors which selectively target these two isoforms over the off-target, cytosolic ones, increased up to 40% the neurological score of experimental animals rats with cerebral artery occlusion (which represents animal model of the disease) (Cesare et al. 2016). The therapeutic opportunities for treating cerebral ischemia are nowadays limited, and this discovery opens new opportunities in the field.

4.3 *Neuropathic Pain*

Up to 8% of the world population is affected by various forms of neuropathic pain and only one drug, gabapentin, has been so far approved for its treatment, but this is also associated with serious side effects, drastically limiting its use (Carta et al. 2015; Supuran 2016c). Kaila's group explained the connection between CA inhibition and neuropathic pain (Asiedu et al. 2014), demonstrating that GABAergic networks and

the neuron-specific potassium-chloride (K^+Cl^-) cotransporter (KCC2) are dependent of the bicarbonate concentration generated by hydration of CO_2 catalyzed by brain CA isoforms. It is not clear which CA isoforms are involved in these processes, but hCA VII and hCA II which are highly expressed in various brain areas, are among the most relevant candidates considered to date as relevant for explaining the above-mentioned phenomena (Asiedu et al. 2010; Supuran 2015, 2016d). Thus, a campaign to develop CA II and/or CA VII-selective inhibitors led to the discovery of sulfonamides (Carta et al. 2015; Angeli et al. 2019c, 2018c; Kalisha Vali et al. 2019) and sulfamates (Bozdag et al. 2019) possessing such an inhibition profile, which were also effective in vivo, in animal models of neuropathic pain (which has been induced by using cytotoxic drugs such as cisplatin) (Angeli et al. 2019c, 2018c; Kalisha Vali et al. 2019; Bozdag et al. 2019).

4.4 Rheumatoid Arthritis

CA IX and XII were observed to be overexpressed in some arthritis. By using sulfonamides/coumarins selective inhibitors against them, in an animal model of the arthritis, interesting and relevant results have been obtained (Margheri et al. 2016; Akgul et al. 2018; Bua et al. 2017). Conjugation of classical non-steroidal anti-inflammatory drugs (belonging to the phenyl-propanoic carboxylic acid type, such as ibuprofen, ketoprofen, etc.), with aromatic sulfonamides (Akgul et al. 2018) or coumarins incorporating hydroxyl and/or amono moieties (Bua et al. 2017), led to hybrids possessing COX and CA inhibitory effects. They efficiently inhibited CA IX/XII in vitro and showed a long-lasting and potent anti-hyperalgesic effect in an animal model of arthritis (Akgul et al. 2018; Bua et al. 2017; Berrino et al. 2019).

4.5 Neurodegeneration

Fossati's group showed that the sulfonamide CAIs acetazolamide **1** and methazolamide **2** (Fossati et al. 2016; Solesio et al. 2018) (Fig. 2) may prevent of mitochondrial dysfunction in animal models of Alzheimer's diseases. The treatment also affected caspase activation as well as cell death associated with amyloid β formation. The two drugs were effective in reducing memory impairment and decreased amyloid β pathology in a transgenic mouse model of Alzheimer's disease (Angiulli et al. 2018). Such findings may be translated to drug design campaigns for finding CAIs effective for the management of this disease, for which no effective therapies are available to date (Provinsi et al. 2019).

5 Conclusions

The wealth of possible binding modes for inhibitors/activators within the CA active site and the new generation isoform-selective inhibitors, most of which were discovered by my group, afforded interesting applications in new research fields, with relevant results being obtained for compounds involved in the management of hypoxic tumors (Supuran 2018d; McDonald et al. 2020), neuropathic pain (Carta et al. 2015; Supuran 2016c), cerebral ischemia (Di Cesare Mannelli et al. 2016), arthritis (Margheri et al. 2016; Akgul et al. 2018; Bua et al. 2017) and neurodegenerative diseases (Fossati et al. 2016; Solesio et al. 2018; Angiulli et al. 2018; Provensi et al. 2019). The CA activators, still in their infancy, may lead to a better understanding of cognition but may as well lead to applications in novel therapeutic areas, among which post-traumatic stress disorders phobias, generalized anxiety, obsessive-compulsive disorder. Indeed, in two recent contributions we demonstrated the role of CA activation in extinction of contextual fear memory or more generally in cognition and emotional memory (Blandina et al. 2020; Schmidt et al. 2020). On the inhibitor side, the search of new chemotypes among the natural products (Atanasov et al. 2021) and the continuous exploration of anti-infectives based on this class of derivatives (Supuran and Capasso 2020) will probably also lead to relevant new applications.

Acknowledgements My present and past research group(s) are probably the most relevant scientific and human adventures I lived and that was and is very rewarding. The collaborations with research groups and the friendship with colleagues from all over the world is another relevant point in my career. To all of them I am extremely grateful. My profound thanks go to my mentors who were highly relevant during all my career: Prof. Alexandru T. Balaban (Texas A & M Univ., USA) and Prof. Andrea Scozzafava (Univ of Florence, Italy) are undoubtedly the most relevant names.

References

- Abbate F, Casini A, Scozzafava A, Supuran CT (2003) Carbonic anhydrase inhibitors: X-ray crystallographic structure of the adduct of human isozyme II with the perfluorobenzoyl analogue of methazolamide. Implications for the drug design of fluorinated inhibitors. *J Enzyme Inhib Med Chem* 18:303–308
- Abbate F, Coetzee A, Casini A et al (2004) Carbonic anhydrase inhibitors: X-ray crystallographic structure of the adduct of human isozyme II with the antipsychotic drug sulpiride. *Bioorg Med Chem Lett* 14:337–441
- Aggarwal M, Kondeti B, McKenna R (2013) Anticonvulsant/antiepileptic carbonic anhydrase inhibitors: a patent review. *Expert Opin Ther Pat* 23:717–724
- Akgul O, Di Cesare ML, Vullo D et al (2018) Discovery of novel nonsteroidal anti-inflammatory drugs and carbonic anhydrase inhibitors hybrids (NSAIDs-CAIs) for the management of rheumatoid arthritis. *J Med Chem* 61:4961–4977
- Alterio V, Vitale RM, Monti SM et al (2006) Carbonic anhydrase inhibitors: X-ray and molecular modeling study for the interaction of a fluorescent antitumor sulfonamide with isozyme II and IX. *J Am Chem Soc* 128:8329–8335

- Alterio V, Di Fiore A, D' Ambrosio K et al (2012) Multiple binding modes of inhibitors to carbonic anhydrases: how to design specific drugs targeting 15 different isoforms? *Chem Rev* 112:4421–4468
- Alterio V, Cadoni R, Esposito D et al (2016) Benzoxaborole as a new chemotype for carbonic anhydrase inhibition. *Chem Commun* 52:11983–11986
- Angeli A, Trallori E, Carta F et al (2018a) heterocoumarins are selective carbonic anhydrase ix and xii inhibitors with cytotoxic effects against cancer cells lines. *ACS Med Chem Lett* 9:947–951
- Angeli A, Ferraroni M, Supuran CT (2018b) Famotidine, an antiulcer agent, strongly inhibits helicobacter pylori and human carbonic anhydrases. *ACS Med Chem Lett* 9:1035–1038
- Angeli A, di Cesare ML, Lucarini E et al (2018c) Design, synthesis and X-ray crystallography of selenides bearing benzenesulfonamide moiety with neuropathic pain modulating effects. *Eur J Med Chem* 154:210–219
- Angeli A, Tanini D, Nocentini A et al (2019a) Selenols: a new class of carbonic anhydrase inhibitors. *Chem Commun (Camb)* 5(5):648–651
- Angeli A, Ferraroni M, Nocentini A et al (2019b) Polypharmacology of epacadostat: a potent and selective inhibitor of the tumor associated carbonic anhydrases IX and XII. *Chem Commun (Camb)* 55:5720–5723
- Angeli A, Di Cesare ML, Ghelardini C et al (2019c) Benzenesulfonamides bearing spirohydantoin moieties act as potent inhibitors of human carbonic anhydrases II and VII and show neuropathic pain attenuating effects. *Eur J Med Chem* 177:188–197
- Angeli A, Carta F, Nocentini A et al (2020) Carbonic anhydrase inhibitors targeting metabolism and tumor microenvironment. *Metabolites* 10:412
- Angiulli F, Solesio ME, Debure L et al (2018) Carbonic anhydrase inhibitors ameliorate neurovascular dysfunction in a mouse model of cerebral amyloid angiopathy. *Alzheimer's Dement J Alzheimer's Assoc* 14:P1296
- Asiedu M, Ossipov MH, Kaila K, Price TJ (2010) Acetazolamide and midazolam act synergistically to inhibit neuropathic pain. *Pain* 148:302–308
- Asiedu MN, Mejia GL, Hübner CA et al (2014) Inhibition of carbonic anhydrase augments GABAA receptor-mediated analgesia via a spinal mechanism of action. *J Pain* 15:395–406
- Aspatwar A, Haapanen S, Parkkila S (2018) An update on the metabolic roles of carbonic anhydrases in the model alga *Chlamydomonas reinhardtii*. *Metabolites* 8:E22
- Atanasov AG, Zotchev SB, Dirsch VM, International Natural Product Sciences Taskforce, Supuran CT (2021) Natural products in drug discovery: advances and opportunities. *Nat Rev Drug Discov* 20:200–216. <https://doi.org/10.1038/s41573-020-00114-z>. Epub ahead of print. PMID: 33510482
- Avvaru BS, Wagner JM, Maresca A et al (2010) Carbonic anhydrase inhibitors. The X-ray crystal structure of human isoform II in adduct with an adamantyl analogue of acetazolamide resides in a less utilized binding pocket than most hydrophobic inhibitors. *Bioorg Med Chem Lett* 20:4376–4381
- Bayram E, Senturk M, Kufrevioglu OI et al (2008) In vitro effects of salicylic acid derivatives on human cytosolic carbonic anhydrase isozymes I and II. *Bioorg Med Chem* 16:9101–9105
- Berrino E, Supuran CT (2019) Novel approaches for designing drugs that interfere with pH regulation. *Expert Opin Drug Discov* 14:231–248
- Berrino E, Milazzo L, Micheli L et al (2019) Synthesis and evaluation of carbonic anhydrase inhibitors with carbon monoxide releasing properties for the management of rheumatoid arthritis. *J Med Chem* 62:7233–7249
- Blandina P, Provensi G, Passani MB, Capasso C, Supuran CT (2020) Carbonic anhydrase modulation of emotional memory. Implications for the treatment of cognitive disorders. *J Enzyme Inhib Med Chem* 35:1206–1214
- Bonneau A, Maresca A, Winum JY et al (2013) Metronidazole-coumarin conjugates and 3-cyano-7-hydroxy-coumarin act as isoform-selective carbonic anhydrase inhibitors. *J Enzyme Inhib Med Chem* 28:397–401
- Bouzina A, Berredjem M, Nocentini A et al (2021) Ninhydrins inhibit carbonic anhydrases directly binding to the metal ion. *Eur J Med Chem* 209:112875

- Bozdag M, Poli G, Angeli A et al (2019) N-aryl-N'-ureido-O-sulfamates: potent and selective inhibitors of the human Carbonic Anhydrase VII isoform with neuropathic pain relieving properties. *Bioorg Chem* 89:103033
- Briganti F, Mangani S, Orioli P et al (1997) Carbonic anhydrase activators: X-ray crystallographic and spectroscopic investigations for the interaction of isozymes I and II with histamine. *Biochemistry* 36:10384–10392
- Bua S, Di Cesare ML, Vullo D et al (2017) Design and synthesis of novel nonsteroidal anti-inflammatory drugs and carbonic anhydrase inhibitors hybrids (NSAIDs-CAIs) for the treatment of rheumatoid arthritis. *J Med Chem* 60:1159–1170
- Cadoni R, Pala N, Lomelino C et al (2017) Exploring heteroaryl-pyrazole carboxylic acids as human carbonic anhydrase XII Inhibitors. *ACS Med Chem Lett* 8:941–946
- Canto de Souza L, Provensi G, Vullo D et al (2017) Carbonic anhydrase activation enhances object recognition memory in mice through phosphorylation of the extracellular signal-regulated kinase in the cortex and the hippocampus. *Neuropharmacology* 118:148–156
- Capasso C, Supuran CT (2015) Bacterial, fungal and protozoan carbonic anhydrases as drug targets. *Expert Opin Ther Targets*. 19:1689–1704
- Carta F, Temperini C, Innocenti A et al (2010) Polyamines inhibit carbonic anhydrases by anchoring to the zinc-coordinated water molecule. *J Med Chem* 53:5511–5522
- Carta F, Garaj V, Maresca A et al (2011) Sulfonamides incorporating 1,3,5-triazine moieties selectively and potently inhibit carbonic anhydrase transmembrane isoforms IX, XII and XIV over cytosolic isoforms I and II: Solution and X-ray crystallographic studies. *Bioorg Med Chem* 19:3105–3119
- Carta F, Supuran CT, Scozzafava A (2012a) Novel therapies for glaucoma: a patent review 2007–2011. *Expert Opin Ther Pat* 22:79–88
- Carta F, Aggarwal M, Maresca A et al (2012b) Dithiocarbamates: a new class of carbonic anhydrase inhibitors. Crystallographic and Kinetic Investigations. *Chem Commun* 48:1868–1870
- Carta F, Maresca A, Scozzafava A et al (2012c) 5- and 6-membered (thio)lactones are prodrug type carbonic anhydrase inhibitors. *Bioorg Med Chem Lett* 22:267–270
- Carta F, Akdemir A, Scozzafava A et al (2013) Xanthates and trithiocarbonates strongly inhibit carbonic anhydrases and show antiglaucoma effects in vivo. *J Med Chem* 56:4691–4700
- Carta F, Di Cesare ML, Pinard M et al (2015) A class of sulfonamide carbonic anhydrase inhibitors with neuropathic pain modulating effects. *Bioorg Med Chem* 23:1828–1840
- Casini A, Antel J, Abbate F et al (2003) Carbonic anhydrase inhibitors: SAR and X-ray crystallographic study for the interaction of sugar sulfamates/sulfamides with isozymes I, II and IV. *Bioorg Med Chem Lett* 13:841–845
- Cianchi F, Vinci MC, Supuran CT et al (2010) Selective inhibition of carbonic anhydrase IX decreases cell proliferation and induces ceramide-mediated apoptosis in human cancer cells. *J Pharmacol Exp Ther* 334:710–719
- Costa G, Carta F, Ambrosio FA et al (2019) A computer-assisted discovery of novel potential anti-obesity compounds as selective carbonic anhydrase VA inhibitors. *Eur J Med Chem*. 181:111565
- D'Ambrosio K, Carradori S, Monti SM et al (2015) Out of the active site binding pocket for carbonic anhydrase inhibitors. *Chem Commun* 51:302–305
- Davis RA, Vullo D, Maresca A et al (2013) Natural product coumarins that inhibit human carbonic anhydrases. *Bioorg Med Chem* 21:1539–1543
- De Simone G, Supuran CT (2012) (In)organic anions as carbonic anhydrase inhibitors. *J Inorg Biochem* 111:117–129
- De Simone G, Di Fiore A, Menchise V et al (2005) Carbonic anhydrase inhibitors. Zonisamide is an effective inhibitor of the cytosolic isozyme II and mitochondrial isozyme V: solution and X-ray crystallographic studies. *Bioorg Med Chem Lett* 15:2315–2320
- De Simone G, Di Fiore A, Capasso C, Supuran CT (2015) The zinc coordination pattern in the eta-carbonic anhydrase from *Plasmodium falciparum* is different from all other carbonic anhydrase genetic families. *Bioorg Med Chem Lett* 25:1385–1389

- De Simone G, Angeli A, Bozdog M et al (2018) Inhibition of carbonic anhydrases by a substrate analog: benzyl carbamate directly coordinates the catalytic zinc ion mimicking bicarbonate binding. *Chem Commun (Camb)* 54:10312–10315
- Del Prete S, De Luca V, De Simone G et al (2016) Cloning, expression and purification of the complete domain of the eta-carbonic anhydrase from *Plasmodium falciparum*. *J Enzyme Inhib Med Chem* 31:54–59
- Del Prete S, Vullo D, Ghobril C et al (2019) Cloning, purification, and characterization of a beta-carbonic anhydrase from *Malassezia restricta*, an opportunistic pathogen involved in dandruff and seborrheic dermatitis. *Int J Mol Sci* 20:E2447
- Di Cesare Mannelli L, Micheli L, Carta F et al (2016) Carbonic anhydrase inhibition for the management of cerebral ischemia: in vivo evaluation of sulfonamide and coumarin inhibitors. *Enzyme Inhib Med Chem* 31:894–899
- Di Fiore A, Pedone C, D'Ambrosio K et al (2006) Carbonic anhydrase inhibitors: Valdecoxib binds to a different active site region of the human isoform II as compared to the structurally related cyclooxygenase II "selective" inhibitor celecoxib. *Bioorg Med Chem Lett*. 16:437–442
- Di Fiore A, Maresca A, Supuran CT et al (2012) Hydroxamate represents a versatile zinc binding group for the development of new carbonic anhydrase inhibitors. *Chem Commun* 48:8838–8840
- Ditte P, Dequiedt F, Svastova E et al (2011) Phosphorylation of carbonic anhydrase IX controls its ability to mediate extracellular acidification in hypoxic tumors. *Cancer Res* 71:7558–7567
- Eldehna WM, Abo-Ashour MF, Nocentini A et al (2019) Enhancement of the tail hydrophobic interactions within the carbonic anhydrase IX active site via structural extension: Design and synthesis of novel N-substituted isatins-SLC-0111 hybrids as carbonic anhydrase inhibitors and antitumor agents. *Eur J Med Chem* 162:147–160
- Ferraroni M, Carta F, Scozzafava A et al (2016) Thioxocoumarins show an alternative carbonic anhydrase inhibition mechanism compared to coumarins. *J Med Chem* 59:462–473
- Fois B, Distinto S, Meleddu R et al (2020) Coumarins from *Magydaris pastinacea* as inhibitors of the tumour-associated carbonic anhydrases IX and XII: isolation, biological studies and in silico evaluation. *J Enzyme Inhib Med Chem* 35:539–548
- Fossati S, Giannoni P, Solesio ME et al (2016) The carbonic anhydrase inhibitor methazolamide prevents amyloid beta-induced mitochondrial dysfunction and caspase activation protecting neuronal and glial cells in vitro and in the mouse brain. *Neurobiol Dis* 86:29–40
- Güzel O, Temperini C, Innocenti A et al (2008) Carbonic anhydrase inhibitors. interaction of 2-(hydrazinocarbonyl)-3-phenyl-1H-indole-5-sulfonamide with 12 mammalian isoforms: kinetic and X-ray crystallographic studies. *Bioorg Med Chem Lett* 18:152–158
- Innocenti A, Vullo D, Scozzafava A et al (2008a) Carbonic anhydrase inhibitors. Interactions of phenols with the 12 catalytically active mammalian isoforms (CA I – XIV). *Bioorg Med Chem Lett* 18:1583–1587
- Innocenti A, Vullo D, Scozzafava A et al (2008b) Carbonic anhydrase inhibitors. Inhibition of mammalian isoforms I – XIV with a series of substituted phenols including paracetamol and salicylic acid. *Bioorg Med Chem* 16:7424–7428
- Isik S, Vullo D, Bozdog M et al (2015) 7-Amino-3,4-dihydro-1H-quinoline-2-one, a compound similar to the substituted coumarins, inhibits α -carbonic anhydrases without hydrolysis of the lactam ring. *J Enzyme Inhib Med Chem* 30:773–777
- Jensen EL, Clement R, Kosta A et al (2019) A new widespread subclass of carbonic anhydrase in marine phytoplankton. *ISME J* 13:2094–2106
- Kalisha Vali Y, Gundla R, Singh OV et al (2019) Spirocyclic sulfonamides with carbonic anhydrase inhibitory and anti-neuropathic pain activity. *Bioorg Chem* 92:103210
- Karioti A, Carta F, Supuran CT (2016) Phenols and polyphenols as carbonic anhydrase inhibitors. *Molecules* 21:E1649
- Kikutani S, Nakajima K, Nagasato C et al (2016) Thylakoid luminal theta-carbonic anhydrase critical for growth and photosynthesis in the marine diatom *Phaeodactylum tricorutum*. *Proc Natl Acad Sci U S A* 113:9828–9833

- Köhler K, Hillebrecht A, Schulze Wischeler J et al (2007) Saccharin inhibits carbonic anhydrases: possible explanation for its unpleasant metallic aftertaste. *Angew Chem Int Ed Engl* 46:7697–7699
- Küçükbay FZ, Küçükbay H, Tanc M, Supuran CT (2016) Synthesis and carbonic anhydrase inhibitory properties of amino acid - coumarin/quinolinone conjugates incorporating glycine, alanine and phenylalanine moieties. *J Enzyme Inhib Med Chem* 31:1198–1202
- Langella E, D'Ambrosio K, D'Ascenzio M et al (2016) A Combined crystallographic and theoretical study explains the capability of carboxylic acids to adopt multiple binding modes in the active site of carbonic anhydrases. *Chemistry* 22:97–100
- Lou Y, McDonald PC, Oloumi A et al (2011) Targeting tumor hypoxia: suppression of breast tumor growth and metastasis by novel carbonic anhydrase IX inhibitors. *Cancer Res* 71:3364–3376
- Maresca A, Supuran CT (2010) Coumarins incorporating hydroxy- and chloro- moieties selectively inhibit the transmembrane, tumor-associated carbonic anhydrase isoforms IX and XII over the cytosolic ones I and II. *Bioorg Med Chem Lett* 20:4511–4514
- Maresca A, Temperini C, Vu H et al (2009) Non-zinc mediated inhibition of carbonic anhydrases: coumarins are a new class of suicide inhibitors. *J Am Chem Soc* 131:3057–3062
- Maresca A, Temperini C, Pochet L et al (2010a) Deciphering the mechanism of carbonic anhydrase inhibition with coumarins and thiocoumarins. *J Med Chem* 53:335–344
- Maresca A, Scozzafava A, Supuran CT (2010b) 7,8-disubstituted- but not 6,7-disubstituted coumarins selectively inhibit the transmembrane, tumor-associated carbonic anhydrase isoforms IX and XII over the cytosolic ones I and II in the low nanomolar/subnanomolar range. *Bioorg Med Chem Lett* 20:7255–7258
- Margheri F, Ceruso M, Carta F, Laurenzana A et al (2016) Overexpression of the transmembrane carbonic anhydrase isoforms IX and XII in the inflamed synovium. *J Enzyme Inhib Med Chem* 31(sup4):60–63
- McDonald PC, Chia S, Bedard PL, Chu Q, Lyle M, Tang L, Singh M, Zhang Z, Supuran CT, Renouf DJ, Dedhar S (2020) A phase 1 study of SLC-0111, a novel inhibitor of carbonic anhydrase IX, in patients with advanced solid tumors. *Am J Clin Oncol* 43:484–490
- Menabuoni L, Scozzafava A, Mincione F et al (1999) Carbonic anhydrase inhibitors. Water-soluble, topically effective intraocular pressure lowering agents derived from isonicotinic acid and aromatic/heterocyclic sulfonamides: is the tail more important than the ring? *J Enzyme Inhib* 14:457–474
- Menchise V, De Simone G, Alterio V et al (2005) Carbonic anhydrase inhibitors: stacking with Phe131 determines active site binding region of inhibitors as exemplified by the X-ray crystal structure of a membrane-impermeant antitumor sulfonamide complexed with isozyme II. *J Med Chem* 48:5721–5727
- Nair SK, Ludwig PA, Christianson DW (1994) Two-site binding of phenol in the active site of human carbonic anhydrase II: structural implications for substrate association. *J Am Chem Soc* 116:3659–3660
- Neri D, Supuran CT (2011) Interfering with pH regulation in tumours as a therapeutic strategy. *Nat Rev Drug Discov* 10:767–777
- Nocentini A, Supuran CT (2018) Carbonic anhydrase inhibitors as antitumor/antimetastatic agents: a patent review (2008–2018). *Expert Opin Ther Pat* 28:729–740
- Nocentini A, Supuran CT (2019) Advances in the structural annotation of human carbonic anhydrases and impact on future drug discovery. *Expert Opin Drug Discov* 14:1175–1197
- Nocentini A, Carta F, Ceruso M et al (2015) Click-tailed coumarins with potent and selective inhibitory action against the tumor-associated carbonic anhydrases IX and XII. *Bioorg Med Chem* 23:6955–6966
- Nocentini A, Supuran CT, Winum JY (2018a) Benzoxaborole compounds for therapeutic uses: a patent review (2010–2018). *Expert Opin Ther Pat* 28:493–504
- Nocentini A, Bonardi A, Gratteri P et al (2018b) Steroids interfere with human carbonic anhydrase activity by using alternative binding mechanisms. *J Enzyme Inhib Med Chem* 33:1453–1459

- Nocentini A, Carta F, Tanc M et al (2018c) Deciphering the mechanism of human carbonic anhydrases inhibition with sulfocoumarins: computational and experimental studies. *Chemistry* 24:7840–7844
- Nocentini A, Gratteri P, Supuran CT (2019) Phosphorus versus sulfur: Discovery of benzenephosphonamidates as versatile sulfonamide-mimic chemotypes acting as carbonic anhydrase inhibitors. *Chemistry* 25:1188–1192
- Pacchiano F, Aggarwal M, Avvaru BS et al (2010) Selective hydrophobic pocket binding observed within the carbonic anhydrase II active site accommodate different 4-substituted-ureido-benzenesulfonamides and correlate to inhibitor potency. *Chem Commun (Camb)* 46:8371–8373
- Pacchiano F, Carta F, McDonald PC et al (2011) Ureido-substituted benzenesulfonamides potently inhibit carbonic anhydrase IX and show antimetastatic activity in a model of breast cancer metastasis. *J Med Chem* 54:1896–1902
- Provensi G, Carta F, Nocentini A et al (2019) A new kid on the block? Carbonic anhydrases as possible new targets in Alzheimer's disease. *Int J Mol Sci* 20:E4724
- Ruzzolini J, Laurenzana A, Andreucci E et al (2020) A potentiated cooperation of carbonic anhydrase IX and histone deacetylase inhibitors against cancer. *J Enzyme Inhib Med Chem* 35:391–397
- Schmidt SD, Costa A, Rani B et al (2020) The role of carbonic anhydrases in extinction of contextual fear memory. *Proc Natl Acad Sci U S A* 117:16000–16008
- Scozzafava A, Menabuoni L, Mincione F et al (1999a) Carbonic anhydrase inhibitors. Synthesis of water-soluble, topically effective, intraocular pressure-lowering aromatic/heterocyclic sulfonamides containing cationic or anionic moieties: is the tail more important than the ring? *J Med Chem* 42:2641–2650
- Scozzafava A, Briganti F, Mincione G et al (1999b) Carbonic anhydrase inhibitors: synthesis of water-soluble, aminoacyl/dipeptidyl sulfonamides possessing long-lasting intraocular pressure-lowering properties via the topical route. *J Med Chem* 42:3690–3700
- Scozzafava A, Supuran CT, Carta F (2013) Antiobesity carbonic anhydrase inhibitors: a literature and patent review. *Expert Opin Ther Pat* 23:725–735
- Sechi M, Innocenti A, Pala N et al (2012) Inhibition of α -class cytosolic human carbonic anhydrases I, II, IX and XII, and β -class fungal enzymes by carboxylic acids and their derivatives: new isoform-I selective nanomolar inhibitors. *Bioorg Med Chem Lett* 22:5801–5806
- Sharma A, Tiwari M, Supuran CT (2014) Novel coumarins and benzocoumarins acting as isoform-selective inhibitors against the tumor-associated carbonic anhydrase IX. *J Enzyme Inhib Med Chem* 2:292–296
- Solesio ME, Peixoto PM, Debure L et al (2018) Carbonic anhydrase inhibition selectively prevents amyloid β neurovascular mitochondrial toxicity. *Aging Cell* 17:e12787
- Supuran CT (2008) Carbonic anhydrases: novel therapeutic applications for inhibitors and activators. *Nature Rev Drug Discov* 7:168–181
- Supuran CT (2015) Acetazolamide for the treatment of idiopathic intracranial hypertension. *Expert Rev Neurother* 15:851–856
- Supuran CT (2016a) Structure and function of carbonic anhydrases. *Biochem J* 473:2023–2032
- Supuran CT (2016b) How many carbonic anhydrase inhibition mechanisms exist? *J Enzyme Inhib Med Chem* 31:345–360
- Supuran CT (2016c) Carbonic anhydrase inhibition and the management of neuropathic pain. *Expert Rev Neurother* 16:961–968
- Supuran CT (2016d) Drug interaction considerations in the therapeutic use of carbonic anhydrase inhibitors. *Expert Opin Drug Metab Toxicol* 12:423–431
- Supuran CT (2017) Advances in structure-based drug discovery of carbonic anhydrase inhibitors. *Expert Opin Drug Discov* 12:61–88
- Supuran CT (2018a) Carbonic anhydrases and metabolism. *Metabolites* 8:E25
- Supuran CT (2018b) Carbonic anhydrase inhibitors and their potential in a range of therapeutic areas. *Expert Opin Ther Pat* 28:709–712

- Supuran CT (2018c) Applications of carbonic anhydrases inhibitors in renal and central nervous system diseases. *Expert Opin Ther Pat* 28:713–721
- Supuran CT (2018d) Carbonic anhydrase inhibitors as emerging agents for the treatment and imaging of hypoxic tumors. *Expert Opin Investig Drugs* 27:963–970
- Supuran CT (2018e) Carbon- versus sulphur-based zinc binding groups for carbonic anhydrase inhibitors? *J Enzyme Inhib Med Chem* 33:485–495
- Supuran CT (2018f) Carbonic anhydrase activators. *Future. Med Chem* 10:561–573
- Supuran CT (2019) The management of glaucoma and macular degeneration. *Expert Opin Ther Pat* 29:745–747
- Supuran CT (2020a) Exploring the multiple binding modes of inhibitors to carbonic anhydrases for novel drug discovery. *Expert Opin Drug Discov* 15:671–686
- Supuran CT (2020b) Experimental carbonic anhydrase inhibitors for the treatment of hypoxic tumors. *J Exp Pharmacol* 12:603–617
- Supuran CT, Capasso C (2020) Antibacterial carbonic anhydrase inhibitors: an update on the recent literature. *Expert Opin Ther Pat* 30:963–982
- Supuran CT, Scozzafava A, Menabuoni L et al (1999) Carbonic anhydrase inhibitors. Part 71. Synthesis and ocular pharmacology of a new class of water-soluble, topically effective intraocular pressure lowering sulfonamides incorporating picolinoyl moieties. *Eur J Pharm Sci* 8:317–328
- Supuran CT, Alterio V, Di Fiore A et al (2018) Inhibition of carbonic anhydrase IX targets primary tumors, metastases, and cancer stem cells: three for the price of one. *Med Res Rev* 38:1799–1836
- Supuran CT, Altamimi ASA, Carta F (2019) Carbonic anhydrase inhibition and the management of glaucoma: a literature and patent review 2013–2019. *Expert Opin Ther Pat* 29:781–792
- Svastová E, Hulíková A, Rafajová M et al (2004) Hypoxia activates the capacity of tumor-associated carbonic anhydrase IX to acidify extracellular pH. *FEBS Lett* 577:439–445
- Tanini D, Capperucci A, Ferraroni M et al (2020) Direct and straightforward access to substituted alkyl selenols as novel carbonic anhydrase inhibitors. *Eur J Med Chem* 185:111811
- Tanpure RP, Ren B, Peat TS et al (2015) Carbonic anhydrase inhibitors with dual-tail moieties to match the hydrophobic and hydrophilic halves of the carbonic anhydrase active site. *J Med Chem* 58:1494–1501
- Tars K, Vullo D, Kazaks A et al (2013) Sulfocoumarins (1,2-benzoxathiine-2,2-dioxides): a class of potent and isoform-selective inhibitors of tumor-associated carbonic anhydrases. *J Med Chem* 56:293–300
- Temperini C, Scozzafava A, Vullo D, Supuran CT (2006a) Carbonic anhydrase activators. Activation of isoforms I, II, IV, VA, VII, and XIV with L- and D-phenylalanine and crystallographic analysis of their adducts with isozyme II: stereospecific recognition within the active site of an enzyme and its consequences for the drug design. *J Med Chem* 49:3019–3027
- Temperini C, Scozzafava A, Vullo D, Supuran CT (2006b) Carbonic anhydrase activators. Activation of isozymes I, II, IV, VA, VII, and XIV with l- and d-histidine and crystallographic analysis of their adducts with isoform II: engineering proton-transfer processes within the active site of an enzyme. *Chemistry* 12:7057–7066
- Temperini C, Innocenti A, Scozzafava A, Supuran CT (2008) Carbonic anhydrase activators: kinetic and X-ray crystallographic study for the interaction of D- and L-tryptophan with the mammalian isoforms I–XIV. *Bioorg Med Chem* 16:8373–8378
- Temperini C, Innocenti A, Scozzafava A et al (2010) The coumarin-binding site in carbonic anhydrase accommodates structurally diverse inhibitors: the antiepileptic lacosamide as an example. *J Med Chem* 53:850–854
- Touissni N, Maresca A, McDonald PC et al (2011) Glycosylcoumarin carbonic anhydrase IX and XII inhibitors strongly attenuate the growth of primary breast tumors. *J Med Chem* 54:8271–8277
- Vistoli G, Aldini G, Fumagalli L et al (2020) Activation effects of carnosine- and histidine-containing dipeptides on human carbonic anhydrases: a comprehensive study. *Int J Mol Sci* 21:E1761
- Vullo D, Durante M, Di Leva FS et al (2016) Monothiocarbamates strongly inhibit carbonic anhydrases in vitro and possess intraocular pressure lowering activity in an animal model of glaucoma. *J Med Chem*. 59:5857–5867

- Weber A, Casini A, Heine A et al (2004) Unexpected nanomolar inhibition of carbonic anhydrase by COX-2-selective celecoxib: new pharmacological opportunities due to related binding site recognition. *J Med Chem* 47:550–557
- Wilkinson BL, Bornaghi LF, Houston TA et al (2006) A novel class of carbonic anhydrase inhibitors: glycoconjugate benzene sulfonamides prepared by “click-tailing.” *J Med Chem* 49:6539–6348
- Winum JY, Supuran CT (2015) Recent advances in the discovery of zinc-binding motifs for the development of carbonic anhydrase inhibitors. *J Enzyme Inhib Med Chem* 30:321–324
- Winum JY, Maresca A, Carta F et al (2012) Polypharmacology of sulfonamides: pazopanib, a multi-targeted receptor tyrosine kinase inhibitor in clinical use, potently inhibits several mammalian carbonic anhydrases. *Chem Commun (Camb)* 48:8177–8179

Polymeric Carriers for Transporting Nucleic Acids—Contributions to the Field



Lilia Clima, Andrei Ioan Dascalu, Bogdan Florin Craciun,
and Mariana Pinteala

Abstract In order to correct the genetic defects that are fundamental reasons for many pathologies, gene therapy uses exogenous nucleic acids for intentional modulation of gene expression in specific cells. Due to the large size and the negative charge of exogenous nucleic acids, the delivery of these macromolecules is typically mediated by carriers or vectors. Viral carriers are known to be very efficient however, they have a severe drawbacks such as toxicity and immunogenicity. In this regard, gene-based therapy using non-viral approaches has drawn increasing attention, and has become an important field of research. The diversity of materials used as of non-viral vectors known today highlights the recent progress of gene-based therapy using non-viral approaches. Herein, we describe the progress made by our group in the development of hybrid vectors that combine key features of classical carriers design rationally or formed by combinatorial approach using dynamic chemistry which are remarkable strategies to address the current challenges in gene delivery.

Keywords Non-viral vectors · Gene delivery · Polymers · Self-assembly · Poly(ethyleneimine) · Poly(ethylene glycol) · Polyplex · Transfection · Cytotoxicity

Abbreviations

pDNA	Plasmid DNA
siRNA	Small interfering RNA
β -CD	β -Cyclodextrin
bPEI	Branched poly(ethyleneimine)
PEG	Poly(ethylene glycol)
pLuc	Luciferase plasmid
pGFP	Green fluorescent protein plasmid

L. Clima (✉) · A. I. Dascalu · B. F. Craciun · M. Pinteala
Centre of Advanced Research in Bionanoconjugates and Biopolymers, “Petru Poni”
Institute of Macromolecular Chemistry, 41A Grigore Ghica Voda Alley, 700487 Iasi, Romania
e-mail: clima.lilia@icmpp.ro

CDC	Constitutional dynamic chemistry
DCF	Dynamical constitutional frameworks
dsDN	Duble stranded DNA
TE	Transfection efficiency
Girard's reagent T	(Carboxymethyl)trimethylammonium chloride hydrazide
HeLa	Human cervix adenocarcinoma
DF	Dynameric frameworks
HEK 293T	Human embryonic kidney 293T cells
pEGFP	Enhanced green fluorescent protein plasmid
N/P	Nitrogen/phosphorus
AFM	Atomic force microscopy

1 Introduction

Nucleic acids (gene therapy) have the unique potential to provide cures for many targets that are currently unavailable and to do so with higher success rates in the clinic. In present, gene therapy, conceptualized since 1972 (Somia and Verma 2000; Yin et al. 2014), has been already successfully applied to treat genetic as well as acquired diseases (Dunbar et al. 2018; Ginn et al. 2018; Hanna et al. 2017; Thapa and Narain 2016), including Parkinson's disease (Olanow 2014), cardiovascular (Hedman et al. 2011) or retinal (Bainbridge et al. 2006; Smith et al. 2012) and various types of cancer (Egger et al. 2004; Semenza 2003). Yet, so far, as restricted by many factors, the gene therapy using either plasmid DNA (pDNA) or small interfering RNA (siRNA) did not achieve ideal effects due to the lack of the targeting ability, efficient drug carrier and an appropriate drug delivery technique. It is still a difficult problem in gene therapy to address how the transfection efficiency of genes could be considerably improved and the gene be delivered to the targeted sites of the organism efficiently without toxic and side effects. To overcome these drawbacks, (Clima et al. 2015) the development of efficient nucleic acid targeted delivery systems (vectors) is critically required. The general requirements for an efficient vector include: (i) strong enough binding to DNA, but on the other hand to allow the release of the DNA into the cell nucleus; (Papadopoulos et al. 2016; Wu et al. 2018) (ii) to be nontoxic and biodegradable; (iii) to be stable towards enzymatic degradation and (iv) to facilitate endocytosis. Moreover, for an efficient transfection the size, shape and surface characteristics of the vectors are crucial (Gordon et al. 2012).

Vectors of the gene therapy mainly include two categories—viral vectors and non-viral vectors. Despite the fact that viral gene vectors have high transfection efficiency and already found their successful in vivo applications (Dunbar et al. 2018; Ginn et al. 2018; Hanna et al. 2017; Muramatsu 2018; Papadopoulos et al. 2016; Thapa and Narain 2016), the preparation of these vectors is complex and they present serious potential risks and failure of repeated applications in human body (Yang et al. 2014). Alternatively, all other approaches are based on non-viral gene

delivery systems, which try to mimic the efficiency of viral vectors by artificial means (Neu et al. 2005; Wu et al. 2018; Zakeri et al. 2018). Non-viral vectors, are artificially synthesized non-bioactive materials, offering advantages such as low toxicity, low immunoreactions and excellent ability of being chemically modified (Neu et al. 2005; Wu et al. 2018). So far, the main candidates used in gene therapy for the nonviral approach are the cationic polymers such as chitosan (Gordon et al. 2012), cationic lipids (Gordon et al. 2012), polypropyleneimines (Gordon et al. 2012) or polyamidoamines (Ailincal et al. 2018, 2019) and poly(ethylenimine) (PEI) (Wang et al. 2011; Zakeri et al. 2018). Preparation of such vectors often involves multistep rational design approach, though a simple design of the vectors towards efficient carrier is in high demand. In the current mini-review we summarized recent results on different approaches and examples for design and properties of non-viral vectors reported by our group.

2 Functional Cyclodextrins and Polyrotaxanes for Gene Delivery

While designing a non-viral vector, the precise control of the size and functionality of the resulting macromolecular or supramolecular construct, can lead to a replication of the characteristics and function of biological entities involved in transport or protective storing of nucleic acids. Despite the numerous synthetic and structural design possibilities for these platforms, their development and use are far more complex than it appears since there are numerous variables to be balanced for a successful transfection including: (i) optimal charge value, (ii) charge distribution, (iii) flexibility, (iv) size, (v) cell internalization and processing. One viable strategy would be the design of a carrier using building blocks with known desired properties and biological effects. One notable example of this concept is the construction of a polycationic vector comprised of functional β -cyclodextrin (β -CD) units as coupling points for branched poly(ethyleneimine) (bPEI) and poly(ethylene glycol) (PEG) chains. The polycationic dendrons would ensure the nucleic acids complexing ability of the vector while the linear PEG chains were included to disrupt the charge density of the edifice and delay the unwanted interactions with biomolecules in the biological fluids during circulation (Dascalu et al. 2017). The synthetic strategy involved an esterification reaction at the primary hydroxyl groups (minor rim of β -CD) in the presence of an excess amount of acryloyl chloride at room temperature. The newly introduced activated double bonds ensured the subsequent coupling of a 750 Da mono-functional PEG derivative bearing an amino group and 2000 Da bPEI, through a Michael addition reaction resulting in a tri-dimensional polycationic carrier.

The *in vitro* cytotoxicity tests performed on the vector/DNA complexes with precise nitrogen/phosphorous compositional ratios (N/P) in comparison with 2000 Da bPEI revealed that at higher N/P ratios the cell viability exceeded 90% while at lower compositional ratios cellular proliferation was induced. The presence of the

PEG segments did not hinder the complex formation between the proposed vector and plasmidic DNA (pLuc) by means of ionic interactions. Moreover, the performed molecular dynamic simulation revealed that in the presence of the double stranded nucleic acid the carrier molecules adapted their conformation in order to maximize the number of ionic interactions between the DNA negatively charged phosphate residues and the positively charged amino groups in the vector. The *in vitro* transfection efficiency on HeLa cells tests revealed a maximum efficiency at $N/P = 80$ indicating the need for a larger number of carrier molecules to effectively protect and transfect the nucleic acid into the tested cells. In comparison, the tested bPEI/pLuc polyplexes transfected poorly which clearly confirmed the proposed carrier design for the cooperative binding, transport and release of the nucleic acid in the cell. This behavior was supported by the TEM images which revealed that the polyplex particle size decreased as the N/P compositional ratio increased.

In a more ambitious attempt (Ardeleanu et al. 2018), cyclodextrins were used in the development of gene delivery vectors based on polyrotaxanes. This type of assembly consist in physically interlocked structures containing a linear molecular axle (guest) threaded through a macrocycle (host) and locked in place by large terminal bulky stopper groups (Jiří et al. 2012). The mechanically linked components are typically characterized by high freedom and mobility. As expected, with such complex structures, the preparation of the supramolecular carriers was achieved in multiple steps starting with β -CD functionalization. The adequate functionality of cyclic oligosaccharide was introduced by the partial esterification of the primary hydroxyl groups with acryloyl chloride. The number and position of the attached activated double bonds were controlled through the reagents compositional ratio, temperature and solvent mixture. In the next step the partially acrylated β -CD molecules where threaded onto a 1 kDa PEG derivative with terminal triple bonds. Although between β -CD and PEG no inclusion complex is usually formed (Harada et al. 1999) the presence of the acryloyl residues on the minor rim of the host molecule and the rigid propargyl residues on the linear guest ensured the formation of the poly(pseudorotaxane) assembly. This transient structure was stabilized through a Copper(I)-catalyzed Azide-Alkyne Cycloaddition reaction with silatrane azide resulting in the base polyrotaxane. The final step in the construction of the supramolecular carriers consisted in the addition of the functional "segments" on the base polyrotaxane through the previously mentioned Michael addition: 2 kDa bPEI braches or a mixture of 2 kDa bPEI and 0.75 kDa methoxypolyethylene glycol chains. A supplementary step was also described for two distinct post-functionalization reactions namely the decoration of polyrotaxane with bPEI with guanidine residues at the primary amino groups in bPEI or the addition of arginine residues. The described synthesis pathway relied on precise and highly reproducible reactions in order to precisely tailor the structure and functionality of the carriers.

In terms of transfection efficiency (pLuc or pGFP plasmids on HeLa cells) all four described vectors demonstrated their ability to transfect. The polyrotaxane carrier decorated solely with bPEI (ROT-PEI) exhibited the highest transfection efficiency, with a maximum yield at N/P 20 (Fig. 1) while the post-modified version with guanidine residues (ROT-PEI-G) was close, with a maximum yield at N/P 30.

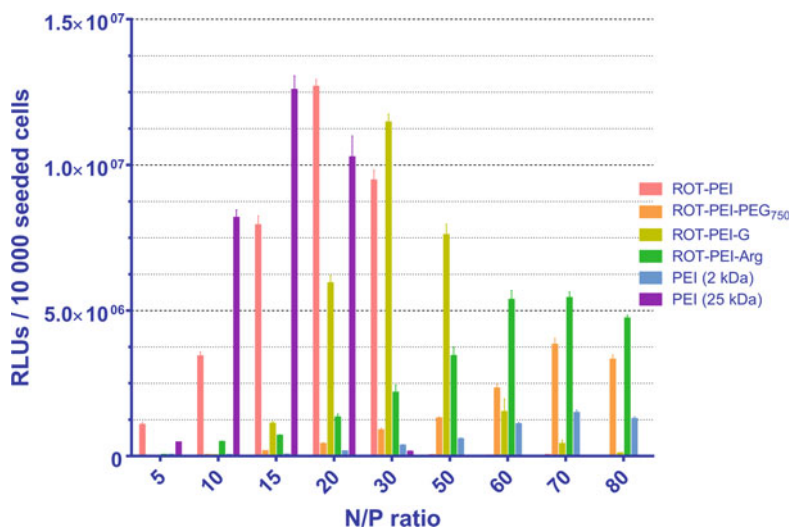


Fig. 1 The transfection efficiency results of ROT-PEI, ROT-PEI-PEG₇₅₀, ROT-PEI-G, ROT-PEI-Arg, PEI 2 kDa, and PEI 25 kDa, with pCS2 + MT-Luc plasmid on HeLa cells, at all tested N/P ratios (from 5 to 80)

The arginine post-decorated vector (ROT-PEI-Arg) vector showed a maximum transfection yield at an N/P ratio of 60. This observation indicated that for this particular study the simple one step guanidinylation is more useful than the arduous attachment of an amino acid with the purpose of mimicking the function of an arginine rich histone (Müller and Muir 2015). Lastly, the polyrotaxane decorated with PEG and bPEI (ROT-PEI-PEG₇₅₀) showed a maximum transfection yield at a higher N/P ratio of 70 which is most likely due to the presence of the PEG chains. The cytotoxicity assay demonstrated that the presence of these chains achieved their purpose of increasing the biocompatibility of the carrier since the test indicated a cell proliferation at lower N/P ratios and a cell viability of approximately 100% throughout the tested range for this particular carrier.

3 Dynamic Combinatorial Systems as Non-viral Vectors

Constitutional dynamic chemistry can be considered a new evolutionary approach to produce chemical diversity. A specific advantage with constitutionally generated systems addresses the possibility to self-adjust to biological target species at a given time, in a certain environment at nanoscale dimensions (Lehn 2012; Zhang and Barboiu 2016). The key concept is exploring the multivalent molecular recognition and self-assembly by using adaptive platforms interacting with biological targets. The use of reversible interactions as dynamic interfaces between the target and Dynamical

Constitutional Frameworks (DCF) components allows one to self-adjust the system's tridimensional geometry and functional properties.

Despite the existing progress, the rational design is sometimes limited to the choice of a low number of components. Within this context, the dynamic combinatorial and constitutional screening approaches appeared to be an attractive strategy for the rapid identification of the active delivery vectors from dynamically exchanging libraries of complex mixtures of components. The construction of dynamic covalent polymers via the incorporation of reversible covalent bonds is therefore a promising strategy for generating effective vectors that allow multivalent interactions for dsDNA binding in biological media (Fig. 2) (Catana et al. 2015; Clima et al. 2019; Clima et al. 2015; Craciun et al. 2018; Marin et al. 2016; Pricope et al. 2018.; Turin-Moleavin et al. 2015; Zhang and Barboiu 2016). DCFs approach is relevant in biological and medicinal research, especially when the biotargets like nucleic acids contain a large number of available reaction units.

The simplicity of the synthetic constitutional strategy using accessible and simple building blocks for easily self-generation DCFs presenting synergistic DNA and cell membrane affinities might be considered as a valuable path toward the systematic discovery of active delivery systems (Fig. 3). In order to enhance transfection efficiency of the DCF-based vectors, several crucially important components like: *cationic heads*, *biocompatible linkers*, *self-assembly triggers* and *multifunctional*

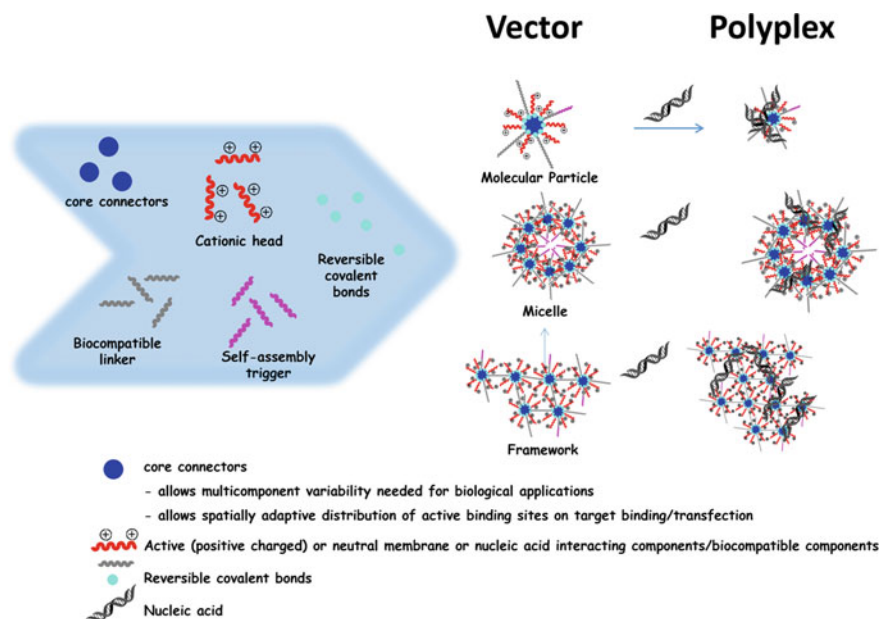


Fig. 2 Concept of the formation of non-viral vectors by dynamic chemistry and combinatorial approach

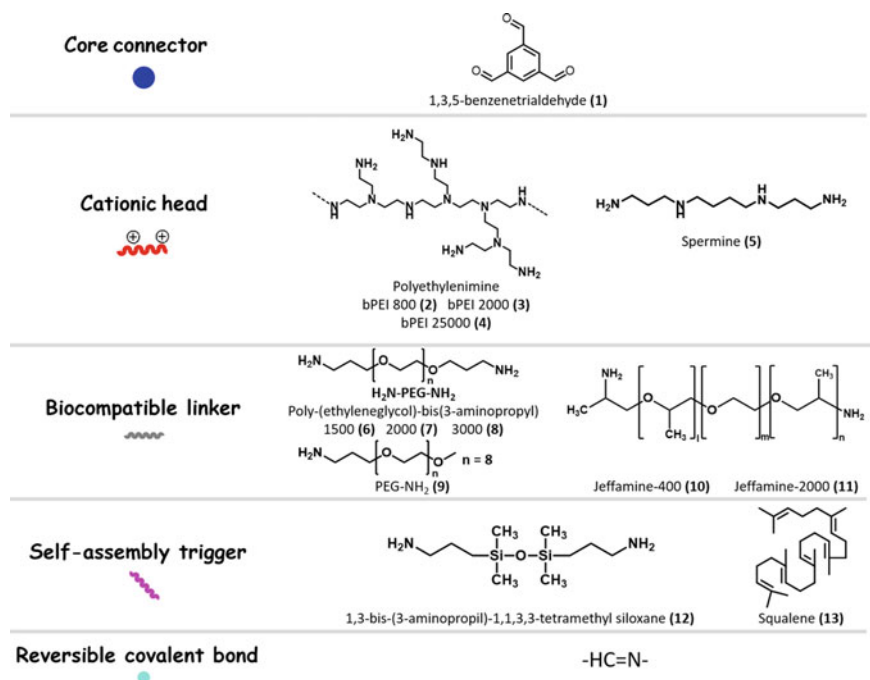


Fig. 3 Building blocks for formation of dynamic combinatorial frameworks

core connectors have to be taken into account to generate specific DCFs for DNA binding (Fig. 3).

PEIs units utilized as *cationic heads*, demonstrated safer alternative to viral vectors and has shown good transfection efficiency (TE) in different types of cells (Ailincai et al. 2018; Funhoff et al. 2004; Neu et al. 2005; Neuberg and Kichler 2014; Wang et al. 2011; Wu et al. 2018). PEI is able to bind DNA by an electrostatic interaction to form small complexes (polyplexes) that are internalized into cells by endocytosis and can be localized to the nucleus as distinct structures (Clima et al. 2015; Neuberg and Kichler 2014; Olden et al. 2018). Commonly, the molecular weight of PEI for the most effective transfection ranges between 5 and 25 kDa (Paul et al. 2014; Zakeri et al. 2018), higher molecular weights lead to increased cytotoxicity in polyplexes, while low molecular weight PEI demonstrate low toxicity in cell culture studies (Godbey et al. 2000; Neu et al. 2005; Yao et al. 2018). A strategy to increase the transfection efficiency with simultaneous decrease in cytotoxicity could be the coupling of the low molecular weight PEIs (maximum 2000 Da) to a core connector, forming conjugates of 8–54 kDa PEI (Ardeleanu et al. 2018; Uritu et al. 2015a, b). Among the *biocompatible linkers* PEGs are considered a powerful tool due to their surface charge shielding ability especially in nucleic acid delivery systems. It forms hydrophilic coating to minimize the interactions of the formed polyplexes with blood components and reduces the polyplex uptake by macrophages, thus increasing the

overall blood circulation time (Suk et al. 2016). Since the conformation, hydrophobicity and electrostatic binding properties change through PEGylation, identifying the degree of the vector PEGylation and the molecular weight is crucial. Excessive PEGylation may lead to a risk of reduction of the DNA-binding capacity leading to considerable drop of in vitro transfection efficiency. Besides biocompatible linkers, some non-viral vectors incorporate a *self-assembly triggers* as hydrophobic or lipid component able to form amphiphile in aqueous medium (Ailincai et al.). These important units contribute to the interaction of the vector with the cell membrane, facilitating cell internalization and increasing gene transfer efficiency.

3.1 Dynamic Constitutional Frameworks (DCF) for DNA Biomimetic Recognition

Catana et al. (2015) first suggested the idea of dynamic constitutional frameworks (DCF) for DNA biomimetic recognition when multifunctional core centers, linear PEG macromonomers and cationic heads were used to produce functional DCFs for DNA binding. The building constituents were: poly(ethylene glycol)-bis(3-aminopropyl) (**6**), Girard's reagent T, monoprotonated N,N-dimethylene amine or aminoguanidine hydrochloride, all linked to 1,3,5-Benzenetri-aldehyde (**1**) via the amino - carbonyl/imine reversible bonds. As the result of the series of components combinations, it was established that compact guanidinium with a cross-linked structure strongly influenced the DNA binding, whereas the frameworks containing Girard's reagent T or monoprotonated N,N-dimethylene amine having linear structure, presented no binding properties. This behavior highlighted dominant coiling versus linear DNA binding mechanism behaviors.

Turin-Moleavin's study (Turin-Moleavin et al. 2015) defining the synthesis and characterization of a class of DNA nanovectors based on unique component and connector center frameworks, connected by reversible covalent bonds, continued further development of the systems. In the presence of interacting DNA biotargets, the dynamic self-assembly of PEG unit (**6**) with bPEI (**2**) cationic binding groups around the 1,3,5-Benzenetri-aldehyde core connector (**1**) has led to adaptive spatial distributions. By forming stable polyplexes with dsDNA, the obtained DCF polyplexes were able to perform as gene nanovectors. Polyplexes possessed sizes ranging between 40 and 125 nm depending on the type and quantity of associated DNA and on the molar ratio of bPEI/PEG. All tested vectors presented DNA transfection ability on HeLa cell line and showed low cytotoxicity, even at high N/P ratio of 200, the viability of cells being over 90% compared to untreated cells as control. This led to the conclusion that both the presence of the PEG component and a moderate amount of bPEI in DCFs were significant in the production of highly transfecting and cyto-friendly polyplexes.

3.2 *Dynamers Based on Hydrophob-Hydrophil Assembly for DNA Transfection*

Another strategy in the development of dynamic vectors was to use hydrophobic/hydrophilic connectors as core-centers (Ailincai et al. 2019; Clima et al. 2019,2015; Craciun et al. 2019; Marin et al. 2016; Pricope et al. 2018) and positively charged molecular heads in the design of 3D Dynameric Frameworks (DFs) as advanced nanomaterials for DNA recognition and transfection. They form modular networks/platforms that self-adapt to the DNA targets, depending on their variable composition due to reversible communication between the constituents of DFs.

A core-shell hydrophobic/hydrophilic structure with a high number of low molecular weight PEI units was expected to create a vector with a transfection efficiency similar to that of high molecular weight PEI, but with much lower toxicity, according to the proposed idea. Nano-noviral vectors with a linear siloxane and aldehyde as hydrophobic core and a hydrophilic shell determined by presence of bPEI 800(2) or bPEI 2000(3) have been designed and synthesized.

The following components were proposed for the DFs according to Marin et al. (2016):

- (i) 1,3,5-Benzenetri-aldehyde (**1**) as tri-carbonyl functionalized core;
- (ii) bis-poly-(propylene glycol), amine-terminated (**6**), Jeffamine-400 and Jeffamine-2000 (**10** and **11**) as cross-linkers contribute to the formation of framework connecting DNA-binding sites by the reversible bond of amino-carbonyl/imine. Additionally **10** and **11** are known for low toxicity and high cellular DNA uptake and are suitable for building of nonviral vectors (Ailincai et al.);
- (iii) Poly(ethylene glycol-3-aminopropyl) terminated (**9**) as specific PEG units, in order to enhance the solubility in aqueous media, increase biocompatibility and diminish the immunogenicity of the vectors;
- (iv) Spermine (**5**), linear-poly(ethylenimine), ($M_n \approx 2500 \text{ gmol}^{-1}$), bPEI (**2**, **3**) as cationic moieties capable of DNA complexation.

Combination of JD1-bPEI800, JD1-bPEI2000 and PEG-ylated JD1-PEG-bPEI800, JD1-PEG-bPEI2000, and JD1-PEG-spermine led to water-soluble DFs (Fig. 4), while formation of DFs from Jeffamine-2000 (**11**) and cationic moieties of linear PEI or Spermine (**5**) in aqueous media led to insoluble precipitate and this system was no longer investigated. The soluble DFs spontaneously self-assembled in aqueous solution as predicted, resulting in spherical nanoparticles. Transmission electron microscopy (TEM) showed that JD1-bPEI800 had a mean diameter of 6 nm, while JD1-bPEI2000 had a mean diameter of 23 nm and mean diameter of 50 nm for the combined JD1-PEG-bPEI800. BPEI-based DFs (PEGylated or non PEGylated) were able to bind DNA effectively as shown in agarose gels by delay of the electrophoretic mobility of formed polyplexes, whereas JD1-PEG-spermine showed

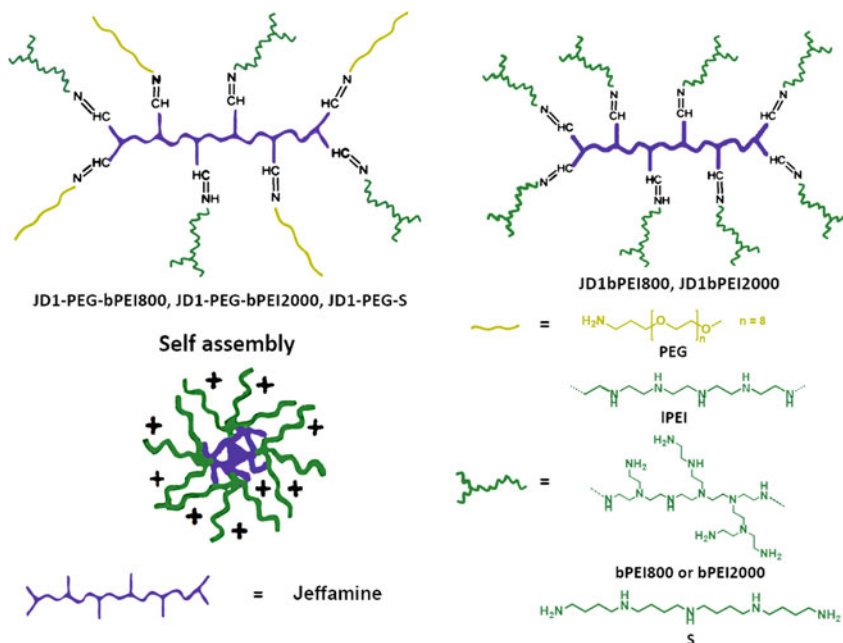


Fig. 4 Dynameric frameworks schematic representation of JD1-PEG-bPEI800, JD1-PEG-bPEI2000, JD1-PEG-Spermine

a low binding capacity even under acidic conditions due to the reduced positive binding sites associated to bPEI DFs.

Formed polyplexes exhibited great tolerance by human embryonic kidney 293 T. JD1-bPEI2000/pEYFP, among the studied polyplexes, confirmed higher gene transfection efficacy on HEK 293T cells, ~9% at N/P 100. This value is 1.2 fold higher than that obtained with SuperFect commercial reagent. Such high performance was explained by the narrow polydispersity observed in AFM for the obtained polyplex, having an average diameter of 100 nm, whereas the higher polydispersity and polyplex diameter resulted in inferior transfection efficiency.

Siloxane structure, viewed as strong hydrophobic units and enhancing high transfection efficiency in non-viral vectors, was investigated as an alternative hydrophobic moiety in a related strategy (Bainbridge et al. 2006).

The diamine-bearing siloxane unit (**12**) has therefore been proposed as suitable hydrophobic core for a library of compounds (Ailincai et al. 2019). In order to build an oligomeric chain of aldehyde functionalities capable of binding the hydrophilic shell in several positions, siloxane (**12**) was reacted with trialdehyde (**1**) in a 1/1 molar ratio (Scheme 1). In the vector architecture, hyperbranched bPEI 800 (**2**) and bPEI 2000 (**3**) were used as hydrophilic moieties (Fig. 5).

UV-VIS spectroscopy has underlined the dynamic aspects of synthesized A1 and A2 amphiphiles.

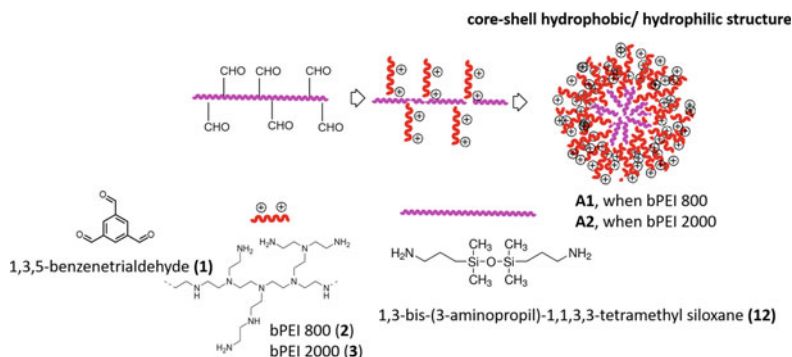


Fig. 5 Formation of core-shell hydrophobic/ hydrophilic structure A1 and A2

Absorption maximum at 300 nm corresponded to benzenetrialddehyde (1) and assigned to electronic transitions $\pi-\pi^*$ of the CHO group, on the other hand, A1 and A2 did not display any absorption maximum in the UV-VIS spectrum since the presence of hyperbranched PEI induces shielding effect of the chromophoric groups, these being hindered. The peak corresponding to the aldehyde occurred however, when the pH reached the value of 6.1, showing that the imine linkages that held the hydrophobic core and the hydrophilic shell together were cleaved by the acid by successive addition of small amounts of HCl. Furthermore, the stability of the two compounds at neutral pH was additionally proven by the NMR spectra of the two amphiphiles recorded in deuterium oxide at different time periods showing no degradation or changes, even after 24 h. The peak corresponding to the carbonyl functionality from trialddehyde occurred by adding a small quantity of HCl to the NMR tubes (pH = 5.8), indicating the cleavage of the imine bond. A1 and A2 were self-assembled in a spherical particles with mean size ranging from 20 to 95 nm. Regardless of the small particle sizes of the vectors, the polyplexes formed with pEGFP tended to have a larger particle size from the vector A1, compared to polyplexes formed from A2. Thus, this behavior of polyplex formed from A2 can be attributed to the presence of bPEI 2000 (3) in its composition, due to multiple protonated amine groups on the surface, these were sufficient to compensate the negative charge of DNA. On the other site, compound A1 with bPEI 800(2) in its composition, formed larger polyplexes, due to the possible aggregation of the A1 entities in order to be able to balance negative charge of DNA.

The cytotoxicity performed on HeLa cell line of the A1/pEGFP and A2/pEGFP polyplexes, showed excellent cell viability (above 90%) even at high N/P ratios (above 400), making them ideal candidates for non-viral vectors. Compared to the free bPEI 800 (2) and bPEI 2000 (3), both compounds had a superior capacity to transfect HeLa cells used as references. This was the product of various synthesized vector properties, such as: (i) high hydrophobicity (Ailincai et al.), (ii) formation of nano-sized particles and spherical morphology (iii) Zeta potential of positive values for the polyplexes (Gordon et al. 2012) and (iv) solubility of the vectors and polyplexes in aqueous milieu.

3.3 Dynamic Combinatorial Frameworks Based on Lipid Hydrophob-Hydrophil Assembly for Nuclei Acid Delivery

Drug carriers with a lipophilic component have long been considered to have a high capacity to cross biological membranes (Banks 2009; Finbloom et al. 2020), including brain barriers (Banks 2009). And because of their hydrophobicity, these molecules are in high demand as non-viral vector components. Direct membrane permeabilization may be caused by specific lipophilic units that interfere with the cell membrane. Due to its propensity to self-assemble in aqueous media, creating amphiphilic compounds, squalene (**13**), a natural triterpene lipid and precursor to cholesterol biosynthesis, has gained attention as a biocompatible material for drug deliver (Couvreur 2009; Craciun et al. 2018; Desmaele et al. 2012; Lepeltier et al. 2013).

Squalene was chemically functionalized and PEGylated before being used as a component in dynamic combinatorial frameworks (DCF). Its DCF composition ratio was designed and optimized to ensure the best possible rapport between self-assembly capacity and nanoassembly shape (Pricope et al. 2018). Constitutional strategy was applied to build DCFs as multivalent DyNAvectors for DNA transfection. The 1,3,5-benzenetrialdhyde (**1**), PEG-ylated squalene (SQ-PEG), H₂N-PEG-NH₂ (**6**) and low molecular weight bPEI 800 (**2**) were combined in different molar ratios to form a library of DCFs (Fig. 6) (Clima et al. 2015).

The DCFs self-assembled in spherical particles with the hydrophobic squalene core and the PEG/PEI hydrophilic shell. Although the shaped particles were in the μm range and could be deemed unsuitable as non-viral vectors due to their large size, their polyplex with plasmid pEYFP showed more compact structures than the

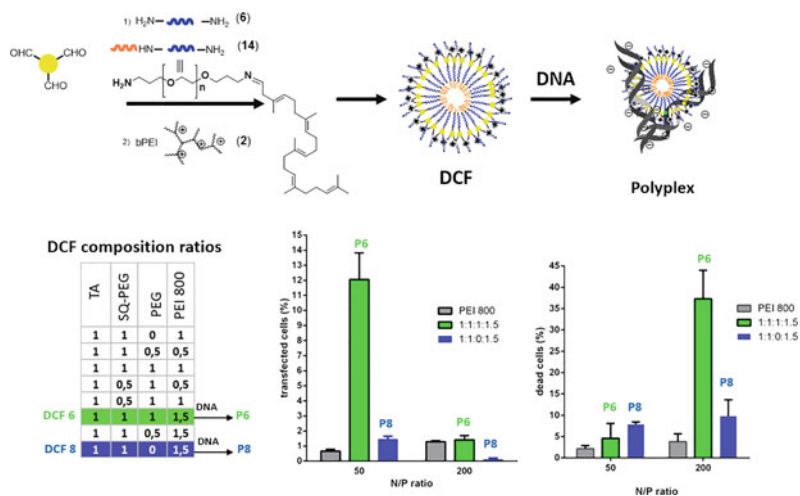


Fig. 6 DCF-squalene based non-viral vectors

noncomplexed DCFs. The sizes of polyplexes were ranged between 20–100 nm, depending on N/P ratio. The improved performance of both P6 and P8 polyplexes at the N/P ratio of 50 compared to bPEI 800 (Fig. 6) depicted the multivalent as in the case of P6 and P8 versus monomeric presentation of the bPEI 800 (2).

The polyplex P6, on the other hand, showed low toxicity and higher transfection values than P8, owing to the presence of H₂N-PEG-NH₂ (6) not only in the SQ-moiety, but also as an external constitutive component that stabilized P6 in a serum-rich environment (Fig. 6).

The particle size of P6 at N/P 50 were about 100 nm, which is in line with the criteria for gene delivery nanoparticles. Shielding the vectors with hydrophilic polymers, especially PEGs, has become a common strategy (Kumar et al. 2014), demonstrating that PEGylation of PEIs resulted in increased solubility of the complexes as well as a reduction in the overall surface charge of the polyplexes (Kursa et al. 2003). Yet, PEGylation has the disadvantage of lowering the cationic polymer's DNA-binding ability, primarily due to sterical hindrance of interactions between polyplexes and targeted cells (Elouahabi and Ruyschaert 2005), lowering in vitro transfection performance. For conjugating to PEI, PEG units of different chain lengths were used, and the results showed that the degree of PEGylation and the molecular weight of PEG have a significant impact on the properties of the resulting PEG-PEI-based non-viral vector.

A systematic investigation of a sequence of DCFs (Fig. 7, NV library) composed from PEGylated squalene (14) (Clima et al. 2015; Craciun et al. 2018), H₂N-PEG-NH₂ of certain length (1500 Da, 2000 Da and 3000 Da), and hiperbranched bPEI

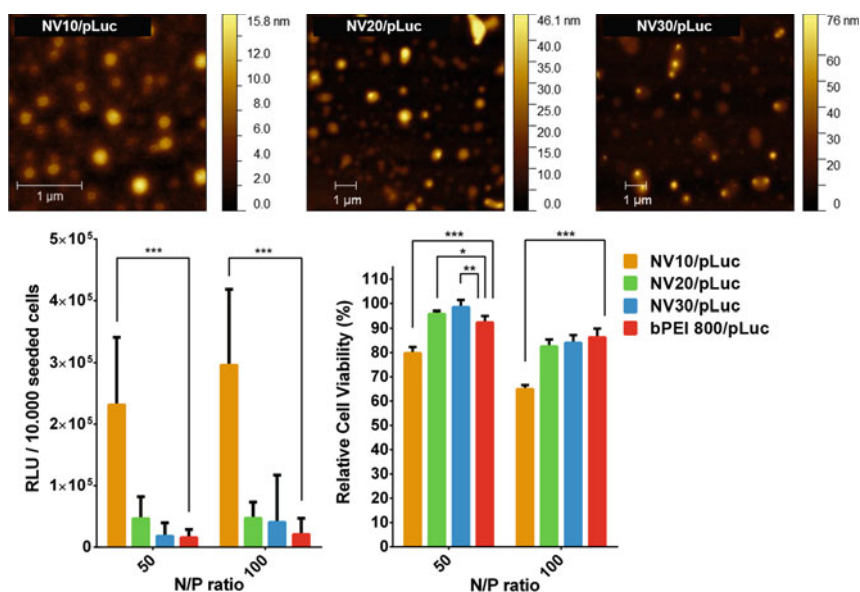


Fig. 7 AFM, transfection efficiency and cell viability for NV10/pLuc, NV20/pLuc and NV30/pLuc

800 of low molecular weight (**2**), all coupled in a hyperbranched structure, revealed some key findings. First, the sterical interactions of PEG units with the framework's components led to the development of smaller size particles as the molecular weight of H₂N-PEG-NH₂ increased from 1500 to 3000 Da, according to TEM and DLS results. Since H₂N-PEG-NH₂ is a linear polymer, it causes larger DCFs to form, resulting in more complex cross-linking and eventual self-assembly of the DCFs in larger particles (Craciun et al. 2019). Likewise, due to the PEG shielding effect over the bPEI 800 (**2**), raising the length of H₂N-PEG-NH₂ in the formulation of NVs resulted in a poorer binding ability of plasmid DNA (pCS2 + MT-Luc). Moreover, we have shown that increasing the ratio of H₂N-PEG-NH₂ from 0.1 to 1 equivalent improved significantly the transfection performance of NV1/pDNA-NV30/pCS2 + MT-Luc polyplexes on the HeLa cell line. In general, transfection efficiency was higher at N/P ratio 100 than at N/P ratio 50 for all studied polyplexes. As a result, using H₂N-PEG-NH₂ with a comparatively high molecular weight within the complex structure improved the vector's biocompatibility, thus highlighting that the molecular weight of H₂N-PEG-NH₂ had an important impact on both transfection performance and cell viability in general.

Another goal of this particular research was understanding the effect of the PEI ratio in the frameworks composition on self-assembling properties, DNA binding affinity, biocompatibility, and transfection properties since these are critical issue for developing a successful gene therapy vector. It is known that the presence of light exes of PEI in composition of non-viral vectors generally facilitate the endosome escape phenomenon. However, since toxicity increases with increasing PEI concentrations, finding the maximum amount of PEI in the composition of DCFs, is critical. Thus, in order to better understand this behavior, a library of frameworks was prepared (Craciun et al. 2019). The 1,3,5-benzenetrialddehyde (**1**), PEGylated squalene derivative (**14**), H₂N-PEG-NH₂ (**6**), and bPEI 2000 were chosen for building the library of DCFs (**3**). To define the toxicity limit, the ratio of bPEI 2000 (**3**) in the investigated DCFs was steadily increased from 1.5 eq to 3.5 eq. As the ratio of PEI in the composition of DCFs approached 3.5 eq, the tested DCFs/DNA polyplexes showed a high cytotoxic behavior at N/P 50. The noticeable cytotoxicity was observed while rising the N/P ratio to 100, regardless of the presence of NH₂-PEG-NH₂.

Unrelatedly to the PEI ratio in DCF composition, the studied polyplexes showed significantly higher transfection rate at N/P ratios of 50 as compared to bPEI 2000 (**3**). At N/P ratio 100, polyplexes showed a poor transfection due to high ratio of PEI in composition of DCFs.

Notably, at N/P ratios of 30 and 50, the presence of H₂N-PEG-NH₂ caused a subtle improvement in transfection efficiency. As the result of the investigation, it was found that the optimum DCF composition ratio of PEI:H₂N-PEG-NH₂ to be 1.5:1 for highest efficiency in transfection of pDNA in HeLa cells.

This study contributed to understanding the correlation and synergy between the constituent elements in dynamic combinatorial frameworks, as well as tuning the structure of DCFs, that are critical issues in the production of an effective nucleic acid carrier.

4 Rational Design Approach for Amphiphilic Squalene-Polyethylenimine Based Conjugates

Novel gene delivery systems based on squalene (Sq) (**13**) and bPEI of 1.8 kDa were synthesized using Michael addition to 1,1',2-trisnorsqualenaldehyde with the goal of developing small controlled structures with good stability and low toxicity. The Sq/bPEI conjugates (Sq-BPEI-NH₂) as well as their guanidinylated derivatives (Sq-BPEI-G) were found to have effective DNA complexation. When used in transfection of HeLa cells, the conjugates achieved highest transfection efficiency at N/P ratios of 20 for the polyplex Sq-BPEI-NH₂/DNA and N/P 15 for the polyplex Sq-BPEI-G/DNA, both being more effective than the reference bPEI/DNA polyplex. A new strategy to release in a controlled manner of encapsulated vectors for improvement of gene delivery yield was explored. Knowing that using a matrix-mediated gene transfer technique enhance gene delivery, increase extent and duration of transgene expression, and ensure a stable gene therapy profile (Cam C and Segura T 2013; Tierney et al. 2013). Thus, the polyplexes fomed from the vector and pEYFP included in a hybrid cryogel (containing natural/synthetic polymers (Atelocollagen, hyaluronic acid derivative, and poly(ϵ -caprolactone)), and PEI functionalized nano-hydroxyapatite (CH10P10/HAp25-15) (Simionescu et al. 2017) yielded a constant release of genetic material for approximately 26 days with a maximal expression on day 5 without any apparent toxic impact on HEK 293T cells.

Tunable material for genetic release, long-term bioavailability, and a relatively simple synthesis process are all features of the evolved systems.

Final Remarks

It is certain that the next generation of non-viral vectors relies on multi-purpose personalized materials with high degree of biocompatibility and biodegradability, which deliver cargo targeted at specific sites in tissues, organs or cells, with no harm to the body, in formulations that are easy to use and convenient for patients. In this context, the concept of simple,combinatoriar modular approach that yield materials with tunable properties is of a great interest. The simplicity of the synthetic strategy and combinatorial approach using accessible and simple building blocks for facile assembly of carriers, can be considered as a valuable path toward the systematic discovery of active delivery systems that aims to translate the scientific progress into clinical benefits for patients.

Acknowledgements This publication is part of a project that has received funding from the H2020 ERA Chairs Project no 667387: SupraChem Lab Laboratory of Supramolecular Chemistry for Adaptive Delivery Systems ERA Chair initiative.

Conflict of Interest The authors declare no conflict of interest.

References

- Ailincăi D, Marin L, Morariu S et al (2016) Dual crosslinked iminoboronate-chitosan hydrogels with strong antifungal activity against *Candida* planktonic yeasts and biofilms *Carbohydr Polym* 152:306–316
- Ailincăi D, Tartau Mititelu L, Marin L (2018) Drug delivery systems based on biocompatible imino-chitosan hydrogels for local anticancer therapy. *Drug Deliv.* 25(1):1080–1090
- Ailincăi D, Peptanariu D, Pinteala M et al (2019) Dynamic constitutional chemistry towards efficient nonviral vectors *Mater Sci Eng C* 94:635–646
- Ardeleanu R, Dascalu AI, Neamtu A et al (2018) Multivalent polyrotaxane vectors as adaptive cargo complexes for gene therapy. *Polym Chem* 9(7):845–859
- Bainbridge JWB, Tan MH, Ali RR (2006) Gene therapy progress and prospects: the eye. *Gene Ther* 13(16):1191–1197
- Banks WA (2009) Characteristics of compounds that cross the blood-brain barrier. *BMC Neurol* 9(1):S3
- Cam C, Segura T (2013) Matrix-based gene delivery for tissue repair. *Curr Opin Biotech* 24(5):855–863
- Catana R, Barboiu M, Moleavin I et al (2015) Dynamic constitutional frameworks for DNA biomimetic recognition. *Chem Commun* 51(11):2021–2024
- Clima L, Peptanariu D, Pinteala M et al (2015) DyNAVectors: dynamic constitutional vectors for adaptive DNA transfection. *Chem Commun* 51(99):17529–17531
- Clima L, Craciun BF, Gavril G et al (2019) Tunable composition of dynamic non-viral vectors over the DNA polyplex formation and nucleic acid transfection. *Polymers* 11(8):1313
- Couvreur P (2009) “Squalenoylation”: a new approach to the design of anticancer and antiviral nanomedicines. *B Acad Nat Med Paris* 193(3):663–673
- Craciun BF, Vasiliu T, Marangoci N et al (2018) Pegylated squalene: a biocompatible polymer as precursor for drug delivery. *Rev Roum Chim* 63(7–8):621–628
- Craciun FB, Gavril G, Peptanariu D et al (2019) synergistic effect of low molecular weight polyethylenimine and polyethylene glycol components in dynamic nonviral vector structure, toxicity, and transfection efficiency. *Molecules* 24(8)
- Dascalu AI, Ardeleanu R, Neamtu A et al (2017) Transfection-capable polycationic nanovectors which include PEGylated-cyclodextrin structural units: a new synthesis pathway. *J Mater Chem B* 5(34):7164–7174
- Desmaele D, Gref R, Couvreur P (2012) Squalenoylation: a generic platform for nanoparticulate drug delivery. *J Control Release* 161(2):609–618
- Dunbar CE, High KA, Joung JK et al (2018) Gene therapy comes of age. *Science* 359(6372):eaan4672
- Egger G, Liang G, Aparicio A et al (2004) Epigenetics in human disease and prospects for epigenetic therapy. *Nature* 429(6990):457–463
- Elouahabi A, Ruysschaert J-M (2005) Formation and intracellular trafficking of lipoplexes and polyplexes. *Mol Ther* 11(3):336–347
- Finbloom JA, Sousa F, Stevens MM et al (2020) Engineering the drug carrier biointerface to overcome biological barriers to drug delivery. *Adv Drug Deliv Rev* 167:89–108
- Funhoff AM, van Nostrum CF, Koning GA et al (2004) Endosomal escape of polymeric gene delivery complexes is not always enhanced by polymers buffering at low pH. *Biomacromol* 5(1):32–39
- Ginn SL, Amaya AK, Alexander IE et al (2018) Gene therapy clinical trials worldwide to 2017: an update. *J Gene Med* 20(5):e3015
- Godbey WT, Barry MA, Saggau P et al (2000) Poly(ethylenimine)-mediated transfection: a new paradigm for gene delivery *Journal of Biomedical Materials Research* 51(3):321–328
- Gordon R, Ranjith R, Leighann S et al (2012) Fungal Biofilm resistance. *Int J Microbiol* 2012
- Hanna E, Rémuizat C, Auquier P et al (2017) Gene therapies development: slow progress and promising prospect. *J Mark Access Health Policy* 5(1):1265293

- Harada A, Okada M, Kawaguchi Y et al (1999) Macromolecular recognition: new cyclodextrin polyrotaxanes and molecular tubes. *Polym Adv Technol* 10(1–2):3–12
- Hedman M, Hartikainen J, Ylä-Herttuala S (2011) Progress and prospects: hurdles to cardiovascular gene therapy clinical trials. *Gene Ther* 18(8):743–749
- Jiří V, Edward SW, Andrey Y et al (2012) Terminology and nomenclature for macromolecular rotaxanes and pseudorotaxanes (IUPAC Recommendations 2012). *Pure Appl Chem* 84(10):2135–2165
- Kumar V, Qin J, Jiang Y et al (2014) Shielding of lipid nanoparticles for siRNA delivery: impact on physicochemical properties, cytokine induction, and efficacy. *Mol Ther Nucleic Acids* 3(11):e210-e
- Kursa M, Walker GF, Roessler V et al (2003) Novel shielded transferrin–polyethylene glycol–polyethylenimine/DNA complexes for systemic tumor-targeted gene transfer. *Bioconjug Chem* 14(1):222–231
- Lehn J-M (2012) Constitutional dynamic chemistry. Barboiu M (ed.) Springer, Heidelberg, p 1–32
- Lepeltier E, Bourgaux C, Rosilio V et al (2013) Self-assembly of squalene-based nucleolipids: relating the chemical structure of the bioconjugates to the architecture of the nanoparticles. *Langmuir* 29(48):14795–14803
- Marin L, Ailincăi D, Cahn M et al (2016) Dynameric frameworks for DNA transfection. *ACS Biomater Sci Eng* 2(1):104–111
- Müller MM, Muir TW (2015) Histones: at the crossroads of peptide and protein chemistry. *Chem Rev* 115(6):2296–2349
- Muramatsu S (2018) Gene therapy using adeno-associated virus vectors *Cancer Sci* 109(1200-).
- Neu M, Fischer D, Kissel T (2005) Recent advances in rational gene transfer vector design based on poly(ethylene imine) and its derivatives. *J Gene Med* 7(8):992–1009
- Neuberg P, Kichler A (2014) *Advances in genetics*. Huang L et al (eds) Academic Press, vol 88, pp 263–288
- Olanow CW (2014) Gene therapy for Parkinson disease—a hope, or a dream? *Nat Rev Neurol* 10(4):186–187
- Olden BR, Cheng YL, Yu JL et al (2018) Cationic polymers for non-viral gene delivery to human T cells. *J Control Release* 282:140–147
- Papadopoulos KI, Wattanaarsakit P, Prasongchean W et al (2016) Polymers and nanomaterials for gene therapy. Narain R (ed) Woodhead Publishing, p 231–56
- Paul A, Eun CJ, Song JM (2014) Cytotoxicity mechanism of non-viral carriers polyethylenimine and poly-L-lysine using real time high-content cellular assay. *Polymer* 55(20):5178–5188
- Pricope G, Pinteala M, Clima L (2018) Dynamic self-organizing systems for DNA delivery. *Rev Roum Chim* 63(7–8):613–619
- Semenza GL (2003) Targeting HIF-1 for cancer therapy. *Nat Rev Cancer* 3(10):721–732
- Simionescu BC, Drobotă M, Timpu D et al (2017) Biopolymers/poly(epsilon-caprolactone)/polyethylenimine functionalized nano-hydroxyapatite hybrid cryogel: Synthesis, characterization and application in gene delivery. *Mat Sci Eng C-Mater* 81:167–176
- Smith AJ, Bainbridge JWB, Ali RR (2012) Gene supplementation therapy for recessive forms of inherited retinal dystrophies. *Gene Ther* 19(2):154–161
- Somia N, Verma IM (2000) Gene therapy: trials and tribulations. *Nat Rev. Genet* 1(2):91–99
- Suk JS, Xu Q, Kim N et al. (2016) PEGylation as a strategy for improving nanoparticle-based drug and gene delivery *Adv Drug Deliver Rev* 99:28–51
- Thapa B, Narain R (2016) Polymers and nanomaterials for gene therapy. Narain R (ed) Woodhead Publishing, p 1–27
- Tierney EG, Duffy GP, Cryan SA et al (2013) Non-viral gene-activated matrices next generation constructs for bone repair. *Organogenesis* 9(1):22–28
- Turin-Moleavin IA, Doroftei F, Coroaba A et al (2015) Dynamic constitutional frameworks (DCFs) as nanovectors for cellular delivery of DNA. *Org Biomol Chem* 13(34):9005–9011
- Uritu CM, Varganici CD, Ursu L et al (2015) Hybrid fullerene conjugates as vectors for DNA cell-delivery. *J Mater Chem B* 3(12):2433–2446

- Uritu CM, Calin M, Maier SS et al (2015) Flexible cyclic siloxane core enhances the transfection efficiency of polyethylenimine-based non-viral gene vectors. *J Mater Chem B* 3(42):8250–8267
- Wang Y, Zheng M, Meng F et al (2011) Branched polyethylenimine derivatives with reductively cleavable periphery for safe and efficient in vitro gene transfer. *Biomacromol* 12(4):1032–1040
- Wu P, Chen H, Jin R et al (2018) Non-viral gene delivery systems for tissue repair and regeneration. *J Transl Med* 16(1):29
- Yang J, Liu H, Zhang X (2014) Design, preparation and application of nucleic acid delivery carriers. *Biotechnol Adv* 32(4):804–817
- Yao WJ, Cheng X, Fu SX et al (2018) Low molecular weight polyethylenimine-grafted soybean protein gene carriers with low cytotoxicity and greatly improved transfection invitro. *J Biomater Appl* 32(7):957–966
- Yin H, Kanasty RL, Eltoukhy AA et al (2014) Non-viral vectors for gene-based therapy. *Nat Rev. Genet* 15(8):541–555
- Zakeri A, Kouhbanani MAJ, Beheshtkhoo N et al (2018) Polyethylenimine-based nanocarriers in co-delivery of drug and gene: a developing horizon. *Nano Rev Exp* 9(1):1488497
- Zhang Y, Barboiu M (2016) Constitutional dynamic materials-toward natural selection of function. *Chem Rev* 116(3):809–834

Development of Novel Versatile Theranostic Platforms Based on Titanate Nanotubes: Towards Safe Nanocarriers for Biomedical Applications



Julien Boudon, Fadoua Sallem, Alexis Loiseau, Lionel Maurizi, Anne-Laure Papa, and Nadine Millot

Abstract The concept of nanomaterials that can be designed and administered into the human body to improve health is of great interest. During the past years there has been an increasing amount of research on the uses of nanomaterials in diverse areas of biomedical research including biological sensing, labelling, imaging, cell separation and therapy. In this chapter, the first evaluation of titanate nanotubes (TiONts) as potential carriers of therapeutic molecules is presented. TiONts with controlled parameters have been developed from a hydrothermal synthesis and their biomedical applications have been explored over the last decade. These nanotubes are elaborated as stable suspensions of nanocarriers by surface chemistry engineering. They can be used as transfection agents for cardiomyocytes and we have shown that TiONts can increase the ionizing effect of radiation therapy in the case of glioblastoma. Furthermore, TiONts' biodistribution has been evaluated by SPECT/CT in male Swiss nude mice and TiONts are quickly cleared. More recently, we have demonstrated that TiONts-docetaxel (DTX) nanohybrids are versatile nanocarriers to limit the systemic toxicity of taxanes and to improve the selectivity of radiotherapy (RT). Our strategy is based on the intraprostatic injection of the TiONts-DTX nanohybrids both in place of brachytherapy and in combination with RT. This is achieved by taking advantage of the TiONts' morphology as well as their radiosensitization effect and by associating them with docetaxel molecules, also recognized for their radiosensitizing potential. We also grafted the surface of TiONts with gold nanoparticles, for a resulting combined radiosensitizing effect. The elaboration of nanohybrid materials, intended for drug delivery systems and based on TiONts coated with chitosan polymer has also been evaluated. Such nanotubes are combined with transresveratrol derivatives for their anti-oxidizing and antitumor effects. All the aspects of a potential toxicity are also considered.

J. Boudon · F. Sallem · A. Loiseau · L. Maurizi · N. Millot (✉)
Laboratoire ICB, UMR 6303, CNRS/Université Bourgogne Franche-Comté,
9 Avenue Alain Savary, 21078 Dijon, France
e-mail: nadine.millot@u-bourgogne.fr

A.-L. Papa
Department of Biomedical Engineering, The George Washington University, Washington,
DC 20052, USA

Keywords Titanate nanotubes · Theranostic platform · Nanomedicine · Nanocarriers · Chemistry · Nanohybrids · Characterizations

1 Introduction

The shape of nanoparticles is an essential element to take into account for the internalization, cytotoxicity, biodistribution and intracellular exchanges of nano-objects in the organism (Ernsting *et al.* 2013).

Diffusion phenomena, through the cells' membrane, have already been observed by anisotropic nanoparticles, allowing the internalization of these biomaterials in the cytoplasm in addition to endocytosis (Kostarelos *et al.* 2007). Besides, it was demonstrated that anisotropic nanoparticles were characterized by a higher blood circulation time and prolonged retention at tumor sites compared to spherical nanoparticles (Agarwal *et al.* 2015). Z. J. Deng et al. have shown that the shape of TiO₂ nanoparticles (nanosphere, nanorod and nanotube) plays an important role in the absorption of proteins on their surface, thus dictating their biokinetics and their behavior *in vivo* (Deng *et al.* 2009).

Intrinsic properties of nanoparticles are also influenced by their shape. It has been shown that magnetic nanoparticles of elongated shape exhibit higher magnetic hyperthermia heating capacities than their spherical equivalents (Das *et al.* 2016). Similarly, gold nanorods have interesting optical properties due to the resonance effects of the surface plasmon. Finally, excellent properties associated with guided geometry nanoparticles have opened up exciting opportunities for new material designs and will potentially revolutionize the current practice in Biology and Medicine (Decuzzi *et al.* 2017). Nanoparticles can be built from different materials and can host a wide range of active components for various biomedical applications, including chemotherapeutics, proteins, contrast agents, and nucleic acids.

The major elongated nanoparticles used in nanomedicine are: carbon nanotubes (Bianco *et al.* 2005), gold nanorods (Awan *et al.* 2018), ZnO nanorods (Jeong *et al.* 2020), silver nanorods (Suganya and Devasena 2015), silica nanotubes (Ma *et al.* 2009), iron oxide nanorods (Singh *et al.* 2020), apatite nanorods (Ge *et al.* 2019), alumina nanotubes (Campos *et al.* 2016), titanium oxide nanorods (Sun *et al.* 2016) and titanate nanotubes (Bavykin and Walsh 2009). Gold nanorods, for instance, have been developed for biomedical applications focus on detection, biocatalysis, imaging, drug delivery, and gene delivery (Wang *et al.* 2013). ZnO nanorods, as for them, are suitable in biosensing and biodetection (Hahm 2016).

Titanate nanotubes (TiONts) have been used in hip prostheses and dental implants (Bavykin and Walsh 2009) and for dopamine detection (Niu *et al.* 2008). Our group is a pioneer in the development of TiONt-based nanocarriers (Mirjolet *et al.* 2013; Papa *et al.* 2013). This chapter aims to summarize the chemical challenges and biomedical opportunities around these fascinating titanate nanotubes.

2 The Preparation of Titanate Nanotubes and their Characterization

2.1 Hydrothermal Synthesis of Titanate Nanotubes

TiONts have historically been synthesized by two methods: (i) *via* hydrothermal synthesis starting from nanometric and spherical TiO_2 precursor (Kasuga *et al.* 1998; Papa *et al.* 2009), which will be described in this chapter, and (ii) *via* electrochemical anodization of a Ti metal foil substrate (Gong *et al.* 2001). The parameters of these reactions (such as temperature, time, pH, agitation, washings, *etc.*) enable a precise control of the physicochemical characteristics of the resulting TiONts such as shapes (Bellat *et al.* 2015) (tubes, sheets, ribbons), dimensions (inner/outer diameters; length), size distribution, specific surface and chemical composition. These parameters can be specifically tuned and optimized to best fit the targeted bioapplications.

The hydrothermal synthesis of TiONts is a single step process starting from TiO_2 spherical nanoparticles (*i.e.* rutile, anatase or P25) under highly basic conditions such as 10 M NaOH (Fig. 1). The hydrothermal treatment (3–4 bar) is maintained over 12 to 72 h and 100 to 180 °C. The formation mechanism of titanate nanotubes is still a matter of debate. Several phenomena are discussed in literature: the dissolution

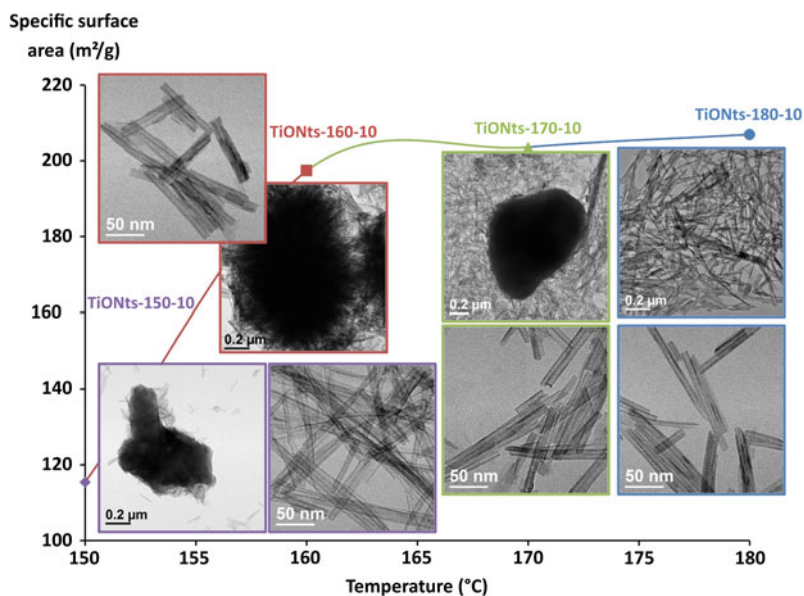


Fig. 1 TEM (Transmission electron microscopy) images and BET specific surface area of TiONts as a function of the reaction temperature (from 150 to 180 °C) at a fixed stirring running for 10 min/h and for 8 h.

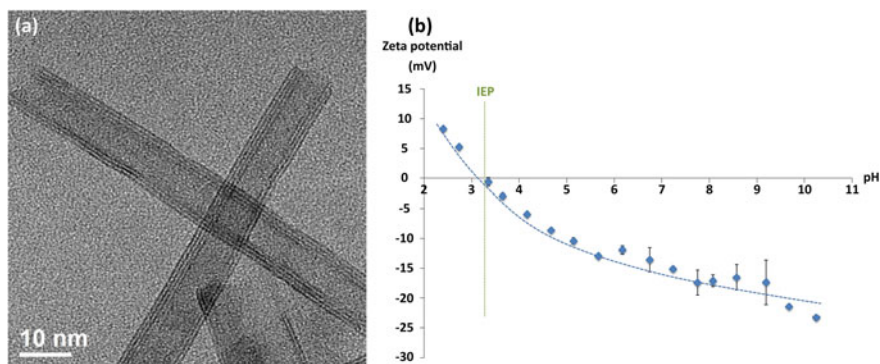
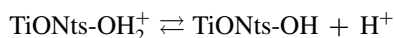


Fig. 2 (a) TEM image of two titanate nanotubes synthesized by static hydrothermal route (no stirring, $T = 150\text{ }^{\circ}\text{C}$, $t = 48\text{ h}$, $[\text{NaOH}] = 10\text{ M}$), (b) zeta potential measurements potential measurements of TiONts as a function of pH in NaCl (10^{-2} M).

of the precursor crystallites in bulk followed by the formation of nanosheets which then curl into nanotubes (Sun and Li 2003; Bavykin *et al.* 2006). After this, the reaction mixture is washed by centrifugation cycles, dialyzed or ultrafiltered until the suspension reaches neutral pH. Finally, the TiONts' suspension is freeze-dried and the resulting lyophilized particles are stable for months at room temperature.

2.2 Titanate Nanotubes' Features and Characterizations

Titanate nanotubes display a large specific surface area (higher than $200\text{ m}^2/\text{g}$) due to their hollow and multilayered assembly (Sallem *et al.* 2017b) (Fig. 2a). Unlike carbon nanotubes, their multilayered morphology is not concentric, rather it is arranged in a spiral fashion. A large number of surface hydroxyls have been estimated by TGA (thermogravimetric analysis) and verified by XPS (X-ray photoemission spectroscopy) surface analyses. The zeta (ζ) potential measurements made on TiONts indicate a maximum zeta potential value around 20 mV and an isoelectric point (IEP) around pH 3 (Fig. 2b). The TiONts' surface charge varies with the pH according to the following equilibria:



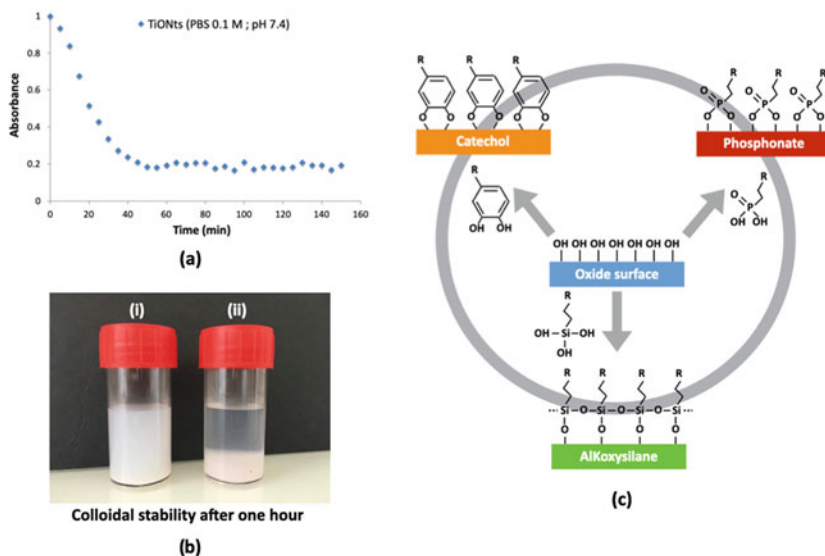


Fig. 3 (a) Colloidal stability of bare TiONts (PBS 0.1 M; pH 7.4) over 150 min following their absorbance at 600 nm by turbidimetry. (b) Picture of bare TiONts' suspensions in (i) ultrapure water and (ii) PBS (0.1 M; pH 7.4) after one hour. (c) Illustration of different pre-functionalization strategies on the TiONts' surface by catechol, phosphonate and alkoxy silane derivatives (only one way of grafting is arbitrarily represented).

3 The Surface Modification of Titanate Nanotubes (Synthesis and Characterizations)

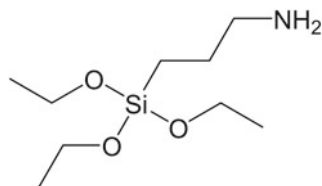
Bare TiONts are not stable enough in physiological conditions (*ca.* 50% of TiONts settled after 20 min and about 80% after one hour, Fig. 3a and b) and require surface modifications to improve their colloidal stability: to do so alkoxy silanes, phosphonates and catechols can be interestingly used to obtain surface-modified TiONts (Fig. 3c), the description of which will be described in the following paragraphs.

3.1 TiONts' Modification by Silane Derivatives

TiONts can easily be modified by silane derivatives to yield silica-coated TiONts with a view to i) stabilize TiONts for further applications and ii) possibly bring new chemical functions provided that the silane used is terminated with an amine or a carboxylic acid group for example.

The mostly used alkoxy silane is 3-aminopropyltriethoxysilane (APTES) for which the silane function reacts with the surface hydroxyls of the TiONts and the amine function makes it possible in particular to have an electrostatic-type repulsion

Fig. 4 Chemical structure of the 3-aminopropyl triethoxysilane molecule.



at the surface of the TiONts. APTES formula is $(\text{CH}_3\text{CH}_2\text{O})_3\text{-Si-(CH}_2)_3\text{-NH}_2$ ($M = 221 \text{ g}\cdot\text{mol}^{-1}$) (Fig. 4). It is commonly used to obtain biocompatible surfaces. This molecule is mainly used to promote protein adhesion and cell growth on biological implants (Balasundaram *et al.* 2006) as well as for biosensing or DNA extraction (Howarter and Youngblood 2006).

Several steps are necessary when grafting APTES on TiONts and any consideration in the following lines could be theoretically applied to any silane derivative: other hydrolyzable groups (3-aminopropyltrimethoxysilane or 3-aminopropyl trichlorosilane); other end groups (3-R-propylalkoxysilane with $R = \text{epoxide, Cl}^-$, N_3^- , *etc.*); and various lengths of alkyl chains bearing the chemical function of interest (ω -R-alkylalkoxysilane). First, a reaction of APTES in aqueous solution forms a silanol with the hydrolysis of three ethanol molecules (Fig. 5a). Then, oligomerization of silanols (intermolecular condensation) leads to the formation of oligosiloxanols with different chain sizes (Fig. 5b). Then, hydrogen bonds appear between oligosiloxanols and the hydroxyls of the TiONts' surface (Fig. 5c). Finally, the last step is the condensation of oligosiloxanols on TiONts with the formation of covalent bonds (Fig. 5d).

It is important to control the different stages of silanization to obtain a monolayer of APTES and to be able to optimize the number of amine functions on the surface of TiONts for subsequent grafting. Indeed, it is possible to create multilayers of APTES during condensation (Fig. 6) and to affect the final structure of the layer of aminosilane on the surface of the inorganic substrate. This is notably due to several parameters such as water content, reaction temperature, concentration, and nature of the silane (White and Tripp 2000). Among these, temperature, and proportion of solvent (ratio water/ethanol) are the main parameters which play on the structure and on the grafting rate of APTES. In fact, an increase in temperature favors the condensation of the polysiloxane on the TiONts' surface as well as the reaction speed, while the proportion of the solvent can affect the competitive reactions between hydrolysis and oligomerization (Liu *et al.* 2013).

Recently, N. Millot *et al.* have developed advanced surface-modified TiONts for biomedical applications including a first coating of silane derivatives (APTES in the following examples) prior to further functionalization(s): polymer-coated TiONts (Papa *et al.* 2015), TiONts as optical probe thanks to phthalocyanines (Boudon *et al.* 2014; Paris *et al.* 2015), docetaxel nanocarriers (Mirjolet *et al.* 2017; Loiseau *et al.* 2017), chitosan-coated TiONts (Sallem *et al.* 2017a), or also TiONts as potential candidate for drug delivery applications across the brain (Sruthi *et al.* 2018).

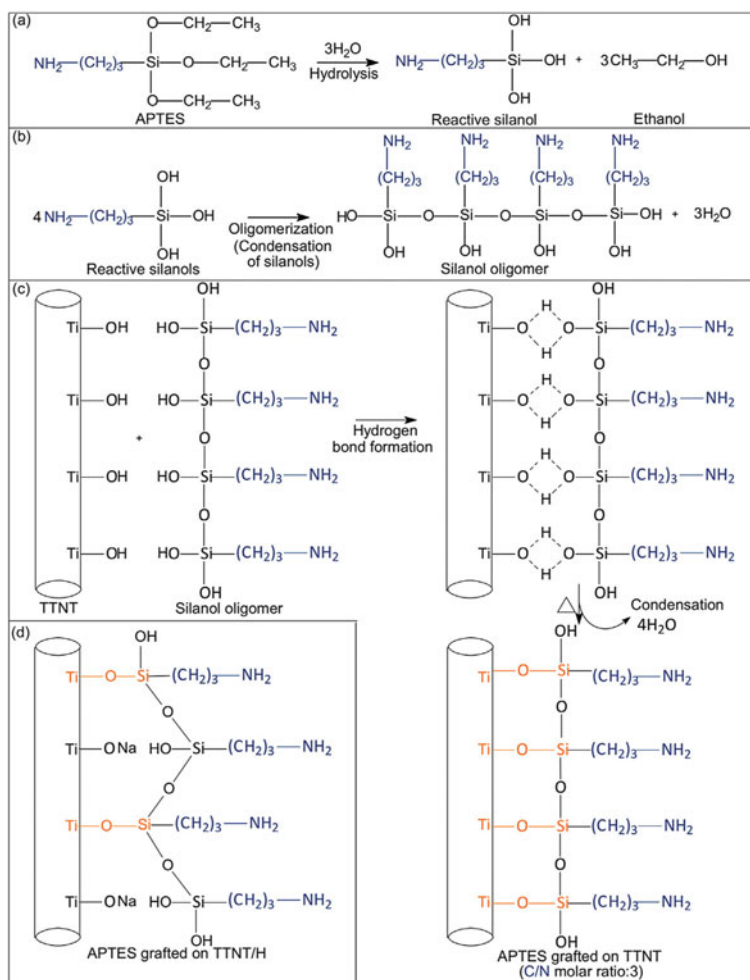


Fig. 5 Functionalization of TiONTs by APTES: (a) hydrolysis of APTES; (b) oligomerization of silanols; (c) creation of hydrogen bridges then formation of covalent bonds by condensation between the oligosiloxanols and the surface of TiONTs; (d) possible incomplete condensation of silanols on the surface of TiONTs. According to (Pontón *et al.* 2014), Copyright © 2014 Elsevier.

3.2 TiONTs' Modification by Phosphonate Derivatives

Phosphonic acids and their derivatives ($\text{R}-\text{PO}(\text{OR}')_2$; $\text{R}, \text{R}' = \text{hydrogen, alkyl}$) have become increasingly attractive due to their strong affinity for hydroxylated surfaces (Ries and Cook 1954). They have already proven themselves in biological fields for biosensors or for medical implants (Mutin *et al.* 2005). The chemisorption mechanisms of phosphonate agents on inorganic substrates are greatly affected by reaction conditions such as temperature, pH of the medium, concentration, solvent and type

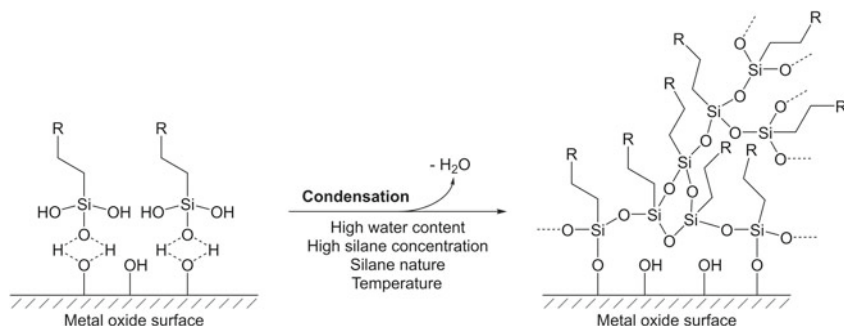


Fig. 6 Scheme of APTES multilayers on the inorganic substrate during condensation. According to (Pujari *et al.* 2014), Copyright © 2014 WILEY-VCH Verlag GmbH & Co. KGaA, Weinheim.

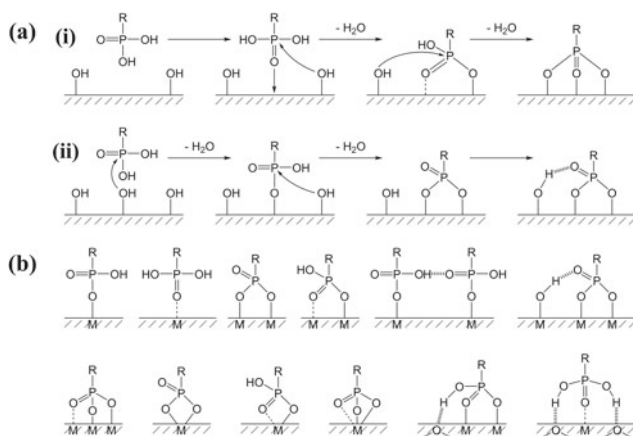
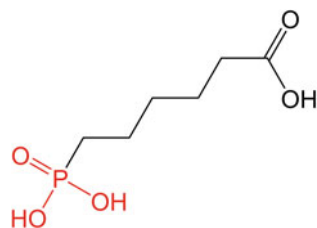


Fig. 7 (a) Presentation of the two main mechanisms for grafting a phosphonate type agent onto a metal oxide surface. (b) Illustration of the different conformations between a phosphonate and the surface of a metal oxide (mono-, bi- and tridentate chelation). According to (Pujari *et al.* 2014), Copyright © 2014 WILEY-VCH Verlag GmbH & Co. KGaA, Weinheim.

of oxide (Pujari *et al.* 2014). The type of interaction between the phosphorus atom and the hydroxyl oxygen can differ depending on the Lewis strength of the atoms on the surface of the metal oxide (Fig. 7a). Indeed, in the case of a surface with high Lewis acidity, the bonds (P-O-M) are even more stable and stronger as the P atom becomes more electrophilic and induces consecutive heterocondensations with hydroxyls. Otherwise, hydrogen bonds can form due to a higher affinity with phosphonate and hydroxyls on the surface of the metal oxide. In addition, the presence of three oxygen atoms on the phosphonates makes it possible to induce three modes of chelation (mono-, bi- and tridentate). The oxygen can then be linked to the same metal site or to different atoms present on the surface (Fig. 7b) (Guerrero *et al.* 2013).

Fig. 8 Chemical structure of the monophosphonate 6-phosphonohexanoic acid molecule.



The phosphonates are then interesting, in comparison with the alkoxyxilanes, because they form stable monolayers. In addition, they are less likely to become detached from the surface of the oxide by self-condensation reactions which can break the bonds formed. However, this can happen under high temperature dehydration conditions (Mutin *et al.* 2005). Also, the handling conditions (phosphonate coupling reactions are often optimized in water) and storage (in air at 20 °C) make them more accessible and less restrictive than aminosilanes or catechols. In addition, phosphonic acids have remarkable affinities with metal oxides having a high degree of oxidation such as titanium (Ti^{4+}) (Guerrero *et al.* 2001). The hydrolytic stabilities of monolayers during the formation of P-O-M bonds are then better than in the case of alkoxyxilanes and are comparable to those of catechols (Daou *et al.* 2007; Pujari *et al.* 2014).

Finally, phosphonates can also be bifunctional molecules. On the one hand, the phosphonate group should have a strong affinity with the surface of TiONts and on the other hand, a reactive function is present to generate an electrostatic effect capable of improving the colloidal stability of the nanotubes and then to graft other molecules. An example of phosphonates is the monophosphonate 6-phosphonohexanoic acid (PHA, Fig. 8): the phosphonic side interacts with the metal oxide surface and the opposite side of the molecule is ended by a carboxylic acid function for further functionalization.

N. Millot *et al.* have investigated three different types of phosphonate grafting to improve the colloidal stability of TiONts: the 6-phosphonohexanoic acid monophosphonate (PHA, Fig. 8), the alendronic acid bisphosphonate (ALD, Fig. 9a) or a PEGylated monophosphonate (Fig. 9b). These agents are all heterobifunctional molecules

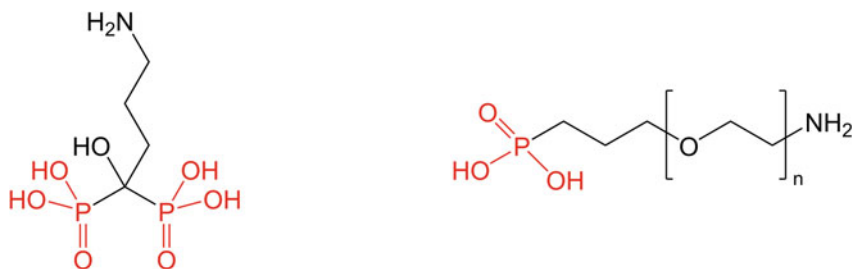


Fig. 9 Chemical structure of (a) the bisphosphonate alendronic acid molecule and (b) the ω -amino-PEG-monophosphonate

and PHA has already been studied in our laboratory on iron oxide nanoparticles but also during initial investigations on TiONts (Paris *et al.* 2015; Thomas *et al.* 2016). PHA has a carboxylic function at one end, while the alendronate and the PEG (polyethylene glycol) derivative have an amine function in addition to the phosphonate function.

The influence of a monophosphonate and a bisphosphonate on colloidal stability under physiological conditions have been compared. The alendronic acid is particularly interesting because it is already used as an anticancer drug (anti-tumor properties), for the treatment of osteoporosis and for other bone diseases (Benyettou *et al.* 2011; Motte *et al.* 2011). Finally, the presence of a long carbon chain, with a phosphonate group on one end and an amine function on the other, allows a steric effect and an electrostatic effect to occur thus improving the colloidal stability with the phosphonate-type polymer.

As depicted in Fig. 10, it should be noted that alendronic acid has five pKa ($\text{pKa}_1 = 0.8$, $\text{pKa}_2 = 2.2$, $\text{pKa}_3 = 6.3$, $\text{pKa}_4 = 10.9$ as regards the pairs of the two phosphonates POOH/POO^- and $\text{pKa}_5 = 12.2$ for the $\text{NH}_3^+/\text{NH}_2$ pair, Fig. 9a). In a previous study, alendronate was grafted to the surface of maghemite nanoparticles at pH 2 *via* two Fe–O–P bonds (corresponding to pKa_1 and pKa_2) (Benyettou *et al.* 2011). In the same study, it is shown that at pH 7.4, the negative charge of the obtained nanohybrid is due to the deprotonation of the OH function of the couple relative to pKa_3 . In theory, to promote the grafting of the alendronate *via* two Fe–O–P bonds, it is preferable to have pH between 2.2 and 6.3. However, the TiONts' IEP is *ca.* 3 (Fig. 2b) (Papa *et al.* 2015). Thus, to form Ti–O–P bonds, it is preferable to have pH below 3 (Fig. 10). Note that at pH 7.4, the agglomeration of TiONts is weaker than at acidic pH (the ζ -potential is -35 mV due to deprotonated hydroxyl groups). It is the same with PHA and $(\text{HO})_2-(\text{O}=\text{P})\text{-PEG-NH}_2$ for which the pKa of phosphonate are between 2 and 8.5. Finally, the choice of pH must consider the pKa of these three molecules, their solubility but also, the IEP and the colloidal stability of the TiONts.

The dispersion state of TiONts, after the different graftings of PHA, ALD and of polymer $(\text{HO})_2-(\text{O}=\text{P})\text{-PEG-NH}_2$ has been analyzed by TEM (Fig. 11). In these

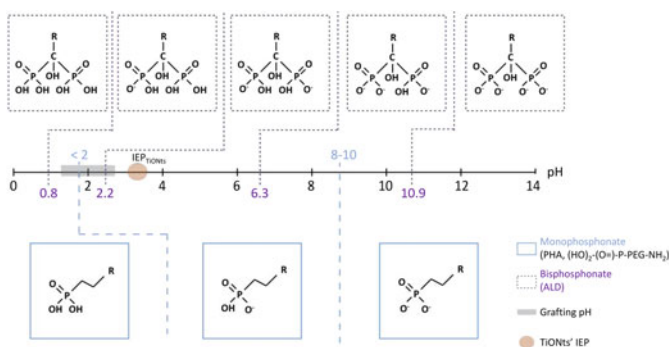


Fig. 10 Different acid–base forms of monophosphonates (PHA and $(\text{HO})_2-(\text{O}=\text{P})\text{-PEG-NH}_2$) and bisphosphonate (ALD) depending on the pH range.

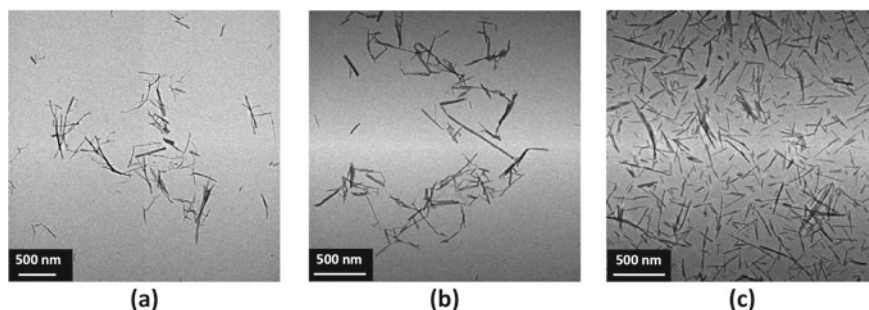


Fig. 11 TEM images showing the dispersion state of different functionalized-TiONTs by phosphate derivatives: (a) TiONTs-PHA, (b) TiONTs-alendronate and (c) TiONTs-PEG-NH₂.

pictures, the grafts for the TiONts-ALD and the TiONts-PHA seem to favor the individualization of the nanohybrids, unlike naked nanotubes which are organized in bundles (Papa *et al.* 2009; Boudon *et al.* 2014) even if they sometimes form a few small agglomerates. This attests that the surface modification of TiONts by ALD and PHA greatly improves their dispersion. However, it is the TiONts-PEG-NH₂ which show better dispersion on the observation grid while they have been found to be less stable by UV-visible spectroscopy. They exhibit a homogeneous dispersion over the entire surface, without agglomerate: it is therefore the polymer chains which contribute sterically to this individualization. This remarkable state of dispersion (better than with the TiONts/APTES/PEG system) allows synthetic by-products to be visualized, such as nanoribbons, but in negligible amount compared to the number of nanotubes.

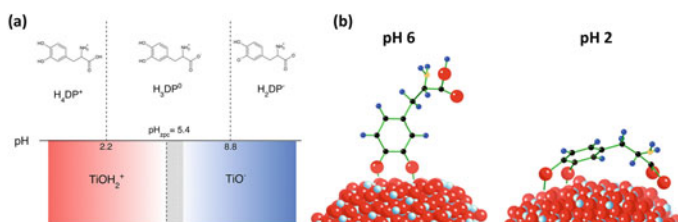


Fig. 12 Illustration of the state (a) of protonation and (b) conformation of catechols (LDOPA) dependent on pH, on a surface of titanium dioxide (Lee *et al.* 2012), Reprinted (adapted) with permission from Langmuir 2012, 28, 50, 17,322–17,330 Copyright © 2012 American Chemical Society.

3.3 TiONts' Modification by Catechols

The applications of nanopowders in suspension are often limited by the insufficient colloidal stability of nanoparticles. Catechols have good properties as stabilizers (Amstad *et al.* 2009, 2011a) to remedy this; they also exhibit antioxidant activity (Lee *et al.* 2003). Catechols generally form a charged monolayer on the surface of metal oxide, which stabilizes nanoparticles to absorb light or to lead to reversible redox reactions and they present as well an interesting potential barrier for photovoltaic and biomedical applications (Pujari *et al.* 2014). Catechol derivatives are used as dispersants for various oxides, in particular with titanium and iron oxides (Amstad *et al.* 2011a; Bahri *et al.* 2011). Despite similar chemical properties between different catechols, the affinities on these oxides vary considerably. Catechols can form weakly reversible or strong bonds, depending on their affinity with the cations of the oxides (Amstad *et al.* 2011b). The grafting mechanism of catechols on oxides is relatively close to that of phosphonates (Sect. 3.2). Briefly, a mono- or bidentate complex can form with one or two oxygen from the catechols and the metal atoms from the oxide, as is the case with titanium.

Moreover, pH is a key parameter in the grafting and conformation of catechols on the surface of metal oxide. In addition to being the main oxidation factor for catechols, the protonation state of the different groups depends on pH (Fig. 12a). Thus, concentration and pH of the reaction medium influence the grafting capacity of catechols (pKa of the catechols' hydroxyls have a value of between 8.5 and 10), as well as the conformation of the molecule on the surface of the oxide (Fig. 12b).

A study related to the grafting of L-3,4-dihydroxyphenylalanine (LDOPA) on TiO₂, has shown that pH 6 favors a stretched conformation and an orientation perpendicular to the surface of nanoparticles (which has also been observed with a high concentration of catechol during grafting) unlike pH 2 for which the molecule seems to be lying on the surface of TiO₂ (Fig. 12b) (Lee *et al.* 2012). It is therefore preferable to have a pH around 6 on a TiO₂ surface to optimize the grafting of catechols and lead to available reactive functions. Furthermore, excessive basic pH promotes the oxidation of catechols (Bahri *et al.* 2011): the choice of pH is therefore essential to obtain an optimal conformation of the molecule while limiting its oxidation for future grafting. The grafting of three hydrophilic catechols has been carried out to modify the surface of TiONts: L-3,4-dihydroxyphenylalanine (LDOPA), 3,4-dihydroxyhydrocinnamic acid (DHCA) and nitrodopamine (NDOPA) (Fig. 13). These molecules have one or many reactive functions in addition to the catechol group so that colloidal stability

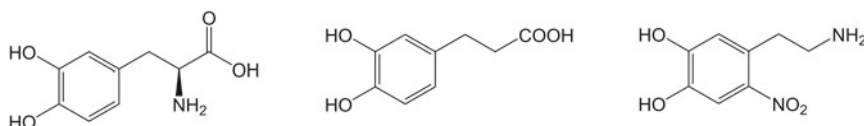


Fig. 13 (a) L-3,4-dihydroxyphenylalanine (LDOPA), (b) 3,4-dihydroxyhydrocinnamic acid (DHCA) and (c) nitrodopamine (NDOPA) molecules.

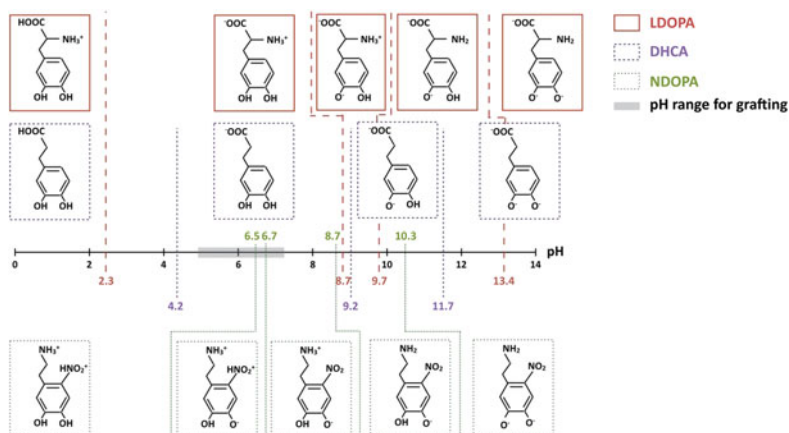


Fig. 14 Diagram of each acid–base form of catechol molecules (LDOPA, DHCA, NDOPA) according to the pH range.

is improved by electrostatic repulsion ($-\text{COOH}$, $-\text{NH}_2$, $-\text{NO}_2$). These same functions allow subsequent grafting of molecules such as polymers, therapeutic or chelating agents. In addition, the hydroxyls of catechols have a very strong affinity with titanium oxides (Amstad *et al.* 2009).

The grafting of DHCA and LDOPA catechols can be carried out under pH 6 because it leads to a fairly good dispersion of TiONts in water (value far from the IEP of bare TiONts), a pH close to the pKa of both catechol hydroxyls (to promote grafting) and allows the oxidation of catechols to be limited as it occurs at strongly acidic or basic pH (LDOPA: $\text{pK}_{\text{aCOOH}} = 2.3$, $\text{pK}_{\text{aNH}_2} = 9.7$, $\text{pK}_{\text{aOH}} = 8.7$ and 13.4 ; DHCA: $\text{pK}_{\text{aCOOH}} = 4.2$, $\text{pK}_{\text{aOH}} = 9.2$ and 11.7 ; NDOPA: $\text{pK}_{\text{aNH}_2} = 8.7$, $\text{pK}_{\text{aNO}_2} = 6.7$, $\text{pK}_{\text{aOH}} = 6.5$ and 10.3) (Amstad *et al.* 2011a; Togashi *et al.* 2012; Thomas *et al.* 2015) (Fig. 14).

Catechol-based stabilizers can be grafted on TiONts: their presence can be proven by several characterization techniques such as FTIR (Fourier Transform InfraRed spectroscopy), XPS, TGA. However, DHCA and LDOPA can transform into quinone at high pH and *via* oxidation or reduction reactions, limiting their grafting. pH 6 seems the most suitable to avoid these phenomena, but to the detriment of a high grafting yield, due to a lower deprotonation of the hydroxyls of the catechol (Fig. 14). For all these reasons, NDOPA has aroused interest (Patil *et al.* 2018; Albu *et al.* 2019) as the use of this molecule allowed the oxidation process to be limited thanks to the close location of NO_2 and NH_2 groups. Furthermore, the grafting rate of NDOPA on TiONts can be improved in selecting the synthesis pH close to the pKa of both hydroxyls of LDOPA and DHCA. These can be proven by TGA with a more significant weight loss for TiONts-NDOPA. In addition, the characterizations carried out by IR and XPS showed a greater rate of formation of the Ti–O–catechol bond. Although, N. Millot *et al.* (Loiseau 2017) showed that grafting the NDOPA

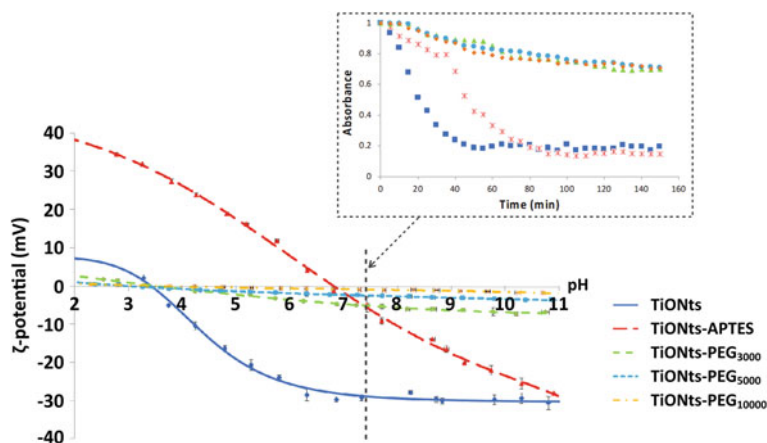


Fig. 15 ζ -potential curves as a function of pH in NaCl (10^{-2} M) of bare TiONts and different functionalized-TiONts (the vertical dashed line corresponds to the physiological pH). In inset, turbidimetric study: colloidal stability of functionalized-TiONts' suspensions (PBS 0.1 M; pH 7.4) over 150 min following their absorbance at 600 nm as a function of time.

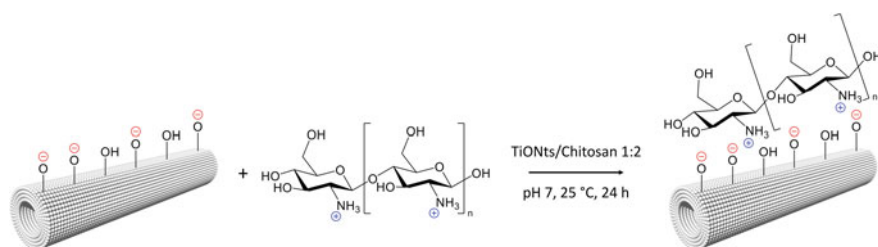


Fig. 16 Surface modification of TiONts by chitosan showing the interaction between the TiONts' negatively-charged surface and positively-charged ammoniums of the chitosan polymer. The large number of dipolar interaction lead to stable chitosan-coated TiONts.

molecules on TiONts did not significantly improve the colloidal stability of TiONts-NDOPA under physiological conditions. It should be noted that TiONts with their elongated morphology and rather large size are often more difficult to stabilize than small spherical nanoparticles. Regardless, catechol-based coatings have proven their effectiveness in many cases such as substrates (Saiz-Poseu et al. 2019; Cheng *et al.* 2019) and nanoparticles (TiO_2 , Fe_3O_4 , etc.) (Benyettou *et al.* 2009; Motte *et al.* 2011; Guenin *et al.* 2014; Thapa *et al.* 2018; Mohammadi *et al.* 2020).

To conclude, catechol derivatives are great stabilizers in most situations and offer new possibilities of further graftings thanks to their amine or carboxylic acid moieties on them. When the criteria of colloidal stability are eventually not met, silanes and phosphonate pathways are excellent alternatives. Other options consist of additional polymer graftings such as polyethyleneglycol (PEG) or polysaccharide (chitosan for instance) derivatives as described in the following section.

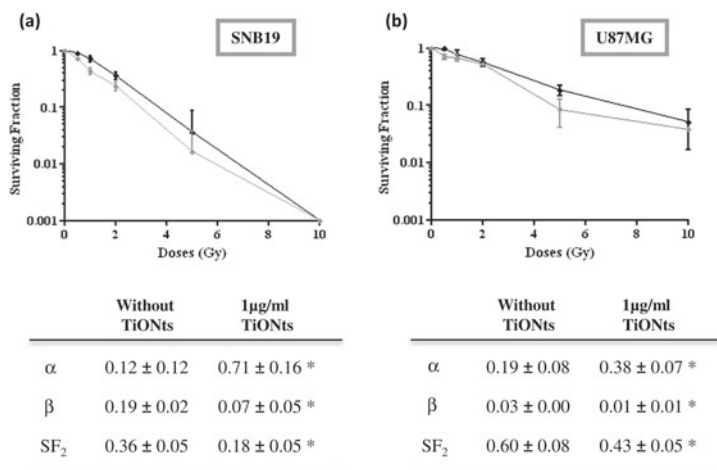


Fig. 17 Survival fraction curves obtained from (a) SNB-19 and (b) U87MG both under the effect of X-Ray exposure without and with TiONts incubation (1 $\mu\text{g}/\text{mL}$). The radiosensitivity parameters obtained by a linear quadratic model (α : initial slope, β : degree of downward curvature and SF_2 : survival fraction at 2 Gy). According to (Mirjolet *et al.* 2013), Reprinted (adapted) with permission from Radiother. Oncol. 2013, 108, 136–142 Copyright © 2013 Elsevier Ireland Ltd. All rights reserved.

3.4 Other TiONts' Surface Modifications

PEGylated chains grafted on nanoparticle (NP) surfaces lead to a charge shielding phenomenon (Maurizi *et al.* 2015), which enables to reduce the hepatic capture. Only a few studies are reporting the effect of PEGylated chain density and length on the biological behavior of TiONts and not much more on other metal oxide NPs (Gref *et al.* 2000; Gratton *et al.* 2008; Jokerst *et al.* 2011; Wu *et al.* 2020). It has been reported that higher PEG density and chain lengths improve the colloidal stability, reduce nonspecific adsorption of proteins and hence minimize the NP detection by the immune system, as well as their uptake by cells (Mosqueira *et al.* 2001; Cruje and Chithrani 2014). That is why the influence of different PEGylated chain lengths (HS-PEG_n-COOH; n = 3,000; 5,000; 10,000) on the colloidal stability of TiONts and on the PEG_n density and conformation has been investigated by N. Millot *et al.* (Loiseau *et al.* 2021).

ζ -potential measurements prove (Fig. 15) the presence of PEG_n on the TiONts-APTES-surface *via* an important charge shielding for the different PEGylated chain lengths (the longer the chain, the most important the shielding). Colloidal stability was also investigated under physiological conditions (PBS 0.1 M; pH 7.4) by turbidimetric analyses (inset in Fig. 15) and correlated with TEM observations (Loiseau *et al.* 2021). The absorbance measurements as a function of time demonstrated a better colloidal stability for TiONts-APTES-PEG_n suspensions than in bare TiONts and TiONts-APTES without PEG. TGA results correlated with FT-IR and XPS

analyses, prove the effective synthesis of TiONts-APTES-PEG_n nanohybrids. In particular, TGA analyses lead to 0.09 PEG_{3,000}/nm²; 0.05 PEG_{5,000}/nm² and 0.03 PEG_{10,000}/nm². These results reflect a relatively dense PEG_n brush conformation.

Chitosan (CT) has been also used to enhance the biocompatibility of hydrothermally synthesized nanotubes in a biological medium as a substitute for polyethylene glycol that is generally used for biocompatibility. CT grafting was carried out using two different approaches; the first one was made by forming covalent bonds using two intermediate molecules, and the second one is based on electrostatic interactions between CT and TiONts (Fig. 16) (Sallem et al. 2017a). The type of linkage on the surface of TiONts was proven to influence the colloidal stability of the elaborated nanohybrids, which were studied in different media (Sallem et al. 2017a).

4 Theranostic Applications of Titanate Nanotubes

Regarding theranostic applications, a key feature of TiONts is their shape. Indeed, beyond composition and surface chemistry (a custom-engineered one according to the application), nanomaterial shape has a tremendous impact on nanoparticle-plasma protein interaction (Nel *et al.* 2009), margination (Blanco *et al.* 2015), biodistribution (Blanco *et al.* 2015) and cellular internalization pathways (Gratton *et al.* 2008). Thus, one can benefit from these unique tubular nanobiomaterials (i) to increase drug, nucleic acid, protein or imaging agent delivery, as well as (ii) to improve the retention of the therapeutic or imaging modality at pathological site (Loiseau *et al.* 2017). This section explores the use of TiONts in the context of transfection, drug delivery, and radiotherapy monitored with medical imaging (theranostic).

4.1 TiONts as New Transfection Agents

The rationale behind using TiONts as a transfection agent was that neonatal cardiomyocytes (CM) are a highly challenging target for nucleic acid delivery (Papa *et al.* 2013). High transfection efficiencies are only achieved with the use of viral vectors as a mean of nucleic acid delivery (*i.e.* transduction). Conventional non-viral methods include liposomal delivery (Hunton *et al.* 2002; Lan *et al.* 2009) (such as Lipofectamine) and electroporation (Louch *et al.* 2011). However, liposomal delivery only achieves limited expression in this challenging CM model and electroporation represents a technical challenge *in vivo*. Because the internalization of tubular nanomaterials is often greater than their spherical counterparts (Gratton *et al.* 2008), there is thus potential to utilize this superior internalization of TiONts within CM. This could fill the current technological gap in non-viral nucleic acid delivery vehicles that achieve safe delivery but lack efficiency. Such a solution could provide non-viral methods that potentially address safety risks with viral techniques, in the context of clinical translation.

For this application, the negative charge of TiONts following their synthesis and purification to pH 6 ($\zeta = -34.5$ mV) was reversed using polyethyleneimine (PEI, $M_n \sim 1,800$ g.mol⁻¹) in order to complex the negatively charged plasmid DNA (linear pmaxGFPTM) at the tube surface, as well as provide the TiONts' suspension with greater stability and dispersion ($\zeta = +39.0$ mV for both 1:1 and 1:10 TiONt:PEI w:w ratios) (Papa *et al.* 2013). TiONt-PEI-DNA complexes were formed in serum-free cell media to ensure no interference with plasma protein adsorption on the tube surface (*i.e.* protein corona) and the resulting net charge at the complex surface was -21.0 mV and $+25.0$ mV for 1:1 and 1:10 TiONt:PEI, respectively. These zeta potential values, coupled with a study of nanohybrid saturation of DNA *via* gel electrophoresis, confirmed that the two carriers had opposite net charge and that the 1:1 TiONt-PEI-DNA was saturated in nucleic acids, compared to the 1:10 TiONt-PEI-DNA complex (that could potentially still increase its loading capacity). The positively charged 1:10 TiONt-PEI-DNA complex failed to achieve transfection, presumably due to a transient cytotoxicity observed solely for the high PEI load formulation as seen with LDH assays. In contrast and interestingly, the negatively charged complex lead to a successful transfection (*i.e.* 33% of CM population was GFP positive) 24-h following a 5-h incubation/transfection of the purified complexes with CM.

Compared to classical non-viral spherical nanoparticles, TiONts offer a new opportunity to mitigate the risks and challenges associated with the use of viral carriers for clinical translation.

4.2 TiONts as New Radiosensitizers

One of the major challenges in radiation oncology is to get therapeutic effects in increasing the ionizing one while minimizing the administered doses whereas the dramatic side effects on healthy surrounding tissue should be minimized. TiONts are good candidates to induce a radiosensitizing effect (Mirjolet *et al.* 2013, 2017; Loiseau *et al.* 2019) – even though titanium has a low atomic number ($Z = 22$) (Maezawa *et al.* 1996; Takakura 1996) – along with an absence of cytotoxicity (see Sect. 5) (Mirjolet *et al.* 2013; Papa *et al.* 2013; Loiseau *et al.* 2017). N. Millot *et al.* studied the incubation of glioblastoma cell lines (SNB-19 and U87MG) with TiONts and under irradiation (Fig. 17). The resulting clonogenic assays showed that radiosensitization is effective by TiONts at both low and high doses with a decrease in the SF₂ parameter for both SNB-19 and U87MG cells. The latter is confirmed by an increase and decrease of α and β parameters, respectively. Biological consequences could be explained by a decrease of DNA repair efficiency after irradiation and amplification of G2/M cell-cycle arrest (Boudon *et al.* 2014). Due to their shape, TiONts have the capability to be internalized in cells better than their spherical counterparts TiO₂ (Papa *et al.* 2013). Moreover, after intratumoral injection, the oblong-shaped TiONts are maintained several days inside the tumor (more than 80%

after 96 h by SPECT/CT imaging (Mirjolet *et al.* 2017) and more than 40% after 20 days by gamma counting (Loiseau *et al.* 2019)).

Thus, these nanomaterials are very interesting as therapeutic platform (intrinsic radiosensitizing properties, delivery of chemotherapeutic and radiotherapeutic agents in tumor sites). To promote TiONts to the theranostic level, superparamagnetic nanoparticles (iron oxide nanoparticles for example) can be associated to get detectable *via* MRI (magnetic resonance imaging) (Papa *et al.* 2011) while still benefiting from their radiosensitizing and shape properties.

4.2.1 TiONts-DTX for the Treatment of Primary Tumor

Combining the ability of radiosensitization and concurrent chemotherapy is of great interest in an effort to improve current management of advanced prostate cancer. Thus, the combination between docetaxel (DTX), an anti-mitotic chemotherapy taxane-type drug, and TiONts has been investigated (Mirjolet *et al.* 2017; Loiseau *et al.* 2017, 2019). The idea is to increase the drug intracellular concentration by maintaining the tubes within the tumor, avoiding repeated injections that can result in chemotherapy resistance, several side effects for patients (Larsen *et al.* 2000; Parhi *et al.* 2012). A grafting strategy of TiONts carrying DTX has been developed by A. Loiseau *et al.* (Loiseau *et al.* 2017) and biological assays showed a satisfactory cytotoxic activity of the TiONt-DTX nanohybrid against two prostate cancer cell lines (PC-3 (Mirjolet *et al.* 2017) (Fig. 18a) and 22RV1 (Loiseau *et al.* 2017) for which IC_{50} is around 360–390 nM) when compared to that of free DTX (IC_{50} : 2–4 nM). Thereafter, the RT efficacy of these nanohybrids was also evaluated *in vivo* after intratumoral injection in PC-3 xenografted prostate tumors into Swiss nude mice (Mirjolet *et al.* 2017; Loiseau *et al.* 2017). The treatment with TiONts-DTX was

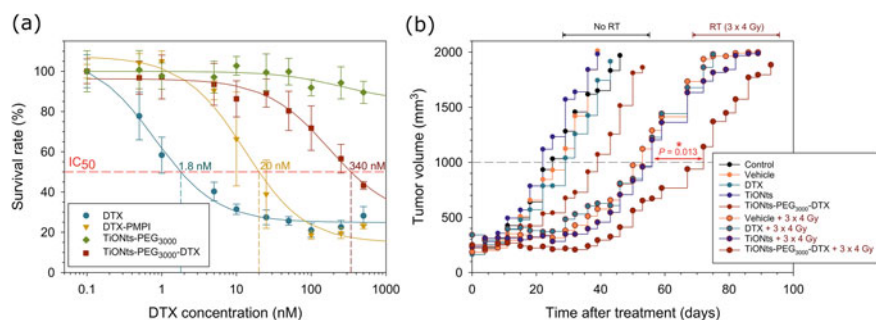


Fig. 18 (a) MTS cytotoxicity assay on PC-3 human prostate cancer cell lines after incubation of DTX, modified-DTX, TiONts-PEG₃₀₀₀ and TiONts-PEG₃₀₀₀-DTX, Reprinted (adapted) with permission from Loiseau *et al.* 2017, Copyright © 2012 American Chemical Society. (b) Evaluation of therapeutic effect of vehicle, free DTX, free TiONts, and TiONts-DTX, associated or not with radiotherapy (RT) administered with three daily fractions of 4 Gy, 24 h after intratumoral injection into PC-3 xenografted tumors.

significantly more effective than that with free DTX. Interestingly, mice treated with TiONts-DTX, without RT, exhibited a trend toward tumor growth delay compared with mice receiving free DTX (40 days vs. 30 days). Finally, tumor growth was significantly slowed down by TiONts-DTX associated with RT (three daily fractions of 4 Gy), compared with free DTX in the same conditions (73 days vs. 56 days to reach a tumor volume of 1,000 mm³, respectively) (Fig. 18b). These results suggest that TiONts-DTX noticeably improved RT efficacy and might enhance treatments of high-risk localized prostate cancers.

4.2.2 TiONts-AuNPs-DTX as Radiosensitizing Agents

The radiosensitizing effect of these nanohybrids has been further improved (when compared to the results presented in Sect. 4.2.1) by grafting gold nanoparticles (Au@DTDTPA NPs) on TiONts. These Au@DTDTPA NPs are biologically well-tolerated and present a low toxicity (Miladi *et al.* 2014; Schuemann *et al.* 2016), they can improve the efficiency of radiation therapy by two-fold after intratumoral injection in animals (Miladi *et al.* 2014; Butterworth *et al.* 2016). However, their potential is probably under-exploited because of their fast renal clearance (Alric *et al.* 2013). Consequently, the association of Au@DTDTPA NPs with TiONts-DTX is expected to overcome this limitation by maintaining them on tumor sites after injection: the resulting TiONts-AuNPs-DTX nanohybrids were elaborated step-by-step by A. Loiseau *et al.* (Loiseau *et al.* 2019). *In vitro* assays on a PC-3 human prostate cancer cell lines were performed (Fig. 19a) (Loiseau *et al.* 2019): Au@DTDTPA NPs and TiONts-AuNPs-PEG₃₀₀₀ did not present any cytotoxicity while TiONts-AuNPs-PEG₃₀₀₀-DTX exhibited a greater cytotoxic activity compared to that observed for TiONts-DTX (IC₅₀: 82 nM vs. 360 nM, respectively).

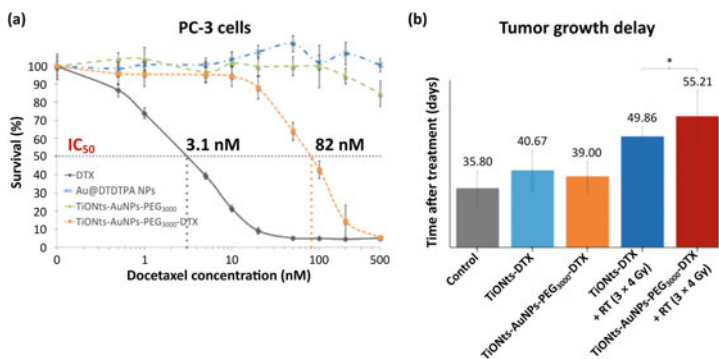


Fig. 19 (a) MTS cytotoxicity assay on PC-3 human prostate cancer cell lines after incubation of DTX, Au@DTDTPA NPs, TiONts-AuNPs-PEG₃₀₀₀ and TiONts-AuNPs-PEG₃₀₀₀-DTX. (b) Evaluation of therapeutic effect of control, TiONts-DTX and TiONts-AuNPs-PEG₃₀₀₀-DTX, associated or not with radiotherapy (RT) administered with three daily fractions of 4 Gy, 24 h after intratumoral injection into PC-3 xenografted tumors. Adapted from (Loiseau *et al.* 2019).

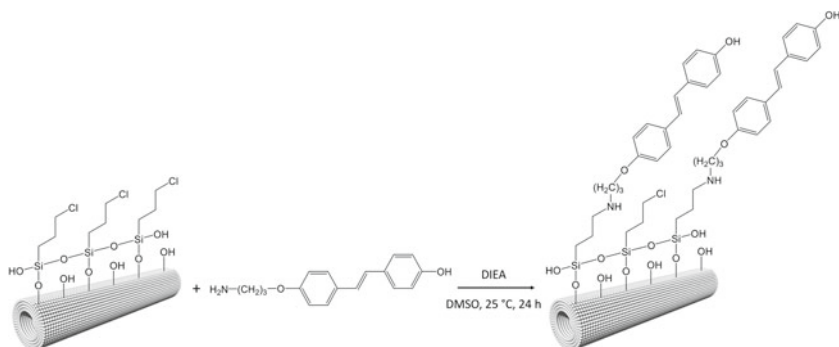


Fig. 20 Scheme of the grafting of the stilbene compound on the surface of TiONts *via* a spacer.

Finally, the synergistic combination between TiONts, DTX and AuNPs in the same entity with RT showed a better therapeutic efficacy by fulfilling their role as carriers and concentrating the radiotherapeutic and chemotherapeutic agents (Fig. 19b). Indeed, tumor growth was significantly slowed down ($p = 0.035$) by the treatment of TiONts-AuNPs-PEG₃₀₀₀-DTX + RT (55 days to reach a tumor volume of 1,000 mm³), compared with TiONts-DTX + RT (50 days) in the same conditions. The elaborated design asserts TiONt-based nanohybrids to be an attractive, and versatile platform for the treatment of prostate cancer.

4.3 TiONts as New Nanocarriers

In 2016, T. Baati *et al.* have shown the effectiveness of a TiONt-based nanocarrier against glioblastoma multiform with a controlled administration of genistein (biologically active flavonoid) in glioblastoma cells (Baati *et al.* 2016). This study showed that these TiONts have a drug loading efficiency of 51.2 wt.% and allows a controlled release of the therapeutic agent. F. Sallem *et al.* have developed the nanocarrier of a therapeutic molecule: a stilbene phenol, 4'-hydroxy-4-(3-aminopropoxy)-*trans*-stilbene (HAPtS), which is a *trans*-resveratrol derivative. *Trans*-resveratrol is a natural stilbenic polyphenol, known to prevent or slow down number of diseases including cardiovascular ones (Hung *et al.* 2000) and cancer (Baur and Sinclair 2006) because of its anti-inflammatory (Xiao *et al.* 2013), antiviral, antitumor and antifungal properties (Pirola and Froejdoe 2008). Despite all the interesting biological properties of *trans*-resveratrol, its low bioavailability and solubility (Lu *et al.* 2009), its rapid metabolism and its rapid elimination in the urine remain its major limitations. The grafting of this molecule on TiONts' surface can circumvent these limitations.

After pre-functionalization with 3-chloropropyltriethoxysilane (CPTES), the stilbenic phenol (HAPtS) was successfully grafted onto TiONts-CPTES surface using a

condensation reaction between HAPtS and CPTES through nucleophilic substitution. The resulting grafting rate was of about 72.5 mg/g of TiONts (Sallem 2017).

5 Biosafety and Nanotoxicity of TiONts

This section intends to discuss the internalization pathways of TiONts, as well as summarize some of the subsequent key aspects of TiONts' cytotoxicity profile that have been discovered thus far (Maurizi *et al.* 2018).

In early studies, TiONts have been detected inside vacuoles of SNB-19 and U87MG cells suggesting an internalization *via* endocytosis/macropinocytosis. In parallel, TiONts were also seen penetrating the plasma membrane, suggesting their diffusion through the lipidic bilayer (Mirjolet *et al.* 2013). Further studies have confirmed this diffusion phenomena as TiONts were still detected within murine microglial BV-2 cells despite their incubation with the endocytosis inhibitor amiloride (Sruthi *et al.* 2018). These observations are in agreement with what has been described regarding the internalization pathways of carbon nanotubes (Raffa *et al.* 2009). Once they cross the plasma membrane, nanoparticles can potentially induce cellular stress, or even cell death, depending on multiple physicochemical factors that modulate their (cyto)toxicity or safety profile (i.e. chemical composition, nanoparticle surface engineering, intracellular concentration). Thus, each TiONts' formulation (depending on the specific synthesis parameters, see Sect. 2) needs to be assessed within the relevant physiological *in vitro* or *in vivo* models. For example, Magrez *et al.* demonstrated that titanate-based nanofilaments have different levels of cytotoxicity in regards to H596 lung carcinoma cells, depending on their chemical composition (Magrez *et al.* 2009). Specifically, the post-synthesis acidic treatment used (to substitute Na⁺ by H⁺) generated a composition that was more cytotoxic to H596 cells when compared to non-acid treated filament counterparts (Magrez *et al.* 2009). This illustrates the complexity and multifaceted behavior of these biomaterials. As previously said, Papa *et al.* evaluated the cytotoxicity of bare (and non-acid treated) TiONts, TiONts-PEI as well as their spherical counterpart P25 TiO₂ in regards to neonatal cardiomyocytes *via* MTT assay (Papa *et al.* 2013). No apparent cytotoxicity was detected within the range of concentrations tested (up to 10 µg/mL) at 24 h (Papa *et al.* 2013). In addition, up to 100 µg/mL TiONts did not induce significant cytotoxicity towards SNB-19 and U87MG cell lines at 72 h, as measured by cell proliferation assay (Mirjolet *et al.* 2013). Overall, the mechanism of diffusion of the TiONts across the cell membrane does not appear to affect cell viability in multiple cell lines, despite inducing transient lipid bilayer disruption.

Microglial activation and associated oxidative burst are major challenges in drug delivery applications across the brain (Bussy *et al.* 2015). In this context, TiONts-APTES have been evaluated *in vitro* using murine microglial BV-2 cells (Sruthi *et al.* 2018). TiONts-APTES exposure (from 5 µg/mL up to 80 µg/mL of TiONts-APTES up to 24 h) lead to an increased ROS (Reactive Oxygen Species) production and transient mitochondrial hyperpolarization. Furthermore, the TiONts-APTES showed

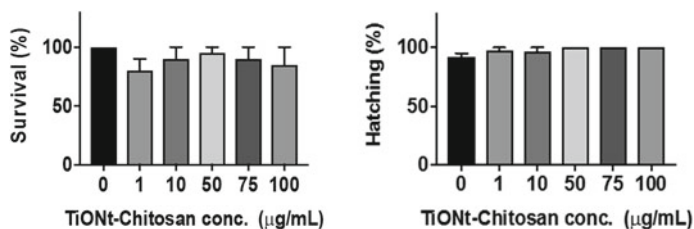


Fig. 21 Percentage of (a) embryo survival and (b) hatching of zebrafish eggs as a function of TiONts-CT concentration. The number of repetitions is three ($n = 3$) and 60 embryos are used in each repetition (therefore 180 animals in total).

good biocompatibility on BV-2 cells as revealed by the plasma membrane integrity, lysosomal membrane integrity, morphology, and viability analysis.

The toxicity assessment on the zebrafish embryo model is a very recent and interesting method for the *in vivo* screening of nanoparticles. This test analyzes toxicity in a much more complex system than cultured cells. It is a less expensive test than large-scale biocompatibility studies in mice or rats (Rizzo *et al.* 2013). Zebrafish embryos are transparent and develop outside their mother, making it easy to follow and understand the cellular mechanism using a simple light microscope. TiONts-chitosan nanohybrid developed in Sect. 3.4 have been evaluated with concentrations varying from 1 to 100 µg/mL. The survival, hatching and development of zebrafish were monitored for 96 h. The survival of zebrafish must be close to 100%, hatching greater than 90% (between 24 and 48 h) and the larval malformations close to 0% conclude on the non-toxicity of nanohybrids. The survival and hatching of zebrafish are not affected by the presence of nanohybrids for the entire concentration range studied from 1 to 100 µg/mL (Fig. 21). No lethality or morphological change was observed even for the highest concentrations. This confirms the non-toxicity of TiONts modified by chitosan.

In these models, TiONts show a good safety profile within the relevant concentrations and doses tested. Nonetheless, further studies including the interaction of TiONts with immune cells, blood cells and plasma proteins, will allow a better understanding of the biological behavior and fate of these bioengineered materials.

6 Conclusions

The aim of this chapter was to illustrate the potential of titanate nanotubes as new potent tools for nanomedicine. The difficulties encountered during their synthesis as well as the different strategies for their necessary surface modification have been illustrated, always *via* a step-by-step approach. Several bioapplications of these engineered TiONts have been outlined: nanocarriers of plasmid DNA or of *trans*-resveratrol derivatives, radiosensitizers *etc.* TiONts have also shown a good safety profile in all the bioassays developed to evaluate their potential toxicity. Finally, these

functionalized TiONts appear as promising versatile tools in the biomedical field to fight some diseases such as cancer. In this context and for these elongated inorganic nanoparticles, intratumoral injection seems to be a relevant way of administration.

Acknowledgements JB, AL, FS, LM and NM acknowledge the funding support from French Government through the CNRS, the “Université de Bourgogne”, the “Conseil Régional Bourgogne Franche-Comté, the European Union (PO FEDER-FSE Bourgogne 2014/2020 programs), the Cancéropôle Est and the EIPHI Graduate School (ANR-17-EURE-0002). ALP acknowledges the support from the George Washington University start-up funds. All the people who contributed in the results presented in this chapter are greatly acknowledged: Sudhakaran Sruthi, Gérard Lizard, Thomas Courant, Johanna Chluba, Laurence Motte, Erwan Guénin, Frédéric Geinguenaud, Laure Dumond, David Vandroux, Céline Mirjolet, Véronique Morgand, Olivier Heintz and Rémi Chasagnon, as well as all the people from the PharmImage® consortium, the 3MIM agreement and the IMAPPI program who are involved but not mentioned in the presented results.

References

- Agarwal R, Journey P, Raythatha M et al (2015) Effect of shape, size, and aspect ratio on nanoparticle penetration and distribution inside solid tissues using 3D spheroid models. *Adv Healthc Mater* 4:2269–2280. <https://doi.org/10.1002/adhm.201500441>
- Albu AM, Draghicescu W, Munteanu T et al (2019) Nitrodopamine vs dopamine as an intermediate layer for bone regeneration applications. *Mater Sci Eng C* 98:461–471. <https://doi.org/10.1016/j.msec.2019.01.014>
- Alric C, Miladi I, Kryza D et al (2013) The biodistribution of gold nanoparticles designed for renal clearance. *Nanoscale* 5:5930–5939. <https://doi.org/10.1039/c3nr00012e>
- Amstad E, Gillich T, Bilecka I et al (2009) Ultrastable iron oxide nanoparticle colloidal suspensions using dispersants with catechol-derived anchor groups. *Nano Lett* 9:4042–4048. <https://doi.org/10.1021/nl902212q>
- Amstad E, Textor M, Reimhult E (2011) Stabilization and functionalization of iron oxide nanoparticles for biomedical applications. *Nanoscale* 3:2819–2843. <https://doi.org/10.1039/c1nr10173k>
- Amstad E, Gehring AU, Fischer H et al (2011) Influence of electronegative substituents on the binding affinity of catechol-derived anchors to Fe₃O₄ nanoparticles. *J Phys Chem C* 115:683–691. <https://doi.org/10.1021/jp1109306>
- Awan UA, Ali S, Rehman M et al (2018) Stable and reproducible synthesis of gold nanorods for biomedical applications: a comprehensive study. *IET Nanobiotechnol* 12:182–190. <https://doi.org/10.1049/iet-nbt.2016.0220>
- Baati T, Kefi BB, Aouane A et al (2016) Biocompatible titanate nanotubes with high loading capacity of genistein: cytotoxicity study and anti-migratory effect on U87-MG cancer cell lines. *Rsc Adv* 6:101688–101696. <https://doi.org/10.1039/c6ra24569b>
- Bahri S, Jonsson CM, Jonsson CL et al (2011) Adsorption and surface complexation study of L-DOPA on rutile (alpha-TiO₂) in NaCl solutions. *Environ Sci Technol* 45:3959–3966. <https://doi.org/10.1021/es1042832>
- Balasundaram G, Sato M, Webster TJ (2006) Using hydroxyapatite nanoparticles and decreased crystallinity to promote osteoblast adhesion similar to functionalizing with RGD. *Biomaterials* 27:2798–2805. <https://doi.org/10.1016/j.biomaterials.2005.12.008>
- Baur JA, Sinclair DA (2006) Therapeutic potential of resveratrol: the *in vivo* evidence. *Nat Rev Drug Discov* 5:493–506. <https://doi.org/10.1038/nrd2060>

- Bavykin DV, Walsh FC (2009) Elongated titanate nanostructures and their applications. *Eur J Inorg Chem* 2009:977–997. <https://doi.org/10.1002/ejic.200801122>
- Bavykin DV, Friedrich JM, Walsh FC (2006) Protonated titanates and TiO₂ nanostructured materials: synthesis, properties, and applications. *Adv Mater* 18:2807–2824. <https://doi.org/10.1002/adma.200502696>
- Bellat V, Chassagnon R, Heintz O et al (2015) A multi-step mechanism and integrity of titanate nanoribbons. *Dalton Trans* 44:1150–1160. <https://doi.org/10.1039/c4dt02573c>
- Benyettou F, Lalatonne Y, Sainte-Catherine O et al (2009) Superparamagnetic nanovector with anti-cancer properties: gamma Fe₂O₃@Zoledronate. *Int J Pharm* 379:324–327. <https://doi.org/10.1016/j.ijpharm.2009.04.010>
- Benyettou F, Lalatonne Y, Chebbi I et al (2011) A multimodal magnetic resonance imaging nanoplat-form for cancer theranostics. *Phys Chem Phys* 13:10020–10027. <https://doi.org/10.1039/c0cp02034f>
- Bianco A, Kostarelos K, Prato M (2005) Applications of carbon nanotubes in drug delivery. *Curr Opin Chem Biol* 9:674–679. <https://doi.org/10.1016/j.cbpa.2005.10.005>
- Blanco E, Shen H, Ferrari M (2015) Principles of nanoparticle design for overcoming biological barriers to drug delivery. *Nat Biotechnol* 33:941–951. <https://doi.org/10.1038/nbt.3330>
- Boudon J, Papa A-L, Paris J, Millot N (2014) Titanate nanotubes as a versatile platform for nanomedicine. In: *Nanomedicine*. One Central Press (OCP), pp 403–428
- Bussy C, Al-Jamal KT, Boczkowski J et al (2015) Microglia determine brain region-specific neurotoxic responses to chemically functionalized carbon nano tubes. *ACS Nano* 9:7815–7830. <https://doi.org/10.1021/acs.nano.5b02358>
- Butterworth KT, Nicol JR, Ghita M et al (2016) Preclinical evaluation of gold-DTTPA nanoparticles as theranostic agents in prostate cancer radiotherapy. *Nanomed* 11:2035–2047. <https://doi.org/10.2217/nmm-2016-0062>
- Campos CH, Diaz CF, Guzman JL et al (2016) PAMAM-conjugated alumina nanotubes as novel nontoxic nanocarriers with enhanced drug loading and releasing performances. *Macromol Chem Phys* 217:1712–1722. <https://doi.org/10.1002/macp.201600136>
- Cheng YF, Zhang JY, Wang YB et al (2019) Deposition of catechol-functionalized chitosan and silver nanoparticles on biomedical titanium surfaces for antibacterial application. *Mater Sci Eng C* 98:649–656. <https://doi.org/10.1016/j.msec.2019.01.019>
- Cruje C, Chithrani DB (2014) Polyethylene glycol density and length affects nanoparticle uptake by cancer cells. *J Nanomed Res* 1 <https://doi.org/10.15406/jnmr.2014.01.00006>
- Daou TJ, Buathong S, Ung D et al (2007) Investigation of the grafting rate of organic molecules on the surface of magnetite nanoparticles as a function of the coupling agent. *Sens Act B-Chem* 126:159–162. <https://doi.org/10.1016/j.snb.2006.11.020>
- Das R, Alonso J, Nemati Porshokouh Z et al (2016) Tunable high aspect ratio iron oxide nanorods for enhanced hyperthermia. *J Phys Chem C* 120:10086–10093. <https://doi.org/10.1021/acs.jpcc.6b02006>
- Decuzzi P, Coclite A, Lee A et al (2017) Nano-Particles for biomedical applications. In: Bhushan B (ed) *Springer handbook of nanotechnology*. Springer, Heidelberg, pp 643–691. https://doi.org/10.1007/978-3-662-54357-3_21
- Deng ZJ, Mortimer G, Schiller T et al (2009) Differential plasma protein binding to metal oxide nanoparticles. *Nanotechnology* 20:455101. <https://doi.org/10.1088/0957-4484/20/45/455101>
- Ernsting MJ, Murakami M, Roy A, Li S-D (2013) Factors controlling the pharmacokinetics, biodistribution and intratumoral penetration of nanoparticles. *J Control Release J Control Release Soc* 172:782–794. <https://doi.org/10.1016/j.jconrel.2013.09.013>
- Ge X, Ren C, Lu X et al (2019) Surfactant-free electrochemical synthesis of fluoridated hydroxyapatite nanorods for biomedical applications. *Ceram Int* 45:17336–17343. <https://doi.org/10.1016/j.ceramint.2019.05.292>
- Gong D, Grimes CA, Varghese OK et al (2001) Titanium oxide nanotube arrays prepared by anodic oxidation. *J Mater Res* 16:3331–3334. <https://doi.org/10.1557/JMR.2001.0457>

- Gratton SEA, Ropp PA, Pohlhaus PD et al (2008) The effect of particle design on cellular internalization pathways. *Proc Natl Acad Sci U S A* 105:11613–11618. <https://doi.org/10.1073/pnas.0801763105>
- Gref R, Luck M, Quellec P et al (2000) “Stealth” corona-core nanoparticles surface modified by polyethylene glycol (PEG): influences of the corona (PEG chain length and surface density) and of the core composition on phagocytic uptake and plasma protein adsorption. *Colloids Surf B-Biointerfaces* 18:301–313. [https://doi.org/10.1016/S0927-7765\(99\)00156-3](https://doi.org/10.1016/S0927-7765(99)00156-3)
- Guenin E, Lalatonne Y, Bolley J et al (2014) Catechol versus bisphosphonate ligand exchange at the surface of iron oxide nanoparticles: towards multi-functionalization. *J Nanoparticle Res* 16:2596. <https://doi.org/10.1007/s11051-014-2596-7>
- Guerrero G, Mutin PH, Vioux A (2001) Anchoring of phosphonate and phosphinate coupling molecules on titania particles. *Chem Mater* 13:4367–4373. <https://doi.org/10.1021/cm001253u>
- Guerrero G, Alauzun JG, Granier M et al (2013) Phosphonate coupling molecules for the control of surface/interface properties and the synthesis of nanomaterials. *Dalton Trans* 42:12569–12585. <https://doi.org/10.1039/c3dt51193f>
- Hahn J (2016) Fundamental properties of one-dimensional zinc oxide nanomaterials and implementations in various detection modes of enhanced biosensing. In: Johnson MA, Martinez TJ (eds) *Annual review of physical chemistry*, vol 67. Annual Reviews, Palo Alto, pp 691–717. <https://doi.org/10.1146/annurev-physchem-031215-010949>
- Howarter JA, Youngblood JP (2006) Optimization of silica silanization by 3-aminopropyl triethoxysilane. *Langmuir* 22:11142–11147. <https://doi.org/10.1021/la061240g>
- Hung LM, Chen JK, Huang SS et al (2000) Cardioprotective effect of resveratrol, a natural antioxidant derived from grapes. *Cardiovasc Res* 47:549–555. [https://doi.org/10.1016/S0008-6363\(00\)00102-4](https://doi.org/10.1016/S0008-6363(00)00102-4)
- Hunton DL, Lucchesi PA, Pang Y et al (2002) Capacitative calcium entry contributes to nuclear factor of activated T-cells nuclear translocation and hypertrophy in cardiomyocytes. *J Biol Chem* 277:14266–14273. <https://doi.org/10.1074/jbc.M107167200>
- Jeong E, Ul Kim C, Byun J et al (2020) Quantitative evaluation of the antibacterial factors of ZnO nanorod arrays under dark conditions: physical and chemical effects on Escherichia coli inactivation. *Sci Total Environ* 712:136574. <https://doi.org/10.1016/j.scitotenv.2020.136574>
- Jokerst JV, Lobovkina T, Zare RN, Gambhir SS (2011) Nanoparticle PEGylation for imaging and therapy. *Nanomed* 6:715–728. <https://doi.org/10.2217/nmm.11.19>
- Kasuga T, Hiramatsu M, Hoson A et al (1998) Formation of titanium oxide nanotube. *Langmuir* 14:3160–3163. <https://doi.org/10.1021/la9713816>
- Kostarelos K, Lacerda L, Pastorin G et al (2007) Cellular uptake of functionalized carbon nanotubes is independent of functional group and cell type. *Nat Nanotechnol* 2:108–113. <https://doi.org/10.1038/nnano.2006.209>
- Lan X, Yin X, Wang R et al (2009) Comparative study of cellular kinetics of reporter probe [131I]FIAU in neonatal cardiac myocytes after transfer of HSV1-tk reporter gene with two vectors. *Nucl Med Biol* 36:207–213. <https://doi.org/10.1016/j.nucmedbio.2008.10.016>
- Larsen AK, Escargueil AE, Skladanowski A (2000) Resistance mechanisms associated with altered intracellular distribution of anticancer agents. *Pharmacol Ther* 85:217–229. [https://doi.org/10.1016/S0163-7258\(99\)00073-X](https://doi.org/10.1016/S0163-7258(99)00073-X)
- Lee KW, Kim YJ, Kim DO et al (2003) Major phenolics in apple and their contribution to the total antioxidant capacity. *J Agric Food Chem* 51:6516–6520. <https://doi.org/10.1021/jf034475w>
- Lee N, Hummer DR, Sverjensky DA et al (2012) Speciation of L-DOPA on nanorutile as a function of pH and surface coverage using surface-enhanced Raman spectroscopy (SERS). *Langmuir* 28:17322–17330. <https://doi.org/10.1021/la303607a>
- Liu Y, Li Y, Li X-M, He T (2013) Kinetics of (3-Aminopropyl)triethoxysilane (APTES) silanization of superparamagnetic iron oxide nanoparticles. *Langmuir* 29:15275–15282. <https://doi.org/10.1021/la403269u>

- Loiseau A (2017) Nanotubes de titanate comme nanovecteurs polyvalents : radiosensibilisants du cancer de la prostate et sondes pour l'imagerie nucléaire. Université Bourgogne Franche-Comté, Theses
- Loiseau A, Boudon J, Mirjolet C, et al (2017) Taxane-grafted metal-oxide nanoparticles as a new theranostic tool against cancer: the promising example of docetaxel-functionalized titanate nanotubes on prostate tumors. *Adv Health Mater* 6. <https://doi.org/10.1002/adhm.201700245>
- Loiseau A, Boudon J, Oudot A et al (2019) Titanate nanotubes engineered with gold nanoparticles and docetaxel to enhance radiotherapy on xenografted prostate tumors. *Cancers* 11:1962. <https://doi.org/10.3390/cancers11121962>
- Loiseau A, Boudon J, Mirjolet C, et al (2021) The influence of the PEGylated length on titanate nanotubes properties and docetaxel nanohybrid cytotoxicity against prostate cancer cells. *Molecules* submitted
- Louch WE, Sheehan KA, Wolska BM (2011) Methods in cardiomyocyte isolation, culture, and gene transfer. *J Mol Cell Cardiol* 51:288–298. <https://doi.org/10.1016/j.yjmcc.2011.06.012>
- Lu Z, Cheng B, Hu Y et al (2009) Complexation of resveratrol with cyclodextrins: solubility and antioxidant activity. *Food Chem* 113:17–20. <https://doi.org/10.1016/j.foodchem.2008.04.042>
- Ma H, Tarr J, DeCoster MA et al (2009) Synthesis of magnetic porous hollow silica nanotubes for drug delivery. *J Appl Phys* 105:07B309. <https://doi.org/10.1063/1.3072048>
- Maezawa H, Furusawa Y, Kobayashi K et al (1996) Lethal effect of K-shell absorption of intracellular phosphorus on wild-type and radiation sensitive mutants of *Escherichia coli*. *Acta Oncol* 35:889–894. <https://doi.org/10.3109/02841869609104042>
- Magrez A, Horváth L, Smajda R et al (2009) Cellular toxicity of TiO₂-based nanofilaments. *ACS Nano* 3:2274–2280. <https://doi.org/10.1021/nn9002067>
- Maurizi L, Papa A-L, Dumont L et al (2015) Influence of surface charge and polymer coating on internalization and biodistribution of polyethylene glycol-modified iron oxide nanoparticles. *J Biomed Nanotechnol* 11:126–136. <https://doi.org/10.1166/jbn.2015.1996>
- Maurizi L, Papa A-L, Boudon J et al (2018) Toxicological risk assessment of emerging nanomaterials: cytotoxicity, cellular uptake, effects on biogenesis and cell organelle activity, acute toxicity and biodistribution of oxide nanoparticles. In: Gomes AC, Sarria MP (eds) *Unraveling the safety profile of nanoscale particles and materials - from biomedical to environmental applications*. InTech, Rijeka, pp 17–36. <https://doi.org/10.5772/intechopen.71833>
- Miladi I, Alric C, Dufort S et al (2014) The *in vivo* radiosensitizing effect of gold nanoparticles based MRI contrast agents. *Small* 10:1116–1124. <https://doi.org/10.1002/sml.201302303>
- Mirjolet C, Papa AL, Créhange G et al (2013) The radiosensitization effect of titanate nanotubes as a new tool in radiation therapy for glioblastoma: a proof-of-concept. *Radiother Oncol J Eur Soc Ther Radiol Oncol*. <https://doi.org/10.1016/j.radonc.2013.04.004>
- Mirjolet C, Boudon J, Loiseau A et al (2017) Docetaxel-titanate nanotubes enhance radiosensitivity in an androgen-independent prostate cancer model. *Int J Nanomedicine* 12:6357–6364. <https://doi.org/10.2147/IJN.S139167>
- Mohammadi F, Moeni M, Li C et al (2020) Interaction of cellulose and nitrodopamine coated superparamagnetic iron oxide nanoparticles with alpha-lactalbumin. *RSC Adv* 10:9704–9716. <https://doi.org/10.1039/C9RA09045B>
- Mosqueira VCF, Legrand P, Morgat JL et al (2001) Biodistribution of long-circulating PEG-grafted nanocapsules in mice: effects of PEG chain length and density. *Pharm Res* 18:1411–1419. <https://doi.org/10.1023/A:1012248721523>
- Motte L, Benyettou F, de Beaucorps C et al (2011) Multimodal superparamagnetic nanoplatform for clinical applications: immunoassays, imaging & therapy. *Faraday Discuss* 149:211–225. <https://doi.org/10.1039/c005286g>
- Mutin PH, Guerrero G, Vioux A (2005) Hybrid materials from organophosphorus coupling molecules. *J Mater Chem* 15:3761–3768. <https://doi.org/10.1039/b505422b>
- Nel AE, Mädler L, Velegol D et al (2009) Understanding biophysicochemical interactions at the nano-bio interface. *Nat Mater* 8:543–557. <https://doi.org/10.1038/nmat2442>

- Niu L, Shao M, Wang S et al (2008) Titanate nanotubes: preparation, characterization, and application in the detection of dopamine. *J Mater Sci* 43:1510–1514. <https://doi.org/10.1007/s10853-007-2374-3>
- Papa A-L, Millot N, Saviot L et al (2009) Effect of reaction parameters on composition and morphology of titanate nanomaterials. *J Phys Chem C* 113:12682–12689. <https://doi.org/10.1021/jp903195h>
- Papa A-L, Maurizi L, Vandroux D et al (2011) Synthesis of titanate nanotubes directly coated with USPIO in hydrothermal conditions: a new detectable nanocarrier. *J Phys Chem C* 115:19012–19017. <https://doi.org/10.1021/jp2056893>
- Papa A-L, Dumont L, Vandroux D, Millot N (2013) Titanate nanotubes: towards a novel and safer nanovector for cardiomyocytes. *Nanotoxicology* 7:1131–1142. <https://doi.org/10.3109/17435390.2012.710661>
- Papa A-L, Boudon J, Bellat V et al (2015) Dispersion of titanate nanotubes for nanomedicine: comparison of PEI and PEG nanohybrids. *Dalton Trans Camb Engl* 44:739–746. <https://doi.org/10.1039/c4dt02552k>
- Parhi P, Mohanty C, Sahoo SK (2012) Nanotechnology-based combinational drug delivery: an emerging approach for cancer therapy. *Drug Discov Today* 17:1044–1052. <https://doi.org/10.1016/j.drudis.2012.05.010>
- Paris J, Bernhard Y, Boudon J et al (2015) Phthalocyanine-titanate nanotubes: a promising nanocarrier detectable by optical imaging in the so-called imaging window. *RSC Adv* 5:6315–6322. <https://doi.org/10.1039/c4ra13988g>
- Patil N, Jérôme C, Detrembleur C (2018) Recent advances in the synthesis of catechol-derived (bio)polymers for applications in energy storage and environment. *Prog Polym Sci* 82:34–91. <https://doi.org/10.1016/j.progpolymsci.2018.04.002>
- Pirola L, Froejdoe S (2008) Resveratrol: one molecule, many targets. *IUBMB Life* 60:323–332. <https://doi.org/10.1002/iub.47>
- Pontón PI, d'Almeida JRM, Marinkovic BA et al (2014) The effects of the chemical composition of titanate nanotubes and solvent type on 3-aminopropyltriethoxysilane grafting efficiency. *Appl Surf Sci* 301:315–322. <https://doi.org/10.1016/j.apsusc.2014.02.071>
- Pujari SP, Scheres L, Marcellis ATM, Zuilhof H (2014) Covalent surface modification of oxide surfaces. *Angew Chem-Int Ed* 53:6322–6356. <https://doi.org/10.1002/anie.201306709>
- Raffa V, Ciofani G, Vittorio O et al (2009) Physicochemical properties affecting cellular uptake of carbon nanotubes. *Nanomed* 5:89–97. <https://doi.org/10.2217/nnm.09.95>
- Ries H, Cook H (1954) Monomolecular films of mixtures. 1. stearic acid with isostearic acid and with tri-para-cresyl phosphate - comparison of components with octadecylphosphonic acid and with tri-ortho-xenyl phosphate. *J Colloid Sci* 9:535–546. [https://doi.org/10.1016/0095-8522\(54\)90056-2](https://doi.org/10.1016/0095-8522(54)90056-2)
- Rizzo LY, Golombek SK, Mertens ME, et al (2013) *In vivo* nanotoxicity testing using the Zebrafish Embryo Assay. *J Mater Chem B Mater Biol Med* 1. <https://doi.org/10.1039/C3TB20528B>
- Saiz-Poseu J, Mancebo-Aracil J, Nador F et al (2019) The chemistry behind catechol-based adhesion. *Angew Chem Int Ed* 58:696–714. <https://doi.org/10.1002/anie.201801063>
- Sallem F (2017) Optimized syntheses and advanced characterizations of titanate nanotubes and their functionalization : towards the development of nanovectors of therapeutic molecules. Université Bourgogne Franche-Comté, Theses
- Sallem F, Chassagnon R, Megriche A et al (2017) Effect of mechanical stirring and temperature on dynamic hydrothermal synthesis of titanate nanotubes. *J Alloys Compd* 722:785–796. <https://doi.org/10.1016/j.jallcom.2017.06.172>
- Sallem F, Boudon J, Heintz O et al (2017) Synthesis and characterization of chitosan-coated titanate nanotubes: towards a new safe nanocarrier. *Dalton Trans*. <https://doi.org/10.1039/C7DT03029K>
- Schuemann J, Berbeco R, Chithrani DB et al (2016) Roadmap to clinical use of gold nanoparticles for radiation sensitization. *Int J Radiat Oncol Biol Phys* 94:189–205. <https://doi.org/10.1016/j.ijrobp.2015.09.032>

- Singh N, Millot N, Maurizi L et al (2020) Taurine-conjugated mussel-inspired iron oxide nanoparticles with an elongated shape for effective delivery of doxorubicin into the tumor cells. *ACS Omega* 5:16165–16175. <https://doi.org/10.1021/acsomega.0c01747>
- Sruthi S, Loiseau A, Boudon J et al (2018) *In vitro* interaction and biocompatibility of titanate nanotubes with microglial cells. *Toxicol Appl Pharmacol* 353:74–86. <https://doi.org/10.1016/j.taap.2018.06.013>
- Suganya TR, Devasena T (2015) Exploring the mechanism of anti-inflammatory activity of phyto-stabilized silver nanorods. *Dig J Nanomater Biostructures* 10:277–282
- Sun X, Li Y (2003) Synthesis and characterization of ion-exchangeable titanate nanotubes. *Chem Eur J* 9:2229–2238. <https://doi.org/10.1002/chem.200204394>
- Sun N, Li X, Wang Z et al (2016) A multiscale TiO₂ nanorod array for ultrasensitive capture of circulating tumor cells. *ACS Appl Mater Interfaces* 8:12638–12643. <https://doi.org/10.1021/acsami.6b02178>
- Takakura K (1996) Double-strand breaks in DNA induced by the K-shell ionization of calcium atoms. *Acta Oncol* 35:883–888. <https://doi.org/10.3109/02841869609104041>
- Thapa B, Diaz-Diestra D, Santiago-Medina C et al (2018) T1- and T2-weighted magnetic resonance dual contrast by single core truncated cubic iron oxide nanoparticles with abrupt cellular internalization and immune evasion. *ACS Appl Bio Mater* 1:79–89. <https://doi.org/10.1021/acsabm.8b00016>
- Thomas G, Demoisson F, Heintz O et al (2015) Functionalized Fe₃O₄ nanoparticles: influence of ligand addition sequence and pH during their continuous hydrothermal synthesis. *RSC Adv* 5:78614–78624. <https://doi.org/10.1039/C5RA17452J>
- Thomas G, Demoisson F, Boudon J, Millot N (2016) Efficient functionalization of magnetite nanoparticles with phosphonate using a one-step continuous hydrothermal process. *Dalton Trans* 45:10821–10829. <https://doi.org/10.1039/C6DT01050D>
- Togashi T, Takami S, Kawakami K et al (2012) Continuous hydrothermal synthesis of 3,4-dihydroxyhydrocinnamic acid-modified magnetite nanoparticles with stealth-functionality against immunological response. *J Mater Chem* 22:9041–9045. <https://doi.org/10.1039/c2jm30325f>
- Wang X, Shao M, Zhang S, Liu X (2013) Biomedical applications of gold nanorod-based multifunctional nano-carriers. *J Nanoparticle Res* 15:1892. <https://doi.org/10.1007/s11051-013-1892-y>
- White LD, Tripp CP (2000) Reaction of (3-aminopropyl)dimethylethoxysilane with amine catalysts on silica surfaces. *J Colloid Interface Sci* 232:400–407. <https://doi.org/10.1006/jcis.2000.7224>
- Wu B, Zhang L-J, Zhang C-J et al (2020) Effect of Poly(ethylene glycol) (PEG) surface density on the fate and antitumor efficacy of redox-sensitive hybrid nanoparticles. *ACS Biomater Sci Eng* 6:3975–3983. <https://doi.org/10.1021/acsbomaterials.0c00516>
- Xiao J, Song J, Hodara V et al (2013) Protective effects of resveratrol on TNF-alpha-induced endothelial cytotoxicity in baboon femoral arterial endothelial cells. *J Diabet Res UNSP* 185172. <https://doi.org/10.1155/2013/185172>

A Microbiological Epilogue—Nosocomial Infections



Irina Rosca, Elena-Laura Ursu, and Adrian Fifere

Abstract This chapter shortly presents our 5 years researching experience within the field nosocomial infections. We present a few research directions that we developed the last years, consisting in: microorganisms' adaptations characterization, testing the antimicrobial activity of different classes of active molecules and finding new and efficient methods for medical devices disinfections. All these studies are gathered by a final purpose to prevent, control and eradicate the nosocomial infections.

Keywords Nosocomial infections · New active molecules · Medical devices disinfection

Abbreviations

MDRO	Multidrug-resistant organisms
PAW	Plasma activated water
EPS	Exopolysaccharides
LAB	Lactic acid bacteria

I. Rosca (✉) · E.-L. Ursu · A. Fifere
Centre of Advanced Research in Bionanoconjugates and Biopolymers, “Petru Poni” Institute of Macromolecular Chemistry, 700487 Iasi, Romania
e-mail: rosca.irina@icmpp.ro

E.-L. Ursu
e-mail: ursu.laura@icmpp.ro

A. Fifere
e-mail: fifere@icmpp.ro

1 Introduction

Who are we? Where are we coming from? Where are we going? How is it possible that after so many years of evolution, and after reaching more than 7.8 billion, the human species, the top of the trophic niches, the most evolved soul of earth, to be so sensitive to microorganisms? How is it possible for the microorganism so small and apparently not evolved to be so harmful to the human kind? When our symbiosis changed so much? It's been a long, long way from the origins, the beginnings, where things came from, where we came from, where life came from. We are constantly evolving, but during the last two decades it has been noted a major increase in the proportion of severe microbial infections paradoxically due to the excessive use of broad-spectrum antibiotics, catheters, and a growing number of immunocompromised patients.

Nosocomial infections or healthcare associated infections occur in patients under medical care, these infections occurring worldwide and being produced by bacteria (*Acinetobacter* sp., *Clostridium difficile*, *Klebsiella* sp., *Escherichia coli*, methicillin-resistant *Staphylococcus aureus*—MRSA), viruses (hepatitis B and C, influenza, HIV, rotavirus and herpes-simplex virus) and fungal strains (*Candida albicans*, *Cryptococcus neoformans*, *Aspergillus* sp) (Vincent 2003; Rosenthal *et al.* 2012; Haque *et al.* 2018). Some of them belong to the natural flora of the patient and may cause infection only when the immune system becomes prone to infections, being called opportunistic pathogens. The most common infections are those of the urinary tract, followed by pneumonias, surgical site infections, and primary bloodstream infections (Emori and Gaynes 1993). Regarding the mortality caused by nosocomial infections, this area is quite controversial since the patients developing these infections are in general sicker and have a greater risk of death compared with other patients (Vincent 2003).

2 Where Are We Now?

Due to the alarming level of nosocomial infections, a phenomenon that has grown and aroused globally, the interest of the researchers on this theme increased proportionally. Within this context, since 2012, in the IntelCentru—Advanced Research Center for Bionanoconjugates and Biopolymers department, within the “Petru Poni” Institute of Macromolecular Chemistry in Iași, we set up a dedicated laboratory, intended to (bio) synthesize and test biologically active molecules with applicability in fighting against nosocomial infections. In this laboratory, a multidisciplinary team tested the antimicrobial activity (antibacterial and antifungal) of various classes of active molecules (bio) synthesized.

2.1 Microorganisms Environmental Adaptations

Our studies started with the estimation of the characteristics of the opportunistic pathogens, which give them resistance to current antibiotics/antifungals. For instance, *Candida albicans* is a member of the normal human microbiome, usually being commensal and harmless, but under certain circumstances, if the defence mechanisms of the host are damaged, it becomes an opportunistic pathogen and produces candidiasis (Kabir *et al.* 2012). *C. albicans* is known to produce two major types of infections: superficial infections, such as oral or vaginal candidiasis, and deep-seated life-threatening systemic infections (such as endocarditis and acute invasive candidiasis as causes of sepsis) (Sanita *et al.* 2013).

Within this context first of our investigations was on the correlation between the infection site and the characteristics of *C. albicans* strains isolated from Romanian patients, in order to quantify the yeas strains evolution. Therefore a total number of 301 isolates from different clinical sites were investigated and clustered in terms of genotype determination, resistogram, phospholipase activity, haemolysis, proteinase activity, and biofilm formation. Biofilm formation is clearly one of the main strategies for microorganisms survival in a variety of sites, the different stages in biofilm formation including initial attachment to the surface, formation of a monolayer along the surface with formation of micro-colonies, biofilm maturation with formation of a three-dimensional structure, and cell dispersion (Fig. 1).

We proved that all the isolated and analysed strains of *C. albicans* had strain-dependent variable levels of enzymatic activity, and there were not all biofilm producers. Although much progress has been made in understanding the phenotypic and genotypic profile of *C. albicans*, still much less is known regarding their interaction with the host. *C. albicans* is a diploid organism and its pathogenicity is linked to a series of inherent and environmental factors and it is mostly related to the host immunological status. No significant correlation was found between the genotype and the infection site (Rosca *et al.* 2018a), but a significant correlation was found between genotype C and isolates from HIV-infected patients proving once

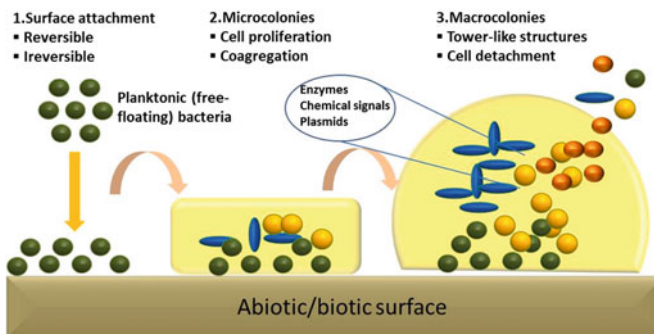


Fig. 1 Scheme of bacterial biofilm and antimicrobial resistance formation

again that *C. albicans* pathogenicity probably relies on factors related to the host (Bostanaru *et al.* 2019).

In the same time the resistance rates to the antifungal agents are increasing because of the selective pressure produced by antifungal treatment. In another study we described the *in vitro* inhibitory and fungicidal activity of the three echinocandins currently use in antifungal therapy such as caspofungin, micafungin, and anidulafungin against a large multicenter derived collection of pathogenic yeasts from Romania. Echinocandins are semisynthetic lipopeptides that block an enzyme complex from the fungal cell membrane, which is responsible for the synthesis of β -glucan, a major component of the cell wall of certain groups of fungi. Although they have a relatively narrow activity spectrum compared with other classes of antifungal agents (Rogers and Frost 2009), echinocandins are very effective against *Candida* and *Aspergillus* strains, the most prevalent invasive fungal pathogens (Meersseman and Wijngaerden 2007; Arendrup *et al.* 2014). This first survey of the susceptibility to echinocandins of pathogenic yeasts from Romania revealed alarming rates of resistance to echinocandins and significant multiple drug resistance to echinocandins and azoles (Mares *et al.* 2018).

2.2 Medical Devices Contamination

On the other hand, the numerous outbreaks of nosocomial infections caused by multidrug-resistant organisms (MDRO) in digestive endoscopy are one of the most worrying effects of recent years (Kovaleva *et al.* 2013). Most nosocomial pathogens exhibit adhesion phenomena at endoscopes in general and duodenoscopes in particular, their persistence at inert surfaces being difficult to access for reprocessing (Schaefer *et al.* 2010). In this regard, the microbiological safety of duodenoscopes has become an ardent topic, constantly on the panel of professional discussions and debates at global level. Duodenoscopes are distinguished by their technological design and the recent data abounds in cases related to nosocomial infections with the most commonly encountered pathogens, such as *Staphylococcus aureus* and *Klebsiella pneumoniae* (Muscarella 2014; Humphries and McDonnell 2015), species that are known due to their ability to form a MDRO, adhering to surfaces and spaces that are difficult to access for reprocessing. Recent data support the fact that inert surfaces at the endoscopes are becoming more susceptible to contamination, and thus to reprocessing, due to the simple repeated use of endoscopes in commonly working cycles, which generate alterations of the interface polymers thus facilitating contamination and subsequently the growth and development of MDRO (Petersen *et al.* 2016).

Within this framework our research described the impact of routine procedural use and reprocessing cycles on the duodenoscope, underling alterations of both coating and working channel polymers due to usage (Balan *et al.* 2019) (Fig. 2). The present study brought new evidences regarding the assessment of duodenoscope reliability concerning the coating materials in both direct and indirect contact with living tissues,

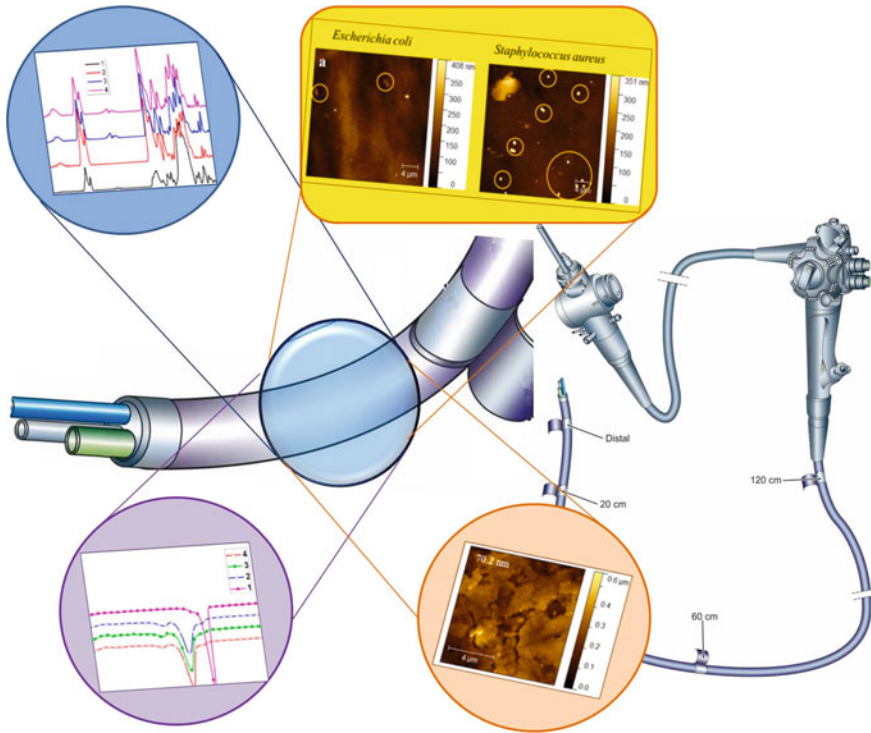


Fig. 2 Scheme of the study of reprocessing cycles on the duodenoscope

via devices manipulated through the working channel. We noticed alterations of both the coating and working channel polymers due to usage, even for a relatively small number of cases. External alterations increased progressively from the distal to the proximal samples, up to the elevator sample. However, the coating surface was proven to still be efficient against bacterial adhesion. All this physical evidences showed that the impact of routine procedural use and reprocessing on the duodenoscope possibly made it susceptible to bacterial contamination and MDRO biofilm formation due to difficult reprocessing of altered surfaces.

3 Where Are We Going Now?

We know so far that we are dealing with menacingly microorganisms adapted to live in all the conditions regardless the organism and environmental characteristics. These microorganisms are quite adapted to all kind of environmental conditions, can elude the drug's effects and populate different hidden places of medical devices producing resistant biofilms. *What can we do to confute them?* In the last decade

studies focused on finding active molecules that can act as new and improved antimicrobial agents, since, generally, nanosystems can interact with microbial cells directly by disrupting/penetrating the cell envelope (Wang *et al.* 2017). Usually, most antifungal drugs possess low water solubility or are unstable in physiological conditions consisting in the decrease of the therapeutic efficiency and leading to the increase of the dosages. Within this context there is a meaningful searching for alternatives in order to improve the antifungal properties of new and effective drugs.

3.1 *New Active Molecules for Nosocomial Infections Control*

While looking for new natural and efficient active molecules in order to fight against fungal infections, another important stop was in exploiting microorganisms in fighting against their own kind. Due to numerous industrial applications such as pharmaceutical, medical and food products and to numerous health benefits, exopolysaccharides (EPS), which are extracellular bio-macromolecules, have received special attention and were selected to be tested as new and efficient antifungal agents. EPS produced by lactic acid bacteria (LAB) have been proved to possess immunomodulatory, antitumor and anti-inflammatory effects, acting as oxidizing agents, their biological activity and technological applications being determinate by their structural properties (Kavitake *et al.* 2016).

We analysed the biosynthesis conditions, structure and the biological applications of an exopolysaccharides (EPS) producing strain, isolated from yogurt, and identified as *Weissella confusa* by 16sDNA gene sequencing. The strain was shown to produce a high amount of EPS (25.2 g/L of freeze-dried EPS/L culture medium) in De Man, Rogosa and Sharpe agar (MRS) culture medium improved with sucrose (80 g/l) and dissolved in UHT milk. EPS are important both from a technological as well as from a medical point of view and both aspects will be taken into account in any envisaged biotechnological applications. The extracted and purified EPS were characterized by FTIR and ¹³C-NMR spectroscopic methods, GPC investigation and thermal analysis (DSC and TGA) showing that the EPS extracted from fermentative culture medium have a dextran structure, with 100% glucose composition.

Dextran is a very complex glycan composed of chains of α -D-glucose with α -(1 \rightarrow 6) linear links and different percentages of α -(1 \rightarrow 4), α -(1 \rightarrow 3) and α -(1 \rightarrow 2) bonds, which depend on the nature of dextransucrase biosynthesized by the microbial strain (Shukla and Goyal 2013). Beside food applications, especially for bakeries (Kajala *et al.* 2015), the biopolymer has various applications in pharmaceutical and light industries (Gloria Hernandez *et al.* 2011), being used in medicine as antithrombotic agent (Naessens *et al.* 2005). Dextran-based nanoparticles have applications in targeted drug therapy, where dextran is used in coating and it can be functionalized (McBain *et al.* 2008). Dextran is also used as coating for protection against oxidation of metal nanoparticles (Bautista *et al.* 2005).

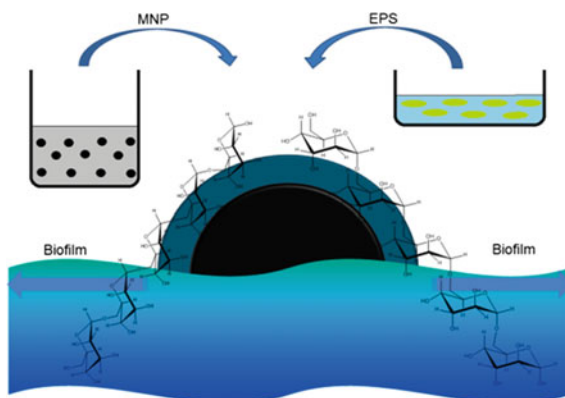
We conducted several studies revealing that the obtained EPS amount after the fermentative processes is strongly influenced by the culture medium composition

and by the fermentation conditions (Petrovici *et al.* 2018a). These EPS had a dextran structure, with 100% glucose composition and high molecular weight. These characteristics classified the pure EPS produced by *W. confusa* as a suitable ecological candidate product for the pharmaceutical and alimentary field (Petrovici *et al.* 2018b). In the end a concentration up to 3 mg/mL of dextran proved to have no cytotoxic effect on normal human dermal fibroblasts (NHDF) and, moreover, at this concentration, dextran broken up to 70% of the biofilms formed by the *C. albicans* SC5314 strain, in the same time having no antimicrobial activity against standard bacterial strains. We concluded also that, due to their characteristics, these EPS are suitable as hydrophilic matrix for controlled release of drugs in pharmaceutical industry (Rosca *et al.* 2018b).

Knowing that biofilm formation is one of the most challenging problems of nowadays, being associated with severe nosocomial infections, we managed to improve the EPS antifungal activity in order to completely destroy the yeast biofilms. One of the handy solutions was the use of nanostructures which interact directly with the microorganism's cell envelope. We engineered dextran coated iron oxide nanoparticles, loaded with propiconazole, in order to test the hypothesis of a combined effect of the polymer and drug, both known for their antifungal activities. Magnetic nanoparticles were coated with the biosynthesized dextran of 1% and 2% concentrations (Fig. 3), followed by the embedding of propiconazole onto the dextran shell. It was proved that while the 2% formulation nanoparticles revealed an activity on *C. albicans* strain, breaking 77% of biofilm, the improved version of the system (loaded with propiconazole) showed a maximum antifungal activity on *C. albicans*, in both planktonic and biofilm phase (Lungoci *et al.* 2018).

Other classes of molecules that our group had studied in terms of microbiological activity during the last years included organic ligands (Bahrin *et al.* 2019), cyclodextrins (Fifere *et al.* 2018), metal oxide nanoparticles (Turin-Moleavin *et al.* 2019) and natural and synthetic epoxy resins (Rosu *et al.* 2018, 2019, 2020).

Fig. 3 Concept illustration of coated magnetic nanoparticles (MNP) with exopolysaccharides (EPS) with antifungal activity



3.2 *New Methods for Medical Devices Disinfection*

Thus we studied the microorganisms responsible for nosocomial infections properties, we tested several types of active molecules in order to better eradicate the opportunistic pathogens, what else could be done? Resistant multi-drug and pan-drug strains have the ability to form biofilms resistant to both physical and chemical cleaning agents in high-grade disinfection reprocessing (Otter *et al.* 2015). The formation of such biofilm is catalysed not only by the difficulties or defects of reprocessing but also by the alterations of the surfaces subjected to reprocessing. Other sources of contamination are either manufacturing defects or secondary to the processes of physical destruction by friction phenomena, abrasion with maximum expression in daily practice in areas of maximum angulation, in areas of post-use handling, or at the level of working channels subject to repeated passage of medical devices (Kovaleva *et al.* 2013).

Plasma activated water (PAW) has been recognized as an effective non-thermal method in decontaminating, disinfecting, and even sterilizing a variety of devices and surfaces for medical and sanitary use (Farin and Grund 1994; Fridman *et al.* 2006; Deng *et al.* 2007; Deilmann *et al.* 2008). The application of non-thermal liquid plasma has proven to be an innovative method of reprocessing surfaces by the lithic activity it exhibits at the level of microorganisms at the same time without causing physical or chemical damage or alteration to treated surfaces or materials (Lerouge *et al.* 2001; Sladek and Stoffels 2005). PAW is a highly active resource against a wide range of microorganisms and is required over other alternative methods of reprocessing by the fact that it is easy to produce and use. It has non-thermal and non-aggressive cytotoxic and cytolytic properties with exposed inert surfaces and last but not least has capacity of penetration and early activity at the level of hard to reach spaces conferred by its fluid character (Sladek and Stoffels 2005).

Within this context our goal was to evaluate if the duodenoscope and its surface components are suited for repeated use of PAW in reprocessing cycles. We also aimed to evaluate the efficacy of PAW in high-level disinfection of endoscopy unit in order to consider PAW as a possible new alternative for duodenoscope reprocessing. Our preliminary study showed that PAW reprocessing is characterized by a significant decrease of bacterial populations, doubled by no surface and composition damage of the duodenoscope polymer coatings. PAW allows also skipping the water-rinsing stage of disinfection and minimizes biofilm formation. Therefore, it could be considered as a new and effective alternative method of disinfection for duodenoscope reprocessing, to be used after current-standard manual cleaning (Balan *et al.* 2018, 2019).

Being still at the road threshold, the conclusions are far from being generally valid, we have the assuredness of fighting on a multi-level way to eradicate the nosocomial infections and promising results are emerging, but we have a long way to go in order to reach the final achievement. Within this context our studies will continue to focus on finding new and efficient biomolecules with antimicrobial effects and able to improve the medical devices disinfection at a high level.

Acknowledgements This project has received funding from the H2020 ERA Chairs Project no 667387: SupraChem Lab Laboratory of Supramolecular Chemistry for Adaptive Delivery Systems ERA Chair initiative. This work was also supported by a grant within the frame of the Complex Projects Partnership Program—PCCDI, under authority of Romanian National Authority for Scientific Research—UEFISCDI, project code PN-III-P1-1.2-PCCDI-2017-0083 (37PCCDI/2018). The authors are extremely grateful and sincerely acknowledge the guidance and collaboration to Professor Dr. Mihai Mares from “Ion Ionescu de la Brad” University, Iasi and MD Gheorghie Balan Jr. from “Grigore T. Popa” University of Medicine and Pharmacy, Iasi.

References

- Arendrup MC, Boekhout T, Akova M et al (2014) ESCMID/ECMM joint clinical guideline for the diagnosis and management of rare invasive yeast infections. *Clin Microbiol Infect* 3:76–98. <https://doi.org/10.1111/1469-0691.12360>
- Bahrin L, Clima L, Shova S, Rosca I, Cojocaru C, Bejan D, Sardaru M, Marangoci N, Lozan V, Rotaru A (2019) Synthesis, structure, computational modeling, and biological activity of two novel bimesitylene derivatives. *Res Chem Intermed* 45(2):453–469. <https://doi.org/10.1007/s11164-018-3611-x>
- Balan G, Rosca I, Ursu E-L, Doroftei F, Bostanaru AC, Hnatiuc E, Nastasa V, Sandru V, Stefanescu G, Trifan A, Mares M (2018) Plasma activated water - a new and effective alternative for duodenoscope reprocessing. *Infect Drug Resist* 11:727–733. <https://doi.org/10.2147/IDR.S159243>
- Balan G, Rosca I, Ursu E-L, Fifere A, Varganici C-D, Doroftei F, Turin-Moleavin I-A, Sandru V, Constantinescu G, Timofte D, Stefanescu G, Trifan A, Sfarti CV (2019) Duodenoscope-associated infections beyond the elevator channel: alternative causes for difficult reprocessing. *Molecules* 24:2343. <https://doi.org/10.3390/molecules24122343>
- Bautista MC, Bomati-Miguel O, Morales MP, Serna CJ, Veintemillas-Verdaguer S (2005) Surface characterisation of dextran coated iron oxide nanoparticles prepared by laser pyrolysis and coprecipitation. *J Magn Magn Mater* 293:20–27. <https://doi.org/10.1016/j.jmmm.2005.01.038>
- Bostanaru A-C, Rosca I, Minea B, Nastasa V, Foia L, Marincu I, Mares M, Mederle O-A (2019) Genotype comparison of *Candida albicans* isolates from different clinical samples. *Rev Rom Med Lab* 27(3):327–332. <https://doi.org/10.2478/rmlm-2019-0027>
- Deilmann M, Halfmann H, Bibinov N, Wunderlich J, Awakowicz P (2008) Low pressure microwave plasma sterilization of polyethylene terephthalate bottles. *J Food Prot* 71(10):2119–2123. <https://doi.org/10.4315/0362-028x-71.10.2119>
- Deng X, Shi JJ, Kong MG (2007) Protein destruction by a helium atmospheric pressure glow discharge: capability and mechanisms. *J Appl Phys* 101:074701. <https://doi.org/10.1063/1.2717576>
- Emori TG, Gaynes RP (1993) An overview of nosocomial infections, including the role of the microbiology laboratory. *Clin Microbiol Rev* 6(4):428–442. <https://doi.org/10.1128/cmr.6.4.428>
- Farin G, Grund KE (1994) Technology of argon plasma coagulation with particular regard to endoscopic applications. *Endosc Surg Allied Technol* 2(2):71–77
- Fifere A, Lungoci LA, Minea B, Rosca I, Duca G, Boldescu V, Marangoci N, Simionescu BC, Pinteala M, Macaeav F (2018) Cyclodextrins as molecular delivery systems for drugs with antifungal activity: from design to application. In: Duca Ghe si Macaeav F (ed) *Compounds and Materials for Drug Development and Biomedical Applications*, Editura Academiei Romane, Muzeul Brailei «Carol I» Editura Istros, Bucuresti-Braila, pp 291–307

- Fridman G, Peddinghaus M, Balasubramanian M, Ayan H, Fridman A, Gutsol A (2006) Blood coagulation and living tissue sterilization by floating electrode dielectric barrier discharge in air barrier. *Plasma Chem Plasma Process* 26(4):425–442. <https://doi.org/10.1007/s11090-006-9024-4>
- Gloria Hernandez H, Livings S, Aguilera JM, Chiralt A (2011) Phase transitions of dairy proteins, dextrans and their mixtures as a function of water interactions. *Food Hydrocolloid* 25(5):1311–1318. <https://doi.org/10.1016/j.foodhyd.2010.12.006>
- Haque M, Sartelli M, McKimm J, Abu Bakar M (2018) Health care-associated infections - an overview. *Infect Drug Resist* 11:2321–2333. <https://doi.org/10.1016/j.apjtb.2017.01.019>
- Humphries RM, McDonnell G (2015) Superbugs on duodenoscopes: the challenge of cleaning and disinfection of reusable devices. *J Clin Microbiol* 53:3118–3125. <https://doi.org/10.1128/JCM.01394-15>
- Kabir MA, Hussain MA, Ahmad Z (2012) *Candida albicans*: a model organism for studying fungal pathogens. *ISRN Microbiol* 2012:538694. <https://doi.org/10.5402/2012/538694>
- Kajala I, Shi Q, Nyssölä A et al (2015) Cloning and characterization of a *Weissella confusa* dextranucrase and its application in high fibre baking. *PLoS ONE* 10(1):e0116418. <https://doi.org/10.1371/journal.pone.0116418>
- Kavitake D, Devi PB, Singh SP, Shetty PH (2016) Characterization of a novel galactan produced by *Weissella confusa* KR780676 from an acidic fermented food. *Int J Biol Macromol* 86:681–689. <https://doi.org/10.1016/j.ijbiomac.2016.01.099>
- Kovaleva J, Peters FT, van der Mei HC, Degener JE (2013) Transmission of infection by flexible gastrointestinal endoscopy and bronchoscopy. *Clin Microbiol Rev* 26(2):231–254. <https://doi.org/10.1128/CMR.00085-12>
- Lerouge S, Wertheimer MR, Yahia LH (2001) Plasma sterilization: a review of parameters, mechanisms, and limitations. *Plasma Polym* 6(3):175–188. <https://doi.org/10.1023/A:1013196629791>
- Lungoci L, Pinteala M, Petrovici AR, Rosca I, Turin-Moleavin I-A, Fifere A (2018) Biosynthesized dextran coated magnetic particles with antifungal activity. *Rev Roum Chim* 63(5–6):495–501
- Mares M, Minea B, Nastasa V, Rosca I, Bostanaru A-C, Marincu I, Toma V, Cristea VC, Murariu C, Pinteala M (2018) In vitro activity of echinocandins against 562 clinical yeast isolates from a Romanian multi-centre study. *Med Mycol* 56(4):442–451. <https://doi.org/10.1093/mmy/myx059>
- McBain SC, Yiu HH, Dobson J (2008) Magnetic nanoparticles for gene and drug delivery. *Int J Nanomedicine* 3:169–180. <https://doi.org/10.2147/IJN.S1608>
- Meersseman W, Van Wijngaerden E (2007) Invasive aspergillosis in the ICU: an emerging disease. *Intensive Care Med* 33:1679–1681. <https://doi.org/10.1007/s00134-007-0792-y>
- Muscarella LF (2014) Risk of transmission of cabapenem-resistant Enterobacteriaceae and related “superbugs” during gastrointestinal endoscopy. *World J Gastrointest Endosc* 6(10):457–474. <https://doi.org/10.4253/wjge.v6.i10.457>
- Naessens M, Cerdobbel AN, Soetaert W, Vandamme EJ (2005) *Leuconostoc* dextranucrase and dextran: production, properties and applications. *J Chem Technol Biotechnol* 80:845–860. <https://doi.org/10.1002/jctb.1322>
- Otter JA, Vickery K, Walker JT et al (2015) Surface-attached cells, biofilms and biocide susceptibility: implications for hospital cleaning and disinfection. *J Hosp Infect* 89(1):16–27. <https://doi.org/10.1016/j.jhin.2014.09.008>
- Petersen BT, Koch J, Ginsberg GG (2016) Infection using ERCP endoscopes. *Gastroenterology* 151:46–50. <https://doi.org/10.1053/j.gastro.2016.05.040>
- Petrovici AR, Nicolescu A, Silion M, Rosca I, Ciolacu D (2018a) Biopolymer biosynthesis by lactic acid bacteria strain in four different culture media. *Rev Roum Chim* 63(7–8):637–642
- Petrovici AR, Rosca I, Stoica I, Silion M, Nicolescu A, Dodi G, Simionescu N, Varganici C-D, Ivanov I-C, Pinteala M (2018b) Biosynthesis of exopolysaccharides by *Weissella confusa* in a new culture medium. *Rom Biotech Lett* 23:13637–13646

- Rogers TR, Frost S (2009) Newer antifungal agents for invasive fungal infections in patients with haematological malignancy. *Br J Haematol* 144:629–641. <https://doi.org/10.1111/j.1365-2141.2008.07412.x>
- Rosca I, Bostanaru A-C, Minea B, Nastasa V, Gherghel I, Mares M, Moroti-Constantinescu VR (2018a) Phenotypic and genotypic profiles of *Candida albicans* isolates from Romanian patients. *Rev Rom Med Lab* 26(4):405–413. <https://doi.org/10.2478/rrlm-2018-0023>
- Rosca I, Petrovici AR, Peptanariu D, Nicolescu A, Dodi G, Avadanei M, Ivanov IC, Bostanaru A-C, Mares M, Ciolacu D (2018b) Biosynthesis of dextran by *Weissella confusa* and their in vitro functional characteristics. *Int J Biol Macromol* 107:1765–1772. <https://doi.org/10.1016/j.ijbiomac.2017.10.048>
- Rosenthal VD, Bijie H, Maki DG et al (2012) International Nosocomial Infection Control Consortium (INICC) report, data summary of 36 countries, for 2004–2009. *Am J Infect Control* 40(5):396–407. <https://doi.org/10.1016/j.ajic.2011.05.020>
- Rosu L, Varganici C–D, Mustata F, Rosu D, Rosca I, Rusu T, (2020) Epoxy coatings based on modified vegetable oils for wood surface protection against fungal degradation. *ACS Appl Mater Interfaces* 12(12):14443–14458. <https://doi.org/10.1021/acsami.0c00682>
- Rosu L, Varganici C-D, Mustata F, Rusu T, Rosu D, Rosca I, Tudorachi N, Teaca C-A (2018) Enhancing the thermal and fungal resistance of wood treated with natural and synthetic derived epoxy resins. *ACS Sustain Chem Eng* 6:5470–5478. <https://doi.org/10.1021/acssuschemeng.8b00033>
- Rosu L, Mustata F, Varganici C-D, Rosu D, Rusu T, Rosca I (2019) Thermal behaviour and fungi resistance of composites based on wood and natural and synthetic epoxy resins cured with maleopimaric acid. *Polym Degrad Stab* 160:148–161. <https://doi.org/10.1016/j.polyimdegradstab.2018.12.022>
- Sanita PV, de Oliveira Mima EG, Pavarina AC, Jorge JH, Machado AL, Vergani CE (2013) Susceptibility profile of a Brazilian yeast stock collection of *Candida* species isolated from subjects with *Candida*-associated denture stomatitis with or without diabetes. *Oral Surg Oral Med Oral Pathol Oral Radiol* 116(5):562–569. <https://doi.org/10.1016/j.oooo.2013.07.002>
- Schaefer MK, Jung M, Dahl M et al (2010) Infection control assessment of ambulatory surgical centres. *JAMA* 303(22):2273–2279. <https://doi.org/10.1001/jama.2010.744>
- Shukla S, Goyal A (2013) Medium optimization of fermentation for enhanced dextrans production from *Weissella confusa* Cab3 by statistical methods. *Curr Biotechnol* 2:39–46. <https://doi.org/10.2174/2211550111302010007>
- Sladek RE, Stoffels E (2005) Deactivation of *Escherichia coli* by the plasma needle. *J Phys D Appl Phys* 38:1716–1721. <https://doi.org/10.1088/0022-3727/38/11/012>
- Turin-Moleavin I-A, Fifere A, Lungoci A-L, Rosca I, Coroaba A, Peptanariu D, Nastasa V, Pasca S-A, Bostanaru A-C, Mares M, Pinteala M (2019) In vitro and in vivo antioxidant activity of the new magnetic-cerium oxide nanoconjugates. *Nanomaterials* 9:1565. <https://doi.org/10.3390/nano9111565>
- Vincent JL (2003) Nosocomial infections in adult intensive-care units. *Lancet* 361(9374):2068–2077. [https://doi.org/10.1016/S0140-6736\(03\)13644-6](https://doi.org/10.1016/S0140-6736(03)13644-6)
- Wang L, Hu C, Shao L (2017) The antimicrobial activity of nanoparticles: present situation and prospects for the future. *Int J Nanomedicine* 12:1227–1249. <https://doi.org/10.2147/IJN.S121956>

New Enkephalin Nanomedicines for Pain Alleviation, Overcoming the Side Effects of Morphine



Sinda Lepetre-Mouelhi, Jiao Feng, and Patrick Couvreur

Abstract Over the last years, the nanomedicines has been recognized as a key element, capable of providing new and innovative medical solution to address unmet medical needs. More specifically, Squalene-based nanoparticles have opened exciting perspectives for drug delivery due to their biodegradability and their non-toxicity. In this study, it was shown for the first time, that the rapidly metabolized Leu-enkephalin (LENK) neuropeptide, once conjugated to the biocompatible lipid squalene (SQ) and formulated into nanoparticles, may become pharmacologically efficient. First, the resulting LENK-SQ bioconjugates were synthesized using different biocleavable chemical linkers, in order to modulate the LENK release from their formulation into nanoparticles (NPs). This nanoformulation led to new nanosystems exhibiting high drug loadings, allowed an efficient protection to LENK from early metabolism and conferred to the released neuropeptide a significant anti-hyperalgesic effect in a rat model of inflammatory pain which lasted longer than after treatment with morphine. A biodistribution study, as well as, the use of brain-permeant and -impermeant opioid receptor antagonists indicated that LENK-SQ NPs acted exclusively through peripherally located opioid receptors. This study showed that LENK-SQ bioconjugates may be beneficial in impacting the opioid crisis as these LENK-SQ NPs (i) exhibited higher affinity toward δ -opioid receptors versus μ -opioid receptors, (ii) showed exclusively peripheral activity (no BBB penetration) so no CNS addiction and (iii) took advantage of the inflammatory process to optimize drug concentrations at the site of injury.

Keywords Nanomedicine · Leu-Enkephalin · Squalene · Prodrug · Bioconjugate · Hyperalgesia · Inflammatory pain · Opioid receptors · Peripheral effect · Rat

S. Lepetre-Mouelhi (✉) · J. Feng · P. Couvreur
Institut Galien Paris-Sud, UMR8612, Université Paris-Saclay,
92290 Châtenay-Malabry, France
e-mail: sinda.lepetre@universite-paris-saclay.fr

© The Author(s), under exclusive license to Springer Nature Switzerland AG 2021
M. J. M. Abadie et al. (eds.), *New Trends in Macromolecular and Supramolecular Chemistry for Biological Applications*, https://doi.org/10.1007/978-3-030-57456-7_10

191

1 Introduction and State-of-Art on Nanomedicines

Conventional chemotherapy is often hampered by poor diffusion through biological barriers such as epithelium, endothelium, cell membranes, and a rapid metabolism and clearance from the body. In addition, it frequently leads to a non-specific biodistribution of the drug in the body thus generating severe side effects due to drug losses in healthy organs and tissues.

To circumvent these drawbacks, the drug can be encapsulated into **nanoparticles** (NPs). This nanoparticulate formulation allows protection to the drug from degradation, an efficient targeting towards diseased tissues, a better intracellular diffusion and a controlled release (Peer et al. 2007; Wang et al. 2012). A nanoparticle is composed of a core surrounded by a corona. Typically, the **core** material encapsulates the drug. It can be made of organic or inorganic compounds from natural and synthetic sources, such as polymeric materials, lipids, metal oxides, etc.... The **corona**, for its part, is a natural protein layer spontaneously formed around nanoparticles when exposed to biological media. The corona is constituted of plasma proteins, such as Albumin, immunoglobulin G (IgG), fibrinogen, apolipoproteins, coagulation factors, complement proteins... The formation of the protein corona around nanoparticles is dependent on physico-chemical properties of NPs including nanoparticle size, surface charge, hydrophobicity, surface chemistry and is characteristic of the environment in which are dispersed NPs. The corona can also be synthetic when designed to (i) confer stealth properties to the nanoparticle against immune system or (ii) enhance their targeting ability. In the first case, the corona is composed of Polyethylene Glycol (PEG) chains covalently linked or adsorbed onto the surface of the NP in order to prevent interactions between the particle surface and the plasma proteins (thus avoiding recognition by reticuloendothelial system). In the second case, for a better targeting, the corona may be constituted of PEG-chains grafted to specific ligands or only specific ligands adsorbed on the surface of the nanoparticle. The corona affects the fate of the nanoparticle in the body. It determines the rate of clearance from the bloodstream, the volume of distribution, the organ disposition, and the rate and route of clearance from the body.

These drug delivery nanosystems may be classified in 2 categories: organic NPs (e.g., polymeric, liposomes, micelles, etc.) and inorganic NPs (e.g., gold, silica, iron oxide, etc.).

Currently, there are a number of nanomedicines that have been approved for clinical use, either by the Food and Drug Administration (FDA) in the United States (51 FDA-approved nanomedicines), or the European Medicines Agency (EMA) in the European Union and more than 77 nanomedicines are in clinical trials (Bobo et al. 2016) (Anselmo and Mitragotri 2016). Among FDA-approved nanomedicines, most of organic NPs are liposomal systems and are mainly used in cancer therapy. The first approved nanomedicine was Doxil (FDA 1995), encapsulating the doxorubicin for cancer treatment (Barenholz and (Chezy) 2012). Then, other liposomes were also developed such as DaunoXome (daunorubicin), Myocet (doxorubicin), Marqibo (vincristine) and most recently, Onivyde (irinotecan) (Fox 1995; Leonard et al.

Leonard et al. 2009; Silverman et al. 2013; Carnevale and Ko 2016). The majority of these formulations are not PEGylated, with the exception of Doxil and Onivyde (Chang et al. 2015). Vyxeos is the first clinically approved liposome to deliver a synergistic combination of 2 drugs, daunorubicin and cytarabine for the treatment of acute myeloid leukemia in August of 2017 (Krauss et al. 2019). All of these nanoformulations are passively targeted with the ability to preferentially accumulate at tumor sites via the enhanced permeation and retention (EPR) effect (Maeda 2012). The liposomes are also used in some others clinical applications, such as general anesthesia with Diprivan (Cummings et al. 1984; Thompson and Goodale 2000). The FDA-approved Visudyne, a light-activated liposome loading verteporfin, was used in photodynamic therapy for choroidal neovascularization due to age-related macular degeneration (Schmidt-Erfurth and Hasan 2000). For the treatment of some bacterial/fungal infections, liposomes loading amphotericin B (AmBisome) have been clinically approved as well as lipid-complexed formulations, such as Abelcet and Amphotec (Hamill 2013; Rust and Jameson 1998). Two other liposomes Inflexal V and Epaxal were commercialized successfully as vaccines. These virosome-based vaccines incorporated inactivated influenza and hepatitis A virus respectively (Fan et al. 2021). It should be noted that the virosomes Inflexal V and Epaxal have since been phased out of the clinic. Other non liposomal organic nanoformulations were also approved. Abraxan, is a protein nanoparticle which is used in cancer therapy with paclitaxel formulated as albumin bound (Tomao et al. 2009). Polymeric nanoparticles were also used, such as Copaxone as immunomodulator, Neulatsa for chemotherapy induced neutropenia, Cimzia for the treatment of several autoimmune diseases, Plegridy treating relapsing multiple sclerosis and adynovate for the treatment of hemophilia A (Bobo et al. 2016). In the past few years, lipid nanoparticles have emerged as one of the most advanced and efficient mRNA delivery platforms. In that respect, the lipid nanoparticles Onpattro (Patisiran) delivering siRNA for the silencing of a specific gene responsible for expression of transthyretin (causing hereditary transthyretin amyloidosis), were recently approved (2018) (Adams et al. 2018). In 2020, an effective vaccine against the severe acute respiratory syndrome coronavirus 2 (SARS-CoV-2) (which emerged in late 2019) was approved (Jackson et al. 2020). The candidate vaccine mRNA-1273 is a lipid nanoparticle encapsulating a nucleoside-modified messenger RNA (mRNA) that encodes the SARS-CoV-2 spike (S) glycoprotein. Hence, approval of the first vaccine using lipid nanoparticles, highly effective against the devastating SARS-CoV-2 pandemic represents a major milestone for nanomedicines.

Approved inorganic NPs, for their part, are mainly iron-based colloids. They are used as iron-replacement therapies for treatment of anemia, such as Cosmofer, Dexferrum, Ferrlecit, Injectafter, in order to increase iron concentration in the body (Coyne and Auerbach 2010). They are also widely used as contrast agents for Magnetic Resonance Imaging (MRI) for imaging a variety of cancers and pathologies (Gupta and Gupta 2005; Wang et al. 2001; Na et al. 2009; Laurent et al. 2008). Recently, BTRX3/Hensify a crystalline hafnium oxide nanoparticle with negatively charged phosphate coating, received approval in 2019 (Bonvalot et al. 2019). These

inorganic nanoparticles enhances external radiotherapy via a physical mode of action that relies on hafnium's natural radioenhancing properties.

However, despite the large number of successful nanomedicines that have reached the market, further development of new nanoformulations is still urgently needed to address current global health challenges, which requires collaborative efforts of scientists arising from different disciplines. In this context, Couvreur's team developed a very promising nanomedicine platform for the treatment of severe diseases, using natural and biocompatible materials such as squalene lipid.

2 The Squalenoylation Nanotechnology: An Innovative and Efficient Nanoformulation

Squalene (SQ), a natural endogenous lipid belonging to the chemical class of triterpenes, is formed by six isoprene units and is an intermediate metabolite in the synthesis of cholesterol. It is widely distributed in nature and with reasonable amounts found in shark liver oil, olive oil, wheat germ oil and rice bran oil. It received its name because of its occurrence in shark liver oil (*Squalus* spp.) (Miettinen and Vanhanen 1994). Because it is of biological origin and frequently used as a dietary supplement, SQ is favourably predisposed from a toxicological standpoint; thus, it has been extensively used as a carrier/adjuvant in therapeutic applications. «The squalenoylation nanotechnology» involves the linkage of a fonctionnalized SQ (squalenic acid, squalenol, squalenamine, SQ maleimide, etc....) to therapeutic agents using a chemical bio-cleavable linkage, such as ester, amide, hydrazone, carbamate, disulfide, etc.... The resulting SQ based bioconjugates, which are prodrugs, are bioreversible derivatives that undergo an enzymatic and/or a chemical transformation *in vivo* to release the active drug. Owing to the rigid structural property of SQ, these SQ-drug bioconjugates may self-assemble spontaneously in aqueous solutions into nanoparticles without the use of any surfactant and with high drug loading. Since its first application in 2006, squalenoylation nanotechnology has showed great potential for the delivery of various therapeutic agents in a safer and more efficient manner. Indeed, this new concept offers various advantages in comparison with the conventional nanocarriers. Contrary to polymer nanoparticles or liposomes nanoformulations which encapsulate physically the drugs into their matrices, the squalene-drug conjugates NPs involve a chemical encapsulation approach, thus preventing the “burst” release phenomenon (Couvreur et al. 2006). The supramolecular organization of these NPs allows protection to the therapeutic agents from degradation/metabolization resulting in greater plasmatic half-life, while controlling and extending the drug release. Furthermore, these nanosystems facilitated drug's passage through biological membranes due to the lipophilic properties of SQ resulting in an enhanced drug concentration within targeted tissues and cells and generating significant increase in drug pharmacological activity. Proofs of this concept have been established with drugs presenting different physicochemical characteristics, like

small hydrophilic or lipophilic molecules. Generally, the squalenylation favorably modifies *in vivo* the pharmacokinetic profile and biodistribution of the carried drug, allowing its intravenous administration as NPs and increasing its therapeutic index (Desmaële et al. 2012; Feng et al. 2017). Thus, this drug delivery platform opened exciting perspectives in the drug delivery field. However, it has been a tremendous challenge to extend the SQ-based bioconjugation approach to molecules with higher molecular weight such as peptides, due to several obstacles in performing successful conjugation reactions. First, peptides are unstable biomolecules. Second, they are hydrophilic molecules, therefore, they have no affinity for lipophilic molecules such as squalene. In addition, the chemical modification of a peptide often results in a loss of its pharmacological activity. Thus, the chemical approach using squalenylation nanotechnology has overcome all these hurdles, allowing the design of a small library of innovative neuropeptide-SQ bioconjugates for pain management. Thus, owing to a simple conjugation with the lipid squalene, the rapidly metabolized Leu-enkephalin (LENK) neuropeptide may become pharmacologically efficient.

3 Squalene-based Nanomedicines for Pain Management: Leu-Enkephalin-Squalene Nanoparticles (LENK-SQ NPs)

According to CDC/NCHS, National Vital Statistics System, every day, more than 115 people in the United States die after overdosing on opioids (Adams 2018). The misuse of and addiction to opioids, especially morphine, represents a serious national crisis in the US that affects public health, as well as, social and economic welfare. This highlights the need to urgently find new painkillers devoided of severe side effects. In this context, endogenous neuropeptides, such as enkephalins, are very promising painkillers which unlike morphin, exhibit a higher affinity towards delta-opioid receptors in comparison with mu (Janecka et al. 2004). This feature is of great importance since δ -opioid receptor ligands are believed to have a much lower abuse potential, as well as, reduced respiratory, gastrointestinal and cognitive disorders (Contet et al. 2004; Kiritsy-Roy et al. 1989; Abbadie and Abbadie 2002; Pasternak and Abbadie 2013; Tavani et al. 1990; Dykstra et al. 2002). However, because of pharmacokinetic issues, and rapid plasma metabolization, the enkephalins were not exploitable up to now.

4 Synthesis of Leu-Enkephalin-SQ Bioconjugates

In this context, in order to exploit its analgesic potential, the currently unusable Leu-enkephalin (LENK) neuropeptide was conjugated to the SQ derivative. Thus, various squalenoyl-Leu-enkephalin (LENK-SQ) conjugates were designed with

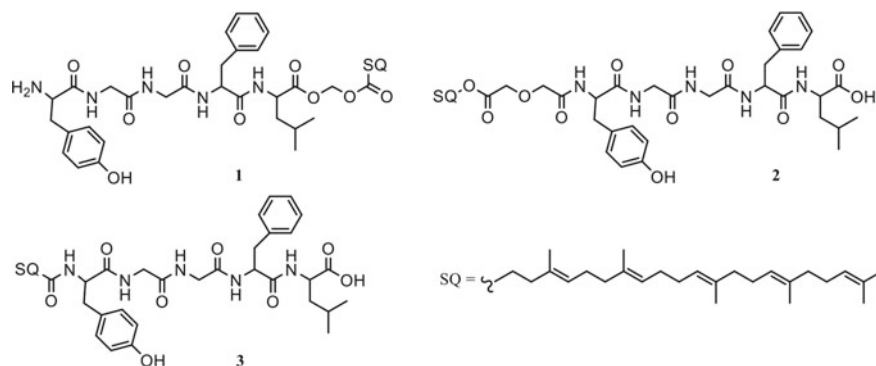


Fig. 1 Chemical structures of the bioconjugates. (1) Leu-enkephalin-squalene with dioxycarbonyl linker (LENK-SQ-Diox), (2) Leu-enkephalin-squalene with diglycolic linker (LENK-SQ-Dig), and (3) Leu-enkephalin-squalene with amide linker (LENK-SQ-Am). Figure reproduced from Ref. Feng et al. (2019), © 2019 AAAS

different chemical linkers using bioconjugation approach (Fig. 1). Therefore, LENK neuropeptide exhibits 2 potential sites for SQ conjugation: C-terminal acid and N-terminal amine. It must be emphasized that the N-terminal of LENK is required for binding to opioid receptors (Büscher et al. 1976). However, based on the fact that the amide bond is susceptible to be cleaved by overexpressed peptidases within inflammation site, (Viswanatha Swamy and Patil 2008) the conjugation on N-terminal was also achieved. Thus, a simple amide bond between SQ and LENK was first considered. Subsequently, two linkers with different sensitivity to hydrolysis were also used in order to modulate the release kinetics of LENK from NPs. Practically, conjugation of the squalenic acid (SQ derivative) on N-terminal LENK was performed through a simple amide bond (LENK-SQ-Am conjugate). Using diglycolic spacer, squalenol was also conjugated to N-terminal LENK (LENK-SQ-Dig conjugate) while through dioxycarbonyl linker the squalenic acid was coupled to C-terminal LENK (LENK-SQ-Diox conjugate).

The LENK-SQ-Diox conjugate was synthesized by alkylation of the carboxylate function of the peptide with the chloromethyl ester of squalenic acid, which resulted from the treatment of squalenic acid with chloromethyl chlorosulfate. Prior to react with the chloromethyl ester of squalenic acid, the LENK was protected by Alloc (allyloxycarbonyl) group on its N-terminal amine, in order to avoid N-terminal conjugation. Subsequent deprotection of Alloc-LENK-SQ under neutral conditions was then achieved by catalytic transfer hydrogenation method using triethylsilane and 10% Pd-C (Mandal and McMurray 2007), affording pure LENK-SQ-Diox in 9.5% yield (Fig. 2). The LENK-SQ-Dig prodrug was obtained from the conjugation between LENK and squalene diglycolic acid, activated by ethyl chloroformate. The squalene diglycolic acid resulted from a reaction between the squalenol and diglycolic anhydride. The LENK-SQ-Dig was obtained with 69% yield (Fig. 3). It was expected that the oxa moiety of the diglycolate linker enhances the susceptibility to hydrolysis by increasing the distance between LENK and SQ and so the accessibility

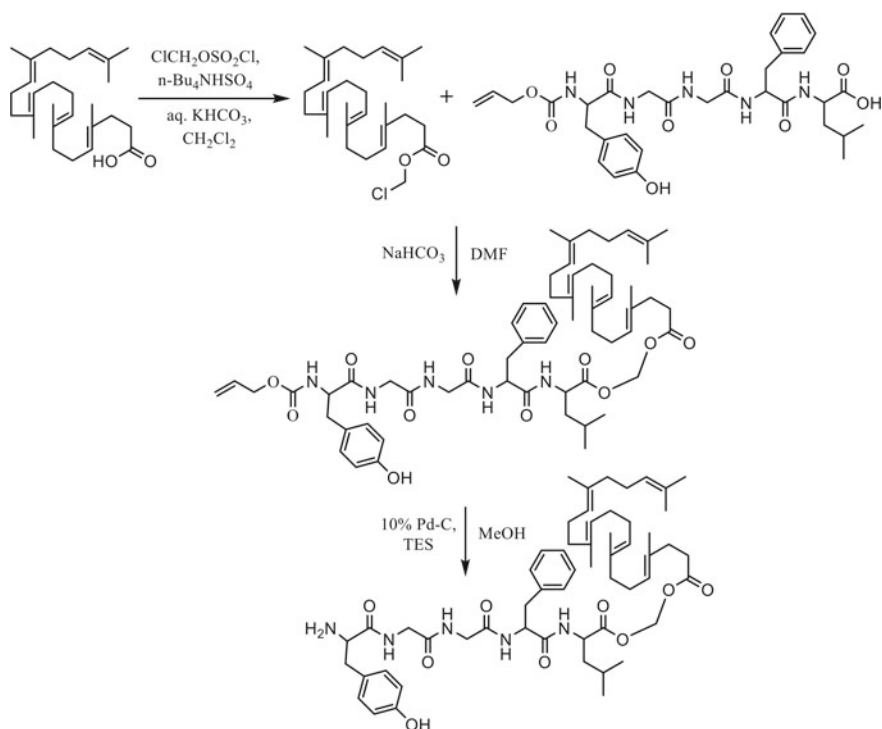


Fig. 2 Synthesis of Leu-enkephalin-squalene with dioxycarbonyl linker (LENK-SQ-Diox). Figure reproduced from Ref. Feng et al. (2019), © 2019 AAAS

to the linkage by enzymes. Direct conjugation between LENK and squalenic acid via amide bond was achieved by acid activation using ethyl chloroformate, affording LENK-SQ-Am in 73% yield (Fig. 4) (Feng et al. 2019).

It was expected that LENK-SQ-Diox released faster the LENK than LENK-SQ-Dig, and LENK-SQ-Am was supposed to trigger the slower release as reported in the literature (Sémiramoth et al. 2012).

5 LENK-SQ Nanomedicines: Preparation and Characterization

The LENK-SQ bioconjugates were then formulated as nanoparticles using simple nanoprecipitation technique without the aid of any surfactant. In that respect, LENK-SQ ethanolic solutions were nanoprecipitated in dextrose solution (2 mg/mL) and exhibited impressively high drug payloads (i.e. 53 to 59%) in comparison with conventional nanoparticles or liposomes which amounted to a maximum of 5% (Betageri et al. 1997; Chen et al. 2008). The size of the NPs varied from 61 to

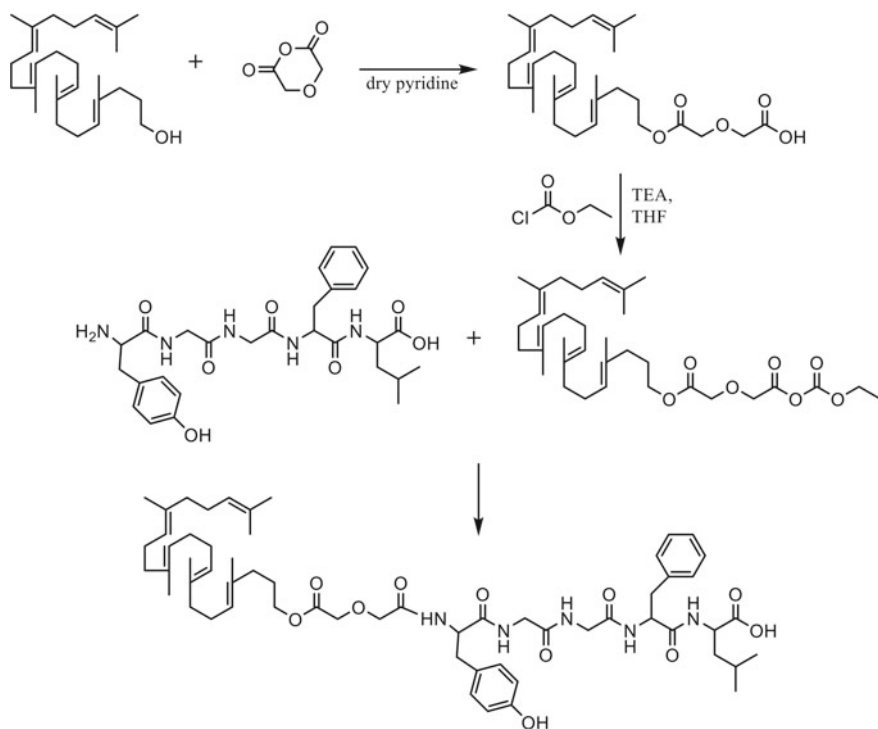


Fig. 3 Synthesis of Leu-enkephalin-squalene with diglycolic linker (LENK-SQ-Dig). Figure reproduced from Ref. Feng et al. (2019), © 2019 AAAS

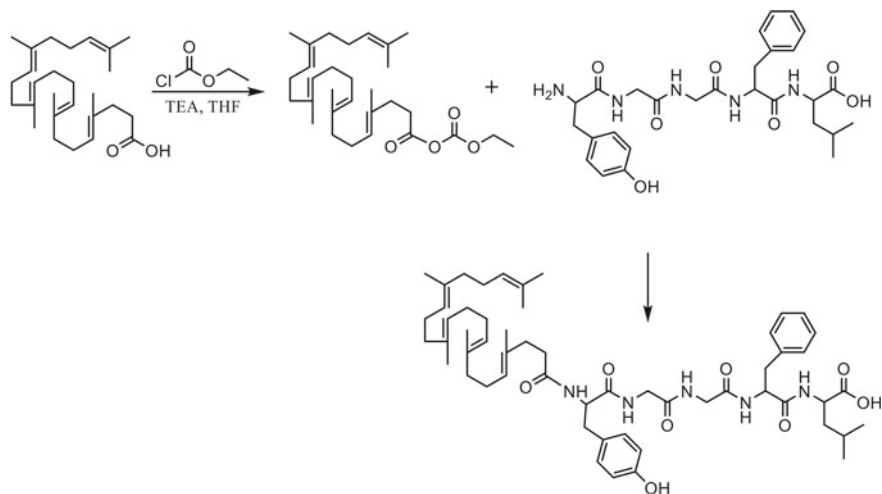


Fig. 4 Synthesis of Leu-enkephalin-squalene with amide linker (LENK-SQ-Am). Figure reproduced from Ref. Feng et al. (2019), © 2019 AAAS

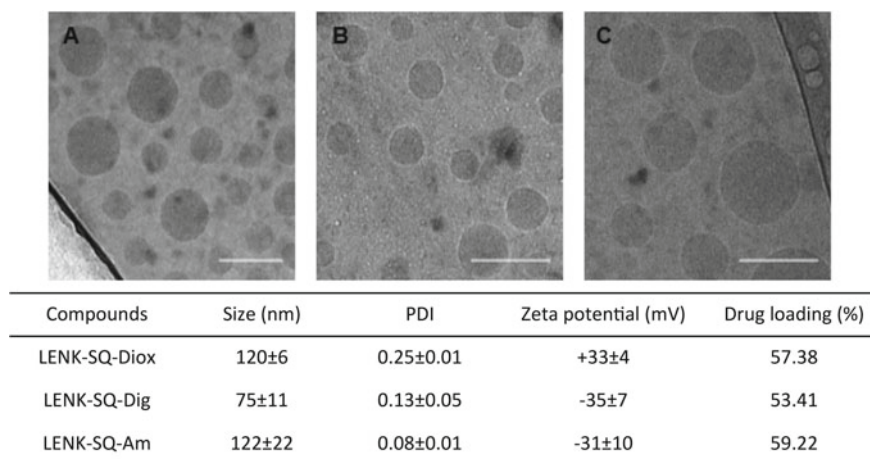


Fig. 5 NP characterization. Representative cryo-TEM images showing the formation of NPs from different bioconjugates: **A** LENK-SQ-Diox NPs, **B** LENK-SQ-Dig NPs, and **C** LENK-SQ-Am NPs. Scale bars, 100 nm. Physicochemical characteristics of NPs [i.e., size, polydispersity index (PDI), zeta potential, and % drug loading] are shown in the table. Figure reproduced from Ref. Feng et al. (2019), © 2019 AAAS

112 nm, depending on the conjugation site and also the linkage between SQ and enkephalin (Fig. 5). The NPs displayed spherical and monodisperse structures with net positive or negative surface charge (Fig. 5), which could be attributed to the free C- or N-terminal function of the peptide depending on the bioconjugation mode. Indeed, in case of the LENK-SQ-Diox bioconjugate, the net positive charge was due to free N-terminus site (primary amino group) of the bioconjugate, resulting from SQ conjugation on the C-terminus of LENK peptide. Conversely, the zeta potential became negative when the conjugation with SQ was performed on the N-terminus LENK peptide (LENK-SQ-Dig and LENK-SQ-Am). The sizes and the surface charges of the LENK-SQ NPs were found to be quite stable at +4 °C during several days (Feng et al. 2019).

6 *In vitro* Release Study of LENK from LENK-SQ Nanoparticles in Serum

The chemical stability of the different linkers (i.e., direct amide or dioxycarbonyl or diglycolate spacers) was studied after incubation of the LENK-SQ NPs with mouse serum in order to ascertain that free LENK peptide could be released from the LENK-SQ nanoparticles (Fig. 6). The study clearly showed that only LENK-SQ-Diox and LENK-SQ-Dig released the peptide. In the case of LENK-SQ-Diox NPs, the experiments highlighted the gradual decrease of bioconjugate concentration in favour

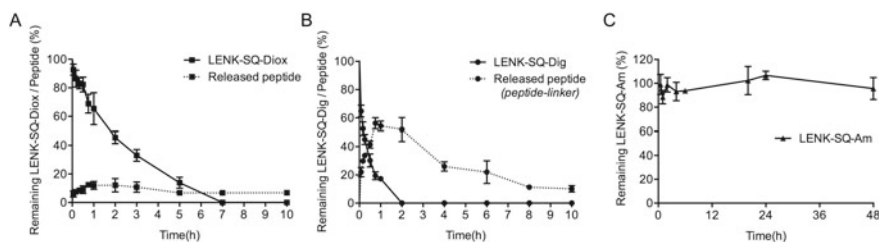


Fig. 6 In vitro bioconversion of LENK-SQ bioconjugates into LENK in the presence of serum. **A** LENK-SQ with dioxycarbonyl linker, **B** LENK-SQ with diglycolic linker, and **C** LENK-SQ with amide bond. Solid lines and dashed lines represent the bioconjugates and the released peptides, respectively. Figure reproduced from Ref. Feng et al. (2019), © 2019 AAAS

of a progressive release of the free LENK peptide which was subsequently slowly degraded by the peptidases of the serum, but still lasted beyond 10 h post-incubation (Fig. 6A). LENK-SQ-Dig NPs, for their part, decreased in serum until complete disappearance at 2 h, but no presence of free peptide was detected. Interestingly, the RP-HPLC analyses evidenced a slow release of the peptide still attached to its linker. The peptide-linker fragment reached a maximum at 45 min before undergoing progressive degradation but it could still be detected over 10 h (Fig. 6B). On the contrary, LENK-SQ-Am NPs remained stable in serum during 48 h, and no peptide was released throughout the experiment (Fig. 6C) (Feng et al. 2019). Interestingly, with the LENK-SQ-Diox bioconjugate, both the LENK and the SQ moieties were each attached to the dioxycarbonyl linker through an ester bond. In the case of the LENK-SQ-Dig bioconjugate, the diglycolate linker was linked on one side to SQ moiety through an ester bond while on the other side it was linked to the LENK through an amide bond. With regards to the LENK-SQ-Am bioconjugate, the LENK was directly connected to the SQ moiety through an amide bond. Given that generally amide bond is chemically and enzymatically more stable than ester bond, the absence of release of LENK from LENK-SQ-Am was not surprising (Simões et al. 2009; Wong and Choi 2015). Moreover, because LENK-SQ-Am and LENK-SQ-Dig are linear peptides, their N-terminal modification increased peptidase resistance (Oliyai 1996). Finally, as mouse serum is extremely rich in esterases, it is most likely that the release of LENK from LENK-SQ NPs was due to enzymatic hydrolysis of ester bond (Simões et al. 2009). Despite these *in vitro* data showing that depending on the type of linker, whether or not the LENK peptide was released, all the 3 bioconjugates were recruited for experimental algosimetry. It was expected that within the inflammation site, the more aggressive *in vivo* enzymatic medium, particularly rich in proteolytic enzymes, will contribute to the release of LENK from all the bioconjugates. Indeed, it was reported that the presence of high concentrations of proteolytic enzymes like chymotrypsin, cathepsin D and other proteases in inflammatory exudates play a crucial role in the inflammatory process (Viswanatha Swamy and Patil 2008).

7 Assessment of the Analgesic Activity of LENK-SQ NPs *in vivo*

The antinociceptive properties of LENK-SQ NPs were evaluated using a carrageenan-induced paw edema model in rats. The inflammation was generated by intraplantar injection of λ -carrageenan into the right hind paw thus inducing a local inflammatory response characterized by marked edema, hyperthermia, and hyperalgesia restricted to the injected right hind paw. Baseline measurements of paw withdrawal latencies (PWL) to a noxious thermal stimulus were first performed prior to carrageenan injection using Hargreaves test (Oliyai 1996) and presented a mean value \pm SEM ($n = 8$) of 6.65 ± 0.37 s. Then, thermal sensitivities were evaluated 3 h after carrageenan injection, which corresponded to the peak inflammatory response, leading to a mean decrease of 52.48% of PWL compared to the basal PWLs in naïve rats (Fig. 8). Anti-hyperalgesic effects were assessed using the same test at various times during 4 h, after acute intravenous administration of the different drug treatments at this 3 h inflammation peak (Fig. 7). The acute treatment with morphine which was used as positive control (1 mg/kg), reduced the thermal hyperalgesia as shown by the resulting significant increase in PWLs. Indeed, the PWL reached 12.87 ± 1.38 s, 10 min after morphine injection, while it remained at 3.05 ± 0.20 s after treatment with a control dextrose solution (Fig. 8A). However, morphine analgesic activity disappeared rapidly and no longer significant effect was observed from 100 min post-morphine administration (Fig. 8A). Then, the anti-hyperalgesic effect of LENK-SQ NPs with the 3 different linkers was evaluated (Fig. 8C–H). All LENK-SQ NPs displayed a significant anti-hyperalgesic effect on inflamed hind paw leading to a significant reduction of thermal hyperalgesia, as expressed by a dramatic increase of respective AUC values in comparison with λ -carrageenan-treated rats injected with either the free LENK peptide or the blank SQ NPs (Fig. 8D, F, H). The anti-hyperalgesic effect was less intense than after morphine administration, but LENK-SQ NPs exhibited a much longer lasting effect. More specifically, the anti-hyperalgesic activity was notable during two hours from 10 to 130 min in rats injected with LENK-SQ Diox NPs or LENK-SQ Am NPs (Fig. 8C, G). Surprisingly, LENK-SQ-Am NPs, which were supposed to release the LENK slower than the two other NPs, have proved to be more potent but with a shorter duration, probably because the enzymatic capability in serum is not predictive of the enzymatic content in the inflamed paw. For their part, LENK-SQ-dig NPs also displayed a significant anti-hyperalgesic effect (Fig. 8E) which lasted twice as long as morphine. Indeed, LENK-SQ-dig NPs exhibited a maximum increase in PWL from 10 to 130 min post-injection, followed by a progressive decrease down to baseline at 220 min. It is interesting to note that the maximal PWL values corresponding to LENK-SQ NPs administration in λ -carrageenan-treated rats were comparable to basal PWL values measured in control naïve rats, before λ -carrageenan treatment (Fig. 8C, E, G), thus revealing a pure anti-hyperalgesic action of these NPs. However, the PWL values corresponding to the injection of morphine in λ -carrageenan-treated rats were twice

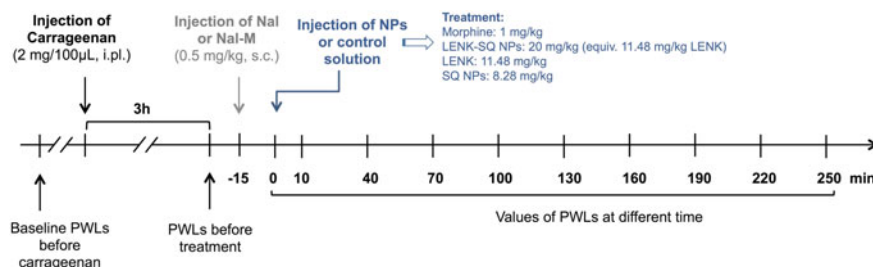


Fig. 7 Experimental design for algometry. The antinociceptive effect of NPs was tested in a pathophysiological context induced by an intraplantar carrageenan injection (2% saline, 100 µL). Involvement of central or peripheral opioid receptors was performed using a brain-permeant opioid antagonist, naloxone (Nal), and a brain-impermeant opioid receptor antagonist, naloxone methiodide (Nal-M). NP suspensions or control solutions were injected intravenously with a dose volume of 10 mL/kg during 30 s. The Hargreaves test was performed 10 min after the NP administration and then every 30 min up to a period of 250 min. The dose of LENK-SQ NPs (20 mg/kg) was equivalent to LENK (11.48 mg/kg) and to SQ NPs (8.28 mg/kg) and corresponded to 20.66 mmol/kg for both LENK-SQ and LENK. s.c., subcutaneous; i.pl., intraplantar. Figure reproduced from Ref. Feng et al. (2019), © 2019 AAAS

as high as those found in control naïve rats (Fig. 8A), which confirm the well established analgesic effect of the opiate agonist in addition to the anti-hyperalgesic effect. Furthermore, the absence of anti-hyperalgesic activity with blank SQ NPs (without the LENK) (Fig. 8), confirmed that the antinociceptive response to LENK-SQ NPs administration were due to the released LENK peptide. All these results seem to indicate that LENK-SQ NPs are particularly effective to treat hyperalgesia and are devoid of analgesic properties as with morphine. However, further studies are required to evaluate this hypothesis (Feng et al. 2019).

8 Effects of Opioid Receptor Blockade Using Naloxone and Naloxone Methiodide

For the purpose of establishing the involvement of central or peripheral opioid receptors during the anti-hyperalgesic effect of LENK-SQ NPs, opioid receptor antagonists such as naloxone (Nal, central and peripheral antagonist) or naloxone methiodide (Nal-M, peripheral antagonist) (Buller et al. 2005) were administered subcutaneously 15 min prior to the injection of NPs (Fig. 7). Pre-administration of either brain-permeant *Nal* or brain-impermeant Nal-M, abolished the anti-hyperalgesic effect of the three LENK-SQ NPs (Fig. 8C–H). Indeed, Nal pre-treatment resulted in a reduction of 66%, 105% or 73% of the AUC values compared to these found in rats injected with LENK-SQ-Diox, LENK-SQ-Dig and LENK-SQ-Am NPs alone, respectively. In the same way, pre-treatment with Nal-M caused a reduction of 81%, 99% and 96%, respectively, showing that the selective blockade of peripheral opioid receptors only

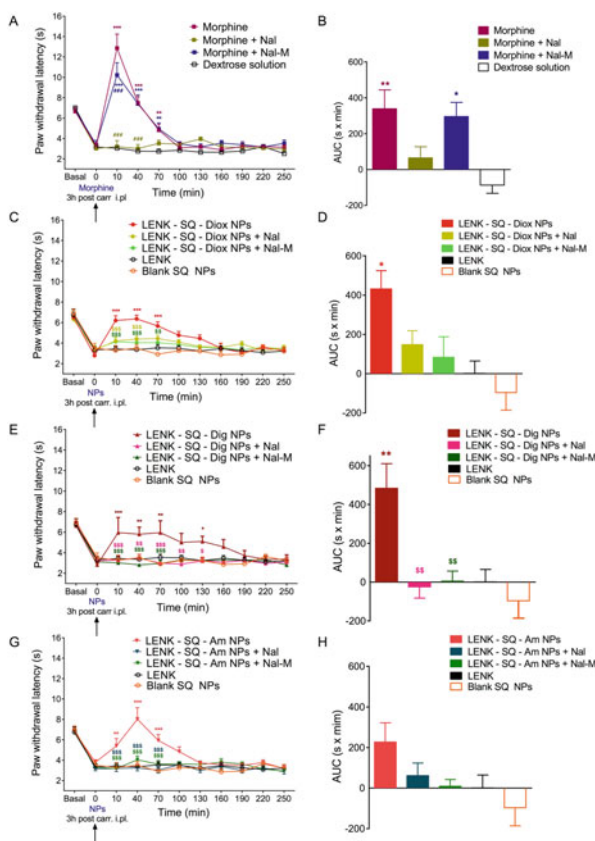


Fig. 8 Antihyperalgesic effect of LENK-SQ NPs and morphine. Antihyperalgesic effects of acute treatment with morphine **A** and **B**, LENK-SQ-Diox NPs **C** and **D**, LENK-SQ-Dig NPs **E** and **F**, and LENK-SQ-Am NPs **G** and **H** in λ -carrageenan–induced inflammatory pain injected rats. Administration of morphine, LENK-SQ NPs, Nal, Nal-M, LENK, blank SQ NPs, or dextrose solution (vehicle) was performed (arrows, 0 on abscissa) 3 h after λ -carrageenan injection into the right hind paw. Morphine (**A**), LENK-SQ-Diox NPs (**C**), LENK-SQ-Dig NPs (**E**), and LENK-SQ-Am NPs (**G**) induced an increase in PWL (in seconds, means \pm SEM of independent determinations in five to nine animals per group) in the Hargreaves test. * $P < 0.05$, ** $P < 0.01$, *** $P < 0.001$, compared to dextrose solution or LENK solution; ### $P < 0.001$, compared to morphine; \$ $P < 0.05$, \$\$ $P < 0.01$, \$\$\$ $P < 0.001$, compared to LENK-SQ NPs. Two-way analysis of variance (ANOVA) with repeated measures, Bonferroni post test. Nal or Nal-M was administered 15 min before morphine or LENK-SQ NP injection. Basal on abscissa: Control (naïve) rats (before λ -carrageenan injection). (**B**, **D**, **F**, and **H**) Bars are the means \pm SEM of AUCs (seconds \times minutes) of the cumulative durations derived from the time course changes (**A**, **C**, **E**, and **G**) in PWL after the various treatments. * $P < 0.05$, ** $P < 0.01$, *** $P < 0.001$, one-way ANOVA, Tukey post test, compared to dextrose (vehicle) or LENK solution; \$ $P < 0.05$, \$\$ $P < 0.01$, \$\$\$ $P < 0.001$, compared to LENK-SQ NPs. Two-way analysis of variance (ANOVA) with repeated measures, Bonferroni post test. Nal or Nal-M was administered 15 min before morphine or LENK-SQ NP injection. Basal on abscissa: Control (naïve) rats (before λ -carrageenan injection). (**B**, **D**, **F**, and **H**) Bars are the means \pm SEM of AUCs (seconds \times minutes) of the cumulative durations derived from the time course changes (**A**, **C**, **E**, and **G**) in PWL after the various treatments. * $P < 0.05$, ** $P < 0.01$, *** $P < 0.001$, one-way ANOVA, Tukey post test, compared to dextrose (vehicle) or LENK solution; \$ $P < 0.05$, \$\$ $P < 0.01$, \$\$\$ $P < 0.001$, compared to LENK-SQ NPs Figure reproduced from Ref. Feng et al. (2019), © 2019 AAAS

was enough to abolish the anti-hyperalgesic effects of LENK-SQ NPs. It is interesting to note that in the case of morphine, pre-administration of Nal abrogated the amplitude and the duration of the anti-hyperalgesic effect of morphine in comparison with the morphine group while pre-treatment with Nal-M only marginally decreased the morphine's effect (by 13%) (Fig. 8A and B) showing that morphine acts mainly through central and, to a lesser extent, peripheral opioid receptors.

All these results clearly demonstrated that all three LENK-SQ NPs acted exclusively through peripherally located opioid receptors (Feng et al. 2019).

9 Biodistribution of LENK-SQ NPs

In order to investigate the ability of LENK-SQ NPs to address the neuropeptide towards the inflamed tissue, biodistribution studies were performed using *in vivo* fluorescence imaging. The *in vivo* biodistribution of LENK-SQ-Am NPs was assessed after intravenous injection of DiD-fluorescently labeled LENK-SQ-Am NPs in a murine λ -carrageenan-induced paw edema model (right hind paw). The fluorescence in tissues was tracked up to 24 h, non-invasively, from the abdomen side using an IVIS Lumina device (Fig. 9). After intravenous injection of fluorescent LENK-SQ-Am NPs, the real-time *in vivo* imaging showed a remarkable increase of fluorescence within the inflamed paw by 2–3 times of the average radiant efficiency in comparison with the healthy paw (Fig. 9A, D, F). In order to ensure that the accumulation of fluorescence in the λ -carrageenan-inflamed paw was not due to the local hind paw injection *per se*, normal mice were injected locally with saline in the hind paw and then intravenously treated with fluorescent LENK-SQ NPs (non-inflamed control). The absence of significant accumulation of fluorescence at hind paw level confirmed that the NPs accumulation is related to inflammation process induced by carrageenan (Fig. 9B, E). The intravenous injection of a single DiD solution (without NPs) in λ -carrageenan administered mice, didn't reveal, here again, significant accumulation of fluorescence in the inflamed paw (Fig. 9C, F).

With the aim of showing that the NPs reached intact the inflamed tissues, the LENK-SQ NPs containing two fluorescent probes, a the fluorescent DiD dye and a fluorescent DiR quencher, were incubated in serum. A progressive appearance of fluorescence indicated a relatively slow dissociation of the NPs in serum (20% after 5 min and 50% after 30 min) suggesting that under our *in vivo* conditions, a significant proportion of intact NPs could reach the inflamed tissues (Fig. 10).

Finally, in a separate experiment, the biodistribution of the fluorescence in different organs was performed. Thus, 4 h after the intravenous injection of fluorescent NPs or DiD solution, mice were euthanized and transcardially perfused with saline to eliminate the fluorescence which was in the blood circulation. The collected organs indicated a strong *ex vivo* fluorescence signal which was observed again in the inflamed paw, but also in the liver, the spleen and the lungs. Interestingly, no fluorescence was detected in the brain of the animals (Fig. 11) thus confirming that the anti-hyperalgesic effect resulted from the targeting of LENK-SQ NPs toward

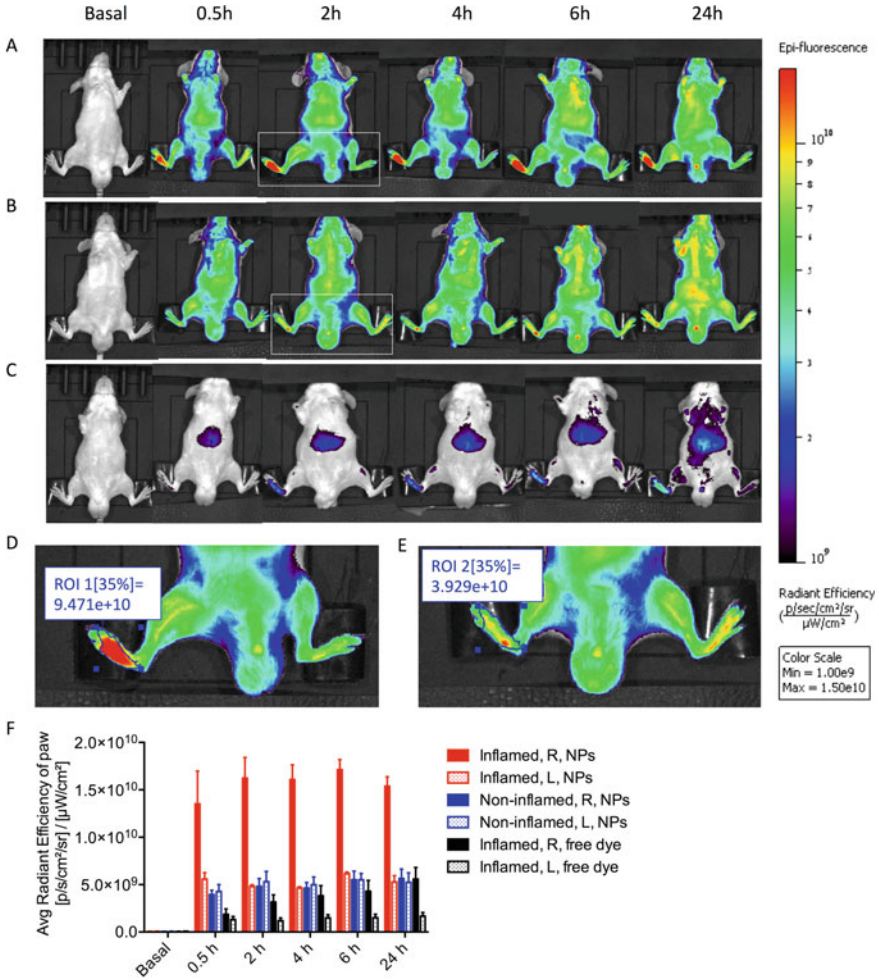


Fig. 9 IVIS Lumina scan of mice and of their organs after intravenous administration of fluorescent LENK-SQ-Am NPs or control fluorescent dye solution (ventral view). **A** Biodistribution of fluorescent LENK-SQ-Am NPs in mice with inflamed right hind paw. **B** Biodistribution of fluorescent LENK-SQ-Am NPs in mice with non-inflamed hind paw (saline injected only into the right hind paw). **C** Biodistribution of free dye in mice with inflamed right paw. **D** Zoom of group A at 2 h. **E**) Zoom of group B at 2 h. **F**) Quantitative analysis of the paws with the same region of interest (ROI). R, right hind paw; L, left hind paw. Figure reproduced from Ref. Feng et al. (2019), © 2019 AAAS

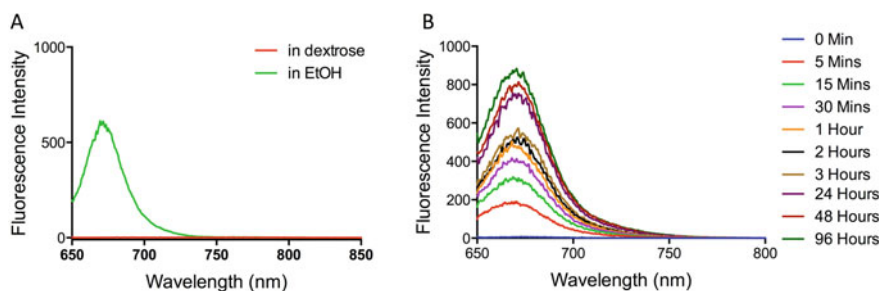


Fig. 10 In vitro colloidal stability of LENK-SQ-Am NPs in mouse serum. **A** Controls: When diluted in 5% dextrose LENK-SQ-Am NPs remained assembled (DiD: reporter dye; DiR: quencher). They disassembled in ethanol; **B** LENK-SQ-Am NPs (DiD: reporter dye; DiR: quencher) incubated in mouse serum (1:4). The fluorescence emission was measured to assess the progressive disassembly of the nanoparticles Figure reproduced from Ref. Feng et al. (2019), © 2019 AAAS

peripheral opioid receptors in inflamed tissue, rather than central opioid receptors (Feng et al. 2019).

10 Toxicity Study

Given that not negligible fluorescence was detected in some organs, indicating the potential presence of NPs in these tissues, the overall toxicity of LENK-SQ NPs was investigated 24 h and 48 h after their intravenous administration (20 mg/kg) in rats and compared to control animals injected with 5% dextrose solution. Concerning the liver, the levels of aspartate transaminase (AST) (Fig. 12A) and alanine transaminase (ALT) (Fig. 12B) were not increased in the LENK-SQ NPs group in comparison with control group, thus indicating no toxicity towards the liver. This was confirmed by histological analysis of this tissue at 24 h and 48 h (Fig. 12C–F). The histology of the spleen (Fig. 12G–J), the kidneys (Fig. 12K–N), the lungs (Fig. 12O–R) and the heart (Fig. 12S–V) didn't reveal any morphological anomaly after LENK-SQ NPs administration, too. All these results confirmed the safety of the LENK-SQ NPs upon systemic intravenous administration at the therapeutic dose of 20 mg/kg (Feng et al. 2019).

11 Conclusion

We describe here a novel nanomedicine approach based on the bioconjugation of endogenous LENK neuropeptide to biocompatible SQ, allowing the specific delivery of LENK for efficient pain control associated with inflammatory events. It was shown that LENK-SQ NPs exhibited an anti-hyperalgesic activity which lasted even longer

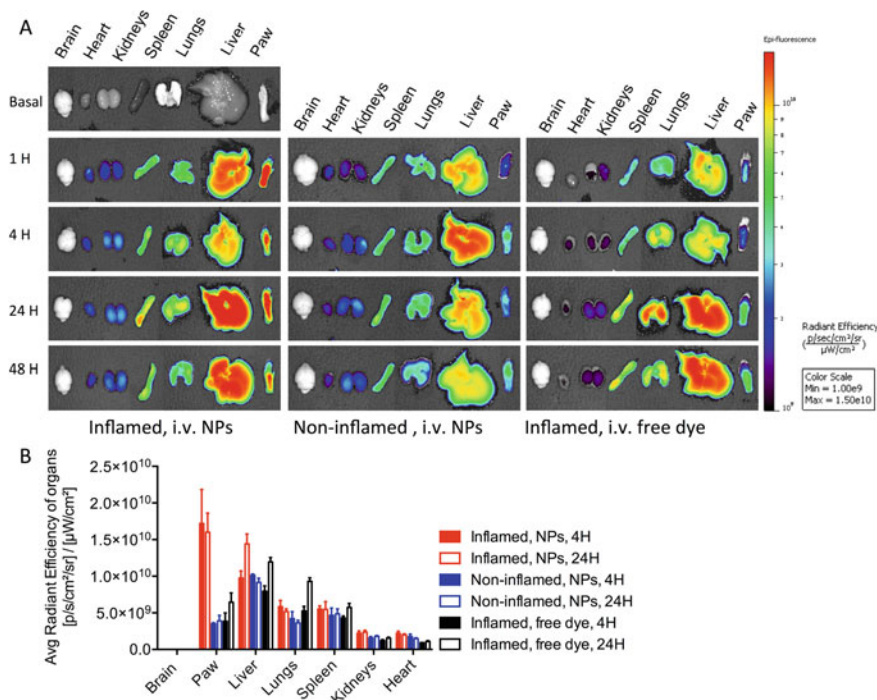


Fig. 11 Biodistribution of fluorescent LENK-SQ-Am NPs or control fluorescent dye solution in mice with or without inflamed paw. 4 h after λ -carrageenan or saline injection into the right paw, fluorescent LENK-SQ NPs or free dye were intravenously introduced into the mice. At different time points, mice were deeply anesthetized with a mixture of ketamine (100 mg/kg, i.p.) and xylazine (10 mg/kg, i.p.) before euthanasia by transcardiac perfusion of 40 ml saline (8 mL/min), until the fluid exiting the right atrium was entirely clear. Then, liver, spleen, kidneys, heart, lungs, brain, and inflamed right hind paw were excised and immediately imaged with the imager. The fluorescence emitted was quantified with Living Image software over the region of interest (ROI) with the threshold of 20%. (A) Ex vivo fluorescence imaging of the harvested brain, heart, kidneys, lungs, liver and paw from fluorescent NPs or free dye-injected SWISS mice. (B) Average radiant efficiency of these organs after 4 or 24 h injection of NPs or free dye. Figure reproduced from Ref. Feng et al. (2019), © 2019 AAAS

than with morphine, by activation of peripherally located opioid receptors. The experimental approach to prepare these NPs is simple, safe and easy, which should facilitate further pharmaceutical development and clinical translation. Although further studies are needed to more precisely determine how the pharmacodynamics of LENK-SQ NPs may affect the clinical outcome, this study opens a new exciting perspective for an efficient treatment of intense pain, devoid of severe side effects associated with morphine or related synthetic opioids.

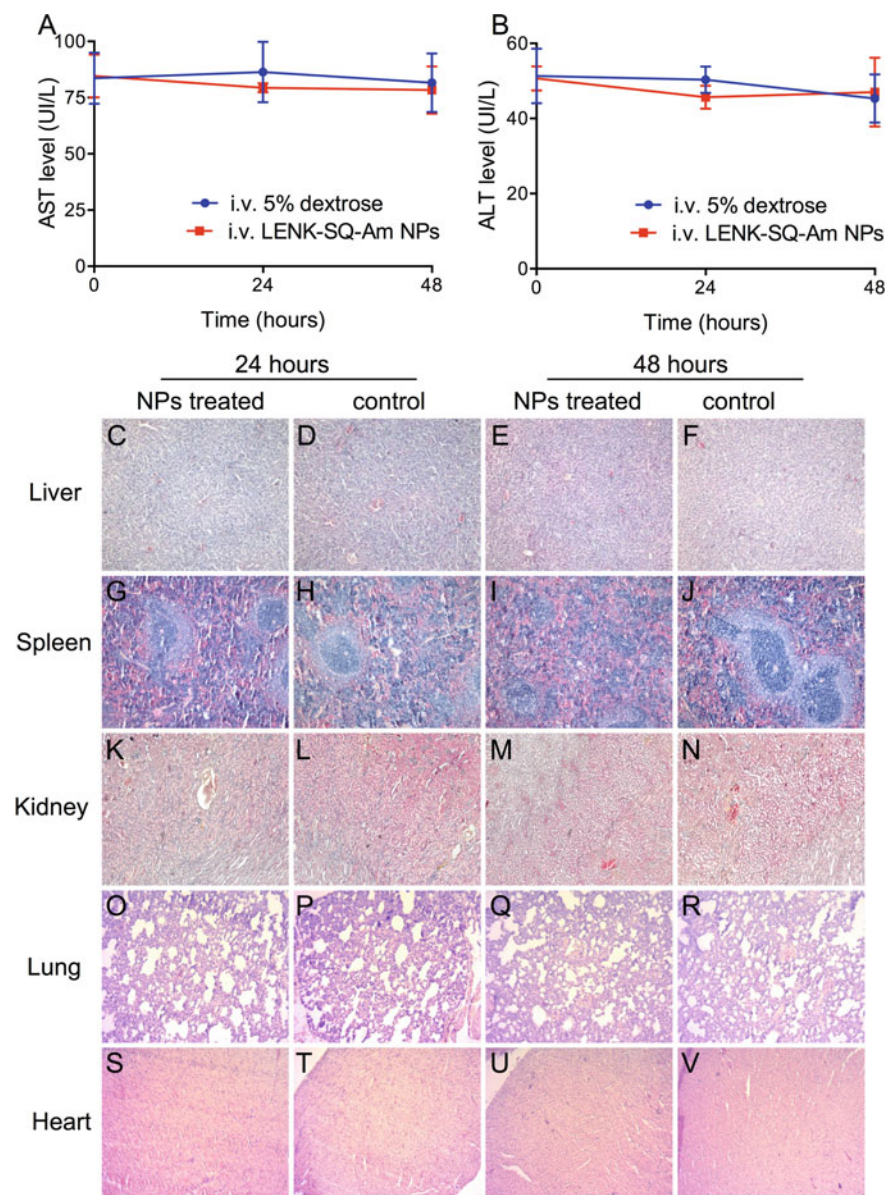


Fig. 12 Toxicity study of LENK-SQ-Am NPs upon systemic administration. LENK-SQ-Am NPs (20 mg/kg) were intravenously administered in rats. The AST (A) and ALT (B) levels in plasma showed no differences compared with dextrose solution (data presented as mean UI/L \pm SED, N = 3 animals per group). Histological analysis of organs after intravenous administration of LENK-SQ-Am NPs (20 mg/kg) did not show any signs of cell or tissue damage at 24 h and 48 h, comparatively to a control 5% dextrose solution. Liver (C-F), spleen (G-J), kidneys (K-N), lungs (O-R) and heart (S-V). All tissue images were analyzed by microscopy at 10 \times magnification except for kidneys which were at 5 \times magnification (Zeiss). Figure reproduced from Ref. Feng et al. (2019), © 2019 AAAS

References

- Abbadie C, Abbadie GW (2002) Endorphins and their receptors. In: Encyclopedia of the human brain. Elsevier (2002), pp 193–200. <https://doi.org/10.1016/B0-12-227210-2/00137-0>
- Adams JM (2018) Increasing naloxone awareness and use: the role of health care practitioners. *JAMA* 319(20):2073. <https://doi.org/10.1001/jama.2018.4867>
- Adams D, Gonzalez-Duarte A, O’Riordan WD, Yang C-C, Ueda M, Kristen AV, Tournev I, Schmidt HH, Coelho T, Berk JL, Lin K-P, Vita G, Attarian S, Planté-Bordeneuve V, Mezei MM, Campistol JM, Buades J, Brannagan TH, Kim BJ, Oh J, Parman Y, Sekijima Y, Hawkins PN, Solomon SD, Polydefkis M, Dyck PJ, Gandhi PJ, Goyal S, Chen J, Strahs AL, Nochur SV, Sweetser MT, Garg PP, Vaishnav AK, Gollob JA, Suhr OB (2018) Patisiran, an RNAi therapeutic, for hereditary transthyretin amyloidosis. *N Engl J Med* 379(1):11–21. <https://doi.org/10.1056/NEJMoa1716153>
- Anselmo AC, Mitragotri S (2016) Nanoparticles in the clinic: nanoparticles in the clinic. *Bioeng Transl Med* 1(1):10–29. <https://doi.org/10.1002/btm2.10003>
- Bobo D, Robinson KJ, Islam J, Thurecht KJ, Corrie SR (2016) Nanoparticle-based medicines: a review of FDA-approved materials and clinical trials to date. *Pharm Res* 33(10):2373–2387. <https://doi.org/10.1007/s11095-016-1958-5>
- Barenholz Y (Chezy). Doxil® — The first FDA-approved nano-drug: lessons learned. *J Control Release* 2012, 160(2): 117–134. <https://doi.org/10.1016/j.jconrel.2012.03.020>
- Betageri GV, Vutla NB, Banga AK (1997) Liposomal formulation and characterization of the opioid peptide leucine enkephalin. *Pharm Sci* 3:587–591. <https://doi.org/10.1111/j.2042-7158.1997.tb00502.x>
- Bonvalot S, Rutkowski PL, Thariat J, Carrère S, Ducassou A, Sunyach M-P, Agoston P, Hong A, Mervoyer A, Rastrelli M, Moreno V, Li RK, Tiangco B, Herraes AC, Gronchi A, Mangel L, Sy-Ortin T, Hohenberger P, de Baère T, Le Cesne A, Helfre S, Saada-Bouزيد E, Borkowska A, Anghel R, Co A, Gebhart M, Kantor G, Montero A, Loong HH, Vergés R, Lapeire L, Dema S, Kacso G, Austen L, Moureau-Zabotto L, Servois V, Wardelmann E, Terrier P, Lazar AJ, Bovée, JVMG, Le Pêcheux C, Papai Z (2019) NBTXR3, a first-in-class radioenhancer hafnium oxide nanoparticle, plus radiotherapy versus radiotherapy alone in patients with locally advanced soft-tissue sarcoma (Act.In.Sarc): a multicentre, phase 2–3, randomised, controlled trial. *Lancet Oncol* 20(8):1148–1159. [https://doi.org/10.1016/S1470-2045\(19\)30326-2](https://doi.org/10.1016/S1470-2045(19)30326-2)
- Buller K, Hamlin A, Osborne P (2005) Dissection of peripheral and central endogenous opioid modulation of systemic interleukin-1 β responses using c- expression in the rat brain. *Neuropharmacology* 49(2):230–242. <https://doi.org/10.1016/j.neuropharm.2005.03.014>
- Büscher HH, Hill RC, Römer D, Cardinaux F, Clossé A, Hauser D, Pless J (1976) Evidence for analgesic activity of enkephalin in the mouse. *Nature* 261(5559):423–425. <https://doi.org/10.1038/261423a0>
- Carnevale J, Ko AH (2016) MM-398 (nanoliposomal irinotecan): emergence of a novel therapy for the treatment of advanced pancreatic cancer. *Future Oncol* 12(4):453–464. <https://doi.org/10.2217/fon.15.333>
- Chang TC, Shiah HS, Yang CH, Yeh KH, Cheng AL, Shen BN, Wang YW, Yeh CG, Chiang NJ, Chang JY, Chen LT (2015) Phase I study of nanoliposomal irinotecan (PEP02) in advanced solid tumor patients. *Cancer Chemother Pharmacol* 75(3):579–586. <https://doi.org/10.1007/s00280-014-2671-x>
- Chen Y, Wang F, Benson HAE (2008) Effect of formulation factors on incorporation of the hydrophilic peptide dalargin into PLGA and MPEG-PLGA nanoparticles. *Biopolymers* 90(5):644–650. <https://doi.org/10.1002/bip.21013>
- Contet C, Kieffer BL, Befort K (2004) Mu opioid receptor: a gateway to drug addiction. *Curr Opin Neurobiol* 14(3):370–378. <https://doi.org/10.1016/j.conb.2004.05.005>

- Couvreur P, Stella B, Reddy LH, Hillaireau H, Dubernet C, Desmaële D, Lepêtre-Mouelhi S, Rocco F, Dereuddre-Bosquet N, Clayette P, Rosilio V, Marsaud V, Renoir J-M, Cattel L (2006) Squalenoyl nanomedicines as potential therapeutics. *Nano Lett* 6(11):2544–2548. <https://doi.org/10.1021/nl061942q>
- Coyne DW, Auerbach M (2010) Anemia management in chronic kidney disease: intravenous iron steps forward. *Am J Hematol NA-NA*. <https://doi.org/10.1002/ajh.21682>
- Cummings GC, Dixon J, Kay NH, Windsor JPW, Major E, Morgan M, Sear JW, Spence AA, Stephenson DK (1984) Dose requirements of ICI 35,868 (propofol, 'Diprivan') in a new formulation for induction of anaesthesia. *Anaesthesia* 39(12):1168–1171. <https://doi.org/10.1111/j.1365-2044.1984.tb06425.x>
- Desmaële D, Gref R, Couvreur P (2012) Squalenoylation: a generic platform for nanoparticulate drug delivery. *J Control Release* 161(2):609–618. <https://doi.org/10.1016/j.jconrel.2011.07.038>
- Dykstra L, Granger AL, Allen RM, Zhang X, Rice KC (2002) Antinociceptive effects of the selective delta opioid agonist SNC80 alone and in combination with mu opioids in the squirrel monkey titration procedure. *Psychopharmacology* 163(3–4):420–429. <https://doi.org/10.1007/s00213-002-1100-8>
- Fan Y, Marioli M, Zhang K (2021) Analytical characterization of liposomes and other lipid nanoparticles for drug delivery. *J Pharm Biomed Anal* 192:113642. <https://doi.org/10.1016/j.jpba.2020.113642>
- Feng J, Lepetre-Mouelhi S, Couvreur P (2017) Design, preparation and characterization of modular SQ-based nanosystems for controlled drug release. *CTMC* 17(25). <https://doi.org/10.2174/1568026617666170719171728>
- Feng J, Lepetre-Mouelhi S, Gautier A, Mura S, Cailleau C, Coudore F, Hamon M, Couvreur P (2019) A new painkiller nanomedicine to bypass the blood-brain barrier and the use of morphine. *Sci Adv* 5(2), eaau5148. <https://doi.org/10.1126/sciadv.aau5148>
- Fox JL (1995) FDA advisors okay NeXstar's DaunoXome. *Nat Biotechnol* 13(7):635–636. <https://doi.org/10.1038/nbt0795-635>
- Gupta AK, Gupta M (2005) Synthesis and surface engineering of iron oxide nanoparticles for biomedical applications. *Biomaterials* 26(18):3995–4021. <https://doi.org/10.1016/j.biomaterials.2004.10.012>
- Gylling H, Miettinen TA (1994) Postabsorptive metabolism of dietary SQ. *Atherosclerosis* 106(2):169–178. [https://doi.org/10.1016/0021-9150\(94\)90122-8](https://doi.org/10.1016/0021-9150(94)90122-8)
- Hamill RJ (2013) Amphotericin B formulations: a comparative review of efficacy and toxicity. *Drugs* 73(9):919–934. <https://doi.org/10.1007/s40265-013-0069-4>
- Jackson LA, Anderson EJ, Rouphael NG, Roberts PC, Makhene M, Coler RN, McCullough MP, Chappell JD, Denison MR, Stevens LJ, Pruijssers AJ, McDermott A, Flach B, Doria-Rose NA, Corbett KS, Morabito KM, O'Dell S, Schmidt SD, Swanson PA, Padilla M, Mascola JR, Neuzil KM, Bennett H, Sun W, Peters E, Makowski M, Albert J, Cross K, Buchanan W, Pikaart-Tautges R, Ledgerwood JE, Graham BS, Beigel JH (2020) An mRNA vaccine against SARS-CoV-2 — preliminary report. *N Engl J Med* 383(20):1920–1931. <https://doi.org/10.1056/NEJMoa202483>
- Janecka A, Fichna J, Janecki T (2004) Opioid receptors and their ligands. *CTMC* 4(1):1–17. <https://doi.org/10.2174/1568026043451618>
- Kiritsy-Roy JA, Marson L, Van Loon GR (1989) Sympathoadrenal, cardiovascular and blood gas responses to highly selective mu and delta opioid peptides. *J Pharmacol Exp Ther* 251(3):1096–1103
- Krauss AC, Gao X, Li L, Manning ML, Patel P, Fu W, Janoria KG, Gieser G, Bateman DA, Przepiorka D, Shen YL, Shord SS, Sheth CM, Banerjee A, Liu J, Goldberg KB, Farrell AT, Blumenthal GM, Pazdur R (2019) FDA approval summary: (daunorubicin and cytarabine) liposome for injection for the treatment of adults with high-risk acute myeloid leukemia. *Clin Cancer Res* 25(9):2685–2690. <https://doi.org/10.1158/1078-0432.CCR-18-2990>

- Laurent S, Forge D, Port M, Roch A, Robic C, Vander Elst L, Muller RN (2008) Magnetic iron oxide nanoparticles: synthesis, stabilization, vectorization, physicochemical characterizations, and biological applications. *Chem. Rev.* 108(6):2064–2110. <https://doi.org/10.1021/cr068445e>
- Leonard RCF, Williams S, Tulpule A, Levine AM, Oliveros S (2009) Improving the therapeutic index of anthracycline chemotherapy: focus on liposomal doxorubicin (Myocet™). *Breast* 18(4):218–224. <https://doi.org/10.1016/j.breast.2009.05.004>
- Maeda H (2012) Macromolecular therapeutics in cancer treatment: the EPR effect and beyond. *J Control Release* 164(2):138–144. <https://doi.org/10.1016/j.jconrel.2012.04.038>
- Mandal PK, McMurray JS (2007) Pd–C-induced catalytic transfer hydrogenation with triethylsilane. *J. Org. Chem.* 72(17):6599–6601. <https://doi.org/10.1021/jo0706123>
- Miettinen TA, Vanhanen H (1994) Serum concentration and metabolism of cholesterol during rapeseed oil and SQ feeding. *Am J Clin Nutr* 59(2):356–363. <https://doi.org/10.1093/ajcn/59.2.356>
- Na HB, Song IC, Hyeon T (2009) Inorganic nanoparticles for MRI contrast agents. *Adv Mater* 21(21):2133–2148. <https://doi.org/10.1002/adma.200802366>
- Oliyai R (1996) Prodrugs of peptides and peptidomimetics for improved formulation and delivery. *Adv Drug Deliv Rev* 19(2):275–286. [https://doi.org/10.1016/0169-409X\(95\)00110-S](https://doi.org/10.1016/0169-409X(95)00110-S)
- Pasternak GW, Abbadie C (2013) Opioid receptor localization. In: Gebhart GF, Schmidt RF (eds) *Encyclopedia of pain*. Springer, Heidelberg, pp 2436–2441. https://doi.org/10.1007/978-3-642-28753-4_2961
- Peer D, Karp JM, Hong S, Farokhzad OC, Margalit R, Langer R (2007) Nanocarriers as an emerging platform for cancer therapy. *Nature Nanotech* 2(12):751–760. <https://doi.org/10.1038/nnano.2007.387>
- Rust DM, Jameson G (1998) The novel lipid delivery system of amphotericin B: drug profile and relevance to clinical practice. *Oncol Nurs Forum* 25(1):35–48
- Schmidt-Erfurth U, Hasan T (2000) Mechanisms of action of photodynamic therapy with verteporfin for the treatment of age-related macular degeneration. *Surv Ophthalmol* 45(3):195–214. [https://doi.org/10.1016/S0039-6257\(00\)00158-2](https://doi.org/10.1016/S0039-6257(00)00158-2)
- Sémiramoth N, Meo CD, Zouhiri F, Saïd-Hassane F, Valetti S, Gorges R, Nicolas V, Poupaert JH, Chollet-Martin S, Desmaële D, Gref R, Couvreur P (2012) Self-assembled squalenoylated penicillin bioconjugates: an original approach for the treatment of intracellular infections. *ACS Nano* 6(5):3820–3831. <https://doi.org/10.1021/nn204928v>
- Silverman JA, Deitcher SR (2013) Marqibo® (vincristine sulfate liposome injection) improves the pharmacokinetics and pharmacodynamics of vincristine. *Cancer Chemother Pharmacol* 71(3):555–564. <https://doi.org/10.1007/s00280-012-2042-4>
- Simões MF, Valente E, Gómez MJR, Anes E, Constantino L (2009) Lipophilic pyrazinoic acid amide and ester prodrugs. *Eur J Pharm Sci* 37(3–4):257–263. <https://doi.org/10.1016/j.ejps.2009.02.012>
- Tavani A, Petrillo P, La Regina A, Sbacchi M (1990) Role of peripheral mu, delta and kappa opioid receptors in opioid-induced inhibition of gastrointestinal transit in rats. *J Pharmacol Exp Ther* 254(1):91–97
- Thompson KA, Goodale DB (2000) The recent development of propofol (DIPRIVAN®). *Intensive Care Med* 26(S3):S400–S404. <https://doi.org/10.1007/PL00003783>
- Tomao, S (2009) Albumin-bound formulation of paclitaxel (Abraxane® ABI-007) in the treatment of breast cancer. *IJN* 99. <https://doi.org/10.2147/IJN.S3061>
- Viswanatha Swamy AHM, Patil P (2008) Effect of some clinically used proteolytic enzymes on inflammation in rats. *Indian J Pharm Sci* 70(1):114. <https://doi.org/10.4103/0250-474X.40347>

- Wang Y-XJ, Hussain SM, Krestin GP (2001) Superparamagnetic iron oxide contrast agents: physicochemical characteristics and applications in MR imaging. *Eur Radiol* 11(11):2319–2331. <https://doi.org/10.1007/s003300100908>
- Wang AZ, Langer R, Farokhzad OC (2012) Nanoparticle delivery of cancer drugs. *Annu Rev Med* 63(1):185–198. <https://doi.org/10.1146/annurev-med-040210-162544>
- Wong PT, Choi SK (2015) Mechanisms of drug release in nanotherapeutic delivery systems. *Chem Rev* 115(9):3388–3432. <https://doi.org/10.1021/cr5004634>

Inverse Problems and Hierarchical Multiscale Modelling of Biological Matter



Alexander Lyubartsev and Aatto Laaksonen

Abstract In solving mathematical and physical problems we generally think that the problem can be condensed to a well-defined equation which then can be solved either analytically or numerically with the provided input data and, if necessary, applying initial and boundary conditions to limit the amount of solutions to something which makes sense and can be accepted as the correct solution. This is the typical practice in “forward” problem solving. Consequently the *solution* can be considered as the *inverse* of the problem. Indeed, it is not uncommon in Science and also in everyday life to have the “solution” without knowing what exactly did “cause” it and “how”. We take an illustrative example from Forensics with a case where a lethal crime is committed with a dead body (solution), but at the time of arrival to the crime scene the details to start to investigate are scattered all over the place. The investigators have the difficult task to mentally reverse the time to get good enough picture of the crime (problem) to start to trace the criminal and murder weapon (input) and possibly also the motive (cause). In this Chapter we discuss on how solving of the Inverse Problems is entering in Chemistry and focus on our own inverse computer modelling method to create a model (force field) from the results we already have. We explain how this method, called the Inverse Monte Carlo, can also be used for systematic hierarchical multi-scale modelling based on successive coarse-graining from first-principles to meso-scale and even further by super-coarse-graining. We show several applications of using it and also vision future prospects of hierarchical multi-scale modelling.

A. Lyubartsev · A. Laaksonen (✉)

Department of Materials and Environmental Chemistry, Arrhenius Laboratory,
Stockholm University, 106 91 Stockholm, Sweden
e-mail: aatto@mmk.su.se

A. Laaksonen

Centre of Advanced Research in Bionanoconjugates and Biopolymers, Petru Poni Institute of
Macromolecular Chemistry, Aleea Grigore Ghica-Voda, 41A, 700487 Iasi, Romania

State Key Laboratory of Materials-Oriented and Chemical Engineering, Nanjing Tech University,
Nanjing 210009, People’s Republic of China

Department of Engineering Sciences and Mathematics, Division of Energy Science, Luleå
University of Technology, 97187 Luleå, Sweden

1 Introduction

1.1 *Inverse and Forward Problems*

Solving the Inverse Problems and practising “Reverse Engineering” must have appeared naturally out of curiosity and necessity along with direct problem-solving we humans have been faced to, first for survival and conformity, successively leading to civilisation, technology and Sciences. Solving Inverse Problems in Science is first of all a mathematical problem (Tarantola 2005; Yaman2013), common in many areas from Chemistry and Biology to Medicine and Astronomy just to mention a few. In Medicine doctors regularly need to suggest a diagnosis and treatment to the illness of the patient, while in Astronomy we may have a mysterious spectrum travelled from a very distant star. In the first example the inverse problem can be solved more or less rigorously either by systematically recognising patterns or empirically and even by guessing, while in the second example there are scientific methods to solve it backward by analysing the wave lengths giving information about the source (and its chemical composition) as a cause of the distinct radiation. For many living species in Nature unconsciously solving of the inverse problem is critically important for their very existence in catching food or navigating.

To solve forward problems can be easy and quickly done “on the back of an envelope” but it may also require powerful supercomputers and complex numerical algorithms to provide the correct result. Modelling a multimillion ensemble of strongly interacting particles to describe biological systems by solving Newton’s equations is a typical example of the latter. Solving inverse problems can become often mathematically incredibly difficult simply because they tend to be improperly posed so that several inputs can give same results as a cause of the forward problem even when the data appears perfectly correct. For example two (or more) different sound sources can produce the same overlapping acoustic pattern. Therefore a unique correspondence is an important requirement for a complete solution of the inverse problem.

2 Design in Chemistry

2.1 *Forward Design*

In Chemistry and in particular in Materials Science, one particular word has lately come very popular and it is “Design”. We now can access and manipulate the building blocks of matter using a variety of experimental techniques and since all matter around us and also inside us is made of molecules, we should be in a good position to “design” material with specific properties and function. However, since there is roughly ten orders of magnitude difference between molecular sizes and sizes of

macroscopic stock material to manufacture products for us humans this design is not always easy or straight-forward. Would it be easy straight-backward? There are many ideas now emerging around it,

Solving inverse problems has during the last decades become an important instrument in many scientific disciplines. In particular they have recently gained popularity in Chemistry and in Materials Sciences. A recent development is called “Inverse Design” (Sanchez-Lengeling and Aspuru-Guzik 2018). However, before introducing it let us first discuss the “Forward Design” which has been the common practise since early attempts to gain metals create explosives and process food and necessities. Finally stoichiometry allowed quantitative studies and chemical synthesis was discovered. Chemistry and chemical engineering are based on and develops with the accumulated and documented knowledge. Chemical intuition of its practiser is always an important component leading to new knowledge. There is no denying that the so called “trial-and error” and “cook-and-look” techniques have been common in many Chemistry laboratories to produce new chemicals and substances with specific desired properties and functions. Serendipity, the complete opposite to design, did appear occasionally to help to give the most important results. Thanks to computers continuously becoming more powerful and numerical search algorithms more efficient together with rapidly growing well-organized and easily accessible molecular and chemical databases, the “Forward Design” has radically changed its strategy from cooking molecules in laboratories to mining of existing molecular data using computers as an important component to shorten the cycle from ideas to products.

2.2 Knowledge-Based Design in Chemistry

During many decades now the chemical research has produced an extensive amount of new molecules with their specific properties tagged, organized and stored in large data bases. This data comes both from experiments and theoretical studies. Having this accumulated knowledge and data publicly open and easily accessible, as well as its correctness verified before storing it, can prevent us making (same) mistakes or discovering the wheel again, but most importantly to help us to discover new knowledge and correlations still hidden there. Along with these big data mines, new disciplines are developed of how to extract the desired information from it (Informatics, Chemometrics, Machine Learning, etc.), we have new options and methods to produce novel materials. By starting to search specific type molecules in the “Molecular Space” containing now virtually all possible molecular structures and by screening to gradually select a “Chemical Space” containing only a handful of candidates having the chemical properties we are looking for. Pharmaceutical industry has many decades been using this type of rational design based on virtual screening and quantitative structure-activity relationship (QSAR) models with carefully designed descriptors to find new compounds (leads) to become efficient medicines with optimal therapeutic effects while showing a minimum amount of side effects. With machine learning techniques entering Chemistry more and more simple regression models are

being substituted with more intelligent methods such as neural networks and others to find hidden correlations in big data structures and even new “physical” rules.

2.3 *Inverse Design in Chemistry*

There are many different strategies to solve inverse problems in Chemistry. Typically in utilizing the “Inverse Design” we can do the opposite to “Forward Design” and start by specifying the property or function of the new material we then look for from the “Chemical Space” and thereafter start to screen the content in “Molecular Space” with suitable descriptors trying to successively narrow the space to a small number of molecules having the property and function we look for (Sanchez-Lengeling and Aspuru-Guzik 2018). This type of search is strongly aided with machine learning and other techniques of artificial intelligence now increasingly applied in Chemistry. The types of materials inversely designed this way so far contain mainly drugs and organic and inorganic materials for optical and electronic devices, including batteries (Sanchez-Lengeling and Aspuru-Guzik 2018). Other approaches to design specific molecules also include so called Variational Particle Number and Alchemical Potentials within density functional theory (von Lilienfeld et al. 2005), Linear Combination of Atomic Potentials (LCAP) (Wang et al. 2006), which can be implemented in classical and quantum mechanical (DFT, tight-binding DFT and time-dependent DFT) Hamiltonians to perform many types of property optimizations. Inverse band-structure problem is solved for finding an atomic configuration with given electronic and optical properties (Franceschetti and Zunger 1999). Struebing et al. (2013) suggest an inverse method to find an optimal solvent to maximally speed up the kinetics for chemical reactions. Inverse methods can be used successfully in Spectroscopy for example to decompose 2D NMR spectra of mixtures of molecules utilizing the technique of blind source separation (BSS) (Cherni et al. 2019). Jonas uses a so called deep imitation learning protocol to solve the chemical structure from molecular formula and NMR spectrum (Jonas 2019). There are many excellent reviews on these topics, such as Machine Learning which is strongly entering into Computational Chemistry and Materials Science via knowledge-based modelling is excellently reviewed in Ferguson (2018), Butler et al. (2018). Several emergent methods of Inverse design are reviewed in (Sanchez-Lengeling and Aspuru-Guzik 2018; Noh et al. 2020; Sherman et al. 2020; Hu et al. 2009; Martinez-Luaces 2012; Hachmann et al. 2018).

2.4 Solving Inverse Problems in Computer Modelling and Simulations

Ideas of solving the inverse problems in Computational Chemistry have their roots in liquid state theories of mid last century (Kunin and Frisch 1969) and started gain popularity in the following decades along with the development of more powerful computers (Rosenfeld and Kahl 1997). In computer simulations the most important input is the interaction potential or Force Field. It can be constructed conceptually based on simple models used to describe interatomic or intermolecular interactions, all having their fundamental origin in how electrons and nuclei in atomic and molecular frameworks feel the presence of each other and the forces they give rise to. Long before the computers did arrive scientists knew that there was a weak attraction even between neutral particles (atoms and molecules) at long distances (order of a few Ångström) which grew stronger at closer distances and became strongly repulsive at short distances. Lennard-Jones (Jones 1924) and contemporary scientists proposed very simple mathematical models to describe it. For charged particles there was Coulomb law describing their mutual strong and long-range interactions. The assumption of additivity of the interactions and that only two particles did interact with each other momentarily were assumed and simplified the theoretical work as effective pair potentials became a common tool to model interacting particles. When parameterized on experimental information they could contain a certain part of many-particle character built in thereby improving their quality.

When studying condensed phases of matter the structural information can be obtained from the pairwise correlations of the neighbouring particles (atoms, ions, molecules etc.). These correlations can be constructed statistically by sitting physically on each particle at a time and looking for the neighbouring particles in any direction radially and adding every hit in a histogram as a function of the mutual distances. When normalized to bulk density these pairwise correlations become radial distribution functions (RDF) or pair correlation functions giving probabilities to find particles at specific distances. Very early it was observed by scientists working in developing liquid theories and so called integral equation models that there was a correlation between pair correlation functions and pair potentials, Indeed, there is an explicit expression allowing, in principle, to compute the RDF from known pair potentials, and approximately it is always possible by particle-based computer simulations. An inverse problem, that is determination of pair potentials if RDF is known is however not a trivial task. Johnson and March did calculate potential of mean forces (PMF) from RDFs obtained in early diffraction studies of liquid metals and iterated them to pair potentials (Johnson and March 1963). An important foundation was the Uniqueness theorem of Henderson for RDFs and pair potentials for systems in equilibrium Henderson (Henderson 1974) which was later shown to be true even for multi-component systems. These theorems however did not say how to obtain one from the other. In 1979 Swendsen published a Monte Carlo method for statistical mechanical simulations and renormalization-group analysis of critical properties applied on the Ising model presenting an effective Hamiltonian and iterative solution

of the problem to obtain an effective pair potential from nearest-neighbor pairs of the spins (Swendsen 1979). Inspired by the work of Swendsen, in 1995 Lyubartsev and Laaksonen suggested a generalized inverse scheme to invert RDFs to effective pair potentials for arbitrary molecular systems (Lyubartsev and Laaksonen 1995), later known to be the Inverse Monte Carlo (IMC) or Newtonian Inversion (NI). This method is discussed in more detail in the next Chapter. Similar structure-based inversion methods have also been suggested (Soper 1996; Reith et al. 2003) being inspired by earlier works of Schommers (1983) and Reatto et al. (1986). Also the method of force-matching based inversion method of Izvekov and Voth should be mentioned (Izvekov and Voth 2005) which in turn was inspired by the force-matching method of Ercolessi and Adams (1994). In addition there are many other promising schemes including Generalized Yvon-Born-Green (YBG) method (Mullinax and Noid 2010; Cho and Chu 2009), relative entropy (Shell 2008) and configurational temperature (Mechelke and Habeck 2013).

3 The Inverse Monte Carlo Method

3.1 Theoretical Foundations

We will describe here the method of Inverse Monte Carlo (IMC). It is a mathematical method to coarse-grain (CG) the molecular interactions based on structural information obtained in underlying accurate studies (theoretical or experimental) of the same molecular system. Also equilibrium thermodynamic information can be used to obtain the CG model. It has some common features with many of the methods discussed above. The general idea in all coarse-graining is to produce a simpler model, or a kind of caricature, of the more accurate model full of details. Like in watching photos or paintings from a long distance the small details become less important. The same is true in modelling matter at longer length scales. Also at longer time scales the fast molecular fluctuations are averaged making molecules effectively more rigid in one or several conformations (geometries). This type of simplification is done in coarse-graining where we remove those degrees of freedom (DoF) from the original detailed potential energy Hamiltonian $H(r_1, \dots, r_n)$ which are less-important while we describe the system by keeping only the important DoFs (R_1, R_2, \dots, R_N), where $N \ll n$.

How to choose the important DoFs is very much a matter of taste (or rather of experience based on chemical and physical intuition) as in many cases it turns out not to be very critical. As CG sites one often chooses centre-of-masses (COM) of the molecular group forming the CG. Generally, the CG coordinates are some functions of atomistic coordinates:

$$R_i = \theta_i(r_1, \dots, r_n) \tag{1}$$

Although in some cases the CG coordinates (R_i) may coincide with coordinates of certain atoms (r_j).

Once a mapping scheme of atomistic coordinates to CG coordinates (1) is chosen, we can describe a coarse-grained (CG) Hamiltonian:

$$H_{CG}(R_1, \dots, R_N) = -\frac{1}{\beta} \ln \int \prod_{i=1}^n dr_i \prod_{j=1}^N \delta(R_j - \theta_j(r_1, \dots, r_n)) \exp(-\beta H(r_1, \dots, r_n)) \quad (2)$$

which is an effective N-body CG potential energy function. However, expression (2) cannot be used directly in CG simulations, therefore we first map or fit it to a pair potential:

$$H^{CG}(R_1, R_2, \dots, R_N) \approx \sum_{i>j} U_{ij}(R_{ij}) \quad R_{ij} = |R_i - R_j| \quad (3)$$

Many methods discussed in previous Section fit the Hamiltonian (3) to reproduce some properties from the underlying simulations with all the DoFs, for example energy, forces, or some features of structure. In IMC we use ensemble averages and RDFs as our first choice.

The IMC method is a powerful general method to invert ensemble averages, and particularly RDFs to effective pair potentials. It completely solves the inverse problem providing a unique solution. For any multi-component system it produces the effective pair potentials between selected sites (atoms, center-of-mass, and any other type of sites) in an inverse process which in forward process (input \rightarrow model \rightarrow simulation \rightarrow results) reproduce completely the RDFs used as input and inverted to produce the effective potentials (model) when same conditions are applied. There may not be much point in doing the full circle this way but now we can increase the size of the system a few orders of magnitude and perform a simulation which we could not afford before when using the original detailed model, typically the all-atom (AA) model. The reason is not only that we have now much less interaction pairs already making simulations faster but the effective potentials between heavier sites are also softer and we can choose a longer time step. Still, the greatest effect using IMC comes from not needing to use any explicit solvent in the CG simulations. This will be discussed in more details below.

In the calculation of an RDF or $g(r)$ in a typical particle simulation of N particles in a volume V the radial particle-particle distances are discretized to histograms S_α which after normalization to bulk particle density (N/V) show the probabilities to find the distances of the neighbouring sites between a chosen pair of atoms (or other type of sites). This histogram or the estimator of the pair-correlations is used in IMC. By discretizing the CG Hamiltonian (3) to two histograms of which one is the normalized estimator S_α from the $g(r)$ and the other is an effective CG pair potential V_α in a table form we will obtain:

$$H = \sum U_\alpha S_\alpha \quad (4)$$

where ensemble average of S_α is related to RDF by:

$$g(r_\alpha) = \frac{1}{4\pi r_\alpha^2 \Delta r} \frac{V}{N^2/2} S_\alpha \quad (5)$$

Besides RDFs between non-bonded CG sites, other structural properties can be included into set of S_α , for example distribution of CG bond lengths, angles and torsion angles. This is very useful when we coarse-grain biomolecules (or other large molecules such as polymers), for which we create models consisting of CG sites connected by CG bonds. Bonded and angular potentials of such models are fitted to reproduce bond and angular distributions originated from the detailed model within the same IMC framework.

While in standard simulations (direct forward problem) we have interaction potential U_α as input, and we can evaluate $\langle S_\alpha \rangle$ and RDF as output, in the coarse graining by IMC we solve the inverse task: from averages $\langle S_\alpha \rangle$ (determined in atomistic simulations) we determine CG potentials. Solution of this non-linear inverse problem can be reached iteratively by the Newton-Raphson method, and by this reason the IMC approach is also referred as ‘‘Newton Inversion’’. Let us determine Jacobian of $S(U)$ dependence:

$$J = \frac{\partial \langle S_\alpha \rangle}{\partial U_\gamma} \quad (6)$$

as well as use the ‘‘vector’’ notations for the sets of potentials and RDFs:

$$\{\langle S_\alpha \rangle\} \equiv \vec{S}; \quad \{U_\alpha\} \equiv \vec{U}$$

Jacobian (6) expresses how changes of potential affect RDFs:

$$\Delta \vec{S} = \hat{J} \Delta \vec{U} \quad (7)$$

From the statistical-mechanical relationships this Jacobian can be computed by doing direct simulations with potential U :

$$\frac{\partial \langle S_\alpha \rangle}{\partial U_\gamma} = -\beta (\langle S_\alpha S_\gamma \rangle - \langle S_\alpha \rangle \langle S_\gamma \rangle) \quad (8)$$

Now we have everything to solve the inverse problem. We start simulation from a trial potential which can be the mean force potential $U_\alpha = -k_{BT} \ln \langle S_\alpha \rangle$ or just zero. We compute from these simulation RDFs and $\langle S_\alpha \rangle$ and determine deviations from the reference RDFs $\langle S_\alpha^{ref} \rangle$ obtained in atomistic simulations:

$$\vec{\Delta S} = \vec{S} - \vec{S}^{ref} \quad (9)$$

Now we can compute which change in the potential is required to get the desired change in corresponding RDF:

$$\Delta\vec{U} = \hat{J}^{-1} \Delta\vec{S} \quad (10)$$

We update the interaction potential $\vec{U} \rightarrow \vec{U} + \Delta\vec{U}$ and repeat the procedure to compute a new corrected estimator. The iterative procedure is repeated until the estimators become identical (within statistical error of the simulations) to those in the original input $g(r)$, also giving back the final RDFs obtained in the fine-grain simulation serving as reference. After convergence, we obtain the CG effective pair potentials which contain all the atomistic details to reproduce the microscopic structure found in the all-atom simulations, considering only the sites chosen to the CG model. It is like to visualize the AA simulation but leaving out the atomistic details and also the solvent. IMC fully includes the cross-correlations between the pair interactions, making the effective pair potentials more accurate in comparison with interactions obtained from using other similar methods. This is one of the properties making IMC a superior inverse method.

3.2 Using the Inverse Monte Carlo Method

In practical computations, and in particular for large molecules, direct use of expressions (8)–(10) may lead to non-convergence since the method is based on linear extrapolation (7) of a generally non-linear relationship. A simple way to regularize the procedure is to go by “small steps” to remain always in the linear regime and to multiply the change of RDF (9) (and respective change of potential (10)) by a damping factor $0 < \lambda < 1$.

What really makes IMC superior compared to other corresponding methods producing effective CG pair potentials is that even the solvent molecules can be considered as uninteresting DoFs. Therefore in using IMC CG pair potentials in simulations no explicit solvent is needed. The solvent is not implicitly there in the simulation cell as a continuum like in common implicit solvent models and most often characterized by the dielectric constant of the bulk solvent. The solvent is in the effective IMC CG potentials and contain specific atom-atom interactions for example to display H-bonds and solvation and hydration structures as in the underlying atomistic simulations. This is an extremely important feature as in all molecular simulations containing explicit solvent (most often water) it is the moving of the solvent around in the simulation cell which consumes major part of the computing time. In other words the IMC CG pair potentials are *solvent-mediated* containing the solvent in their functional forms. When used for example in simulations of biomolecular systems in water solution with ions and salt, all types of interaction forces are still there (hydrophobic, hydrophilic, H-bonds, steric, etc.). Self-assembly and other typical biological processes can be described accurately without explicit water molecules

as the water is still there in the effective potentials. The IMC potentials both supply the specific solute-solvent interactions and provide the collective effect of water to hydrophobicity and hydrophilicity as in AA simulations. Indeed, the IMC CG potentials for soft meso-scale particles while containing the atomistic interactions are so accurate that they can be coarse-grained again. This super-coarse graining allows us to perform reliable CG simulations of truly large systems like chromatin as will be described below.

The IMC CG pair potentials are produced in a tabulated form and their functional form can be very different from that of standard potentials like Lennard-Jones used often as empirically parameterized CG potentials. This is because it does have all types of intermolecular interactions together. Also, as it is solvent-mediated it has an oscillatory form at short distances reflecting the structure of solvation and hydration layers while this behaviour weakens and disappears at longer distances.

At long distances the IMC CG potential becomes overlapping with Coulombs law for charged particles as might be expected. Indeed, the Coulomb potential can be separated from the overall IMC CG potential and treated separately so that Ewald summation can be used in CG simulations. This divides in a natural way the CG potential to a specific short-range potential and long-range potential. Separating short-range and long-range Coulombic in CG simulations was also shown to produce more reliable overall results (Wang et al. 2013). Also, by making use of the inherent temperature dependency of the dielectric constant (Mirzoev and Lyubartsev 2011) the results obtained from IMC CG simulations can be made much less sensitive to temperature changes. In principle, the simulations with IMC CG potentials should be carried out at or close to the conditions applied in the underlying detailed simulations to calculate the RDFs as will be discussed below.

Intramolecular IMC CG potentials may also substantially deviate from the harmonic potentials bonded interactions are known to give rise to. However, in some cases they are close enough to harmonic so harmonic springs can be used, at least initially. In constructing IMC CG force field it is not necessary to follow the concept of dividing interactions for bond-stretching, angle-bending and rotation around bonds as in common atomistic force fields, as these can be substituted by a matrix of bead-bead interactions. IMC converges rapidly for systems with small molecules but for large biomolecular systems constructing converged potentials can become time-consuming and to do the inversion process manually becomes in practise out of question for biomolecular systems. Auxiliary tools are needed.

3.3 *MagiC*

There is a software package *MagiC* (Mirzoev and Lyubartsev 2013) developed which performs the structure-based coarse-graining of IMC described above for arbitrary molecular systems and models which has been recently updated to version 3 (Mirzoev et al. 2019). *MagiC* is an essential tool and integral part of IMC to perform systematic coarse-graining. It can take the input from several common simulation packages

while it produces CG potentials to be run on many coarse-grained simulation program packages like the GPU-Accelerated LARge-scale MOlecular Simulation Toolkit (GALAMOST) (Zhu et al. 2013), the Large-scale Atomic/Molecular Massively Parallel Simulator LAMMPS (Plimpton 1995) and the GRONingen MACHine for Chemical Simulations Gromacs (Van Der Spoel et al. 2005). MagiC software has many additional functions from diagnostics to visualisation.

3.4 Applications of Inverse Monte Carlo

The method of Inverse Monte Carlo was presented in mid-90's (Lyubartsev and Laaksonen 1995) and had to be soon applied on demanding systems to verify its power. 25 years ago a fairly “demanding” system was already to study NaCl in water even with the access to national supercomputers. We did study this solution at different salt concentrations. The number of molecules did range from 256 to 2000 with up to 20 ion pairs included. The simulations did cover a few nanoseconds (Lyubartsev and Laaksonen 1996). One reason why these were demanding simulations was that we did need very well converged RDFs for many different concentrations to accurately invert them to effective solvent-mediated Na-Cl Na-Na and Cl-Cl ion-ion potentials (Lyubartsev and Laaksonen 1997). We then did apply them to compute both the osmotic and activity coefficients for the hydrated ions. To obtain reliable results we did need 200 ion pairs. Systems of this size would not have been feasible to simulate using all-atom models with the computer power available for us at that moment. The water-mediated CG ion-ion potentials gave excellent results within the entire concentration range from 0.001 to 5 M. We did then perform a detailed MD simulation study about alkali metal ion (Li+, Na+, K+, and Cs+) condensation around double helix DNA in water solution (Lyubartsev and Laaksonen 1998) from which we obtained ion-DNA RDFs to invert them in IMC to effective CG potentials (Lyubartsev and Laaksonen 1999). Now already having water-mediated ion-ion CG potentials (we did compute them also for Li+, K+ and Cs+) we now had a complete set of CG potentials to perform simulations of a large double strand DNA chain in water in a box of $100 \times 100 \times 68 \text{ \AA}^3$. Using our water-mediated CG potentials we could find the order $\text{Cs+} > \text{Li+} > \text{Na+} \approx \text{K+}$ for counter ion binding to DNA in agreement with several independent experimental studies.

We did also perform Car-Parrinello simulations for liquid water to compute effective water mediated CG potentials from first-principles MD simulations (Lyubartsev and Laaksonen 2000). In this way we calculated a new atomistic water interaction potential from RDFs obtained in simulations with electronic degrees of freedom. We then did calculate hydration of Li+ ions from Car-Parrinello (Lyubartsev et al. 2001). In this way we could show that IMC was a true multi-scale modelling method where we could start from first-principles simulations and inverting the RDFs we would obtain AA interaction potentials and when using them in simulations (after increasing the size of the cell two orders of magnitude) we could construct a meso-scale effective pair potentials. This would allow us to hierarchically connect three

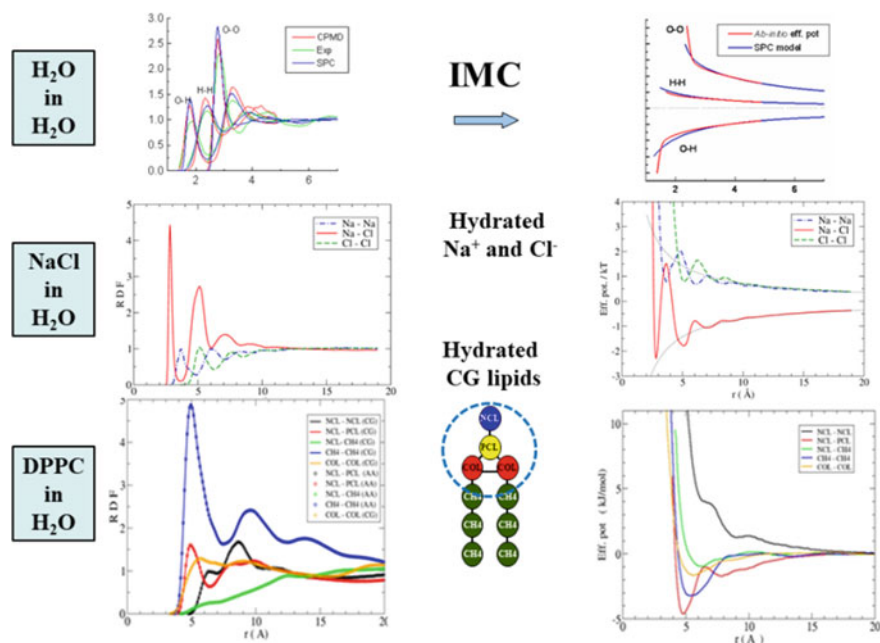


Fig. 1 RDFs from AA simulations and IMC inverted solvent-mediated CG potentials

scales: quantum, classical and mesoscale and start the whole multiscale modelling without any empirical information (Lyubartsev et al. 2009). We have previously summarized our work in (Lyubartsev et al. 2010; Lyubartsev et al. 2015) where there are more examples of the application of IMC. Much of the work done on biological systems is about nucleic acids.

In Fig. 1 we can see three different solvent-separated IMC CG effective pair potentials and the corresponding reference RDFs from which they are calculated. In all cases water is the solvent. Notice the oscillating nature of the potentials due to the presence of solvent built in them. In the top panel on the left we have RDFs from CPMD simulations of liquid water, classical simulations of SPC water and experimental water RDFs. On the right side are the corresponding inverted RDFs as pair potentials. For SPC we obtain back the SPC water model used in simulations to produce the RDFs. Note that although the RDFs are fairly similar the effective potentials from CPMD show much steeper repulsion compared to SPC model while at the long distance the models coincide as they should at Coulomb regime. Also the CPMD simulations of Li^+ in water gave much steeper repulsion in the effective IMC ion water-oxygen potentials (not shown here, see Ref. (Lyubartsev et al. 2001)) compared to common ion-water potentials models reflecting the exponential decay of repulsion based on Quantum Mechanical description. It could be fitted perfectly to $V_{\text{eff}}(\mathbf{r}) = A \exp(-B\mathbf{r})$ with $A = 37,380 \text{ kJ/mol}$ and $B = 3.63 \text{ \AA}^{-1}$ indicating that Buckingham type of potential is to prefer. In fact, in the Lennard-Jones potential the

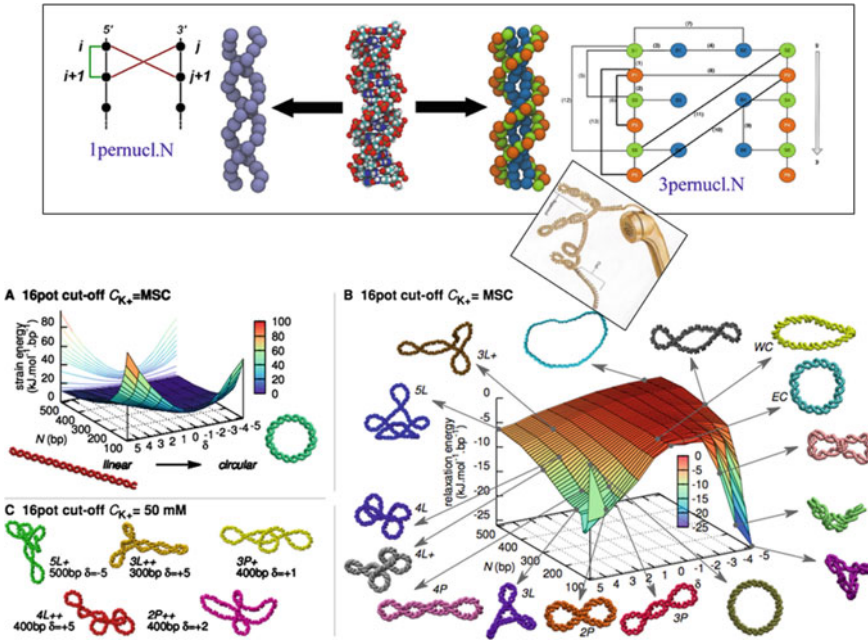


Fig. 2 Possible topologies (top) and twist and writhe oc minicircles of DNA (bottom) from Ref. (Naômé et al. 2014)

exponential decay of repulsion is approximated with the $1/r^{12}$ dependence making the calculations very much easier. In the middle panel are the water-mediated pair potentials calculated from the ion-ion RDFs, obtained in the aqueous solution of NaCl. Observe the distinct contact and water-separated potential wells in the $\text{Na}^+ - \text{Cl}^-$ potentials and the additional hydration shells after them at longer distances seen as oscillations. At long distances they coincide with Coulombs law (dotted line) as can be seen in the figure. At the bottom there the IMC potentials for DPPC phospholipids obtained from AA simulations of randomly placed lipids in the water box. These IMC CG lipid models reproduce accurately all phases and morphologies these amphiphilic systems can form in water depending on the applied conditions. For more details see references (Lyubartsev and Laaksonen 1997; Lyubartsev et al. 2009, 2010). In Fig. 2 we apply IMC on DNA mini-circles up to 500 base pairs. In top two typical topologies are shown to coarse-grain DNA. Mechanical energies for linear and circular DNA are shown in bottom. For details see Ref. (Naômé et al. 2014, 2015).

3.5 Transferability of IMC CG Potentials

An important issue with the IMC CG potentials, and for that matter with most other CG potentials based on underlying fine-grain simulations, is that they describe the system at a specific thermodynamic state and the CG potentials automatically inherit the same condition and therefore should be used accordingly. It means that the effective potentials cannot be used to cover large intervals in temperature, concentrations, densities etc. But can they be used to study the same type of systems exhibiting very different topologies at same conditions? In our studies of multi-scale modelling of human telomeric quadruplexes (Rebic et al. 2015, 2017) we did construct the IMC potentials from AA MD simulations for the topomer, a [3 + 1] hybrid with a 26-nucleobase sequence d[AAAGGG(TTAGGG)₃AA] with K⁺ counter ions stabilizing the Hoogsteen structure (PDB id 2HY9). We later used successfully the same IMC potentials to model another quadruplex topology (PDB id 1KF1) also known to form from the human telomeric DNA sequence d[AGGG(TTAGGG)₃] differing from 2HY9 in its loop topology and its G-strand relative orientation. The results are encouraging suggesting a certain degree of transferability in simulating quadruplexes with different topologies. Since the IMC potentials are normally not fit to any simple mathematical functions any general transferability is out of question due to their inherent complexity and difficulties to construct combination rules (Fig. 3).

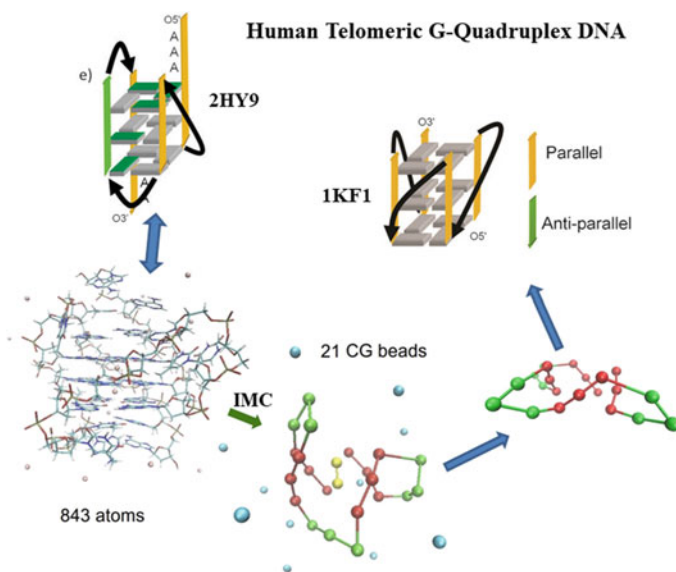


Fig. 3 IMC CG model for 2HY9 topology can be used in CG simulations of 1KF1. For more details see Refs. (Rebic et al. 2015, 2017)

3.6 *IMC Effective Potentials and Dynamical Properties*

An important issue in creating and using effective potentials based on structural information only is their capability to predict dynamical properties in CG simulations. It is reasonable to expect that CG potentials, being softer than AA potentials, create an energy surface where soft mesoscopic particles, even if heavier, move too fast compared to AA simulations or experiments. As no dynamical information goes in to the process in inverting the solely structural information to is also difficult to estimate the effect of its absence to dynamics of the particles. Also, even the fact that no explicit solvent is needed; making the simulations fast, the lack of friction normally generated by the solvent molecules affects the overall internal motion of the solute molecules. In our study of mini-circles of DNA (90–500 bp) at different salt concentrations using IMC CG potentials (Naômé et al. 2014, 2015), we did also study the dynamical properties for linear 18-mers of DNA in water solution with ions. We did observe that the counter-ions did diffuse roughly 220 times faster than in AA MD simulations while end-to-end fluctuations of DNA were 4.5 times faster and its total twist fluctuations 21 times faster than in AA MD simulations. Using Langevin dynamics gave us the opportunity to adjust the friction coefficient to give reasonable results for the dynamics. For example, using a friction coefficient 35 ps⁻¹, which is comparable to the collision frequency of water molecules, brings the diffusion of the counter-ions close to the experimental values. In general as the degree of coarse-graining is different for DNA and for ions their dynamics differ so no general scaling factor is difficult to establish. Even if it is difficult to obtain quantitatively correct dynamics the relative trends can be reproduced normally well. Scaling CG potentials to reproduce experimental or AA-simulation results is needed otherwise.

3.7 *Fine Graining*

The opposite to coarse-graining is fine-graining (FG) or back-mapping, which is far from trivial as it requires inserting (re-inventing) the degrees-of-freedom which were deleted in coarse-graining. FG is not simple because the problem is under-determined. For polymeric systems, including biopolymers like nucleic acids, it is somewhat easier because the back-bone geometry and the topology of the monomeric units are known, this way providing several geometric constraints. For DNA there are the sequence information, the distance constraints for Watson-Crick base-pairs, the grooves and stacking to guide the FG. Common strategy is to start by a random placement, followed with a relaxation without adding any constraints. Thereafter check the chiralities, and first after that to start to apply the constraints. We have followed this strategy in (Lyubartsev et al. 2015; Naômé et al. 2014). Some software packages already have features for performing back-mapping, such as newer versions of Gromacs.

3.8 *Bottom-Up Meets Top-Down*

At the same time as multi-scale modelling based on the successive coarse-graining is a “from-bottom-up” technique to reach the mesoscale beyond, many sophisticated “from-top-down” experimental methods such as 3D imaging, microscopies, single-molecule manipulation and force measurements can come down to the meso-scale and even under. This means that these two approaches (bottom-up and top-down) can be made to meet at the mesoscale. A probable future scenario is mapping of images and forces from experiments on mesoscopic simulation models so that we start have good quality meso-scale force fields for CG simulations (as the AA force fields we have today) with experimental origin which also can be cross-fertilized with theoretical CG force fields inverted from underlying accurate FG simulations to make them more detailed. For example, AFM can supply vertical and lateral force-distance data which can be used to create a force field between particles and surfaces which is currently completely missing in modelling. All this would also allow us to improve the resolution of these experimental techniques all the way to the atomistic level by applying fine-graining techniques discussed in the previous section. Once atomistic level is reached quantum calculations can be performed to explore any possible reactive parts of the system. “Top-down meets bottom-up” will be a common theme in many integrative studies with multi-instrument experimental and multi-scale modelling is performed for the insight, discovery and design of novel products.

3.9 *Advanced Use of IMC*

We give here two more recent examples of multi-scale modelling based on hierarchical coarse-graining using the Inverse Monte Carlo method. The first deals with the important topic of bio-toxicity of nanomaterials and the second example is about super-coarse-graining of genetic materials.

3.10 *Safety of Nanomaterials—Multiscale Modelling Using IMC*

Nanomaterials ranging from carbon nanotubes and graphene structures to metal and metal oxide nanoparticles and quantum dots provide a virtually endless line of bioengineering applications, as well as offer use in modern nanomedicine as potential carriers for targeted drug delivery. On the other hand, the nanotoxic hazard associated with the penetration of small nanoparticles in biological tissues is a vividly debated subject. Concern is raised on both direct and potential long-term hazard to human health caused by nanomaterials since the immune system, developed during

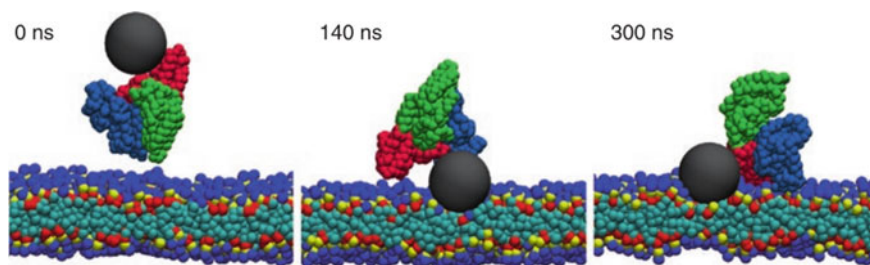


Fig. 4 Time sequence of CG simulation snapshots illustrating the interaction of a complex of negatively charged hydrophobic nanoparticle (2 nm radius) and Human Serum Albumin (HSA) protein with DMPC lipid bilayer. Reprinted from Hender et al., “Multiscale Modelling of Bionano Interface”, in *Modelling the Toxicity of Nanoparticles*, L. Tran et al. (eds.), *Advances in Experimental Medicine and Biology*, Vol. 947, 2017, https://doi.org/10.1007/978-3-319-47754-1_7, with permission from Springer International Publishing

millions years of evolution, is not familiar with engineered nanoparticles. Existing methodologies of *in-vivo* toxicological evaluation require long time, are expensive and also connected with ethical concerns. This is why *in-silico* methods of prediction of toxic effects are of high demand (see Fig. 4). It is however extremely challenging task to model what is really happening from the first contact of a nanoparticle with biological matter on the molecular level to the effects of the nanomaterial on the whole organism.

Here we come to the point when hierarchical multiscale modelling, starting from atomistic description of the interface between nanomaterial surface and biomolecules (Brandt and Lyubartsev 2015) and proceeding to several levels of coarse-graining, handshakes with system biology, and in particular the Adverse Outcomes Pathways (AOP) concept (Halappanavar et al. 2020). An AOP relates the first biological effect of a nanoparticle taken up by an organism (called the Molecular Initiating Event), through a series of “Key Events” (measurable changes at organelle, cell, organ level), with an adverse outcome for the whole organism (and even for populations). First attempt to use multiscale simulations to predict some molecular initiating events in AOP, such as protein corona formations around a nanoparticle or membrane rupture using multiscale simulations have been recently published (Lopez et al. 2017; Power et al. 2019).

Necessity of validated tools for evaluation of potential toxic effects has led to appearance of “Safe by Design” concept (Schwarz-Plaschg et al. 2017) in design of nanomaterials. Toxicological safety should be considered as a compulsory property of all newly developed materials, alongside with the functional properties for which the material is developed. While performing the “Inverse Design”, it is imperative to include the toxicological chain relating properties of molecular bio-nano interface with adverse outcomes, into the search in Chemical Space for specific materials satisfying these properties.

3.11 Super Coarse-Graining Using Inverse Monte Carlo

To apply hierarchical multi-scale methods there is hardly anything more suitable than the genome material which is strictly hierarchically built in consecutive orders (primary sequences, secondary, tertiary, quaternary, etc.) from underlying structures. The hierarchical order for modelling is: [DNA + histones] – [beads and strings of nucleosome core particles (NCP)] – [fibres of packed nucleosomes] – [chromatin loops] – [chromatin domains] – [extended and condensed chromosome]. Also, in terms of number of base-pairs there are six orders of magnitude from NCP to chromosome (10^2 to 10^8). We have in our previous studies demonstrated the importance of the electrostatic interactions and the power and accuracy of the IMC method by simulating these hierarchical building blocks in physiologically relevant conditions and with varied ion concentrations and observed the same condensation behaviour as in experiments while obtaining stable structures (Korolev et al. 2004; Korolev et al. 2006; Korolev et al. 2010). The CG simulation methodology developed by us is so detailed that even the coarse-grained model of nucleosome core particles can be coarse-grained while maintaining their molecular properties (Fig. 5).

We did simulate a clustering of 5000 NCPs obtaining an excellent agreement with small angle X-ray scattering spectra for a corresponding system (Fan et al. 2013; Sun et al. 2019). Also, we simulated large amount of DNA oligonucleotides (up to 400 oligonucleotides each of 100 base pairs of DNA) in presence of CoHex3+ ions

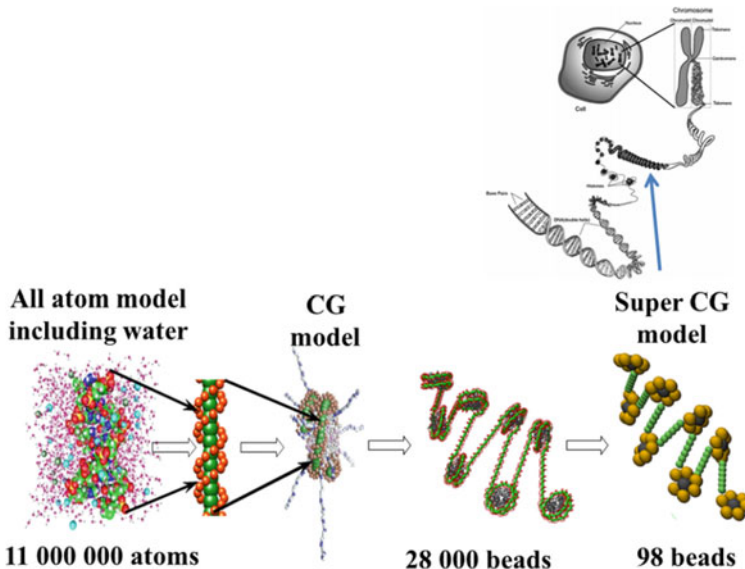


Fig. 5 Systematic hierarchical multi-scale modeling from DNA to chromatin where higher order coarse-graining (super coarse-graining) is used. 98 beads corresponds a system of 11 million atoms in corresponding all-atom simulation Ref. (Fan et al. 2010)

and found aggregation of DNA's in ordered hexagonal structures (Sun et al. 2019). Furthermore, using super coarse grained DNA model which represent DNA as beads in a chain with interaction potential derived by IMC from atomistic simulations including effects of ions and water, we simulated a very long (40,000 base pairs) DNA and found that it, in presence of CoHex^{3+} ions, form toroidal structures which were also observed in electron microscopy studies (Sun et al. 2019) (Fig. 6).

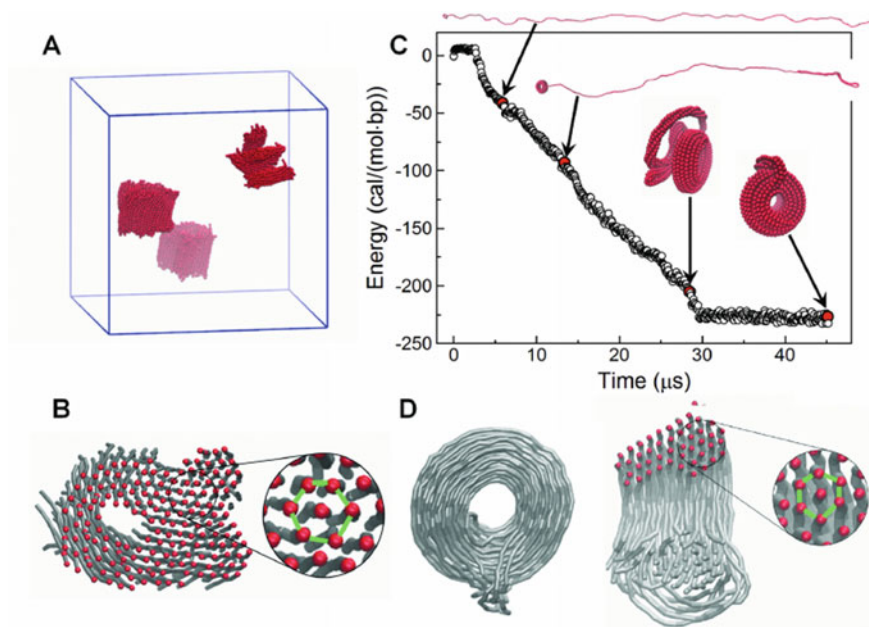


Fig. 6 DNA aggregation and toroid formation induced by CoHex^{3+} ions simulated by the super coarse-grained DNA model. **A:** Final configuration of DNA aggregation in a simulation with 400 DNA oligonucleotides of 100 base pairs each. **B:** Cross-section of one of the DNA condensed particle shown in **A**. **C** and **D:** Formation of toroidal structures in the super coarse-grained simulations of a 10,200 base pairs DNA. **C:** Energy profile and snapshots (normalised per DNA base pair) from one of the simulations. **D:** Structure of the DNA toroid. Cartoon on the right-hand side shows cross-section through the toroid where the red dots illustrate DNA double helices near the cutting plane. The zoom-in illustrated in **B** and **D** show the DNA packing within the aggregates with green lines highlighting hexagonal arrangement of the DNA molecules. *Reprinted* from Sun et al. (2019) with permission from Oxford University Press

4 Future Prospects

4.1 Chromosome Modelling

The hierarchical multiscale modelling of chromatin can be extended to reach what can be still considered as a grey-zone and to study the organization of the chromosomes inside the cell nucleus. This is a highly challenging “Bottom-up meets the Top-Down” project and is recognized as such by many colleagues (Langowski and Heermann 2007; Ozer et al. 2015; Moller and Pablo 2020; Bendandi et al. 2020; Caudai et al. 2019). In doing so modelling is not enough but we need to use a more integrative approach where we combine competences from other areas including bioinformatics (Ozer et al. 2015) and advanced instrumentation (Moller and Pablo 2020). Successively we also need to complement the purely physics and particle based methods by adding knowledge and rule-based models in the toolbox. We need experimental information about topologically associated domains (TAD) to insert in the models (Caudai et al. 2019).

We also will to study the role (structure and function) of nuclear lamina in the organisation of the chromosome, including the nuclear envelope proteins lamins (globular regulators of chromatin) bound to the lamina and other inner membrane proteins interacting with the chromosome (Dittmer and Misteli 2011; Ho and Lammerding 2012; Nora et al. 2013). Mutations in polymerizing lamins (laminopathies) are connected to a diversity of genetic human diseases (currently 17 are known) giving indication of their close role in cellular functions being important modulators in transcriptional regulation while affecting chromatin structure and organization. We will apply our multi-scale methodology to these higher-order polymeric proteins with alpha-helical rod-domains and study their roles as regulators of chromatin.

The function of the genes is not only what is encoded linearly in the sequences but it is now known that the topological organization of the DNA in chromatin and how it interacts with the nuclear environment are important in transcriptional regulation. Also, chromatin may have different structures inside the cell nucleus depending of the cell cycle. Chromosome Conformation Capture (3C) and its many extensions and other related methods have become highly valuable to decipher the spatial organisation of chromatin although they do not give information about the dynamical processes (Emmett et al. 2015; Lieberman-Aiden et al. 2009). Local DNA contacts are important in communications between the enhancers and promoters and these take place in TADs which in turn shape the chromosome landscape. 3C methods are used to quantify the number of interaction between the chromosome positions. Among the most popular of the 3C methods currently is the Hi-C (Reddy and Feinberg 2013) which can also combined with other methods, for example three-dimensional fluorescence in situ hybridization (3D-FISH) (<https://www.ncbi.nlm.nih.gov/geo/>). This method gives a picture and behaviour of packed chromosome as fractal globule. The Hi-C (extension of 3C methods) is becoming more accurate due to better regression-based correction schemes.

4.2 *Genome-Wide Modeling*

Hi-C maps (available for example from Gene Expression Omnibus (Ibrahim et al. 2013)) can be converted into a matrix of average pairwise distances that can be used as restraints in many simulation models. This is analogous to when NOE distances are added to all-atom force fields in determination of protein structures using NMR. This allows for the first time a genome-wide modelling for example by using Brownian Dynamics simulations. Currently restraint-base modelling has been performed for chromatin using (1) rule-based spatial modelling (Doyle et al. 2014; Imakaev et al. 2015; Serra et al. 2015), (2) polymer models (Gruenert et al. 2010; Carstens et al. 2016) and (3) bead models (Szałaj et al. 2016). The resolution of the used models depends on the resolution in the genome data sets. However it is increasing continuously. As an example of a bead model with resolution of 50kbp requires 3330 beads to represent the X chromosome (Szałaj et al. 2016). The parameterization of the bead models is very much ad hoc with input from experiments, while we wish to be able to use super-coarse-graining based on underlying molecular information. Genome-wide modelling is becoming a very vital area. To become more acquainted we suggest following excellent reviews for multi-scale modelling and other new approaches (Molitor et al. 2017; Xia 2018; Sewitz et al. 2017; Bsascom and Schlick 2017).

5 Final Remarks

In this Chapter we introduce and discuss “Inverse Problem” in Chemistry and focus on its applications in Computational Chemistry where we can produce models for interacting molecular systems (interaction potentials and force fields) backward from the already obtained simulation results. We demonstrate that by proceeding systematically and hierarchically this inverse procedure can be made through hierarchical coarse-graining to a powerful and accurate multiscale modelling methodology called the Inverse Monte Carlo (IMC) alternatively Newtonian Inversion, which can be used all the way from first-principles quantum mechanics to meso-scale and beyond meaning in such a way that no empirical information would be needed. We do not do this yet routinely as computers need to become much faster for first-principles simulations of biological material as an example. We start normally from all-atom classical simulations. We discuss both the benefits and limitations of the IMC methods while illustrating some important applications, especially applications where the method is clearly superior to other similar methods in its accuracy. We show examples of higher-order coarse-graining (super-coarse-graining). We then discuss future aspects of the method and introduce the area of genome-wide modelling where we expect to make an impact with IMC combined informatics and knowledge/rule-based methods including machine learning and closely carried out with several sophisticated experimental techniques currently used in genome research.

Acknowledgements A. Laaksonen acknowledges Swedish Research Council for financial support (project: 2019-03865), and partial support from a grant from Ministry of Research and Innovation of Romania (CNCS-UEFISCDI, project number PN-III-P4-ID-PCCF-2016-0050, within PNCDI III). A. Lyubartsev acknowledges Swedish Research Council (project: 2017-03950) and Horizon 2020 framework programme (SmartNanoTox project) for financial support.

Conflict of Interest The authors declare no conflict of interest.

Ethical Approval The authors declare that this article does not contain any studies with human participants or animals.

References

- Bascom G, Schlick T (2017) Linking chromatin fibers to gene folding by hierarchical looping. *Biophys J* 112:434–445
- Bendandi A, Dante S, Zia SR, Diaspro A, Rocchia W (2020) Chromatin compaction multiscale modeling: a complex synergy between theory, simulation, and experiment. *Front Mol Biosci* 7:1–14
- Brandt EG, Lyubartsev AP (2015) Molecular dynamics simulations of adsorption of amino acid side chain analogues and a titanium binding peptide on the TiO_2 (100) surface. *J Phys Chem C* 119:18126–18139
- Butler KT, Davies DW, Cartwright H, Isayev O, Walsh A (2018) Machine learning for molecular and materials science. *Nature* 559:547–555
- Carstens S, Nilges M, Habeck M (2016) Inferential structure determination of chromosomes from single-cell Hi-C data. *PLoS Comput Biol* 12:e1005292
- Cudai C, Salerno E, Zoppe M, Tonazzini A (2019) Estimation of the spatial chromatin structure based on a multiresolution bead-chain model. *IEEE/ACM Trans Comput Biol Bioinform* 16:550–559
- Cherni A, Piersanti E, Anthoine S, Chau C, Shintu L, Yemloul M, Torresani B (2019) Challenges in the decomposition of 2D NMR spectra of mixtures of small molecules. *Faraday Discuss* 218:459–480
- Cho HM, Chu J-W (2009) Inversion of radial distribution functions to pair forces by solving the Yvon-Born-Green equation iteratively. *J Chem Phys* 131:134107
- Dans PD, Walther J, Gomez H, Orozco M (2016) Multiscale simulation of DNA. *Curr Opin Struct Biol* 37:29–45
- Dittmer T, Misteli T (2011) The lamin protein family. *Genome Biol* 12:222
- Doyle B, Fudenberg G, Imakaev M, Mirny LA (2014) Chromatin loops as allosteric modulators of enhancer-promoter interactions. *PLoS Comput Biol* 10:e1003867
- K Emmett, B Schweinhart, R Rabadan (2015) Multiscale topology of chromatin folding. In: Proceedings of the 9th EAI international conference on bio-inspired information and communications technologies (formerly BIONETICS), BICT 2015, pp 177–180
- Ercolessi F, Adams JB (1994) Interatomic potentials from first-principles calculations: the force-matching method. *Europhys Lett* 26(8):583–588
- Fan Y, Korolev N, Lyubartsev AP, Nordenskiöld L (2013) An advanced coarse-grained nucleosome core particle model for computer simulations of nucleosome-nucleosome interactions under varying ionic conditions. *PLoS ONE* 8:e54228
- Ferguson AL (2018) Machine learning and data science in soft materials engineering. *J Phys Condens Matter* 30:1–27
- Franceschetti A, Zunger A (1999) The inverse band-structure problem of finding an atomic configuration with given electronic properties. *Nature* 402:60–63

- Gruenert G, Ibrahim B, Lenser T, Lohel M, Hinze T, Dittrich P (2010) Research article rule-based spatial modeling with diffusing, geometrically constrained molecules. *BMC Bioinform* 11:307
- Hachmann J, Afzal MAF, Haghghatdari M, Pal Y (2018) Building and deploying a cyberinfrastructure for the data-driven design of chemical systems and the exploration of chemical space. *Mol Simul* 44:921–929
- Halappanavar S, van den Brule S, Nymark P, Gaté L, Seidel C, Valentino S, Zhernovkov V, Danielsen P, De Vizcaya A, Wolff H, Stöger T, Boyadziev A, Poulsen SS, Sørli JB, Vogel U (2020) Adverse outcome pathways as a tool for the design of testing strategies to support the safety assessment of emerging advanced materials at the nanoscale. *Part Fibre Toxicol* 17. Article number: 16
- Henderson RL (1974) A uniqueness theorem for fluid pair correlation functions. *Phys Lett* 49A:197–198
- Ho CY, Lammerding J (2012) Lamins at a glance. *J Cell Sci* 125:2087–2093
<https://www.ncbi.nlm.nih.gov/geo/>
- Hu XQ, Beratan DN, Yang WT (2009) Emergent strategies for inverse molecular design. *Sci China Ser B Chem* 52:1769–1776
- Ibrahim B, Henze R, Gruenert G, Egbert M, Huwald J, Dittrich P (2013) Spatial rule-based modeling: a method and its application to the human mitotic kinetochore. *Cells* 3:506–544
- Imakaev MV, Fudenberg G, Mirny LA (2015) Modeling chromosomes: beyond pretty pictures. *FEBS Lett* 589:3031–3036
- Izvekov S, Voth GA (2005) Multiscale coarse graining of liquid-state systems. *J Chem Phys* 123:134105
- Johnson MD, March NH (1963) Long-range oscillatory interaction between ions in liquid metals. *Phys Lett* 4:313–314
- Jonas E (2019) Deep imitation learning for molecular inverse problems. In: *Proceedings of the 33rd Conference on Neural Information Processing Systems (NeurIPS 2019)*, Vancouver, Canada
- Jones JE (1924) On the determination of molecular fields. II. From the equation of state of a gas. *Proc Roy Soc Lond Ser A* 106:463–477
- Korolev N, Lyubartsev AP, Laaksonen A (2004) Electrostatic background of chromatin fiber stretching. *J Biomol Struct Dyn* 22:215–226
- Korolev N, Lyubartsev AP, Nordenskiöld L (2006) Computer modeling demonstrates that electrostatic attraction of nucleosomal DNA is mediated by histone tails. *Biophys J* 90:4305–4316
- Korolev N, Allahverdi A, Yang Y, Fan Y, Lyubartsev AP, Nordenskiöld L (2010) Electrostatic origin of salt-induced nucleosome array compaction. *Biophys J* 99:1896–1905
- Kunkin W, Frisch HL (1969) Inverse problem in classical statistical mechanics. *Phys Rev* 177:282–287
- Langowski J, Heermann DW (2007) Computational modeling of the chromatin fiber. *Semin Cell Dev Biol* 18:659–667
- Lieberman-Aiden E, van Berkum NL, Williams L, Imakaev M, Ragozcy T, Telling A, Amit I, Lajoie BR, Sabo PJ, Dorschner MO, Sandstrom R, Bernstein B, Bender MA, Groudine M, Gnirke A, Stamatoyannopoulos J, Mirny LA, Lander ES, Dekker J (2009) Comprehensive mapping of long-range interactions reveals folding principles of the human genome. *Science* 326:289–294
- Lopez H, Brandt EG, Mirzoev A, Zhurkin D, Lyubartsev A, Lobaskin V (2017) Multiscale modelling of bionano interface. In: *Tran L et al (eds) Modelling the toxicity of nanoparticles. Advances in experimental medicine and biology*, vol 947
- Lyubartsev AP, Laaksonen A (1995) Calculation of effective interaction potentials from radial distribution functions: A reverse Monte Carlo approach. *Phys Rev E* 52:3730–3737
- Lyubartsev AP, Laaksonen A (1996) Concentration effects in aqueous NaCl solutions. A molecular dynamics simulation. *J Phys Chem* 100:16410–16418
- Lyubartsev AP, Laaksonen A (1997) Osmotic and activity coefficients from effective potentials for hydrated ions. *Phys Rev E* 55:5689–5696
- Lyubartsev A, Laaksonen A (1998) Molecular dynamics simulations of DNA in solution with different counter-ions. *J Biomol Struct Dyn* 16(3):579–592

- Lyubartsev AP, Laaksonen A (2000) Determination of effective pair potentials from *ab initio* simulations: application to liquid water. *Chem Phys Lett* 325(1–3):15–21
- Lyubartsev AP, Laaksonen A (1999) Effective potentials for ion-DNA interactions. *J Chem Phys* 111(24):11207–11215
- Lyubartsev AP, Laaksonen K, Laaksonen A (2001) Hydration of Li⁺ ion. An *ab initio* molecular dynamics simulation. *J Chem Phys* 114(7):3120–3126
- Lyubartsev A, Tu Y, Laaksonen A (2009) Hierarchical multiscale modelling scheme from first principles to mesoscale. *J Theor Comput Nanosci* 6(5):951–959
- Lyubartsev A, Mirzoev A, Chen LJ, Laaksonen A (2010) Systematic coarse-graining of molecular models by the Newton inversion method. *Faraday Discuss* 144:43–56
- Lyubartsev A, Naome A, Laaksonen A (2015) Systematic Hierarchical Coarse-Graining with the Inverse Monte Carlo Method. *J Chem Phys* 143(24):243120/1–243120/8
- Martinez-Luaces V (2012) Chemical kinetics and inverse modelling problems. In: Patel V (ed) *Chemical Kinetics*. Intech Publishing
- Mechelke M, Habeck M (2013) Estimation of interaction potentials through the configurational temperature formalism. *J Chem Theory Comput* 9:5685–5692
- Mirzoev A, Lyubartsev AP (2011) Effective solvent mediated potentials of Na⁺ and Cl[−] ions in aqueous solution: temperature dependence. *Phys Chem Chem Phys* 13:5722–5727
- Mirzoev A, Lyubartsev AP (2013) MagiC: software package for multiscale modeling. *J Chem Theory Comput* 9:1512–1520
- Mirzoev A, Nordenskiöld L, Lyubartsev A (2019) Magic v.3: an integrated software package for systematic structure-based coarse-graining. *Comput Phys Commun* 237:263–273. Software MagiC can be downloaded from: <https://www.fos.su.se/~sasha/magic/>
- Molitor J, Mallm J-P, Rippe K, Erdel F (2017) retrieving chromatin patterns from deep sequencing data using correlation functions. *Biophys J* 112:473–490
- Moller J, de Pablo JJ (2020) Bottom-up meets top-down: the crossroads of multiscale chromatin modeling. *Biophys J* 118:2057–2065
- Mullinax JW, Noid WG (2010) A generalized-Yvon-Born-Green theory for determining coarse-grained interaction potentials. *J Phys Chem C* 114:5661–5674
- Naômé A, Laaksonen A, Vercauteren DP (2014) A solvent-mediated coarse-grained model of DNA derived with the systematic Newton inversion method. *J Chem Theory Comput* 10(8):3541–4354
- Naômé A, Laaksonen A, Vercauteren D (2015) A CG simulation study of the structures, energetics, and dynamics of linear and circular DNA with its ions. *J Chem Theory Comput* 11:2813–2826
- Noh J, Gu GH, Kim S, Jung Y (2020) Machine-enabled inverse design of inorganic solid materials: promises and challenges. *Chem Sci* 11:4871–4881
- Nora EP, Dekker J, Heard E (2013) Segmental folding of chromosomes: a basis for structural and regulatory chromosomal neighborhoods? *BioEssays* 35:818–828
- Ozer G, Luque A, Schlick T (2015) The chromatin fiber: multiscale problems and approaches. *Curr Opin Struct Biol* 31:124–139
- Plimpton S (1995) Fast parallel algorithms for short-range molecular dynamics. *J Comput Phys* 117:1–19
- Pombo A, Dillon N (2015) Three-dimensional genome architecture: players and mechanisms. *Nat Rev* 16:245–257
- Power D, Rouse I, Poggio S, Brandt E, Lopez H, Lyubartsev A, Lobaskin V (2019) A multiscale model of protein adsorption on a nanoparticle surface. *Model Simul Mater Sci Eng* 27:084003
- Reatto L, Levesque D, Weis JJ (1986) Iterative predictor-corrector method for extraction of the pair interaction from structural data for dense classical liquids. *Phys Rev A* 33:3451–3465
- Rebic M, Mocci F, Laaksonen A, Ulicny J (2015) Multiscale simulations of human telomeric G-quadruplex DNA. *J Phys Chem B* 119(1):105–113
- Rebic M, Mocci F, Ulicny J, Lyubartsev A, Laaksonen A (2017) Coarse-grained simulation of rodlike higher-order quadruplex structures at different salt concentrations. *ACS Omega* 2(2):386–396
- Reddy KL, Feinberg AP (2013) Higher order chromatin organization in cancer. *Semin Cancer Biol* 23:109–115

- Reith D, Putz M, Muller-Plathe F (2003) Deriving effective mesoscale potentials from atomistic simulations. *J Comput Chem* 24:1625–1636
- Rosenfeld Y, Kahl G (1997) The inverse problem for simple classical liquids: a density functional approach. *J Phys Condens Matter* 9:L89–L98
- Sanchez-Lengeling B, Aspuru-Guzik A (2018) Inverse molecular design using machine learning: generative models for matter engineering. *Science* 361:360–365
- Schommers W (1983) Pair potentials in disordered many-particle systems: a study for liquid gallium. *Phys Rev A* 28:3599–3605
- Schwarz-Plaschg C, Kallhoff A, Eisenberger I (2017) Making nanomaterials safer by design? *Nanoethics* 11:277–281
- Serra F, Di Stefano M, Spill YG, Cuartero Y, Goodstadt M, Baù D, Marti-Renom MA (2015) Restraint-based three-dimensional modeling of genomes and genomic domains. *FEBS Lett* 589:2987–2995
- Sewitz SA, Fahmi Z, Lipkow K (2017) Higher order assembly: folding the chromosome. *Curr Opin Struct Biol* 42:162–168
- Shell MS (2008) The relative entropy is fundamental to multiscale and inverse thermodynamic problems. *J Chem Phys* 129:144108
- Sherman ZM, Howard MP, Lindquist BA, Jadrlich RB, Truskett TM (2020) Inverse methods for design of soft materials. *J Chem Phys* 152:140902
- Soper AK (1996) Empirical potential Monte Carlo simulation of fluid structure. *Chem Phys* 202:295–306
- Struebing H, Ganase Z, Karamertzanis PG, Sioungkrou E, Haycock P, Piccione PM, Armstrong A, Galindo A, Adjiman CS (2013) Computer-aided molecular design of solvents for accelerated reaction kinetics. *Nature Chem* 5:952–957
- Sun T, Mirzoev A, Minhas V, Korolev N, Lyubartsev AP, Nordenskiöld L (2019) A multiscale analysis of DNA phase separation: from atomistic to mesoscale level. *Nucleic Acids Res* 47:5550–5562
- Swendsen RH (1979) Monte Carlo renormalization group. *Phys Rev Lett* 42:859–861
- Szalaż P, Tang Z, Michalski P, Pietal MJ, Luo OJ, Sadowski M, Li X, Radew K, Ruan Y, Plewczynski D (2016) An integrated 3-dimensional genome modeling engine for data-driven simulation of spatial genome organization. *Genome Res* 26:1697–1709
- Tarantola A (2005) Inverse problem theory and methods for model parameter estimation. SIAM, Philadelphia. ISBN 0-89871-572-5
- Van Der Spoel D, Lindahl E, Hess B, Groenhof G, Mark AE, Berendsen HJ (2005) GROMACS: fast, flexible, and free. *J Comput Chem* 26:1701–1718
- van Berkum NL, Lieberman-Aiden E, Williams L, Imakaev M, Gnirke A, Mirny LA, Dekker J, Lander ES (2010) Hi-C: a method to study the three-dimensional architecture of genomes. *JOVE J Vis Exp* 39:e1869
- von Lilienfeld OA, Lins RD, Rothlisberger U (2005) Variational particle number approach for rational compound design. *Phys Rev Lett* 95:153002
- Wang M, Hu X, Beratan DN, Yang W (2006) Designing molecules by optimizing potentials. *J Am Chem Soc* 128:3228–3232
- Wang Y-L, Lyubartsev A, Lu Z-Y, Laaksonen A (2013) Effect of the electrostatic interactions on the multiscale coarse-graining simulations of ionic liquids. *Phys Chem Chem Phys* 16:1–12
- Xia K (2018) Sequence-based multiscale modeling for high-throughput chromosome conformation capture (Hi-C) data analysis. *PLoS ONE* 13:e0191899
- Yaman F, Yakhno VG, Potthast R (2013) A survey on inverse problems for applied sciences. *Math Probl Eng* 1–19. Article ID: 976837
- Zhu Y-L, Liu H, Li Z-W, Qian H-J, Milano G, Lu Z-Y (2013) GALAMOST: GPU-accelerated large-scale molecular simulation toolkit. *J Comput Chem* 34:2197–2211

Non-viral Vectors and Drug Delivery: In Vitro Assessment



Dragos Peptanariu, Marc J. M. Abadie, and Mariana Pinteala

Abstract Advances in nanotechnology, chemistry and molecular biology are making possible the transformation of conventional medicine into a personalized one where we are increasingly talking about intelligent drug carriers and targeted delivery of drugs and genes. Gene therapy emerges as a new field in biomedical research and seeks to establish a roadmap to the clinic and the market by promising solutions to incurable diseases. Various approaches are being tried for the implementation of gene therapy, on the one hand viral transporters and on the other hand non-viral solutions. Along with non-viral transfection vector design and synthesis, *in vitro* biological evaluation is required to investigate both the ability of vectors to transfect, and their good biocompatibility. For accurate and reliable outcomes, the choice of the correct method is essential.

Keywords Gene therapy · Drug delivery · Non-viral vectors · Polyethylenimine · Bioassays · Transfection · Cytotoxicity

Abbreviations

AM	Acetoxymethyl
AMP	Adenosine monophosphate
ATP	Adenosine triphosphate
CRISPR	Clustered regularly interspaced short palindromic repeats
DMSO	Dimethyl sulfoxide
GFP	Green fluorescent protein
GR	GelRed

D. Peptanariu (✉) · M. Pinteala
“Petru Poni” Institute of Macromolecular Chemistry, 700487 Iasi, Romania
e-mail: peptanariu.dragos@icmpp.ro

M. J. M. Abadie
Aggregates, Interfaces and Materials Energy (ICGM-AIME, UMR CNRS 5253), Institute
“Charles Gerhardt” of Montpellier, Montpellier, France

MTS	3-(4,5-dimethylthiazol-2-yl)-5-(3-carboxymethoxyphenyl)-2-(4-sulfophenyl)-2H-tetrazolium
MTT	3-(4,5-dimethyl-2-thiazolyl)-2, 5-diphenyl-2H-tetrazolium bromide
PEI	Polyethylenimine
PEG	Polyethylene glycol
PLL	Poly-L-lysine
TALEs	Transcription activator-like effectors
X-gal	5-Bromo-4-chloro-3-indolyl- β -D-galactopyranoside
XTT	2,3-bis-(2-methoxy-4-nitro-5-sulfophenyl)-2H-tetrazolium-5-carboxanilide
ZFPs	Zinc-finger proteins

1 Introduction

The advancement in scientific fields like biochemistry and molecular biology has contributed to a greater understanding of the causes of disease and its genetic basis. It has intensified the drive to pursue new and more successful therapies, and it has gradually introduced the idea of gene therapy as a promising choice in modern medicine.

Severe inherited or acquired genetic diseases such as leukemia, multiple myeloma, Parkinson's disease cystic fibrosis, muscular dystrophy, hemophilia those are some of the conditions whose patients are unsatisfied with traditional therapies and are currently seeking a therapeutic remedy.

Gene therapy promises the prospect of genetic disease curative treatment by inserting genes into the cells of patients, rather than using traditional medications that only offer symptomatic care.

Gene therapy is becoming more and more common, as of 2017 almost 2600 clinical trials have been performed and although viral therapies dominate the market for approved products, there is a growing interest in non-viral technologies (Ginn et al. 2018).

2 Gene Therapy Overview

With the advent of genetic engineering in the early 1970s a new avenue for gene therapy opened up. Two main instruments were necessary for the technique: a method of cloning unique genes for diseases and an efficient gene transfer tool.

The US scientists Theodore Friedmann and Richard Roblin demonstrated the promise of the gene therapy technology. In 1972 they published an article in Science (Friedmann and Roblin 1972) indicating that genetically engineered tumor viruses

could be used to move the genetic material required to treat patients with genetic disorders.

This system was first evaluated in the case of beta-thalassemia which is a severe blood condition caused by a genetic mutation in beta-globin gene. In 1976, scientists from the Cold Spring Harbor Laboratory and Harvard University cloned the beta-globin gene (Maniatis et al. 1976). This was the first gene to cause disease ever cloned.

In 1980, Dr. Martin Cline from the University of California in Los Angeles made the first attempt to use gene therapy in humans (Sun 1982). Cline and his team were unsuccessful in the treatment of two patients with beta-thalassemia by injecting the recombinant gene into their bone marrow and then reinfusing the cells. The findings of the experiment were inconclusive, unpublished and posed legal questions and public debate.

Later on, in the 1980s, retroviruses paved the way in developing more efficient carriers for gene therapy. Richard Charles Mulligan from Massachusetts Institute of Technology, along with his collaborators, managed to genetically alter a mouse leukemia retrovirus so that it could transport and deliver DNA sequences without reproducing in humans (Mann et al. 1983).

Benefiting from these new advances, the first approved gene therapy trial in humans is carried out by Michael Blaese, French Anderson and colleagues at NIH in 1990. It used a retroviral-mediated delivery of adenosine deaminase gene (ADA) to the T cells of two children affected by serious combined immunodeficiency disease (SCID) (Blaese et al. 1995; Sheridan 2011). That proved to be effective in one of the patients and encouraged the launch of numerous gene therapy trials in the following decades. The technique expanded by introducing new vectors, such as adenoviruses.

Eventually, the first commercial gene therapies appeared on the market. In 2003, Genetecin, a recombinant adenovirus treatment for squamous cell carcinoma in the head and neck (Pearson et al. 2004) was approved in China. In 2012, Glybera is licensed, the first for Europe, as a gene therapy suggested in the treatment of lipoprotein lipase deficiency (Burnett and Hooper 2009; Miller 2012).

The journey of gene therapy was not without issues, with the death of some patients or side effects including leukemia caused by viral vectors requiring legislative and ethical reconsideration.

Motivated by the problems encountered by viral vectors, research on non-viral vectors began to develop in parallel. In 1980 it was first demonstrated how phospholipid phosphatidylserin-based liposomes could transport DNA from SV40 virus to monkey kidney cells (Fraley et al. 1980).

Vectors based on cationic polymers represent a very wide class due to their chemical diversity; they are very versatile and can have countless functional groups and targeting elements. Within them, the poly-L-lysine polypeptide (PLL) was the first such vector to demonstrate the ability to bind DNA (Olins et al. 1967; Laemmli 1975). PLL is followed by PEI, a cationic polymer rich in amino groups, which has demonstrated the ability to bind and transfect DNA since the 1990s (Boussif et al. 1995).

Then, non-viral vectors began to diversify, comprising a wide range of liposomes, cationic polymers, dendrimers, peptides, vectors to which a number of chemical modifications were made to improve transfection and targeting properties (Yin et al. 2014; Lostalé-Seijo and Montenegro 2018).

In recent years, genomic editing techniques involving zinc-finger proteins (ZFPs), transcription activator-like effectors (TALEs) and clustered regularly interspaced short palindromic repeats (CRISPR)—Cas systems have gained increasing interest (Cong et al. 2013; Gaj et al. 2013; Mali et al. 2013; Urnov et al. 2010). They aim to accurately edit a genomic sequence and are an important step towards personalized medicine.

3 Viral or Non-viral

Among the viral ones, adenoviral vectors are probably of the most common. These vectors have the advantage that they function well in non-dividing cells, which is something hard to achieve by non-viral vectors. From the retroviruses, lentiviral vectors are also very popular, especially human immunodeficiency virus and the herpes simplex virus. Besides the fact that they do operate in non-dividing cells, these carriers could pack big DNA molecules, making them suitable for larger genes. Unfortunately it is hard to control the place of insertion into genome, raising safety concerns. They are better used *in vitro* in difficult to transduce cells.

Both viral and non-viral gene carriers have drawbacks and benefits which are summarized in Table 1.

Non-viral methods of introducing genetic material into cells, also called transfection methods, are numerous and comprise physical methods like electroporation, magnetofection, microinjection, gene gun, sonication, optical transfection and chemical methods which rely mostly on liposomes, dendrimers and cationic polymers. Among the first non-viral agents invented were cationic lipids, PLL and PEI.

PEI is perhaps the most studied cationic polymer used in transfection. Our research group has developed several vectors made of low molecular weight PEI stable attached through covalent bonds (Uritu et al. 2015a; Uritu et al. 2015b; Dascalu et al. 2017; Ardeleanu et al. 2018) to different hydrophobic cores (Fig. 1), as well as vectors based on dynamic chemistry where components were linked through reversible imine bonds (Clima et al. 2015; Turin-Moleavin et al. 2015; Ailincai et al. 2019; Craciun et al. 2019).

In general, high molecular weight PEI (15–25 kDa) is very effective in transfection, but this comes with a price, increased cytotoxicity. At the opposite pole is low molecular weight PEI, which has a good biocompatibility but also a low efficiency in transfection. Our approach was to combine low mass PEI molecules for good biocompatibility and the use of hydrophobic cores to improve transfection.

Table 1 Risks and benefits of viral and non-viral vectors

Viral vectors	
Benefits	Risks
Very high efficiency Could be applied to different human cell types	Limited carrier capacity Usually infect more than one type of cell, not always a desirable aspect Random genomic integration Risk of Weismann barrier breach and germline modification Overexpression of transgene Strong immune reaction Risk of transmission from the patient to other individuals or into the environment High costs
Non-viral vectors	
Benefits	Risks
Low costs Large scale production Reduced safety concerns Low immunogenic potential Increased cargo capacity Flexibility	Lower efficiency Increased toxicity at efficient concentrations

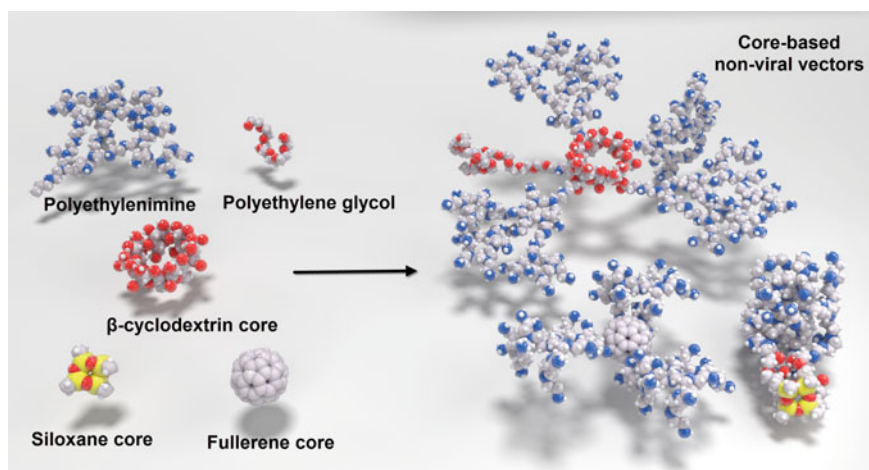


Fig. 1 Non-viral vectors. Their synthesis was done by attaching PEI and PEG molecules to hydrophobic cores such as fullerene, siloxane, β -cyclodextrin

4 Polyethylenimine Vectors, Mechanism of Action

The process of DNA packaging by PEI is due to the electrostatic forces between the positive charges of the polymer and the negative ones of the nucleic acids. The result is the formation of polyplexes, which are particles with a certain degree of polydispersity. The nitrogen/phosphorus ratio (N/P ratio) which depends on the polymer/DNA ratio has a very important role in the transfection efficiency, particles with electric positive surface being more efficient in the interaction with the negatively charged surface of the cell membrane. The interaction process between polyplexes and cells requires endocytosis (Bieber et al. 2002; Rejman et al. 2005) and is facilitated by syndecans and the catabolism of the extracellular matrix (Demeneix and Behr 2005; Kopatz et al. 2004; Christianson and Belting 2014). Polyplexes make contact with the cell membrane through syndecans, transmembrane proteins that present in their distal extracellular portion heparan sulfate, anionic components that interact with the extracellular matrix and cationic particles. The process is continued with the agglomeration of several syndecan molecules and the activation of cytoskeletal proteins with which syndecans react through the intracytoplasmic domain. Eventually the action of the cytoskeleton will pull the cell membrane inward, resulting in its invagination and sequestration of polyplexes into endosomal vesicles (Fig. 2).

The endosomal sequestration of PEI/DNA complexes can be problematic because the physiological maturation of endosomes results in either fusion with lysosomes

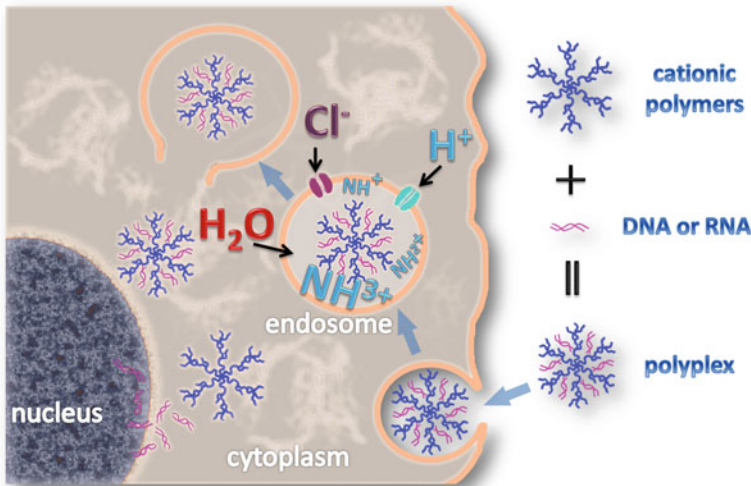


Fig. 2 Endosomal escape. First, the polyplexes interact with the cell membrane and enter the cell through endocytosis. In the endosome ATPase proton pumps actively translocate protons from the cytosol into the endosomes but PEI based vectors with ‘proton sponge’ property will become protonated and will resist the acidification. The protons influx is followed by passive entry of chloride ions leading to water influx, osmotic pressure and possible rupture of the endosome.

or direct transformation into lysosomes. The lysosomal acidic environment, rich in degradable enzymes, would not be a friendly space for any drug.

But here PEI emphasizes its feature of proton sponge by using amino groups capable of protonation, which can absorb much of the protons pumped into the endosomes by proton pumps, thus resisting the tendency to acidify. The active inflow of protons will be followed by the passive influx of anions, such as chloride, and the increased ionic concentration will facilitate the penetration of water by osmotic pressure and the swelling and rupture of the endosome with the release of polyplexes in the cytosol.

The exact mechanism of endosomal escape is controversial and not fully understood (Won et al. 2009).

Some researchers argue that there is no change in lysosomal pH due to the presence of PEI and V-ATPases proton pumps could overcome the buffering capacity of PEI (Benjaminsen et al. 2013). Moreover, the bursting of endosome could actually be detrimental for cell health due to the release of apoptosis inducing enzymes (Roberg et al. 2002).

Once released into the cytosol, the journey of polyplexes does not end here, for gene expression to take place, DNA must reach the nucleus. The cytosol is not a safe place for DNA, on the one hand it is a very crowded space, through which it diffuses hard and at the same time it contains nucleases that can quickly degrade nucleic acids. This is why it is important that DNA does not break down from polyplexes yet. The most advantageous time for polyplexes to reach the nucleus is during mitosis.

5 Addressing Efficiency and Biocompatibility Using *in vitro* Assays

In order to support the research of transfection vectors, regardless of whether their destination is *in vivo* or *in vitro* use, it is necessary first of all to test them *in vitro*. The tests must tackle, on the one hand, the transfection potential and, on the other hand, their cytotoxicity.

5.1 Gel Retardation Assay and Dye Exclusion Assay

Before transfection experiments begin, the ability of vectors to bind DNA must be investigated first. There is no reason to make transfections on cells with molecules that do not prove the ability to pack nucleic acids.

One of the most common and oldest tests to evaluate the packaging capacity of non-viral vectors is gel retardation assay. This technique is actually nothing else but a variation of affinity electrophoresis procedure used to test protein-nucleic acids

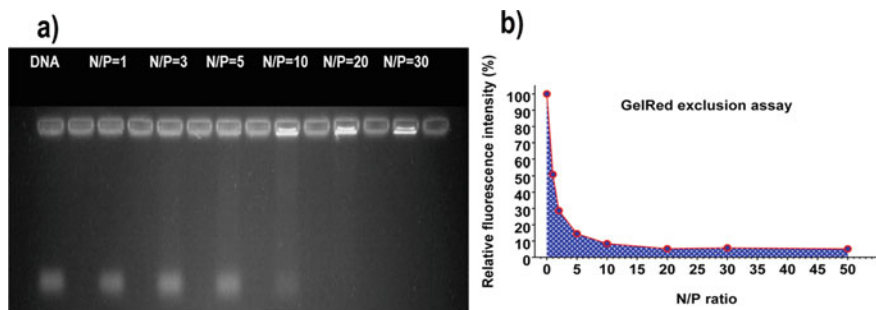


Fig. 3 Binding capacity of vectors. A vector based on PEI and fullerene core was the subject of testing using a) gel retardation assay and b) dye exclusion assay

interactions which can identify if a protein or a protein mixture will attach to a specific DNA or RNA sequence (Scott et al. 1994).

Unlike the classic use of this test in protein-nucleic acid interactions, here the place of the protein is taken by our vector, and the specificity of the interaction with certain nucleic acid sequences interests us less, being more important the ability to bind DNA and RNA in general.

The assay is usually performed as electrophoresis on an agarose gel. Free DNA is placed in one well of the gel, and polyplexes in increasing N/P ratios are placed in the next wells. As expected, once electric current is applied, DNA being an electronegative molecule will begin to migrate into the electric field. In the case of polyplexes, however, this migration will be slowed down with the increase of the N/P ratio, being completely abolished over a certain N/P. At the same time, the bands corresponding to polyplexes will be less bright due to the displacement of the staining agent by the polymeric vector (Fig. 3a).

A test called GelRed (GR) dye exclusion assay is another one that we have used in our work (Vasiliu et al. 2018; Craciun et al. 2019) to investigate the binding capacity of vectors. GR is a sensitive dye used to stain nucleic acids and is safer to use than ethidium bromide because it is impermeable to the cell membrane and therefore cannot penetrate living cells.

GR fluorescence increases significantly as it interacts and binds to double-stranded DNA molecules. Due to this fact, it can also be used to investigate the ability of vectors to bind DNA. Thus, for this test, samples with polyplexes DNA-vector are first prepared individually at various N/P ratios, after which GR is added to each of them. As the N/P ratio increases, more and more GR will be excluded by the vector from the DNA complex resulting in a decrease in fluorescence (Fig. 3b). The result is read with the help of a plate reader. This test is more sensitive than gel retardation assay, requires much smaller amounts of reagents and provides a quantitative result, allowing comparison between the binding powers of various vectors.

5.2 Evaluation of Transfection Efficiency and Biocompatibility

Once the ability to bind nucleic acids by vectors has been proven, we can move on to testing the efficiency of transfection, i.e. the purpose for which we created these chemical structures.

In general, such studies generate libraries of chemical compounds that must be tested in different concentrations, ultimately raising the number of samples a lot. Thus, it is very important that the chosen assays meet a number of characteristics such as: efficiency in simultaneous running on a large number of samples, the ability to generate reproducible data, and last but not least to be economically feasible.

To help us get results more easily, polyplexes are prepared using test vectors and a plasmid containing a reporter gene such as luciferase, β -galactosidase or a fluorescent protein like green fluorescent protein (GFP) (Bono et al. 2020). The purpose of these reporter genes is to generate an easily detectable result in the case of a successful transfection (Fig. 4).

Performing a cell transfection experiment must take into account several aspects.

Cellular mitosis is important for the success of transfection, for this reason it is good for the cells to be in the exponential growth phase and their confluence to be between 70 and 90% for adherent cells. The optimal cell density must be found to obtain the best possible transfection result (Malloggi et al. 2015).

Cell lines are preferable in transfection experiments precisely because they have a high rate of division, in contrast to aging primary cells, which rarely replicate and are very difficult to transfect (Pezzoli et al. 2017). The health of the cells is

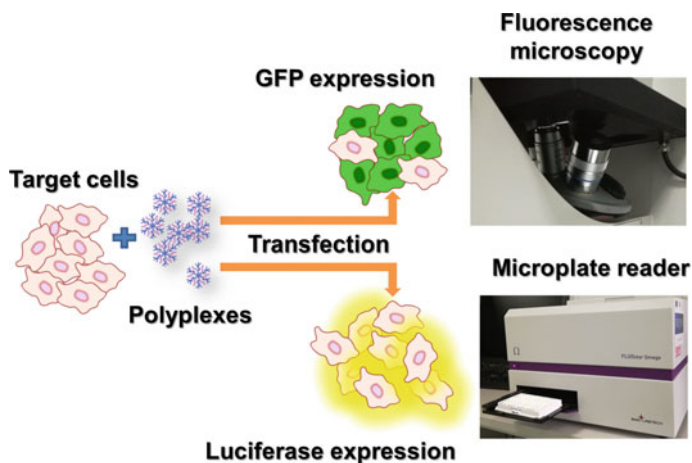


Fig. 4 Evaluation of transfection efficiency. Cells are transfected with polyplexes containing reporter genes. Efficient transfection results in cells expressing either a fluorescent protein which can be seen in fluorescence microscopy, or luciferase which could be quantified after reaction with luciferin by reading light emitted with a luminometer

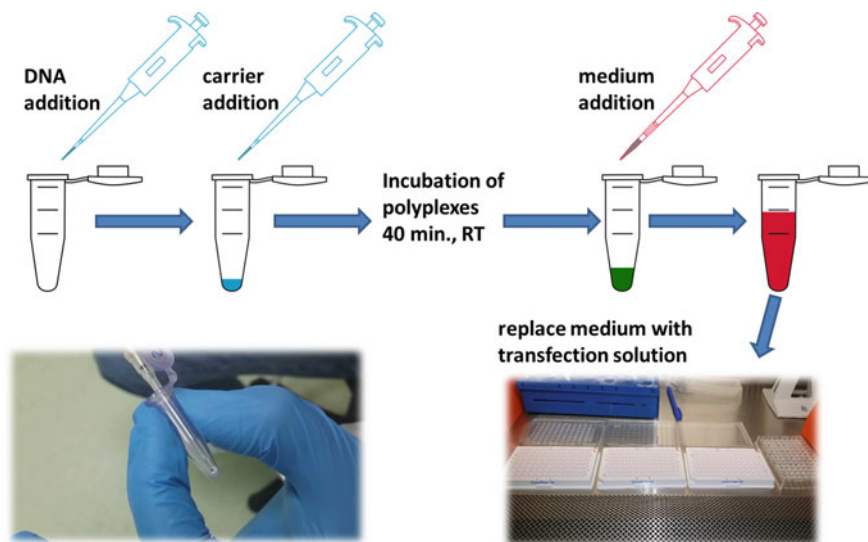


Fig. 5 Preparation of transfection solution. Polyplexes are created by mixing the vector with plasmid DNA, after which the cell culture medium is added. The final solution is used to treat the cells.

ensured by the culture conditions, among them their nutritional environment being very important. Thus, the cells cannot be bathed directly in a polyplex solution and expected to maintain their full viability. For this reason, it is preferable for the transfection to take place in a culture medium in which polyplexes are also present. The experiment begins by forming a polyplex solution by mixing vectors with plasmid DNA in the absence of the culture medium, after which the latter is added (Fig. 5).

It is important that things are done in this order because the presence of the culture medium during the formation of polyplexes can interfere with the process.

The preparation of polyplexes in a salt environment leads to their aggregation over time, which facilitates sedimentation and improves transfection by increasing the concentration in the vicinity of adherent cells (Jones et al. 2013; Hill et al. 2016).

For the reason mentioned above related to good cell viability, the polyplex solution is good to represent a small fraction of the final volume that will be used for the treatment of cells (van Gaal et al. 2011).

Serum can be present, although serum proteins can interact with polyplexes, the serum culture medium improves the quality of transfection because it ensures better cellular health.

Because cationic polymers destabilize the cell membrane (Hong et al. 2006; Leroueil et al. 2008), it is preferable not to use antibiotics in the transfection medium since they could penetrate cells more easily and induce an increase in toxicity.

Several N/P ratios will be tested to find those optimal for transfection. To establish the range of N/P concentrations, the data from the DNA binding experiment will be

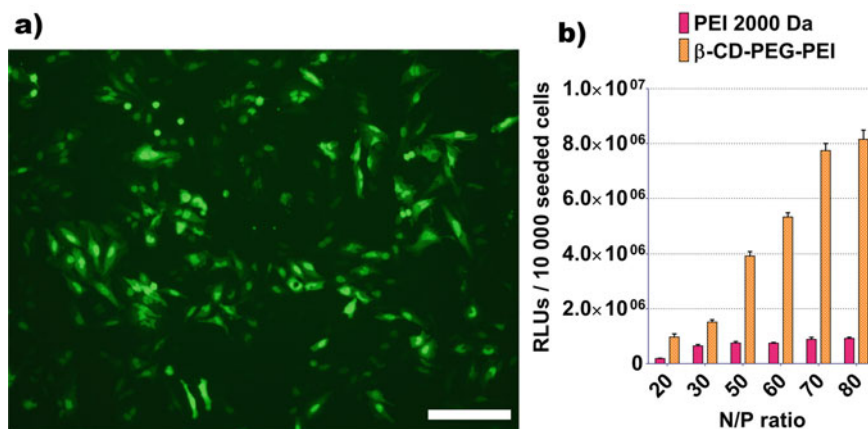


Fig. 6 Typical transfection results. a) Fluorescence microscopy of HeLa cells 48 h after transfection with GFP and vector based on polyethylenimine attached to a rotaxane core. Scale bar 200 μ m (Ardeleanu et al. 2018). b) Luciferase assay on HeLa cells 48 h after transfection with luciferase gene carried by a vector made of β -cyclodextrine core with PEI and PEG. Results expressed in RLUs \pm S.E.M (standard error of the mean). RLUs = relative light units (Dascalu et al. 2017).

used, in general the N/P values at which the maximum binding capacity begins to be reached are the ones where an optimal transfection takes place.

Transfection with the GFP reporter gene gives us a qualitative result by visualizing the transfected cells under a microscope. A plasmid carrying the GFP gene fused to the gene of a nuclear localization peptide will lead to the accumulation of the GFP protein in the cell nucleus, allowing an easier view of the results (Fig. 6a).

Fluorescence microscopy will bring a qualitative result, but it may be subjective, transfection with the reporter gene for luciferase (Fig. 6b) is a more sensitive test that provides a valuable quantitative result that allows the detection of more subtle transfections and permits comparison between the efficiency of various vectors or at various N/P ratios. In the case of this assay, a global response, mediated on the entire amount of cells in the sample is given.

Luciferase is an oxidative enzyme present in certain animal species that manifest bioluminescence.

Light is released in the luciferase reaction as luciferase acts on its specific substrate, luciferin, in the presence of ATP (Fig. 7).

Luciferase assay is very reliable: because the luciferase bioluminescence does not require light excitation, there is limited auto-fluorescence and thus practically background-free fluorescence.

Light sensitive devices such as luminometers or microplate readers equipped with luminescence module can measure light emission.

In the case of β -galactosidase gene transfection, the successfully transfected cells will express the β -galactosidase enzyme and after treatment with the substrate X-gal,

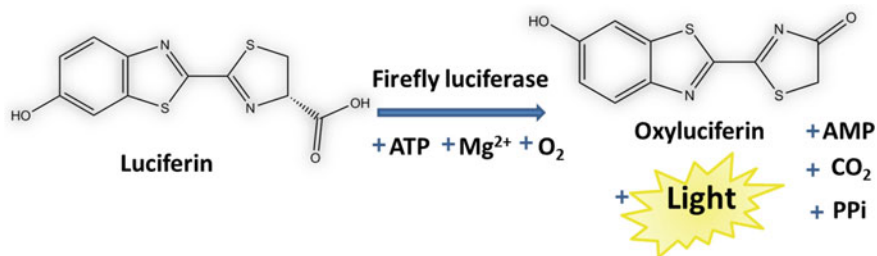


Fig. 7 Luciferase reaction. Luciferin protein is converted in the presence of ATP by the enzyme luciferase into oxyluciferin. The reaction occurs with photon emission which can be quantified by a luminometer.

an intensely blue-colored product is obtained. Thus, the transfection can be quantified by reading the absorbance to a microplate reader.

Flow cytometry is another method to quantitatively evaluate transfection performed with reporter genes for fluorescent proteins, such as GFP. However, it should be noted that unlike the luciferase assay, larger amounts of cells are required for flow cytometry. Also, the method involves a longer time to prepare the samples for reading, with the risk of introducing differences between the first and last samples read. However, this method is very useful to find out the percentage of cells that have been transfected.

The purpose of non-viral vectors is to transfect cells; however it is important that this process takes place without harmful effects on cell viability. Therefore, *in vitro* testing of vectors should also include the analysis of their biocompatibility. Microplate assays are of choice to analyze the large number of samples required by a library of compounds at different concentrations.

Metabolic colorimetric assays are often used for their simplicity; they do not directly determine viability and proliferation, but do so indirectly by measuring the cell's ability to convert a tetrazolium salt (MTT, MTS, XTT) to formazan.

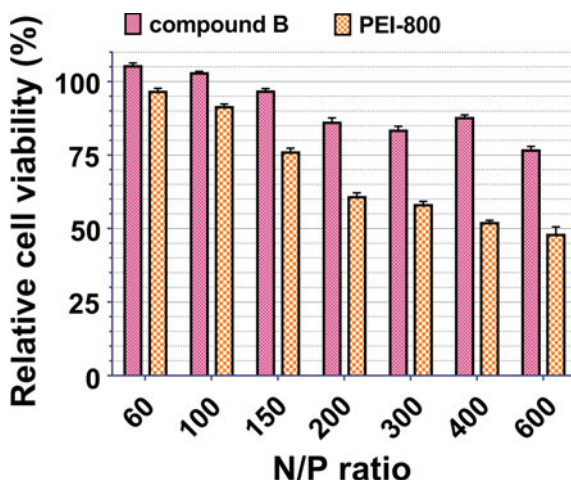
MTT is a colorimetric test described by Mosmann (Mosmann 1983) to quantify the proliferation and survival of mammalian cells. This test is based on the ability of cellular oxidoreductase enzymes in living cells to reduce a tetrazolium salt into a water-insoluble purple formazan.

In a typical MTT experiment, the cells of interest are cultured in the presence of the test substance for a certain amount of time (1–2 days) after which the cell cultures are treated with the MTT agent for several hours. At the end a formazan is obtained which will be dissolved by the addition of DMSO and the absorbance at 560 nm will be read on a microplate reader. The absorbance value of formazan is directly proportional to the number of healthy cells.

Very similar, in the case of MTS it is another tetrazolium salt that produces a water-soluble formazan, thus eliminating the solubilization stage at the end of the MTT test (Fig. 8).

These tests cannot discriminate between reduced proliferative activity or slowed cellular metabolic rate, but they could be complemented with other viability tests such

Fig. 8 MTS assay. Relative viability of HeLa cells 48 h after transfection with compound B, a non-viral vector constructed with a linear siloxane core with low molecular mass PEI attached through imine linkage. Results expressed as percentage relative to viability of untreated cells \pm S.D. (standard error of the mean). The results show a better biocompatibility of compound B compared to the PEI from which it was synthesized (Ailincai et al. 2019).



as live-dead staining. One such familiar test is the staining with propidium iodide and calcein AM (acetoxymethyl). Calcein AM stains living cells in fluorescent green, while propidium iodide, impermeable to the living cell membrane, stains dead cells in fluorescent red by binding to nucleic acids.

Flow cytometry can be used both to quantify transfection and to evaluate cell viability. But as we mentioned, care must be taken in experiments involving a large number of samples and in the time elapsed between the acquisitions of various samples.

6 Final Notes

Medicine is evolving and although not perfect, gene therapy is here to stay, enhancing its methods each year. Improved synthesis techniques in the field of non-viral vectors have made new molecular structures possible. The number of transfection compounds has become impressive and there is an increasing demand for bioassay screening.

In-vitro biological assays for non-viral vectors must be carefully selected for their sensitivity, specificity, reproducibility and the option to be easily applied. As none of the transfection assessment tests provide all the information, it is good practice to combine them. For example, transfection with GFP and luciferase provides a comprehensive picture of transfection efficiency by providing both qualitative and quantitative information.

Acknowledgements This work has received funding from the H2020 ERA Chairs Project no 667387: SupraChem Lab Laboratory of Supramolecular Chemistry for Adaptive Delivery Systems ERA Chair initiative and Grant of the Romanian National Authority for Scientific Research and Innovation, CNCS/CCCDI – UEFISCDI, project number PN-III-P3-3.6-H2020-2016-0011, within PNCDI III.

References

- Ailincăi D, Peptanariu D, Pinteala M, Marin L (2019) Dynamic constitutional chemistry towards efficient nonviral vectors. *Mater Sci Eng C* 94:635–646. <https://doi.org/10.1016/j.msec.2018.10.002>
- Ardeleanu R, Dascalu AI, Neamtu A, Peptanariu D, Uritu CM, Maier SS, Nicolescu A, Simionescu BC, Barboiu M, Pinteala M (2018) Multivalent polyrotaxane vectors as adaptive cargo complexes for gene therapy. *Polym Chem* 9(7):845–859. <https://doi.org/10.1039/C7PY01256J>
- Benjaminsen RV, Matthebjerg MA, Henriksen JR, Moghimi SM, Andresen TL (2013) The possible “proton sponge” effect of polyethylenimine (PEI) does not include change in lysosomal pH. *Mol Ther* 21(1):149–157. <https://doi.org/10.1038/mt.2012.185>
- Bieber T, Meissner W, Kostin S, Niemann A, Elsasser H-P (2002) Intracellular route and transcriptional competence of polyethylenimine–DNA complexes. *J Control Release* 82(2):441–454. [https://doi.org/10.1016/S0168-3659\(02\)00129-3](https://doi.org/10.1016/S0168-3659(02)00129-3)
- Blaese RM, Culver KW, Miller AD, Carter CS, Fleisher T, Clerici M, Shearer G, Chang L, Chiang Y, Tolstoshev P, Greenblatt JJ, Rosenberg SA, Klein H, Berger M, Mullen CA, Ramsey WJ, Muul L, Morgan RA, Anderson WF (1995) T lymphocyte-directed gene therapy for ADA- SCID: initial trial results after 4 years. *Science* 270(5235):475–480. <https://doi.org/10.1126/science.270.523.5.475>
- Bono N, Ponti F, Mantovani D, Candiani G (2020) Non-viral in vitro gene delivery: it is now time to set the bar! *Pharmaceutics* 12(2):183. <https://doi.org/10.3390/pharmaceutics12020183>
- Boussif O, Lezoualc’h F, Zanta MA, Mergny MD, Scherman D, Demeneix B, Behr JP (1995) A versatile vector for gene and oligonucleotide transfer into cells in culture and in vivo: polyethylenimine. *Proc Natl Acad Sci U S A* 92(16):7297–7301. <https://doi.org/10.1073/pnas.92.16.7297>
- Burnett JR, Hooper AJ (2009) Alipogene tiparvec, an adeno-associated virus encoding the Ser(447)X variant of the human lipoprotein lipase gene for the treatment of patients with lipoprotein lipase deficiency. *Curr Opin Mol Ther* 11(6):681–691
- Christianson HC, Belting M (2014) Heparan sulfate proteoglycan as a cell-surface endocytosis receptor. *Matrix Biol* 35:51–55. <https://doi.org/10.1016/j.matbio.2013.10.004>
- Clima L, Peptanariu D, Pinteala M, Salic A, Barboiu M (2015) DyNAvectors: dynamic constitutional vectors for adaptive DNA transfection. *Chem Commun* 51(99):17529–17531. <https://doi.org/10.1039/C5CC06715D>
- Cong L, Ran FA, Cox D, Lin S, Barretto R, Habib N, Hsu PD, Wu X, Jiang W, Marraffini LA, Zhang F (2013) Multiplex genome engineering using CRISPR/Cas systems. *Science* 339(6121):819–823. <https://doi.org/10.1126/science.1231143>
- Craciun BF, Gavril G, Peptanariu D, Ursu LE, Clima L, Pinteala M (2019) Synergistic effect of low molecular weight polyethylenimine and polyethylene glycol components in dynamic nonviral vector structure, toxicity, and transfection efficiency. *Molecules* 24(8):1460
- Dascalu AI, Ardeleanu R, Neamtu A, Maier SS, Uritu CM, Nicolescu A, Silion M, Peptanariu D, Calin M, Pinteala M (2017) Transfection-capable polycationic nanovectors which include PEGylated-cyclodextrin structural units: a new synthesis pathway. *J Mater Chem B* 5(34):7164–7174. <https://doi.org/10.1039/C7TB01722G>
- Demeneix B, Behr JP (2005) Polyethylenimine (PEI). In: *Advances in Genetics*, vol 53. Academic Press, pp 215–230. [https://doi.org/10.1016/S0065-2660\(05\)53008-6](https://doi.org/10.1016/S0065-2660(05)53008-6)
- Fraley R, Subramani S, Berg P, Papahadjopoulos D (1980) Introduction of liposome-encapsulated SV40 DNA into cells. *J Biol Chem* 255(21):10431–10435
- Friedmann T, Roblin R (1972) Gene therapy for human genetic disease? *Science* 175(4025):949–955. <https://doi.org/10.1126/science.175.4025.949>
- Gaj T, Gersbach CA, Barbas CF 3rd (2013) ZFN, TALEN, and CRISPR/Cas-based methods for genome engineering. *Trends Biotechnol* 31(7):397–405. <https://doi.org/10.1016/j.tibtech.2013.04.004>

- Ginn, SL, Amaya, AK, Alexander, IE, Edelstein, M, Abedi, MR (2018) Gene therapy clinical trials worldwide to 2017: an update. *J Gene Med.* 20:e3015. <https://doi.org/10.1002/jgm.3015>
- Hill AB, Chen M, Chen CK, Pfeifer BA, Jones CH (2016) Overcoming gene-delivery hurdles: physiological considerations for nonviral vectors. *Trends Biotechnol* 34(2):91–105. <https://doi.org/10.1016/j.tibtech.2015.11.004>
- Hong S, Leroueil PR, Janus EK, Peters JL, Kober MM, Islam MT, Orr BG, Baker JR Jr, Banaszak Holl MM (2006) Interaction of polycationic polymers with supported lipid bilayers and cells: nanoscale hole formation and enhanced membrane permeability. *Bioconjug Chem* 17(3):728–734. <https://doi.org/10.1021/bc060077y>
- Jones CH, Chen CK, Ravikrishnan A, Rane S, Pfeifer BA (2013) Overcoming nonviral gene delivery barriers: perspective and future. *Mol Pharm* 10(11):4082–4098. <https://doi.org/10.1021/mp400467x>
- Kopatz I, Remy J-S, Behr J-P (2004) A model for non-viral gene delivery: through syndecan adhesion molecules and powered by actin. *J Gene Med* 6(7):769–776. <https://doi.org/10.1002/jgm.558>
- Laemmli UK (1975) Characterization of DNA condensates induced by poly(ethylene oxide) and polylysine. *Proc Natl Acad Sci U S A* 72(11):4288–4292. <https://doi.org/10.1073/pnas.72.11.4288>
- Leroueil PR, Berry SA, Duthie K, Han G, Rotello VM, McNerny DQ, Baker JR Jr, Orr BG, Holl MM (2008) Wide varieties of cationic nanoparticles induce defects in supported lipid bilayers. *Nano Lett* 8(2):420–424. <https://doi.org/10.1021/nl0722929>
- Lostalé-Seijo I, Montenegro J (2018) Synthetic materials at the forefront of gene delivery. *Nat Rev Chem* 2(10):258–277. <https://doi.org/10.1038/s41570-018-0039-1>
- Mali P, Yang L, Esvelt KM, Aach J, Guell M, DiCarlo JE, Norville JE, Church GM (2013) RNA-guided human genome engineering via Cas9. *Science* 339(6121):823–826. <https://doi.org/10.1126/science.1232033>
- Malloggi C, Pezzoli D, Magagnin L, De Nardo L, Mantovani D, Tallarita E, Candiani G (2015) Comparative evaluation and optimization of off-the-shelf cationic polymers for gene delivery purposes. *Polymer Chemistry* 6(35):6325–6339. <https://doi.org/10.1039/C5PY00915D>
- Maniatis T, Kee SG, Efstratiadis A, Kafatos FC (1976) Amplification and characterization of a beta-globin gene synthesized in vitro. *Cell* 8(2):163–182. [https://doi.org/10.1016/0092-8674\(76\)90001-5](https://doi.org/10.1016/0092-8674(76)90001-5)
- Mann R, Mulligan RC, Baltimore D (1983) Construction of a retrovirus packaging mutant and its use to produce helper-free defective retrovirus. *Cell* 33(1):153–159. [https://doi.org/10.1016/0092-8674\(83\)90344-6](https://doi.org/10.1016/0092-8674(83)90344-6)
- Miller N (2012) Glybera and the future of gene therapy in the European Union. *Nat Rev Drug Discov* 11(5):419. <https://doi.org/10.1038/nrd3572-c1>
- Mosmann T (1983) Rapid colorimetric assay for cellular growth and survival: application to proliferation and cytotoxicity assays. *J Immunol Methods* 65(1–2):55–63. [https://doi.org/10.1016/0022-1759\(83\)90303-4](https://doi.org/10.1016/0022-1759(83)90303-4)
- Olins DE, Olins AL, Von Hippel PH (1967) Model nucleoprotein complexes: studies on the interaction of cationic homopolypeptides with DNA. *J Mol Biol* 24(2):157–176. [https://doi.org/10.1016/0022-2836\(67\)90324-5](https://doi.org/10.1016/0022-2836(67)90324-5)
- Pearson S, Jia H, Kandachi K (2004) China approves first gene therapy. *Nat Biotechnol* 22(1):3–4. <https://doi.org/10.1038/nbt0104-3>
- Pezzoli D, Giupponi E, Mantovani D, Candiani G (2017) Size matters for in vitro gene delivery: investigating the relationships among complexation protocol, transfection medium, size and sedimentation. *Sci Rep* 7(1):44134. <https://doi.org/10.1038/srep44134>
- Rejman J, Bragonzi A, Conese M (2005) Role of clathrin- and caveolae-mediated endocytosis in gene transfer mediated by lipo- and polyplexes. *Mol Ther* 12(3):468–474. <https://doi.org/10.1016/j.ymthe.2005.03.038>

- Roberg K, Kågedal K, Öllinger K (2002) Microinjection of cathepsin D induces caspase-dependent apoptosis in fibroblasts. *Am J Pathol* 161(1):89–96. [https://doi.org/10.1016/S0002-9440\(10\)64160-0](https://doi.org/10.1016/S0002-9440(10)64160-0)
- Scott V, Clark AR, Docherty K (1994) The gel retardation assay. In: Harwood AJ (ed) *Protocols for gene analysis*. Humana Press, Totowa, pp 339–347. <https://doi.org/10.1385/0-89603-258-2:339>
- Sheridan C (2011) Gene therapy finds its niche. *Nat Biotechnol* 29(2):121–128. <https://doi.org/10.1038/nbt.1769>
- Sun M (1982) Martin cline loses appeal on NIH grant. *Science* 218(4567):37. <https://doi.org/10.1126/science.7123214>
- Turin-Moleavin I-A, Doroftei F, Coroaba A, Peptanariu D, Pinteala M, Salic A, Barboiu M (2015) Dynamic constitutional frameworks (DCFs) as nanovectors for cellular delivery of DNA. *Org Biomol Chem* 13(34):9005–9011. <https://doi.org/10.1039/C5OB01315A>
- Uritu CM, Calin M, Maier SS, Cojocaru C, Nicolescu A, Peptanariu D, Constantinescu CA, Stan D, Barboiu M, Pinteala M (2015) Flexible cyclic siloxane core enhances the transfection efficiency of polyethylenimine-based non-viral gene vectors. *J Mater Chem B* 3(42):8250–8267. <https://doi.org/10.1039/C5TB01342A>
- Uritu CM, Varganici CD, Ursu L, Coroaba A, Nicolescu A, Dascalu AI, Peptanariu D, Stan D, Constantinescu CA, Simion V, Calin M, Maier SS, Pinteala M, Barboiu M (2015) Hybrid fullerene conjugates as vectors for DNA cell-delivery. *J Mater Chem B* 3(12):2433–2446. <https://doi.org/10.1039/C4TB02040E>
- Urnov FD, Rebar EJ, Holmes MC, Zhang HS, Gregory PD (2010) Genome editing with engineered zinc finger nucleases. *Nat Rev Genet* 11(9):636–646. <https://doi.org/10.1038/nrg2842>
- van Gaal EV, van Eijk R, Oosting RS, Kok RJ, Hennink WE, Crommelin DJ, Mastrobattista E (2011) How to screen non-viral gene delivery systems in vitro? *J Control Release Official J Control Release Soc* 154(3):218–232. <https://doi.org/10.1016/j.jconrel.2011.05.001>
- Vasiliu T, Cojocaru C, Peptanariu D, Dascalu AI, Pinteala M, Rotaru A (2018) Polyplex formation between cyclodextrin-based non-viral vector and dsDNA: molecular dynamic study with experimental validation. *Rev Roum Chim* 63(7–8):629–636
- Won Y-Y, Sharma R, Konieczny SF (2009) Missing pieces in understanding the intracellular trafficking of polycation/DNA complexes. *J Control Release* 139(2):88–93. <https://doi.org/10.1016/j.jconrel.2009.06.031>
- Yin H, Kanasty RL, Eltoukhy AA, Vegas AJ, Dorkin JR, Anderson DG (2014) Non-viral vectors for gene-based therapy. *Nat Rev Genet* 15(8):541–555. <https://doi.org/10.1038/nrg3763>

Biodegradable Nanoparticles for Specific Drug Transport



Karin Danz, Hagen von Briesen, and Sylvia Wagner

Abstract Biodegradable nanoparticles are highly versatile and adaptable delivery systems for pharmaceutical drugs. The nanoparticles can be targeted to specific cell types and tissues, modified to overcome biological barriers the contained drugs cannot overcome on their own and at the same time mask the undesirable side effects of pharmacological substances. The nanoparticle characteristics can be tailored to specific targets by modifications such as the addition of antibodies to the particle surface or coating them in substances altering their circulation behaviour. Different approaches and examples for targeted drug delivery with biodegradable nanoparticles are discussed, as well as model systems for the advanced evaluation of the used formulations shown.

Keywords Biodegradable nanoparticles · Specific drug targeting · Overcome biological barriers · Blood-brain barrier

Abbreviations

ApoE	Apolipoprotein E
BBB	Blood-brain barrier
EGFR	Epidermal growth factor receptor
EPR	Enhanced Permeability and Retention
EMA	European Medicines Agency
FDA	Food and Drug Administration
HSA	Human serum albumin
HER2	Human epidermal growth factor receptor-2
PLA	Poly(lactic acid)
PLGA	Poly(lactic-co-glycolic) acid

K. Danz · H. von Briesen · S. Wagner (✉)
Department Bioprocessing and Bioanalytics, Fraunhofer Institute for Biomedical Engineering,
Joseph-von-Fraunhofer-Weg 1, 66280 Sulzbach, Germany
e-mail: sylvia.wagner@ibmt.fraunhofer.de

PVA	Polyvinyl alcohol
TER	Transendothelial electrical resistance

1 Introduction

The targeted delivery of drugs within the human organism is an ongoing challenge in pharmaceutical circles. To this day, the administration of drugs by oral or intravenous means leads to a nearly uniform distribution within the body once initial absorption e.g. through the gastrointestinal tract by oral delivery has occurred. This is followed by enrichment in tissues capable of metabolising or storing the substances, specifically liver, kidney and spleen. The only exception in this systemic distribution in many cases is the brain environment. Here, the blood-brain barrier (see Sect. 4.2) due to its highly selective character prevents more than 98% of all pharmaceutical drugs from crossing into the brain environment (Pardridge 2005). The general systemic distribution provides an advantage when tackling systemic illnesses but, in many cases, a targeted approach would be preferable. Modern drugs still carry the potential for both unwanted side effects of a single drug or problematic drug interactions in case of application of multiple substances. The possibility to deliver a drug only to the tissue or organ of interest has been a research target for decades. One of the most promising options to achieve this goal are nanoparticulate delivery systems. Since their first descriptions in the 1970s, nanoparticles have been investigated for a number of potential applications, not limited to targeted drug delivery (Birrenbach and Speiser 1976; Kreuter and Speiser 1976; Scheffel et al. 1972). The use in diagnostic context for example is of particular interest as well. Here, metallic nanoparticles specifically have proven useful (Mody et al. 2010). Yet, for drug delivery approaches, especially in the case of long-term or continuous medication, the nanoparticle systems need to be biocompatible to such a degree as to not build up over time of administration or instigate an immune response for clearing (Mirabello et al. 2015). A base of biodegradable polymers, that can be degraded and metabolised within existing cellular metabolic pathways, have been the solution of choice for some time.

2 Nanoparticulate Drug Delivery Systems

For drug delivery approaches, nanoparticles are classified as structures with a mean size of 1 to 1000 nm. While a colloidal shape is most common, other shapes including cubic or rod-like are possible (Saraiva et al. 2016). The base material, as mentioned above, is usually comprised of biodegradable polymers. This includes both natural macromolecules like human serum albumin (HSA), gelatine, chitosan or alginate, as well as synthetic polymer blocks like polylactic acid (PLA), poly(lactic-co-glycolic) acid (PLGA), polyacrylic acid and its derivatives and others (Kumari et al. 2010).

The resulting particles exhibit a natural electric charge, that can range from positive to negative with varying degrees of strength. The drugs are either trapped within the particle matrix itself or bound to the particles surface. Additionally, surface modifications are possible to achieve specific characteristics or target certain cells types, organs or tissues (Fig. 1).

The nanoparticle production itself is largely dependent on the base material. Both chemical polymerisation reactions as well as dispersion-based methods have been described (Kreuter 1983). Chemical polymerisation reactions establish crosslinks between the polymer blocks. Controlling this chemical reaction provides a certain degree of adjustability concerning the appearance and characteristics of the produced nanoparticles. With dispersion methods, the polymer blocks are allowed to form nucleation cores and grow within a solution without establishing chemical links

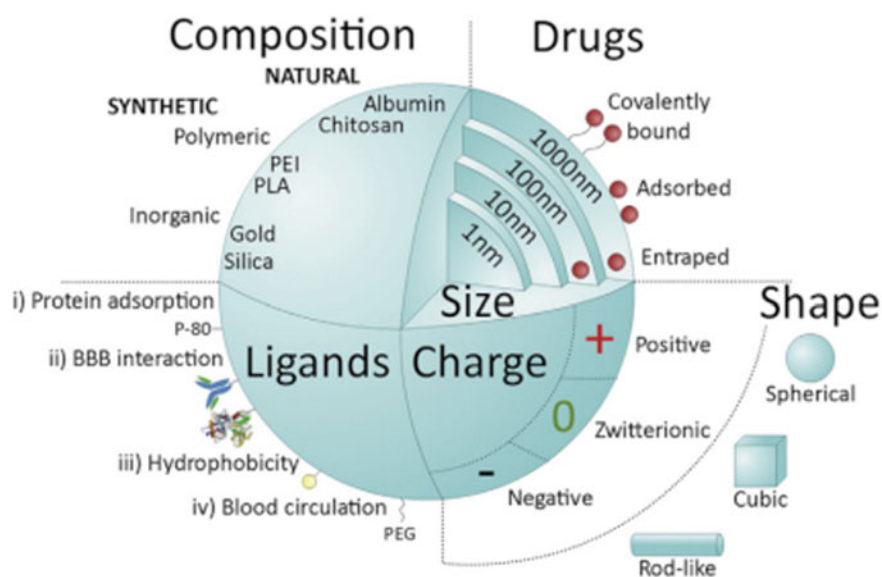


Fig. 1 Key nanoparticle characteristics influencing circulation behaviour and cellular targeting. Nanoparticles can be comprised of natural biopolymers, like albumin, chitosan or gelatin, or of synthetically produced building blocks, such as synthetic polymers, including polylactic acid (PLA), poly(lactic-co-glycolic) acid (PLGA) and poly(ethylenimine) (PEI), or inorganic substances, usually metals (Gold, Silica, Iron). Nanoparticle sizes can range from 1 to 1000 nm and the transported drugs can be covalently bound or adsorbed to the particle surface, as well as entrapped within the particle structure. The shapes of nanoparticles vary, from spherical to cubic, rod-like or tubular, any number of configurations are possible. Nanoparticles can also exhibit charges ranging from positive to negative, including a zwitterionic characteristic. Functionalisation of nanoparticles is achieved by utilising ligands with desired characteristics. The main interactions that can be induced through ligands are: (i) enabling adsorption of specific proteins through surfactants like polysorbate 80 (P-80); (ii) allowing direct interaction with the blood-brain barrier (BBB) through transferrin proteins, antibodies or similar; (iii) increase the hydrophobic character of the nanoparticles by attaching amphiphilic peptides; or (iv) alter the duration of blood circulation of the nanoparticles, e.g. by binding poly(ethylene) glycol (PEG) to the particle surface (Saraiva et al. 2016).

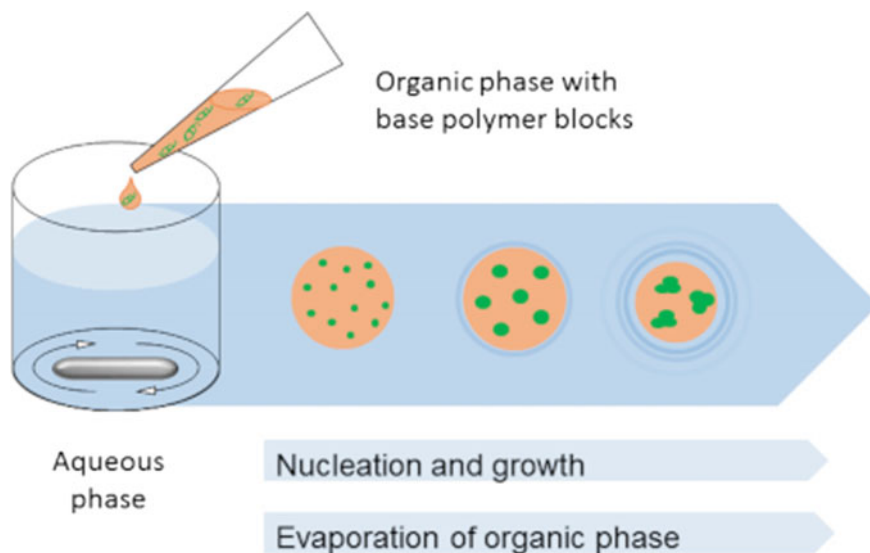


Fig. 2 Schematic illustration of nanoparticle preparation by dispersion method. To prepare nanoparticles, the base polymers are dissolved in an organic phase and then added to an aqueous phase with continuous agitation. Agitation methods can include stirring, ultrasound, mechanical mixing or others. The polymer blocks in the finely dispersed organic phase form nucleation cores. These cores grow by accretion of further polymer blocks to the cores, encouraged through continuous evaporation of the remaining organic phase

(Fig. 2). In order to influence the produced particle, different parameters, including the dispersion method itself, the complexity and characteristics of the used solvents, the polymer blocks as well as the ratio of potentially more than one base polymer can be adjusted to achieve a certain aim. For both methods, the drugs to be delivered can be trapped within the developing particle structure or linked covalently or chemically to the particle surface (Vauthier and Bouchemal 2009). The nanoparticle surface also provides an area for further development and specific modifications.

Historically, the first pharmaceutically developed nanoparticles were “bare” on the surface, but already Akasaka et al. (1988) published an albumin-based nanoparticle modified with cell-specific antibodies for targeted delivery. In 2001, the first albumin-based nanoparticles for tumour therapy advanced to clinical studies (Damascelli et al. 2001) and in 2005, the first albumin-nanoparticles were approved by the “Food and Drug Administration” (FDA) as medicinal product, followed by approval through the European Medicines Agency (EMA) in 2008. This drug is called Abraxane, a formulation of HSA nanoparticles containing the cytostatic agent paclitaxel, and is used in cancer treatment (Miele et al. 2009).

Surface modifications can encompass any number of substances, including peptides, proteins, antibodies, small molecules and even polymers different from the base polymers. They can be attached through covalent bonds or simple adsorption and will have different effects, allowing either passive or active targeting approaches,

but also increasing the circulation time of the nanoparticles in the blood stream (Gref et al. 1994). This is necessary to allow sufficient absorption of the nanoparticles in the targeted tissues (Zara et al. 2002) and is achieved by masking the nanoparticles from being recognised as foreign by the immune system (Storm et al. 1995). Potential ways to mask them include hydrophilic surfaces modifications (van Vlerken et al. 2007; Kaul and Amiji 2002) as well as addition of surfactants (Troster and Kreuter 1992) or serum components (Wagner et al. 2012), forming so called “stealth”-particles with increased retention time in circulation (Moghimi and Hunter 2001). Combining this effect with further targeting, either passive or active, provides a highly specific delivery system for drugs.

2.1 Passive Targeting

The passive targeting approach is most common in tumour targeting. Tumour growth is usually accompanied by increased angiogenesis and decreased lymphatic drainage (Maeda et al. 2000). The formed blood vessels tend to be imperfect in as far as the endothelial cells lining the vessels do not form a continuous, unbroken structure. The normal tight endothelial configuration prevents nanoparticles circulating in the blood stream from simply being taken up into the surrounding tissue. When the endothelial barrier is thus riddled with imperfections, the particles can simply penetrate through these into the surrounding tissue. The vessels found in tumours show holes between endothelial cells with a diameter of 200 to 600 nm, thus allowing nanoparticles to be taken up into the tumour tissue and accumulate there (Noguchi et al. 1998). This effect is known as the “Enhanced Permeability and Retention” (EPR) effect and forms the basis for passive targeting. This effect is especially useful when combined with the above-mentioned “stealth”-particles.

2.2 Active Targeting

Active targeting makes use of cellular structures of the target cells and uses established cellular uptake mechanisms for the nanoparticle transport into the cells. Ligands like polysaccharides, proteins or antibodies are bound to the nanoparticle surface and will interact with their specific receptors present on the cellular surface (Nobs et al. 2004). This enables the active uptake of the nanoparticles in the cells of interest. Based on the specific ligand selected for the particle modification, specific cells and tissues can be targeted as destination of the nanoparticles.

3 Nanoparticles for Specific Tumour Therapy

Therapeutic intervention for cancer treatment and tumour targeting is a major area of interest in nanoparticle development. Due to the nature of tumour growths as highly proliferating and adaptable tissues, successful drugs often have a general cytotoxic effect and a wide variety of negative side effects. Encapsulating these drugs in nanoparticles has the potential of masking undesirable side effects while still delivering them to the areas where their effects are of use, namely the tumours themselves. This masking has been shown for the chemotherapeutic doxorubicin, whose cytotoxic side effects on heart tissue and testes were significantly lowered when encapsulated in HSA nanoparticles (Pereverzeva et al. 2007). Examples for tumour specific targeting are the targeting of breast cancer or melanoma cells based on receptor expression and making photosensitisers a viable treatment option despite their challenging side effects.

3.1 *HER2-Overexpressing Breast Cancer*

The human epidermal growth factor receptor-2 (HER2) is one of three important receptors that can be found in breast cancer and is an important prognostic factor. A humanised monoclonal antibody targeting HER2 called trastuzumab was approved by the FDA in 2008 and improved prognosis of patients with this type of cancer significantly. Modifying nanoparticles with this agent allows for making use of the effect trastuzumab can achieve on its own while simultaneously delivering a second drug to combat the tumour. Incorporating doxorubicin as chemotherapeutic agent into HSA nanoparticles and modifying them on the surface with covalently bound trastuzumab has allowed for specific targeting of HER2-overexpressing breast cancer cells, improved internalisation (Fig. 3) and prolonged the effect of doxorubicin in these cells (Anhorn et al. 2008).

The nanoparticle base of HSA is rapidly degraded after cellular uptake allowing the encapsulated doxorubicin to be released and therefore significantly increasing its intracellular concentration and effectiveness. The uptake into the target cells is insured through the monoclonal antibody trastuzumab. When bound on the nanoparticle surface, the antibodies are still capable of binding to their target receptor HER2 on the tumour cells and are quickly internalised. Due to the covalent bond with the nanoparticles, these are internalised in the same process and thus become accessible for the intracellular degradation and doxorubicin release (Fig. 4).

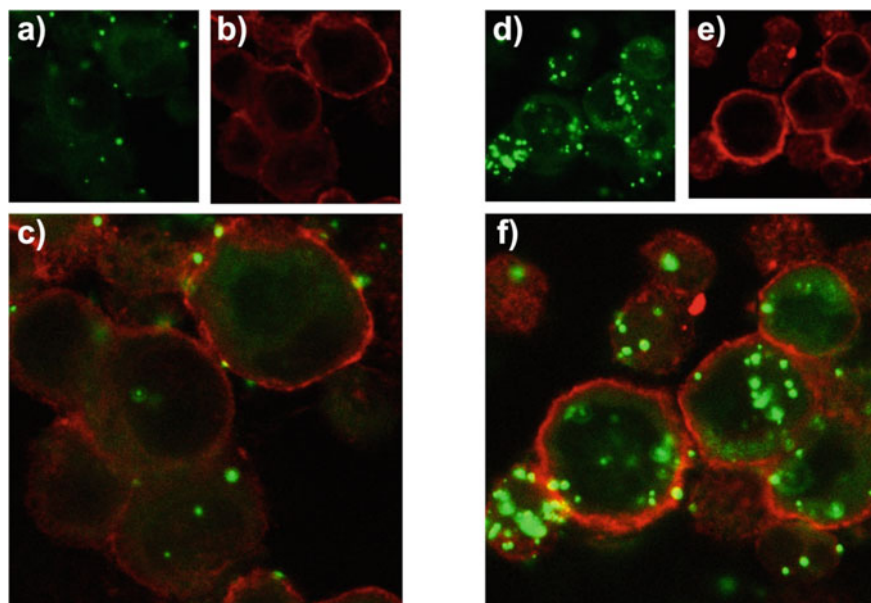


Fig. 3 Cellular uptake and intracellular distribution of HSA nanoparticles analysed by confocal laser scanning microscopy. HER2-overexpressing breast cancer cells SK-Br-3 were cultured on glass slides and treated with either (a–c) doxorubicin-loaded control nanoparticles without antibody modification or (d–f) doxorubicin-loaded nanoparticles modified with the specific HER2-recognizing antibody trastuzumab for 4 h at 37 °C. Nanoparticles show autofluorescence (green channel, (a) and (d)) and cell membranes were stained with Concanavalin A AlexaFluor 594 (red, (b) and (e)). Images (c) and (f) show an overlay of the dedicated channels. All images were taken of inner sections of the cells (Anhorn et al. 2008)

3.2 Melanomas

The same principles as described above can be used to target any number of different cancers based on the expression of specific receptors. A second example is the targeting of melanoma cells based on their overexpression of integrin $\alpha_V\beta_3$ (Wagner et al. 2010b). This integrin is involved in angiogenesis and is overexpressed in a number of cancers including melanomas. A monoclonal antibody called DI17E6 has been described, that can inhibit the growth of melanomas both in vitro and in vivo. When this antibody is covalently bound to doxorubicin-loaded HSA nanoparticles, its own effect can be enhanced through the cytotoxic effect of the doxorubicin when delivered directly to the melanoma cells (Fig. 5). This leads to an increased cytotoxicity in the target cells ($\alpha_V\beta_3$ -high expressing melanoma cells) when compared to either free doxorubicin or the DI17E6 antibody alone, while not showing cytotoxicity in cells low in expressing integrin $\alpha_V\beta_3$, as shown in Table 1:

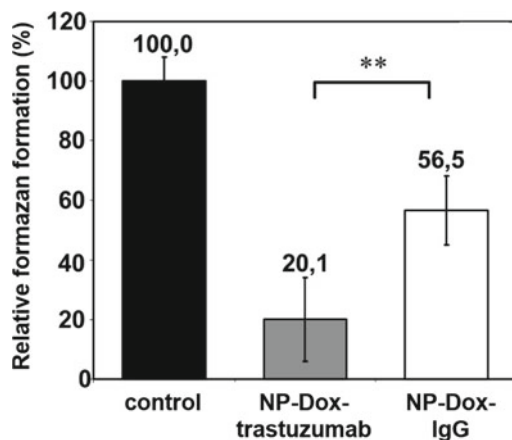


Fig. 4 Cell viability assay comparing doxorubicin-loaded trastuzumab-modified nanoparticles (NP-Dox-trastuzumab) with doxorubicin-loaded IgG-modified control nanoparticles (NP-Dox-IgG). HER2-overexpressing breast cancer cells SK-Br-3 were incubated with the same concentration of either specific NP-Dox-trastuzumab or control NP-Dox-IgG in PBS for 4 h at 37 °C. After washing the cells were incubated for a further 7 d at 37 °C. WST-1 reagent was used to determine the cell viability by measuring the formazan formation. The 100% standard was set with untreated cells (internal control of each experiment $n = 9$, one representative experiment out of three independent experiments is shown). **: The two samples are significantly different ($P < 0.01$, two-tailed Mann-Whitney U Test equivalent to Wilcoxon rank sum test) (Anhorn et al. 2008)

3.3 Nanoparticulate Photosensitisers for Tumour Therapy

Photosensitisers are compounds capable of producing highly reactive oxygen species and inducing cellular death when exposed to light of a certain wavelength. The second generation photosensitiser mTHPC (trade name Foscan) was approved for the treatment of advanced head and neck cancer by the EMA in 2001 and has shown a significant phototoxicity in many cancer cells *in vitro*. Yet, due to its poor water solubility and dark toxicity the applicability to a wider variety of cancer *in vivo* has proven difficult. Therefore nanoparticles were developed encapsulating mTHPC in order to decrease its dark toxicity and improve water solubility. PLGA nanoparticles loaded with mTHPC were shown to accumulate mTHPC in colon carcinoma cells in an amount comparable to the free substance (Löw et al. 2011). While the phototoxic effect after light exposure was similar in cells treated with either the encapsulated or free mTHPC, the dark toxicity was significantly reduced in cells exposed to nanoparticulate mTHPC (Fig. 6). Therefore encapsulating mTHPC ameliorates the negative side effects of the drug while maintaining its intended effect. Combining the encapsulation of mTHPC with targeting approaches as discussed above could open up a number of avenues where mTHPC can be used in cancer treatments without the significant side effects that prevent the wider use of the free substance.

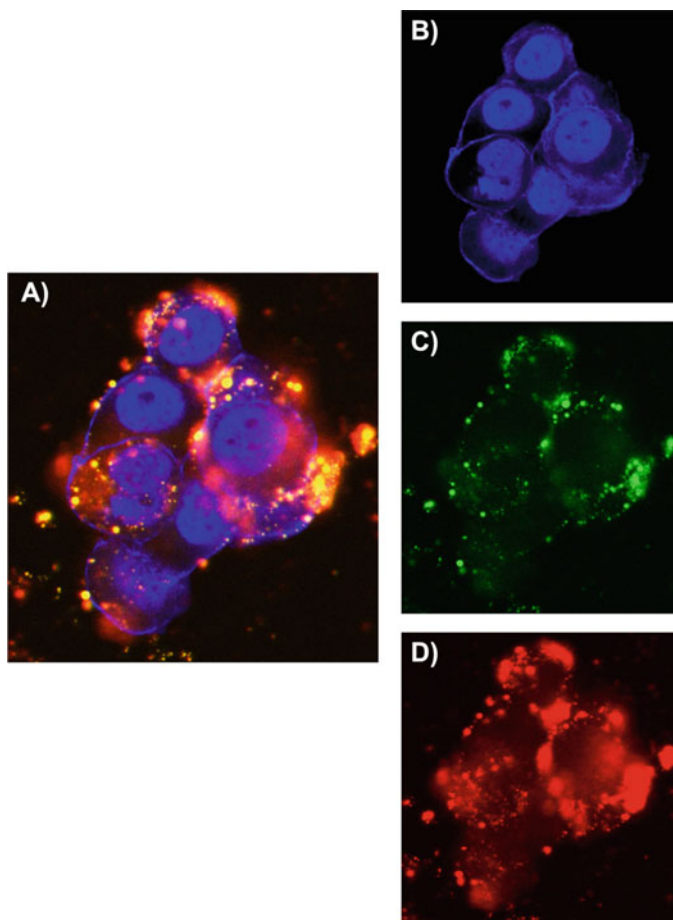


Fig. 5 Cellular uptake and intracellular distribution of doxorubicin-loaded DI17E6-modified HSA nanoparticles studied by confocal laser scanning microscopy. $\alpha_v\beta_3$ -high expressing melanoma cells M21 were cultured on glass slides and treated with 10 ng/ μ L doxorubicin-loaded DI17E6-modified HSA nanoparticles for 4 h at 37 °C. Nanoparticles were visualised using their green autofluorescence, doxorubicin showed red autofluorescence and cell membranes were stained with Concanavalin A AlexaFluor 350 (blue). Images were taken within the inner cell sections. **A** overlay of all channels, **B** cell membranes stained blue, **C** green autofluorescence of HSA nanoparticles, **D** red autofluorescence of doxorubicin (Wagner et al. 2010b)

4 Nanoparticles for Crossing Biological Barriers

Nanoparticulate development for improved drug delivery does not only have to take the ultimate target of the particle delivery into account, but also needs to consider the route the particles have to take to reach that target. The initial application of nanoparticles is theoretically possible through all routes also used for non-encapsulated drugs.

Table 1 IC-50 values of different nanoparticulate formulations in $\alpha_V\beta_3$ -high expressing melanoma cells (M21) or $\alpha_V\beta_3$ -low expressing melanoma cells (M21L) (Wagner et al. 2010b)

	M21 [ng/ml]	M21L [ng/ml]
<i>Nanoparticle preparation</i>		
NP-Dox unmodified	30.8 ± 3.5	75.4 ± 8.3
NP-Dox-Peg	>100	>100
NP-Dox-DI17E6	8.0 ± 0.2	>100
NP-Dox-IgG	>100	>100
<i>Controls</i>		
free doxorubicin	57.5 ± 3.7	70.7 ± 0.8
free DI17E6	>100	>100

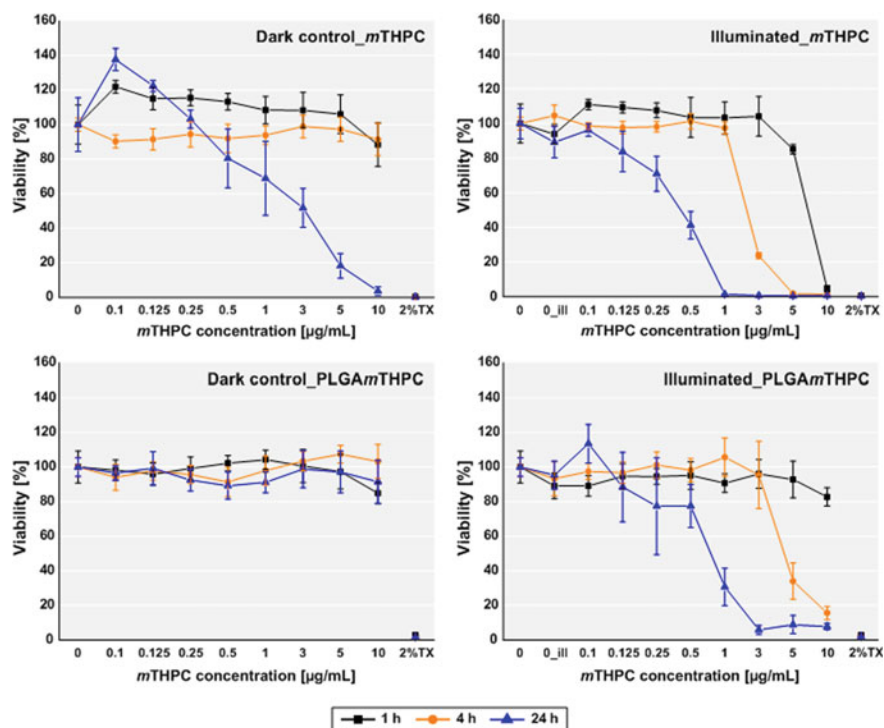


Fig. 6 Determination of cell viability. Colon carcinoma cells HT29 were exposed to varying concentrations of free mTHPC or mTHPC-loaded PLGA nanoparticles (corresponding to a photosensitizer concentration of 0.1–10 $\mu\text{g ml}^{-1}$) for 1, 4, and 24 h followed by illumination (652 nm; 5 J cm^{-2}). Control experiments were not illuminated (Dark control). The cell viability was measured by WST-1 assay. Each result represents the mean viability \pm standard deviation (SD) of three independent experiments and each of these was performed in biological triplicates. Cell viability was calculated as percentage of viable cells compared to untreated control cells. Untreated cells were used as negative control (0; 0_ill:illuminated control cells) and 2% Triton X-100 (2% TX) treated cells as positive control (L ow et al. 2011)

The main routes used are topical, oral or intravenous delivery. Especially in the case of topical and oral delivery, additional barriers have to be overcome for the nanoparticles to reach the blood stream. Next to topical administration, oral delivery has high patient compliance and is therefore the preferred mode of administration when it comes to a wide variety of drugs. The absorption occurs in the gastrointestinal tract, mainly the duodenum and small intestine, as long as the nanoparticles are capable of interacting with this gastrointestinal barrier (Ensign et al. 2012).

4.1 The Gastrointestinal Barrier

The gastrointestinal tract provides a significant barrier for the absorption of drugs and nanoparticles. Different areas have different pH values, which affect the chemical properties and thus absorption rates of substances based on their structure and properties. Additionally, the intestinal tract is covered by a mucus layer of varying thickness depending on the area of intestine. To either overcome or utilise this mucus barrier, administered nanoparticles need to be specifically modified to either attach to or cross the mucus layer (Ensign et al. 2012). Successful mucus penetration or permeation has been shown with PLGA nanoparticles loaded with mTHPC as a model drug and duodenal cancer as target (unpublished data). The nanoparticles were modified with specific surfactants to change their surface properties in such a way, that they were preferentially bound to the intestinal mucus. Their size in combination with physical characteristics then allowed them to either penetrate the mucus layer and reach the underlying duodenal cells, or caused them to be stuck in the mucus layer and degraded there, releasing the contained drugs at this specific side. The produced nanoparticles showed increased accumulation in cellular models of duodenal cells with a mucus layer in contrast to intestinal cells without this layer.

Excursion: The Mucus Chip—An Initial Advanced Testing Module

Considering both the complexity of the gastrointestinal system in general and the challenging nature of the intestinal mucus layer specifically, advanced testing systems are necessary to investigate the properties and behaviour of orally administered nanoparticles (Elberskirch et al. 2019). As the first hurdle to either encountering intestinal cells or absorption into the general circulation is the mucus layer itself, a specific test system for mucus penetration and retention was devised. The mucus chip contains a defined layer of intestinal mucus suspended between permeable membranes (Fig. 7). To simulate the intestinal situation, substances are applied from the apical side in a static system, while a peristaltic flow of buffer solution is maintained on the basolateral side to simulate natural peristalsis. Based on the amount of nanoparticles found in the basolateral compartment at different time points, the mucus permeation can be measured and further optimisation steps considered.

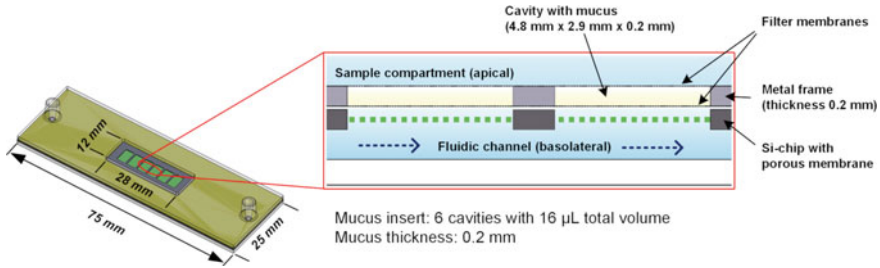


Fig. 7 Microfluidic mucus-chip module. **A** Assembled cartridge with mucus insert, **B** cross-section view of mucus insert, micro-membrane chip and compartments (Elberskirch et al. 2019)

4.2 The Blood-Brain Barrier

Another region of the human body, that poses a significant challenge for drug delivery, is the brain. Any drugs, substances or nanoparticles, that want to reach brain tissue, have to pass the blood-brain barrier (Pardridge 2005). This barrier is comprised of the endothelial cells forming the brain capillaries, the surrounding basement membrane with embedded pericytes and the end feet of associated astrocytes (Keaney and Campbell 2015; Fig. 8). What makes the capillaries within the brain unique in contrast to the

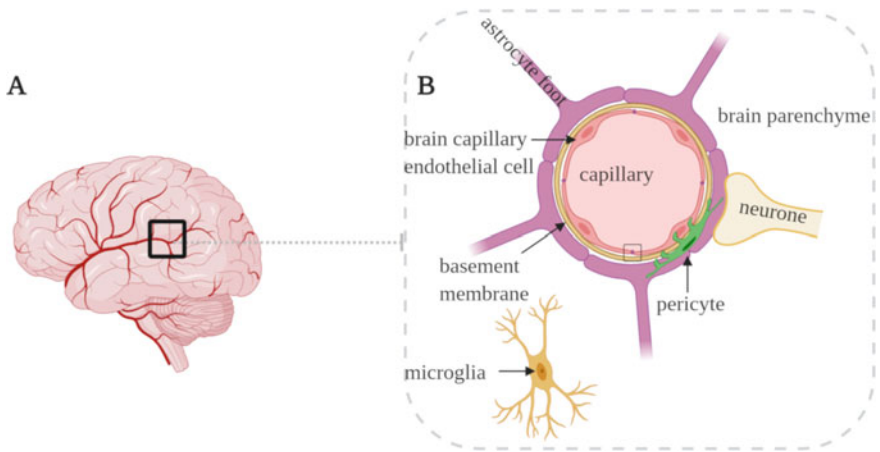


Fig. 8 The human blood-brain barrier. **A** An overview of the human brain with vasculature and **B** a graphical representation of the organisation of cells surrounding brain capillaries, known as neurovascular unit. The capillary wall is comprised of brain capillary endothelial cells (red) connected by tight junctions (little square). The endothelial cells are surrounded by a basement membrane (yellow), in which pericytes (green) are embedded. On the brain side of the basement membrane, the capillaries are encompassed by the endfeet of astrocytes (purple), which can be connected to neuronal axons (beige). The only cell type not directly associated with the neurovascular unit are microglia (orange) present in the brain parenchyme. Created with [BioRender.com](https://www.biorender.com)

rest of the body is the fact that the endothelial cells are connected by tight junctions all around, leaving no gaps at all and restricting even small molecular diffusion in the intracellular space (Daneman and Prat 2015). The main options to overcome this barrier are active or passive transport processes. Only a small number of either water- or lipid-soluble molecules can cross the blood-brain barrier independently. The transport processes used for uptake are adsorptive transcytosis, receptor-mediated transcytosis or the use of transport proteins (Saunders et al. 2013; Tuma and Hubbard 2003). Nanoparticles, due to their size, are restricted to making use of one of these processes. The exact route nanoparticles take in order to reach neuronal cells has been extensively discussed and investigated (Wohlfart et al. 2012; Wagner et al. 2012). It has been shown that nanoparticles modified to present apolipoprotein E (ApoE) on their surface are internalised into brain capillary endothelial cells through receptor-mediated endocytosis by the LRP1 receptor, as shown through mechanism studies (Wagner et al. 2012), followed by transcytosis to neighbouring cells, specifically astrocytes (Begley 2012), and can be found in different regions of the brain as soon as 30 min after intravenous injection (Fig. 9) in a mouse model (Zensi et al. 2009). ApoE or other ligands like ApoA1 (Zensi et al. 2010), transferrin (Ulbrich et al. 2009) or insulin (Ulbrich et al. 2011) have dedicated receptors expressed in the brain capillaries. These receptors can be targeted for nanoparticle transport using specific antibodies for these receptors similar to tumour targeting (Ulbrich et al. 2009) or by presenting the receptor-specific proteins on the nanoparticle surface. To achieve this, the proteins can be covalently bound or non-covalently recruited to the nanoparticles. Specific modifications are necessary to achieve this and examples are shown in the following paragraphs.

4.2.1 Covalently Bound ApoE

ApoE can be bound to the surface of different base nanoparticles and used for a variety of treatments.

In one study, HSA nanoparticles with covalently bound ApoE have been developed and used to transport oximes across an *in vitro* blood-brain barrier model (Wagner et al. 2010a). Oximes are used in the treatment of organophosphate poisoning by reactivating the blocked acetylcholine esterase in cells, but cannot cross the blood-brain barrier in therapeutically relevant doses. Thus, they are unable to ameliorate the neurological effects caused by an imbalance in acetylcholine as neurotransmitter. Therefore, they were adsorbed to HSA nanoparticles. These particles had ApoE bound to their surface and were then applied to an *in vitro* blood-brain barrier model. It was shown that only particles with the ApoE modification were taken up into the capillary endothelial cells in a significant amount. These nanoparticles were also capable of transporting oximes across the *in vitro* barrier model while maintaining their functionality in combating organophosphate poisoning (Dadparvar et al. 2011).

In a second study, the base particle consisted of PLA (Stab et al. 2016). Here, the ApoE-modified nanoparticles showed as well higher accumulation in brain capillary endothelial cells than unmodified nanoparticles (Fig. 10).

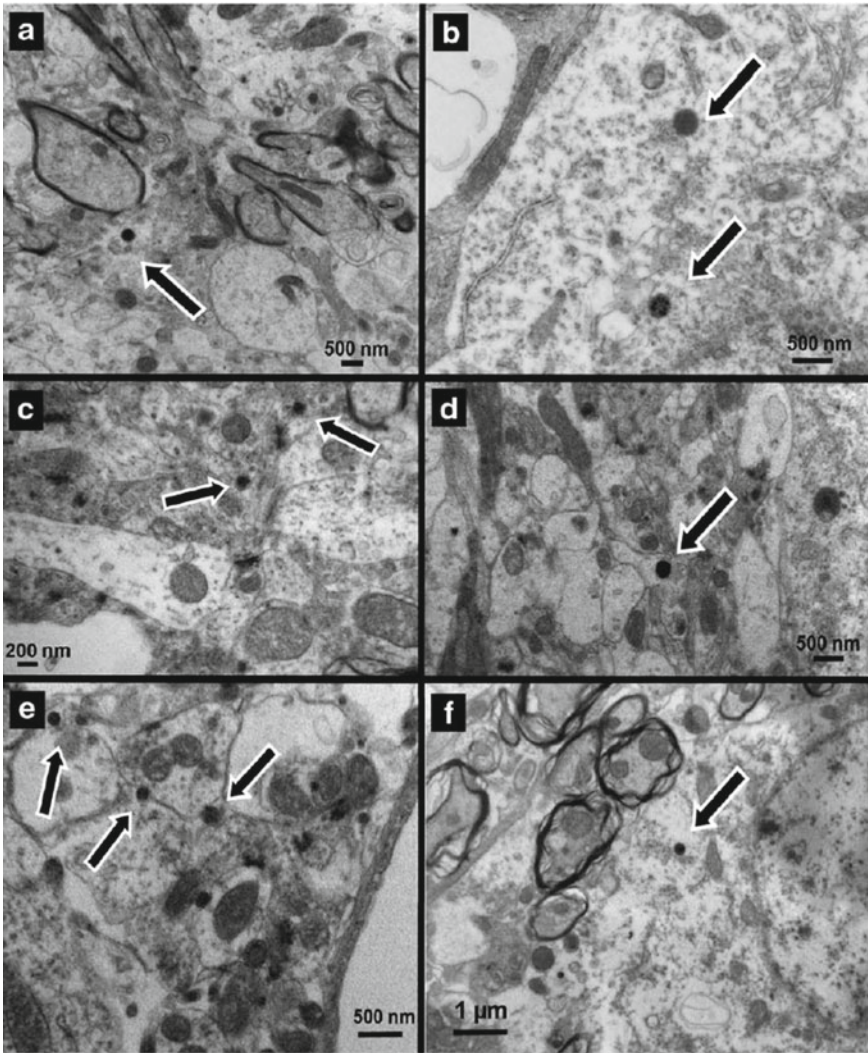


Fig. 9 Apo-E modified HSA nanoparticles in different brain regions in a SV 129 mouse model. SV 129 mice were injected in the tail vein with 200 μg ApoE-modified HSA nanoparticles per g body weight. 30 min after application transcardiac perfusion with a fixative was initiated, brains removed and sliced. Samples corresponding separate sections of the brain were embedded in resin and stained with uranyl acetate for electro microscopy. Nanoparticles are indicated by arrows and were found in **a** the olfactory bulb, **b** the cortex, **c** the striatum, **d** the hippocampus, **e** the cerebellum and **f** the brain stem (Zensi et al. 2009)

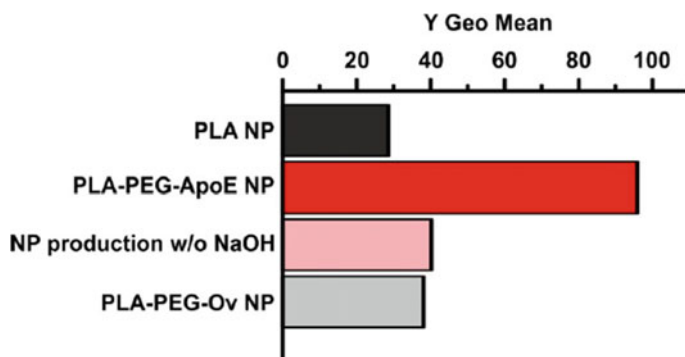


Fig. 10 Influence of ApoE3-modification on binding and uptake characteristics of nanoparticles studied via flow cytometry experiments. Primary porcine brain capillary endothelial cells pBCEC were incubated for 4 h at 37 °C with unmodified control nanoparticles (PLA NP); ApoE3-modified nanoparticles (PLA-PEG-ApoE NP); ApoE3-modified nanoparticles prepared without NaOH in the buffer (NP production w/o NaOH) or nanoparticles modified with the control protein ovalbumin (PLA-PEG-Ov NP). Binding intensity was assessed by measuring the Y Geo Mean (Stab et al. 2016)

4.2.2 Non-covalent ApoE Recruitment

The protein ApoE cannot only be bound to nanoparticles before they are administered, it is also present in human serum and circulates freely in the blood stream. Thus, if a reliable way to attract it to the surface of circulating nanoparticles is identified, the natural reservoir of this apolipoprotein can be used for targeting the nanoparticles. Meister et al. (2013) have shown that PLA nanoparticles produced in the presence of polyvinyl alcohol (PVA) are capable of attracting and maintaining a so-called protein corona of plasma proteins. This corona contained both ApoE and ApoA1 among other proteins. Flurbiprofen-loaded PLA-PVA nanoparticles were successfully taken up into brain capillary endothelial cells, capable of crossing an in vitro blood-brain barrier model and could reduce the γ -secretase activity though in vitro release of the contained flurbiprofen (Meister et al. 2013). They were also capable of decreasing the amount of $A\beta_{42}$ produced by an in vitro cellular model of Alzheimer's disease (Stab et al. 2016, Fig. 11).

Excursion: Blood-Brain Barrier Model Systems

The decision, whether a covalent or non-covalent binding of targeting modifications is necessary or advisable needs to be made on a case by case basis. Every particle system is unique in its properties and behaviour dependent on particle material, contained substance and targeted application. To analyse and evaluate this, reliable, advanced model systems for the targeted areas are vital. This is especially true in the case of the blood-brain barrier. Reliable, reproducible model systems closely mimicking the in vivo situation and reactions are essential for evaluating nanoparticles developed for BBB crossing (Helms et al. 2016). Initial model systems were based on immortalised cell lines and maintained the receptor and transporter status of the in vivo BBB, but

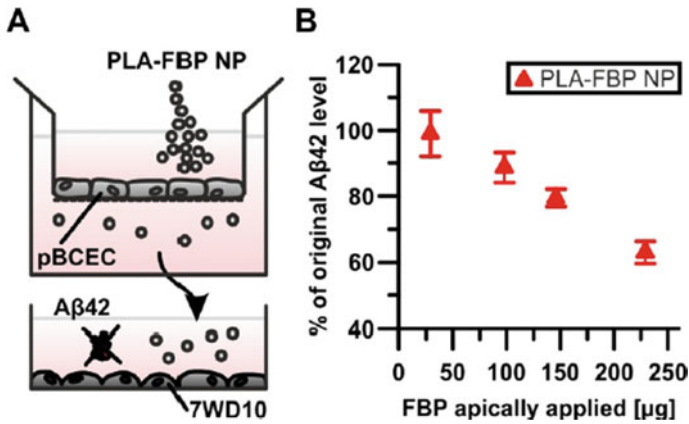


Fig. 11 Aβ42-lowering capacity of nanoparticles after in vitro BBB Crossing. **A** Schematic drawing of experimental design: Primary porcine brain capillary endothelial cells pBCEC were cultivated on transwell inserts simulating the BBB. When Transendothelial Electrical Resistance (TER) was adequate, drug-loaded nanoparticles (PLA-FBP NP) were added for 4 h. Then, the apical compartment and pBCEC were discarded and basolateral medium was transferred to culture plates seeded with Aβ42 producing Alzheimer's disease model cells 7WD10 for 72 h. **B** Analysis of 7WD10 supernatants by a human Aβ42 recognizing ELISA assay. Data from at least 3 independent experiments (Stab et al. 2016)

the characteristic barrier tightness could not be replicated. This barrier tightness is characterised by the transendothelial electrical resistance (TER) value, which can be determined and monitored in model systems. Immortalised cell lines achieved at most values of 40 Ωcm². As achieving a certain tightness or TER value is one basis for the selectivity, these lines were useful for binding and uptake but not transport studies. A step towards replicating the barrier transport behaviour was taken with the development of in vitro BBB models based on isolated primary cells (Nakhband and Omid 2011; Stab et al. 2016). These capillary endothelial cells were isolated from animal sources like bovine, porcine or rodent material. But these models, due to their non-human origin, do not express the identical receptors and transporters as found in humans. A model system presenting all relevant characteristics, both in protein expression and transport behaviour of an intact, sufficiently selective barrier has been published in recent years (Lippmann et al. 2012). The specifically necessary brain capillary endothelial cells are differentiated from human induced pluripotent stem cells (Fig. 12). This human origin ensures a high transferability of the results obtained in this model system based on transporter status and the barrier tightness obtained is comparable or superior to that achieved in primary cell models (Lippmann et al. 2014). The source material of human induced pluripotent stem cells also presents the opportunity to develop specific models for neurological diseases and investigate whether the uptake and transport processes are altered in a diseased state and if so, how this impacts therapeutic options.

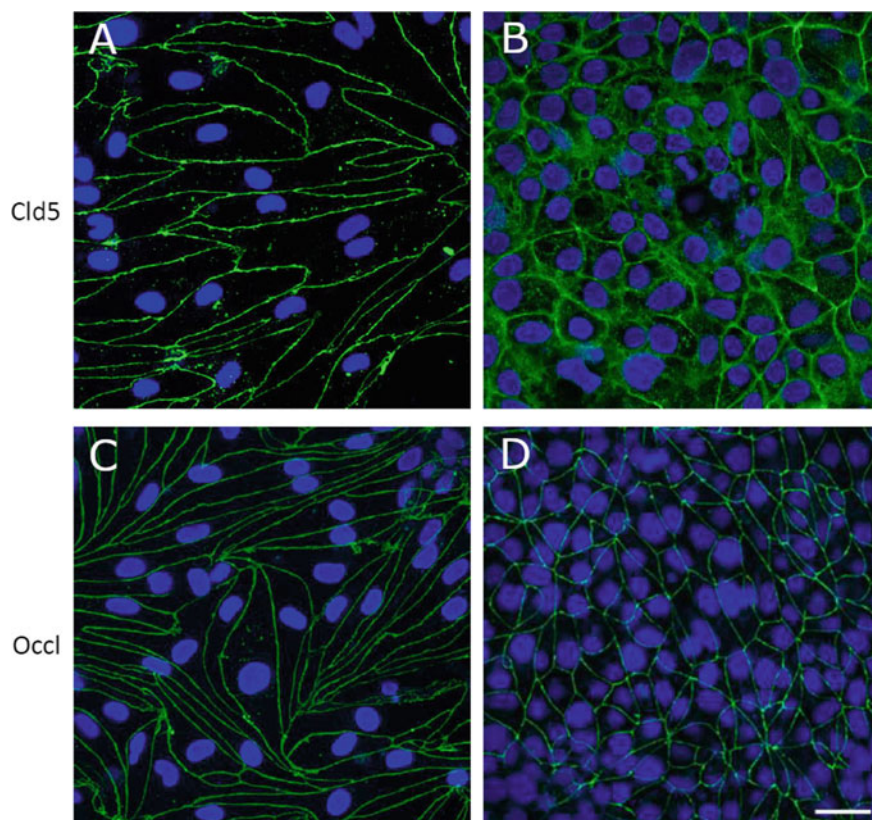


Fig. 12 Comparison of protein expression of primary porcine- and human induced pluripotent stem cell-derived blood-brain barrier models by confocal laser scanning microscopy. Primary porcine brain capillary endothelial cells (**A** and **C**) and stem cell-differentiated brain capillary endothelial cells (**B** and **D**) were cultivated on polycarbonate membrane inserts with 3.0 μm pores for 3 days at 37 $^{\circ}\text{C}$ before fixation with an acetone:methanol (7:3) mixture. Separate sections of the inserts were stained (**A**, **B**) for Claudin-5 (Cld5) with a rabbit anti-Claudin-5 antibody and (**C**, **D**) for Occludin (Occl) with a rabbit anti-Occludin antibody before counterstaining with a goat anti-rabbit AlexaFluor 488 antibody (green). Nuclei were DAPI stained (blue). Membranes were immobilised between two cover slides for microscopic analysis. Images **A** and **B** show Claudin-5 (green) and DAPI (blue) staining, images **C** and **D** show Occludin (green) and DAPI (blue) staining. Size bar 25 μm

5 Final Remarks

Overall, it is clear that nanoparticles are a highly adaptable option for drug formulations capable of masking undesirable side effects of drugs while allowing them to maintain their therapeutic effect upon release in the target cells or tissue. Especially when it comes to at present unsolved issues, like the dark toxicity and hydrophobic characteristics of mTHPC or the selectivity of the blood-brain barrier preventing

most drugs from crossing into the brain, nanoparticles open up new avenues for the application of existing substances or advancing the development of new therapeutic treatments. Based on the possibilities to modify just about every characteristic of a nanoparticle, they can be tailored to achieve specific effects and present targeted properties. But nanoparticles are not limited to applications in drug delivery. Depending on what is incorporated, nanoparticles can be used in theragnostics (Fang and Zhang 2010), diagnostic applications (Mirabello et al. 2015), for gene therapy (Cullis and Hope 2017) or to improve stem cell differentiation (Dayem et al. 2016).

Acknowledgements The authors would like to thank the European Commission, BMBF and BMVg for funding several parts of this work. The authors thank the Faerber GmbH (Zweibruecken, Germany) for the supply of the porcine intestine and skull/brain.

Conflict of interest The authors declare no conflict of interest.

References

- Akasaka Y, Ueda H, Takayama K et al (1988) Preparation and evaluation of bovine serum albumin nanospheres coated with monoclonal antibodies. *Drug Des Deliv* 3(1):85–97
- Anhorn MG, Wagner S, Kreuter J et al (2008) Specific targeting of HER2 overexpressing breast cancer cells with doxorubicin loaded trastuzumab modified human serum albumin nanoparticles. *Bioconjugate Chem* 19(12):2321–2331
- Begley D (2012) Brain superhighways. *Sci Transl Med* 4(147):147fs29
- Birrenbach G, Speiser PP (1976) Polymerized micelles and their use as adjuvants in immunology. *J Pharm Sci* 65(12):1763–1766
- Cullis PR, Hope MJ (2017) Lipid nanoparticle systems for enabling gene therapies. *Mol Ther* 25(7):1467–1475
- Dadparvar M, Wagner S, Wien SL et al (2011) HI 6 human serum albumin nanoparticles – development and transport over an in vitro blood-brain barrier model. *Toxicol Lett* 206(1):60–66
- Damascelli B, Cantu G, Mattavelli F et al (2001) Intraarterial chemotherapy with polyoxyethylated castor oil free paclitaxel, incorporated in albumin nanoparticles (ABI-007): phase II study of patients with squamous cell carcinoma of the head and neck and anal canal: preliminary evidence of clinical activity. *Cancer* 92(10):2592–2602
- Daneman R, Prat A (2015) The blood-brain barrier. *Cold Spring Harb Perspect Biol* 7(1):
- Dayem AA, Choi HY, Yang GM et al (2016) The potential of nanoparticles in stem cell differentiation and further therapeutic applications. *Biotechnol J* 11(12):1550–1560
- Elberskirch L, Knoll T, Moosmann A et al (2019) A novel microfluidic mucus-chip for studying the permeation of compounds over the mucus barrier. *J Drug Deliv Sci Tech* 54:
- Ensign LM, Cone R, Hanes J (2012) Oral drug delivery with polymeric nanoparticles: the gastrointestinal mucus barrier. *Adv Drug Deliv Rev* 64(5):557–570
- Fang C, Zhang M (2010) Nanoparticle-based theragnostics: integrating diagnostic and therapeutic potentials in nanomedicine. *J Control Release* 146(1):2–5
- Gref R, Minamitake Y, Peracchia MT et al (1994) Biodegradable long-circulating polymeric nanospheres. *Science* 263(5153):1600–1603
- Helms HC, Abbott NJ, Burk M et al (2016) In vitro models of the blood-brain barrier: an overview of commonly used brain endothelial cell culture models and guidelines for their use. *J Cereb Blood Flow Metab* 36(5):862–890
- Kaul G, Amiji M (2002) Long-circulating poly(ethylene glycol)-modified gelatin nanoparticles for intracellular delivery. *Pharm Res* 19(7):1061–1067

- Keaney J, Campbell M (2015) The dynamic blood-brain barrier. *FEBS J* 282:4067–4079
- Kreuter J (1983) Evaluation of nanoparticles as drug-delivery systems I: preparation methods. *Pharm Acta Helv* 58:196–209
- Kreuter J, Speiser PP (1976) New adjuvants on a polymethylmethacrylate base. *Infect Immun* 13(1):204–210
- Kumari A, Yadav SK, Yadav SC (2010) Biodegradable polymeric nanoparticles based drug delivery systems. *Colloids Surf B Biointer*. 75(1):1–18
- Lippmann ES, Azarin SM, Kay JE et al (2012) Human blood-brain barrier endothelial cells derived from pluripotent stem cells. *Nat Biotechnol* 30(8):783–791
- Lippmann ES, Al-Ahmad A, Azarin SM et al (2014) A retinoic acid-enhanced, multicellular human blood-brain barrier model derived from stem cell sources. *Sci Rep* 4:4160
- Löw K, Knobloch T, Wagner S et al (2011) Comparison of intracellular accumulation and cytotoxicity of free mTHPC and mTHPC-loaded PLGA nanoparticles in human colon carcinoma cells. *Nanotech* 22:
- Maeda H, Wu J, Sawa T et al (2000) Tumor vascular permeability and the EPR effect in macromolecular therapeutics: a review. *J Control Release* 65(1–2):271–284
- Meister S, Zlatev I, Stab J et al (2013) Nanoparticulate flurbiprofen reduces amyloid- β 42 generation in an in vitro blood-brain barrier model. *Alzheimers Res Ther* 5(6):91
- Miele E, Spinelli GP, Miele E et al (2009) Albumin-bound formulation of paclitaxel (Abraxane ABI-007) in the treatment of breast cancer. *Int J Nanomed* 4:99–105
- Mirabella V, Calatayud DG, Arrowsmith RL et al (2015) Metallic nanoparticles as synthetic building blocks for cancer diagnostics: from materials design to molecular imaging applications. *J Mater Chem B* 3(28):5657–5672
- Mody VV, Siwale R, Singh A et al (2010) Introduction to metallic nanoparticles. *J Pharm Bioallied Sci* 2(4):282–289
- Moghimi SM, Hunter AC (2001) Capture of stealth nanoparticles by the body's defences. *Crit Rev Ther Drug Carrier Syst* 18(6):527–550
- Nakhlband A, Omidi Y (2011) Barrier functionality of porcine and bovine brain capillary endothelial cells. *Bioimpacts* 1(3):153–159
- Nobs L, Buchegger F, Gumy R et al (2004) Current methods for attaching targeting ligands to liposomes and nanoparticles. *J Pharm Sci* 93(8):1980–1992
- Noguchi Y, Wu J, Duncan R et al (1998) Early phase tumor accumulation of macromolecules: a great difference in clearance rate between tumor and normal tissues. *Jpn J Cancer Res* 89(3):307–314
- Pardridge WM (2005) The blood-brain barrier: bottleneck in brain drug development. *NeuroRX* 2:3–14
- Pereverzeva E, Treschalin I, Bodyagin D et al (2007) Influence of the formulation on the tolerance profile of nanoparticle-bound doxorubicin in healthy rats: focus in cardio- and testicular toxicity. *Int J Pharm* 337(1–2):346–356
- Saraiva C, Praca C, Ferreira R et al (2016) Nanoparticle-mediated brain drug delivery: overcoming blood-brain barrier to treat neurodegenerative diseases. *J Control Release* 235:34–47
- Saunders NR, Daneman R, Dziegielewska KM et al (2013) Transporters of the blood-brain and blood-CSF interfaces in development and in the adult. *Mol Aspects Med* 34(2–3):742–752
- Scheffel U, Rhodes BA, Natarajan TK et al (1972) Albumin microspheres for study of the reticuloendothelial system. *J Nucl Med* 13(7):498–503
- Stab J, Zlatev I, Raudszus B et al (2016) Flurbiprofen-loaded nanoparticles can cross a primary porcine in vitro blood-brain barrier model to reduce Amyloid- β 42 burden. *J Nanomed Biother Discov* 6:140
- Storm G, Belliot SO, Daemen T et al (1995) Surface modification of nanoparticles to oppose uptake by the mononuclear phagocyte system. *Adv Drug Deliv Rev* 17:31–48
- Troster SD, Kreuter J (1992) Influence on the surface properties of low contact angle surfactants on the body distribution of 14C-poly(methyl methacrylate) nanoparticles. *J Microencapsul* 9(1):19–28
- Tuma PL, Hubbard AL (2003) Transcytosis: crossing cellular barriers. *Physiol Rev* 83(3):871–932

- Ulbrich K, Hekmatara T, Herbet E et al (2009) Transferrin- and transferrin-receptor-antibody-modified nanoparticles enable drug delivery across the blood-brain barrier. *Eur J Pharm Biopharm* 71(2):251–256
- Ulbrich K, Knoblich R, Kreuter J (2011) Targeting the insulin receptor: nanoparticles for drug delivery across the blood-brain barrier (BBB). *J Drug Target* 19(2):125–132
- van Vlerken LE, VyasTK AM (2007) Poly(ethylene glycol)-modified nanocarriers for tumor-targeted and intracellular delivery. *Pharm Res* 24(8):1405–1414
- Vauthier C, Bouchemal K (2009) Methods for the preparation and manufacture of polymeric nanoparticles. *Pharm Res* 26(5):1025–1058
- Wagner S, Kuffleitner J, Wien SL et al (2010a) Nanoparticulate transport of oximes over an in vitro blood-brain barrier model. *PLoS One* 5(12):e14213
- Wagner S, Rothweiler F, Anhorn MG et al (2010b) Enhanced drug targeting by attachment of an anti α v-integrin antibody on doxorubicin loaded human serum albumin nanoparticles. *Biomater* 31:2388–2398
- Wagner S, Zensi A, Wien SL et al (2012) Uptake mechanism of ApoE-modified nanoparticles on brain capillary endothelial cells as a blood-brain barrier model. *PLoS ONE* 7(3):
- Wohlfart S, Gelperina S, Kreuter J (2012) Transport of drugs across the blood-brain barrier by nanoparticles. *J Control Release* 161(2):264–273
- Zara GP, Cavalli R, Bargoni A et al (2002) Intravenous administration to rabbits of non-stealth and stealth doxorubicin-loaded solid lipid nanoparticles at increasing concentrations of stealth agent: pharmacokinetics and distribution of doxorubicin in brain and other tissues. *J Drug Target* 10(4):327–335
- Zensi A, Begley D, Pontikis C et al (2009) Albumin nanoparticles targeted with ApoE to enter the CNS by transcytosis and are delivered to neurones. *J Control Release* 137(1):78–86
- Zensi A, Begley D, Pontikis C et al (2010) Human serum albumin nanoparticles modified with apolipoprotein A-I cross the blood-brain barrier and enter the rodent brain. *J Drug Target* 18(10):842–848

Smart Polymeric Materials for Drug Delivery



Gheorghe Fundueanu, Sanda Bucatariu, and Marieta Constantin

Abstract Smart polymers or polymers sensitive to external stimuli are remarkable materials because they behave similarly to living organisms. Basically, these polymers as linear molecules or cross-linked networks modify their physico-chemical properties such as hydrophilic/ hydrophobic balance, solubility, degree of swelling in response to the action of external stimuli present in the human body. Among stimuli-sensitive polymers, those sensitive to pH and temperature are the most useful in biomedical area because in the human body, these physico-chemical parameters change in different body compartments. All of these changes were exploited to control the moment and release rates of drugs. Moreover, these systems have the ability of reacting to the presence of biomolecules released by the body under pathological conditions.

Keywords Poly(*N*-isopropylacrylamide) · Smart polymers · Drug delivery · Hydrogels

Abbreviations

AA	Acrylic acid
AAM	Acrylamide
BMA	Butyl methacrylate
CAB	Cellulose acetate butyrate
DF	Diclofenac

G. Fundueanu (✉) · S. Bucatariu · M. Constantin
Department of Natural Polymers, Bioactive and Biocompatible Materials, “Petru Poni” Institute of Macromolecular Chemistry, 700487 Iassy, Romania
e-mail: ghefun@icmpp.ro

S. Bucatariu
e-mail: sanda.bucatarui@icmpp.ro

M. Constantin
e-mail: marieta@icmpp.ro

MA	Methacrylic acid
MM	Methyl methacrylate
SEM	Scanning electron microscopy
LCST	Lower critical solution temperature
NIPAAm	<i>N</i> -Isopropylacrylamide
NIPMAAm	<i>N</i> -Isopropylmethacrylamide
NVP	<i>N</i> -Vinylpyrrolidone
PBS	Phosphate buffer solution
PVA	Poly(vinyl alcohol)
T _g	Glass transition temperature

1 Introduction

Controlled drug delivery systems have represented a huge improvement in the way of drug administration compared to conventional formulations (Noorian et al. 2020; Krause et al. 2019; Kim et al. 2019). These systems have the advantage that they can maintain the concentration of the drug in the blood and tissues in the therapeutic field, reduce the frequency of drug administration and increase patient comfort and compliance. However, there are several medical disorders (diabet, heart disorders, etc.) when the continuous release of drugs in shorter or longer periods is not appropriate. For these cases, the pharmaceutical formulations must release the drug when one of the parameters that regulates the body's functions changes. These systems are generally based on intelligent or stimuli sensitive polymers (Liu et al. 2019; Jamwal et al. 2019; Alsuraifi et al. 2018).

Smart polymers are a category of macromolecules that in aqueous solution suffer a phase transition when small changes of the external parameters occur. These parameters can be temperature (Lee and Bae 2020), pH (Sapre et al. 2020), ionic strength (Zhang et al. 2005), electric field (Shang et al. 2007), magnetic field (Manouras and Vamvakaki 2017), light (Sedlacek et al. 2019), redox potential (Singh et al. 2020), the presence of biomolecules (Fundueanu et al. 2013), etc. Among polymers sensitive to external stimuli, those sensitive to temperature and pH are the most used for biomedical applications because both parameters vary most frequently in the human body. Changes in temperature and pH cause modifications in the physico-chemical properties of polymeric pharmaceutical formulation that result in modulation of the release profiles of loaded drugs (Wang et al. 2020; Zheng et al. 2019).

2 Thermosensitive Drug Delivery Systems

Drug delivery systems sensitive to temperature have the ability to control the moment of drug delivery only when the human body temperature is above or below the physiological temperature.

Poly (N-isopropylacrylamide) (poly(NIPAAm)) is the most used thermoresponsive polymer in biomedical applications because it shows a sharp phase transition around 32 °C, which is close to the human body temperature (Fig. 1) (Heskins and Guillet 1968).

The temperature at which this transition takes place is called the lower critical solution temperature (LCST). Below the LCST the polymer chains are surrounded by water molecules bound by hydrogen bonds, exposing an extended coil conformation and making the polymer soluble in water. However, when the temperature exceeds the LCST, the polymer loses the hydration water, becomes hydrophobic and precipitates (Fig. 1). Consequently, the cross-linked hydrogels obtained from these polymers swell under the LCST and shrink above the LCST (Fig. 2) (Fundueanu et al. 2009a).

This swelling/shrinking process has been exploited for the development of thermosensitive drug delivery systems based on poly(NIPAAm-co-hydroxyethylacrylamide) microspheres (Fundueanu et al. 2013). The drug is usually released when the hydrogel is in the swollen state (below LCST). Above the LCST, the matrix shrinks and the release of drug is stopped. The pulsatile effect depends to the size of hydrogel microspheres. It was established that microspheres with the diameter ranging between 5 and 60 μm release the drug with almost the same rate below (in the swollen state) and above the LCST (in the collapsed state). On the contrary, microspheres with the diameter ranging between 125 and 220 μm release a significantly higher amount of indomethacin below than above the LCST. This difference was enough pronounced to ensure a pulsatile release mechanism when the temperature changes cyclically below and above the LCST.

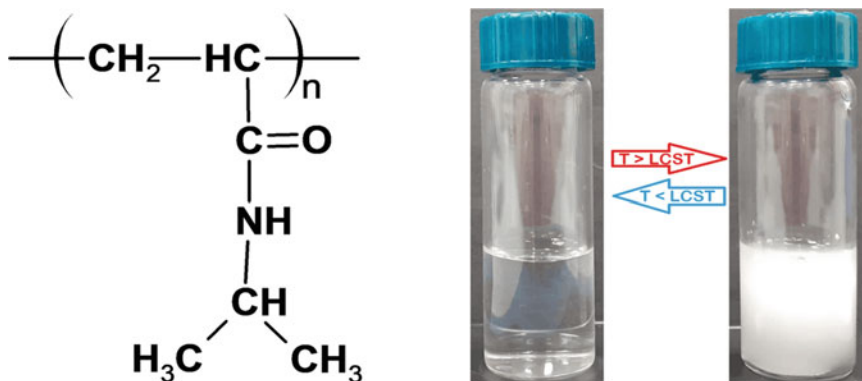


Fig. 1 Poly(N-isopropylacrylamide) aqueous solution below and above the LCST

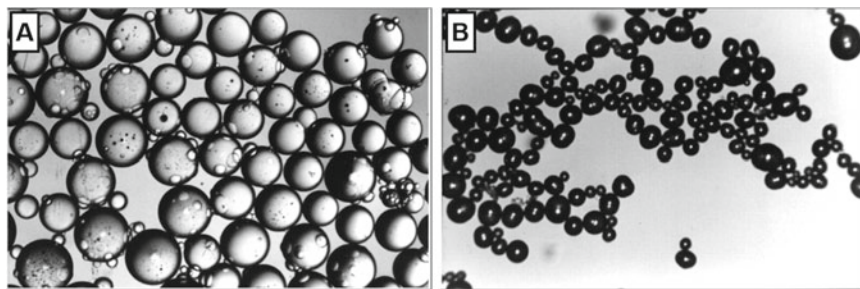


Fig. 2 Optical photomicrographs of poly(NIPAAm-co-acrylamide) microspheres in the swollen state in phosphate buffer below the LCST value at 22 °C (panel A) and above the LCST value at 45 °C (panel B). Reproduced with permission from Acta Biomaterialia (Fundueanu et al. 2009a)

In addition, the amount of entrapped drug influences the pulsatile release mechanism. Microspheres from poly(NIPAAm-co-N-vinylpyrrolidone) (poly(NIPAAm-co-NVP)) with a low loading degree (7.62%), display a substantial difference between the diclofenac (DF) release rate at temperatures situated below and above the LCST (Fig. 3A); this difference guarantees a pulsatile release mechanism (Fig. 3B). On the opposite, the release profiles of DF from microspheres with high loading degree (13.08%) at temperatures lower and higher the LCST are almost superimposable (Fig. 3C), therefore the cyclically variation of temperature does not ensure a pulsatile mechanism (Fig. 3D) (Fundueanu et al. 2020a).

As it was mentioned, the LCST of the poly(NIPAAm) in aqueous solution is around 32 °C, which is slightly lower than the temperature of the human body. In order to increase the transition temperature, NIPAAm is copolymerized with hydrophilic co-monomers (Khan 2007; Liu et al. 2004). In fact, by copolymerization with hydrophilic monomers, the hydrophilic/hydrophobic balance is disturbed and higher energy (temperature) is necessary to break the hydrogen bonds between copolymer and water. In addition, the insertion of hydrophilic co-monomers along the main chain in a higher proportion alters the amide and isopropyl sequences of poly(NIPAAm) and can lead to a decrease or even loss of thermosensitive properties (Feil et al. 1933). On the opposite, the copolymerization of the NIPAAm with hydrophobic monomers leads to a decrease of the LCST below 32 °C (Luan et al. 2016). An atypical behaviour was observed for poly(N-isopropylmethacrylamide) (poly(NIPMAAm)) with structure similar to that of NIPAAm with the exception of methyl groups. Although poly(NIPMAAm) is more hydrophobic than poly(NIPAAm), the phase transition temperature of poly(NIPMAAm) in aqueous solution is higher (≈ 46 °C) (Djokpé and Vogt 2001), reflecting the conformation of the monomeric structure in poly(NIPMAAm). The presence of methyl groups throughout the main polymeric chain hinders the hydrophobic interactions, therefore a higher temperature is necessary for polymer precipitation. The copolymerization of NIPAAm with increasing amount of NIPMAAm gives copolymers with increased values of LCST (Table 1) (Fundueanu et al. 2016).

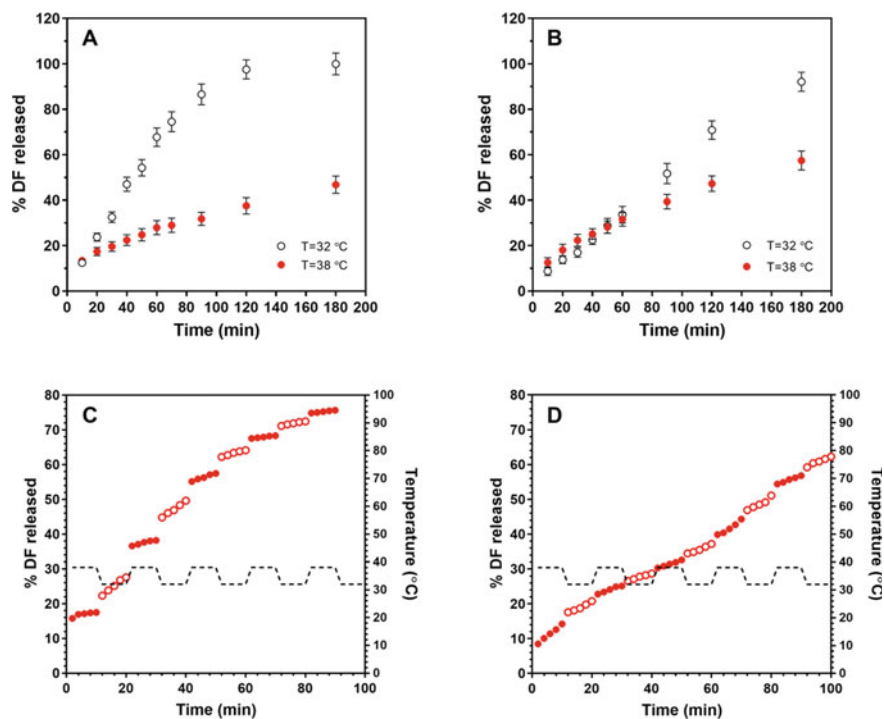


Fig. 3 Effect of temperature (panels A and B) and temperature cycling (panels C and D) (32 °C (empty symbols) and 38 °C (full symbols)) on DF release profiles from poly(NIPAAm-co-NVP) microspheres. The release studies were performed in PBS at pH = 7.4, using microspheres with 7.62% (w/w) DF (panel A and C) and with 13.08% (w/w) DF (panel B and D). Reproduced with permission from Express Polymer Letters (Fundueanu et al. 2020)

Table 1 Dependence of LCST on the co-monomer ratio in the feed and in the copolymer. The concentration of the copolymer solution was 1% (w/v). Reproduced with permission from Macromolecular Chemistry and Physics (Fundueanu et al. 2016)

Sample	Co-monomer composition (% mol ratio)				LCST (°C)		
	In the feed		In copolymer		pH 7.4	pH 1.2	H2O
	NIPAAm	NIPMAAm	NIPAAm	NIPMAAm			
S ₀	100	0	100	0	29.9 ± 0.2	31.6 ± 0.2	32.6 ± 0.2
S ₁	66.67	33.33	55.00	45.00	35.9 ± 0.3	– ^a	– ^a
S ₂	60	40	51.00	49.00	36.8 ± 0.3	38.2 ± 0.3	38.8 ± 0.2
S ₃	50	50	41.75	58.25	38.3 ± 0.3	– ^a	– ^a
S ₄	33.33	66.67	28.75	71.25	40.9 ± 0.2	– ^a	– ^a
S ₅	0	100	0	100	44.7 ± 0.3	45.0 ± 0.2	45.5 ± 0.3

Data are the results of two independent experiments.

^a not done.

Practically, the LCST of poly(NIPAAm-co-NIPMAAm) increases almost linearly with the percentage of NIPMAAm in the copolymer; comparable results were found by Djokpé and Vogt (Djokpé and Vogt 2001).

In fact, the phase transition of the copolymer is situated between the LCST of poly(NIPAAm) homopolymer and that of poly(NIPMAAm). Under simulated physiological conditions (phosphate buffer at pH 7.4) poly(NIPAAm) displays a LCST of 29.9 °C while poly(NIPMAAm) has a LCST at 44.8 °C, which both are lower than that determined in aqueous solution. This decrease in the transition temperature is due to the high ionic strength of the phosphate buffer which weakens the interaction between the polymer chains and the water.

However, the most used pharmaceutical form for these polymers in biomedical applications are hydrogels (Andrei et al. 2016; Sung et al. 2015). They are obtained by copolymerization of corresponding co-monomers in the presence of small amounts of cross-linkers. The resulted hydrogels should preserve the thermosensitive properties of the linear polymer. Moreover, they should display fast swelling/deswelling rates to small changes of the temperature to ensure a pulsatile drug delivery (Fig. 4) (Fundueanu et al. 2016).

Swelling/deswelling rates of thermosensitive hydrogels depend mainly by the diffusion rate of water molecules into and out of the hydrogel. The diffusion rate

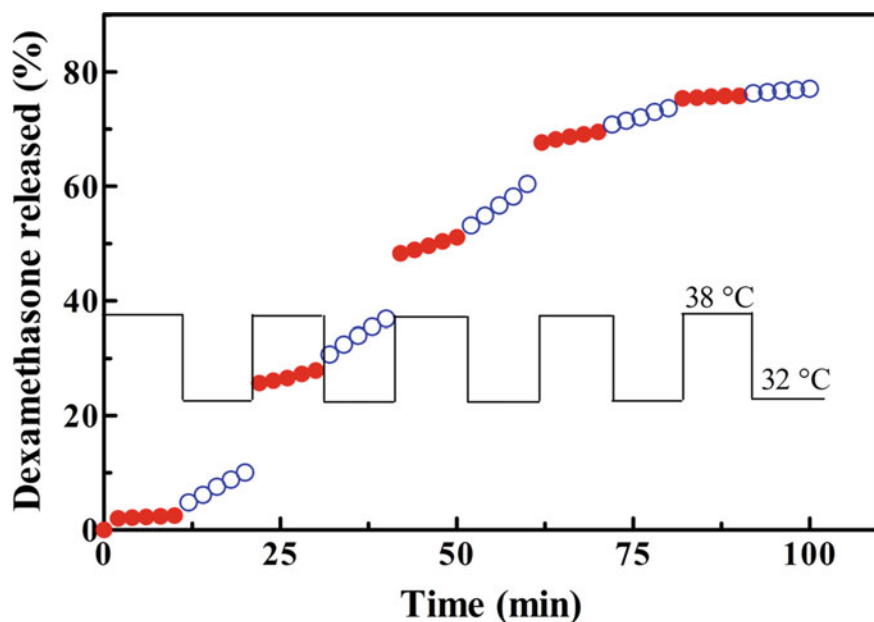


Fig. 4 Influence of cyclically temperature change on dexamethasone release from the poly(NIPAAm-co-NIPMAAm) microgels. Data were obtained in simulated physiological conditions (PBS at pH = 7.4) at 32 °C (empty symbols) and 38 °C (full symbols). Reproduced with permission from Macromolecular Chemistry and Physics (Fundueanu et al. 2016)

of water molecules is governed by the dimension and porosity of the hydrogel. Certainly, the smaller is the size the faster is the diffusion rate; in addition a high porosity allows a rapid diffusion of water (Sato-Matsuo and Tanaka 1988; Tanaka and Fillmore 1979). The creation of a porous structure in a three-dimensional network is one of the best procedure used to avoid the „skin effect” that hinders the diffusion of water and promotes a rapid volume change of hydrogel in response to temperature modifications (Strachotova et al. 2007). In hydrogels with porous structures, the water is ejected or absorbed by convection, a much faster process than by conventional diffusion. Usually, porous poly(NIPAAm) hydrogels were prepared in the presence of a template molecule. Tokuyama and Kanehara (2007) have synthesized hydrogels by free radical copolymerization of NIPAAm and N,N-methylene-bis-acrylamide, as cross-linker, in an oil-in-water emulsion (Tokuyama and Kanehara 2007). At the end of polymerization, the dispersed oil minidroplets used as template are removed by washing with appropriate solvents resulting a porous hydrogel. Thermally reversible macroporous poly(NIPAAm) hydrogel has also been synthesized in aqueous solution at a temperature above the LCST. As long as the reaction takes place at a temperature above the LCST, the polymer collapses as it reaches a certain degree of polymerization. The hydrophobic interactions that take place later between the aggregates create bridges that generate a heterogenous macroporous structure (Yan and Hoffman 1995). Hydrogels with large pores were also obtained in the presence of hydroxypropyl cellulose as a pore-forming agent. The response rate to the temperature changes was much faster for these hydrogels than those obtained without porogens. However, since the polymerization occurred above LCST, the macroporous hydrogel displayed a heterogeneous structure (Wu et al. 1992). Microgels with homogeneous pore size and size distribution were obtained by chemical cross-linking of preformed poly(NIPAAm-co-AAm) in the presence of poly(NIPAAm) thermosensitive oligomers, taken as porogen (Fundueanu et al. 2009b). The porous microspheres were obtained both below and above the LCST of the poly(NIPAAm) oligomer. The size of the pores is obviously influenced by the amount of the porogen in the reaction mixture. In the absence of the porogen no pores are formed and the microspheres show a compact internal structure and a smooth surface. The best size distribution and homogeneity of the pores were obtained under the LCST of porogen because the synthesis process takes place in a homogeneous solution of the polymer and oligomer (Fig. 5).

Due to the porous structure and hydrophilic character of the co-monomers, the microgels display relatively high values of water regain and swelling degree. Also, they are characterized by a very rapid response rate when the temperature changes below and above the body temperature. The porous microspheres have proven to be suitable matrix for loading and temperature-controlled release of the high molecular weight model drug blue dextran (Fig. 6).

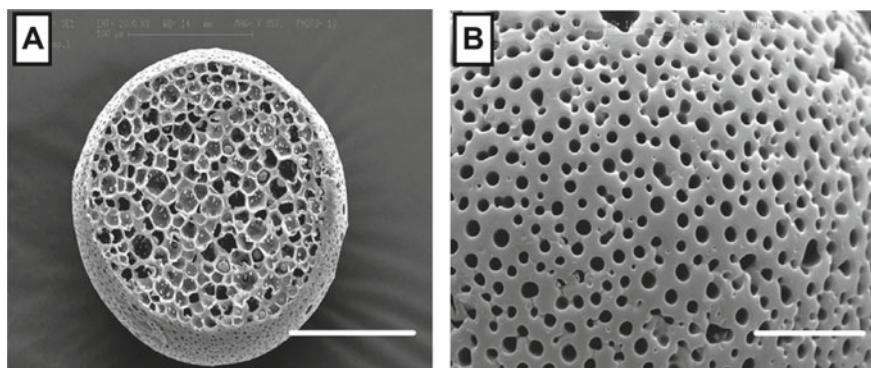


Fig. 5 SEM micrographs of porous poly(NIPAAm-co-AAm) microspheres obtained using poly(NIPAAm) oligomers as porogens: cross-section (panel A) and surface detail (panel B). The bars correspond to 100 and 20 μm in panels A and B, respectively. Reproduced with permission from International Journal of Pharmaceutics (Fundueanu et al. 2009b)

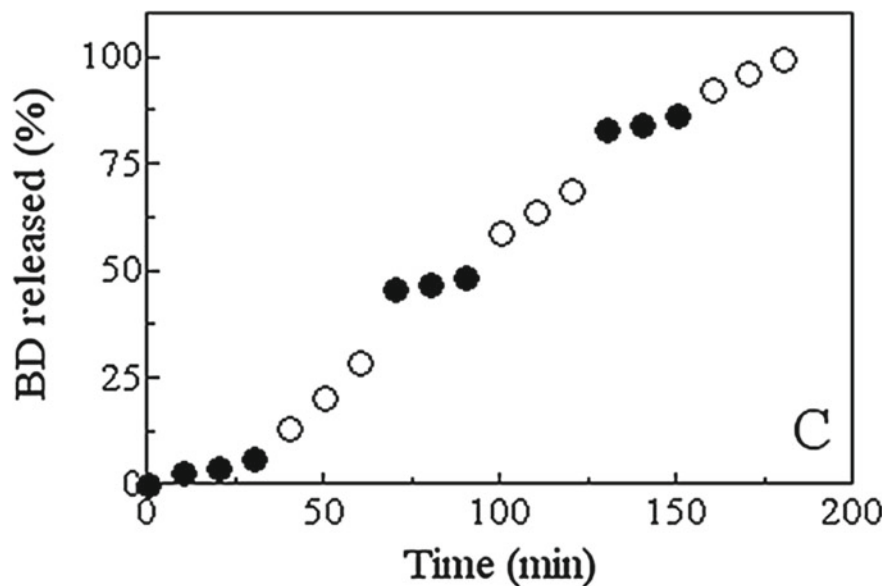


Fig. 6 Effect of temperature cycling (33 $^{\circ}\text{C}$ (empty symbols) and 38 $^{\circ}\text{C}$ (full symbols)) on Blue Dextran release from poly(NIPAAm-co-AAm) microspheres in phosphate buffer at pH 7.4. Reproduced with permission from International Journal of Pharmaceutics (Fundueanu et al. 2009b)

3 PH-Sensitive Drug Delivery Systems

Drug delivery systems sensitive to pH were designed and developed to exploit the pH variations in the human body. For example, the pH varies from 1–2 in the stomach

to 7.4 and even 8 in the blood and duodenum, respectively. Additionally, the pH-sensitive systems have appealed an enormous interest because the differences in pH between normal tissue and tumoral tissues can be used to design pH-sensitive drug delivery carriers that can target tumors and release loaded drugs at the tumor site (Xu et al. 2020; Men et al. 2020; Sim et al. 2019).

Generally, the pH-sensitive polymers comprise weakly acidic (carboxylic) or weakly basic (amine) functional groups (Riyajan 2019; Liu et al. 2018). The most important properties of these polymers result from the protonation/deprotonation of the pH-sensitive groups to small pH change in the range of physiological conditions. The linear polymers change their hydrophilic / hydrophobic character and consequently their solubility. The cross-linked hydrogels synthesized from these polymers swell and shrink as a result of protonation/deprotonation of functional groups (Vaghani and Patel 2011; Sabzi et al. 2020). Basically, hydrogels possessing carboxylic pH-sensitive groups become protonated at low pH, below the pKa and therefore is relatively not swollen (Fig. 7A). As the pH rises above the pKa value,

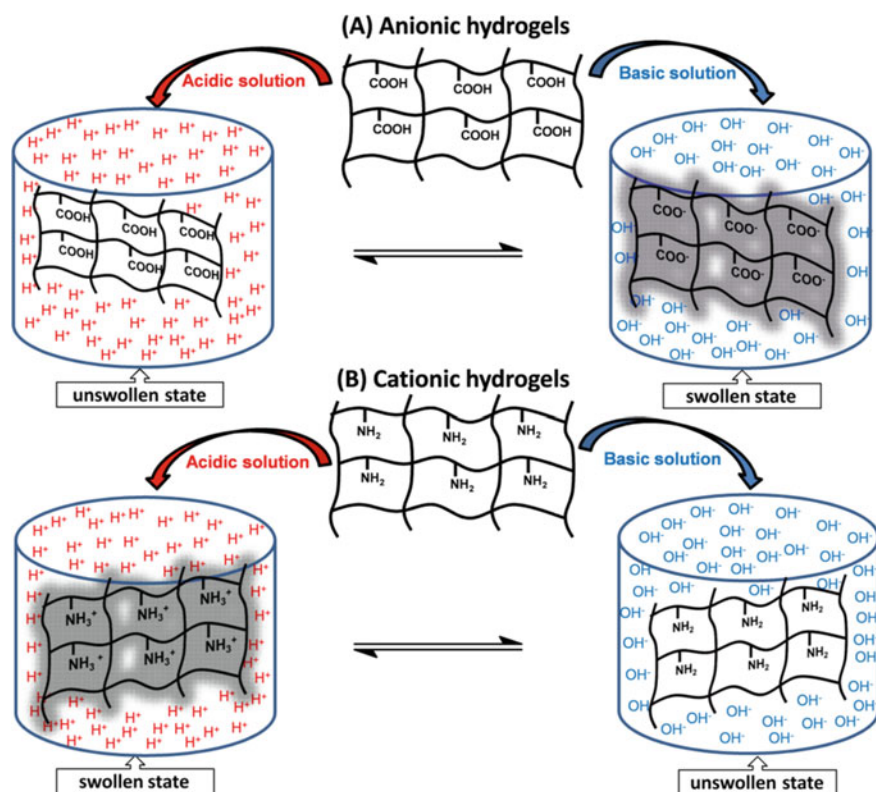


Fig. 7 Swelling behavior of an anionic (panel A) and cationic hydrogel (panel B) in acidic and basic solution

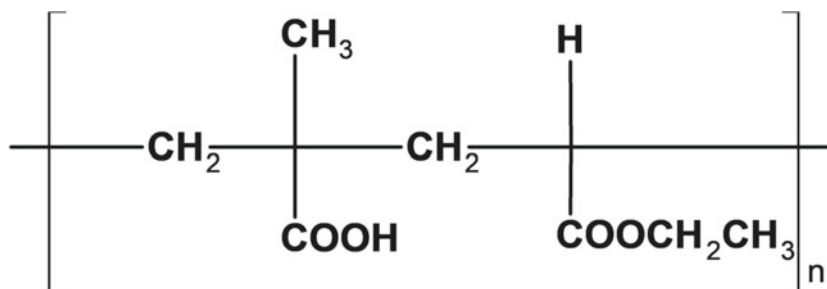


Fig. 8 Chemical structure of Eudragit L 100–55

the carboxylic groups ionize, become hydrophilic and the hydrogel swells. Hydrogels with amino pH-sensitive groups have a completely opposite behavior. At low pH, under the pKa, the amino groups are protonated (ionized) and the hydrogel swells while at higher pH values, above pKa, the amino groups are non-ionized, less hydrophilic and the hydrogel is in a collapsed state (Fig. 7B).

The most commonly used pH-sensitive polymers in the linear form are methacrylic acid copolymers, known as Eudragit R (a registered trademark of Rohm Pharmaceuticals; Darmstadt, Germany). For example, Eudragit L 100-55 T forms salts and dissolves above pH 5.5 and is insoluble in gastric fluids (Fig. 8). This property has been exploited to deliver drugs to the large intestine by way of pH sensitive enteric coatings or as micro- and nano-particles (Hao et al. 2013).

Besides Eudragits, other pH-sensitive polymers such as derivatives of cellulose are largely used for drug targeting to the small intestine. Among these, cellulose acetate phthalate (pKa ~ 5.5), also known as cellacefate is a cellulose derivative where about half of the hydroxyl groups are esterified with acetyls and a quarter is esterified with one or two carboxyls of the phthalic acid (Fig. 9). It is a commonly used polymer in the formulation of pharmaceuticals, such as the enteric coating of tablets or capsules for controlled release formulations (Jagdale and Chandekar 2017).

However, the most important drawback of these polymers is the lack of biodegradability. This inconvenience is not so severe for pharmaceutical formulations with oral application, instead, for other types of administrations such as parenteral ones, the biodegradability becomes a very acute problem. Therefore, natural polymers with native pH-sensitive units were frequently used for delivery of drugs modulated by the pH. Among these, alginic acid (Boi et al. 2020) and chitosan (Ata et al. 2020) are the most representative anionic and cationic natural polymers, respectively, used in biomedical applications. Concerning the chemical structure, alginic acid is described as a linear block copolymer composed of sequences with consecutive β -1,4-D-mannuronic acid residues (M-blocks), α -L-guluronic acid residues (G-blocks) and alternating M and G residues (MG-blocks) (Fig. 10).

The pKa of mannuronic and guluronic acid in 0.1 M NaCl are known to be 3.38 and 3.65, respectively. Owing to its pH-sensitivity, biocompatibility, low toxicity and muco-adhesive properties, alginic acid is considered a noticeable polymer

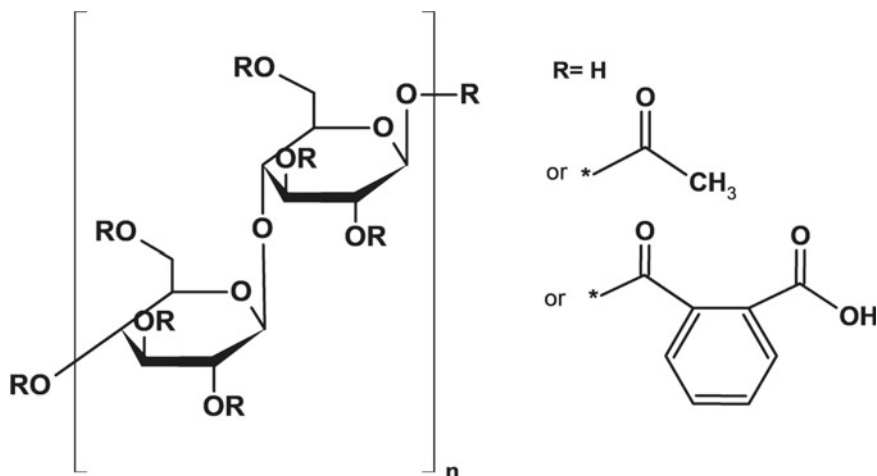


Fig. 9 Chemical structure of cellulose acetate phthalate

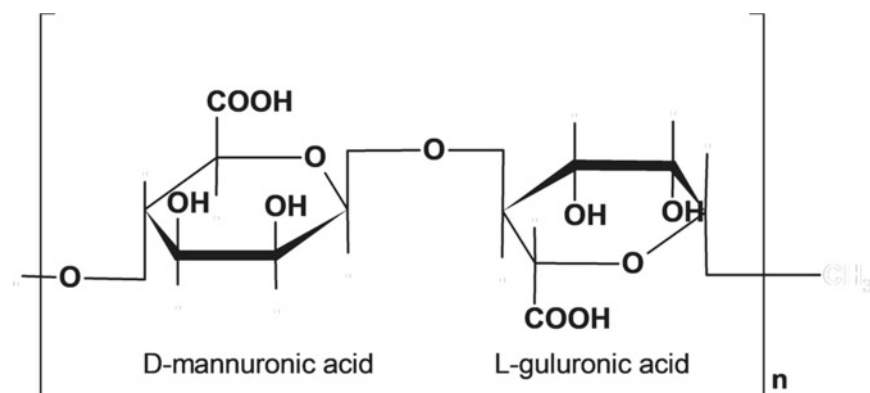


Fig. 10 Chemical structure of alginic acid

for biomedical applications. Therefore, George and Abraham (2007) developed a pH-sensitive alginate–guar gum hydrogel cross-linked with glutaraldehyde for oral administration of protein drugs (George and Abraham 2007). It is well-known that protein instability mainly in gastric fluids is one of the major motives by which proteins are administered usually through injection rather than taken by oral route. Due to the protonation of alginate, the amount of released protein from test hydrogels was minimal at pH 1.2 (~20%), but it was found to be significantly higher (~90%) at pH 7.4., when the carboxylic groups are in ionized form and the hydrogel swells.

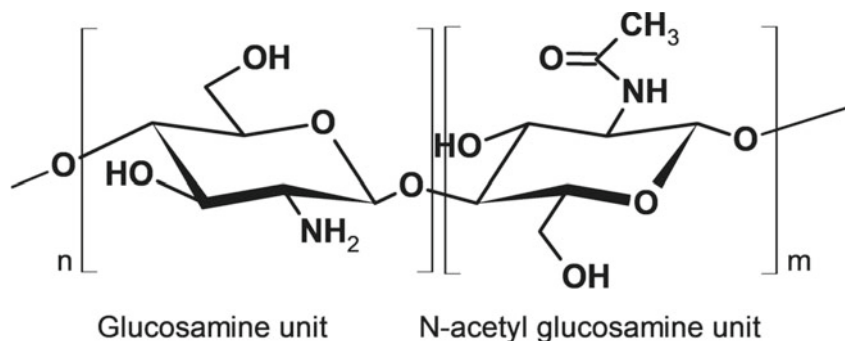


Fig. 11 Chemical structure of chitosan showing the repeating subunits

With the aim to enhance the drug entrapment efficiency and control the swelling properties and stability of drug delivery system in different pH media, Ca²⁺ cross-linking and freeze-thawing cycle techniques were used to prepare sodium alginate/poly(vinyl alcohol) (PVA) hydrogel beads (Hua et al. 2010). The alginate/PVA mixture was firstly cross-linked with Ca²⁺ to form beads and then subjected to freezing–thawing cycles for additional crosslinking. It was proved that the swelling, drug release profiles, and degradation of the developed beads were influenced by pH of the testing medium and PVA content.

Chitosan is another linear polysaccharide composed of randomly distributed β-linked D-glucosamine and N-acetyl-D-glucosamine (Fig. 11).

Like alginate, it is biocompatible, biodegradable and the degradation by-products are not toxic. It is the second abundant biomass-derived polysaccharide and is obtained by treating the chitin shells of shrimp and other crustaceans with sodium hydroxide. If alginate-based hydrogels collapse in an acidic environment and swell in a weakly basic environment, chitosan hydrogels have an opposite behaviour; they swell in acidic pH and collapse in basic media. This compartment is given by the presence of abundant amino groups with a pK_a of around 6.5. Since the pK_a value is situated in the pH range of tumor environment, it is widely used for controlled delivery of anticancer drugs (Ghaffari et al. 2020; Wang et al. 2019). As follows, an interesting hydrogel was designed and developed from the cross-linking of chitosan, graphene, and cellulose nanowhisker via Schiff base reaction by a synthetic dialdehyde (Omidi et al. 2020). The hydrogel was loaded with two antitumoral drugs, doxorubicin and curcumin.

The drug release profiles demonstrated that the rate of release is dependent on switching pHs from neutral pH to the acidic conditions. By decreasing of pH from 7.4–5.4, the strength of cross-linking imine bonds decreases and as well the repulsive ionic interactions between the protonated amino groups increase which leads to an expanded structure.

Chitosan was also used for the preparation of microcapsules for cell encapsulation and cell culture (Fundueanu et al. 2020b). Since the encapsulation process must take place in mild conditions and the neutral chitosan is soluble in just in acidic conditions,

harmful to cells, the amino groups were protonated and the chitosan was transformed in the hydrochloride form. Thus, the chitosan derivative was easily solubilized in isotonic solutions and cell encapsulation was successfully performed with no cell damage. Moreover, the protonated chitosan microcapsules allow the cells to adhere to their surface.

One of the most important drawbacks of hydrogels prepared from simple alginate or chitosan is their low stability in physiological fluids. Therefore, core-shell nanoparticles from polyelectrolytes complexes between chitosan and alginate were prepared for oral insulin administration (Mukhopadhyay et al. 2015).

The nanoparticles displayed an almost spherical shape, an average diameter of 100–200 nm determined by dynamic light scattering, and high insulin encapsulation efficiency. In simulated gastric fluid, the nanoparticles retained almost entire amount of encapsulated insulin while in simulated intestinal conditions a sustained release was achieved. Additionally, *in vivo* experiments presented substantial intestinal absorption of insulin, showing noticeable hypoglycaemic effects with enhanced insulin bioavailability in diabetic mice. After oral administration, the core-shell nanoparticles displayed no systemic toxicity.

4 pH/Temperature-Sensitive Drug Delivery Systems

pH/temperature sensitive drug delivery systems were designed and developed to exploit the variation of both pH and temperature of the human body. They are obtained either in the form of linear or cross-linked polymers by copolymerization of NIPAAm with pH-sensitive monomers. The pH-sensitive co-monomer can increase or decrease the LCST if they are in the un-protonated or protonated state (Yoo et al. 2000). Also, the modification of pH and temperature can modulate the solubility, if the polymer is in the linear form, or swelling behavior for cross-linked hydrogels.

Thus, stimuli-sensitive statistical terpolymers of N-isopropylacrylamide (temperature-sensitive), butyl methacrylate (BMA) and acrylic acid (AA) (pH-sensitive) of various molecular weights were used to prepare microcapsules for modulating the release of insulin (Ramkissoo-Ganorkar et al. 1999). This system has the advantage that only physical interactions polymer/polymer and polymer/protein were used to prepare insulin-loaded microcapsules in mild conditions.

The release rate of insulin was controlled by the pH, temperature and molecular weights of polymers. In gastric fluid at pH = 1.2 and body temperature, the beads were not soluble, and therefore no drug is released in the stomach. At pH 7.4 and body temperature, the low molecular weight polymeric beads shown a dump-like profile and dissolved within 2 h (release mechanism controlled by bead dissolution), while the high molecular weight polymeric beads swelled only and released insulin gradually over a period of 8 h (release mechanism controlled by bead swelling and insulin diffusion).

In another work, the escape of DNA loaded poly(vinyl alcohol) microspheres from multinucleated microcapsules took place through the holes induced by dissolution

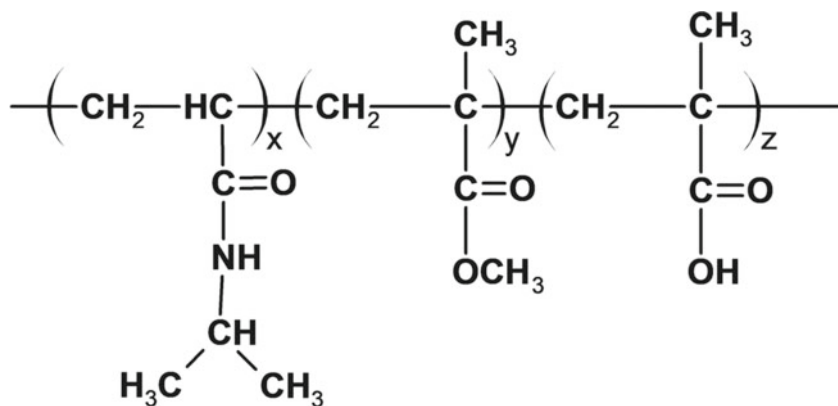


Fig. 12. Chemical structure of poly(NIPAAm-co-MM-MA)

of the pH/temperature sensitive polymer at colonic pH and temperature (Fundueanu et al. 2007).

Fundueanu et al. (2009) developed a pH/temperature sensitive copolymer based on NIPAAm, methyl methacrylate (MM) and methacrylic acid (MA) (Fig. 12) (Fundueanu et al. 2009).

Poly (NIPAAm-co-MM-co-MA) with a co-monomer molar ratio of 79:13:8 is insoluble in the gastric fluid (pH = 1.2), but soluble in the intestinal fluid (pH = 6.8 and 7.4), at the body temperature (37 °C). This copolymer was mixed with the hydrophobic cellulose acetate butyrate (CAB) and vitamin B12 (taken as a water soluble drug model system) and transformed in spherical microparticles by oil-in-water solvent evaporation method. With the aim to determine the compatibility between the two components of the microspheres (CAB with pH/temperature sensitive copolymer), the glass transition temperatures (T_g) of separated polymers and of microspheres were determined.

The occurrence of two T_g values validated that there is no interaction between the two components; they precipitated separately during microsphere preparation, the smart polymer forming small micro-domains on the surface and within the microspheres (Fig. 13A).

At pH = 1.2 and 37 °C, poly(NIPAAm-co-MM-co-MA) is not soluble, therefore the amount of vitamin B12 released is very low. When the temperature is lowered to 20 °C, below LCST, the copolymer solubilizes and an increased percentage of vitamin B12 is released. In phosphate buffer at pH = 6.8, the copolymer is less soluble than at pH = 7.4, therefore the release rate is lower but is much higher than at pH = 1.2. Obviously, the highest amount of vitamin is released at pH = 7.4, when the copolymeric domains solubilize totally creating pores within three-dimensional network (Fig. 13B).

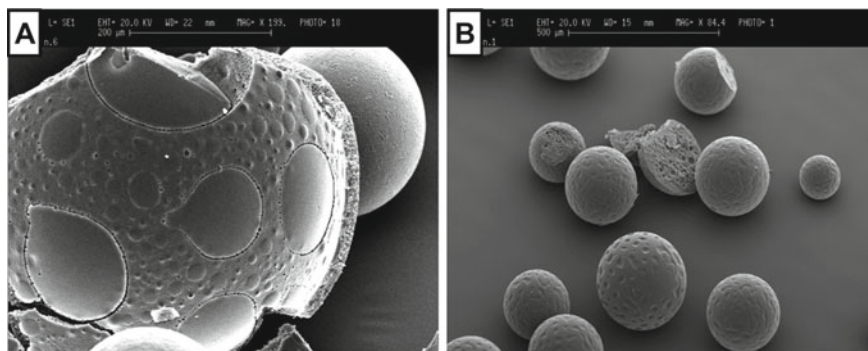


Fig. 13 SEM micrographs of CAB/poly(NIPAAm-co-MM-co-MA) microspheres before (panel A) and after (panel B) release studies in PBS at pH = 7.4. Reproduced with permission from Journal of Materials Science-Materials in Medicine (Fundueanu et al. 2009)

The copolymerization of NIPAAm with ionic co-monomers can increase or decrease the LCST if the charged co-monomers are in the protonated/unprotonated state (Yoo et al. 2000). However, the charged co-monomers, due to their high hydrophilicity in the ionized state, diminish dramatically or even annihilate the thermosensitivity of the copolymer (Constantin et al. 2014).

Remarkably, when the pH-sensitive units interact electrostatically with hydrophobic oppositely charged bioactive compounds like diclofenac (Fundueanu et al. 2013), propranolol (Constantin et al. 2014), diphenhydramine (Fundueanu et al. 2017), indomethacin (Constantin et al. 2020), the copolymers restore the thermosensitive properties. Correspondingly, the hydrogels synthesized from these copolymers are in the “inactivated” state in the absence of specific biomolecules at normal physiological pH and temperature (pH = 7.4 and T = 36 °C). However, in the presence of bioactive biomolecules, hydrogels undergo “activation”, shrink and expel mechanically a certain amount of drug (Fig. 14).

It must be mentioned that the pH-sensitive component plays the role of a biosensor, the biomolecule acts as a triggering agent, and the poly(NIPAAm) represents the delivery component (actuator).

The proposed hydrogels represent the support of the next generation of self-regulated drug delivery systems based on a sensor (pH-sensitive units) able to detect the perturbation of physiological conditions and a delivery component (thermosensitive units) able to push the necessary dose of drug.

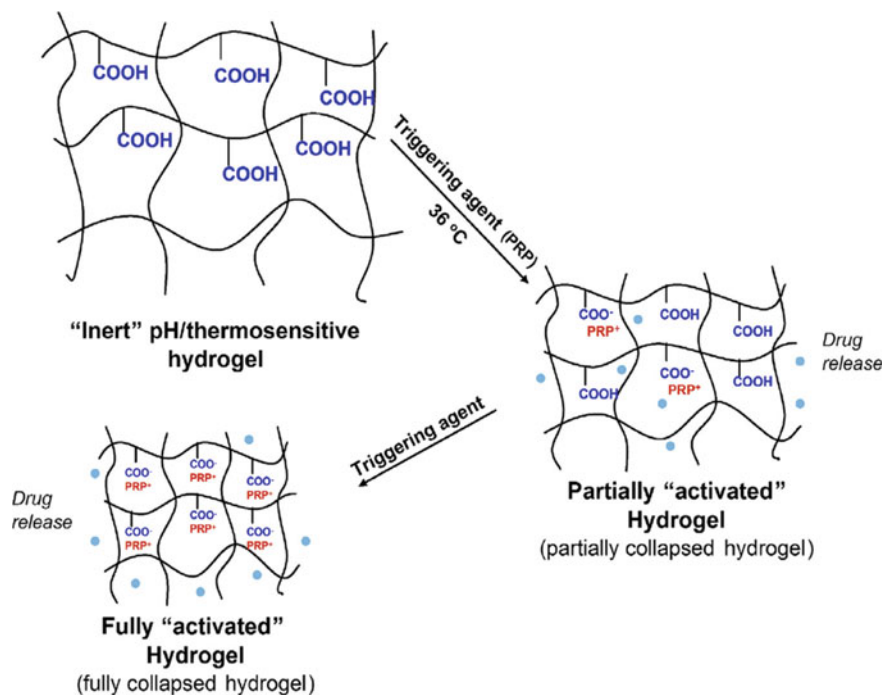


Fig. 14 Schematic representation of the principle of operation of pH/thermosensitive poly(NIPAAm-co-MA) microgels in the presence of the triggering agent, under simulated physiological conditions. Reproduced with permission from European Journal of Pharmaceutical Sciences (Constantin et al. 2014)

5 Conclusions

While the basic concepts of the stimuli-sensitive hydrogels are sound, the practical applications necessitate significant improvements in the hydrogel properties. For example, hydrogels do not have the mechanical strength indispensable in many applications. In addition, the response rate to the input signal is low for large-scale hydrogels. Difficulties to achieve pH/thermo-sensitivity within a narrow pH or temperature range (from pH 7.4 to pH = 7.0 or 6.5; from $T = 36.5\text{ °C}$ to 37 °C) often appear since the transition temperature of the cross-linked hydrogels is not as abrupt as for linear polymers. Drug loading and drug retention within microgels for a long period of time could be a major drawback. Also, the selectivity of these systems must be substantially improved.

Acknowledgements The project leading to this application has received funding from the H2020 ERA Chairs Project no 667387: SupraChem Lab Laboratory of Supramolecular Chemistry for Adaptive Delivery Systems ERA Chair initiative. This work was supported also by a grant of the Romanian Ministry of Research and Innovation, CCDI-UEFISCDI, project number PN-III-P1-1.2.-PCCDI-2017-0697/contract nr. 13 PCCDI/2018 within PNCDI III.

References

- Alsuraifi A, Curtis A, Lamprou DA, Hoskins C (2018) Stimuli responsive polymeric systems for cancer therapy. *Pharmaceutics* 10(3):136. <https://doi.org/10.3390/pharmaceutics10030136>
- Andrei M, Turturica G, Stanescu PO, Teodorescu M (2016) Thermosensitive injectable hydrogels from poly(N-isopropylacrylamide)-dextran aqueous solutions: thermogelation and drug release properties. *Soft Mater* 14(3):162–169. <https://doi.org/10.1080/1539445X.2016.1172317>
- Ata S, Rasool A, Islam A, Bibi I, Rizwan M, Azeem MK, Qureshi AUR, Iqbal M (2020) Loading of Cefixime to pH sensitive chitosan based hydrogel and investigation of controlled release kinetics. *Int J Biol Macromol* 155:1236–1244. <https://doi.org/10.1016/j.ijbiomac.2019.11.091>
- Boi S, Rouatbi N, Dellacasa E, Di Lisa D, Bianchini P, Monticelli O, Pastorino L (2020) Alginate microbeads with internal microvoids for the sustained release of drugs. *Int J Biol Macromol* 156:454–461. <https://doi.org/10.1016/j.ijbiomac.2020.04.083>
- Constantin M, Bucatariu S, Harabagiu V, Popescu I, Ascenzi P, Fundueanu G (2014) Poly(N-isopropylacrylamide-co-methacrylic acid) pH/thermo-responsive porous hydrogels as self-regulated drug delivery system. *Eur J Pharm Sci* 62:86–95. <https://doi.org/10.1016/j.ejps.2014.05.005>
- Constantin M, Bucatariu S, Ascenzi P, Butnaru M, Fundueanu G (2020) Smart drug delivery system activated by specific biomolecules. *Mat Sci Eng C* 108:110466. <https://doi.org/10.1016/j.msec.2019.110466>
- Djoké E, Vogt W (2001) N-Isopropylacrylamide and N-Isopropylmethacrylamide: cloud points of mixtures and copolymers. *Macromol Chem Phys* 202(5):750–757. [https://doi.org/10.1002/1521-3935\(20010301\)202:5%3c750::AID-MACP750%3e3.0.CO;2-8](https://doi.org/10.1002/1521-3935(20010301)202:5%3c750::AID-MACP750%3e3.0.CO;2-8)
- Feil H, Bae YH, Feijen J, Kim SW (1933) Effect of comonomer hydrophilicity and ionization on the lower critical solution temperature of N-isopropylacrylamide copolymers. *Macromolecules* 26:2496–2500. <https://doi.org/10.1021/ma00062a016>
- Fundueanu G, Constantin M, Bucatariu S, Ascenzi P (2016) Poly(N-isopropylacrylamide-co-N-isopropylmethacrylamide) thermo-responsive microgels as self-regulated drug delivery system. *Macromol Chem Phys* 217 (22):2525–2533. <https://doi.org/10.1002/macp.201600324>
- Fundueanu G, Constantin M, Asmarandei I, Harabagiu V, Ascenzi P, Simionescu BC (2013) The thermosensitivity of pH/thermo-responsive microspheres activated by the electrostatic interaction of pH-sensitive units with a bioactive compound. *J Biomed Mater Res A* 101(6):1661–1669. <https://doi.org/10.1002/jbm.a.34469>
- Fundueanu G, Constantin M, Ascenzi P (2009) Poly(N-isopropylacrylamide-co-acrylamide) cross-linked thermoresponsive microspheres obtained from preformed polymers: Influence of the physico-chemical characteristics of drugs on their release profiles. *Acta Biomater* 5(1):363–373. <https://doi.org/10.1016/j.actbio.2008.07.011>
- Fundueanu G, Constantin M, Asmarandei I, Bucatariu S, Harabagiu V, Ascenzi P, Simionescu BC (2013) Poly(N-isopropylacrylamide-co-hydroxyethylacrylamide) thermosensitive microspheres: The size of microgels dictates the pulsatile release mechanism. *Eur J Pharm Biopharm Part A* 85(3):614–623. <https://doi.org/10.1016/j.ejpb.2013.03.023>
- Fundueanu G, Constantin M, Bucatariu S, Ascenzi P (2020a) Poly(N-isopropylacrylamide-co-N-vinylpyrrolidone) thermoresponsive microspheres: the low drug loading ensures the pulsatile release mechanism. *EXPRESS Polym Lett* 14(1):63–76. <https://doi.org/10.3144/expresspolymlett.2020.6>
- Fundueanu G, Constantin M, Ascenzi P (2009) Fast-responsive porous thermoresponsive microspheres for controlled delivery of macromolecules. *Int J Pharm* 379(1):9–17. <https://doi.org/10.1016/j.ijpharm.2009.05.064>
- Fundueanu G, Constantin M, Bucatariu S, Nicolescu A, Ascenzi P, Moise LG, Tudor L, Trusca VG, Gafencu AV, Fikai D, Fikai A, Andronescu E (2020b) Simple and dual cross-linked chitosan millicapsules as a particulate support for cell culture. *Int J Biol Macromol* 143:200–212. <https://doi.org/10.1016/j.ijbiomac.2019.12.045>

- Fundueanu G, Constantin M, Bortolotti F, Cortesi R, Ascenzi P, Menegatti E (2007) Cellulose acetate butyrate-pH/thermosensitive polymer microcapsules containing aminated poly(vinyl alcohol) microspheres for oral administration of DNA. *Eur J Pharm Biopharm* 66(1):11–20. [https://doi.org/10.1016/S0939-6411\(07\)00176-2](https://doi.org/10.1016/S0939-6411(07)00176-2)
- Fundueanu G, Constantin M, Stanciu C, Theodoridis G, Ascenzi P (2009) pH- and temperature-sensitive polymeric microspheres for drug delivery: the dissolution of copolymers modulates drug release. *J Mater Sci Mater Med* 20(12):2465–2475. <https://doi.org/10.1007/s10856-009-3807-0>
- Fundueanu G, Constantin M, Bucatariu S, Ascenzi P (2017) pH/thermo-responsive poly(N-isopropylacrylamide-co-maleic acid) hydrogel with a sensor and an actuator for biomedical applications. *Polymer* 110:177–186. <https://doi.org/10.1016/j.polymer.2017.01.003>
- George M, Abraham TE (2007) pH sensitive alginate–guar gum hydrogel for the controlled delivery of protein drugs. *Int J Pharm* 335:123–129. <https://doi.org/10.1016/j.ijpharm.2006.11.009>
- Ghaffari SB, Sarrafzadeh MH, Salami M, Khorramizadeh MR (2020) A pH-sensitive delivery system based on N-succinyl chitosan-ZnO nanoparticles for improving antibacterial and anti-cancer activities of curcumin. *Int J Biol Macromol* 151:428–440. <https://doi.org/10.1016/j.ijb iomac.2020.02.141>
- Hao S, Wang Y, Wang B, Deng J, Liu X, Liu J (2013) Rapid preparation of pH-sensitive polymeric nanoparticle with high loading capacity using electrospray for oral drug delivery. *Mater Sci Eng C* 33:4562–4567. <https://doi.org/10.1016/j.msec.2013.07.009>
- Heskins M, Guillet JE (1968) Solution properties of poly(N-isopropylacrylamide). *J Macromol Sci Chem* 2:1441–1455. <https://doi.org/10.1080/10601326808051910>
- Hua S, Ma H, Li X, Yang H, Wang A (2010) pH-sensitive sodium alginate/poly(vinyl alcohol) hydrogel beads prepared by combined Ca²⁺-crosslinking and freeze-thawing cycles for controlled release of diclofenac sodium. *Int J Biol Macromol* 46:517–523. <https://doi.org/10.1016/j.ijb iomac.2010.03.004>
- Jagdale S, Chandekar A (2017) Optimization of chitosan and cellulose acetate phthalate controlled delivery of methylprednisolone for treatment of inflammatory bowel disease. *Adv Pharm Bull* 7(2):203–213. <https://doi.org/10.15171/apb.2017.025>
- Jamwal S, Ram B, Ranote S, Dharela R, Chauhan GS (2019) New glucose oxidase-immobilized stimuli-responsive dextran nanoparticles for insulin delivery. *Int J Biol Macromol* 123:968–978. <https://doi.org/10.1016/j.ijbiomac.2018.11.147>
- Krause J, Bogdahn M, Schneider F, Koziol M, Weitschies W (2019) Design and characterization of a novel 3D printed pressure-controlled drug delivery system. *Eur J Pharm Sci* 140:105060. <https://doi.org/10.1016/j.ejps.2019.105060>
- Khan A (2007) Preparation and characterization of N-isopropylacrylamide/acrylic acid copolymer core–shell microgel particles. *J Colloid Interf Sci* 313:697–704. <https://doi.org/10.1016/j.jcis.2007.05.027>
- Kim C, Jeong D, Kim S, Kim Y, Jung S (2019) Cyclodextrin functionalized agarose gel with low gelling temperature for controlled drug delivery systems. *Carbohydr Polym* 22215:115011. <https://doi.org/10.1016/j.carbpol.2019.115011>
- Lee CH, Bae YC (2020) Thermodynamic framework for switching the lower critical solution temperature of thermo-sensitive particle gels in aqueous solvent. *Polymer* 195:122428. <https://doi.org/10.1016/j.polymer.2020.122428>
- Liu F, Huang PL, Huang D, Liu SF, Cao QY, Dong XM, Zhang HW, Ko R, Zhou WY (2019) Smart “on-off” responsive drug delivery nanosystems for potential imaging diagnosis and targeted tumor therapy. *Chem Eng J* 365:358–368. <https://doi.org/10.1016/j.cej.2019.02.037>
- Liu XM, Wang LS, Wang L, Huang J, He C (2004) The effect of salt and pH on the phase-transition behaviors of temperature-sensitive copolymers based on N-isopropylacrylamide. *Biomaterials* 25(25):5659–5666. <https://doi.org/10.1016/j.biomaterials.2004.01.019>
- Liu YX, Liu KY, Zhao MN, Wang SH, Zhou ZX, Shen YQ, Jiang LM (2018) A pH-responsive fragrance release system based on pseudopeptide polymeric micelles. *React Funct Polym* 132:138–144. <https://doi.org/10.1016/j.reactfunctpolym.2018.09.021>

- Luan B, Muir BW, Zhu J, Hao X (2016) A RAFT copolymerization of NIPAM and HPMA and evaluation of thermo-responsive properties of poly(NIPAM-co-HPMA). *RSC Adv* 6:89925–89933. <https://doi.org/10.1039/C6RA22722H>
- Manouras T, Vamvakaki M (2017) Field responsive materials: photo-, electro-, magnetic- and ultrasound-sensitive polymers. *Polym Chem* 8(1):74–96. <https://doi.org/10.1039/C6PY01455K>
- Men WF, Zhu PY, Dong SY, Liu WK, Zhou K, Bai Y, Liu XL, Gong SL, Zhang SG (2020) Layer-by-layer pH-sensitive nanoparticles for drug delivery and controlled release with improved therapeutic efficacy in vivo. *Drug Deliv* 27(1):180–190. <https://doi.org/10.1080/10717544.2019.1709922>
- Mukhopadhyay P, Chakraborty S, Bhattacharya S, Mishra R, Kundu PP (2015) pH-sensitive chitosan/alginate core-shell nanoparticles for efficient and safe oral insulin delivery. *Int J Biol Macromol* 72:640–648. <https://doi.org/10.1016/j.ijbiomac.2014.08.040>
- Noorian SA, Hemmatinejad N, Navarro JAR (2020) Bioactive molecule encapsulation on metal-organic framework via simple mechanochemical method for controlled topical drug delivery systems. *Micropor Mesopor Mater* 302:110199. <https://doi.org/10.1016/j.micromeso.2020.110199>
- Omidi S, Pirhayati M, Kakanejadifard A (2020) Co-delivery of doxorubicin and curcumin by a pH-sensitive, injectable, and in situ hydrogel composed of chitosan, graphene, and cellulose nanowhisker. *Carbohydr Polym* 231:115745. <https://doi.org/10.1016/j.carbpol.2019.115745>
- Ramkissoon-Ganorkar C, Liu F, Baudys M, Kim SW (1999) Modulating insulin-release profile from pH/thermosensitive polymeric beads through polymer molecular weight. *J Control Release* 59:287–298. [https://doi.org/10.1016/S0168-3659\(99\)00006-1](https://doi.org/10.1016/S0168-3659(99)00006-1)
- Riyajan SA (2019) Development of a novel pH-sensitive polymer matrix for drug encapsulation from maleated poly(vinyl alcohol) grafted with polyacrylamide. *Polym Bull* 76(9):4585–4611. <https://doi.org/10.1007/s00289-018-2615-4>
- Sabzi M, Afshari MJ, Babaahmadi M, Shafagh N (2020) pH-dependent swelling and antibiotic release from citric acid crosslinked poly(vinyl alcohol) (PVA)/nano silver hydrogels. *Colloids Surf B* 188:110757. <https://doi.org/10.1016/j.colsurfb.2019.110757>
- Sapre N, Chakraborty R, Purohit P, Bhat S, Das G, Bajpe SR (2020) Enteric pH responsive cargo release from PDA and PEG coated mesoporous silica nanoparticles: a comparative study in *Drosophila melanogaster*. *RSC Adv* 10:11716–11726. <https://doi.org/10.1039/C9RA11019D>
- Sato-Matsuo E, Tanaka T (1988) Kinetics of discontinuous volume phase transition of gels. *J Chem Phys* 89:1695–1703. <https://doi.org/10.1063/1.455115>
- Sedlacek O, Filippov SK, Svec P, Hruby M (2019) SET-LRP synthesis of well-defined light-responsive block copolymer micelles. *Macromol Chem Phys* 220(19):1900238. <https://doi.org/10.1002/macp.201900238>
- Shang J, Chen X, Shao ZZ (2007) the Electric-Field-Sensitive Hydrogels. *Prog Chem* 19(9):1393–1399
- Sim T, Han SM, Lim C, Won WR, Lee ES, Youn YS, Oh KT (2019) A pH-sensitive polymer for cancer targeting prepared by one-step modulation of functional side groups. *Macromol Res* 27(8):795–802. <https://doi.org/10.1007/s13233-019-7112-6>
- Singh S, Kumar V, Kumar B, Priyadarshi R, Deeba F, Kulshreshtha A, Kumar A, Agrawal G, Gopinath P, Negi YS (2020) Redox responsive xylan-SS-curcumin prodrug nanoparticles for dual drug delivery in cancer therapy. *Mater Sci Eng C- Mater* 107:110356. <https://doi.org/10.1016/j.msec.2019.110356>
- Sung B, Kim C, Kim MH (2015) Biodegradable colloidal microgels with tunable thermosensitive volume phase transitions for controllable drug delivery. *J Colloid Interf Sci* 450:26–33. <https://doi.org/10.1016/j.jcis.2015.02.068>
- Strachotova B, Strachota A, Uchman M, Slouf M, Brus J, Plestil J, Matejka L (2007) Super porous organic-inorganic poly(N-isopropylacrylamide)-based hydrogel with a very fast temperature response. *Polymer* 48:1471–1482. <https://doi.org/10.1016/j.polymer.2007.01.042>
- Tanaka T, Fillmore DJ (1979) Kinetics of swelling of gels. *J Chem Phys* 70:1214–1218. <https://doi.org/10.1063/1.437602>

- Tokuyama H, Kanehara A (2007) Novel synthesis of macroporous poly(Nisopropylacrylamide) hydrogels using oil-in water emulsions. *Langmuir* 23:11246–11251. <https://doi.org/10.1021/la701492u>
- Vaghani SS, Patel MM (2011) pH-sensitive hydrogels based on semi-interpenetrating network (semi-IPN) of chitosan and polyvinyl pyrrolidone for clarithromycin release. *Drug Dev Ind Pharm* 37(10):1160–1169. <https://doi.org/10.3109/03639045.2011.563422>
- Wang X, Xu JX, Xu XX, Fang Q, Tang RP (2020) pH-sensitive bromelain nanoparticles by ortho ester crosslinkage for enhanced doxorubicin penetration in solid tumor. *Mater Sci Eng C- Mater* 113:111004. <https://doi.org/10.1016/j.msec.2020.111004>
- Wang YL, Khan A, Liu YX, Feng J, Dai L, WGH, Alam N, Tong L, Ni YH (2019) Chitosan oligosaccharide-based dual pH responsive nano-micelles for targeted delivery of hydrophobic drugs. *Carbohydr Polym* 223:115061. <https://doi.org/10.1016/j.carbpol.2019.115061>
- Wu XS, Hoffman AS, Yager P (1992) Synthesis and characterization of thermally reversible macroporous poly(N-isopropylacrylamide) hydrogels. *J Polym Sci Part A Polym Chem* 30:2121–2129. <https://doi.org/10.1002/pola.1992.080301005>
- Xu YQ, Liu DX, Hu J, Ding PR, Chen MW (2020) Hyaluronic acid-coated pH sensitive poly (beta-amino ester) nanoparticles for co-delivery of embelin and TRAIL plasmid for triple negative breast cancer treatment. *Int J Pharm* 573:118637. <https://doi.org/10.1016/j.ijpharm.2019.118637>
- Yan Q, Hoffman AS (1995) Synthesis of macroporous hydrogels with rapid swelling and deswelling properties for delivery of macromolecules. *Polymer* 36:887–889. [https://doi.org/10.1016/0032-3861\(95\)93123-4](https://doi.org/10.1016/0032-3861(95)93123-4)
- Yoo MK, Sung YK, Lee YM, Cho CS (2000) Effect of polyelectrolyte on the lower critical solution temperature of poly(Nisopropylacrylamide) in the poly(NIPAAm-co-acrylic acid) hydrogel. *Polymer* 41:5713–5719. [https://doi.org/10.1016/S0032-3861\(99\)00779-X](https://doi.org/10.1016/S0032-3861(99)00779-X)
- Zhang RS, Tang MG, Bowyer A, Eisenthal R, Hubble J (2005) A novel pH- and ionic-strength-sensitive carboxy methyl dextran hydrogel. *Biomaterials* 26(22):4677–4683. <https://doi.org/10.1016/j.biomaterials.2004.11.048>
- Zheng YT, Wang WF, Zhao JL, Wu CY, Ye CQ, Huang MX, Wang SG (2019) Preparation of injectable temperature-sensitive chitosan-based hydrogel for combined hyperthermia and chemotherapy of colon cancer. *Carbohydr Polym* 222:115039. <https://doi.org/10.1016/j.carbpol.2019.115039>

Inorganic Nanoparticles as Free Radical Scavengers



Adrian Fifere, Ioana-Andreea Turin Moleavin, Ana-Lacramioara Lungoci, Narcisa Laura Marangoci, and Mariana Pinteala

Abstract Inorganic nanoparticles have received special attention in recent years, mainly due to the interesting electronic properties of transition metals. Inorganic nanoparticles have redox, optical and magnetic properties that allow them to function as therapeutic agents and as diagnostic tools, leading to a theranostic approach of biomedical applications.

Oxidative stress is an imbalance between the production of reactive species and their overproduction due to disruptive factors, so that reactive species overwhelm the antioxidant defense of the human body. It can cause various pathologies, those related to inflammatory phenomena, cardiovascular problems and aging being notorious. Nanotechnologies can provide solutions in reducing oxidative stress at the systemic or targeted level, being known the applications of nanoparticles as targeted drug delivery agents.

Due to the incomplete electron-occupied *d* or *f* orbitals of transition metals, cumulated with crystalline defects, the inorganic nanoparticles had redox properties that allow them to be involved in biochemical redox processes. In this context, the up-to-date results regarding the obtaining and antioxidant activity of the nanoparticles with core-shell structure will be discussed here. The study will be done both from the perspective of the intrinsic activity of the inorganic core of the nanoparticles with core-shell structure, and of the activity added by the coating polymer layer, which may itself be active, or may contain antioxidants. A large part of this essay is

A. Fifere (✉) · I.-A. T. Moleavin · A.-L. Lungoci · N. L. Marangoci · M. Pinteala
Centre of Advanced Research in Bionanoconjugates and Biopolymers Department, “Petru Poni”
Institute of Macromolecular Chemistry, 700487 Iassy, Romania
e-mail: fifere@icmpp.ro

I.-A. T. Moleavin
e-mail: moleavin.ioana@icmpp.ro

A.-L. Lungoci
e-mail: lungoci.lacramioara@icmpp.ro

N. L. Marangoci
e-mail: nmarangoci@icmpp.ro

M. Pinteala
e-mail: mpinteala@icmpp.ro

dedicated to magnetic nanoparticles (MNP) with free radical scavenging properties. Two particular examples are discussed in details: magnetic nanoparticles as platforms for the transport and protection of natural antioxidants and MNP conjugated with nanoceria as synthetic inorganic antioxidants.

Keywords Reactive oxigene species · Antioxidants · Iron oxide · Cerium oxide · Magnetic nanoparticles

Abbreviations

SOD	Superoxide dismutase
CAT	Catalase
MNP	Magnetic nanoparticles
PEI	Polyethyleneimine
SBE β CD	Sulfobutyl ether- β -cyclodextrin
PCA	Protocatehuic acid
SBE β CD/PCA	Inclusion complex of sulfobutyl ether- β -cyclodextrin with protocatehuic acid
MPEI	Magnetite nanoparticles coated with branched polyethyleneimine
MPEI-PCA	Magnetite nanoparticles coated with branched polyethyleneimine and loaded with protocatehuic acid
MPEI-SBE β CD/PCA	Magnetite nanoparticles coated with branched polyethyleneimine and loaded with the sulfobutyl ether- β -cyclodextrin inclusion complex with protocatehuic acid
CeNP	Cerium oxide nanoparticles
CePEI	Cerium oxide nanoparticles coated with branched polyethyleneimine
CePEI-GA	Cerium oxide nanoparticles coated with crosslinked polyethyleneimine with glutaric aldehyde
MPEI-GA	Magnetite nanoparticles coated with glutaric aldehyde crosslinked polyethyleneimine containing active aldehyde groups
MCePEI-GA	Interconnected magnetite and cerium oxide nanoparticles of crosslinked polyethyleneimine with glutaric aldehyde

1 Introduction. Antioxidants and Prooxidants

The most important factors that govern the functioning of living organisms are the pH and the redox state. Both are closely correlated, so that the pH can be changed by redox transformations depending on their mechanism, while the pH can determine a specific reaction path that leads to a specific redox state. Therefore, acid–base and redox characterization of cell tissues becomes extremely important. Studies have shown that it is impossible to characterize a cell by a specific redox state or a specific pH. Thus, each cellular organelle or cell subdivision can be characterized by the parameters mentioned above, having extremely different values from other cellular or intracellular environment (Sies et al. 2017).

A decisive role in modulating cellular signaling processes is played by chemically unstable or metastable species, having an active atomic center or chemical group characterized by high reactivity, namely reactive oxygen species and reactive nitrogen species, abbreviated in the literature as ROS and RNS. Nowadays it has become more and more obvious that ROS and RNS not only model, but also constitute themselves into signaling molecules for the regulation of physiological processes (Sies and Jones 2020).

Molecular oxygen is gradually reduced in aerobic processes from zero oxidation state to -2 oxidation state. In the intermediate stages of the reaction occurs the most important range of radical ROS species, such as: $O_2^{\cdot-}$, $HO\cdot$, $HO_2\cdot$, H_2O_2 . It is accepted that mitochondria are the main cellular organs in which ROS are generated (Lenaz 2012; Drose and Brandt 2012).

ROS generated in living organisms can contain only paired electrons, such as: hydrogen peroxide (H_2O_2), organic hydroperoxides ($RCOOH$), ozone (O_3), singlet oxygen (1O_2 - electronically excited molecular oxygen), and excited carbonyl ($RCH = O^*$) which can transfer energy from O_2 to 1O_2 . Of higher importance are ROS in the form of free radicals, with unpaired electrons: superoxide anion radical ($O_2^{\cdot-}$), hydroxyl radical ($HO\cdot$), peroxy radical ($ROO\cdot$) and the radical alkoxide ($RO\cdot$).

The presence of external factors, such as temperature, intense physical activity, pollution/toxins, smoking, pathogens, alcohol, ionizing radiation, UV radiation, can cause disorders of normal metabolic processes. The stress caused to living organisms by external and internal factors lead to the augmentation of the ROS concentration above the limits of normal body functioning. This condition leads to undesirable phenomena that modify the cellular metabolism and determines the oxidative stress. The concept of stress appeared in 1936 with Hans Selye and was later developed, establishing a scale of oxidative stress that starts from physiological oxidative stress (eustres), to excessive oxidative stress and, to the extreme, toxic oxidative stress (distress) (Lushchak 2014; Yan 2014).

Oxidative stress is an imbalance between the production and accumulation of ROS and RNS in cells and their ability to inactivate reactive species using enzymatic or other redox reactions (Espinosa et al. 2020). Consequently, cell damage is produced by excess ROS, which can lead to various pathologies. Oxidative stress is correlated with the exacerbation of inflammatory phenomena and cardiovascular disease, in which

atherosclerosis plays a crucial role, being related to the oxidation of LDL and lipid peroxidation (Pizzino et al. 2017). Several studies show that tolerance to oxidative stress decreases dramatically with age due to reduced concentrations of antioxidant enzymes such as superoxide dismutase (SOD) and catalase (CAT) (Abete et al. 1999).

Since it has been established that oxidative stress plays an important role in the pathogenesis of many clinical conditions and aging, antioxidants play a key role in restoring redox balance in living organisms. The term antioxidant has a general meaning, being substances that inhibit the oxidation of a substrate (Halliwell and Gutteridge 1995) or has a kinetic effect of slowing down the oxidation reaction, ultimately (Halliwell 2007). Later, the meaning was expanded to substances that prevent or eliminate oxidative damage, directly ROS scavenges, able to regulate the defence against ROS or inhibit the natural production of ROS in the body (Khlebnikov et al. 2007).

The human body re-establishes the oxidative balance using a series of antioxidants with different structural complexity, including enzymatic antioxidants and non-enzymatic antioxidants, the last group being composed of small molecules, such as vitamins (Carocho and Ferreira 2013). Enzymatic antioxidants act specifically, some acting directly on ROS, eliminating them, while others act in a synergistic way, regenerating other antioxidants, such as glutathione reductase that regenerates glutathione or glucose-6-phosphate that regenerates NADPH.

Enzymatic antioxidants that directly inactivate ROS are made up of three enzymes, as it follows:

- Superoxide dismutase (SOD) - converts the superoxide anion to hydrogen peroxide;
- Catalase (CAT) - converts hydrogen peroxide into water and oxygen with remarkable efficiency;
- Glutathione peroxidase - reduces peroxides, decreasing lipid peroxidation and Fenton reaction levels.

Non-enzymatic endogenous antioxidants generally have low molecular weight molecules compared to enzymatic ones and act less specifically. This class includes: glutathione, vitamin A, coenzyme Q10, and uric acid.

Over time, humans have evolved to live in symbiosis with the environment. Therefore, due to the large number of antioxidants present in nature, natural antioxidants from the diet began to supplement or act synergistic with the endogenous antioxidants set forth above. The classes of natural antioxidants taken through diet are: phenolic acids, flavonoids, carotenoids and vitamins (Xu et al. 2017). Natural antioxidants are able to easily pass into oxidized forms in the process of reducing the oxidation state of ROS and inactivating free radicals (Choe and Min 2009).

Nanoparticles have aroused intense interest in the scientific world in the last ten years due to the combination of the native properties of ordinary materials, with high surface area at nanometric scale, which determine unique physicochemical properties. They can be classified into different categories, depending on the composition, structure, dimensions, shape and properties (Jeevanandam et al. 2018; Khan et al. 2019). Inorganic nanoparticles comprise metallic nanoparticles made of pure metals,

up to combinations of metals in the form of alloys, oxides or salts, transition metals offering a wide range of possibilities for obtaining nanoparticles with various tunable properties (Sytnyk et al. 2013; Lane et al. 2019). Transition metals are notorious in technical and biomedical applications due to the energy or electron transfer facilitated by partial occupied orbitals. The *d* and *f* orbitals from transition metals allow them to adopt a wide range of oxidation states into stable or metastable compounds. The existence of several oxidation states of the same metal that can coexist in the same compound suggests that inorganic nanoparticles, especially those of metal oxides, may be involved in redox reactions by which ROS or RNS can be inactivated. This process occurs due to the establishment of redox equilibrium between the upper and lower oxidation states of the metal ions in the nanoparticles. An intrinsic ability of inorganic nanoparticles to scavenge free radicals has been noted, with literature documenting this aspect in numerous particular cases (Kassem et al. 2020; Wang et al. 2019). Very often metallic nanoparticles and derivatives with some intrinsic biologic properties (antibacterial, antifungal or antioxidant) are coated with natural or artificial antioxidants (Chahardoli et al. 2020; Khalil et al. 2020). In most cases, the antioxidant activity of products of this kind with a core-shell structure increases significantly, proving much more efficient than in the case of exclusive use of the inorganic core (Shah et al. 2017; Swietek et al. 2019a). Bibliographic references in this regard indicate that these nanoparticles are more stable in water and biological fluids, with a reduced dimensional dispersion, which is very important for biomedical applications (Rao et al. 2019; Guerrini et al. 2018).

There are numerous essays describing individual problems of natural antioxidants, intrinsic inorganics antioxidants or nanoantioxidants with core-shell structure having an active shell. This review combines the available information on uncoated inorganic nanoantioxidants with those on core-shell coated nanoantioxidants based on natural antioxidants. The most recent results concerning antioxidant and prooxidant features of inorganic nanoparticles will create a picture with enough details to understand today's complex problems regarding the interaction of nanotechnologies with biomedical applications on ROS-associated diseases (Fig. 1).

Most of the papers develop in detail the characteristics of nanoantioxidants based on iron oxide nanoparticles with magnetic properties. Nanoantioxidants as magnetic nanoparticles are guided in the magnetic field, being targetable drug delivery agents with applications in medical imaging, so that they offer a teranostic approach (Richard et al. 2016; Dadfar et al. 2019) (Fig. 1). In this context, two types of magnetic nanoantioxidants containing natural and inorganic artificial antioxidants will be particularly described. In these sections are presented all the details concerning the synthesis strategies, morphology and results regarding the key features characteristics for magnetic nanoantioxidants.

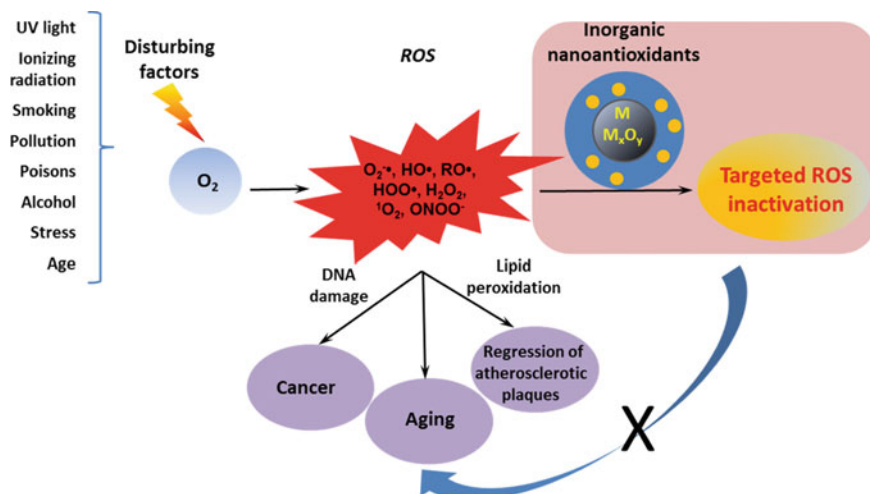


Fig. 1 General illustration of the motivation of using inorganic antioxidant

2 Inorganic Antioxidants

The importance of inorganic chemical elements in the control of redox balance in the human body is obvious taking into consideration two main factors: the ability of transition metals to adopt a whole range of oxidation states and the presence of transition metals and metalloids in enzymes responsible for establishing cell oxidative balance. These findings may lead to the idea that transition metals can restore redox balance on their own. However, minerals, in most cases, do not act directly on free radicals, being rather indispensable components of most antioxidant enzymes. Examples can be given by the most important representatives, zinc which is found in SOD, and selenium, which is found in glutathione peroxidase, or manganese found in many enzymes, such as CAT (Prasad et al. 2004; Tabassum et al. 2010). Magnesium is involved in many biological processes and clinical studies have shown that magnesium deficiency causes an increase in oxidative stress, which leads to oxidative changes in proteins and DNA, while reducing the body's ability to defend itself against oxidizing agents (Zheltova et al. 2016).

2.1 Metal-Based Nanoparticles as Inducers of Oxidative Stress

Mineral and inorganic compounds can form stable nanoparticles, their synthesis, physico-chemical and biological properties being intensively studied in the last decades (Domenico et al. 2019). Concerning the inorganic nanoparticles, toxic or

beneficial effects were observed in correlation with the redox properties, which led to the idea that inorganic nanoparticles decisively influence the change of the oxidative balance. In a suitable environment inorganic nanoparticles can produce ROS (Sarkar et al. 2014). Over time, the toxicity of oxide nanoparticles related to ROS production has been exploited for the development of nanoparticles with antitumor and antimicrobial effects (Vinardell and Mitjans 2015). Zinc oxide can induce ROS, especially if it is in an acidic environment, resulting in altered DNA (Hala et al. 2018). Toxicity related to ROS formation was also observed in copper oxide nanoparticles (Fahmy and Cormier 2009; Reddy and Lonkala 2019) or titanium oxide (Xue et al. 2010).

Iron oxide nanoparticles have multiple applications in medicine and are excellent candidates in theranostic applications. However, depending on the concentration, they can cause ROS through complex mechanisms in which iron participates at competing process such as complexation/chelation, affecting enzymatic factors, and reacting with prooxidants and hydrogen peroxide in Fenton-type reactions (Hayyan et al. 2016; Christina and Sedlak 2008). Robert J. Wydra *et al.* describe the acceleration of free radical formation of iron oxide nanoparticles when introduced into the alternating magnetic field, the discovery having potential applications in magnetic hyperthermia (Wydra et al. 2015).

Inorganic nanoparticles are often agents for the delivery of endogenous or exogenous natural antioxidants, with numerous reviewers documenting these applications (Boubbou Boubbou 2018; Palanisamyab and Wang 2019), this aspect being further developed in the following sections. In this context, it should be mentioned that, despite the fact that natural antioxidants have been designed by living organisms to reduce oxidative stress, there are certain conditions in which they can generate oxidative stress. Consequently, the use of natural antioxidants as therapeutic drugs loaded onto inorganic nanoparticles must be done responsibly, because under certain conditions they can have antagonistic effects, acting as oxidants, or favouring oxidation reactions. Chemical species that induce oxidative stress by favoring the formation of reactive species (ROS or RNS) or inhibiting the antioxidant system are called prooxidants (such as O_2 , H_2O_2 , Fe^{3+} etc.).

Despite the fact that polyphenols are among the most effective natural antioxidants, there are a large number of representatives in this class that can act as prooxidants under certain conditions (Jomov et al. 2019; Yordi et al. 2012). Degeneration of phenols from antioxidants to prooxidants may be favored by other prooxidants or the presence of transition metals. An example is the presence of molecular oxygen and iron or copper, which will catalyze the formation of phenoxyl radicals able to oxidize biological molecules, altering DNA structure (Galati and O'Brien 2004).

Vitamins are notorious antioxidants but can become prooxidant under certain conditions. For example, ascorbic acid inactivates radicals, becoming a less active radical, being deactivated by supplementation with other amounts of ascorbic acid or other antioxidants. If not inactivated, the resulting radical is sufficiently reactive to promote linoleic acid self-oxidation (Cillard et al. 1980). Vitamin C can also react with copper or iron, reducing them to lower oxidation states, which can further contribute to secondary reactions of hydroxyl radical formation by Fenton-type reactions (Duarte and Lunec 2005).

2.2 Inorganic Nanoparticles as Radical Scavengers

Metallic nanoparticles and their oxides under specific conditions and in suitable quantities can inactivate ROS efficiently, having intrinsic antioxidant properties. This property does not depend on the functionalization of the particles, but on the surface properties related to oxidation state of the metals, crystalline structure and defects. Given the complex relationship between structure and function of the inorganic nanoparticles, especially in metallic oxides, they can inactivate free radicals by mimicking the endogenous antioxidants of the human body. Oxides of cerium (CeO_4) (Baldim et al. 2018), cobalt (Co_3O_4) (Dong et al. 2014) in the form of nanoparticles, as well as a number of metallic nanoparticles such as platinum, gold deposited on platinum, manganese oxides (Mn_3O_4) (Waldo and Penner-Hahn 1995) can mimic the activity of CAT to decompose the hydrogen peroxide in water and molecular hydrogen.

The process is pH dependent, being favoured by high pH, while low pH can determine a prooxidant activity of nanoparticles, in which hydrogen peroxide undergoes a redox process of decomposition into hydroxyl radicals and hydroxide ions. The mechanism of antioxidant action of metal oxide nanoparticles is related to the exchange between two oxidation states of the metal, such as cerium oxide nanoparticles, in which cerium is in a state of oxidation +4 in bulk, while on the surface there are defects with Ce^{3+} , responsible for antioxidant activity. Cerium-based nanoparticles (CeNP) are excellent antioxidant agents that mimic the activity of SOD, along with zirconium oxide (ZrO_2), Co_2O_4 (Guo et al. 2020) and Mn_3O_4 (Singh et al. 2017). Nanometals such as palladium (Ge et al. 2016) and platinum (Liu et al. 2014) can successfully mimic the SOD activity.

2.3 Coated Inorganic Nanoparticles as Nanoantioxidants

Metal nanoparticles and their oxides are excellent drug delivery agents, because they are stable, can be functionalized and have small and controllable dimensions. In addition to the intrinsic properties of inorganic nanoparticles, other interesting properties are added by the coating with natural and synthetic polymers (Lungoci et al. 2018).

The addition of antioxidants on the surface of nanoparticles obviously modifies the intrinsic antioxidant activity, improving it. At the same time, the antioxidant activity of the natural antioxidant deposited on the surface of the nanoparticles can be modified, attenuated or can become selective. For example, silica nanoparticles were easily coated with caffeic acid in core shell structures, protecting caffeic acid from the degradative action of external factors (Arriagada et al. 2019). The results showed that free radical scavenging activity of caffeic acid was attenuated, increasing the chelating capacity of Fe^{2+} ions and the ability to inactivate singlet oxygen. Similar results were obtained by Deligianakis *et al.* by chemical grafting of gallic acid on the

surface of SeO_2 nanoparticles (Deligiannakis et al. 2012). *In the same vein, it has been noted that antioxidants can be degraded on the surface of metal oxides where they have been deposited. Through this redox process, the degradation of nanoparticles can be achieved by changing the oxidation state of the transition metals, modifying the surface properties.* This statement can be suggested by the catalytic properties of metal nanoparticles that can lead to degradation reactions (Bhatia et al. 2013), such as zinc oxide (Kumar et al. 2014a), titanium oxide (Him et al. 2019), cobalt oxide (Adekunle et al. 2020; Saravana et al. 2020), redox processes established between cerium nanoparticles and polyphenols being also documented (Andrei et al. 2016; Hayat et al. 2014).

Nanoparticles coated with pure natural antioxidants, mixtures of antioxidants or natural extracts have remarkable antioxidant activity, to which is often added antimicrobial activity. Therefore, Sutradhar *et al.* synthesized aluminum dioxide nanoparticles coated with coffee extract (Sutradhar et al. 2014), while Ansari *et al.* obtained Al_2O_3 nanoparticles using *Cymbopogon citratus* leaf extract. In both cases the stability of Al_2O_3 nanoparticles increased, adding new antioxidant properties (Ansari and Khan 2015). Metal oxides based on transition metals, such as Fe, Co and Ce were synthesized in the presence of natural extracts, in which the natural extract has a double role: acts as a reducing agent and stabilizes the colloidal suspension of nanoparticles, reducing aggregation. Most natural extracts used for this purpose are of the polyphenols type, which offer excellent antioxidant and antimicrobial properties.

Metallic nanoparticles are generally subject to oxidation, being less stable, except for noble metals (Auffana et al. 2009). There are numerous reports in specialized journals on the synthesis of metal nanoparticles where their surface is passivated by natural extracts (Jurasin et al. 2016). For example, since gold nanoparticles can be easily synthesized due to their high ability to reduce the oxidation state from auric salts, they can be easily precipitate as nanoparticles from many synthetic and natural antioxidant, resulting in core-shell structures. Abdulrahman M. Elbagory *et al.* synthesized particles with different morphology and different sizes using 17 different plant extracts (Elbagory et al. 2016). Palladium nanoparticles were synthesized in the same manner using *Evolvulus alsinoides* leaf extract (Gurunathan et al. 2015) or *Gardenia jasminoides* extract (Jia et al. 2009) and copper nanoparticles, using *Labeo rohita* extract (Sinha and Ahmaruzzaman 2015).

A particular attention is paid to silver nanoparticles (AgNP). The use of silver as a microbial agent dates back more than 4,000 years, where silver-based products were used by ancient peoples as eating utensils, food storage or drinking tools. The mechanism of antimicrobial action of silver is still under debate, but enough data is known so that a picture can be provided. The mechanism is connected with the reactivity of silver with thiols, which can block certain enzymatic pathways by binding silver to sulfur-containing amino acids such as cysteine (Jung et al. 2008). Anna Kedziora *et al.* make an interesting comparison between the action of Ag^+ and AgNP in terms of antibacterial activity (Kedziora et al. 2018).

AgNP synthesis involves the use of surfactants with reducing character in order to reduce the oxidation state of silver cations and to regulate their dimensions. Being a

noble metal, the oxidation state of silver is easily reduced, so that natural extracts are excellent reducers of Ag^+ to Ag^0 in AgNP synthesis by green chemistry methods. Plant-based synthesis methods involve mixing a plant extract with an aqueous solution of a metal salt. This process takes place at room temperature, requiring a few hours to complete in non toxic milieu. The main mechanism is the reaction mediated by some phytochemicals, such as terpenoids, flavones, ketones, aldehydes, amines and carboxylic acids involved in the reduction of silver ions (Souza 2019).

The advantage of AgNPs obtained with natural products is obvious, but the most important is the fact that natural extracts bring with them additional antioxidant and antimicrobial properties, given that silver is not an intrinsic antioxidant. Among many others, Andreia Corciova and coworkers undertook extensive studies regarding the antioxidant and antimicrobial activity of AgNP coated with natural products. Thus, AgNPs coated with *Phyllanthus amarus* extract have antioxidant properties due to components such as p-coumaric, ferulic acid, isocvercitrin, cvercitrin, rutoside, hispidulin, stigmaterol, beta-sitosterol and campesterol (Corciova et al. 2018a). The products have been shown to be effective against *Staphylococcus aureus* and *Pseudomonas aeruginosa*. *Tilia cordata* led to the production of AgNP with a yield and size modulated by the amount of extract (Corciova et al. 2018b). The *T. cordata* extract have remarkable antioxidant properties, with antimicrobial activity against a wide palate of microorganisms, such as: *S. aureus*, *E. coli*, *P. aeruginosa*, *Candida albicans* and *Candida parapsilosis*, the last two being fungal strains. Similar results were obtained with bee propolis extract, the resulting nanoparticles also having photodegradation properties (Corciova et al. 2019a). Licorice extract led to obtaining AgNPs whose antioxidant properties were better than those of the original extract (Corciova et al. 2019b).

3 Magnetic Nanoparticles as Tools in Biomedical Applications for Reducing Oxidative Stress

Magnetic nanoparticles have supported the interest of researchers in recent years, today being the most important transport agents of inorganic core drugs, many reviews in the field documenting this fact (Thomsen et al. 2015; Price et al. 2018). Their special properties are primarily related to the existence of paramagnetic atoms that confer magnetism to magnetic nanoparticles. The magnetism of the nanoparticles makes them temporally and spatially guided in the magnetic field, being guidable in the human body, which is the golden key in the field of targeted drug delivery agents. Therefore, in addition to the targeting selectivity offered by dimensional or functional segregation, magnetic nanoparticles can be literally forced by a magnetic field with the right power and orientation, to focus on the desired place. Additionally, the magnetic properties allow them to be applied in magnetic resonance imaging (MRI) by scanning longitudinal time (T1) and transverse relaxation time (T2). Among the most important nanoparticles of metal oxides used as contrast agents in the field of

medical imaging are those based on iron oxides (Na et al. 2009; Ni et al. 2017). Iron oxides include hematite ($\alpha\text{-Fe}_2\text{O}_3$), byxbyite ($\beta\text{-Fe}_2\text{O}_3$), maghemite ($\gamma\text{-Fe}_2\text{O}_3$), $\epsilon\text{-Fe}_2\text{O}_3$ wustite (Fe-O) and magnetite (Fe_3O_4). Of all the forms of iron oxides, the most studied nanoparticles for applications in medical imaging are magnetite nanoparticles with inverted spinel crystal structure (Marashdeha et al. 2019). Also, the magnetic properties allow them to heat up in alternative magnetic fields, making them suitable in hyperthermic cancer therapy (Giustini et al. 2010).

Undoubtedly, the chemical functionality offered by functional groups -OH on the surface of magnetic nanoparticles is very important since these chemical groups show reactivity with organic compounds. Magnetic nanoparticles with a core-shell structure are nanostructured materials stabilised by chemical and physical bonds, as illustrated in Fig. 2. Mariana Pinteala and collaborators had remarkable results in terms of the synthesis of magnetite nanoparticles with a core-shell type structure where most of the strategies to stabilise nanoparticles illustrated in Fig. 2 were applied. Thus, it was possible to obtain organotryethoxysilanes coated nanoparticles (Durdureanu-Angheluta et al. 2008) or amphiphilic polymers based on siloxanes (Pricop et al. 2010; Durdureanu-Angheluta et al. 2010), the synthesis and properties of nanomagnetite functionalized with amino groups were studied in detail (Durdureanu-Angheluta et al. 2012). Advanced nanoparticles with anticoagulant properties were obtained (Durdureanu-Angheluta et al. 2014a), grafted with enzymes (Durdureanu-Angheluta et al. 2014b), having remarkable properties with a saturation magnetization of over 50 emu/g.

In view of the above, magnetic nanoantioxidants are formed in most cases from metal oxide nanoparticles based on iron, nickel, cobalt, manganese and other paramagnetic transitional elements. Although, as previously seen, even though metal oxides of the MNP may have intrinsic antioxidant properties, it is preferable to use core-shell

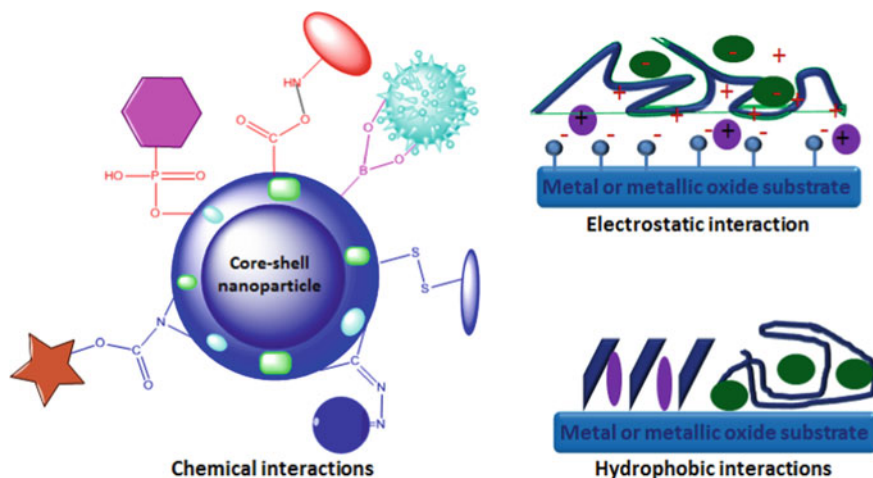


Fig. 2 Connections made to the functionalization and coating of core-shell nanoparticles

nanoparticles in medical applications instead of naked nanoparticles. Nanoparticles coated with antioxidant polymers or antioxidant active substances offer several main advantages: drastically reduce aggregation phenomena, significantly increase the antioxidant effect and reduce cytotoxicity.

An important class of MNPs with antioxidant activity is that of nanoparticles coated with natural polymers, synthesized using green chemistry methods. Natural polymers reduce the number of toxic reagents used in synthesis because they can act as active reducing agents in the nanoparticle formation, confer new functions or accentuate existing ones, simultaneously with the coating and protecting metal oxide surfaces, serving as dimensional control agents. For example, MNPs were synthesized at room temperature in the presence of green tea leaves (*Camellia sinensis*), where the resulting polyphenols showed active reducing properties in the iron oxides formation (Hoag et al. 2009; Nadagouda et al. 2010). The extensive study of MNP coated with green tea extract showed that in addition to the characteristic functions of polyphenols, the surface properties of the metal oxide of the core are also preserved. Therefore, the coated MNP can participate in degradation processes through Fenton-type reactions (Shahwan et al. 2011; Kuang et al. 2013). Consequently, there is a dual activity of MNP coated with natural polymers, characteristic of polymers and the oxide nature of the magnetic core. Another advantage of these nanoparticles is the antimicrobial effects, acting against a whole range of pathogens, such as *S. aureus* and *Bacillus subtilis*, having antifungal effects, against *Mucor piriformis* and *Aspergillus niger* (Gautham et al. 2019; Amutha et al. 2018).

3.1 Magnetic Nanoantioxidants Based on Phenolic Acids. Magnetic Nanoparticles Loaded with Protocatechuic Acid

In the great diversity of core-shell MNP with antioxidant properties relatively few studies are with MNP loaded with small molecule natural antioxidants such as phenolic acids, flavonoids or carotinoids, most reports focusing on natural polymers from extracts of plants. Regarding the phenolic antioxidants, they can be anchored to MNP by chelating the iron ions in the crystal lattice on the surface through phenolic and carboxylic groups, in a manner similar to that presented in Fig. 2. In this respect, ortho-phenolic groups have defined a universal method of functionalization of metallic oxide surfaces based on catecholic chemistry (Amstad et al. 2009; Guenin et al. 2014). In regard to this manner, Jun Lee and coworkers functionalize superparamagnetic oxide nanoparticles (SPION) with folic acid (Kim et al. 2016). The authors linked folic acid to caffeic acid through a polyethylene glycol spacer, and finally, caffeic acid to MNP via catecholic groups, demonstrating the feasibility of this system. The resulting product can be used in MRI, having also antitumor properties (Alpsoy et al. 2017).

MNPs may exert a stabilizing effect on antioxidants incorporated into coating polymers. For example, gallic acid was loaded on chitosan-coated MNP leading to

increased thermal stability of the antioxidant (Dorniani et al. 2012). The final product has high anticancer activity, studied on the HT29 and MCF7 cell line, but the authors did not study the antioxidant effects of nanoparticles. Later, in 2017, T. Sayed *et al.* (Shah et al. 2017) directly attached gallic acid to the surface of the fiber nanooxides and obtained low-sized MNP, with gallic acid acting as a surfactant. The study showed a remarkable antioxidant activity, 2–4 times higher than the intrinsic activity of MNP, adding an antimicrobial activity. Two synthesis methods were adapted in this work, the *in-situ* addition of gallic acid and the addition of gallic acid after the synthesis of uncovered MNP.

Comparing the studies with antioxidant-coated MNPs loaded directly on the surface with those in which antioxidants are loaded on polymer-coated MNPs (dextran, chitosan, synthetic polymers) the latter become predominant. In this context, most of the published works studied biomedical applications from the perspective of various pathologies and less the antioxidant effects. In an early example, quercetin, a very important representant of natural antioxidants, is loaded on dextran coated MNP demonstrating anticancer activity against MCF7 cells (Kumar et al. 2014b). Later, Elnas Amazadeh and co-workers use the same synthetic pathway to obtain quercetin loaded iron oxide nanoparticles to obtain drugs useful in memory health (Amanzadeh et al. 2019). The antioxidant properties of this system are studied by Sayed Tawab Shah *et al.* (Shah et al. 2017) by adopting a modified synthesis method, linking quercetin to MNP through the catecholic arrangement. The authors show by the DPPH test the significant activity of quercetin-conjugated MNP, 2–3 times higher than the intrinsic activity characteristic of uncovered iron oxide nanoparticles.

An interesting study is undertaken by covering MNP (γ -Fe₂O₃) with heparin, a polysaccharide anticoagulant, without antioxidant properties (Swietek et al. 2019b). These products are compared with chitosan-coated MNPs loaded with several types of phenolic antioxidants (gallic acid, hydroquinone and phloroglucinol). In this paper, tests of antioxidant effects were made with the DPPH method showing the efficiency of nanoparticles conjugated with phenolic antioxidants and the obvious lack of antioxidant activity of MNP loaded with heparin. Due to the fact that heparin allows a higher cellular uptake, MNP that combines the effect of heparin and antioxidants become promising tools for biomedical applications.

The above mentioned studies demonstrate the versatility of MNP as drug delivery agents when coated with antioxidant-loaded polymers compared to those with phenolic antioxidants deposited directly on their surface. In the latter case, the phenolic functional groups of antioxidants are binding elements with nanoparticles, with the possibility of reducing their efficiency. Other advantage to choose nanoparticles coated polymers in order to load antioxidants is given by the bioavailability conferred by the coating polymers and the possibility of releasing the antioxidants in a controllable manner (Ayyanaar et al. 2020). In this context, an extensive study was made by the group M. Pinteala and collaborators on nanostructured magnetite with core-shell structure loaded with protocatechuic acid (PCA), so as to preserve the magnetic and antioxidant properties, and to add other interesting properties from a biological point of view (Lungoci et al. 2019). In this work the authors present the results obtained from the synthesis and characterization of some MNP coated with

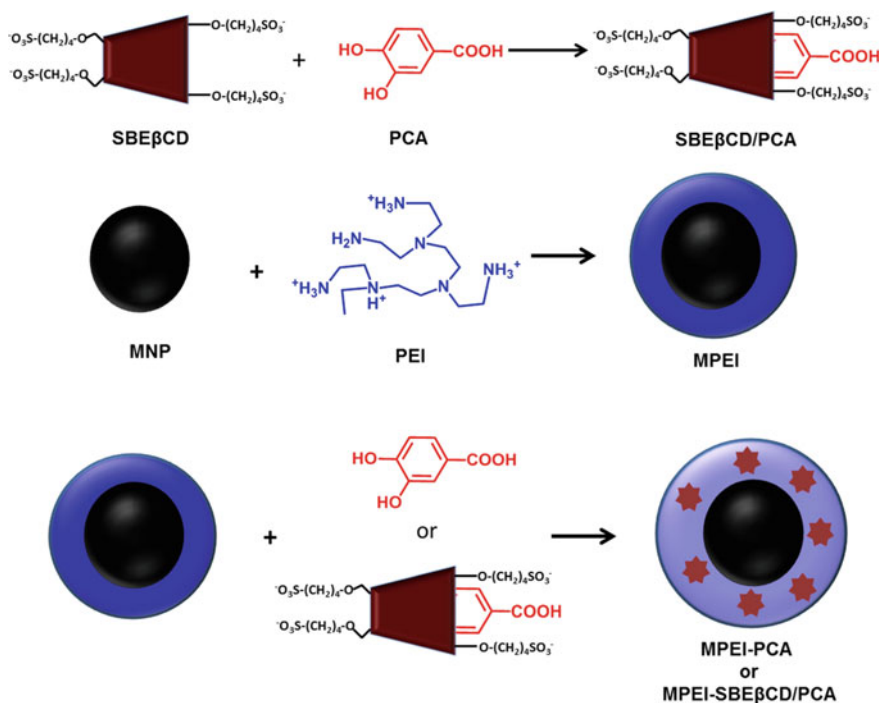


Fig. 3 Schematic representation of the synthesis of SBEβCD/APC, MPEI, MPEI-APC and MPEI-SBEβCD/APC

PEI (MPEI) with free radical scavenging properties due to the loading with natural antioxidants (Fig. 3). *The objective of this study is part of a general objective of group M. Pinteala to obtain MNPs loaded with natural and inorganic antioxidants as adjuvant therapy in percutaneous coronary interventions in atherosclerosis therapy. Oxidative stress and endothelial dysfunction in the blood vessel are thought to cause restenosis after a certain period of application of the metal stent, a process that can be delayed or even stopped by the local use of antioxidant therapies capable of capturing and inactivating free radicals.*

PEI used to coat MNP in this study is a polymer whose behaviour related to cytotoxicity is well known since this polymer is often used in transfection studies, to deliver gene intracellularly (Uritu et al. 2015; Ardeleanu et al. 2018). It was chosen to coat MNP due to its polycationic character which favors the electrostatic binding to negatively charged surface of the nanoparticles (Fig. 4). In addition, PEI shell of MPEI facilitates the incorporation of any negatively charged compounds (therapeutic agents) and their subsequent release *in vivo* in specific conditions. The therapeutic agent considered in this paper is PCA which has the role of reducing oxidative stress in tissues. The stabilization of the nanooxidant takes place through the interaction of PCA with PEI, due to the acid-base dissociation of PCA which results in the formation of negative species able to develop electrostatic attractive forces with the

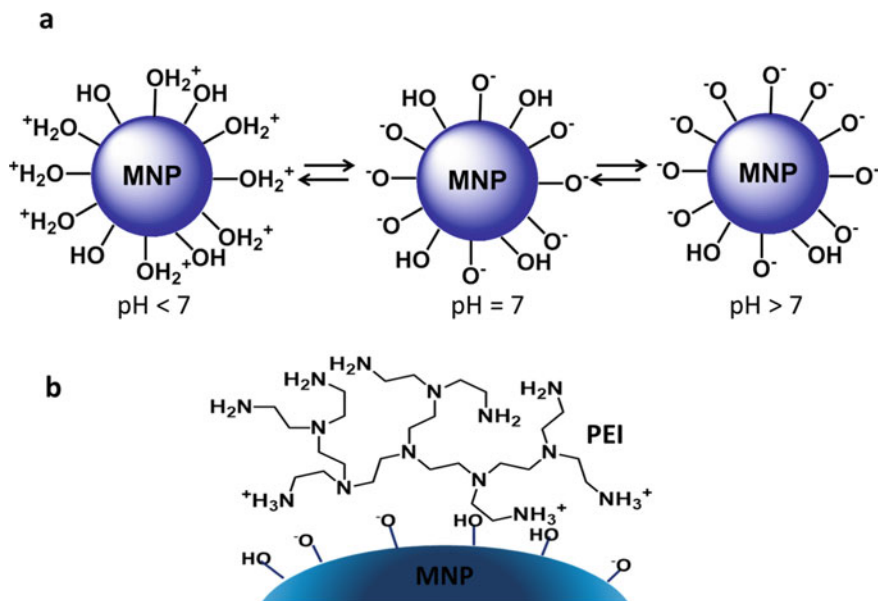


Fig. 4 Illustration of chemical processes on the MNP surface as a function of pH (a) and interactions between PEI and MNP (b)

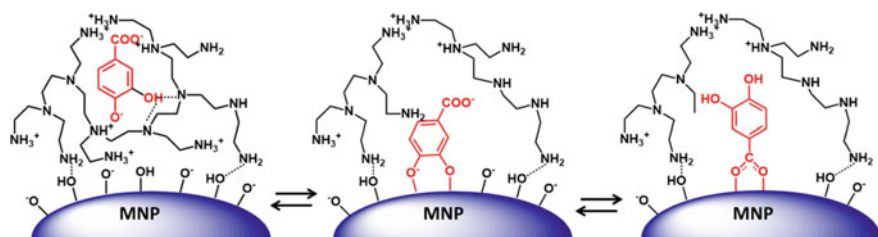


Fig. 5 Illustration of possible interactions between PCA and MPEI nanoparticles

PEI layer (Fig. 5). The attraction interactions that are established between MPEI and PCA can take other forms, also, due to the complexation of iron atoms by means of hydroxyl or carboxylic groups, as illustrated in Fig. 5. These processes can occur at the interaction of any polyphenolic compound with MNP coated with PEI or other polication, such as chitosan. Therefore, MPEI loaded with PCA (MPEI-PCA) are considered a particular model for MNP loaded with any natural phenolic acid.

PCA is a polyphenol extracted from various exotic herbs (*Hibiscus sabdariffa*). It has antioxidant and anti-inflammatory effects and is protective against changes induced by various toxins in the liver; the literature also attests various antitumor effects, especially in the case of leukemia (Anter et al. 2011). The mechanisms

behind its antioxidant activity are the chelation of metal transition ions, as well as the inactivation of free radicals by changing hydrogen atoms (H) or electrons (e).

In the same study of MPEI loaded PCA, MPEIs loaded with an inclusion complex formed between sulfobutyl ether β -cyclodextrin (SBE β CD) and APC (SBE β CD/APC) were also taken into account; the resulting magnetic nanoparticles were denoted by MPEI-SBE β CD/PCA. Inclusion in cyclodextrins can increase the stability of various therapeutic agents and improve their bioavailability by increasing solubility in aqueous media. SBE β CD is negatively charged when dissociate in water, since it has ionic groups $-\text{SO}_3^-$, which facilitates the absorption in the PEI polycation layer covering the magnetite, in the same manner as PCA. The embedding efficiency of MPEI was measured and 56% was obtained for PCA and 44% for the SBE β CD/PCA inclusion complex, highlighting an increased efficiency of MPEI in uncomplexed PCA absorption compared to that complexed with SBE β CD.

The advantage of the synthesis of MNPs coated with inclusion complexes formed with cyclodextrins is given by the fact that by complexing with cyclodextrins, MNP can be loaded with classes of water-insoluble antioxidants, such as carotenoids (Oliveira et al. 2011), that are normally fat-soluble or in other hydrophobic solvents. *Therefore MNPs covered with PEI are true delivery platforms for hydrophilic and hydrophobic natural antioxidants.*

The size and shape of such nanoparticles could vary due to the coating polymer, but also to the embedded therapeutic agents, as the electrical charge and molecular volume of the PCA and the inclusion complex vary widely. The analysis of TEM images shows that MNP have an average diameter of 7.5 nm, having a uniform spherical shape. Coating MNP with PEI and loading with APC or SBE β CD/PCA inclusion complex did not alter the spherical shape of the final conjugates, but led to a subtle increase in mean diameter (7–13 nm). Being a supramolecular compound, obviously the molecular volume of the SBE β CD/APC inclusion complex is larger than that of the APC. Therefore the diameter of the conjugates is correlated with the molecular volume of the chemical species loaded in the coating layer of the nanoparticles.

In aqueous solution the dimensions of the nanoparticles change due to the solvation of the coating polymers. Dimensional analysis in aqueous solution shows that MNPs have a hydrodynamic diameter of 480 nm in water; while the Zeta potential indicates a negative value of -24 mV at pH 11 and -1 mV at pH 7 (see Fig. 4 for explanations). By coating the magnetic nanoparticles with PEI is promoting an increase in hydrodynamic diameter to 690 nm due to solvation and spatial expansion in water of PEI chains. Due to the ionization of amino groups in water by acid–base processes, the PEI layer gives MPEI nanoparticles a high positive potential ($+40$ mV). Loading MPEI with the SBE β CD/APC leads to a decrease in the hydrodynamic diameter from 690 to 573 nm of the MPEI-SBE β CD/APC nanoparticles due to the compensation of the electrical charges of the PEI with the negative ones from SBE β CD/APC. Therefore, the folding process of the inclusion complex in the PEI shell leads to an effect of packaging and compaction of the polymeric coating layer.

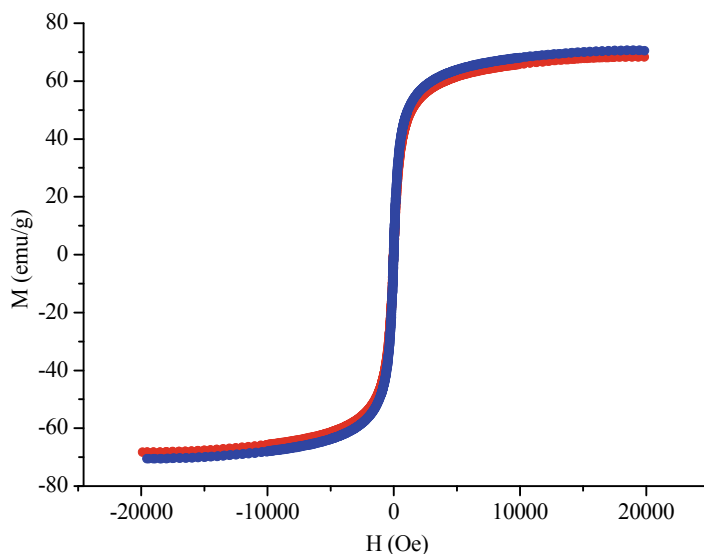


Fig. 6 Magnetization curves of MNP (blue) and MPEI (red)

Having a magnetite core, the studied nanoparticles have magnetic properties, the magnitude of the magnetization offering an estimate of the applicability of these nanosystems in the expected biomedical applications. The saturation magnetization is about 70 emu/g, specific for uncovered MNP. Low values of saturation magnetization and magnetic coercivity make the hysteresis effect almost imperceptible, suggesting that nanoparticles have superparamagnetic properties (Fig. 6). It is interesting to note that when MNP are coated with PEI (MPEI), the value of saturation magnetization is close to the value of uncovered nanoparticles, which makes them very important for biomedical applications (Laurent et al. 2014; Viota et al. 2013).

Free radical scavenging capacity was tested by the DPPH method which showed that nanoparticles loaded with free APC or included in SBE β CD have excellent antioxidant properties (Fig. 7). In the low concentration range, the ratio of MPEI-APC free radical inhibition capabilities to MPEI-SBE β CD/APC shows that MPEI-APC is more effective.

PCA from nanoparticles exhibit its antioxidant activity when encapsulated PEI layer of MPEI, but probably is released first in water and then participate in the redox reaction. MPEI release profiles loaded with free PCA or inclusion complex show preservation of PCA release rate from MPEI-PCA and MPEI-SBE β CD/PCA for three days (Fig. 8).

Antioxidant release was slower from MPEI-SBE β CD/PCA than from MPEI-PCA, since electrostatic interactions between polyethyleneimine and APC or SBE β CD/PCA are different. The different release rates may be due to differences in the diffusion coefficients of PCA and SBE β CD/PCA in the PEI layer. This observation is supported by the lower embedding efficiency of SBE β CD/PCA than APC

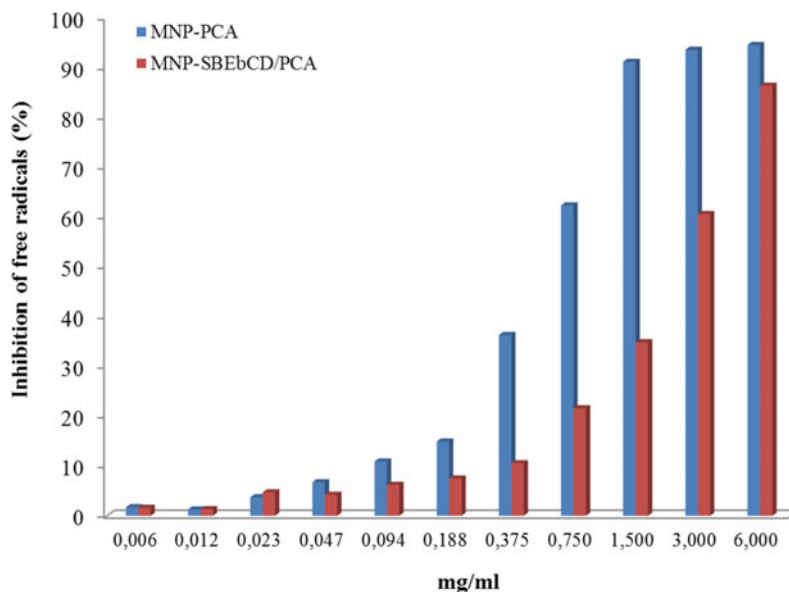


Fig. 7 The antioxidant activity of APC loaded on MPEI in various formulations by the DPPH method

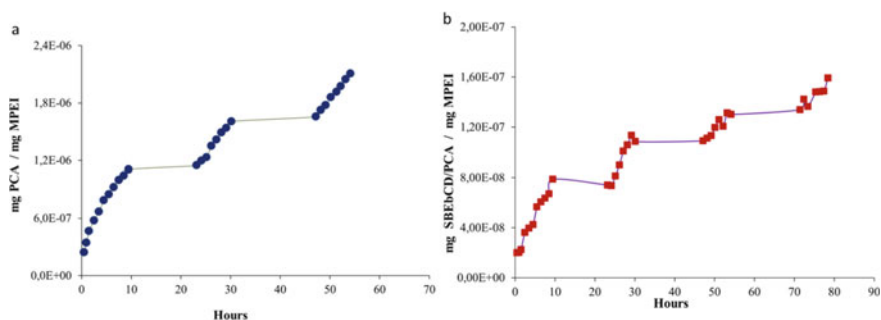


Fig. 8 Controlled release curves for **a** MPEI-APC and **b** MPEI-SBEβCD-APC

in MPEI. On the other hand, there may be different release mechanisms. Thus, SBEβCD/PCA may decompose in a first step, followed by the release of PCA or the inclusion complex may first be released followed by the release of APC from the SBEβCD cavity, which greatly complicates the release kinetics of SBEβCD/PCA.

In conclusion, core-shell systems based on PEI-type coating polymers can offer multiple opportunities by loading with antioxidants having very different physico-chemical properties in terms of polarity and electrical charges due to the involvement of modified cyclodextrins able to facilitate interactions between antioxidants

and PEI layer. Through this approach, the release of antioxidants from nanoparticles and antioxidant properties can be modulated, creating the possibility of using two or more antioxidants with different physicochemical properties, which interact synergistically.

3.2 Two Types of Metallic Oxide in One Magnetic Nanoantioxidant. Magnetic Nanoparticles Conjugated with Cerium Nanoparticles

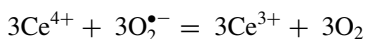
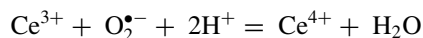
A very interesting topic is the conjugation of two types of metal oxides having complementary functions necessary for certain biomedical applications. There are two key approaches to this. One involves obtaining hybrid nanoparticles containing two distinct solid phases (mixtures of oxides or nanoalloys), and the second involves obtaining a type of nanoparticles decorated with the second type. Of course, if we refer to nanostructured materials, there is also the approach of nanocomposites, but this topic is beyond the subject of this review.

A pleiada of hybrid nanoparticles were obtained where nanoparticles formed of one type of metal oxide were coated with a layer of the second type of metal oxide (Anzorena et al. 2019; Pham et al. 2020). In most cases, the principle of synthesis consisted in obtaining the first type of nanoparticles that represented the seeds of crystallization in the second stage of synthesis, when is crystallized the second solid phase, obtaining inorganic core-shell particles.

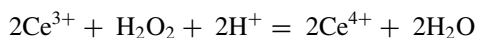
Regarding magnetic nanoantioxidants, no hybrid nanoparticles based on iron oxide have been obtained so far, to study in detail both magnetic and antioxidant properties in order to evaluate these nanostructured systems as potential tools in biomedical applications. In this regard, very recently significant progress has been made using the second approach, where core-shell nanoparticles decorated with the second type of nanoparticles are obtained. One of the most recent reports is by Hang T. Ta *et al.* which obtained CeNP-conjugated MNPs where poly(acrylic acid) ensures the integrity of the nanoaggregate by physical forces (Wua et al. 2018). Due to the coating with poly(acrylic acid) able to dissociate in water, the nanoparticles have a high negative Zeta potential, up to -56 mV, which suggests a high stability. The authors study in detail the activity of ROS inactivation, a characteristic of CeNP, and correlate with Ce^{3+} concentration. Also, nanoparticles are good contrast agents in MRI due to MNP, proving the teranostic potential of such products. Regarding the magnetic properties, the saturation magnetization, or the variation of this parameter at the transition from MNP to the CeNP conjugate, was not measured. These parameters help to estimate the guidability in magnetic field of such nanoaggregate.

Cerium oxide nanoparticles have aroused great interest in recent days in biomedical applications related to its redox properties. Nanoceria is known in the literature for its antioxidant activity, having an enzymatic activity that mimics the activity of superoxide dismutase, catalase, phosphatase, oxidase or peroxidase. Antioxidant

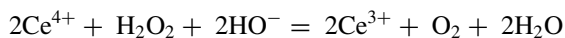
and catalytic properties are correlated with oxygen deficiency in the surface crystal lattice, leading to the existence of two oxidation states, Ce^{3+} and Ce^{4+} , onto CeNP (Baldini et al. 2018). Ce^{3+} on the surface of nanoparticles is correlated with the increased number of crystalline defects or oxygen vacancies, leading to an increase in the specific surface area and of ROS quenching capability (Charbgoon et al. 2017). In this context, the redox process evolve so that the Ce^{3+} ions undergo oxidation reactions in the presence of radical species, reducing the oxidation state of the ractive species (Patel et al. 2018). Through this CeNP mechanism they can fulfill the function of the SOD enzyme:



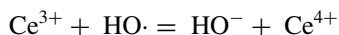
Among other things, the importance of using CeNP lies in their ability to regenerate their active centers by transforming oxygen peroxide, in a manner similar to the CAT enzyme (Reed et al. 2014):



These processes seem to be in competition, the reaction pathway being correlated with the concentration of Ce^{3+} at the surface of the nanoparticles, so that at a lower ratio of $\text{Ce}^{3+}/\text{Ce}^{4+}$ dominates the CAT specific catalytic activity, to which can be added the reaction (Celardo et al. 2011; Nelson et al. 2016):



Furthermore, it has been observed that CeNP can also inactivate $\text{HO}\cdot$ radicals that have high reactivity (Karakoti et al. 2008; Ivanov et al. 2009):



In the above reactions, trivalent and tetravalent cerium ions are not dissociated in solution, they are anchored in the crystal lattice of oxides in nanoparticles.

Very recently, a different approach from Hang T. Ta et al. is that of the M. Pinteala group, in which MNPs conjugated with CeNP are obtained by means of crosslinked polymers, this time ensuring the integrity of the nanoaggregate by chemical forces (Turin-Moleavin et al. 2019). The nanoparticles were coated with PEI, considering that this polymer is a polyamine with multiple possibilities of chemical functionalization through specific reactions of amines that can be easily and rapidly crosslinked with monomers such as dialdehydes. This synthesis strategy is more versatile than

MNP coated with the oxides of another metal, because, theoretically, it can interconnect any type of different metal oxides. As previously discussed, such a nanoconjugate is a hybrid nanocomposite, where the constituent nanoparticles can individually perform their function of interest.

The aim of this study was to design a nanostructured system capable of delivering antioxidant chemical species in a pharmacologically controlled and spatially guided manner MNP magnetic nanoparticles coated with PEI and conjugated with CeNP were synthesized, resulting in systems with antioxidant and magnetic properties. The involvement of MNP in the design of these nanostructured systems is intended to provide additional functionality, making them able to be guided in the magnetic field and visualized by imaging methods, such as medical nuclear magnetic resonance, determining a teranostic approach.

The synthesis strategy adopted involved the initial synthesis of PEI coated CeNP stabilized by physical bonds (CePEI), followed by chemical crosslinking of PEI with glutar aldehyde (CePEI-GA). MPEI activated with glutar aldehyde was also synthesized; whose reactive carbonyl groups were reacted with CePEI in order to obtain the hybrid MNP-CeNP conjugates further abbreviated MCePEI-GA as in Fig. 9.

These types of nanoparticles can have various shapes and sizes. The morphology was studied with TEM, whose images show a matrix composed of spherical nanoparticles, with a small diameter, ranging from 7–8 nm. It should be noted that the TEM images cannot discriminate between MNP (7 nm) and CeNP (5 nm), the average diameter of MCePEI-GA nanoparticles being approximately 8 nm. It can be concluded that MCePEI-GA is not composed of MPEI nanoparticles decorated with CePEI-GA-PEI, these being rather formed by a polymeric matrix stabilized by chemical bonds formed between the coatings of the two types of nanoparticles. The result is normal, because the two types of nanoparticles are close in size, with a difference between the average diameters of only 2 nm.

TEM shows the size and morphology of dry nanoparticles. Often the dimensions measured by TEM are different from those measured in solution due to the interaction of nanoparticles with the solvent. The hydrodynamic dimensions are often larger in solution than in the dry state, and this is of significant importance because the measured hydrodynamic dimensions largely correspond to those in biological fluids. Ultimately, the comparison between the absolute diameter measured by TEM and the hydrodynamic one can provide an estimation of the behavior of nanoparticles when circulating through the capillaries of the human body. The hydrodynamic diameter of MCePEI-GA-PEI nanoparticles is much larger than that measured by TEM with a value of 210 nm. This value is less than the hydrodynamic diameter of the nanoparticles that make up the nanoconjugate, with values of 680 nm for MPEI and 641 nm for CePEI-GA-PEI. The differences between the hydrodynamic diameters of the individual components (MPEI and CePEI-GA) and of the MCePEI-GA may be due to the increase in the degree of crosslinking of the PEI in the final product. Also, similar to the MPEIs discussed earlier, MCePEI-GA has a potential positive Zeta of approximately +30 mV due to the ionization of PEI in water.

Because nanoparticles are claimed to be magnetic nanoantioxidants, one of the most important properties is magnetic, saturation magnetization parameter giving

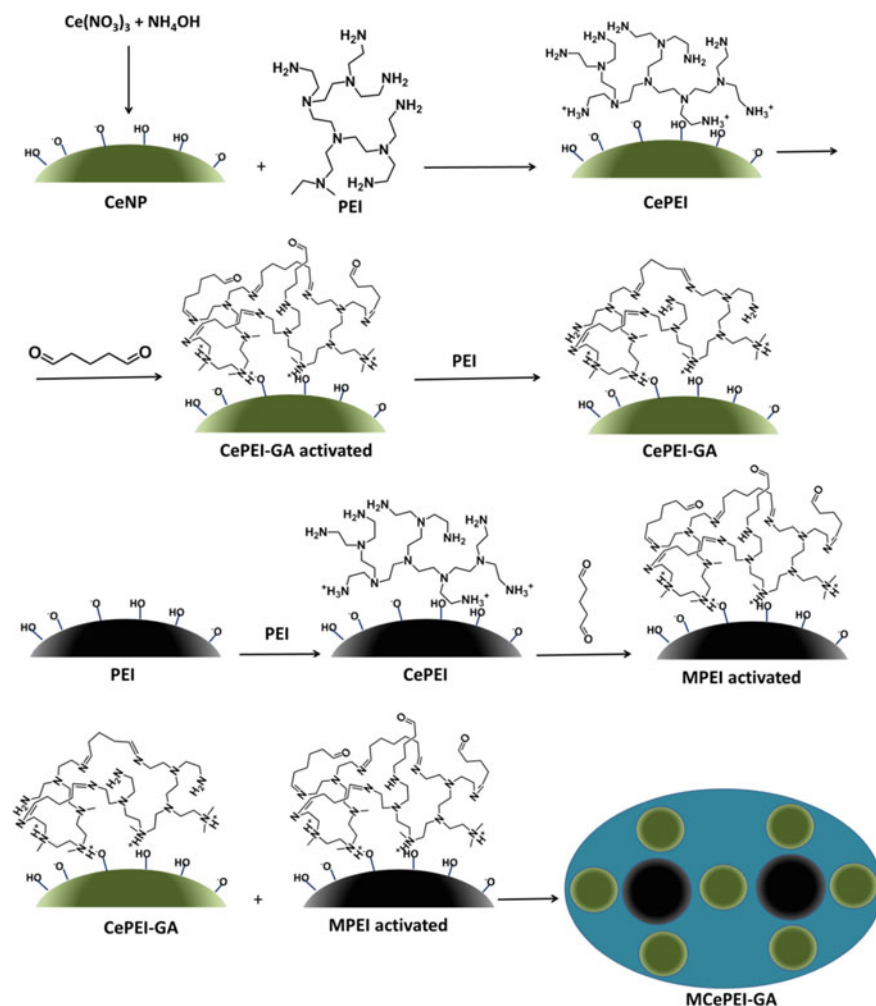


Fig. 9 Schematic representation of the synthesis reactions of MCePEI-GA-PEI

an estimate of the guidance of these nanoparticles in the human body. Magnetization curves indicate that all samples have superparamagnetic properties, suggested by low values of magnetic coercivity and residual magnetization (Fig. 10). It is considered that the addition of PEI for the inactivation of carbonyl groups in the CePEI-GA synthesis step of the process of obtaining CePEI-GA-PEI nanoparticles has a major contribution to the decrease of MCePEI-GA-PEI magnetization. The physical mixture of MNP, CeNP and PEI, without crosslinking with glutaraldehyde, leads to a product with a saturation magnetization of 68, 34 emu/g, which is between 70.63 emu/g for MNP and 7.41 emu/g for MCePEI-GA. The order of the magnetization values highlights the importance of the PEI crosslinking steps in decreasing the

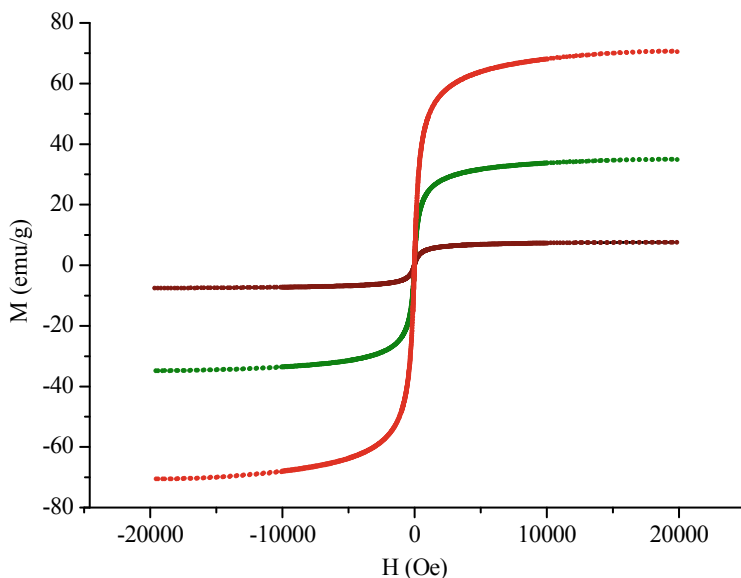


Fig. 10 Magnetization curves of nanoparticles MNP (red); physical mixture MNP, CeNP and PEI (green); and MCEPEI-GA (brown)

saturation magnetization, probably due to the diamagnetic effect of the crosslinked polymeric layer.

In addition to their magnetic properties, their antioxidant properties complete the picture of the fundamental characteristics of magnetic nanoantioxidants, and they can provide an estimate of their ability to quench ROS. The free radical scavenging properties were evaluated using the DPPH test, which showed a higher percentage inhibition of radicals of MCEPEI-GA than in the case of CePEI-GA nanoparticles. This result is unusual knowing that MCEPEI-GA has a lower content of cerium oxide (Fig. 11a). The increase in antioxidant activity was attributed to the amino groups in PEI and imines ($-C = N-$), in the structure of PEI crosslinked with glutar aldehyde.

To highlight the effects of crosslinking on antioxidant properties, the percentage inhibitions of CePEI (nanoparticles stabilized only by physical bonds, without crosslinking) and CePEI-GA (PEI is crosslinked) at different concentrations were compared. The measurements showed that CePEI-GA nanoparticles have a higher percentage inhibition than CePEI, which suggests that crosslinking PEI with glutaric aldehyde improves their free radical scavenging properties. This can be explained by the appearance of $-HC = N-$ imine double bonds, which can themselves, contribute to increasing the antioxidant capacity of the final system (Kotora et al. 2016).

Analysis of composition by XPS method of the CePEI-GA-PEI conjugate showed that the Ce^{3+}/Ce^{4+} ratio is higher than in CePEI (PEI non-crosslinked). Probably, during the process of crosslinking PEI with glutar aldehyde, Ce^{4+} is reduced to Ce^{3+} , which can catalyze the oxidation of aldehydes in the crosslinking process of PEI

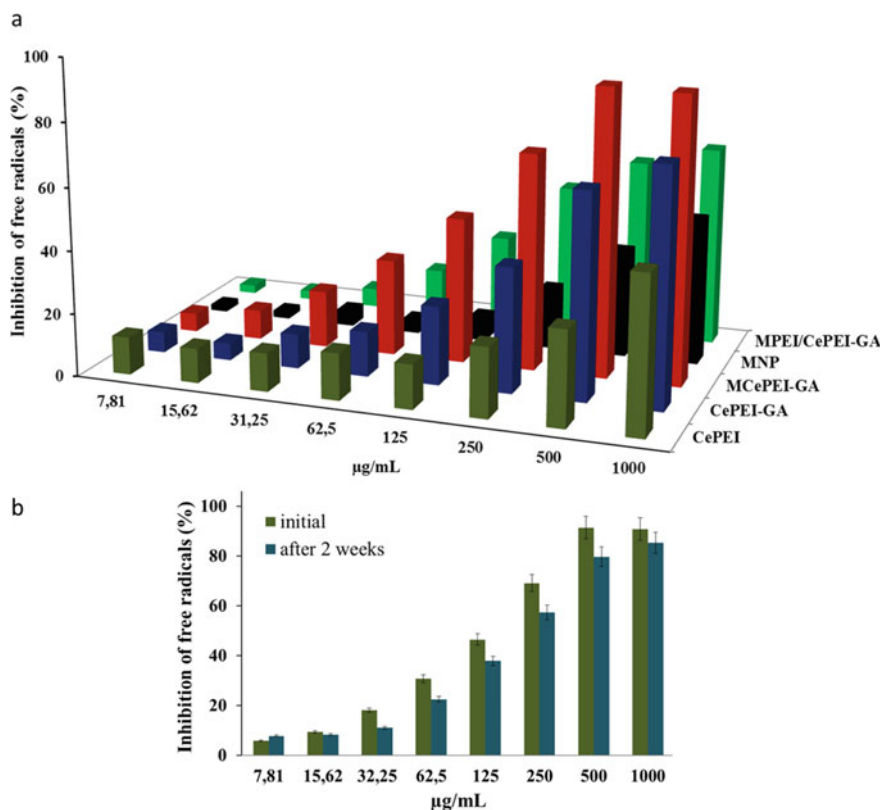


Fig. 11 The antioxidant activity measured by the DPPH method of CePEI, CePEI-GA, MCEPEI-GA, MNP nanoparticles and the MPEI/CePEI-GA physical mixture (a) and the variation of the antioxidant activity of MCEPEI-GA nanoparticles over time (b)

(Orozco et al. 2017). The increase in Ce^{3+} concentration due to crosslinking with glutaric aldehyde of PEI may be another cause of the increased antioxidant activity of the MCEPEI-GA nanoconjugate compared to the activity of its nanoparticles, MPEI and CePEI-GA.

MCEPEI-GA-PEI nanoconjugates form a nanostructured system with stable free radical scavenging properties over time, suggested by the very small decrease in the antioxidant activity of MCEPEI-GA-PEI after two weeks (Fig. 11b).

Due to the antioxidant nature of cerium oxide-based nanoparticles, it is important to investigate the effects of their administration on the oxidative-reducing status of certain organs and biological fluids in living organisms. Therefore, the total antioxidant capacity of mice was measured and expressed in Trolox equivalents using the ABTS method (<https://www.sigmaldrich.com/catalog/product/sigma/mak187?lang=en®ion=RO>). Injection of mice with CePEI-GA and MCEPEI-GA led to an increase in the reducing character of homogenates obtained from animal fluids

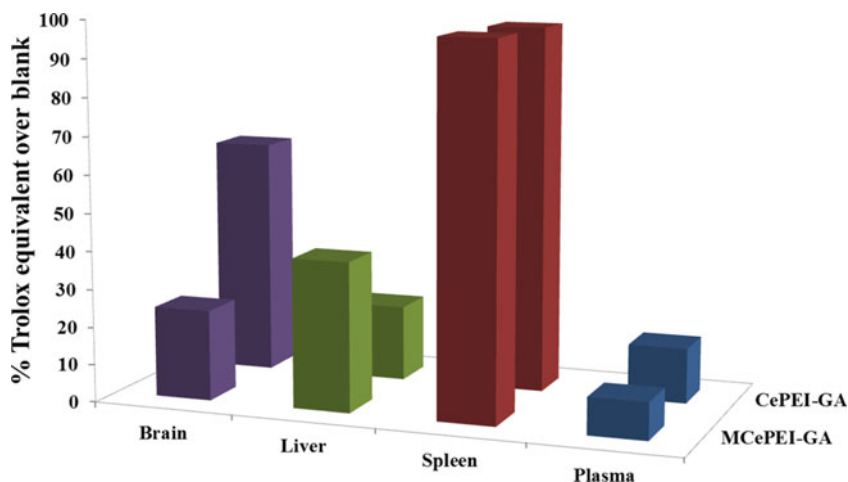


Fig. 12 Increase in total antioxidant capacity relative to the control sample (in Trolox equivalents) for samples treated with CePEI-GA and MCEPEI-GA

and organs. The largest increases in antioxidant capacity are found in the spleen and brain (Fig. 12).

In the spleen, the increase in the amount of antioxidant is large, with approximately 97% compared to the control samples for CePEI-GA and 97.5% for MCEPEI-GA (Fig. 12). In the brain, the increase in the amount of antioxidants is very different for the two types of nanoparticles, higher for CePEI-GA (62.6%) than for MCEPEI-GA (23.95%). The liver naturally has a significant amount of antioxidants (Casas-Grajales and Muriel 2015). Despite this, the amount of antioxidant increases in the liver, following the administration of nanoparticles, by 20% in the case of CePEI-GA and by 39.47% in the case of MCEPEI-GA compared to the control samples, the increase being higher than in plasma.

When the magnetic properties were evaluated it was observed that crosslinking with glutaraldehyde led to a decrease in the saturation magnetization of MCEPEI-GA nanoconjugates compared to that of the physical mixture of nanoparticles, in which crosslinking was excluded. The effect is attributed to the increase in the fraction of the final product of the diamagnetic materials represented by crosslinked PEI. This trend is reversed when analyzing the free radical scavenging capacity. The nanoparticles MPEI, CePEI-GA together with PEI crosslinked with glutaraldehyde have an effect that seems to be synergistic, for the benefit of antioxidant properties. In conclusion, the physico-chemical properties of interest for biomedical applications of MCEPEI-GA, magnetic and free radical scavenging vary in opposite directions with increasing degree of crosslinking of PEI, whereas glutaraldehyde is the means of firm connection between the constituent nanoparticles. Therefore, in the synthesis of nanoconjugates of this kind, which unite CeNP and MNP, when MPEI and CePEI-GA are interconnected, a compromise must be made between the decrease/increase of magnetization and the antioxidant capacity due to crosslinking with glutaraldehyde.

In conclusion, studies undertaken on nano-magnetic antioxidants based on MNP composed of iron oxide and PEI composed of hyperbranch polietilenimine with low molecular mass (1.8 kDa) provides data regarding the preparation and the investigation of the biomedical application of the complex structured nano-entity able to deliver antioxidant chemical species in a pharmacologically controlled and spatially guided manner. More specifically these types of nanooxidants are cargo-complex having a magnetic core with PEI shell, able to load and to deliver precise amounts of radical scavengers of natural antioxidant, PCA, or to conjugate with cerium oxide nanoparticulate. Consequently the nanoantioxidants can be spatially guided in the human body by means of magnetic field and supplying species capable of inactivation of active radical species. Since these magnetic nanoantioxidants can be concentrated in affected regions (acting as scavengers of free radicals) together with their potential applications in MRI (due to their magnetic properties) *these kinds of products can be considered as new excellent candidates for theranostic applications.*

4 Conclusions and Future Perspectives

Oxidative stress has multiple causes and a number of pathologies are connected to it, such as cardiovascular diseases or cancer, for which no healing solutions have yet been found. At the cellular level, the body tries to shift the redox balance from an uncharacteristic oxidative state to one that allows the normal functioning of the human body. To regulate redox balance, the human body uses endogenous antioxidants able to reduce oxidative stress in stage through complex biochemical mechanisms. Human's interaction with nature has determined a symbiotic relationship that has allowed the exchange of matter with beneficial effects on human health. Thus, it was inherent the supplementation of the the endogenous antioxidants with the exogenous ones, determining a dependence of the human body on the addition of antioxidants found in natural products.

Throughout history, man has indirectly understood the benefits of natural antioxidants, so that ancient medicine relied on the use of natural products, such as teas, propolis or fruits, which brought important intakes of natural antioxidants to the body. Nowadays, the approach to limiting oxidative stress is much more complex, and this complexity is due to the increasingly alert social life, which increases the efforts of specialists to keep the human body in normal functioning parameters. In the context of the development of nanotechnology, it is a challenge to provide antioxidants using nanoobjects that optimize the necessary therapeutic doses due to the protective effect of antioxidants and the targetability of chemically functionalized nanoobjects.

This review highlights recent advances in the suitability of using inorganic nanoparticles as nanoantioxidants. It provides a measure of the comparison between different ways or formulations in which nanoparticles can be used as antioxidants. Therefore, the redox effects in the body of metal nanoparticles in zero oxidation state and their oxides with intrinsic free radical scavenging properties are described. The general conclusion is that, with few exceptions, the antioxidant activity is amplified

by nanoparticles coated with natural antioxidants in the form of natural extracts or with pure antioxidants loaded as therapeutic agents in core-shell nanoparticles.

Magnetic nanoparticles have lately become the vectors of a teranostic approach in biomedical research. The issue of magnetically guided nanoantioxidants is discussed in detail in the review from the perspective of functionality in the process of free radical scavenging. In this section the physicochemical characterization of magnetic nanoparticles is described to highlight the relationships of structure properties and the minimum conditions that must be met to have an effective nanoantioxidant. This approach is due to the finding that some nanoparticles of metal oxides have different biological properties depending on the synthesis methods. In this context, the review describes a product formed from the conjugation of two metal oxides, iron and cerium, which together with the polymeric conjugation system, determined a synergistic free radical scavenging effect.

In this context, it has been shown that the systems formed by magnetic nanoparticles and hyperbranched polyethyleneimine are reliable precursors in the synthesis of nanoantioxidants. The loading with protocatechuic acid of magnetic nanoparticles coated with polyethyleneimine shows the feasibility of obtaining such nanoantioxidants. On the other hand, obtaining nanoparticles loaded with inclusion complexes based on modified cyclodextrins and natural antioxidants, which have been shown to have good antioxidant properties, shows the versatility of these systems, which can adapt to loading nanoparticles with water-insoluble antioxidants.

Regarding intrinsically inorganic antioxidants, very recent research has shown that the conjugation of magnetic nanoparticles with nanoceria provides a reliable way to obtain magnetic nanoantioxidants. The use of the conjugation platform composed of magnetic nanoparticles coated with polyethyleneimine led to the obtaining of magnetic nanoantioxidants based on cerium oxide. The components of these interconnected systems act synergistically in a particular way that has not been observed in the physical mixture.

All these findings lead to the idea that such nanostructured systems show great potential for treatment and diagnosis of ROS-related inflammatory and cardiovascular diseases.

Inorganic nanoantioxidants are still in an early stage of characterization and development into final products as therapeutic agents. In sufficiently low amounts they are not toxic, but in higher amounts or under inappropriate pH conditions, usually at low pH, inorganic nanoparticles can induce oxidative stress. Oxidative stress induced by inorganic and organic nanoantioxidants is a well-documented property, being sometimes used for the antimicrobial activity induced through ROS. The redox processes in which nanoantioxidants are involved appear to be different sometimes when describing the results of *ex vivo*, *in vitro* or *in vivo* experiments used to create experimental models, requiring more knowledge for a full understanding of redox processes in the living world. This finding highlights the complexity of redox processes in the body and the difficulties encountered in designing effective nanoantioxidants. It is a continuous challenge of fundamental science to better understand the redox processes caused by inorganic nanoparticles in the human body in order to characterize as accurately as possible the dual antioxidant or oxidant behavior of inorganic nanoparticles.

Therefore, a challenge today, in terms of inorganic antioxidants, is to find a correct relationship between structure and properties, so that through low therapeutic doses to amplify the redox processes of free radical scavenging to the detriment of those that generate reactive species in human body.

Acknowledgements This project has received funding from the H2020 ERA Chairs Project no 667387: SupraChem Lab Laboratory of Supramolecular Chemistry for Adaptive Delivery Systems ERA Chair initiative. This work was also supported by a grant from the Romanian Ministry of Research and Innovation, CCCDI–UEFISCDI, project number PN-III-P1-1.2-PCCDI-2017-0697/13PCCDI/2018, within PNCDI III.

References

- Abete P, Napoli C, Santoro G (1999) Age-related decrease in cardiac tolerance to oxidative stress. *J Mol Cell Cardiol* 31(1):227–236. <https://doi.org/10.1006/jmcc.1998.0862>
- Adekunle AS, Oyekunle JA, Durosinmi LM, Oluwafemi OS, Olayanju D, Akinola AS, Olaoluwa R, Akinyele O, Ajayeoba T (2020) Nano-Struct Nano-Objects 21(100):405. <https://doi.org/10.1016/j.nanoso.2019.100405>
- Alpsoy L, Baykal A, Kurtan U (2017) Superparamagnetic iron oxide nanoparticles (SPION) functionalized by caffeic acid (CFA). *J Supercond Nov Magn* 30:2699–2706. <https://doi.org/10.1007/s10948-017-4088-3>
- Amanzadeh E, Esmaeili A, Najaf Abadi RE, Kazemipour N, Pahlevanneshan Z, Beheshti S (2019) Quercetin conjugated with superparamagnetic iron oxide nanoparticles improves learning and memory better than free quercetin via interacting with proteins involved in LTP. *Sci Rep* 9(1):6876. <https://doi.org/10.1038/s41598-019-43345-w>
- Amstad E, Gillich T, Bilecka I, Textor M, Reimhult E (2009) Ultrastable iron oxide nanoparticle colloidal suspensions using dispersants with catechol-derived anchor groups. *Nano Lett* 9(12):4042–4048. <https://doi.org/10.1021/nl902212q>
- Amutha S, Sridhar S, Sridhar S (2018) Green synthesis of magnetic iron oxide nanoparticle using leaves of *glycosmis mauritiana* and their antibacterial activity against human pathogens. *J Innov Pharm Biol Sci* 5(2):22–26
- Andrei V, Sharpe E, Vasilescu A, Andreescu S (2016) A single use electrochemical sensor based on biomimetic nanoceria for the detection of wine antioxidants. *Talanta* 156–157:112–118. <https://doi.org/10.1016/j.talanta.2016.04.067>
- Ansari MA, Khan HM (2015) Green synthesis of Al₂ O₃ nanoparticles and their bactericidal potential against clinical isolates of multi-drug resistant *Pseudomonas aeruginosa*. *World J Microbiol Biotechnol* 31:153–164. <https://doi.org/10.1007/s11274-014-1757-2>
- Anter J, Romero-Jimenez F-B, Villatoro-Pulido M, Analla M, Alonso-Moraga A, Munoz-Serrano A (2011) Antigenotoxicity, cytotoxicity, and apoptosis induction by apigenin, bisabolol, and protocatechuic acid. *J Med Food* 14(3):276–283. <https://doi.org/10.1089/jmf.2010.0139>
- Anzorena RS, Mazan MO, Soldatic A, Larrondo SA (2019) The effect of incorporation of iron in cerium oxide structure on reducibility and catalytic performance for methane oxidation in diluted streams. *Ceram Int* 45:19,757–19,765. <https://doi.org/10.1016/j.ceramint.2019.06.229>
- Ardeleanu R, Dascalu AI, Neamtu A, Peptanariu D, Uritu CM, Maier SS, Nicolescu A, Simionescu BC, Barboiu M, Pinteala M (2018) Multivalent polyrotaxane vectors as adaptive cargo complexes for gene therapy. *Polym Chem* 9:845–859. <https://doi.org/10.1039/c7py01256j>
- Arriagada F, Gunther G, Nos J, Nonell S, Olea-Azar C, Morales J (2019) Antioxidant nanomaterial based on core-shell silica nanospheres with surface-bound caffeic acid: a promising vehicle for oxidation-sensitive drugs. *Nanomaterials* 9:214. <https://doi.org/10.3390/nano9020214>

- Auffana M, Roseb J, Wiesner MR, Botterob JY (2009) Chemical stability of metallic nanoparticles: a parameter controlling their potential cellular toxicity in vitro. *Environ Pollut* 157(4):1127–1133. <https://doi.org/10.1016/j.envpol.2008.10.002>
- Ayyanaar S, Kesavan MP, Balachandra C, Rasala S, Rameshkumar P, Aoki P, Rajesh J, Webster TJ, Rajagopal G (2020) Iron oxide nanoparticle core-shell magnetic microspheres: applications toward targeted drug delivery. *Nanomed Nanotechnol Biol Med* 24(102):134. <https://doi.org/10.1016/j.nano.2019.102134>
- Baldim V, Bedioui F, Mignet N, Margailc I, Berret JF (2018) The enzyme-like catalytic activity of cerium oxide nanoparticles and its dependency on Ce³⁺ surface area concentration. *Nanoscale* 10:6971–6980. <https://doi.org/10.1039/C8NR00325D>
- Baldini E, Palmieri T, Dominguez A (2018) Phonon-driven selective modulation of exciton oscillator strengths in anatase TiO₂ nanoparticles. *Nanoletters* 18:5007–5014. <https://doi.org/10.1021/acs.nanolett.8b01837>
- Bhatia M, Girdhar A, Chandrakar B, Tiwari A (2013) Implicating nanoparticles as potential biodegradation enhancers: a review. *J Nanomed Nanotechnol* 4(4):1–7. <https://doi.org/10.4172/2157-7439.1000175>
- Boubbou KE Magnetic iron oxide nanoparticles as drug carriers: preparation, conjugation and delivery. *Nanomedicine* 13(8):929–952. <https://doi.org/10.2217/nmm-2017-0320>
- Carocho M, Ferreira I (2013) A review on antioxidants, prooxidants and related controversy: natural and synthetic compounds, screening and analysis methodologies and future perspectives. *Food Chem Toxicol* 51:15–25. <https://doi.org/10.1016/j.fct.2012.09.021>
- Casas-Grajales S, Muriel P (2015) Antioxidants in liver health. *WJGPT* 6(3):59–72. <https://doi.org/10.4292/wjgpt.v6.i3.59>
- Celardo I, Pedersen JZ, Traversa E, Ghibelli L (2011) Pharmacological potential of cerium oxide nanoparticles. *Nanoscale* 3:1411–1420. <https://doi.org/10.1039/C0NR00875C>
- Chahardoli A, Karimi N, Ma X (2020) Effects of engineered aluminum and nickel oxide nanoparticles on the growth and antioxidant defense systems of *Nigella arvensis*. *Sci Rep* 10:3847. <https://doi.org/10.1038/s41598-020-60841-6>
- Charbgoon F, Ahmad M, Darroudi M (2017) Cerium oxide nanoparticles: green synthesis and biological applications. *Int J Nanomedicine* 12: 1401–1413. <https://doi.org/10.2147/IJN.S124855>
- Choe E, Min DB (2009) Mechanisms of antioxidants in the oxidation of foods. *CRFSFS* 8(4):345–358. <https://doi.org/10.1111/j.1541-4337.2009.00085.x>
- Christina R, Sedlak KDL (2008) Ligand-enhanced reactive oxidant generation by nanoparticulate zero-valent iron and oxygen. *Environ Sci Technol* 42(18):6936–6941. <https://doi.org/10.1021/es801438f>
- Cillard J, Cillard P, Cormier M, Girre L (1980) Tocopherol prooxidants effect in aqueous media: increased autoxidation rate of linoleic acid. *J Am Oil Chem Soc* 57:252–255. <https://doi.org/10.1007/BF02668254>
- Corciova A, Mircea C, Tuchilus C, Cioanca O, Burlec AF, Ivanescu B, Vlase A, Gheldiu AM, Fifere A, Lungoci AL, Hancianu M (2018) Extract and characterization of newly synthesized silver nanoparticles. *Farmacia* 66(5):831–838. <https://doi.org/10.31925/farmacia.2018.5.13>
- Corciova A, Ivanescu B, Tuchilus C, Fifere A, Doroftei F, Lungoci AL, Marangoci N, Mircea C (2018) Biosynthesis of silver nanoparticles (AgNPs) using *Tilia cordata* flowers extracts and evaluation of some biological activities. *Environ Eng Manag J* 17(12):2957–2968. <https://doi.org/10.30638/eemj.2018.296>
- Corciova A, Mircea C, Burlec AF, Cioanca O, Tuchilus C, Fifere A, Lungoci AL, Marangoci N, Hancianu M. (2019) Antioxidant, antimicrobial and photocatalytic activities of silver nanoparticles obtained by bee propolis extract assisted biosynthesis. *Farmacia* 67(3):482–489. <https://doi.org/10.31925/farmacia.2019.3.16>
- Corciova A, Burlec AF, Gheldiu AM, Fifere A, Lungoci AL, Marangoci N, Mircea C (2019) Biosynthesis of silver nanoparticles using licorice extract and evaluation of their antioxidant activity. *Rev Chim -Bucharest-Original Edition* 70(11):4053–4059. <https://doi.org/10.37358/RC.19.11.7700>

- Dadfar SM, Roemhild M, Drude N, Stillfried S, Knuchel R, Kiessling F, Lammers T (2019) Iron oxide nanoparticles: diagnostic, therapeutic and theranostic applications. *Adv Drug Deliv Rev* 138:302–325. <https://doi.org/10.1016/j.addr.2019.01.005>
- de Souza TA (2019) Silver nanoparticles: an integrated view of green synthesis methods, transformation in the environment and toxicity. *Ecotoxicol Environ Saf* 171:691–700. <https://doi.org/10.1016/j.ecoenv.2018.12.095>
- Deligiannakis Y, Sotiriou GA, Pratsinis SE (2012) Antioxidant and antiradical SiO₂ nanoparticles covalently functionalized with gallic acid. *ACS Appl Mater Interfaces* 4:6609–6617. <https://doi.org/10.1021/am301751s>
- Domenico L, Kiselev MA, Caccamo MT (2019) Smart nanoparticles for drug delivery application: development of versatile nanocarrier platforms in biotechnology and nanomedicine. *J Nanomater* ID 3(702):518. <https://doi.org/10.1155/2019/3702518>
- Dong J, Song L, Yin JJ, He W, Wu Y, Gu N, Zhang Y (2014) Co₃O₄ nanoparticles with multi-enzyme activities and their application in immunohistochemical assay. *ACS Appl Mater Interfaces* 6:1959–1970. <https://doi.org/10.1021/am405009f>
- Dorniani D, Hussein ZB, Kura AU, Fakurazi S, Shaari AH, Ahmad ZA (2012) Preparation of Fe₃O₄ magnetic nanoparticles coated with gallic acid for drug delivery. *Int J Nanomedicine* 7:5745–5756. <https://doi.org/10.2147/IJN.S35746>
- Drose S, Brandt U (2012) Molecular mechanisms of superoxide production by the mitochondrial respiratory chain. *Adv Exp Med Biol* 748:145–169. <https://doi.org/10.1016/j.bbabo.2013.03.009>
- Duarte TL, Lunec J (2005) Review: when is an antioxidant not an antioxidant? A review of novel actions and reactions of vitamin C. *Free Radic Res* 39:671–686. <https://doi.org/10.1080/10715760500104025>
- Durdureanu-Angheluta A, Ardeleanu R, Pinteala M, Harabagiu V, Chiriac H, Simionescu BC (2008) Silane covered magnetite particles. Preparation and characterization. *Dig J Nanomater Biostruct* 3:33–40
- Durdureanu-Angheluta A, Pricop L, Stoica I, Peptu CA, Dascalu A, Marangoci N, Doroftei F, Chiriac H, Pinteala M, Simionescu, BC (2010) Synthesis and characterization of magnetite particles covered with α -triethoxysilil-polydimethylsiloxane. *J Magn Magn Mater* 322(19):2956–2968. <https://doi.org/10.1016/j.jmmm.2010.05.013>
- Durdureanu-Angheluta A, Dascalu A, Fifere A, Coroaba A, Pricop L, Chiriac H, Tura V, Pinteala M, Simionescu BC (2012) Progress in the synthesis and characterization of magnetite nanoparticles with amino groups on the surface. *J Magn Magn Mater* 324:1679–1689. <https://doi.org/10.1016/j.jmmm.2011.11.062>
- Durdureanu-Angheluta A, Uritu CM, Coroaba A, Minea B, Doroftei F, Calin M, Maier SS, Pinteala M, Simionescu M, Simionescu BC (2014) Heparin-anthranoid conjugates associated with nanomagnetite particles and their cytotoxic effect on cancer cells. *J Biomed Nanotechnol* 10(1):131–142. <https://doi.org/10.1166/jbn.2014.1690>
- Durdureanu-Angheluta A, Ignat ME, Maier SS, Pricop L, Coroaba A, Fifere A, Pinteala M, Chiriac A (2014) Lipolytic biocatalyst based on recyclable magnetite-polysiloxane nanoparticles. *Appl Surf Sci* 292:898–905. <https://doi.org/10.1016/j.apsusc.2013.12.077>
- Elbagory AM, Cupido CN, Meyer M, Hussein AA (2016) Large scale screening of southern African plant extracts for the green synthesis of gold nanoparticles using microtitre-plate method. *Molecules* 21:1498. <https://doi.org/10.3390/molecules21111498>
- Espinos C, Galindo MI, Garcia-Gimeno MA, Ibanez-Cabellos JS, Martinez-Rubio D, Millan JM, Rodrigo R, Sanz P, Seco-Cervera M, Sevilla T, Tapia A, Pallardo FV (2020) Oxidative Stress, a crossroad between rare diseases and neurodegeneration. *Antioxidants* 9(4):313. <https://doi.org/10.3390/antiox9040313>
- Fahmy B, Cormier SA (2009) Copper oxide nanoparticles induce oxidative stress and cytotoxicity in airway epithelial cells. *Toxicol In Vitro* 23(7):1365–1371. <https://doi.org/10.1016/j.tiv.2009.08.005>

- Galati G, O'Brien PJ (2004) Potential toxicity of flavonoids and other dietary phenolics: significance for their chemopreventive and anticancer properties. *Free Radic Biol Med* 37:287–303. <https://doi.org/10.1016/j.freeradbiomed.2004.04.034>
- Gautham B, Jegadeesan K, Srimathi N, Santosh Srinivas S, Manishkanna D (2019) Green synthesis of iron oxide nanoparticles using *Terminalia bellirica* and *Moringa oleifera* fruit and leaf extracts: antioxidant, antibacterial and thermoacoustic properties. *Biocatal Agric Biotechnol* 21(101):354. <https://doi.org/10.1016/j.bcab.2019.101354>
- Ge C, Fang G, Shen X, Chong Y, Wamer WG, Gao X, Chai Z, Chen C, Yin JJ (2016) Facet energy versus enzyme-like activities: the unexpected protection of palladium nanocrystals against oxidative damage. *ACS Nano* 10:10,436–10,445. <https://doi.org/10.1021/acsnano.6b06297>
- Giustini AJ, Petryk AA, Cassim SM, Tate JA, Baker I, Hoopes PJ (2010) Magnetic nanoparticle hyperthermia in cancer treatment. *Nano Life* 1(01n02):17–32. <https://doi.org/10.1142/S1793984410000067>
- Guenin E, Lalatonne Y, Bolley J, Milosevic I, Platas-Iglesias C, Motte L (2014) Catechol versus bisphosphonate ligand exchange at the surface of iron oxide nanoparticles: towards multi-functionalization. *J Nanopart Res* 16:2596. <https://doi.org/10.1007/s11051-014-2596-7>
- Guerrini L, Alvarez-Puebla RA, Perez NP (2018) Surface modifications of nanoparticles for stability in biological fluids materials. *Materials* 11(7):1154. <https://doi.org/10.3390/ma11071154>
- Guo S, Han Y, Guo L (2020) Mechanistic study of catalase and superoxide dismutation-mimic activities of cobalt oxide nanozyme from first-principles microkinetic modeling. *Catal Surv Asia* 24:70–85. <https://doi.org/10.1007/s10563-019-09290-4>
- Gurunathan S, Kim E, Han JW, Park JH, Kim J-H (2015) Green chemistry approach for synthesis of effective anticancer palladium nanoparticles. *Molecules* 20:22,476–22,498. <https://doi.org/10.3390/molecules201219860>
- Hala A, Howaida N, Manal S (2018) Zinc oxide nanoparticles induced oxidative DNA damage, inflammation and apoptosis in rat's brain after oral exposure. *6(2):29*. <https://doi.org/10.3390/toxics6020029>
- Halliwell B (2007) Biochemistry of oxidative stress. *Biochem Soc Trans* 35:1147–1150. <https://doi.org/10.1042/BST0351147>
- Halliwell B, Gutteridge JM (1995) The definition and measurement of antioxidants in biological systems. *Free Radic Biol Med* 18:125–126. [https://doi.org/10.1016/0891-5849\(95\)91457-3](https://doi.org/10.1016/0891-5849(95)91457-3)
- Hayat A, Andreescu D, Bulbul G, Andreescu S (2014) Redox reactivity of cerium oxide nanoparticles against dopamine. *J Colloid Interface Sci*. 418:240–245. <https://doi.org/10.1016/j.jcis.2013.12.007>
- Hayyan M, Hashim MA, AlNashef IM (2016) Superoxide ion: generation and chemical implications. *Chem Rev* 116(5):3029–3085. <https://doi.org/10.1021/acs.chemrev.5b00407>
- Him C, Tsangab A, Lia K, Zenga Y, Zhao W, Zhangab T, Zhan Y, Xie R, Leungd DY, Huang H (2019) Titanium oxide based photocatalytic materials development and their role of in the air pollutants degradation: overview and forecast. *Environ Int* 125:200–228. <https://doi.org/10.1016/j.envint.2019.01.015>
- Hoag GE, Collins JB, Holcomb JL, Hoag JR, Nadagouda MN, Varma RS (2009) Degradation of bromothymol blue by “greener” nano-scale zero-valent iron synthesized using tea polyphenols. *J Mat Chem* 19(45):8671–8677. <https://doi.org/10.1039/B909148C>
- Ivanov VK, Shcherbakov AB, Usatenko AV (2009) Structure-sensitive properties and biomedical applications of nanodispersed cerium. *Russ Chem Rev* 78(9):855–871. <https://doi.org/10.1070/RC2009v078n09ABEH004058>
- J, Kim KS, Na K, Lee J, (2016) Caffeic acid-coated multifunctional magnetic nanoparticles for the treatment and bimodal imaging of tumours. *J Photochem Photobiol B Biol* 160:210–216. <https://doi.org/10.1016/j.jphotobiol.2016.03.058>
- Jeevanandam J, Barhoum A, Chan YS, Dufresne A, Danquah MK (2018) Review on nanoparticles and nanostructured materials: history, sources, toxicity and regulations. *Beilstein J. Nanotechnol* 9:1050–1074. <https://doi.org/10.3762/bjnano.9.98>

- Jia L, Zhang Q, Li Q, Song H (2009) The biosynthesis of palladium nanoparticles by antioxidants in *Gardenia jasminoides* Ellis: long lifetime nanocatalysts for p -nitrotoluene hydrogenation. *Nanotechnology* 20:1–10. <https://doi.org/10.1088/0957-4484/20/38/385601>
- Jomov K, Hudecova L, Lauro P, Simunkova M, Alwasel SH., Alhazza IM, Valko M (2019) Switch between antioxidant and prooxidant properties of the phenolic compounds myricetin, morin, 30,40-dihydroxyflavone, taxifolin and 4-hydroxy-coumarin in the presence of copper(II) ions: a spectroscopic, absorption titration and DNA damage study. *Molecules* 24:4335. <https://doi.org/10.3390/molecules24234335>
- Jung WK, Koo HC, Kim KW, Shin S, Kim SK, Yo P (2008) Antibacterial activity and mechanism of action of the silver ion in *Staphylococcus aureus* and *Escherichia coli*. *Appl Environ Microbiol* 74(7):2171–2178. <https://doi.org/10.1128/AEM.02001-07>
- Jurasin DD, Curlin M, Capjak I, Crnkovic T, Lovric M, Horak D, Vrcek IV, Gajovic S (2016) Surface coating affects behavior of metallic nanoparticles in a biological environment. *Beilstein J Nanotechnol* 7:246–262. <https://doi.org/10.3762/bjnano.7.23>
- Karakoti AS, Monteiro-Riviere NA, Aggarwal R, Davis JP, Narayan RJ, Self WT, McGinnis J, Seal S (2008) Nanoceria as antioxidant: synthesis and biomedical applications. *JOM* 60(3):33–37. <https://doi.org/10.1007/s11837-008-0029-8>
- Kassem S, Mohamed M, Sayour H, Canfarotta F, Piletsky S, Soliman MAM (2020) Functionalized core-shell yttrium oxide nanoparticles as antioxidants agents in heat stressed rats. *Biol Trace Elem Res*. <https://doi.org/10.1007/s12011-020-02036-8>
- Kedziora A, Speruda M, Krzyzewska E, Rybka J, Lukowiak A, Bugla-Ploskonska (2018) Similarities and differences between silver ions and silver in nanoforms as antibacterial agents. *Int J Mol Sci* 19:444. <https://doi.org/10.3390/ijms19020444>
- Khalil I, Yehye WA, Etxeberria AE, Alhadi AA, Dezfooli SM, Binti N, Julkapli M, Basirun WJ, Seyfoddin A (2020) Nanoantioxidants: recent trends in antioxidant delivery. *Antioxidants* 9(1):24. <https://doi.org/10.3390/antiox9010024>
- Khan I, Saeed K, Khan I (2019) Nanoparticles: properties, applications and toxicities. *Arab J Chem* 12(7):908–931. <https://doi.org/10.1016/j.arabjc.2017.05.011>
- Khlebnikov AI, Schepetkin IA, Domina NG, Kirpotina LN, Quinn MT (2007) Improved quantitative structure–activity relationship models to predict antioxidant activity of flavonoids in chemical, enzymatic, and cellular systems. *Bioorg Med Chem* 15:1749–1770. <https://doi.org/10.1016/j.bmc.2006.11.037>
- Antioxidant Assay Kit CS0790 (Sigma-Aldrich). <https://www.sigmaaldrich.com/catalog/product/sigma/mak187?lang=en®ion=RO>
- Kotora P, Sersen F, Filo J, Loos D (2016) The scavenging of DPPH, galvinoxyl and ABTS radicals by imine analogs of resveratrol. *Molecules* 21(1):127. <https://doi.org/10.3390/molecules21010127>
- Kuang Y, Wang Q, Chen Z, Megharaj M, Naidu R (2013) Heterogeneous Fenton-like oxidation of monochlorobenzene using green synthesis of iron nanoparticles. *J Colloid Interface Sci* 410:67–73. <https://doi.org/10.1016/j.jcis.2013.08.020>
- Kumar SR, Priyatharshni S, Babu VN, Mangalaraj D, Viswanathan C, Kannan S, Ponpandian N (2014) Quercetin conjugated superparamagnetic magnetite nanoparticles for in-vitro analysis of breast cancer cell lines for chemotherapy applications. *J Colloid Interface Sci* 436:234–242. <https://doi.org/10.1016/j.jcis.2014.08.064>
- Kumar R, Kumar G, Umar A (2014a) Zinc oxide nanomaterials for photocatalytic degradation of methyl orange: a review. *Nanosci Nanotechnol Lett* 6:631–650. <https://doi.org/10.1166/nnl.2014.1879>
- Lane MK, Julie B, Zimmerman C (2019) Controlling metal oxide nanoparticle size and shape with supercritical fluid synthesis. *Green Chem* 21:3769–3781. <https://doi.org/10.1039/C9GC01619H>
- Laurent S, Saei AA, Behzahi S, Panahifar A, Mahmoudi M (2014) Superparamagnetic iron oxide nanoparticles for delivery of therapeutic agents: opportunities and challenges. *Expert Opin Drug Del* 11(9):1449–1470. <https://doi.org/10.1517/17425247.2014.924501>
- Lenaz G (2012) Mitochondria and reactive oxygen species. Which role in physiology and pathology? *Adv Exp Med Biol* 942:93–136. <https://doi.org/10.3390/ijms14036306>

- Liu Y, Wu H, Li M, Yin JJ, Nie Z (2014) pH dependent catalytic activities of platinum nanoparticles with respect to the decomposition of hydrogen peroxide and scavenging of superoxide and singlet oxygen. *Nanoscale* 6:11,904–11,910. <https://doi.org/10.1039/C4NR03848G>
- Lungoci AL, Pinteala M, Petrovici AR, Rosca I, Turin-Moleavin IA, Fifere A (2018) Biosynthesized dextran coated magnetic nanoparticles with antifungal activity. *Rev Roum Chim* 63(5–6):497–503
- Lungoci A-L, Turin-Moleavin I-A, Corciova A, Mircea C, Arvinte A, Fifere A, Marangoci NL, Pinteala M (2019) Multifunctional magnetic cargo-complexes with radical scavenging properties. *Mat Sci Eng Sci C* 94:608–618. <https://doi.org/10.1016/j.msec.2018.10.013>
- Lushchak VI (2014) Free radicals, reactive oxygen species, oxidative stress and its classification. *Chem Biol Interact* 224C:164–75. <https://doi.org/10.15407/ubj87.06.011>
- Marashdeha MWB, Ababneh OM, Leminea A, Alsadigc K, Omrid L, Mire A Suliemanf E (2019) The significant effect of size and concentrations of iron oxide nanoparticles on magnetic resonance imaging contrast enhancement. *Results Phys* 15:1,026,512. <https://doi.org/10.1016/j.rinp.2019.102651>
- Na HB, Song IC, Hyeon T (2009) Inorganic nanoparticles for MRI contrast agents. *Adv Mater* 21(21):2133–2148. <https://doi.org/10.1002/adma.200802366>
- Nadagouda MN, Castle AB, Murdock RC, Hussain SM, Varma RS (2010) In vitro biocompatibility of nanoscale zerovalent iron particles (NZVI) synthesized using tea polyphenols. *Green Chem* 12(1):114–122. <https://doi.org/10.1039/B921203P>
- Nelson BC, Johnson ME, Walker ML, Riley KR, Sims CM (2016) Antioxidant cerium oxide nanoparticles in biology and medicine. *Antioxidants* 5:15. <https://doi.org/10.3390/antiox5020015>
- Ni D, Bu W, Ehlerding EB, Cai W, Jianlin S (2017) Engineering of inorganic nanoparticles as magnetic resonance imaging contrast agents. *Chem Soc Rev* 46(23):7438–7468. <https://doi.org/10.1039/C7CS00316A>
- Oliveira VE, Almeida EVC, Castro HV, Edwards HG, Dos Santos HF, de Oliveira LF (2011) Carotenoids and β -cyclodextrin inclusion complexes: Raman spectroscopy and theoretical investigation. *J Phys Chem A* 115(30):8511–8519. <https://doi.org/10.1021/jp2028142>
- Orozco LM, Renz M, Corma A (2017) Cerium oxide as a catalyst for the ketonization of aldehydes: mechanistic insights and a convenient way to alkanes without the consumption of external hydrogen. *Green Chem* 19:1555–1569. <https://doi.org/10.1039/C6GC03511F>
- Palanisamyab S, Wang YM (2019) Superparamagnetic iron oxide nanoparticulate system: synthesis, targeting, drug delivery and therapy in cancer. *Dalton Trans* 48:9490–9515. <https://doi.org/10.1039/C9DT00459A>
- Patel P, Kansara K, Singh R (2018) Cellular internalization and antioxidant activity of cerium oxide nanoparticles in human monocytic leukemia cells. *International. J Nanomedicine* 15: 39–41. <https://doi.org/10.2147/IJN.S124996>
- Pham XH, Hahm E, Kim HM, Son BS, Jo A, An J, Tran Thi TA, Nguyen DQ, Jun BH (2020) Silica-coated magnetic iron oxide nanoparticles grafted onto graphene oxide for protein isolation. *Nanomaterials* 10:117. <https://doi.org/10.3390/nano10010117>
- Pizzino G, Irrera N, Cucinotta M, Pallio G, Mannino F, Arcoraci V, Squadrito F, Altavilla D, Hindawi AB (2017) Oxidative stress: harms and benefits for human health. *Oxidative Med Cell Longevity* 8,416,763:1–13. <https://doi.org/10.1155/2017/8416763>
- Prasad AS, Bao B, Beck FWJ, Kuck O, Sarkar FH (2004) Antioxidant effect of zinc in humans. *Free Radic Biol Med* 37:1182–1190. <https://doi.org/10.1016/j.freeradbiomed.2004.07.007>
- Price PM, Mahmoud WE, Al-Ghamdi AA, Bronstein LM (2018) Magnetic drug delivery: where the field is going. *Front Chem* 6:619. <https://doi.org/10.3389/fchem.2018.00619>
- Pricop L, Durdureanu-Angheluta A, Spulber M, Stoica I, Fifere A, Marangoci NL, Dascalu AI, Tigoianu R, Harabagiu V, Pinteala M, Simionescu BC (2010) Synthesis and micellization of polydimethylsiloxane-carboxy terminated poly(ethylene oxide) graft copolymer in aqueous and organic media and its application for synthesis of core-shell magnetic particles. *E-Polymers* 093:1–19. <https://doi.org/10.1515/epoly.2010.10.1.1043>

- Rao L, Yu GT, Meng QF, Bu LL, Tian R, Lin LS, Deng H, Yang W, Zan M, Ding J, Li A, Xiao H, Sun ZJ, Liu W, Chen X (2019) Cancer cell membrane-coated nanoparticles for personalized therapy in patient-derived xenograft models. *Adv Funct Mater* 29:1,905,671. <https://doi.org/10.1002/adfm.201905671>
- Reddy ARN, Lonkala S (2019) In vitro evaluation of copper oxide nanoparticle-induced cytotoxicity and oxidative stress using human embryonic kidney cells. *Toxicol Ind Health* 35(2):159–164. <https://doi.org/10.1177/0748233718819371>
- Reed K, Cormack A, Kulkarni A, Mayton M, Sayle D, Klaessig F, Stadler B (2014) Exploring the properties and applications of nanoceria: is there still plenty of room at the bottom? *Environ Sci Nano* 1:390–405. <https://doi.org/https://doi.org/10.1039/C4EN00079J>
- Richard S, Saric A, Boucher M, Slomianny C, Geffroy F, Meriaux S, Lalatonne Y, Petit P, Motte L (2016) Antioxidative theranostic iron oxide nanoparticles toward brain tumors imaging and ROS production. *ACS Chem Biol* 11(10):2812–2819. <https://doi.org/10.1021/acscchembio.6b00558>
- Saravana RS, Muthukumarab M, Mubasherac SM, Abinaya M, Prasathb V, Parthibana R, Moham-madd F, Chun W, Sagadevanf SO (2020) Evaluation of the photocatalytic efficiency of cobalt oxide nanoparticles towards the degradation of crystal violet and methylene violet dyes. *Optik* 207(164):428. <https://doi.org/10.1016/j.ijleo.2020.164428>
- Sarkar A, Ghosh M, Si PC (2014) Nanotoxicity: oxidative stress mediated toxicity of metal and metal oxide nanoparticles. *J Nanosci Nanotechnol* 14(1):730–743. <https://doi.org/10.1166/jnn.2014.8752>
- Shah ST, Yehye WA, Saad O, Simarani K, Chowdhury ZZ, Alhadi AA, Al-Ani LA (2017) Surface functionalization of iron oxide nanoparticles with gallic acid as potential antioxidant and antimicrobial agents. *Nanomaterials* 7(306). <https://doi.org/10.3390/nano7100306>
- Shahwan T, Sirriah SA, Nairat M (2011) Green synthesis of iron nanoparticles and their application as a Fenton-like catalyst for the degradation of aqueous cationic and anionic dyes. *Chem Eng J* 172(1):258–266. <https://doi.org/10.1016/j.cej.2011.05.103>
- Sies H, Jones DP (2020) Reactive oxygen species (ROS) as pleiotropic physiological signalling agents. *Nat Rev Mol Cell Biol* 21:363–383. <https://doi.org/10.1038/s41580-020-0230-3>
- Sies H, Berndt C, Jones DP (2017) Oxidative stress. *Annu Rev Biochem* 86:715–748. <https://doi.org/10.1146/annurev-biochem061516-045037>
- Singh N, Savanur MA, Srivastava S, D’Silva P, Mugesh G (2017) A manganese oxide nanozyme prevents the oxidative damage of biomolecules without affecting the endogenous antioxidant system. *Angew Chem Int Ed* 56:14,267–14,271. <https://doi.org/10.1039/C8NR09397K>
- Sinha T, Ahmaruzzaman M (2015) Green synthesis of copper nanoparticles for the efficient removal (degradation) of dye from aqueous phase. *Environ Sci Pollut Res* 22:20,092–20,100. <https://doi.org/10.1007/s11356-015-5223-y>
- Sutradhar P, Saha M, Maiti D (2014) Microwave synthesis of copper oxide nanoparticles using tea leaf and coffee powder extracts and its antibacterial activity *CuO* 4:86. <https://doi.org/10.1007/s40097-014-0086-1>
- Swietek M, Lu YC, Konefal R, Ferreira LP, Cruz MM, Ma YH, Horak D (2019) Scavenging of reactive oxygen species by phenolic compound-modified maghemite nanoparticles. *Beilstein J Nanotechnol* 10:1073–1088. <https://doi.org/10.3762/bjnano.10.108>
- Swietek M, Lu YC, Konefal R, Ferreira LP, Cruz MM, Ma YH, Horak D (2019a) Scavenging of reactive oxygen species by phenolic compound-modified maghemite nanoparticles. *Beilstein J Nanotechnol* 10:1073–1088. <https://doi.org/10.3762/bjnano.10.108>
- Sytnyk M, Kirchschrager R, Bodnarchuk MI, Primetzhofer D, Kriegner D, Enser H, Stangl J, Baue P, Voith M, Hassel AW, Krumeich F, Ludwig F, Meingast A, Kothleitner G, Kovalenko MV, Heiss W (2013) Tuning the magnetic properties of metal oxide nanocrystal heterostructures by cation exchange. *Nano Lett* 13(2):586–593. <https://doi.org/10.1021/nl304115r>
- Tabassum A, Bristow RG, Venkateswaran V (2010) Ingestion of selenium and other antioxidants during prostate cancer radiotherapy: a good thing? *Cancer Treat Rev* 36:230–234. <https://doi.org/10.1016/j.ctrv.2009.12.008>

- Thomsen LB, Thomsen M, Moos T (2015) Targeted drug delivery to the brain using magnetic nanoparticles. *Ther Deliv* 6(10):1145–1155. <https://doi.org/10.4155/tde.15.56>
- Turin-Moleavin IA, Fifere A, Lungoci AL, Rosca I, Coroaba A, Peptanariu D, Pasca SA, Bostanaru AC, Mares M, Pinteala M (2019) Vitro and in vivo antioxidant activity of the new magnetic-cerium oxide nanoconjugates. *Nanomaterials (Basel)* 9(11):1565. <https://doi.org/10.3390/nano9111565>
- Uritu CM, Calin M, Maier SS, Cojocaru C, Nicolescu A, Peptanariu D, Constantinescu CA, Stan D, Barboiu M, Pinteala M (2015) Flexible cyclic siloxane core enhances the transfection efficiency of polyethylenimine-based non-viral gene vectors. *J Mater Chem B* 3(42):8250–8267. <https://doi.org/10.1039/C5TB01342A>
- Vinardell MP, Mitjans M (2015) Antitumor activities of metal oxide nanoparticles. *Nanomaterials* 5:1004–1021. <https://doi.org/10.3390/nano5021004>
- Viota JL, Carazo A, Munoz-Gamez JA, Rudzka K, Gomez-Sotomayor R, Ruiz-Extremera A, Salmeron J, Delgado AV (2013) Functionalized magnetic nanoparticles as vehicles for the delivery of the antitumor drug gemcitabine to tumor cells. Physicochemical in vitro evaluation. *Mater Sci and Eng C* 33(3):1183–1192. <https://doi.org/10.1016/j.msec.2012.12.009>
- Waldo GS, Penner-Hahn JE (1995) Mechanism of manganese catalase peroxide disproportionation: determination of manganese oxidation states during turnover. *Biochemistry* 34(5):1507–1512. <https://doi.org/10.1021/bi00005a006>
- Wang Z, Shen X, Gao X, Zhao Y (2019) Simultaneous enzyme mimicking and chemical reduction mechanisms for nanoceria as a bio-antioxidant: a catalytic model bridging computations and experiments for nanozymes. *Nanoscale* 11:13,289–13,299. <https://doi.org/10.1039/C9NR03473K>
- Wua Y, Yanga Y, Zhaoa W, Xua ZP, Littled P, Whittakera VK, Zhanga R, Ta HT (2018) Novel iron oxide-cerium oxide core-shell nanoparticle as a potential theranostic material for ROS related inflammatory diseases. *J Mater Chem B* 6:4937–4951. <https://doi.org/10.1039/C8TB00022K>
- Wydra RJ, Oliver CE, Anderson KE, Dziubla TD, Hilt JZ (2015) Accelerated generation of free radicals by iron oxide nanoparticles in the presence of an alternating magnetic field. *RSC Adv* 5(24):18888–18893. <https://doi.org/10.1039/C4RA13564D>
- Xu DP, Li Y, Meng X, Zhou T, Zhou Y, Zheng J, Zhang JJ, Bin Li H (2017) Natural antioxidants in foods and medicinal plants: extraction, assessment and resources *Int J Mol Sci* 18(1):96. <https://doi.org/10.3390/ijms18010096>
- Xue C, Wu J, Lan F, Liu W, Yang X, Zeng F, Xu H (2010) Nano titanium dioxide induces the generation of ROS and potential damage in HaCaT cells under UVA irradiation. *J Nanosci Nanotechnol* 10(12):8500–8507. <https://doi.org/10.1166/jnn.2010.2682>
- Yan LJ (2014) Positive oxidative stress in aging and aging-related disease tolerance. *Redox Biol* 2C:165–169. <https://doi.org/10.1016/j.redox.2014.01.002>
- Yordi EG, Perez EM, Matos MJ, Villares EU (2012) Antioxidant and pro-oxidant effects of polyphenolic compounds and structure–activity relationship evidence. *Nutr. Well-Being Health* 2:23–48. In: Bouayed, J, Bohn T (ed.). <https://doi.org/https://doi.org/10.5772/29471>
- Zhelstova AA, Kharitonova MV, Iezhitsa IN, Spasova AA (2016) Magnesium deficiency and oxidative stress: an update. *BioMedicine* 6(4):8–14. <https://doi.org/10.7603/s40681-016-0020-6>

Supramolecular Guanosine-Quadruplex Hydrogels and Hydrogel Composites for Cell Growth Applications



Elena Laura Ursu and Alexandru Rotaru

Abstract Supramolecular Chemistry have for decades played an important role in developing of functional systems for biomedical applications. In the current work, we summarize our results obtained during the implementation of the SupraChemLab project with the focus on supramolecular hydrogels or systems for cell staining applications. Supramolecular hydrogels composed of natural components and increased water content are of high interest in drug delivery and tissue engineering. We have proposed the use of synthesized guanosine dimers as building blocks for the construction of hydrogels with cation dependent assembly involving the formation of guanosine quartets. The hydrogel properties could be tuned by the use of cations able to either form the guanosine quartet, or participate in framework cross-linking thus considerably improving hydrogel properties. Besides cation tuning, we have investigated insertion of dispersed carbon nanotubes into the hydrogel matrix with the aim of improving hydrogels mechanical properties. The prepared and characterized materials supported cell growth and did not show visible signs of degradation. Tests showed excellent cell viability, of up to 75%, on these supramolecular hydrogels after 24 h.

In a parallel research, we have in detail investigated supramolecular host-guest inclusion complex formation between a fluorescent indoliziny-pyridinium salt and β -cyclodextrin in view of testing this assembly as fluorescent probes for staining cells or cell components. The investigated supramolecular system displayed several important advantages including strong decrease of inclusion complex cytotoxicity when compared to starting compound, long-lived fluorescence in cells, and specific accumulation in lysosomes. These findings make the investigated supramolecular approach attractive for testing on dyes in all spectral regions with intrinsic disadvantages like low solubility or elevated toxicity, as fluorescent probes for cells or cell component labelling or staining.

E. L. Ursu · A. Rotaru (✉)

Centre of Advanced Research in Bionanoconjugates and Biopolymers, “Petru Poni” Institute of Macromolecular Chemistry, 700487 Iasi, Romania

e-mail: rotaru.alexandru@icmpp.ro

E. L. Ursu

e-mail: ursu.laura@icmpp.ro

Keywords Supramolecular chemistry · Guanosine quartet · Cell support · Carbon nanotubes · Fluorescent probes · Cell staining

Abbreviations

BDBA	Benzene-1,4-diboronic acid
CD	β -cyclodextrin
ESI-MS	Electrospray ionization mass spectroscopy
G4Q	Guanosine quartet
HeLa	Human cervical adenocarcinoma cells
IPS	Indolizinylium-pyridinium salt
NHDF	Normal human dermal fibroblasts
SEM	Scanning electron microscopy
SHs	Supramolecular Hydrogels
SWNTs	Single-walled carbon nanotubes
TEM	Transmission electron microscopy

1 Introduction

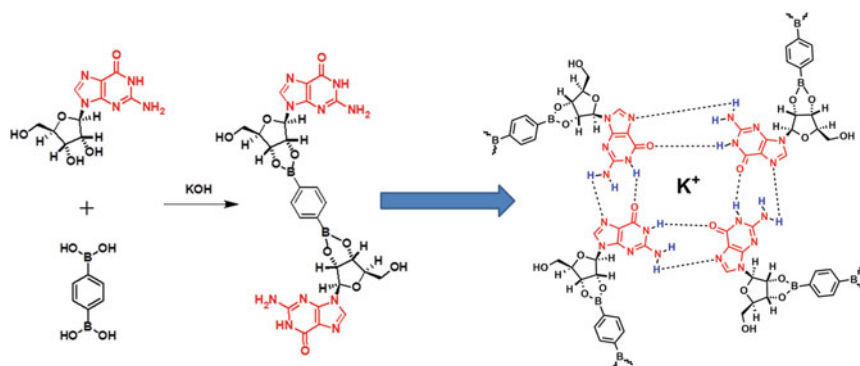
The development of next-generation materials for biomedical purposes should comprise new approaches which may include natural or nature-inspired materials and a strategy to straightforward assembly of these entities into functional units. Supramolecular chemistry, defined as ‘chemistry beyond the molecule’ (Aida et al. 2012; Dong et al. 2015; Lehn, 1988) may represent a viable solution to the design of functional materials due to its specific and unique interactions, based on the rational design of molecular recognition motifs. The designed motifs are hold together by non-covalent interactions including π - π interactions, hydrogen bonding, or van der Waals interactions and contribute to the preparation of final supramolecular systems whose properties resemble the dynamic nature of their constituents (Appel et al. 2012; Seiffert and Sprakel, 2012). So far, supramolecular approaches in the design of functional biomaterials have resulted in reported outstanding in vitro and in vivo protocols for therapy or diagnostics (Dong et al. 2015; Ghosh et al. 2020; Webber et al. 2016, 2013). In the current work, we will give an overview on the supramolecular approaches developed by our group in the field of materials for cell support applications and supramolecular systems for staining of living cells or cellular components. We summarize the conditions for the design and preparation of optimal guanosine-based precursors for the construction of suitable, non-toxic and tunable support for the sustainable cellular growth and development. We discuss the advantages of supramolecular host-guest inclusion complexes approach in the development of

long-lived non-toxic fluorescent probes for extranuclear cytoplasm staining and in time specific accumulations of probes in cell acidic organelles.

2 Guanosine-Based Supramolecular Hydrogels for Cell Support Applications

Since hydrogels, defined as a three-dimensional network of interconnected and cross-linked constituent building blocks, are capable of retention impressive amounts of water (Jha et al. 2010; Yu and Ding, 2008), they have found numerous applications ranging from tissue engineering (Cai et al. 2011; Lin et al. 2014) and cell culture scaffolds (Benoit et al. 2008; Khetan et al. 2013) to drug delivery (Banerjee et al. 2009; Cornwell and Smith, 2015; Hirst et al. 2008; Lim et al. 2019; Sangeetha and Maitra, 2005). A particular class of hydrogels, Supramolecular Hydrogels (SHs), where the constituent molecules are held together by non-covalent interactions, have recently gained particular attention due to the possibility of the stimuli response of such systems. These particularities of SHs owe to the reversibility of the involved non-covalent interactions utilized in the SHs design and preparation, comprising host-guest inclusion complex formation, extensive hydrogen bonding, self-assembly, electrostatic interactions, self-assembly and metal-ligand coordination. For SHs to be successfully used for biomedical applications, it is important for them to be synthesized from biocompatible materials (Lim et al. 2019; Singh et al. 2013). Consequently, designing SHs consisting of naturally occurring molecules (e.g. nucleobases, peptides, polysaccharides, etc.) are of a particular interest. We and others (Peters et al. 2016–2015; Plank and Davis 2016; Rotaru et al. 2017) have focused our research on preparation of guanosine-based hydrogels with the subsequent biomedical applications. The gelation mechanism of the proposed materials primarily involves cation-templated formation of the guanosine quartet (G4Q) core, a macrocycle formed by four hydrogen-bonded guanosines. The cation also stabilizes the assembly by coordinating to the eight carbonyl oxygens of two sandwiched G-quartets. The resulting G-quadruplex, a columnar structure formed by the vertical stacking of multiple G4Qs may further self-assemble via supplementary reversible covalent bonds or other non-covalent interactions. Besides the formation of guanosine-based columnar structures, the investigated materials are reticulated by boric acid (Peters et al. 2014) or phenyl diboronic acid (Rotaru et al. 2017) under basic conditions by condensation of the 2',3'-diol units of guanosine with borate anion (Scheme 1).

Since boric acid based hydrogels possess high cytotoxicity and thus cannot be properly utilized in the biomedical field, our group proposed to modify the properties of the gel and its water retention capacity by substituting boric acid linker with benzene-1,4-diboronic acid (BDDBA), and employ mono and bivalent ions for stabilizing the guanosine quartet (Rotaru et al. 2017). Following this strategy and using KOH in the first attempts, we succeeded in preparation of stable and transparent hydrogels (K-G-BDDBA) but with a relatively low water retention capacity when



Scheme 1 Reaction pathways for the preparation of guanosine dimer as precursor for guanosine-based hydrogels (Rotaru et al. 2017)

compared with the boric acid analog. To overcome this disadvantage, a strategy of changing the templating cation in hydrogel synthesis was adopted by replacing Ba(OH)₂ instead of KOH. The experiment has also resulted in the formation of a transparent Ba-G-BDBA hydrogel with a water retention capacity of 5 times higher when compared to the K-G-BDBA. Following this trend and taking into account the nature of the BDBA-guanosine dimer, we have investigated the possibility of further internal reticulation of the hydrogel structure by bivalent cations. Impressively, the use of Mg²⁺ cations after the formation of the K-G-BDBA hydrogel, led to the creation of new Mg-K-G-BDBA hydrogels able to retain 15 times greater amount of water.

In order to verify the biomedical applicability of K-G-BDBA, Ba-G-BDBA and Mg-K-G-BDBA hydrogels, cell growth and viability tests were performed on the NHDF (normal human dermal fibroblasts) cell line. The performed tests demonstrated well to excellent cell viability cultured on these hydrogels after a 24-h interval, as well as good attachments of cells to the hydrogels surfaces (Fig. 1). Among the tested hydrogels, Mg-K-G-BDBA hydrogel showed the best results as a support for cell growth applications due to higher water content when compared to the others.



Fig. 1 Images of NHDF cells grown on K-G-BDBA (left), Ba-G-BDBA (middle) and Mg-K-G-BDBA (right) guanosine-based hydrogels (Rotaru et al. 2017)

Unfortunately, the high water retention capacity offered by the use of Ba^{2+} and Mg^{2+} ions in the formation of hydrogels led to the lower stability of their internal structure which led to difficulties in handling the samples during the experiments. To overcome these disadvantages, we investigated alternative crosslinking agents both to improve the properties of hydrogels and to maintain high water retention capacities. Literature survey has shown that various nanomaterials including carbon nanotubes and graphene oxides have been reported as being used to form composite hydrogels and to enhance their mechanical properties by intercalation in the polymeric or supramolecular structure of the hydrogel (Adewunmi et al. 2016; Bellingeri et al. 2018; Kouser et al. 2018; Tan et al. 2011). Among these materials, single-walled carbon nanotubes (SWNTs) have demonstrated their efficiency in strengthening hydrogel structures, leading to the formation of composite hydrogels with superior properties (Hough et al. 2006; Tan et al. 2011). Additionally, their non-toxic and biocompatible character makes them excellent candidates in the field of tissue engineering.

In order to efficiently introduce SWNTs into the internal structure of K-G-BDBA hydrogel, we have designed the experiment in such a way that it would be possible to first disperse the SWNTs followed by a trigger for the formation of the hydrogel matrix (Ursu et al. 2020). Using the developed strategy, it was possible to controllably introduce various amounts of SWNTs (Fig. 2) into the hydrogel structure and correspondingly to increase the water retention ability by factor three. The SWNT-hydrogel composites' structure was investigated using scanning electron microscopy (SEM), Raman spectroscopy and transmission electron microscopy (TEM), supported by the data on the rheological investigations of the samples with different amounts of SWNTs. All the obtained data suggested the dispersion of the SWNTs inside the hydrogel matrix and clear influence of the SWNTs on the improvement of the hydrogel porosity and overall properties.

Further studies were performed for the evaluation of the hydrogels ability to be used as efficient supports for cell growth applications. Cytotoxicity studies on the optimized SWNTs composites have shown good to excellent values for cell growth (>70%), and revealed the fact that the cytotoxicity values were not dependent on the concentration of SWNTs in the investigated samples.

Next, human dermal fibroblast (NHDF) cells were cultured on the surface of the composite hydrogels using the drop seeding technique, followed by periodical monitoring over an extended period of time. In order to visualize the cell growing progress, the cells cultured on the surface of the hydrogels were subsequently labeled using live/dead assay, this being used as a qualitative method, complementary to the quantitative MTS cytotoxicity test. By this method we were able to selectively mark and visualize living cells (using AM calcein, green cells) and dead cells (using propidium iodide, red blood cells). Analysis of images obtained by fluorescence microscopy 24 h after incubation confirmed the results obtained in cytotoxicity studies, showing a predominant number of viable cells (green) compared to dead cells (red).

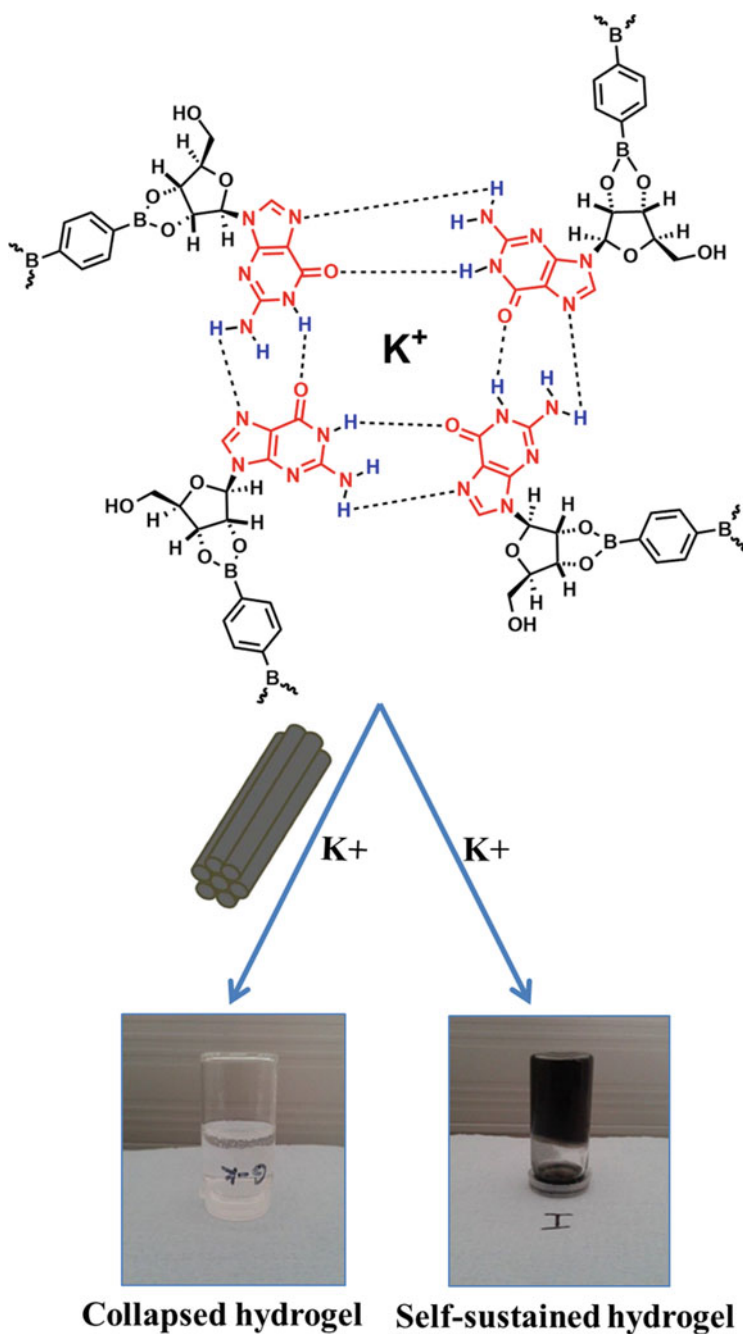
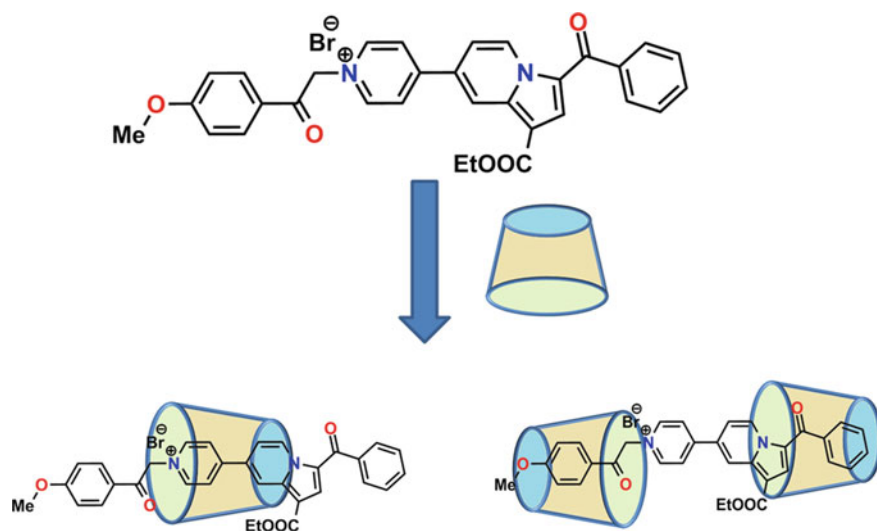


Fig. 2 Schematic representation of SWNTs dispersion by guanosine-based hydrogel with the formation of SWNT-composite hydrogels with increased water retention ability (Ursu et al. 2020)

3 Host-Guest Inclusion Complexes as Fluorescent Probes for Staining Living Cells

Fluorescence imaging is an effective tool used in living systems to image and track specific biological targets or processes (Stennett et al. 2014; Xia et al. 2013), thus supporting an extensive search for suitable fluorescent dyes. Since synthesized fluorescent molecules may possess unsuitable properties (toxicity, low water solubility and poor membrane permeability) (Qin et al. 2012; Vegesna et al. 2013) for in vitro or in vivo applications, various synthetic approaches are utilized for mitigation of existing disadvantages (Feng et al. 2010; Maruyama et al. 2002; Woodroffe et al. 2004; Zhang et al. 2015). We and others have suggested the use of supramolecular approaches to include cucurbit[8]uril or cyclodextrins host-guest inclusion complexes in the development of methods to solve both solubility and toxicity problems (Di Donato et al. 2016; Edetsberger et al. 2011; Ghosh et al. 2014; Konda et al. 2017; Pricope et al. 2018). Our group has proposed novel long-lived supramolecular fluorescent probes capable of penetrating cell membrane and selectively staining cell acidic organelles by using pH-sensitive indoliziny-pyridinium salt derivative and β -cyclodextrin (CD) (Scheme 2) (Pricope et al. 2018).

The designed indoliziny-pyridinium salt (IPS) with pH-dependent fluorescent properties was used in the complexation reaction with CD as a guest molecule in our strategy. Complexation was supposed to decrease the high toxicity of IPS and to



Scheme 2 Schematic representation for the preparation of supramolecular host-guest inclusion complexes between cyclodextrin and indoliziny-pyridinium salt derivative with the formation of 1:1 and 1:2 complexes (Pricope et al. 2018)

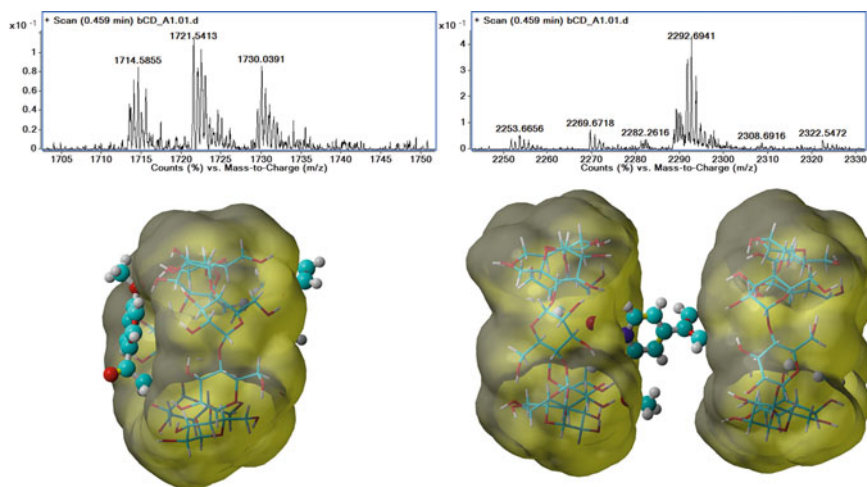


Fig. 3 Examples of ESI-MS spectra for the IPS and β -CD reaction mixture: observed masses for 1:1 inclusion complex ($1654 - M^+ - Br + CD$) and a 1:2 complex ($2788 - M^+ - Br + 2CD$); molecular docking models of IPS in complex with β -CD showing the possibility of the 1:1 (left) and 1:2 (right) inclusion complex formation (Pricope et al. 2018)

increase the overall solubility of dye water. In order to observe full water solubilization of IPS, we have experimented with variable ratios between IPS and CD, beginning with the 1:1.5 ratio (guest:host). The higher solubilization ratio between IPS and CD implies that more complex supramolecular assemblies formed of an inclusion complex consisting of one IPS molecule and two or more CD units were formed. Indeed, the formation of 1:1 and 1:2 species was confirmed by ESI-MS experiments of the reaction mixture and supported by the molecular docking theoretical calculations (Fig. 3).

Interestingly, the large increase in stoichiometry between the host and the guest did not change the equilibrium towards the formation of just 1:2. The complexation process was additionally monitored for the changes in supramolecular arrangements of the starting CD in comparison to the aggregation of the inclusion complex. A mixture of large sheets and parallelogram-like crystals of various sizes were presented in the TEM images for CD, while the IPS inclusion complex showed needle-like crystals of several micrometers in length.

The cytotoxicity of IPS and IPS inclusion complexes was investigated against two human cancer and normal cell lines (HeLa and NHDF) prior to cell staining experiments. The data obtained showed that IPS exhibited very high toxicity values at all five concentrations investigated (0% cell viability) on the HeLa cell line and relatively high to medium toxicity on the NHDF cells (Pricope et al. 2018). On the other hand, the solutions of the IPS inclusion complexes at the same studied concentrations exhibited remarkably high cell viability values (above 95%) in the case of HeLa cells and high cell viability values (above 80%) in the case of NHDF cells.

The ability of the IPS inclusion complex to stain living cells was tested on two cell lines (HeLa and NHDF), different concentrations of inclusion complexes were incubated over a period of 24 h, with image recording every 15 min (Pricope et al. 2018). The results of the incubation suggested the penetration of the IPS complex through the membranes of both the cell lines studied, suggesting mainly uniform extranuclear localization. Surprisingly, after 24 h, the picture changed significantly, and when comparing the images after 15 min and 24 h, the overall strong increase in brightness of both the investigated cell lines was observed. Interestingly, the bright accumulations within the cytoplasm were smaller and more regular in the case of NHDF cells than the ones found in HeLa cells. A particular interaction of the dye with specific cell components was demonstrated by large and localized bright accumulations in HeLa cells (Fig. 4).

We presume that the deposition of the dye takes place preferentially in the acidic organelles of the cells, taking into account the characteristics of the IPS compound and its properties of providing a higher intensity of fluorescence at a lower pH. A co-staining experiment was conducted with LysoTracker Red DND-99, a commercial agent used for staining acidic cell organelles, to verify this assumption. A similar accumulation of both staining agents was observed when the images stained with IPS complex and LysoTracker Red DND-99 were overlapped in the same localized spots of the HeLa cells examined. Our proposal on the unique accumulations in the acidic organelles of the cell was confirmed by the results obtained. Therefore, our future efforts will focus on the synthesis and testing of non-toxic fluorescent derivatives based on the pyridyl-indolizine core molecule, the development and application of the corresponding cyclodextrin inclusion complexes in staining specific organelles of the cells.

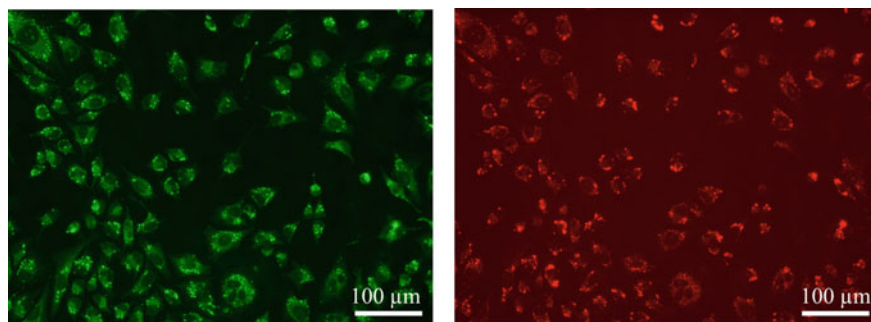


Fig. 4 Comparison of cellular accumulation and distribution in HeLa cells of IPS (left) after 24 h (GFP filter) and LysoTracker Red DND-99 (right) after 30 min (N2.1 filter)

4 Conclusions

During the implementation of the SupraChemLab project within the H2020 Call, we have succeeded in designing systems and developing protocols for the preparation of novel functional supramolecular assemblies which found applications as cell supports matrixes or fluorescent cell staining probes. The main focus of the research in the field of cell support systems concerted around the concept of guanosine quartet formation of the specifically designed dimers able to yield extensive supramolecular frameworks with the subsequent formation of hydrogels. These flexible and biocompatible materials exhibited tunable properties conditioned by the used cations to reticulate the framework, and were able to sustain impressive amounts of water in their structure. Besides the cation exchange, the insertion of dispersed carbon nanotubes was also used to improve and tune the hydrogels' mechanical properties, making them even better materials for cell support applications. All the investigated supramolecular materials demonstrated good cytotoxicity and successful adhesion of NHDF cells to their surfaces, making them interesting candidates as materials for tissue engineering.

The supramolecular approach in the design of novel fluorescent probes for cell staining applications was proposed and successfully tested. Host-guest inclusion complex formation between a fluorescent indoliziny-pyridinium salt and β -cyclodextrin was investigated and the obtained complex evaluated for cellular permeability, intracellular fluorescence and selective accumulation within acidic organelles. A series of interesting observation including: (i) a strong decrease of inclusion complex cytotoxicity when compared to starting compound; (ii) long-lived fluorescence in cells and (iii) specific accumulation in lysosomes accompanied by strong fluorescent signal increase in corresponding accumulations in time, make the investigated supramolecular approach attractive for testing on dyes in all spectral regions with intrinsic disadvantages like low solubility or elevated toxicity, as fluorescent probes for cells or cell component labelling or staining.

Acknowledgements The project leading to this application has received funding from the H2020 ERA Chairs Project no 667387: SupraChem Lab Laboratory of Supramolecular Chemistry for Adaptive Delivery Systems ERA Chair initiative. This work was supported also by a grant of the Romanian Ministry of Research and Innovation, CCDI-UEFISCDI, project number PN-III-P1-1.2.-PCCDI-2017-0697/contract nr. 13 PCCDI/2018 within PNCDI III.

Conflict of Interest The authors declare no conflict of interest.

References

- Adewunmi AA, Ismail S, Sultan AS (2016) Carbon nanotubes (CNTs) nanocomposite hydrogels developed for various applications: a critical review. *J Inorg Organomet Polym* 26:717–737. <https://doi.org/10.1007/s10904-016-0379-6>

- Aida T, Meijer EW, Stupp SI (2012) Functional supramolecular polymers. *Science* 335:813–817. <https://doi.org/10.1126/science.1205962>
- Appel EA, del Barrio J, Loh XJ, Scherman OA (2012) Supramolecular polymeric hydrogels. *Chem Soc Rev* 41:6195–6214. <https://doi.org/10.1039/C2CS35264H>
- Banerjee S, Das RK, Maitra U (2009) Supramolecular gels 'in action.' *J Mater Chem* 19:6649–6687. <https://doi.org/10.1039/B819218A>
- Bellingeri R, Mulko L, Molina M, Picco N, Alustiza F, Grosso C, Vivas A, Acevedo DF, Barbero CA (2018) Nanocomposites based on pH-sensitive hydrogels and chitosan decorated carbon nanotubes with antibacterial properties. *Mater Sci Eng C Mater Biol Appl* 90:461–467. <https://doi.org/10.1016/j.msec.2018.04.090>
- Benoit DSW, Schwartz MP, Durney AR, Anseth KS (2008) Small functional groups for controlled differentiation of hydrogel-encapsulated human mesenchymal stem cells. *Nat Mater* 7:816–823. <https://doi.org/10.1038/nmat2269>
- Cai X, Chen L, Jiang T, Shen X, Hu J, Tong H (2011) Facile synthesis of anisotropic porous chitosan/hydroxyapatite scaffolds for bone tissue engineering. *J Mater Chem* 21:12015–12025. <https://doi.org/10.1039/C1JM11503K>
- Cornwell DJ, Smith DK (2015) Expanding the scope of gels – combining polymers with low-molecular-weight gelators to yield modified self-assembling smart materials with high-tech applications. *Mater Horiz* 2:279–293. <https://doi.org/10.1039/C4MH00245H>
- Di Donato C, Lavorgna M, Fattorusso R, Isernia C, Isidori M, Malgieri G, Piscitelli C, Russo C, Russo L, Iacovino R (2016) Alpha- and beta-cyclodextrin inclusion complexes with 5-fluorouracil: characterization and cytotoxic activity evaluation. *Molecules* 21 <https://doi.org/10.3390/molecules21121644>
- Dong R, Zhou Y, Huang X, Zhu X, Lu Y, Shen J (2015) Functional supramolecular polymers for biomedical applications. *Adv Mater Weinheim* 27:498–526. <https://doi.org/10.1002/adma.201402975>
- Edetsberger M, Knapp M, Gaubitzer E, Miksch C, Gvichiya KE, Köhler G (2011) Effective staining of tumor cells by coumarin-6 depends on the stoichiometry of cyclodextrin complex formation. *J Incl Phenom Macrocycl Chem* 70:327–331. <https://doi.org/10.1007/s10847-010-9894-1>
- Feng X, Liu L, Wang S, Zhu D (2010) Water-soluble fluorescent conjugated polymers and their interactions with biomacromolecules for sensitive biosensors. *Chem Soc Rev* 39:2411–2419. <https://doi.org/10.1039/B909065G>
- Ghosh S, Chatteraj S, Chattopadhyay N (2014) Interaction of β -cyclodextrin with Nile red in a single live CHO cell: an initiative towards developing a prospective strategy for the excretion of adsorbed drugs from the cell membrane. *Analyst* 139:5664–5668. <https://doi.org/10.1039/C4AN01114G>
- Ghosh T, Biswas A, Gavel PK, Das AK (2020) Engineered dynamic boronate ester-mediated self-healable biocompatible G-quadruplex hydrogels for sustained release of vitamins. *Langmuir* 36:1574–1584. <https://doi.org/10.1021/acs.langmuir.9b03837>
- Hirst AR, Escuder B, Miravet JF, Smith DK (2008) High-tech applications of self-assembling supramolecular nanostructured gel-phase materials: from regenerative medicine to electronic devices. *Angew Chem Int Ed Engl* 47:8002–8018. <https://doi.org/10.1002/anie.200800022>
- Hough LA, Islam MF, Hammouda B, Yodh AG, Heiney PA (2006) Structure of semidilute single-wall carbon nanotube suspensions and gels. *Nano Lett* 6:313–317. <https://doi.org/10.1021/ml051871f>
- Jha AK, Malik MS, Farach-Carson MC, Duncan RL, Jia X (2010) Hierarchically structured, hyaluronic acid-based hydrogel matrices via the covalent integration of microgels into macroscopic networks. *Soft Matter* 6:5045–5055. <https://doi.org/10.1039/C0SM00101E>
- Khetan S, Guvendiren M, Legant WR, Cohen DM, Chen CS, Burdick JA (2013) Degradation-mediated cellular traction directs stem cell fate in covalently crosslinked three-dimensional hydrogels. *Nat Mater* 12:458–465. <https://doi.org/10.1038/nmat3586>

- Konda SK, Maliki R, McGrath S, Parker BS, Robinson T, Spurling A, Cheong A, Lock P, Pigram PJ, Phillips DR, Wallace L, Day AI, Collins JG, Cutts SM (2017) Encapsulation of mitoxantrone within cucurbit[8]uril decreases toxicity and enhances survival in a mouse model of cancer. *ACS Med Chem Lett* 8:538–542. <https://doi.org/10.1021/acsmchemlett.7b00090>
- Kouser R, Vashist A, Zafaryab M, Rizvi MA, Ahmad S (2018) Biocompatible and mechanically robust nanocomposite hydrogels for potential applications in tissue engineering. *Mater Sci Eng C Mater Biol Appl* 84:168–179. <https://doi.org/10.1016/j.msec.2017.11.018>
- Lehn J-M (1988) Supramolecular chemistry—scope and perspectives molecules, supermolecules, and molecular devices (nobel lecture). *Angew Chem Int Ed Engl* 27:89–112. <https://doi.org/10.1002/anie.198800891>
- Lim JYC, Lin Q, Xue K, Loh XJ (2019) Recent advances in supramolecular hydrogels for biomedical applications. *Mater Today Adv* 3:100021. <https://doi.org/10.1016/j.mtadv.2019.100021>
- Lin Y-J, Hsu F-C, Chou C-W, Wu T-H, Lin H-R (2014) Poly(acrylic acid)-chitosan-silica hydrogels carrying platelet gels for bone defect repair. *J Mater Chem B* 2:8329–8337. <https://doi.org/10.1039/c4tb01356e>
- Maruyama S, Kikuchi K, Hirano T, Urano Y, Nagano T (2002) A novel, cell-permeable, fluorescent probe for ratiometric imaging of zinc ion. *J Am Chem Soc* 124:10650–10651. <https://doi.org/10.1021/ja026442n>
- Peters GM, Skala LP, Davis JT (2016) A molecular chaperone for G4-quartet hydrogels. *J Am Chem Soc* 138:134–139. <https://doi.org/10.1021/jacs.5b08769>
- Peters GM, Skala LP, Plank TN, Hyman BJ, Manjunatha Reddy GN, Marsh A, Brown SP, Davis JT (2014) A G4-K+ hydrogel stabilized by an anion. *J Am Chem Soc* 136:12596–12599. <https://doi.org/10.1021/ja507506c>
- Peters GM, Skala LP, Plank TN, Oh H, Manjunatha Reddy GN, Marsh A, Brown SP, Raghavan SR, Davis JT (2015) G4-Quartet-M+ borate hydrogels. *J Am Chem Soc* 137:5819–5827. <https://doi.org/10.1021/jacs.5b02753>
- Plank TN, Davis JT (2016) A G4-K+ hydrogel that self-destructs. *Chem Commun* 52:5037–5040. <https://doi.org/10.1039/C6CC01494A>
- Pricope G, Ursu EL, Sardaru M, Cojocaru C, Clima L, Marangoci N, Danac R, Mangalagiu II, Simionescu BC, Pinteala M, Rotaru A (2018) Novel cyclodextrin-based pH-sensitive supramolecular host-guest assembly for staining acidic cellular organelles. *Polym Chem* 9:968–975. <https://doi.org/10.1039/C7PY01668A>
- Qin W, Ding D, Liu J, Yuan WZ, Hu Y, Liu B, Tang BZ (2012) Biocompatible nanoparticles with aggregation-induced emission characteristics as far-red/near-infrared fluorescent bioprobes for in vitro and in vivo imaging applications. *Adv Func Mater* 22:771–779. <https://doi.org/10.1002/adfm.201102191>
- Rotaru A, Pricope G, Plank TN, Clima L, Ursu EL, Pinteala M, Davis JT, Barboiu M (2017) G-Quartet hydrogels for effective cell growth applications. *Chem Commun* 53:12668–12671. <https://doi.org/10.1039/C7CC07806D>
- Sangeetha NM, Maitra U (2005) Supramolecular gels: functions and uses. *Chem Soc Rev* 34:821–836. <https://doi.org/10.1039/B417081B>
- Seiffert S, Sprakel J (2012) Physical chemistry of supramolecular polymer networks. *Chem Soc Rev* 41:909–930. <https://doi.org/10.1039/C1CS15191F>
- Singh A, Zhan J, Ye Z, Elisseeff JH (2013) Modular multifunctional poly(ethylene glycol) hydrogels for stem cell differentiation. *Adv Func Mater* 23:575–582. <https://doi.org/10.1002/adfm.201201902>
- Stennett EMS, Ciuba MA, Levitus M (2014) Photophysical processes in single molecule organic fluorescent probes. *Chem Soc Rev* 43:1057–1075. <https://doi.org/10.1039/C3CS60211G>
- Tan Z, Ohara S, Naito M, Abe H (2011) Supramolecular hydrogel of bile salts triggered by single-walled carbon nanotubes. *Adv Mater* 23:4053–4057. <https://doi.org/10.1002/adma.201102160>
- Ursu E-L, Gavril G, Morariu S, Pinteala M, Barboiu M, Rotaru A (2020) Single-walled carbon nanotubes–G-quadruple hydrogel nanocomposite matrixes for cell support applications. *Mater Sci Eng C* 111:110800. <https://doi.org/10.1016/j.msec.2020.110800>

- Vegesna GK, Sripathi SR, Zhang J, Zhu S, He W, Luo F-T, Jahng WJ, Frost M, Liu H (2013) Highly water-soluble BODIPY-based fluorescent probe for sensitive and selective detection of nitric oxide in living cells. *ACS Appl Mater Interfaces* 5:4107–4112. <https://doi.org/10.1021/am303247s>
- Webber MJ, Appel EA, Meijer EW, Langer R (2016) Supramolecular biomaterials. *Nat Mater* 15:13–26. <https://doi.org/10.1038/nmat4474>
- Webber MJ, Berns EJ, Stupp SI (2013) Supramolecular nanofibers of peptide amphiphiles for medicine. *Isr J Chem* 53:530–554. <https://doi.org/10.1002/ijch.201300046>
- Woodrooffe CC, Masalha R, Barnes KR, Frederickson CJ, Lippard SJ (2004) Membrane-permeable and -impermeable sensors of the Zinpyr family and their application to imaging of hippocampal zinc in vivo. *Chem Biol* 11:1659–1666. <https://doi.org/10.1016/j.chembiol.2004.09.013>
- Xia T, Li N, Fang X (2013) Single-molecule fluorescence imaging in living cells. *Annu Rev Phys Chem* 64:459–480. <https://doi.org/10.1146/annurev-physchem-040412-110127>
- Yu L, Ding J (2008) Injectable hydrogels as unique biomedical materials. *Chem Soc Rev* 37:1473–1481. <https://doi.org/10.1039/B713009K>
- Zhang Z-X, Guo X-F, Wang H, Zhang H-S (2015) Capillary electrophoresis strategy to monitor the released and remaining nitric oxide from the same single cell using a specially designed water-soluble fluorescent probe. *Anal Chem* 87:3989–3995. <https://doi.org/10.1021/acs.analchem.5b00191>

Hydrogelation of Chitosan with Monoaldehydes Towards Biomaterials with Tuned Properties



Luminita Marin, Daniela Ailincai, Manuela Maria Iftime, Anda-Mihaela Craciun, Andrei Bejan, Mariana Pinteala, and Marc Jean M. Abadie

Abstract Chitosan based hydrogels are a class of materials intensely investigated for real life applications. This is because their main component, chitosan, is a naturally originated biopolymer, sustainable, biocompatible, biodegradable and possessing many other useful biologic properties. The traditional pathways of chitosan hydrogelation, i.e. physical and covalent crosslinking, present advantages but also disadvantages which limit their applications. The present chapter presents a new strategy of chitosan hydrogelation with monoaldehydes, which exist in a large variety in nature. The mechanism of the hydrogelation was demonstrated by experimental methods, and the ability of these unusual hydrogels, acting as drug delivery formulation, soil conditioner and heavy metal adsorbent, is shortly described.

Keywords Chitosan · Monoaldehydes · Hydrogelation

L. Marin (✉) · D. Ailincai · M. M. Iftime · A.-M. Craciun · A. Bejan
Polycondensation and Thermostable Polymers Department, “Petru Poni”
Institute of Macromolecular Chemistry, 700487 Iași, Romania
e-mail: lmarin@icmpp.ro

D. Ailincai
e-mail: daniela.ailincai@icmpp.ro

M. M. Iftime
e-mail: ciobanum@icmpp.ro

A.-M. Craciun
e-mail: olaru.anda@icmpp.ro

A. Bejan
e-mail: bejan.andrei@icmpp.ro

M. Pinteala · M. J. M. Abadie
Centre of Advanced Research in Bionanoconjugates and Biopolymers, “Petru Poni”
Institute of Macromolecular Chemistry, 700487 Iași, Romania
e-mail: pinteala@icmpp.ro

M. J. M. Abadie
e-mail: marc.abadie@umontpellier.fr

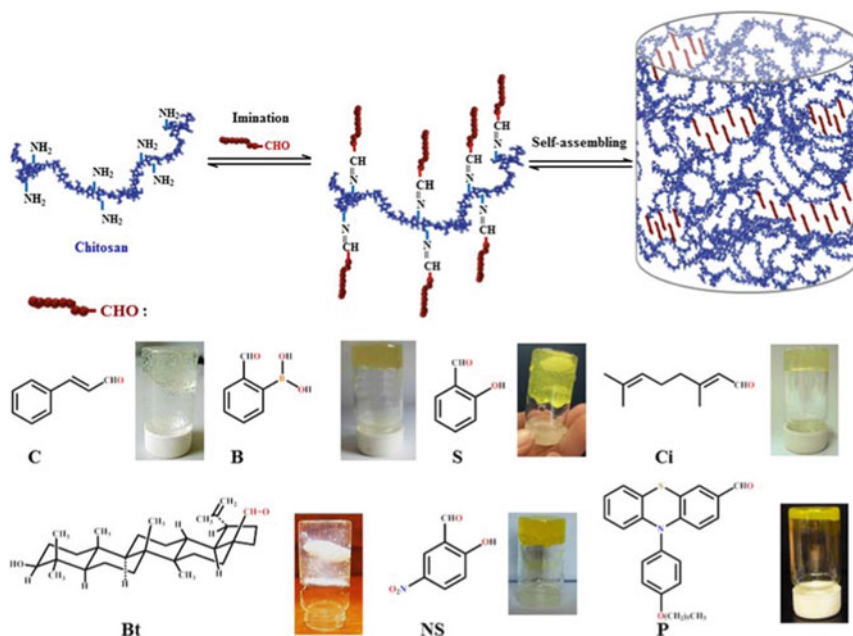
1 Introduction

Chitosan is a biopolymer derived from the natural chitin, which proved valuable properties, such as biocompatibility, biodegradability, antimicrobial, antitumor, hemostatic activity, and so on (Rinaudo 2006). This rich bio-activity encouraged a tremendous activity in the chitosan field directed to its exploitation in medicine, agriculture, food industry, environment protection, cosmetics, and hygiene (Ravi Kumar 2000). To amplify a specific applicative potential, two strategies were addressed: (i) reacting with other active species and (ii) preparation of materials based on it. Consequently, a large variety of chitosan based biopolymers and materials based on them were developed. Investigations on manufacturing chitosan as nanoparticles, films and coatings, hydrogels and fibers were pursued. Among them, chitosan based hydrogels proved suitable properties for all the fields listed above. They can absorb large amounts of water, allow solute diffusion and fluid exchange, mimic the viscoelastic properties of extracellular matrix, and have modulable structure and functions, being suitable as matrix for tissue engineering, carriers for drugs and cells, adsorbents for various liquids and pollutants. In this light, there is a continuous concern on the preparation of chitosan based hydrogels. Two principal crosslinking methods were validated. (i) Physical crosslinking, more specific ionotropic gelation, which base on the electrostatic interaction of the polycationic chitosan with low molecular weight anions, such as citrate, glycerophosphate, tripolyphosphate and sulfate (Domalik-Pyzik et al. 2019). The hydrogels yielded by ionotropic gelation present the advantage of a high degree of sensitivity and temperature responsiveness. On the other hand, they contain a large amount of water and loose three-dimensional architecture leading to the disadvantage of low mechanical strength and fast dissolution, which limits their application. (ii) Chemical crosslinking consists in the covalent reaction of chitosan with multi-functional crosslinkers, often bi-functional, such as glutaraldehyde, formaldehyde and glyoxal (Domalik-Pyzik et al. 2019). The hydrogels resulted by this method have good mechanical properties, good environmental stability and slower enzymatic degradation. Besides, the pore size can be simple controlled by varying the crosslinking density. These advantages make chitosan based covalent crosslinked hydrogels more suitable for long term in vivo applications. On the other hand, the low molecular weight chemical crosslinkers have a toxicity degree in their unreacted form yielding cytotoxic effects (Beauchamp et al. 1992; Berger et al. 2004). This limits the in vivo applications of the hydrogels containing them, encouraging research for friendlier crosslinkers. From this perspective, the use of crosslinkers of natural origin appeared as a promising alternative towards harmless hydrogels. In this light genipin, a natural product extracted from gardenia fruits, proved ability to crosslink the chitosan chains leading to hydrogels with excellent biocompatibility and mechanical properties, suitable for tissue engineering (Manickam et al. 2014; Muzzarelli et al. 2015). A new strategy developed in the last years revealed the possibility to crosslink chitosan with monoaldehydes (Marin et al. 2014,2017; Ailincai et al. 2016; Iftime et al. 2017; Olaru et al. 2018; Bejan et al. 2018; Iftime and Marin 2018). This is a very promising synthetic route, considering that aldehydes exist in

a large variety in nature, being non-toxic and biocompatible. Moreover, many aldehydes have intrinsic bioactivity, creating premises to endow the hydrogels with new valuable characteristics. The aim of this paper is to expose the route of the chitosan hydrogelation with monoaldehydes, and the potential of this method to generate valuable materials for a large variety of applications.

2 Hydrogelation Mechanism. Structural and Supramolecular Evidences

The idea of hydrogelation with a monofunctional compound seems unreasonable from chemical point of view, considering that the fundamental condition for crosslinking is the binding of at least two different chains requiring at least two functionalities. The validation of this unusual hydrogelation of chitosan with monoaldehydes was done on a series of seven aldehydes with aliphatic, aromatic or terpene structure (Scheme 1). The aldehydes had different structure and properties, the aim being to validate a hydrogelation model and also to prepare products suitable for applications. They were reacted with chitosan in acidic medium ($\text{pH} = 6.3$) when soft hydrogels, luminescent under an UV lamp were obtained (Scheme 1). For a



Scheme 1 Schematic representation of the hydrogel synthesis and the structure of the monoaldehydes. For each system were given images of the obtained hydrogels. The monoaldehyde codes were used as codes of the corresponding hydrogels

correct interpretation of the structural data, model compounds were prepared for each system by reacting the aldehydes with glucosamine.

In a system composed from chitosan and monoaldehydes, the most probably chemical reaction is the acid condensation of the amine with aldehyde groups yielding a linear chain grafted with imine units. The obvious question which arises is related to the crosslinking mechanism enabling the hydrogelation. To decipher the events which governs this unusual crosslinking, structural and supramolecular analysis were performed.

A first clue was offered by NMR spectroscopy recorded on the hydrogels prepared by varying the ratio of the amine to aldehyde functional groups. For the system obtained from chitosan and nitrosalicylaldehyde it was noted the chemical shifting characteristic for the imine protons and the absence of the aldehyde protons. For all the other six systems the chemical shifting of the aldehyde and imine protons co-existed in a different ratio of their integrals, which varied with the aldehyde nature, the ratio between functional groups and the reaction time (Fig. 1). This indicates that imination is a chemical process influencing the hydrogelation. Secondly, it points out that the chitosan imination is a reversible process, which equilibrium is shifted to the products depending by the aldehyde reactivity and its concentration in the system. Interestingly, the time was also an important factor accounting for the equilibrium shifting towards the products. This indicates that another process interfering with the imination over time exists.

FTIR spectra recorded on the xerogels (lyophilized hydrogels) displayed even more challenging data. The vibration band characteristic to the newly formed imine units was present in the spectra, shifted to higher wavenumbers for aliphatic units and to lower wavenumbers for aromatic ones (Fig. 2). However, in contradiction with the $^1\text{H-NMR}$ spectra, no clear aldehyde band was evidenced in the FTIR spectra. This indicated that the imination equilibrium was shifted to the products once the water was removed during the lyophilisation. Besides, the spectral domain characteristic

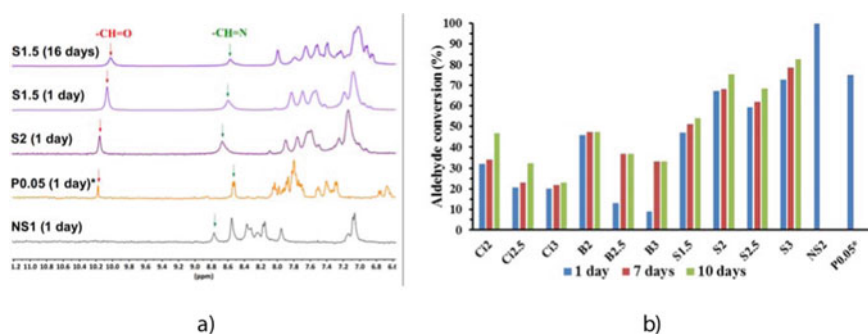


Fig. 1 **a** $^1\text{H-NMR}$ spectra of some representative hydrogels. **b** Graphical representation of the imine/aldehyde ratio over time, obtained from the integral ratio. The number next to codes represents the NH_2/CHO ratio of the functional groups. In the brackets was indicated the ageing time of the hydrogels before spectra recording. * the phenothiazine based aldehyde allowed the hydrogel formation only for small NH_2/CHO ratios (<0.05).

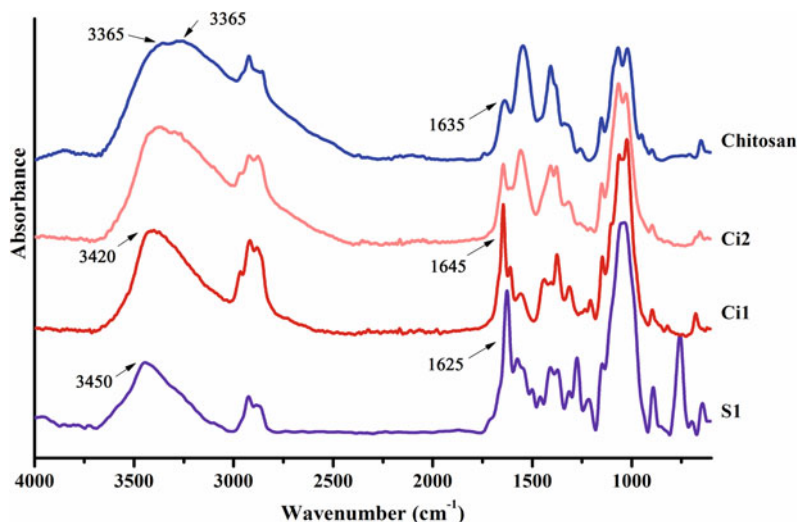


Fig. 2 Representative FTIR spectra of the xerogels

to the H-bond network in chitosan ($3000\text{--}3600\text{ cm}^{-1}$) suffered visible modifications, consisting in the shifting to higher wavelength. This shows that the imination reaction was accompanied by significant rearrangements of the H-bond network, in accordance with modifications at supramolecular level.

X-ray diffraction clearly evidenced these modifications at supramolecular level, mainly by the presence of a distinct reflection in the smaller angle domain (Fig. 3). This is the signature of a layered architecture, which interlayer distance was in good agreement with the length of the resulted imine unit, indicating the self-ordering of the newly formed imine units as being the process interfering with the covalent imination. Taking into considering the reversibility of the imine units, it was envisaged that the self-ordering process was favoured by imination and transimination processes. Consequently, there were formed clusters of the ordered imine units. As the imine units belong to different chitosan chains, the ordered clusters acted as crosslinking nodes. In such a way the crosslinking is in fact the result of the imination reaction correlated with the self-assembling of the newly formed imines. This crosslinking mechanism is in agreement with the NMR observation which noted the slowly shifting of the imination to the products over time. It can be supposed that the ordered clusters have a hydrophobic character, and their separation from the aqueous medium induces the decreasing of the imine content in the reaction medium, pushing the imination equilibrium to the formation of new imine units.

The hypothesis of the formation of the ordered clusters was further confirmed by single crystal X-ray diffraction on the model compounds, which revealed a hydrophobic-hydrophilic segregation giving alternant layers of hydrophobic imine units and hydrophilic glucosamine units. This specific self-assembling pattern

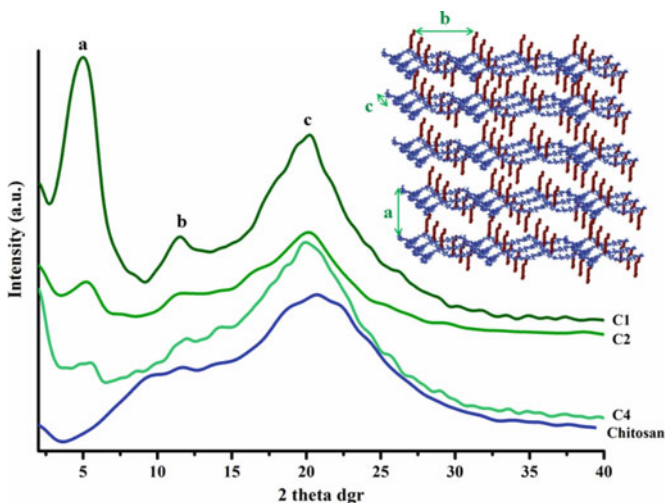


Fig. 3 X-ray diffraction of cinnamyl-chitosan hydrogel. The number next to code represents the ratio of the NH_2/CHO functional groups. It can be observed that once the content of aldehyde was increased, the reflection characteristic to the layering increased in intensity

expressed as a banded texture under polarized light, similar to the textures visualized for the hydrogels and xerogels (Fig. 4). This common feature correlates the single crystal X-ray data of the model compounds and the wide angle X-ray diffraction of the xerogels, confirming once more that the layering of the imine units is the driving force of this unusual chitosan hydrogelation.

3 Confirmation of the Hydrogel State by Rheological Measurements

All the studied systems formed soft transparent solids with smooth texture, which passed the test of the inverted tube for different ratios of the amine/aldehyde functional groups. The minimum amount of aldehyde necessary for hydrogelation was determined by the aldehyde nature. This was the first clue of the hydrogel formation. Beyond the visual confirmation, rheological measurements brought the objective validation of the hydrogel state for the unusual crosslinking of chitosan with monoaldehydes. It is well known that the gel-like behavior is a combination of both elastic and viscous behavior, with the dominance of the elastic one. This is expressed by a higher elastic modulus compared to the viscous one. In the particular case of the chitosan hydrogels crosslinked with monoaldehydes, the elastic modulus increased along with the content of aldehyde, demonstrating a strengthening of the network once the number of crosslinking nodes increased. Moreover, the elastic modulus

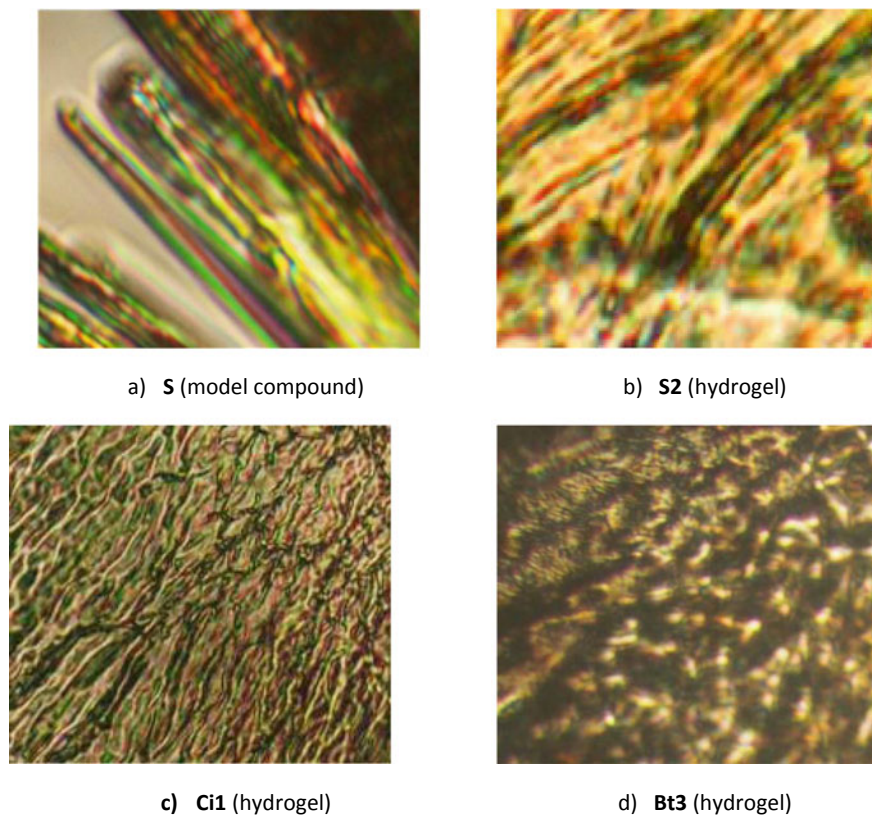


Fig. 4 Representative POM images of model compounds and hydrogels

progressively increased when the temperature increased above 30 °C. This was associated with the shifting of the reaction equilibrium towards the imine units which resulted in the strengthening of the crosslinking nodes. All the investigated systems showed a pseudoplastic behavior, with the dropping of the viscosity to 0 at the shear rate of 10^2 s^{-1} . For some ratios of the amine/aldehyde functional groups, the hydrogels showed a thixotropic behavior, with a recovery degree higher than 70% for the third stepwise (Marin et al. 2014; Iftime et al. 2017; Olaru et al. 2018). The time necessary for the recovery of the supramolecular architecture of the hydrogels was correlated with the crosslinking degree; it was lower for a higher crosslinking degree, and higher for a lower one. The hydrogels with recovery degree higher than 70%, displayed a self-healing behavior, some hydrogels showing reshaping after cutting or crushing.

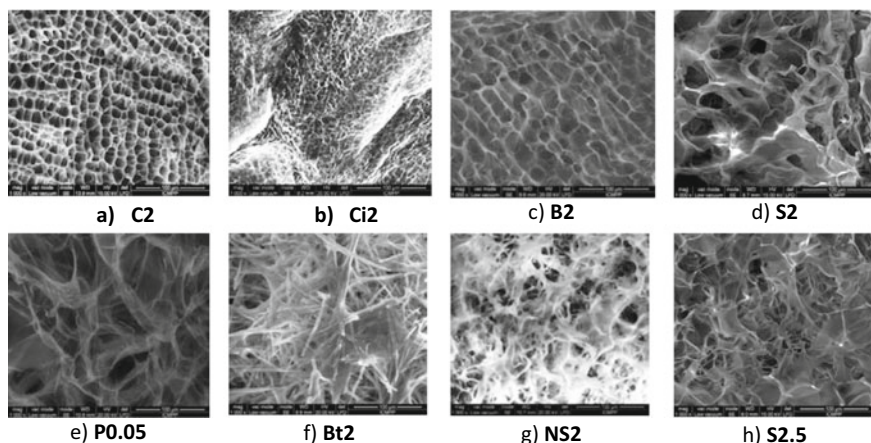


Fig. 5 Representative SEM images

4 Hydrogels Morphology

All hydrogels showed a porous morphology, with pores in the range 15–60 μm . The pore dimension respected the general rule for hydrogels, being smaller for higher crosslinking density and larger for lower crosslinking density. Nevertheless, particular morphological characteristics were observed for the hydrogels generated by different aldehydes. Thus, the hydrogels generated by the cinnamaldehyde crosslinker presented a porous morphology, with an extremely homogeneous distribution of the pores into honey-comb architecture (Fig. 5a). When the crosslinker was the hydrophobic citral monoaldehyde, the hydrogel morphology was distinguished by smaller pores, a maximum diameter of 26 μm being reached for the lowest crosslinking density (Fig. 5b). For the bulky phenothiazine based aldehydes, the pores were large with extremely thin walls (Fig. 5e), while in the case of hydrophobic bulky betulinaldehyde an acicular morphology was observed (Fig. 5f). The presence of a hydroxyl group in ortho position to the formyl unit (salicylaldehyde, nitrosalicylaldehyde, 2 formylphenylboronic acid) led to intercommunicating pores of various dimensions with a less uniform distribution, converging in the case of salicylaldehyde crosslinker to a fibrous morphology once the crosslinking degree diminished (Fig. 5c, d, g, h).

5 Hydrogel Behavior in Aqueous Media. Swelling, Stability, Enzymatic Degradation

All the hydrogels completely rehydrated in acidic (pH = 4), neutral (pH = 7) or physiological (pH = 7.4) media. Their swelling behavior was closely correlated

with the nature of the aldehyde crosslinker and the microstructure. The use of more hydrophobic aldehydes (e.g. citral, cinnamaldehyde, betulinolaldehyde, phenothiazine based aldehyde) led to hydrogels with lower swelling ability, while the aldehydes containing hydrophilic hydroxyl endowed the hydrogels with higher swelling ability, reaching a mass equilibrium swelling of 240 for the hydrogel with fibrous microstructure. As a general rule, the hydrogels dissolved in the medium of acidic pH and were stable in neutral or physiological media. The stability in acidic medium varied from few minutes to 5 days, closely correlated with the hydrophilicity of the aldehyde and crosslinking degree; e.g. by citral crosslinking a stability in acidic media up to 5 days was gained, while crosslinking with salicylaldehyde inflicted a rapid dissolution in 10 min. Except to this rule was the hydrogel prepared with nitrosalicylaldehyde crosslinker, which demonstrated stability in acidic medium over three months of investigation. This was attributed to the complete shifting of the imination equilibrium to the products by a “clip effect”, which reinforced the hydrophobic clusters hindering their dissolution (Kovaricek and Lehn 2012). In physiological and neutral media the hydrogels were stable over a period of 3 months of investigation. This led to the conclusion that by self-ordering of the imine units into tight structures are formed hydrophobic clusters, stable in aqueous media. It should be highlighted that the hydrogels completely rehydrated and preserved quite well their shape in physiological medium, an important advantage for tissue engineering.

On the other hand, adding lysozyme to the swelling media, the hydrogels lose weight over time proving enzymatic degradation. It should be highlighted that lysozyme is a human enzyme found in various bodily fluids which have the ability to hydrolyse the chitosan by an acid catalysed reaction. The enzymatic degradation rate was correlated with the nature of the aldehyde crosslinker. The hydrogels based on the citral hydrophobic crosslinker lost 12% in 21 days (Ailincai et al. 2018), while the hydrogels based on the more hydrophilic aldehydes lost around 40% in a similar investigation period (Craciun et al. 2019; Iftime et al. 2020). Interesting, the crosslinking of the PEGylated chitosan with citral, improved the enzymatic rate, reaching 45% weight loss after 21 days (Ailincai et al. 2020). This indicates the solubility of the residue resulting after the enzymatic cleavage of the O–C bonds of chitosan playing a crucial role in the enzymatic degradation. It was stressed that the electron withdrawing character of the aldehyde crosslinker can play an important role in increasing the rate of the O–C cleavage under the influence of lysozyme (Craciun et al. 2019).

6 Biocompatibility

The motivation behind using natural originating monoaldehydes as chitosan crosslinkers, was the attaining of biocompatible hydrogels suitable for in vivo long term use. In this line of thought, the hydrogels prepared with citral, salicylaldehyde, and nitrosalicylaldehyde were in vivo investigated to see their impact on the blood, biochemical formula and immune system of the experimental animals (mice

or rats) (Marin et al. 2017; Olaru et al. 2018; Ailincai et al. 2018,2020; Craciun et al. 2019; Iftime et al. 2020). No cytotoxic effect was noted nor after one day, neither after seven days after administration, confirming their safe use for in vivo applications.

7 Ability of Hydrogels to Act as Matrix for Drug Delivery

The hydrogels prepared with natural aldehydes were tested for their ability to encapsulate model drugs (Ailincai et al. 2018, 2020; Craciun et al. 2019; Iftime et al. 2020). It was established that by in situ hydrogelation the maximum dose of drug *per* kg, in agreement with the pharmaceutical recommendations, was encapsulated in the pore walls of the hydrogels. This favoured a prolonged release of the drug, certainly increasing its bioavailability compared to the systemic administration, up to 5 days (Craciun et al. 2019; Iftime et al. 2020; Ailincai et al. 2020). Moreover, by proper choice of the aldehyde, it can be ensured a complementary effect, such as antitumor activity, which augments the activity of the drug (Craciun et al. 2019). These results confirmed that the chitosan hydrogelation with monoaldehyde provides valuable matrixes for controlled drug release systems, which properties can be easily tuned by the aldehyde nature.

8 Preparation of Soil Conditioners

Generally speaking, the hydrogels are excellent candidates for soil conditioners, due to their ability to adsorb large amounts of water and to encapsulate and prolong release fertilizers. The ability to encapsulate fertilizers was tested on the hydrogels which demonstrated high swelling ability, using urea as fertilizer model (Iftime et al. 2019). It was demonstrated that the hydrogels were able to efficiently embed a high amount of urea, up to 66% from the mass of formulations. Further, they released urea in a prolonged manner over 35 days, improved the water holding capacity and reduced water evaporation. All these stimulated the plant growth up to 70% higher compared to the variants seeded in the reference soil. Besides, the hydrogels were biodegradable and chitosan proved to be an intrinsic soil fertilizer. All these data show that chitosan hydrogelation with natural monoaldehydes can be an excellent pathway to ecological soil conditioners.

9 Heavy Metal Sensing and Adsorption

The hydrogels prepared from chitosan and phenothiazine based aldehyde showed an excellent ability for heavy metal sensing, such as copper, chromium and mercury. A deeper investigation of the mercury sensing revealed a peculiar behavior, consisting

in the transformation of the hydrogel into a rubber like material. This was attributed to the morphology reinforcing through a secondary crosslinking by the formation of inverse coordination complexes, nitrogen and oxygen centred. This specific behaviour was effective for mercury sensing and its removal as well.

10 Conclusions

The paper presents a new crosslinking pathway of chitosan with monofunctional aldehydes. The mechanism of the unusual hydrogelation has been proved by structural and supramolecular methods of analysis. It was demonstrated that hydrogelation take place by two mutual processes, formation of imine units and their self-order into layered clusters, which play the role of crosslinking nodes. The hydrogelation method was validated on seven different systems, proving to be a successful pathway for preparing valuable materials with properties targeted for specific applications, by simple choice of the aldehydes.

Acknowledgements The project leading to this application has received funding from the H2020 ERA Chairs Project no 667387: SupraChem Lab Laboratory of Supramolecular Chemistry for Adaptive Delivery Systems ERA Chair initiative.

References

- Ailincăi D, Marin L, Morariu S, Mares M, Bostanaru AC, Pinteala M, Simionescu BC, Barboiu M (2016) Dual crosslinked iminoboronate-chitosan hydrogels with strong antifungal activity against *Candida* planktonic yeasts and biofilms. *Carbohydr Polym* 152:306–316. <https://doi.org/10.1016/j.carbpol.2016.07.007>
- Ailincăi D, Mititelu-Tartau L, Marin L (2018) Drug delivery systems based on biocompatible imino-chitosan hydrogels for local anticancer therapy. *Drug Deliv* 25:1080–1090. <https://doi.org/10.1080/10717544.2018.1466937>
- Ailincăi D, Mititelu-Tartau L, Marin L (2020) Citryl-imine-PEG-ylated chitosan hydrogels – promising materials for drug delivery applications. *Int J Biol Macromol* 162:1323–1337. <https://doi.org/10.1016/j.ijbiomac.2020.06.218>
- Beauchamp RO, St Clair MB, Fennell TR, Clarke DO, Morgan KT (1992) A critical review of the toxicology of glutaraldehyde. *Crit Rev Toxicol* 22:143–174. <https://doi.org/10.3109/10408449209145322>
- Bejan A, Ailincăi D, Simionescu BC, Marin L (2018) Chitosan hydrogelation with a phenothiazine based aldehyde–toward highly luminescent biomaterials. *Polym Chem* 9:2359–2369. <https://doi.org/10.1039/C7PY01678F>
- Berger J, Reist M, Mayer JM, Felt O, Peppas NA, Gurny R (2004) Structure and interactions in covalently and ionically crosslinked chitosan hydrogels for biomedical applications. *Eur J Pharm Biopharm* 57:19–34. [https://doi.org/10.1016/S0939-6411\(03\)00161-9](https://doi.org/10.1016/S0939-6411(03)00161-9)
- Craciun AM, Mititelu-Tartau L, Pinteala M, Marin L (2019) Nitrosalicyl-imine-chitosan hydrogels based drug delivery systems for long term sustained release in local therapy. *J Colloid Interface Sci* 536:196–207. <https://doi.org/10.1016/j.jcis.2018.10.048>

- Domalik-Pyzik P, Chlopek J, Pielichowska K (2019) Chitosan-based hydrogels: preparation, properties, and applications. In: Mondal M (ed) Cellulose-based superabsorbent hydrogels. Polymers and polymeric composites: a reference series. Springer, pp 1665–1693. https://doi.org/10.1007/978-3-319-77830-3_55
- Iftime MM, Marin L (2018) Chiral betulin-imino-chitosan hydrogels by dynamic covalent sonochemistry. *Ultrason Sonochem* 45:238–247. <https://doi.org/10.1016/j.ultsonch.2018.03.022>
- Iftime MM, Morariu S, Marin L (2017) Salicyl-imine-chitosan hydrogels: Supramolecular architecture as a crosslinking method toward multifunctional hydrogels. *Carbohydr Polym* 165:39–50. <https://doi.org/10.1016/j.carbpol.2017.02.027>
- Iftime MM, Ailiesei GL, Ungureanu E, Marin L (2019) Designing chitosan based eco-friendly multifunctional soil conditioner systems with urea controlled release and water retention. *Carbohydr Polym* 223:115040. <https://doi.org/10.1016/j.carbpol.2019.115040>
- Iftime MM, Mititelu Tartau L, Marin L (2020) New formulations based on salicyl-imine-chitosan hydrogels for prolonged drug release. *Int J Biol Macromol* 160:398–408. <https://doi.org/10.1016/j.ijbiomac.2020.05.207>
- Kovaricek P, Lehn JM (2012) Merging constitutional and motional covalent dynamics in reversible imine formation and exchange processes. *J Am Chem Soc* 134:9446–9455. <https://doi.org/10.1021/ja302793c>
- Manickam B, Sreedharan R, Elumalai M (2014) Genipin' - the natural water soluble cross-linking agent and its importance in the modified drug delivery systems: an overview. *Curr Drug Deliv* 11(1):139–145. <https://doi.org/10.2174/15672018113106660059>
- Marin L, Morariu S, Popescu MC, Nicolaescu A, Zgardan C, Simionescu BC, Barboiu M (2014) Out-of-water constitutional self-organization of chitosan–cinnamaldehyde dynagels. *Chem Eur J* 20:4814–4821. <https://doi.org/10.1002/chem.201304714>
- Marin L, Ailincăi D, Morariu S, Tartau-Mititelu L (2017) Development of biocompatible glycodynameric hydrogels joining two natural motifs by dynamic constitutional chemistry. *Carbohydr Polym* 170:60–71. <https://doi.org/10.1016/j.carbpol.2017.04.055>
- Muzzarelli RAA, El Mehtedi M, Bottegoni C, Aquili A, Gigante A (2015) Genipin-crosslinked chitosan gels and scaffolds for tissue engineering and regeneration of cartilage and bone. *Mar Drugs* 13(12):7314–7338. <https://doi.org/10.3390/md13127068>
- Olaru AM, Marin L, Morariu S, Pricope G, Pinteala M, Tartau-Mititelu L (2018) Biocompatible based hydrogels for potential application in local tumour therapy. *Carbohydr Polym* 179:59–70. <https://doi.org/10.1016/j.carbpol.2017.09.066>
- Ravi Kumar MNV (2000) A review of chitin and chitosan applications. *React Funct Polym* 46:1–27. [https://doi.org/10.1016/S1381-5148\(00\)00038-9](https://doi.org/10.1016/S1381-5148(00)00038-9)
- Rinaudo M (2006) Chitin and chitosan: properties and applications. *Prog Polym Sci* 31:603–632. <https://doi.org/10.1016/j.progpolymsci.2006.06.001>

Molecular Dynamics Simulations and *in silico* Analysis of Supramolecular Self-assembled Structures



Corneliu Cojocaru, Andrei Neamtu, Tudor Vasiliu, Dragos Lucian Isac,
and Mariana Pinteala

Abstract In this contribution, we summarize the results that we have attained throughout the implementation of the SupraChemLab project (running from 2015 to 2020). Herein, we have focused on molecular dynamics simulations and *in silico* analysis of the supra-molecular structures and systems (such as water channels, biomembranes, and polyplexes). Molecular dynamics simulations were performed using dedicated professional software packages, *i.e.* GROMACS and YASARA. Computational outcomes revealed valuable insights concerning the supra-molecular self-assembled systems.

Keywords Molecular dynamics · Force fields · Computational chemistry · Supramolecular chemistry · Artificial water channels · Polyplexes · Solute-solvent interactions

C. Cojocaru

Department of Inorganic Polymers, “Petru Poni” Institute of Macromolecular Chemistry,
700487 Iasi, Romania
e-mail: cojocaru.corneliu@icmpp.ro

A. Neamtu (✉)

Physiology Department, “Grigore T. Popa” University of Medicine and Pharmacy, Str.
Universitatii nr. 16, 700115 Iasi, Romania
e-mail: andrei.neamtu@umfiiasi.ro

T. Vasiliu · M. Pinteala

Centre of Advanced Research in Bionanoconjugates and Biopolymers, “Petru Poni” Institute of
Macromolecular Chemistry, 700487 Iasi, Romania
e-mail: vasiliu.tudor@icmpp.ro

M. Pinteala

e-mail: pinteala@icmpp.ro

D. L. Isac

Department of Physical Chemistry of Polymers, “Petru Poni” Institute of Macromolecular
Chemistry, 700487 Iasi, Romania
e-mail: isac.dragos@icmpp.ro

Abbreviations

AMC	<i>Azobenzene maleimide compound</i>
AQPs	Aquaporins
AWC	Artificial water channels
b-PEI	Branched poly(ethylene imine)
β -CD	B-cyclodextrin
cD_4^{H}	2,4,6,8-tetramethylcyclotetrasiloxane,
DFT	Density functional theory
DNA	Deoxyribonucleic acid
dsDNA	Double-stranded deoxyribonucleic acid
DOTA	1,4,7,10-tetraazacyclododecane-1,4,7,10-tetraacetic acid
HBA	Hydrogen bond acceptor
HBD	Hydrogen bond donor (HBD)
MD	Molecular dynamics
MM	Molecular mechanics
PEG	Polyethylene glycol
PEI	Poly(ethylene imine)
PLL	Poly(L-Lysine)
POPC	Phosphatidylcholine
RNA	Ribonucleic acid
QM	Quantum mechanics
TIP3P	Three-site water model of rigid geometry

1 Introduction: Molecular Mechanics and Dynamics in Brief

Computational chemistry represents an essential molecular modeling tool employed in modern chemistry and biochemistry. Molecular modeling is very important nowadays to detail the structures and dynamics of molecules, macromolecules and complexes. Generally, computational chemistry comprises two main parts: (1) quantum mechanics (QM), and (2) molecular mechanics (MM) (Jensen 2007; Lewars 2004). In quantum mechanics (QM), the smallest particles subjected to modeling (by Schrödinger equation) are electrons and nuclei. Hence, QM treats electrons explicitly and enables to explore the small and medium-sized molecules with electronic structure methods. By contrast, in molecular mechanics, the nuclei and electrons are not treated explicitly; they are lumped together and treated as unified atom-like particles. Consequently, the atom-like particle is commonly treated as a sphere (ball) having certain size, mass and assigned partial charge. Moreover, in MM the bonds between atoms are viewed as springs (harmonic oscillators). Assuming classical mechanical principles, the MM permits to model efficiently large molecular structures (with thousands of atoms and even more). According to MM theory, the interactions between

atoms are treated using potential functions. For instance, the mathematics of spring deformation (Hooke's Law) is employed to model the bonded interactions, *i.e.* the ability of bonds to stretch, bend and twist. Non-bonded interactions are assessed by considering the Van der Waals attraction, steric repulsion, as well as electrostatic attraction/repulsion between non-bonded atoms. Commonly, the Van der Waals interactions are modeled by using Lennard-Jones 12-6 potentials and considering a fixed cut-off (*i.e.*, a short-range interacting distance, typically of 8–10 Å). In turn, the long-range electrostatic interactions are calculated by Coulombic model and Ewald summation. The total potential energy (U) of a molecule can be expressed as the summation of energy contributions from bond stretching, angle bending, torsional motion (rotation) around the single bonds, and interactions between non-bonded atoms (Lewars 2004):

$$U = \sum_{\text{bonds}} U_{\text{stretch}} + \sum_{\text{angles}} U_{\text{bend}} + \sum_{\text{dihedrals}} U_{\text{torsion}} + \sum_{\text{pairs}} U_{\text{nonbond}} \quad (1)$$

Each energy contribution term is detailed in the textbooks (Jensen 2007; Lewars 2004; MacKerell Jr 2001). The mathematical expression of the potential energy and associated parameters is known as a *force-field*. Therefore, the MM approaches are sometimes called *force-field* methods (Jensen 2007; Lewars 2004). During the last decades, many different types of force-fields were developed. Some of them include additional energy terms in order to improve the accuracy of the mechanical model. The force-field parameters must be optimized for a particular set of potential energy functions. This procedure is known as force-field parametrization. The classical force-fields that handle molecules involving much elements of the periodic table are MM2, MM3, MM4, UFF, and Sybyl (Lewars 2004). For modeling of biological macromolecules (proteins, nucleic acids) other important force-fields are employed such as AMBER, CHARMM, GROMOS, OPLS, YASARA, NOVA, and YAMBER (Guvench and MacKerell 2008; Krieger et al. 2002; Krieger and Vriend 2015).

A versatile computational tool relying on force-field approach is the *molecular dynamics* simulation approach. In fact, *molecular dynamics* (MD) is a technique that uses numerical integration of Newton's equation of motion ($F_i = m_i \ddot{r}_i$) to simulate the time evolution of atoms in the molecular and polymeric systems. For example, by using the Verlet integration (based on finite-difference technique) the evolution of the atomic position against time can be estimated as (Becker and Watanabe 2001):

$$\mathbf{r}_{(n+1)} = \mathbf{r}_n + \mathbf{v}_n \Delta t + 0.5(\mathbf{F}_n/m) \Delta t^2 \quad (2)$$

where, \mathbf{r}_n indicate the particle position (vector of all atomic coordinates) at step n (at time t), and \mathbf{r}_{n+1} indicates the position at the next step $n + 1$ (at time $t + \Delta t$), \mathbf{m} —mass of involved particles; \mathbf{v}_n —velocity of particles and \mathbf{F}_n —force acting on particles at step n . The velocity at the next step ($n + 1$) can be roughly ascertained as $\mathbf{v}_{n+1} = (\mathbf{r}_{n+1} - \mathbf{r}_n)/\Delta t$. Note that the force, in this approach, is determined by the gradient of the potential energy function, as given by (Becker and Watanabe 2001):

$$\mathbf{F}_n = -\nabla U(\mathbf{r}_n) \quad (3)$$

It is worth mentioning that in the last decades more accurate numerical algorithms have been developed to solve the equations of motions (by adopting the same kind of reasoning). Generally, the MD simulation protocol consists of several main steps (Becker and Watanabe 2001), detailed in the following.

1. *Preparation of modeling system*: This step implies the model generation, preparation of the initial coordinates for the structures and assignment of initial velocities (e.g. by Maxwell-Boltzmann distribution). Likewise, this initial phase involves the adding of missing hydrogen atoms; defining the simulation cell/box; solvation of the molecular structures by adding explicit solvent molecules (like TIP3P for water); defining the cell boundaries like periodic-type or wall-type, etc. Moreover, the system relaxation is performed by minimization of the initial structure to diminish the local strain and then gradually heating-up the system to the desired temperature.
2. *Equilibration*: In this phase, a ‘short-term’ dynamic simulation is performed that lasts from tens of picoseconds (ps) to several hundred of ps. The purpose of equilibration phase is to verify that the simulation is stable and free of irregular fluctuations.
3. *Production*: After equilibration, the system is considered reliable for long-term dynamics simulations. In a MD simulation with no pressure control, the volume of the simulation cell is held fixed. Instead, at constant-pressure MD the volume of the system may fluctuate. Nowadays, the production runs take from several nanoseconds up to microsecond-scale (depending on the system size and computer power). Note that the typical time-step for integration of equations of motion is 1 or 2 fs (femtoseconds, 10^{-15} s). The generated trajectories in the production phase are stored for further analysis.
4. *Analysis*: The last phase is dedicated to the careful analysis of the resulting molecular dynamics trajectories that was stored as ‘snapshots’ taken at equal time intervals. In this phase the time-dependent plots are developed to understand the dynamics (averages and fluctuations) of the investigated system.

In summary, molecular dynamics (MD) simulation is essential for studying structures, interactions and dynamics of (macro)/molecular systems. Therefore, MD has been successfully applied in supra-molecular chemistry to assess many important aspects, such as (a) the dynamics of conformations, (b) dynamics of intermolecular interactions (protein-protein, protein-drug, protein-DNA), (c) functionality of water/ionic channels in biological membranes, (d) stability of receptor-ligand complexes and polyplexes, (e) solute-solvent interactions, and others. Molecular dynamics simulations can be carried out using special program packages developed for this purpose, such as GROMACS, NAMD/VMD, AMBER, YASARA, LAMMPS, SCIGRESS, and others.

2 Molecular Dynamics of Water Permeation Across DOTA-Based Artificial Channels

Transport of substances (e.g. water, ions) across biological membranes represents a fundamental process in all living cells. In this respect, the proteins embedded in the lipid bilayer membranes play a crucial role. Such proteins (acting as accessing gates and channels) constitute in fact the highly selective diffusive pathways that control the inflow and outflow of substances through cellular membranes. Nowadays, simulations on membrane proteins deal with water and ion channels, as well as various transporters (Khalili-Araghi et al. 2009). Aquaporins (AQPs) are special type of channel-proteins (embedded into the biological membranes), which have the function of fast water transport (Barboiu 2016); thereby facilitating the moving of water molecules between intracellular and extracellular environments. For biological processes it is of great importance to understand the dynamics of the transport through the confined space of protein channels. In the last years, the artificial water channels (AWC) have attracted much attention (Barboiu 2016; Murail et al. 2018). The development of AWC is aimed to mimic the high water permeability observed for biological systems such as AQPs, as well as their selectivity to reject ion permeation simultaneously. Recently, Murail and co-workers (Murail et al. 2018) showed (by using molecular dynamics) that the self-assembling alkylureidoethylimidazole compounds have formed imidazole-quartet channels (I-quartets) that can act as artificial water channels.

In this report, we assessed the self-assembling of DOTA molecules into a supra-molecular aggregate aiming to be tested as the potential artificial water channel. Note that DOTA represents an organic compound (1,4,7,10-tetraazacyclododecane-1,4,7,10-tetraacetic acid), which is mainly used as a complexing agent (chelator). The investigations were done by molecular dynamics simulations, where phosphatidylcholine (POPC) was employed as the main lipid constituent of the simulated bio-membrane. Thus, we investigated the DOTA self-assembly in the phospholipid (POPC) membrane and the water permeation through this artificial channel. The analysis of self-assembling simulations (starting from fully random mixtures of DOTA/POPC/water/ions) revealed the formation of DOTA aggregates in phospholipid membrane environments. Computational results disclosed that DOTA molecules preferred to “stay together” but still, with no phase separation. Stacks of two DOTA molecules could be identified which seems to strongly interact as they move together as a whole (i.e. the central ring and the nearby -NH-CO- moieties of the adjacent molecules display collective motions). The central cycles were arranged in a parallel orientation and the inter-molecular interaction was strengthened by H-bonds formed between -N-H groups of one DOTA molecule and the -C = O group of the next molecule. This stable arrangement may favor formation of stacks composed of several DOTA molecules with a proper dimension to completely traverse the membrane from one face to the other. This could provide a pathway for water permeation. In order to study the stability of such assemblies and water passage along them we constructed stacks of 6 DOTA molecules and inserted them in the POPC-based membrane. The

number of DOTA molecules had been chosen on the basis of hydrophobic match between the POPC bilayer core and the stack height (we tried with 4–7 molecules). In order to determine the mechanism through which DOTA molecules create water channels in a lipid bilayer we stacked 6 DOTA molecules and inserted them in a lipid bilayer consisting of 130 POPC molecules using ‘membed’ algorithm from the GROMACS 5.1 software. This simulation is called 1DOTA in the following. The insertion led to the deletion of 8 POPC molecules to a final count of 122. The system was hydrated with 7027 water molecules. The main results of the above described simulations are illustrated in Figs. 1, 2, 3, giving the short explanations in the figure captions.

Thus, the computation results unveiled that the water permeation events occur basically at lateral positions from the central rings. And, the water wire, in this case, emerged as jumping effects of water molecules between the binding sites pinpointed in between the -N-H and -C = O moieties of the rings (Figs. 1, 2, 3).

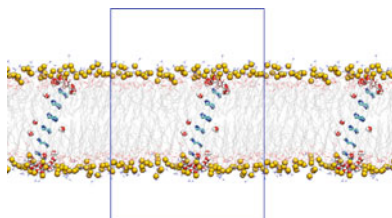


Fig. 1 Snapshot of the simulated system at the end of 1DOTA simulation (1 μ s). The alkyl tails of DOTA molecules were removed for clarity. Some water molecules can be seen in the vicinity of the central ring of DOTA; phosphorus atoms of POPC have been represented as vdw spheres in yellow

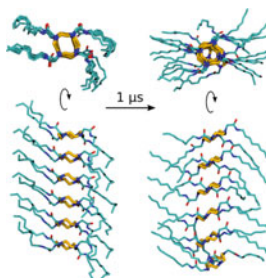


Fig. 2 Snapshots of the 6 DOTA stack at the beginning and at the end of the 1DOTA simulation. Very good conservation of the stacked configuration could be observed even after 1 μ s of simulation within the membrane environment. Alkyl tails of DOTA prefer to align in a parallel configuration and also parallel to the membrane plane

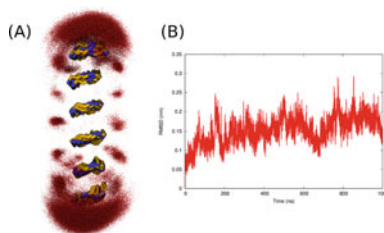


Fig. 3 **A** Water density around the DOTA central ring stack in simulation 1DOTA. Water oxygen atoms were represented as red dots overlaid for multiple frames during simulation. The DOTA stack in each frame was fitted to the starting structure using the nitrogen atoms of the central ring as alignment subset. Water binding sites located in between the -N-H and -C = O groups on both sides of the rings could be identified. Visual inspection of the trajectories revealed jumping events of water molecules between these sites. **B** RMSD of DOTA stack with respect to the starting configuration

3 Molecular Dynamics for Assessing the Formation of Polyplexes

The molecular dynamics (MD) also have found its applicability in ascertaining the formation of polyplexes. The polyplexes are special types of complexes formed between nucleic acids (DNA/RNA) and (macro)molecular entities (*e.g.*, polycations, polyelectrolytes, polypeptides). In the last decades, the polyplexes have received distinct attention due to their potential usage in gene therapy. This therapy implies the insertion of nucleic acids into cells; thereby altering the gene expression aiming to correct gene defects (Anderson 1984). Two main approaches are actually adopted in gene therapy, the first one deal with *viral vectors* for transporting the genetic material (Hawley et al. 1994; Kay et al. 2001; Vannucci et al. 2013), and the second approach uses the cationic non-viral vectors (Li and Huang 2000; Wu and Wu 1987). In the last decade, the focus of the research has started to shift from viral vectors to non-viral vectors. This is because the usage of viruses for gene therapy implies some risks. The main assets of non-viral vectors involve (1) the inferior specific immune reaction, (2) the safer responses, (3) the simpler design, and (4) chemical properties for various purposes (Han et al. 2000; Luo and Saltzman 2000; Mintzer and Simanek 2009; Tang and Szoka 1997). As non-viral vectors, cationic polymers are often employed owing to their capacity to interact readily with nucleic acids by forming polyplexes. The most explored polymers as non-viral vectors deal with linear or branched poly(ethylene imine) (PEI) and polypeptide-type poly(L-Lysine) (PLL) (Mintzer and Simanek 2009; Nicolas et al. 2013). According to previous studies, PLL is more advantageous in comparison to PEI in terms of cytotoxicity (Godbey et al. 1999). This is because PLL is more biodegradable *in vivo* than PEI. However, PLL demonstrated a lower transfection efficiency if compared to PEI (Tang and Szoka 1997).

Ziebarth and co-workers carried out molecular dynamics simulations of a short DNA duplex d(CGCGAATTCGCG) in the presence of PEI or PLL to reveal the specific interactions in the course of polyplexes formation (Ziebarth and Wang 2009).

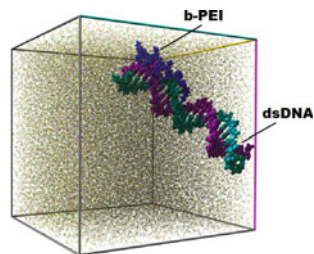
In their study, all simulations were carried out using the Amber Parm99 force field and the AMBER-8 software package for the molecular dynamics. After an initial separation of about 50 Å, the DNA and polycation interacted by forming a stable polyplex within 10 ns (ns). The DNA did not undergo any major structural changes on complexation and remained in the B-form. The polyplexes were formed by the interaction of the charged amine groups of polycations and DNA phosphate groups. Thus, polycations were able to intrude into the major and minor grooves of DNA, depending on the identity and the charge state of the polycation. Ultimately, these authors (Ziebarth and Wang 2009) outlined that, in comparison with PLL, PEI was able to neutralize the charge of DNA in a more efficient way.

In another study undertaken by Sun and collaborators (Sun et al. 2011), the molecular dynamics simulation was performed towards understanding the mechanisms of DNA complexation with PEI. These authors investigated the effect of PEI branching and its protonation state. Drew-Dickerson dodecamer was employed as simulated DNA. And, its initial structure was built to be canonical B-form using the AMBER NAB tool. Four molecular structures of PEI were considered with similar molecular mass (570 Da), but different degrees of branching: (1) pure linear chain, (2) semi-linear, (3) moderately branched geometry and (4) hyper-branched structure. These authors employed the NAMD package for MD simulations using the CHARMM-27 force field. Finally, they found that the degree of branching had a smaller influence on the DNA binding than the protonation state of the polymeric vectors. In addition, it was reported that 46% of protonated PEI formed more stable complexes with DNA than the 23% protonated PEI. Likewise, these authors highlighted that PEI interacted with the DNA through the formation of hydrogen bonding with the backbone oxygens. Two types of hydrogen bonding were evidenced, *i.e.* direct hydrogen bonding and indirect hydrogen bonding (mediated through water molecules).

Regarding the flexibility of DNA macromolecule, a seminal MD study was reported evidencing the relative flexibility in aqueous solutions of DNA compared to RNA (Noy et al. 2004). The essential dynamics analysis (of 10 ns trajectories) suggested that the pattern of the flexibility of DNA and RNA duplexes was different. Moreover, MD simulations (performed by means of AMBER6-1 program) demonstrated that the concepts of flexibility, stiffness, and deformability are much complex. For instance, the DNA duplex can be more flexible for some perturbations and more rigid for others (Noy et al. 2004). Another study dealt with molecular dynamics (assuming the OPLS-AA force field) to approximate localization of structural water molecules in DNA (Neder et al. 2005). Thus, these authors unveiled by MD simulation the first hydration shell of double-helix DNA in the A- and B-conformations. It is worth noting that the MD simulations were also employed for assessing DNA-protein and DNA-drug interactions, detailing the dynamics, and stability of such types of complexes (Lei et al. 2012; MacKerell Jr and Nilsson 2001).

Our group started to approach the subject of the formation of the polyplexes back from 2015. For example, in reference (Clima et al. 2015) it was reported the experimental design, modeling, and optimization of the polyplex formation between double-stranded oligonucleotides (dsDNA) and branched poly(ethylene imine) (b-PEI). A design of experiments was adopted to investigate experimentally the binding

Fig. 4 Rendering of the dsDNA/b-PEI polyplex resulted from MD simulation (at $t = 21$ ns) in a simulation box with explicit water molecules (solvent) (Clima et al., 2015)



efficiency of DNA and branched-PEI under various conditions. Moreover, the molecular dynamics simulation was performed to disclose the mechanism of polyplex formation at the atomic-scale. In this work, the dsDNA composed of 50 nucleotides was exploited in modeling study and experimental validation. Thus, the sense strand of dsDNA was 5'-CAAGCCCTTAACGAACTTCAACGTA-3', and correspondingly, the antisense strand was 5'-TACGTTGAAGTTCGTTAAGGGCTTG-3'. The molecular dynamics simulations were carried out by means of the YASARA-Structure software package (Krieger et al. 2014), which is an all-in-one program for molecular modeling. In fact, YASARA is a molecular-graphics, -modeling and -simulation program with an intuitive user interface and photorealistic graphics (Krieger and Vriend 2014). It contains all AMBER force fields as well as its own force fields (like NOVA, YASARA, and YAMBER). Note that, the YASARA-Structure program includes an automatic parameterization method ('AutoSMILES'), which is very facile to get the molecular mechanics parameters for the unknown structures. According to the report of the developers (Krieger and Vriend 2014), the YASARA program has been developed to boost molecular dynamics simulations in the frame of the all-in-one program environment. In the published study (Clima et al. 2015), the molecular dynamics simulation was done at the level of the YASARA force field, which includes the self-parameterizing knowledge-based potentials. Hence, the resulted DNA/PEI polyplex (at 21 ns simulation time) in an explicit solvent (water model TIP3P) is illustrated in Fig. 4.

Finally, the results of the simulation disclosed that hydrogen atoms from b-PEI amine groups mainly interacted with oxygen atoms from dsDNA phosphate groups. These interactions conducted to the formation of hydrogen bonds between dsDNA and b-PEI macromolecules; thereby stabilizing the polyplex structure. As regards the polyplex conformation, the polycation chain remained close to the DNA making contacts in the vicinity of a minor groove site (Clima et al. 2015).

A continuation of studies dealing with polyplexes (Dascalu et al. 2017; Vasiliu et al. 2018; Vasiliu et al. 2017) has been performed in the frame of ERA Chair SupraChemLab project implemented at the Centre of Advanced Research in Bionanoconjugates and Biopolymers at ICMPP from Iasi, Romania. For instance, the optimization of polyplex formation between dsDNA and poly(L-Lysine) (PLL) has been reported in reference (Vasiliu et al. 2017). Here, the MD simulations were performed at the level of the YASARA force field to reveal the formation of dsDNA-PLL polyplexes at different solution pH, and consequently at different protonation degree of PLL (see Fig. 5).

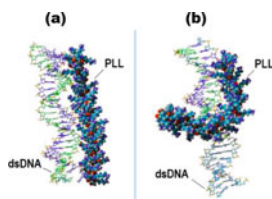


Fig. 5 Rendering of the dsDNA/PLL polyplex indicated by MD simulation (at $t = 35$ ns), (a) pH 5.4 (100% protonation of PLL), (b) pH 7.4 (50% protonation of PLL); explicit water molecules omitted for clarity (Vasiliu et al., 2017)

Thus, MD results disclosed that the binding rate between macromolecules was changed with the variation of PLL protonation. More detailed, at pH 5.4 (*i.e.*, 100% PLL protonation), the distance between dsDNA and PLL decreased from 40 Å to 18 Å in just a few nanoseconds of simulation. Instead, at pH 7.4 (*i.e.*, 50% PLL protonation), the same effect was achieved only after 31 ns. Moreover, MD simulation outcomes suggested that hydrogen bonds were mainly formed between the backbone oxygen atoms of dsDNA and hydrogen atoms of amine groups from PLL. Likewise, computational data showed that the PLL was the most flexible macromolecule, which could be bent and twisted to a greater extent at physiological pH value. In contrast, the dsDNA conformation in polyplex was minimally perturbed during MD simulations. It should be specified here that the formation of the dsDNA-PLL polyplex was validated experimentally using gel electrophoresis assays. The optimal conditions of complexation (pH 5.4 and N/P ratio of 125) were established by means of the response surface methodology (Vasiliu et al. 2017). Likewise, it should be noticed that the binding interaction between dsDNA and PLL was proved also by other authors using different experimental techniques such as fluorescamine assay (Read et al. 1999) and time-resolved multi-angle laser light scattering (Lai and van Zanten 2001).

In another study (Vasiliu et al. 2018) it was shown (by MD simulations in YASARA) the possibility of the polyplex formation between a cyclodextrin-based vector and two oligomeric chains of dsDNA. The non-viral vector represented a polycationic-conjugate assembly comprising beta-cyclodextrin (β -CD) as a core that was grafted with one chain of poly(ethylene glycol) (PEG) and six branches of PEI. The conjugated vector/carrier was denoted as (β -CD-PEG-PEI). The molecular dynamics trajectories revealed that the polycationic conjugate (β -CD-PEG-PEI) was flexible and interacted very fast with both dsDNA macromolecules (Vasiliu et al. 2018). For example, at simulation time $t = 2.5$ ns, five of PEI branches interacted evidently with the nucleotides from both dsDNA helices (Fig. 6). This computational study was also supported by the Gel Red staining assay for experimental validation of the polyplex formation (Vasiliu et al. 2018).

More advanced studies were also performed to shed light on the supramolecular interactions between several molecules of the conjugate (β -CD-PEG-PEI) and a longer chain of dsDNA helix (Dascalu et al. 2017). In this respect, the molecular modeling, dynamics simulations, and trajectories analysis were carried out using the high-performing software packages like YASARA (Krieger and Vriend 2014),

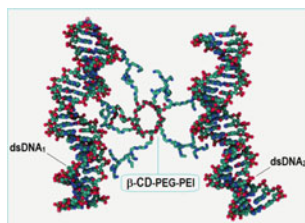
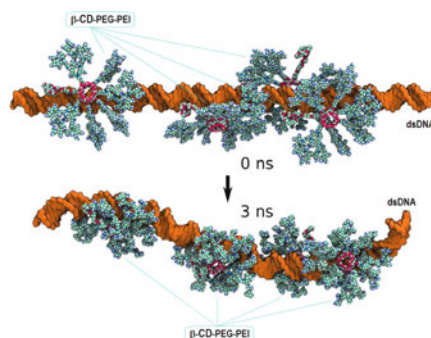


Fig. 6 Rendering of the polyplex supramolecular structure derived from MD simulation (at $t = 2.5$ ns) showing the interaction between the polycationic conjugate vector (β -CD-PEG-PEI) and two macromolecules of dsDNA; explicit water molecules omitted for clarity (Vasiliu et al., 2018)

Fig. 7 Rendering of the polyplex supramolecular conformation resulted from MD simulation showing the bending of the dsDNA chain (96 bp long) in the presence of four polycationic vectors (β -CD-PEG-PEI); explicit water molecules omitted for clarity (Dascalu et al., 2017)



Maestro simulation environment, GROMACS (Abraham et al. 2015), and VMD (Humphrey et al. 1996). In one of the simulations, four entities of β -CD-PEG-PEI conjugate vector were placed in the vicinity of a dsDNA helix (96 base-pairs long), in a “face-on” orientation as starting conformation. After 3 ns of MD simulation, the dsDNA fragment started to bend (Fig. 7). And, the four vectors (β -CD-PEG-PEI) revealed a conformational adaptation to dsDNA surface as a consequence of maximization of the number of *anionic-cationic contacts* (i.e. electrostatic interactions). The more advanced *in silico* molecular modeling performed in this study (Dascalu et al. 2017) suggested that the developed non-viral vector (β -CD-PEG-PEI) can mimic to some extent the function of histones.

In another report (Uritu et al. 2015), a siloxane-based conjugate carrier was assessed as a non-viral vector for the polyplex formation. This vector (denoted as cD_4^H -AGE-PEI) comprised a cyclic siloxane ring (2,4,6,8-tetramethylcyclotetrasiloxane, cD_4^H) as a core that was conjugated with polyethyleneimine (PEI) chains as cationic branches. The MD simulations (performed at the level of the YASARA force field) disclosed the interaction of the cD_4^H -AGE-PEI with the Drew-Dickerson dodecamer $d(CGCGAATTCGCG)_2$. The MD simulation results proved the interaction between cD_4^H -AGE-PEI and dsDNA with the formation of hydrogen bonds that stabilized the polyplex conformation (Fig. 8).

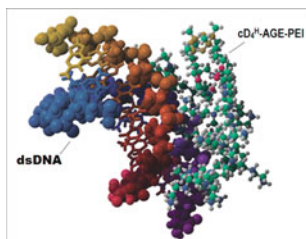


Fig. 8 Rendering of the polyplex structure resulted from MD simulation ($t = 2$ ns), showing the interaction between the non-viral vector (cD_4^H -AGE-PEI) and dsDNA helix; explicit water molecules omitted for clarity (Uritu et al., 2015)

4 Molecular Dynamics Simulation to Estimate Solute-Solvent Interactions

The molecular dynamics (MD) simulation can be employed in the exploration of the solute-solvent interactions by providing dynamic pictures and valuable insights of such complex systems (Zhao et al. 2013). In this respect, the reference (Airinei et al. 2017) reported the solvatochromic analysis and computational study of the *azobenzene maleimide compound* (AMC). It should be mentioned that *azobenzene derivatives* are molecular entities of real interest. These molecules are able to provide a response to external stimuli, which allow the control of their photophysical properties (Cojocaru et al. 2013). Owing to their particular trans/cis isomerization reaction (Isac et al. 2019), the azobenzene derivatives have found the applicability in various fields such as photoresponsive materials, optical data storage, liquid crystal displays, and others (Cojocaru et al. 2013; Isac et al. 2019).

In the reference (Airinei et al. 2017), the molecular dynamics (MD) simulations were carried out to detail the solvation of azobenzene maleimide molecule in two polar solvents (acetone and ethylene glycol). Both solvents were modeled as explicit molecules surrounding the solute. Hence, short-term MD simulations were done using the YASARA force-field. Results of the MD simulation highlighting the solute-solvent interactions are illustrated in Fig. 9.

Simulation outcomes suggested the formation of hydrogen bonds (H-bonds) between the solute (AMC – *azobenzene maleimide compound*) and both polar

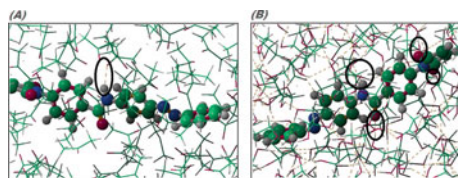


Fig. 9 Rendering of the solute-solvent systems showing the interactions of the solute molecule (*azobenzene maleimide*) with explicit solvents: (A) acetone and (B) ethylene glycol; equilibrated solute-solvent systems after energy minimization and short molecular dynamics (10 ps); computations were done using the YASARA force field

solvents. These H-bonds are represented as dot lines in Fig. 9. The emerged H-bonds, as a consequence of solute-solvent interactions, were encircled in Fig. 9 just for clarity. As one can see from Fig. 9A, the AMC solute formed one hydrogen bond with a molecule of the acetone solvent. Here, the NH group from the amide moiety of AMC acted as hydrogen bond donor (HBD), while the oxygen atom from acetone acted as hydrogen bond acceptor (HBA). The computed distance of the hydrogen bond was equal to 1.94 Å. And, the associated energy was found to be 5.47 kcal/mol.

In the case of ethylene glycol as solvent (Fig. 9B), the calculation results revealed the formation of many hydrogen bonds between solvent molecules in the simulating environment. In addition, the simulation indicated the formation of four H-bonds between the solute (*azobenzene maleimide*) and solvent (ethylene glycol) (see Fig. 9B). Thus, the carbonyl groups from amide and maleimide moieties of AMC acted as proton acceptors (HBA) yielding the formation of three hydrogen bonds. The fourth H-bond appeared between amide NH of the solute (HBD) and the oxygen atom (HBA) from ethylene glycol molecule (Fig. 9B). The calculated distances of these hydrogen bonds ranged from 1.71 Å to 1.85 Å. And, the total hydrogen bond energy was equal to 22.23 kcal/mol for the system *azobenzene maleimide/ethylene glycol*.

A more detailed computational chemistry study of azobenzene maleimide compounds was given in the reference (Isac et al. 2019). These computations were done to explore the electronic structures and to reveal the charge-transfer excitation effects at the level of the density functional theory (DFT) (Isac et al. 2019). Likewise, the solute-solvent interactions were assessed by computational chemistry methods and for other organic molecules, such as pyrazoline derivative compounds (Chibac et al. 2019).

5 Conclusions

In the course of implementation of the SupraChemLab project within the H2020 Call, we have investigated by means of molecular dynamics the formation and evolutions of different supra-molecular assemblies and systems. The computer-aided simulations by molecular dynamics have contributed considerably to understanding of the investigated structures and phenomena. Thus, MD simulations revealed the stability of DOTA self-assembly aggregate in the phospholipid (POPC) membrane and its functionality as the artificial channel for water permeation. Dynamic simulations disclosed also important insights regarding the stability of the studied polyplexes formed as the supra-molecular assemblies between dsDNA and non-viral vectors. Likewise, the MD method can be applied to evaluate the solute-solvent interactions.

Acknowledgements The project leading to this application has received funding from the H2020 ERA Chairs Project no 667387: SupraChem Lab Laboratory of Supramolecular Chemistry for Adaptive Delivery Systems ERA Chair initiative.

Conflict of interest The authors declare no conflict of interest.

References

- Abraham MJ, Murtola T, Schulz R, Páll S, Smith JC, Hess B, Lindahl E (2015) GROMACS: high performance molecular simulations through multi-level parallelism from laptops to supercomputers. *SoftwareX* 1–2:19–25. <https://doi.org/10.1016/j.softx.2015.06.001>
- Airinei A, Isac DL, Homocianu M, Cojocaru C, Hulubei C (2017) Solvatochromic analysis and DFT computational study of an azomaleimide derivative. *J Mol Liq* 240:476–485. <https://doi.org/10.1016/j.molliq.2017.05.096>
- Anderson WF (1984) Prospects for human gene therapy. *Science* 226(4673):401–409
- Barboiu M (2016) Artificial water channels—incipient innovative developments. *Chem Commun* 52(33):5657–5665
- Becker OM, Watanabe M (2001) Dynamics methods. In: Becker OM, MacKerell Jr AD, Roux B, Watanabe M, Marcel Dekker (eds) *Computational biochemistry and biophysics*. New York, pp 39–67
- Chibac AL, Roman G, Cojocaru C, Shova S, Sacarescu G, Simionescu M, Sacarescu L (2019) Bichromophoric pyrazoline derivative with solvent-selective photoluminescence quenching. *J Mol Liq* 278:156–163. <https://doi.org/10.1016/j.molliq.2019.01.067>
- Clima L, Ursu EL, Cojocaru C, Rotaru A, Barboiu M, Pinteala M (2015) Experimental design, modeling and optimization of polyplex formation between DNA oligonucleotides and branched polyethylenimine. *Org Biomol Chem* 13(36):9445–9456
- Cojocaru C, Airinei A, Fifere N (2013) Molecular structure and modeling studies of azobenzene derivatives containing maleimide groups. *SpringerPlus* 2(1):586. <https://doi.org/10.1186/2193-1801-2-586>
- Dascalu A, Ardeleanu R, Neamtu A, Maier S, Uritu C, Nicolescu A, Silion M, Peptanariu D, Calin M, Pinteala M (2017) Transfection-capable polycationic nanovectors which include PEGylated-cyclodextrin structural units: a new synthesis pathway. *J Mater Chem B* 5(34):7164–7174
- Godbey W, Wu KK, Mikos AG (1999) Tracking the intracellular path of poly (ethylenimine)/DNA complexes for gene delivery. *Proc Natl Acad Sci* 96(9):5177–5181
- Guvench O, MacKerell AD (2008) Comparison of protein force fields for molecular dynamics simulations. In: Kukol A (eds) *Molecular modeling of proteins*. methods molecular biology, vol 443. Humana Press/Springer, pp 63–88. https://doi.org/10.1007/978-1-59745-177-2_4
- Han S-O, Mahato RI, Sung YK, Kim SW (2000) Development of biomaterials for gene therapy. *Mol Ther* 2(4):302–317
- Hawley R, Lieu F, Fong A, Hawley TS (1994) Versatile retroviral vectors for potential use in gene therapy. *Gene Ther* 1(2):136
- Humphrey W, Dalke A, Schulten K (1996) VMD: visual molecular dynamics. *J Mol Graph* 14(1):33–38. [https://doi.org/10.1016/0263-7855\(96\)00018-5](https://doi.org/10.1016/0263-7855(96)00018-5)
- Isac DL, Airinei A, Maftai D, Humelnicu I, Mocci F, Laaksonen A, Pinteală M (2019) On the charge-transfer excitations in Azobenzene Maleimide compounds: a theoretical study. *J Phys Chem A* 123(26):5525–5536. <https://doi.org/10.1021/acs.jpca.9b02082>
- Jensen F (2007) *Introduction to computational chemistry*, 2nd edn. Wiley, Chichester, pp 22–77
- Kay MA, Glorioso JC, Naldini L (2001) Viral vectors for gene therapy: the art of turning infectious agents into vehicles of therapeutics. *Nat Med* 7(1):33–40
- Khalili-Araghi F, Gumbart J, Wen P-C, Sotomayor M, Tajkhorshid E, Schulten K (2009) Molecular dynamics simulations of membrane channels and transporters. *Curr Opin Struct Biol* 19(2):128–137
- Krieger E, Koraimann G, Vriend G (2002) Increasing the precision of comparative models with YASARA NOVA—a self-parameterizing force field. *Proteins Struct Function Bioinform* 47(3):393–402
- Krieger E, Vriend G (2014) YASARA View—molecular graphics for all devices—from smart-phones to workstations. *Bioinformatics* 30(20):2981–2982
- Krieger E, Vriend G (2015) New ways to boost molecular dynamics simulations. *J Comput Chem* 36(13):996–1007

- Lai E, van Zanten JH (2001) Monitoring DNA/Poly-L-Lysine polyplex formation with time-resolved multiangle laser light scattering. *Biophys J* 80(2):864–873. [https://doi.org/10.1016/S0006-3495\(01\)76065-1](https://doi.org/10.1016/S0006-3495(01)76065-1)
- Lei H, Wang X, Wu C (2012) Early stage intercalation of doxorubicin to DNA fragments observed in molecular dynamics binding simulations. *J Mol Graph Model* 38:279–289
- Lewars E (2004) Computational chemistry. Introduction to the theory and applications of molecular and quantum mechanics. Kluwer Academic Publishers, pp 43–79
- Li S-D, Huang L-Y (2000) Nonviral gene therapy: promises and challenges. *Gene Ther* 7(1):31–34
- Luo D, Saltzman WM (2000) Synthetic DNA delivery systems. *Nat Biotechnol* 18(1):33–37
- MacKerell Jr AD (2001) Atomistic models and force fields. In: Becker OM, MacKerell Jr AD, Roux B, Watanabe M (eds) Computational biochemistry and biophysics. Marcel Dekker, New York pp 7–38
- MacKerell Jr AD, Nilsson L (2001) Nucleic acid simulations. In: Becker OM, MacKerell Jr AD, Roux B, Watanabe M (eds) Computational biochemistry and biophysics. Marcel Dekker, New York, pp 441–463
- Mintzer MA, Simanek EE (2009) Nonviral vectors for gene delivery. *Chem Rev* 109(2):259–302
- Murail S, Vasiliu T, Neamtu A, Barboiu M, Sterpone F, Baaden M (2018) Water permeation across artificial I-quartet membrane channels: from structure to disorder. *Faraday Discuss* 209:125–148
- Neder ADVF, de Oliveira Neto M (2005) A simple low-cost simulation protocol for approximate localization of structural water molecules in DNA oligonucleotides. *J Braz Chem Soc* 16(3B):597–606
- Nicolas J, Mura S, Brambilla D, Mackiewicz N, Couvreur P (2013) Design, functionalization strategies and biomedical applications of targeted biodegradable/biocompatible polymer-based nanocarriers for drug delivery. *Chem Soc Rev* 42(3):1147–1235
- Noy A, Perez A, Lankas F, Luque FJ, Orozco M (2004) Relative flexibility of DNA and RNA: a molecular dynamics study. *J Mol Biol* 343(3):627–638
- Read ML, Etrych T, Ulbrich K, Seymour LW (1999) Characterisation of the binding interaction between poly(L-lysine) and DNA using the fluorescamine assay in the preparation of non-viral gene delivery vectors. *FEBS Lett* 461(1–2):96–100. [https://doi.org/10.1016/s0014-5793\(99\)01435-0](https://doi.org/10.1016/s0014-5793(99)01435-0)
- Sun C, Tang T, Uludağ H, Cuervo JE (2011) Molecular dynamics simulations of DNA/PEI complexes: effect of PEI branching and protonation state. *Biophys J* 100(11):2754–2763
- Tang M, Szoka F (1997) The influence of polymer structure on the interactions of cationic polymers with DNA and morphology of the resulting complexes. *Gene Ther* 4(8):823–832
- Uritu CM, Calin M, Maier SS, Cojocaru C, Nicolescu A, Peptanariu D, Constantinescu CA, Stan D, Barboiu M, Pinteala M (2015) Flexible cyclic siloxane core enhances the transfection efficiency of polyethylenimine-based non-viral gene vectors. *J Mater Chem B* 3(42):8250–8267. <https://doi.org/10.1039/C5TB01342A>
- Vannucci L, Lai M, Chiappesi F, Ceccherini-Nelli L, Pistello M (2013) Viral vectors: a look back and ahead on gene transfer technology. *New Microbiol* 36(1):1–22
- Vasiliu T, Cojocaru C, Peptanariu D, Dascalu AI, Pinteala M, Rotaru A (2018) Polyplex formation between cyclodextrin-based non-viral vector and dsDNA: molecular dynamic study with experimental validation. *Rev Roum Chim* 63(7–8):629–636
- Vasiliu T, Cojocaru C, Rotaru A, Pricope G, Pinteala M, Clima L (2017) Optimization of polyplex formation between dna oligonucleotide and poly (L-Lysine): experimental study and modeling approach. *Int J Mol Sci* 18(6):1291
- Wu GY, Wu CH (1987) Receptor-mediated *in vitro* gene transformation by a soluble DNA carrier system. *J Biol Chem* 262(10):4429–4432
- Zhao Y, Liu X, Wang J, Zhang S (2013) Effects of anionic structure on the dissolution of cellulose in ionic liquids revealed by molecular simulation. *Carbohydr Polym* 94(2):723–730. <https://doi.org/10.1016/j.carbpol.2013.02.011>
- Ziebarth J, Wang Y (2009) Molecular dynamics simulations of DNA-polycation complex formation. *Biophys J* 97(7):1971–1983